

PL ISSN 1731-6103

2'2007

PRZEGLĄD ELEKTROTECHNICZNY KONFERENCJE

ROK 5



 SIGMA-NOT
Spółka z o.o.

cena 80 zł
(w tym "0" VAT)

8th International Workshop
COMPUTATIONAL PROBLEMS OF ELECTRICAL
ENGINEERING

September 14-16, 2007 – Wilkasy, Poland

Welcome from the Chairman



On behalf of the Scientific and Organizing Committees I would like to welcome all attendees to the 2007 VIIIth International Workshop "Computational Problems of Electrical Engineering" in Wilkasy. Especially warm greetings are directed to our guests from Ukraine, Czech Republic and Romania. We appreciate your participation and look forward to a very rewarding event. The CPEE series was organized to allow scientists, engineers and students of different disciplines, yet having common interests, to report their recent achievements in the interdisciplinary field of research on electrical circuits and signals, electromagnetic field analysis, inverse problems, artificial intelligence, bioengineering, software engineering and electrical engineering education.

During this conference we would like to commemorate the centenary of birth of famous Polish electrician, professor Tadeusz Cholewicki (1907-1988). He was a Polish pioneer of matrix theory application in electrical engineering. Nowadays matrices are common and well known foundation for computational methods and thus in some sense we all follow his original concepts of matrix applications. He was also a founder of Chair of the Theory of Electrical Engineering, which was later transformed into Division of Theory of Electrical Engineering and Applied Informatics—one of the organizers of this event. Many of the Program Committee members, including me, were students and later collaborators of Professor Cholewicki. We shall remember Him forever.

The workshops are alternatively organized in Poland and Ukraine. The first was held in 1999 in Alushta in Crimea, as the common initiative of researchers from National University "Lvivska Polytechnica" and from Warsaw University of Technology. Currently our colleagues from Lodz Technical University have joined this collaboration.

This is the first CPEE workshop held in Polish Masurian Lake District. I faith you will enjoy the beauty of the Masurian nature and, especially the unique climate of the "land of a thousand lakes." I believe that all of us like wild forests, beautiful lakes full of yachts and admirable architectural monuments. This event, beside of our scientific activity, will be a good opportunity to face today's attractiveness and rich history of this region. Many nations lived here, and all of them left here some of their culture. People were fighting for this land, but also for many years they lived here together in peaceful mixture of customs and traditions. Today this history can be inspiring for nations of uniting Europe.

We hope that the scenic Tajty Hotel will create a colloquial and informal atmosphere in order to help the knowledge exchanges and the creation of new collaborations. We believe that the excellent presentations and informal discussions during CPEE 2007 will set new impulses to the development of research of all attendees of the workshop.

I wish the great success of this scientific event and a pleasant stay at Wilkasy.

Stanisław Bolkowski
Chairman of the Program Committee

VIIIth INTERNATIONAL WORKSHOP

"Computational Problems of Electrical Engineering"

*Commemorating the centenary
of Professor Tadeusz Cholewicki*

Organized by



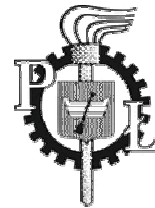
**WARSAW UNIVERSITY
OF TECHNOLOGY**

Institute of the Theory of
Electrical Engineering,
Measurement and
Information Systems



**LVIV POLYTECHNIC
NATIONAL UNIVERSITY**

Department of Theoretical
and Electrical Engineering



**TECHNICAL UNIVERSITY
OF LODZ**

Institute of Computer Science

under auspices of



Wilkasy, Poland
September 14-16, 2007

Program Committee

Prof. S. Bolkowski - Warsaw University of Technology - chairman
Prof. P. Stakchiv - National University "Lvivska Polytechnica" - deputy chairman
Prof. B. Bridge - South Bank University of London
Prof. Ju. Bobalo - National University "Lvivska Polytechnica"
Prof. L. Byczkowska-Lipizska - Technical University of Lodz
Prof. A. Cichocki - Brain Science Institute RIKEN Tokyo
Prof. Z. Ciok - Polish Academy of Sciences
Prof. I. Dolezel - Czech Academy of Sciences
Prof. T. Glinka - Silesian University of Technology
Prof. T. Kaczorek - Polish Academy of Sciences
Prof. P. Kazmierkowski - Warsaw University of Technology
Prof. O. Kyrylenko - Ukrainian Academy of Sciences
Prof. A. Lozinsky - National University "Lvivska Polytechnica"
Prof. K. Mikolajuk - Warsaw University of Technology
Prof. M. Myslovitch - Ukrainian Academy of Sciences
Prof. S. Osowski - Warsaw University of Technology
Prof. N. Shydlovska - Ukrainian Academy of Sciences
Prof. J. Sikora - Warsaw University of Technology
Prof. R. Sikora - Technical University of Szczecin
Prof. L. Synytskiy - Ivan Franko National University of Lviv
Prof. M. Tadeusiewicz - Technical University of Lodz
Prof. B. Ulrych - University of West Bohemia
Prof. S. Wincenciak - Warsaw University of Technology

Organizing Committee

Prof. Stanislaw Osowski - Chairman of the Organizing Committee
J. Starzynski – secretary
S. Rendzinyak – secretary
Z. Filipowicz
B. Sawicki
K. Siwek
R. Szmurlo

Address

IETiSIP Warsaw University of Technology
ul. Koszykowa 75
00-661 Warszawa
POLAND
E-mail: cpee@iem.pw.edu.pl

PRZEGLĄD ELEKTROTECHNICZNY KONFERENCJE, Vol. 2007, No. 2

Contents

| | | |
|----|---|-----|
| 01 | Introduction | 1 |
| 02 | Contents | 3 |
| 03 | Spis treści | 5 |
| 04 | Lubomír BRANČÍK - Procedures for matrix exponential function derivative in Matlab | 7 |
| 05 | Jiří BŮLLOW, Ivo DOLEŽEL, Josef KABELÁČ, Pavel KARBAN, Bohuš ULRYCH - Control of movement of artificial satellites by geomagnetic field | 11 |
| 06 | Tadeusz KACZOREK, Przemysław PRZYBOROWSKI - Positive discrete-time linear Lyapunov systems with delays | 16 |
| 07 | Stanisław HAŁGAS, Michał TADEUSIEWICZ - Finding parametric characteristics in diode-transistor circuits | 20 |
| 08 | Sergiy Ye.SAUKH, Evelina P.SEMAGINA - Economical mathematical model for Ukrainian electroenergetic complex management | 24 |
| 09 | Mariana DUMITRESCU, Toader MUNTEANU, Dan FLORICAU - Optimal electric power flow computation | 29 |
| 10 | Zygmunt PIĄTEK - Eddy currents induced in the screen of a non-coaxial cable | 33 |
| 11 | Tomasz MARKIEWICZ, Piotr WIŚNIEWSKI, Wojciech KOZŁOWSKI, Janusz PATERA - Automatic cell counting in neuroblastoma | 37 |
| 12 | Sorin POPA, Drăghiciu NICOLAE, Simona CASTRASE, Morgos LUCIAN - Fading channels modelation in digital communication systems | 41 |
| 13 | Ioan POPA, Ioan CAUTIL, Dan FLORICAU, Florin OCOLEANU - Modeling of high currents dismountable contacts | 44 |
| 14 | Zdzisław TRZASKA - Characterization of particular circuit elements requisite for studying the electrochemical processes | 48 |
| 15 | Mariana DUMITRESCU - Using Stochastic Petri Nets for power system dependability computation | 53 |
| 16 | Krzysztof DEBOWSKI - Comparison between classical and fuzzy optimization in one-phase electrical circuits | 57 |
| 17 | Jacek REZMER, Przemysław JANIK, Tadeusz ŁOBOS, Zbigniew WACŁAWEK, Torbjörn THIRINGER - Estimation of transients' parameters in wind converter systems using advanced signal processing algorithms | 61 |
| 18 | Dariusz SPAŁEK, Krzysztof WALECZEK - Electromagnetic torque, power losses analysis for spherical electromechanical converters with anisotropy rotor | 65 |
| 19 | Michał TADEUSIEWICZ, Stanisław HAŁGAS - Finding operating points of the diode-transistor circuits via homotopy approach | 69 |
| 20 | Vasyl TKACHUK, Lidiya KASHA - Mathematical model for M-phases switched reluctance motor | 73 |
| 21 | Olga BEZNOVA, Evelina SEMAGINA - Mathematical models for wave propagation analysis in distributed and lumped parameter networks | 77 |
| 22 | Tadeusz ŁOBOS, Jacek REZMER, Piotr RUCZEWSKI, Tomasz SIKORSKI - Development in power quality specification using Time-Frequency Analysis | 80 |
| 23 | Bogdan BLAGITKO, Volodymyr BRIHILEVYCH, Igor JARMOLOWSKYJ - Dynamic system decomposition for diagnosis of mechatronic systems | 84 |
| 24 | Yuri BOBALO, Bogdan MANDZIY, Yaroslav MATVIYCHUK - Analysis of reliability of power supply system on the basis of macro-modeling | 88 |
| 25 | Andrzej KUCZYŃSKI, Marek OSSOWSKI - GA optimization of wavelet analysis of dynamic current supply applied to fault diagnosis | 91 |
| 26 | Maria TRZASKA, Anna Maria BIAŁOSTOCKA - Electrodes modeling in the copper electrocrystallization process | 95 |
| 27 | Zbigniew LEONOWICZ, Ying XIN, Jacek REZMER, Zhengjian CAO, Yang WANG - Investigations of influence on power quality of superconducting fault current limiter | 99 |
| 28 | Dawid BUŁA, Marcin MACIAZEK, Marian PASKO - Optimization of time delays in Active Power Filter control algorithm | 102 |
| 29 | Janusz WALCZAK, Anna ROMANOWSKA - Analysis of second order LTV section with exponentially varying parameters | 106 |
| 30 | Liliana BYCZKOWSKA-LIPIŃSKA, Marcin CEGIELSKI - Parallel computations of transient processes in the electric circuits in cluster systems | 110 |
| 31 | Krzysztof POLAKOWSKI, Stefan F. FILIPOWICZ, Zygmunt FILIPOWICZ - 2.5D tomographic imaging for ultrasonic investigations | 113 |
| 32 | Petro. STAKHIV, Marcin CEGIELSKI - Stability of parallel computations of transient processes in the electric circuits | 116 |
| 33 | Kazimierz MIKOŁAJUK, Andrzej TOBOŁA - A time-varying capacitance: control function of active power filters | 119 |
| 34 | Ryszard SZUPILUK, Krzysztof SIWEK, Piotr WOJEWNIK, Tomasz ZĄBKOWSKI - Multistage filtration via blind signal separation for prediction improvement | 123 |
| 35 | Magdalena STASIAK, Przemysław BEROWSKI, Jan SIKORA - Level Set Method for capacitor optimization problem | 127 |
| 36 | Dan FLORICAU, Guillaume GATEAU, Mircea COVRIG, Ioan POPA, Mariana DUMITRESCU - Calculus of total losses in three-levels voltage source converters | 131 |
| 37 | Virginia IVANOV, Sergiu IVANOV, Maria BROJBOIU, Silvia Maria DIGA - The design of electrical system with microcontroller for the measurement of electrical parameters | 135 |
| 38 | Alexander V. IVANOV, Valerii K. KONONENKO, Ivan S. MANAK - Output power characteristics of the GaInAs lasers emitting in the spectral range of 1.0 μm | 139 |
| 39 | Vsevolod HORYACHKO, Mariya HOWYKOWYCH - Analysis of electromagnetic processes in power system elements on the basis of unique-flux methodology | 142 |
| 40 | Sergei DENYSYUK, Katerina MINAZOVA - Increasing of effectiveness of electromagnetic process analysis in nonlinear time-varying circuits due to separation of equivalence classes | 146 |
| 41 | Nikolay KOSTIN, Oleg BONDAR', Oksana REUTSKOVA - The analysis of self-oscillatory processes in a nonlinear electrochemical circuit | 150 |
| 42 | Serhiy RENDZINYAK, Andriy KORUD, Bohdan MELNYK - Features of subcircuits matching with components described by discrete parameters during analysis of electric circuits transient processes | 154 |
| 43 | Anatoly BELOUS, Anthon EMELYANOV, Valentine SYAKERSKY, Ryhor CHYHIR - Model for forecasting good yield of microcircuit chips by results of test control | 157 |
| 44 | Volodymyr EMETS, Jan ROGOWSKI - Effective computation of high-frequency plane waves field scattered on electrically resistive strip | 161 |
| 45 | Bartłomiej STASIAK, Mykhaylo YATSYMIRSKYY - Fast orthogonal neural networks for 2D signal processing | 167 |

| | | |
|----|--|-----|
| 46 | Tomasz GRZYWACZ, Stefan WOJTOWICZ - A Visibility Matrix determination using space subdivision methods for Diffuse Optical Tomography | 171 |
| 47 | Andrii O. WOLTERS, Mikle V. MISLOVICH, Lesia G. SOBOLEVSKA - Experimental validation of diagnostic symptoms for technical state estimation of several units of rotary electric-power machines | 173 |
| 48 | Bartosz ŚWIDERSKI, Stanisław OSOWSKI, Andrzej CICHOCKI - Epileptic seizure detection using single-class SVM | 177 |
| 49 | Wiesław BROCIK, Robert WILANOWICZ - Modeling and simulation of the interaction of the nonlinear load and traction power system | 181 |
| 50 | Yuriy VASETSKY, Iryna MAZURENKO, Yuriy ARISTOV - Thin toroidal superconducting magnetic energy storage (SMES) with tilted coils: magnetic fields, forces and support system requirements | 185 |
| 51 | Janusz WALCZAK, Dariusz GRABOWSKI - Application of equivalent circuits in power theory for systems with nonsinusoidal waveforms – critical remarks | 190 |
| 52 | Janusz WALCZAK, Dariusz GRABOWSKI - Application of equivalent circuits in power theory for systems with nonsinusoidal waveforms – new optimization concept | 194 |
| 53 | Piotr ŚWISZCZ - Models of nonlinear one-ports supplied with periodic and discontinuous waveforms | 198 |
| 54 | Leszek MOSZCZYŃSKI, Jarosław KUREK - Sensitivity analysis of linear regression solution based on modified York's equation | 202 |
| 55 | Yaroslav SHMYGELSKY - Steady state calculation of nonlinear circuits by the secants method | 205 |
| 56 | Vitaliy V. MARTINOV, Dmitro V. TRUSHAKOV - Simulation of physical processes in eddy-current transformer during its interaction with the tested ferromagnetic specimen | 208 |
| 57 | Tomasz ADRIKOWSKI, Marian PASKO - High-pass elliptic filter using the wide-band biquadratic structure VES OPA–RC „b” - 02 | 211 |
| 58 | Przemysław PŁONECKI, Bartosz SAWICKI, Jacek STARZYŃSKI, Stanisław WINCENCIAK - Mathematical description of eddy-currents in a non-homogenous area with using electric scalar potential | 215 |
| 59 | Paweł WIELEBA, Jan SIKORA - Open source boundary element method library for diffusion optical tomography | 219 |
| 60 | Michał ŚMIAŁEK, Albert AMBROZIEWICZ, Jacek BOJARSKI, Wiktor NOWAKOWSKI, Tomasz STRASZAK - Requirements Specification Language | 223 |
| 61 | Michał KRUK, Stanisław OSOWSKI, Robert KOKTYSZ - Segmentation and characterization of granular ducts in microscopic colon image | 227 |
| 62 | Jarosław KUREK, Adam BIERNAT, Jan SZCZYPIOR - Rotor bar fault diagnosis of induction motor based on single-class SVM | 231 |
| 63 | Ivan PRUDYUS, Leonid LAZKO, Serhiy SEMENOV - Pixel level data fusion based on local correlation in remote sensing systems | 235 |
| 64 | Yuriy BOBALO, Leonid NEDOSTUP, Oxana LAZKO - Generalized robust parameters distribution model | 237 |
| 65 | Stanisław GRATKOWSKI, Mieczysław KOMOROWSKI, Tomasz PIETRUSEWICZ - Simplified theoretical analysis of measuring systems for eddy current testing of low conductivity materials | 238 |
| 66 | Tadeusz KACZOREK, Łukasz SAJEWSKI - Realization problem for positive 2D hybrid systems with one delay in state and input vectors | 242 |
| 67 | Ryszard SIKORA, Tomasz CHADY, Przemysław ŁOPATO, Mieczysław KOMOROWSKI - Differential eddy current transducer with high spatial resolution | 247 |
| 68 | Vasyl MALYAR, Andriy MALYAR - Optimization of starting characteristics of asynchronous motor with phase rotor | 250 |
| 69 | Łukasz STELMACH - Performance tuning of the ray tracing process running in a multi-processor environment | 252 |
| 70 | Piotr SIDYK - Ambiguity groups in linear dynamic analog circuit | 255 |
| 71 | Konrad NITA, Stefan F. FILIPOWICZ - Active source localization in 3D BEM multilayer model | 259 |
| 72 | Anastasia V.BASOVA, Victor F.IVANKOV, Stanislav S.KOKOSHYN, Ivan V.KHIMJUK - Numerical research of the electromagnetic fields in powerful transformers and reactors | 261 |
| 73 | Cornel PANAIT, George CĂRUNTU - The magnetic microsensors response | 265 |
| 74 | George CARUNTU, Cornel PANAIT - The magnetic sensitive MOS structures | 269 |
| 75 | Marek KORZYBSKI, Marek OSSOWSKI - The selection of genetic algorithm parameters for soft fault diagnosis | 272 |
| 76 | Robert SZMURŁO, Jacek STARZYŃSKI, Stanisław WINCENCIAK - Evaluation of bidomain model parameters for simulation of a nerve bundle | 276 |
| 77 | Michał CHOJNOWSKI, Jacek KORYTKOWSKI - Evaluation of 2D model of vagus nerve stimulation with harmonic magnetic field | 280 |

The papers are in order according to time of delivery.

Guest Editor – Jacek Starzyński

PRZEGLĄD ELEKTROTECHNICZNY KONFERENCJE, Rok 2007, Nr. 2

Spis treści

| | | |
|----|--|-----|
| 01 | Wstęp | 1 |
| 02 | Contents | 3 |
| 03 | Spis treści | 5 |
| 04 | Lubomír BRANČÍK - Procedury wyznaczania pochodnych macierzowych funkcji wykładniczych w MATLABie | 7 |
| 05 | Jiří BÜLLOW, Ivo DOLEŽEL, Josef KABELÁČ, Pavel KARBAN, Bohuš ULRYCH - Sterowanie ruchem satelitów z wykorzystaniem ziemskiego pola magnetycznego | 11 |
| 06 | Tadeusz KACZOREK, Przemysław PRZYBOROWSKI - Dodatnie dyskretne układy Lapunowa z opóźnieniem | 16 |
| 07 | Stanisław HAŁGAS, Michał TADEUSIEWICZ - Wyznaczanie charakterystyk parametrycznych w układach diodowo-tranzystorowych | 20 |
| 08 | Sergiy Ye.SAUKH, Evelina P.SEMAGINA - Ekonomiczny model matematyczny dla ukraińskiego systemu elektroenergetycznego | 24 |
| 09 | Mariana DUMITRESCU, Toader MUNTEANU, Dan FLORICAU - Obliczenia numeryczne optymalnego rozplywu mocy | 29 |
| 10 | Zygmunt PIĄTEK - Prądy wirowe indukowane w ekranie kabla niewspółosiowego | 33 |
| 11 | Tomasz MARKIEWICZ, Piotr WIŚNIEWSKI, Wojciech KOZŁOWSKI, Janusz PATERA - Automataczne zliczanie komórek w barwieniu immunohistochemicznym | 37 |
| 12 | Sorin POPA, Drăghiciu NICOLAE, Simona CASTRASE, Morgos LUCIAN - Modelowanie zanikania fali w systemach komunikacji cyfrowej | 41 |
| 13 | Ioan POPA, Ioan CAUTIL, Dan FLORICAU, Florin OCOLEANU - Modelowanie zanikania fali w systemach komunikacji cyfrowej | 44 |
| 14 | Zdzisław TRZASKA - Wykorzystanie Metody Elektrochemicznej Spektroskopii Impedancyjnej(MESI) do przedstawienia pewnych procesów chemicznych za pomocą zjawisk w obwodzie elektrycznym | 48 |
| 15 | Mariana DUMITRESCU - Wykorzystanie Sieci Petriego do analizy niezawodności sieci energetycznych | 53 |
| 16 | Krzysztof DĘBOWSKI - Porównanie optymalizacji klasycznej i rozmytej w odniesieniu do obwodów elektrycznych | 57 |
| 17 | Jacek REZMER, Przemysław JANIK, Tadeusz ŁOBOS, Zbigniew WACŁAWEK, Torbjörn THIRINGER - Oszacowanie składowych przejściowych elektrowni wiatrowych przy wykorzystaniu algorytmów przetwarzania sygnału | 61 |
| 18 | Dariusz SPAŁEK, Krzysztof WALECZEK - Analiza momentu elektromagnetycznego i strat mocy przetwornika elektromechanicznego z anizotropowym wirnikiem | 65 |
| 19 | Michał TADEUSIEWICZ, Stanisław HAŁGAS - Obliczanie punktów pracy układów diodowo-tranzystorowych z użyciem metody homotopii | 69 |
| 20 | Vasyl TKACHUK, Lidiya KASHA - Model matematyczny M-fazowego silnika o przełączanej reluktancji | 73 |
| 21 | Olga BEZNOVA, Evelina SEMAGINA - Model matematyczny propagacji fal w sieciach zasilających w przypadkach przełączeń i zwarć | 77 |
| 22 | Tadeusz ŁOBOS, Jacek REZMER, Piotr RUCZEWSKI, Tomasz SIKORSKI - Rozwój zagadnień oceny jakości energii elektrycznej z wykorzystaniem analizy czasowo-częstotliwościowej | 80 |
| 23 | Bogdan BLAGITKO, Volodymyr BRIHILEVYCH, Igor JARMOLOWSKYJ - Dekompozycja systemu dynamicznego dla diagnozy systemów mechatroniki | 84 |
| 24 | Yuri BOBALO, Bogdan MANDZIY, Yaroslav MATVIYCHUK - Analiza niezawodności systemów zasilania bazująca na modelowaniu w skali makro | 88 |
| 25 | Andrzej KUCZYŃSKI, Marek OSSOWSKI - Optymalizacja metody falkowej zastosowanej do diagnostyki obwodów | 91 |
| 26 | Maria TRZASKA, Anna Maria BIAŁOSTOCKA - Elektrody modelujące w procesie elektrokryształizacji miedzi | 95 |
| 27 | Zbigniew LEONOWICZ, Ying XIN, Jacek REZMER, Zhengjian CAO, Yang WANG - Badanie wpływu nadprzewodzącego dławika przetężeniowego na jakość energii elektrycznej | 99 |
| 28 | Dawid BUŁA, Marcin MACIĄZEK, Marian PASKO - Optymalizacja opóźnień w algorytmie sterowania energetycznego filtru aktywnego | 102 |
| 29 | Janusz WALCZAK, Anna ROMANOWSKA - Analiza sekcji parametrycznych z parametrami zmiennymi eksponencjalnie | 106 |
| 30 | Liliana BYCZKOWSKA-LIPIŃSKA, Marcin CEGIELSKI - Równoległe obliczenia w modelowaniu stanów nieustalonych w obwodach elektrycznych przy pomocy systemów klastrowych | 110 |
| 31 | Krzysztof POLAKOWSKI, Stefan F. FILIPOWICZ, Zygmunt FILIPOWICZ - Tomograficzne obrazowanie z wykorzystaniem przestrzeni 2,5D w badaniach ultradźwiękowych | 113 |
| 32 | Petro. STAKHIV, Marcin CEGIELSKI - Stabilność obliczeń równoległych w symulacji stanów nieustalonych w obwodach elektrycznych | 116 |
| 33 | Kazimierz MIKOŁAJUK, Andrzej TOBOŁA - Zmienna pojemność – funkcja sterowania aktywnych filtrów mocy | 119 |
| 34 | Ryszard SZUPILUK, Krzysztof SIWEK, Piotr WOJEWNIK, Tomasz ZĄBKOWSKI - Poprawa dokładności prognozowania przy wykorzystaniu wieloetapowej filtracji z pośrednictwem ślepej separacji sygnałów | 123 |
| 35 | Magdalena STASIAK, Przemysław BEROWSKI, Jan SIKORA - Metoda zbiorów poziomicowych w optymalizacji kształtu kondensatora | 127 |
| 36 | Dan FLORICAU, Guillaume GATEAU, Mircea COVRIG, Ioan POPA, Mariana DUMITRESCU - Wyznaczanie całkowitych strat w trzypoziomowych konwerterach źródeł napięcia | 131 |
| 37 | Virginia IVANOV, Sergiu IVANOV, Maria BROJBOIU, Silvia Maria DIGA - Projektowanie systemu elektrycznego z mikrokontrolerem do pomiaru parametrów | 135 |
| 38 | Alexander V. IVANOV, Valerii K. KONONENKO, Ivan S. MANAK - Charakterystyki mocy laserów GaINAs, emitujących w zakresie 1 mikrometra | 139 |
| 39 | Vsevolod HORYACHKO, Mariya HOWYKOWYCH - Analiza procesów elektromagnetycznych w elementach systemów zasilających bazująca na metodologii unikalnego-strumienia | 142 |
| 40 | Sergei DENYSYUK, Katerina MINAZOVA - Zwiększenie efektywności analizy procesów elektromagnetycznych w stanach nieustalonych obwodów nieliniowych za pomocą wyróżniania klas zgodności | 146 |

| | | |
|----|--|-----|
| 41 | Nikolay KOSTIN, Oleg BONDAR', Oksana REUTSKOVA - Analiza procesów oscylacyjnych w nieliniowym obwodzie elektrochemicznym | 150 |
| 42 | Serhiy RENDZINYAK, Andriy KORUD, Bohdan MELNYK - Analiza procesów oscylacyjnych w nieliniowym obwodzie elektrochemicznym | 154 |
| 43 | Anatoly BELOUS, Anthon EMELYANOV, Valentine SYAKERSKY, Ryhor CHYHIR - Model do przewidywania niezawodności mikroukładów na podstawie wyników testów jakościowych | 157 |
| 44 | Volodymyr EMENTS, Jan ROGOWSKI - Efektywne obliczanie rozpraszania płaskich fal o wysokiej częstotliwości przez taśmę przewodzącą | 161 |
| 45 | Bartłomiej STASIAK, Mykhaylo YATSYMIRSKYY – Wykorzystanie szybkich ortogonalnych sieci neuronowych do dwuwymiarowego przetwarzania sygnałów | 167 |
| 46 | Tomasz GRZYWACZ, Stefan WOJTOWICZ , - Tworzenie macierzy widoczności dla dyfuzyjnej tomografii optycznej z użyciem technik podziału przestrzeni | 171 |
| 47 | Andrii O. WOLTERS, Mikle V. MISLOVICH, Lesia G. SOBOLEVSKA - Eksperymentalna walidacja cech diagnostycznych użytecznych w ocenie stanu technicznego części maszyn elektrycznych | 173 |
| 48 | Bartosz ŚWIDERSKI, Stanisław OSOWSKI, Andrzej CICHOCKI - Wykrywanie napadu padaczkowego przy pomocy jednoklasowych sieci SVM | 177 |
| 49 | Wiesław BROCIK, Robert WILANOWICZ - Modelowanie i symulacja interakcji nieliniowego obciążenia i systemu zasilania trakcji | 181 |
| 50 | Yuriy VASETSKY, Iryna MAZURENKO, Yuriy ARISTOV - Cienki toroidalny kondycjoner mocy z cewką nadprzewodzącą: pole magnetyczne, siły i wymagania dla systemu mocującego | 185 |
| 51 | Janusz WALCZAK, Dariusz GRABOWSKI - Zastosowanie obwodów równoważnych w teorii mocy układów z przebiegami niesinusoidalnymi – uwagi krytyczne | 190 |
| 52 | Janusz WALCZAK, Dariusz GRABOWSKI - Zastosowanie obwodów równoważnych w teorii mocy układów z przebiegami niesinusoidalnymi – nowa koncepcja optymalizacyjna | 194 |
| 53 | Piotr ŚWISZCZ - Modele nieliniowych dwójników dla wymuszeń okresowych i nieciągłych | 198 |
| 54 | Leszek MOSZCZYŃSKI, Jarosław KUREK - Analiza wrażliwości relacji liniowej uwzględniająca niepewności oszacowania danych pomiarowych | 202 |
| 55 | Yaroslav SHMYGELSKY - Analiza stanów nieustalonych w obwodach nieliniowych przy pomocy metody siecznych | 205 |
| 56 | Vitaliy V. MARTINOV, Dmitro V. TRUSHAKOV - Symulacja procesów fizycznych w transformatorze o stałej wartości prądu uzwojenia wtórnego w czasie jego interakcji z badanym obiektem ferromagnetycznym | 208 |
| 57 | Tomasz ADRIKOWSKI, Marian PASKO - Górnoprzepustowy filtr eliptyczny z użyciem szerokopasmowej struktury bikwadratowej VES OPA-RC „b” - 02 | 211 |
| 58 | Przemysław PŁONECKI, Bartosz SAWICKI, Jacek STARZYŃSKI, Stanisław WINCENIAK - Matematyczny opis prądów wirowych w obszarze niejednorodnym z wykorzystaniem skalarnego potencjału elektrycznego | 215 |
| 59 | Paweł WIELEBA, Jan SIKORA - Biblioteka MEB dla dyfuzyjnej tomografii optycznej realizowana na licencji GNU | 219 |
| 60 | Michał ŚMIAŁEK, Albert AMBROZIEWICZ, Jacek BOJARSKI, Wiktor NOWAKOWSKI, Tomasz STRASZAK - Język specyfikacji wymagań | 223 |
| 61 | Michał KRUK, Stanisław OSOWSKI, Robert KOKTYSZ - Charakterystyka i segmentacja cew gruczołowych w obrazie mikroskopowym jelita | 227 |
| 62 | Jarosław KUREK, Adam BIERNAT, Jan SZCZYPIOR - Diagnostyka uszkodzeń prętów klatki wirnika silnika indukcyjnego za pomocą jednoklasowej sieci SVM | 231 |
| 63 | Ivan PRUDYUS, Leonid LAZKO, Serhiy SEMENOV - Zastosowanie integracji informacji na poziomie pikseli na podstawie lokalnej korelacji w systemach teledetekcji | 235 |
| 64 | Yuriy BOBALO, Leonid NEDOSTUP, Oxana LAZKO - Uogólniony odporny model rozkładu parametrów | 237 |
| 65 | Stanisław GRATKOWSKI, Mieczysław KOMOROWSKI, Tomasz PIETRUSEWICZ - Uogólniony odporny model rozkładu parametrów | 238 |
| 66 | Tadeusz KACZOREK, Łukasz SAJEWSKI - Problem realizacji dla dodatnich dwuwymiarowych układów hybrydowych z jednym opóźnieniem w wektorze stanu i wektorze sterowania | 242 |
| 67 | Ryszard SIKORA, Tomasz CHADY, Przemysław ŁOPATO, Mieczysław KOMOROWSKI - Różnicowy przetwornik wiroprowodowy o dużej rozdzielczości przestrzennej | 247 |
| 68 | Vasyl MALYAR, Andriy MALYAR - Optymalizacja charakterystyki rozruchowej pierścieniowego silnika asynchronicznego | 250 |
| 69 | Łukasz STELMACH - Poprawa wydajności metody śledzenia promieni w środowisku wieloprocesorowym | 252 |
| 70 | Piotr SIDYK - Grupy niejednoznaczności w liniowych dynamicznych układach analogowych | 255 |
| 71 | Konrad NITA, Stefan F. FILIPOWICZ - Lokalizacja aktywnych źródeł w przestrzennych modelach wielowarstwowych | 259 |
| 72 | Anastasia V.BASOVA, Victor F.IVANKOV, Stanislav S.KOKOSHYN, Ivan V.KHIMJUK - Lokalizacja aktywnych źródeł w przestrzennych modelach wielowarstwowych | 261 |
| 73 | Cornel PANAIT, George CĂRUNTU - Analiza odpowiedzi mikroczipnika magnetycznego | 265 |
| 74 | George CARUNTU, Cornel PANAIT - Struktura MOS czuła na pole magnetyczne | 269 |
| 75 | Marek KORZYBSKI, Marek OSSOWSKI - Dobór parametrów algorytmu genetycznego w diagnostyce uszkodzeń parametrycznych | 272 |
| 76 | Robert SZMURŁO, Jacek STARZYŃSKI, Stanisław WINCENIAK - Ocena parametrów dwuobszarowego modelu nerwu | 276 |
| 77 | Michał CHOJNOWSKI, Jacek KORYTKOWSKI - Ocena dwuwymiarowego modelu stymulacji nerwu błędnego (harmonicznym polem magnetycznym) | 280 |

Artykuły uszeregowano zgodnie z kolejnością ich nadsyłania do redakcji.

Numer pod redakcją Jacka Starzyńskiego

Procedures for matrix exponential function derivative in Matlab

Abstract. The paper deals with a few approaches how to determine a derivative of the matrix exponential function in the Matlab language. A usefulness for such the computation appears in many branches of the electrical engineering when various simulation tasks are solved. A Taylor series expansion, an augmented matrix utilization, an eigenvalues decomposition, a Laplace transform approach, a convolution integral evaluation and a Padé approximation method are discussed in the paper.

Streszczenie. Artykuł porównuje kilka algorytmów wyznaczania pochodnych macierzowych funkcji eksponentjalnych w Matlabie. Pochodne funkcji eksponentjalnych mają zastosowanie w kilku działach elektrotechniki, przy rozwiązywaniu rozmaitych problemów. W artykule przedyskutowano następujące przykłady: rozwinięcie w szereg Taylora, zastosowanie macierzy rozszerzonych, rozkład na wartości własne, przekształcenie Laplace'a, obliczanie całek splotowych i aproksymacja Padé. (**Procedury wyznaczania pochodnych macierzowych funkcji wykładniczych w MATLABie**).

Keywords: matrix exponential function, derivative, Matlab, simulation.

Słowa kluczowe: pochodne macierzowe, funkcje eksponentjalne, Matlab.

Introduction

Six possible methods how to compute a first derivative of a matrix exponential function are discussed being used in the Matlab language. A usefulness for such the computation appears in many branches of the electrical engineering simulation. For example, in the field of the circuit theory, it has arisen in the process of a sensitivity determination in the electrical circuits containing multiconductor transmission lines (MTLs) [1, 2]. The properties of an $(n+1)$ -conductor TL in the s -domain can be expressed using a chain matrix

$$(1) \quad \Phi(x, s) = e^{\mathbf{M}(s)x},$$

where x denotes a geometrical coordinate along the MTL and $\mathbf{M}(s)$ is an square matrix of the order $N = 2n$

$$(2) \quad \mathbf{M}(s) = \begin{bmatrix} \mathbf{0} & -\mathbf{Z}_0(s) \\ -\mathbf{Y}_0(s) & \mathbf{0} \end{bmatrix},$$

with

$$(3) \quad \mathbf{Z}_0(s) = \mathbf{R}_0 + s\mathbf{L}_0, \quad \mathbf{Y}_0(s) = \mathbf{G}_0 + s\mathbf{C}_0$$

as the series impedance and shunting admittance matrices, respectively, \mathbf{R}_0 , \mathbf{L}_0 , \mathbf{G}_0 and \mathbf{C}_0 are the MTL's per-unit-length matrices, and $\mathbf{0}$ stands for a zero matrix, all of the order n . The sensitivities can be got resulting from the first derivative of (1), with respect to a parameter $\gamma \in \mathbf{M}(s)$ [1]. Thus, γ is the element of one of the per-unit-length matrix stated above. The x parameter is considered as a constant in this case.

Taylor series expansion

As is well known, the matrix exponential function (1) can be expanded into the Taylor (MacLaurine) series as

$$(4) \quad \Phi(x, s) = \sum_{k=0}^{\infty} \frac{x^k}{k!} \mathbf{M}^k(s).$$

Then, we can write

$$(5) \quad \frac{\partial \Phi(x, s)}{\partial \gamma} = \sum_{k=1}^{\infty} \frac{x^k}{k!} \frac{\partial \mathbf{M}^k(s)}{\partial \gamma},$$

where a derivative of the k -th power of the matrix is stated as follows. If we consider e.g. an identity $\mathbf{M}^k(s) = \mathbf{M}(s)\mathbf{M}^{k-1}(s)$ the first derivative is written as

$$(6) \quad \frac{\partial \mathbf{M}^k(s)}{\partial \gamma} = \frac{\partial \mathbf{M}(s)}{\partial \gamma} \mathbf{M}^{k-1}(s) + \mathbf{M}(s) \frac{\partial \mathbf{M}^{k-1}(s)}{\partial \gamma},$$

that can be processed recursively, starting with $k = 2$.

Depending on the parameter γ and considering (2) and (3) the derivative $\partial \mathbf{M}(s)/\partial \gamma$ in (6) can be formed as a block matrix according to Table 1 [1].

Table 1. Matrix $\mathbf{M}(s)$ derivative with respect to γ

| $\gamma \in \mathbf{R}_0$ | $\gamma \in \mathbf{L}_0$ | $\gamma \in \mathbf{G}_0$ | $\gamma \in \mathbf{C}_0$ |
|--|--|--|--|
| $\begin{bmatrix} \mathbf{0} & -\frac{\partial \mathbf{R}_0}{\partial \gamma} \\ \mathbf{0} & \mathbf{0} \end{bmatrix}$ | $\begin{bmatrix} \mathbf{0} & -s \frac{\partial \mathbf{L}_0}{\partial \gamma} \\ \mathbf{0} & \mathbf{0} \end{bmatrix}$ | $\begin{bmatrix} \mathbf{0} & \mathbf{0} \\ -\frac{\partial \mathbf{G}_0}{\partial \gamma} & \mathbf{0} \end{bmatrix}$ | $\begin{bmatrix} \mathbf{0} & \mathbf{0} \\ -s \frac{\partial \mathbf{C}_0}{\partial \gamma} & \mathbf{0} \end{bmatrix}$ |

In practice, the infinite sum (5) will only be evaluated for a finite number of terms. The sufficiently rapid convergence is ensured if the product $\mathbf{M}(s)x$ is close enough to a null matrix. Therefore, the derivative is found for a transformed chain matrix $\Phi(x/r, s)$, for such the r in order to meet the Euclidian norm $\|\mathbf{M}(s)x/r\| < (0.15 \text{ to } 0.20)$ (the values are recommended in [3] for 3×3 matrices). This temporal result is transformed back to get the final derivative. A procedure is based on so-called scaling and squaring processes [3]. First, considering the formula based on (1) of the form

$$(7) \quad \Phi(x, s) = \Phi^r(x/r, s),$$

and choosing $r = 2^M$, M integer, the restoring $\Phi(x, s)$ from $\Phi(x/r, s)$ can effectively be done by a squaring process

$$(8) \quad \Phi(x/2^{m-1}, s) = \Phi^2(x/2^m, s),$$

successively for $m = M, M-1, \dots, 1$. Then, the recursive formula for restoring $\partial \Phi(x, s)/\partial \gamma$ from $\partial \Phi(x/r, s)/\partial \gamma$ follows (8) as

$$(9) \quad \frac{\partial \Phi(x/2^{m-1}, s)}{\partial \gamma} = \frac{\partial \Phi(x/2^m, s)}{\partial \gamma} \Phi(x/2^m, s) + \Phi(x/2^m, s) \frac{\partial \Phi(x/2^m, s)}{\partial \gamma}$$

processing it M -times, successively for $m = M, M-1, \dots, 1$. This recursive formula contains (8) as its part. During evaluating (5) the successive increments are used to obtain temporary errors enabling to stop the summation process.

Augmented matrix utilization

In principle the chain matrix (1) figures in the solution of the matrix ordinary differential equation of the first order

$$(10) \quad \frac{d\mathbf{W}(x,s)}{dx} = \mathbf{M}(s)\mathbf{W}(x,s),$$

where $\mathbf{W}(x,s) = [\mathbf{V}(x,s), \mathbf{I}(x,s)]^T$ is composed of the Laplace transforms of voltages and currents, respectively. Namely

$$(11) \quad \mathbf{W}(x,s) = \mathbf{\Phi}(x,s)\mathbf{W}(0,s),$$

with $\mathbf{W}(0,s)$ as a boundary condition. A further technique is based on the concept in [3]. When putting together (11) with its first derivative with respect to γ of the form

$$(12) \quad \frac{\partial \mathbf{W}(x,s)}{\partial \gamma} = \frac{\partial \mathbf{\Phi}(x,s)}{\partial \gamma} \mathbf{W}(0,s) + \mathbf{\Phi}(x,s) \frac{\partial \mathbf{W}(0,s)}{\partial \gamma},$$

the only augmented matrix equation can be written as

$$(13) \quad \begin{bmatrix} \mathbf{W}(x,s) \\ \frac{\partial \mathbf{W}(x,s)}{\partial \gamma} \end{bmatrix} = \begin{bmatrix} \mathbf{\Phi}(x,s) & \mathbf{0} \\ \frac{\partial \mathbf{\Phi}(x,s)}{\partial \gamma} & \mathbf{\Phi}(x,s) \end{bmatrix} \begin{bmatrix} \mathbf{W}(0,s) \\ \frac{\partial \mathbf{W}(0,s)}{\partial \gamma} \end{bmatrix}.$$

Similarly, combining (10) with its first derivative with respect to γ of the form

$$(14) \quad \frac{d}{dx} \left(\frac{\partial \mathbf{W}(x,s)}{\partial \gamma} \right) = \frac{\partial \mathbf{M}(s)}{\partial \gamma} \mathbf{W}(x,s) + \mathbf{M}(s) \frac{\partial \mathbf{W}(x,s)}{\partial \gamma},$$

we get the only augmented matrix differential equation as

$$(15) \quad \frac{d}{dx} \begin{bmatrix} \mathbf{W}(x,s) \\ \frac{\partial \mathbf{W}(x,s)}{\partial \gamma} \end{bmatrix} = \begin{bmatrix} \mathbf{M}(s) & \mathbf{0} \\ \frac{\partial \mathbf{M}(s)}{\partial \gamma} & \mathbf{M}(s) \end{bmatrix} \begin{bmatrix} \mathbf{W}(x,s) \\ \frac{\partial \mathbf{W}(x,s)}{\partial \gamma} \end{bmatrix}.$$

A solution of the last differential equation can be written as

$$(16) \quad \begin{bmatrix} \mathbf{W}(x,s) \\ \frac{\partial \mathbf{W}(x,s)}{\partial \gamma} \end{bmatrix} = \exp \left(\begin{bmatrix} \mathbf{M}(s) & \mathbf{0} \\ \frac{\partial \mathbf{M}(s)}{\partial \gamma} & \mathbf{M}(s) \end{bmatrix} x \right) \begin{bmatrix} \mathbf{W}(0,s) \\ \frac{\partial \mathbf{W}(0,s)}{\partial \gamma} \end{bmatrix},$$

with boundary conditions given by the right column vector. Now denoting $\mathbf{\Psi}(x,s) = [\mathbf{\Psi}_{ij}(x,s)]$, $i,j=1,2$, as a transient matrix defined by the exponential function in (16) and comparing it to the system matrix in (13), the chain matrix derivative can be determined by its homothetic submatrix $\mathbf{\Psi}_{21}(x,s)$.

The derivative $\partial \mathbf{M}(s)/\partial \gamma$ is given according to Tab. 1. In a Matlab language the built-in 'expm' function based on Padé approximation and scaling and squaring can be utilized with advantages to evaluate $\mathbf{\Psi}(x,s)$.

Eigenvalues decomposition

An another Matlab function can be utilized to get a matrix exponential function derivative, namely 'eig' built-in function for the matrix eigenvalues and eigenvectors calculation. A procedure is based on a concept in [4]. Let us assume the matrix $\mathbf{M}(s)$ in (2) has distinct eigenvalues $q_j(s)$, $j=1,2,\dots,N$, with associated eigenvectors $\mathbf{u}_j(s)$, $j=1,2,\dots,N$. Then creating the diagonal matrix $\mathbf{Q}(s) = \text{diag}(q_1(s), q_2(s), \dots, q_N(s))$ and $N \times N$ modal matrix $\mathbf{U}(s)$ composed of the eigenvectors $\mathbf{u}_j(s)$ which form its columns, a similarity transformation leads to

$$(17) \quad \mathbf{M}(s) = \mathbf{U}(s)\mathbf{Q}(s)\mathbf{U}^{-1}(s).$$

Then, the chain matrix (1) can be expressed as

$$(18) \quad \mathbf{\Phi}(x,s) = \mathbf{U}(s)e^{\mathbf{Q}(s)x}\mathbf{U}^{-1}(s),$$

and its derivative as [4]

$$(19) \quad \frac{\partial \mathbf{\Phi}(x,s)}{\partial \gamma} = \mathbf{U}(s)\mathbf{P}_\gamma(x,s)\mathbf{U}^{-1}(s).$$

In the last equation $\mathbf{P}_\gamma(x,s)$ is an $N \times N$ matrix with elements

$$(20) \quad p_{ij}^{(\gamma)}(x,s) = h_{ij}^{(\gamma)}(s) \frac{e^{q_i(s)x} - e^{q_j(s)x}}{q_i(s) - q_j(s)}, \quad i \neq j,$$

$$p_{ii}^{(\gamma)}(x,s) = h_{ii}^{(\gamma)}(s) x e^{q_i(s)x}, \quad i = j,$$

and $h_{ij}^{(\gamma)}(s)$ are the (i,j) -th elements of the matrix

$$(21) \quad \mathbf{H}_\gamma(s) = \mathbf{U}^{-1}(s) \frac{\partial \mathbf{M}(s)}{\partial \gamma} \mathbf{U}(s).$$

The derivative $\partial \mathbf{M}(s)/\partial \gamma$ is given according to Tab. 1. The calling Matlab 'eig' function with the argument $\mathbf{M}(s)$ will return both $\mathbf{Q}(s)$ and $\mathbf{U}(s)$ matrices. In case of repeated eigenvalues a more complex method based on a Jordan canonical decomposition can be applied instead, however, it happens rarely in practice [3, 4].

Laplace transform approach

This technique is based on the fact that the derivative $\partial \mathbf{\Phi}(x,s)/\partial \gamma$ is easier to find in the (q,s) -domain compared to the original one. Therefore, another Laplace transform can be applied, with respect to a coordinate x . A commutativity property of the integration and derivative operations leads to the equality

$$(22) \quad \frac{\partial \mathbf{\Phi}(x,s)}{\partial \gamma} = \mathbf{L}_x^{-1} \left\{ \frac{\partial}{\partial \gamma} \mathbf{L}_x \{ \mathbf{\Phi}(x,s) \} \right\},$$

where $\mathbf{L}_x\{\cdot\}$ stands for the Laplace transform operation with respect to x , resulting in

$$(23) \quad \mathbf{L}_x \{ \mathbf{\Phi}(x,s) \} = \int_0^\infty e^{-[q\mathbf{E}-\mathbf{M}(s)]x} dx = [q\mathbf{E}-\mathbf{M}(s)]^{-1},$$

and $\mathbf{L}_x^{-1}\{\cdot\}$ stands for its inversion. From (22) and (23) we can finally write

$$(24) \quad \frac{\partial \mathbf{\Phi}(x,s)}{\partial \gamma} = \mathbf{L}_x^{-1} \left\{ [q\mathbf{E}-\mathbf{M}(s)]^{-1} \frac{\partial \mathbf{M}(s)}{\partial \gamma} [q\mathbf{E}-\mathbf{M}(s)]^{-1} \right\},$$

where the derivative $\partial \mathbf{M}(s)/\partial \gamma$ is given according to Tab. 1. A Laplace transform inversion has to be done numerically in general. Therefore, a numerical method applied determines an achievable accuracy. In the experimental error analysis shown later, a modified NILT method based on a FFT in conjunction with a quotient-difference algorithm is used [5]. This approach is notably useful for getting derivatives for the whole set of equally spaced discrete points along the x coordinate very effectively, as is e. g. in cases when MTL voltage or current waves sensitivities are solved [2, 5].

Convolution integral evaluation

This method is a consequence of the Laplace transform technique in the last section. Namely, an argument of $\mathbf{L}_x^{-1}\{\cdot\}$ operation in (24) has the form of a product of matrices,

therefore it can formally be transformed into the original domain through a convolution integral. Taking (23) into account the result is (see also [4])

$$(25) \quad \frac{\partial \Phi(x, s)}{\partial \gamma} = \int_0^x \Phi(x-u, s) \frac{\partial \mathbf{M}(s)}{\partial \gamma} \Phi(u, s) du ,$$

where u stands for an integration variable. The derivative $\partial \mathbf{M}(s)/\partial \gamma$ is again given according to Tab. 1. As in the NILT method, this integral could be evaluated numerically with an accuracy dependent on the method applied. In [4], however, an efficient technique is developed the accuracy of which is firstly given by the evaluation of the chain matrix (1) and the matrix (2) inversion. Namely, based on [4], and denoting (2) as $\mathbf{M}(s) = [m_{ij}(s)]$, the last equation can be expressed as

$$(26) \quad \frac{\partial \Phi(x, s)}{\partial \gamma} = \sum_{i=1}^N \sum_{j=1}^N \frac{\partial m_{ij}(s)}{\partial \gamma} \int_0^x \Phi(x-u, s) \mathbf{B}_{ij} \Phi(u, s) du ,$$

with \mathbf{B}_{ij} as a square matrix with the (i, j) -th element 1, while 0 elsewhere. Denoting the integral in (26) as $\mathbf{S}_{ij}(x, s)$, it is

$$(27) \quad \left[\begin{array}{l} \mathbf{S}_{ij}(x, s) = \left[\sum_{k=0}^{N-1} (-1)^{N-k-1} (k+1) R_{N-k-1}^N(s) \mathbf{M}^k(s) \right]^{-1} \times \\ \left\{ \sum_{k=0}^{N-1} (-1)^{N-k+1} \frac{\partial R_{N-k}^N(s)}{\partial m_{ij}(s)} \mathbf{M}^k(s) \right\} x \Phi(x, s) - \\ \sum_{u=0}^{N-2} \sum_{k=u+2}^N (-1)^{N-k} (k-u-1) R_{N-k}^N(s) \mathbf{M}^{k-u-2}(s) \mathbf{C}_{ij}(x, s) \mathbf{M}^u(s) \end{array} \right] ,$$

where $\mathbf{C}_{ij}(x, s) = \mathbf{B}_{ij} \Phi(x, s) - \Phi(x, s) \mathbf{B}_{ij}$ is a commutator, and the $R_k^N(s)$ coefficients and their derivatives w.r. to $m_{ij}(s)$ can be stated treating the characteristic polynomial of $\mathbf{M}(s)$, or as sums of certain subdeterminants of $\mathbf{M}(s)$, see [4] for details. The above formulae are valid provided the inverse matrix in (27) exists. What is important is that a special structure of $\mathbf{M}(s)$ in (2) (i.e. the presence of zero diagonal submatrices) will lead to a significant simplification. The $\Phi(x, s)$ can again be evaluated by the 'expm' directly, or by the 'eig' via (18).

Padé approximation method

As was pointed out earlier the Matlab built-in function 'expm' uses a Padé approximation method in conjunction with scaling and squaring techniques [6]. A similar method can be applied to determine a matrix exponential function derivative. Let us consider the Padé approximation of the matrix exponential function (1) as

$$(28) \quad \Phi(x, s) \square \mathbf{D}_{pq}^{-1}(x, s) \mathbf{N}_{pq}(x, s) ,$$

where

$$(29a) \quad \mathbf{N}_{pq}(x, s) = \sum_{j=0}^p \frac{(p+q-j)! p!}{(p+q)! j! (p-j)!} (\mathbf{M}(s)x)^j ,$$

$$(29b) \quad \mathbf{D}_{pq}(x, s) = \sum_{j=0}^q \frac{(p+q-j)! q!}{(p+q)! j! (q-j)!} (-\mathbf{M}(s)x)^j$$

are polynomials of the matrix argument. Now we can follow (28) to get the derivative with respect to γ as

$$(30) \quad \frac{\partial \Phi(x, s)}{\partial \gamma} \square \frac{\partial \mathbf{D}_{pq}^{-1}(x, s)}{\partial \gamma} \mathbf{N}_{pq}(x, s) + \mathbf{D}_{pq}^{-1}(x, s) \frac{\partial \mathbf{N}_{pq}(x, s)}{\partial \gamma} .$$

The substitution for $\partial \mathbf{D}_{pq}^{-1}(x, s)/\partial \gamma$ and further arrangements lead to a formula

$$(31) \quad \frac{\partial \Phi(x, s)}{\partial \gamma} \square \mathbf{D}_{pq}^{-1}(x, s) \left(\frac{\partial \mathbf{N}_{pq}(x, s)}{\partial \gamma} - \frac{\partial \mathbf{D}_{pq}(x, s)}{\partial \gamma} \Phi(x, s) \right) ,$$

where

$$(32a) \quad \frac{\partial \mathbf{N}_{pq}(x, s)}{\partial \gamma} = \sum_{j=0}^p \frac{(p+q-j)! p!}{(p+q)! j! (p-j)!} \frac{\partial \mathbf{M}^j(s)}{\partial \gamma} x^j ,$$

$$(32b) \quad \frac{\partial \mathbf{D}_{pq}(x, s)}{\partial \gamma} = \sum_{j=0}^q \frac{(p+q-j)! q!}{(p+q)! j! (q-j)!} \frac{\partial \mathbf{M}^j(s)}{\partial \gamma} (-x)^j$$

result directly from (29) and $\partial \mathbf{M}(s)/\partial \gamma$ can be stated by the recursive formula (6). To guarantee the sufficiently fast convergence the scaling and squaring are applied in accord with (7) – (9). Here the matrix $\mathbf{M}(s)x$ is scaled to get an Euklidian norm less than $\frac{1}{2}$. Besides, it is convenient to choose $p = q$ in the sums (29) and (32), which leads to a good numerical stability and some simplification. In practice, $p = q = 6$ is usually sufficient, as e.g. the Matlab 'expm' built-in function uses. A generalized Matlab function 'dexpm' has been developed based on the above theory.

Experimental error analysis

Herein, the discussed methods will be elaborated as for their accuracy considering a second-order chain matrix that can analytically be differentiated. The derivatives should be accurate enough for a wide range of the complex variable s to be able to use the results for getting the time-domain sensitivities via a proper NILT method. Therefore, the errors will be investigated for a usual set of complex frequencies $\{s_i = \sigma + j\omega_i\}$ used in the FFT-based NILT method [7].

Let us consider the second-order chain matrix (1) as

$$(33) \quad \Phi(x, s) = \exp \left(- \begin{bmatrix} 0 & Z_0(s) \\ Y_0(s) & 0 \end{bmatrix} x \right) ,$$

with $Z_0(s) = R_0 + sL_0$ and $Y_0(s) = G_0 + sC_0$ in accordance with (3), however, being the scalars. This matrix can analytically be arranged, see e.g. Baker's formula in [8], leading to

$$(34) \quad \Phi(x, s) = \begin{bmatrix} \cosh \Gamma(s)x & -Z_c(s) \sinh \Gamma(s)x \\ -Y_c(s) \sinh \Gamma(s)x & \cosh \Gamma(s)x \end{bmatrix} ,$$

where $\Gamma(s) = [Z_0(s)Y_0(s)]^{1/2}$ and $Z_c(s) = 1/Y_c(s) = [Z_0(s)/Y_0(s)]^{1/2}$ are secondary parameters, a propagation constant and a characteristic impedance (admittance), respectively. Now we can differentiate the chain matrix (34) with respect to primary parameters to get exact results. The solution is split into the categories depending on γ , see Tab. 2.

The relative errors based on Euklidian norms have been stated as

$$(35) \quad E_r(l, s) = \left\| \frac{\partial \Phi_{ana}(l, s)}{\partial \gamma} - \frac{\partial \Phi_{num}(l, s)}{\partial \gamma} \right\| \left/ \left\| \frac{\partial \Phi_{ana}(l, s)}{\partial \gamma} \right\| \right. ,$$

with $\partial \Phi_{ana}(l, s)/\partial \gamma$ and $\partial \Phi_{num}(l, s)/\partial \gamma$ as the analytical solutions according to Tab. 2 and the numerical solutions discussed above, respectively, all in case of the line's end, $x = l$.

Table 2. Derivatives of the 2nd-order chain matrix $\Phi(x,s) = [\Phi_{ij}(x,s)]$

| | |
|--|--|
| Deriv. \ Param. | $\gamma \equiv R_0$ |
| $\frac{\partial \Phi_{11}(x,s)}{\partial R_0}$ | $\frac{Y_c(s)}{2} x \sinh \Gamma(s)x$ |
| $\frac{\partial \Phi_{12}(x,s)}{\partial R_0}$ | $-\frac{1}{2} \left(x \cosh \Gamma(s)x + \frac{1}{\Gamma(s)} \sinh \Gamma(s)x \right)$ |
| $\frac{\partial \Phi_{21}(x,s)}{\partial R_0}$ | $-\frac{Y_c(s)}{2} \left(x \cosh \Gamma(s)x - \frac{1}{\Gamma(s)} \sinh \Gamma(s)x \right)$ |
| Deriv. \ Param. | $\gamma \equiv L_0$ |
| $\frac{\partial \Phi(x,s)}{\partial L_0}$ | $s \frac{\partial \Phi(x,s)}{\partial R_0}$ |
| Deriv. \ Param. | $\gamma \equiv G_0$ |
| $\frac{\partial \Phi_{11}(x,s)}{\partial G_0}$ | $\frac{Z_c(s)}{2} x \sinh \Gamma(s)x$ |
| $\frac{\partial \Phi_{12}(x,s)}{\partial G_0}$ | $-\frac{Z_c(s)}{2} \left(x \cosh \Gamma(s)x - \frac{1}{\Gamma(s)} \sinh \Gamma(s)x \right)$ |
| $\frac{\partial \Phi_{21}(x,s)}{\partial G_0}$ | $-\frac{1}{2} \left(x \cosh \Gamma(s)x + \frac{1}{\Gamma(s)} \sinh \Gamma(s)x \right)$ |
| Deriv. \ Param. | $\gamma \equiv C_0$ |
| $\frac{\partial \Phi(x,s)}{\partial C_0}$ | $s \frac{\partial \Phi(x,s)}{\partial G_0}$ |

The transmission line is described by primary parameters $R_0 = 75 \Omega/m$, $L_0 = 494.6 \text{ nH/m}$, $G_0 = 0.1 \text{ S/m}$, $C_0 = 62.8 \text{ pF/m}$, with a length $l = 0.04 \text{ m}$ [9]. The computation processes the complex frequency set $\{s_i\}$ that is required for an application of the FFT-based NILT method [7]. Herein $s_i = \sigma + j\omega_i$, with $\sigma = 9.1744 \cdot 10^8$ and ω_i ranging as shown in Fig. 1. For this frequency set the considered NILT method allows to obtain the time-domain sensitivities in the interval $t \in \langle 0; 9 \rangle \text{ ns}$.

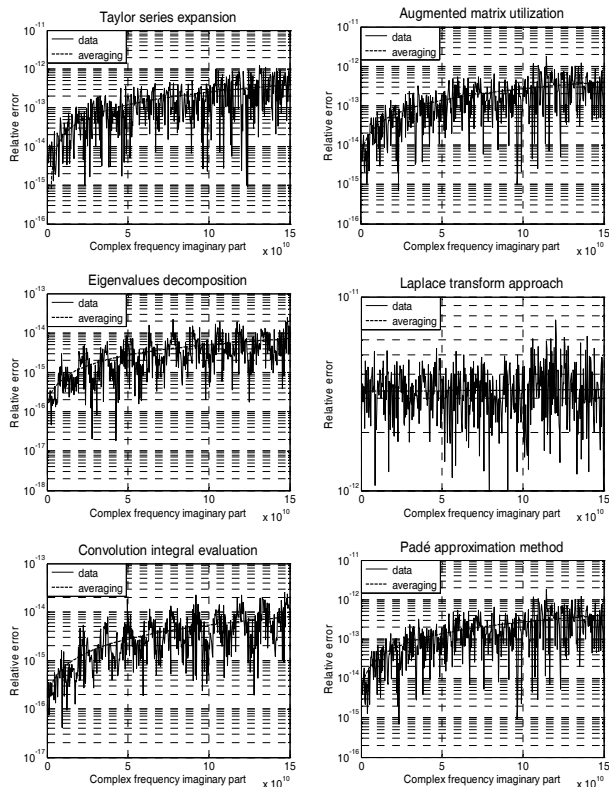


Fig. 1. Relative errors for chain matrix derivatives w.r. to R_0

Table 3. Mean values of the relative errors $E_r(L,s)$

| Taylor series | Augmented matrix | Eigenvalues dec. |
|------------------------|------------------------|------------------------|
| $2.047 \cdot 10^{-13}$ | $2.193 \cdot 10^{-13}$ | $4.098 \cdot 10^{-15}$ |
| Laplace transf. | Convolution eval. | Padé approxim. |
| $3.292 \cdot 10^{-12}$ | $4.367 \cdot 10^{-15}$ | $2.192 \cdot 10^{-13}$ |

Conclusion

To illustrate the errors quantitatively by a simple number their mean values are shown in Tab. 3. The most accurate methods are those based on an eigenvalues decomposition and a convolution integral evaluation. However, they can directly be applied only for $\mathbf{M}(s)$ with distinct eigenvalues (otherwise some generalization is further possible [4]). The second method is further dependent on a technique used to evaluate $\Phi(x,s)$. The methods with generally good stability are those based on a Taylor series expansion and a Padé approximation, even if less accurate. The first one is more CPU-time consuming due to a big number of terms in the Taylor series. The augmented matrix utilization depends on a method being used to evaluate $\Psi(x,s)$. Its accuracy is near the Padé approximation method in case the 'expm' function is used, however, due to a double order of $\Psi(x,s)$ matrix it is more CPU-time consuming. The Laplace transform method seems to be least accurate, however, another NILT method could improve it. On the other hand, the FFT-based NILT [5] permits to get a solution for the whole set of x_k directly. All the procedures have been programmed as M-file functions in the Matlab. The presented Padé approximation method is originally developed and a respective M-file function, called as 'dexpm', generalizes the Matlab 'expm' function enabling to get both $\Phi(x,s)$ and $\partial \Phi(x,s)/\partial \gamma$ matrices simultaneously. To evaluate errors more rigorously, however, it should be necessary to handle another higher-order matrices.

ACKNOWLEDGMENTS

Research in the paper was financially supported by the Czech Ministry of Education under the MSM 0021630503 Research Project MIKROSYN.

REFERENCES

- [1] Brančík L., Novel techniques for sensitivity evaluation in multiconductor transmission line systems, *WSEAS Transactions on Communications*, 4 (2005), No. 5, 216–223.
- [2] Brančík L., Voltage/current waves sensitivity in hybrid circuits with nonuniform MTLs, in *Proceedings of the 10th IEEE Workshop on SPI'06*, Berlin (Germany), 2006, 177–180.
- [3] Fung T. C., Computation of the matrix exponential and its derivatives by scaling and squaring, *International Journal for Numerical Methods in Engineering*, 59 (2004), 1273–1286.
- [4] Tsai H., Chan K. S., A note on parameter differentiation of matrix exponentials, with applications to continuous-time modeling, *Technical report #311*, Univ. of Iowa, 2001, 1–22.
- [5] Brančík L., Chain matrix derivative via Laplace transform method with applications to distributed circuits simulation, In *Proceedings of IMAPS CS International Conference EDS'06*, Brno (Czech Republic), 2006, 58 – 63.
- [6] Moler C., Loan C. V., Nineteen dubious ways to compute the exponential of a matrix, twenty-five years later, *SIAM Review*, (45) 2003, No. 1, 1–46.
- [7] Brančík L., Improved numerical inversion of Laplace transforms applied to simulation of distributed circuits, in *Proceedings of the XI. ISTET'01*, Linz (Austria), 2001, 51–54.
- [8] Angot A., *Užitá matematika pro elektrotechnické inženýry*, (Applied Mathematics for Electrical Engineers), Prague: SNTL 1971, 819 p.
- [9] Lum S., Nakhla M. S., Zhang Q. J., Sensitivity analysis of lossy coupled transmission lines, *IEEE Trans. on Microw. Theory and Techniques*, (39) 1991, No. 12, 2089–2099.

Author: doc. Ing. Lubomír Brančík, CSc., Brno University of Technology, Institute of Radio Electronics, Purkyňova 118, 612 00 Brno, Czech Republic, E-mail: brancik@feec.vutbr.cz

Control of movement of artificial satellites by geomagnetic field

Abstract. The paper deals with a possibility of influencing the movement of artificial satellites of the Earth by its geomagnetic field using “tethers”, i.e. long, direct current carrying superconductive cables moving together with the satellite. Derived is the continuous mathematical model of the problem consisting of an ordinary nonlinear differential vector equation. Its solution is carried out numerically. The algorithm is illustrated on a typical example whose results are discussed.

Streszczenie. Artykuł dotyczy możliwości sterowania ruchem satelitów z wykorzystaniem ziemskiego pola magnetycznego. Sterowanie realizowane jest za pomocą pętli kabli nadprzewodnikowych przewodzących prąd stały. W pracy wyprowadzono analityczny model takiego zagadnienia w postaci zwyczajnych równań różniczkowych dla wielkości wektorowych. Równania te są rozwiązywane numerycznie. Algorytm zilustrowany jest typowym przykładem. Pracę kończy omówienie uzyskanych wyników. (Sterowanie ruchem satelitów z wykorzystaniem ziemskiego pola magnetycznego).

Keywords: geomagnetic field, artificial satellites, control of velocity, numerical analysis.

Słowa kluczowe: ziemskie pole magnetyczne, satelity, sterowanie prędkością, analiza numeryczna

Introduction

In a simplified fashion, the existence of Earth’s magnetic field (geomagnetic field) can be explained as a consequence of the different rotation of the external liquid layer of Earth’s core and the internal, solid layer of Earth’s shell (see Fig. 1). The free electrons in the liquid external layer of the core move with respect to the shell, which gives rise to a magnetic field analogously as in the case of a direct current flowing through an electrically conductive loop. But the real situation is much more complicated. In connection with nonhomogeneities in both mentioned media (core and shell) and subsequent complex turbulent processes in the external liquid layers of the core the geomagnetic field is also turbulent, considerably nonuniform and varies in time (see Figs. 2 and 3).

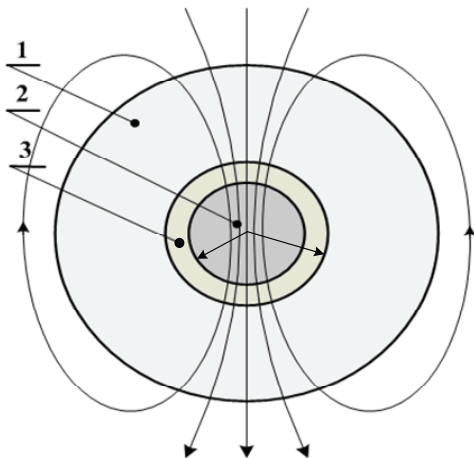


Fig. 1. Geomagnetic field – classical laminar conception: 1 - shell, 2 – internal core, 3 – external molten layer of the core

All these facts have to be taken into account at eventual practical employment of this field. While in the past the geomagnetic field was used only for orientation in the naval navigation (the compass was known in China already in the sixth century after Christ) nowadays this field is (or is seriously considered to be) employed in a number of other human activities. Mentioned can be, at random, the prospecting geophysical activity in the domain of the ferrous ores (Ground Penetrating Radar or DC Magnetic Radiometer, see, for example [7]), determination of the temporal data in geology and prehistoric archeology and, last but not least, a number of the modern space technologies (see, for example, [5], [6] and other references provided there).

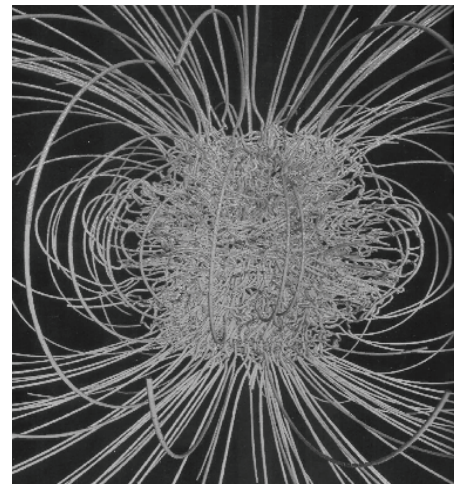


Fig. 2. Geomagnetic field – modern turbulent conception (see [2])

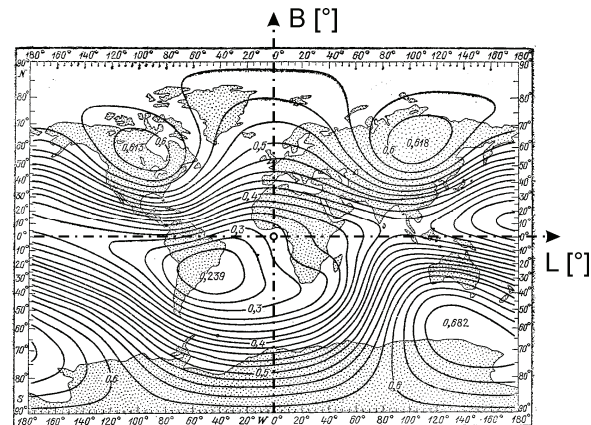


Fig. 3. Distribution of the geomagnetic field along the Earth surface (in [Gs] $\approx 10^{-4}$ [T], see [3])

The paper deals with one of such prospective space applications – control of the movement of the artificial satellites of the Earth by means of the tethers, which are electrically conductive cables connected with the satellite that carry direct current. Employed is here the force interaction between the cable and surrounding geomagnetic field. The aim of the paper is to show that this problem may relatively easily be solved by means of the classical macroscopic electrodynamics together with the utilization of the space geodesy.

Mathematical model of the problem

The principal scheme of influencing the movement of the artificial satellites of Earth by its geomagnetic field by means of a conductive cable carrying direct current (so called tether) is depicted in Fig. 4.

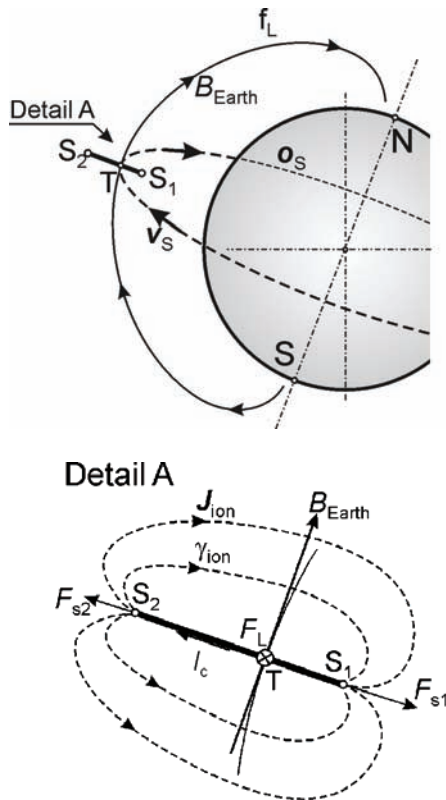


Fig. 4. Principal scheme of control of artificial satellites of the Earth by the geomagnetic field by means of the tether: above - overall situation, below - detail of the tether

The system is formed by two bodies (the satellite itself S_1 and an auxiliary body S_2) firmly connected by a conductive cable – tether – of length $l \approx \overline{S_1 S_2}$ armed by some of light and firm materials such as *Kevlar* (an aromatic polyamide) or *Spektra* (highly solid polyethylene). In the case that the system $\overline{S_1 S_2}$ moves around the Earth (in the space of ionized plasma in the Earth magnetosphere – see Note¹) along an orbit o_s at a velocity v_s , the balance of the gravitational and centrifugal forces will set up in its centre of gravity. While the satellite S_1 is affected by a mildly dominant gravitational, (centripetal) force F_{s1} , the auxiliary body S_2 is affected by a centrifugal force F_{s2} . As a consequence of the mutual repulsion of parts S_1 and S_2 the tether $\overline{S_1 S_2}$ will remain tensed in the radial direction with respect to the Earth, compare Fig. 4. If the tether carries a direct current I_C (see the Note), it starts to be (in common with the whole system $\overline{S_1 S_2}$) in the Earth geomagnetic field B_{Earth} influenced by the Lorentz force F_L (see equation (6)), in the perpendicular direction to the direction $\overline{S_1 S_2}$, see

¹ The current flows not only through the tether $\overline{S_1 S_2}$ itself, but through a closed electric circuit where the tether represents only one of its parts. The current will close through (see Fig. 4, Detail A) the practically unbounded environment that is ionized, and, consequently electrically conductive, particularly due to the solar wind.

Figure 4, Detail A. Its orientation (sign) is given by the direction of current I_C .

But this situation leads to the problem of continuity of transition of the current density J_{ion} from a finite surface of the body S_2 into the unbounded weakly electrically conductive environment. This is, in fact a problem of practically incommensurable rotationally axisymmetric electric field. With respect to a limited space of the paper, no attention is paid to it, even when it is fully solvable by the modern computational tools.

As far as the force F_L acting in the center of gravity of the system $\overline{S_1 S_2}$ is oriented in the direction of its movement (at the velocity v_s), it is accelerated, which leads to its shift (due to the higher centrifugal force) on an orbit with a longer radius vector. In an opposite case the satellite will be dragged and pulled (due to prevailing gravitational force) to an orbit with a shorter radius vector.

The paper is aimed at the quantification of the presented scenario by means of the laws of the classical macroscopic electrodynamics together with the utilization of the knowledge of astrodynamics and space geodesy. In order to solve a real situation, beside the Lorentz force F_L even further forces (in astrodynamics called perturbations) affect the movement that are caused by the perturbation gravitational potential of the Earth and several more effects listed, for example, in [11]. Nevertheless, with the exception of the perturbation gravitational potential of the Earth that will be respected, all remaining perturbations may be considered practically negligible, because their effects on the satellite are by several orders smaller than the primarily investigated influence of the tether providing the Lorentz force F_L .

Mathematical model of the problem

Approximate computation of the Earth magnetic field

The computation of the force effects of the geomagnetic field on the system $\overline{S_1 S_2}$ cannot be done without its knowledge at the place of the actual position of the satellite. An approximate calculation of its value may be realized by the modeling of the

- field of a magnetic dipole (or, more accurately, of a system of magnetic dipoles, see, for example [9]).
- field of a system of fictitious conductive loops merged into the liquid external layer of the Earth core (compare Fig. 1, $R_{min} = 1300$ km, $R_{max} = 3500$ km) that carry direct currents of such densities that the corresponding uniform magnetic field would reach at the Earth surface ($R_0 = 6381$ km) the mean value of the nonuniform geomagnetic field depicted in Fig. 3.

The conception starts from the second possibility that better corresponds to the assumed physical reality (compare the paragraph 1). The solution was performed using the professional FEM-based program QuickField (see [10]) for the mean value of the magnetic field on the Earth surface $H_{SE} = 34$ A/m that corresponds to T. The “regula falsi” method [17] then provided the corresponding current density of value $|J| = 0.00105$ A/m². These computations were also accompanied by testing the convergence of the obtained numerical solutions. For example, accuracy of two valid digits of $|H_{SE}|$ was reached for the discretization mesh with 64500 elements.

The qualitative distribution of the force lines of the calculated magnetic field is depicted in Fig. 5. Fig. 6 then shows the quantitative dependence of $|B_{Earth}|$ on the

distance h from the Earth surface. This dependence was used in the equations of motion, particularly for the computation of the Lorentz force F_L , see equation (6).

Equations of motion of a satellite

The mathematical description of the motion equations of an Earth satellite must start from the definition of suitable coordinate systems. In our case, the most advantageous is probably the equator system related to the Greenwich (Fig. 7) that is characterized by coordinates

- geographic (astronomical) latitude φ ,
- geographic (astronomical) longitude λ .

The motion of the satellite may be then (with respect to the assumptions given at the end of par. 1) described at an arbitrary point (x_S, t) , $x_S \in o_S$, $x_S \equiv (x_S, y_S, z_S)$, x_S being the position of the satellite that is given by equations

$$(1) \quad m_S \frac{dv_S}{dt} = F_1 + F_2$$

$$(2) \quad v_S = \frac{dx_S}{dt}$$

where m_S is the mass of the satellite and v_S is the vector of its velocity and $F_1 = F_L$ while F_2 being the force due to the perturbation of the gravitational potential of the Earth.

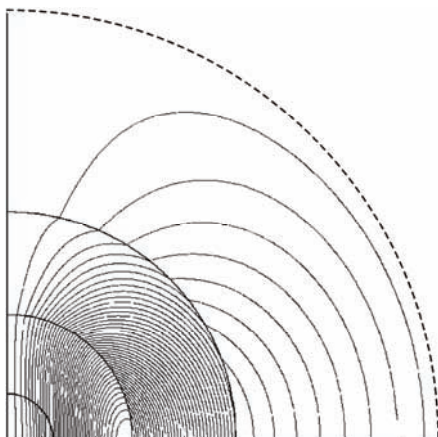


Fig. 5. Result of an approximate computation of the geomagnetic field by code QuickField

The solution of (1) and (2) is carried out in Cartesian coordinate system (x, y, z) , see, for example, Fig. 7. On the other hand, computation of some parameters of the force F_2 (see equations (7)–(8)) needs working with a coordinate system related to the Greenwich meridian. The uniqueness of the equations (1) and (2) is enforced by the boundary conditions

$$(3) \quad (x_S, t=0) = x_{S0}, \quad (v_S, t=0) = v_{S0}$$

where x_{S0} is a certain (initial) point of the trajectory o_S of the satellite, from which the movement of the satellite starts to be investigated ($t=0$) and at which its velocity is v_{S0} (compare Table 1).

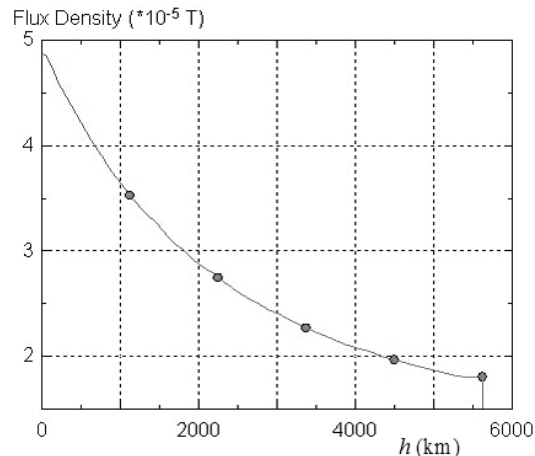


Fig. 6. Dependence of the geomagnetic field $|B_{Earth}|$ on the height h above the Earth surface

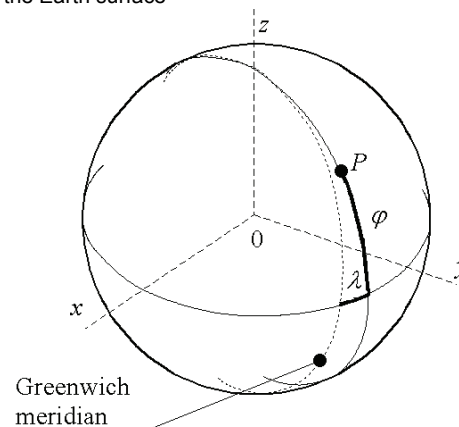


Fig. 7. The equator coordinate system related to the Greenwich meridian (point P denotes the projection of the satellite on the Earth surface)

The knowledge of both vectors $x_S \equiv (x_S, y_S, z_S)$ and $v_S \equiv (v_{xS}, v_{yS}, v_{zS})$ then allows determining the module of velocity

$$(4) \quad |v_S| = \sqrt{v_{xS}^2 + v_{yS}^2 + v_{zS}^2}$$

and its height above the Earth surface

$$(5) \quad h = \sqrt{x_S^2 + y_S^2 + z_S^2} - R_0.$$

The vectors of the forces F_1 , F_2 occurring in (1) can be expressed (details see in [11]) by the following relations

- $F_1 = F_L$ – is the vector of the Lorentz force produced by the direct current I_C in the cable $l \approx \overline{S_1 S_2}$ (Fig. 4) that is given ([12], [18]) by integral

$$(6) \quad F_L = I_C \cdot \int_{S_1}^{S_2} (dl \times B_{Earth})$$

where dl is an oriented element of the length of the tether and B_{Earth} is the magnetic flux density of the geomagnetic field at point x_S .

- $F_I = F_{GPE}$ – is the vector of a perturbation force caused by the perturbation gravitational potential of the Earth – for details see [11] – that is given as

$$(7) \quad F_{GPE} = \text{grad } R_E$$

where

$$(8) \quad R_E = \frac{GM_E}{r_S} \sum_{n=2}^{\infty} \sum_{k=0}^n \left(\frac{a_E}{r_S} \right)^n \cdot (C_n^{(k)} \cos k\Lambda + S_n^{(k)} \sin k\Lambda) P_n^{(k)}(\sin \Phi).$$

here: R_E is the perturbation potential of the Earth, GM_E is the geocentric gravitational constant of the Earth, r_S is the geocentric radius vector of the satellite (measured from the Earth barycentre), a_E is the radius of the equator (corresponds to R_0), $C_n^{(k)}$, $S_n^{(k)}$ are the Stokes parameters (geopotential harmonic coefficients), n is the degree of the parameter, k is the order of the parameter, $P_n^{(k)}(\sin \Phi)$ are the Legendre polynomials for $k = 0$ and Legendre associated functions for $k \neq 0$, Φ and Λ are the geocentric latitude and longitude ($\approx \varphi, \lambda$, see Fig. 7).

Numerical solution of the model

The above mathematical model given by a system of differential equations (1) and (2) was solved by the user code written in MatLab, containing the Adams-Bashfort-Moulton method [16] for the solution of ordinary differential equations formulated as the initial problems. The solution was carried out with an error of the order of 10^{-9} .

Illustrative example

The aim of this example was to

- demonstrate the possibility of controlling the movement of the artificial satellites of the Earth by means of the force effects of the geomagnetic field on a tether – a cable connected with the satellite and carrying direct current – from the viewpoints of both deceleration and acceleration of the satellite;
- allow a quantitative evaluation of all basic parameters of the tether – its length $l \approx \overline{S_1 S_2}$ and its current I_C (see Fig. 4, Detail A);

The input data

Investigated is the problem of control of the movement of an artificial Earth satellite *RHESSI* [13] (Ramaty High Solar Spectroscopic Imager) that belongs to the category of the scientific satellites, its producer is Spectrum Astro, USA and operator NASA, USA (Fig. 8). The basic information about the satellite is in Table 1.

Table 1. Basic data about the satellites

| satellite | | <i>RHESSI</i> | |
|----------------------------|----------------------|---------------|-------|
| mass | m_S | kg | 293 |
| perigee | A | km | 564 |
| apogee | B | km | 586 |
| decline of trajectory | l_d | ° | 38.04 |
| Initial altitude | h_{s0} | km | 564 |
| module of Initial velocity | $\text{mod}(v_{s0})$ | km/s | 7.583 |

The computation of the motion of the satellite was carried out on the assumption that

- it is equipped with the tether of length l whose mass is negligible with respect to the mass of the corresponding satellite,
- at time $t = 0$ when the satellite is in position x_{s0} of its trajectory at velocity v_{s0} (compare equation (3) and Tab. 1), the tether starts carrying a direct current I_C .

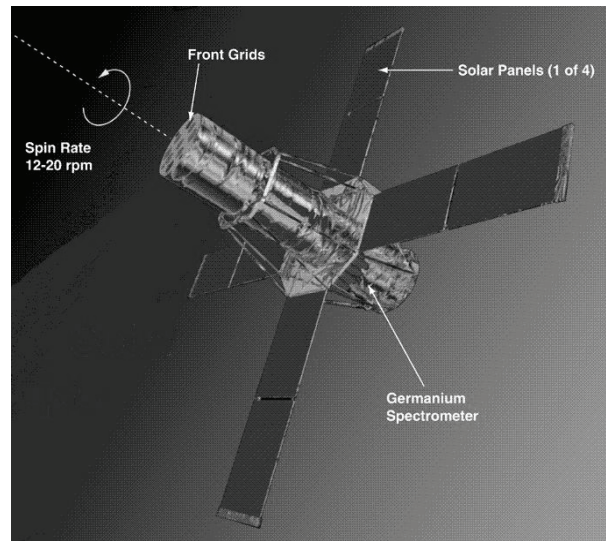


Fig. 8. Satellite *RHESSI* (see [13])

Results and their discussion

The results obtained may be summarized in the following figures that allow evaluating the most important influences on the control of movement of artificial satellites by means of the tethers.

Influence of the geomagnetic field

This influence follows from Figs. 9a, b (increase of the height of the satellite above Earth). Both cases concern the satellite *RHESSI* (see [13] or Tab. 1) equipped with a tether of length $l = 1$ km that carries current $I_C = 60$ A. The direction of this current (and, consequently, direction of the Lorentz force F_L) may be changed.

These figures show that the tether of the given parameters is really able to significantly change the movement of the satellite, that is pulled, for example, up on a higher orbit, see Fig. 9a, b.

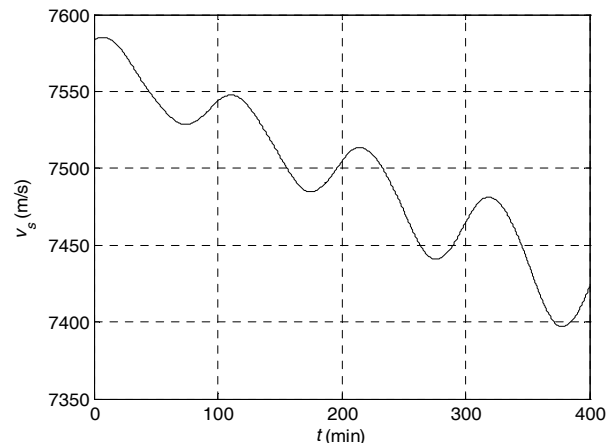


Fig. 9a. Raising of the position of the satellite *RHESSI* [13], length of the tether $l = 1$ km, current $I_C = 60$ A – velocity versus time

The function of the tether also results in the enlargement of the amplitude of oscillations of the altitude h , i.e. increase of the apogee A to perigee B brought about by an

analogous distribution of the Lorentz force F_L (see 9b) that is caused (for constant current I_C) by the distribution of magnetic flux density B_{Earth} of the geomagnetic field at altitude h (compare Fig. 6 and eq. (6)). This effect (that can sometimes be undesirable) of the tether may be suppressed by suitable regulation of current I_C such that the force F_L would remain constant. It is clear that an appropriate control of current I_C and force F_L would lead to an arbitrary ratio $A/B \geq 1$.

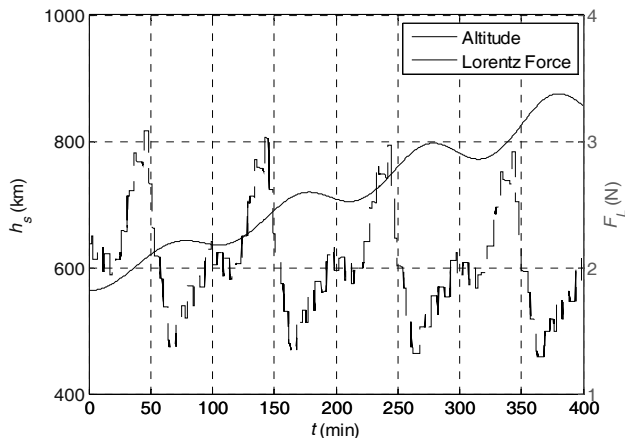


Fig. 9b. Raising of the position of the satellite RHESSI [13], length of the tether $l = 1$ km, current $I_C = 60$ A – altitude and Lorentz force versus time

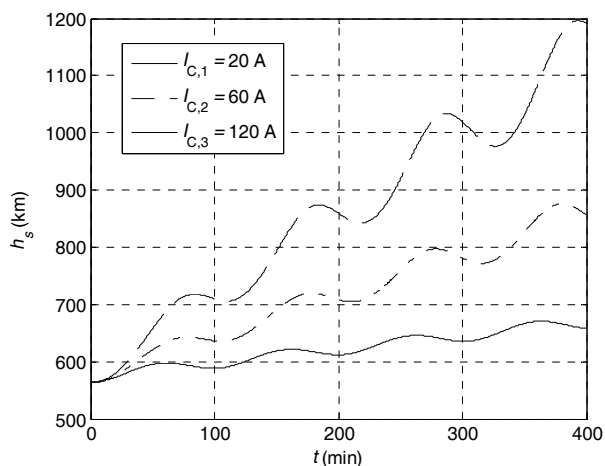


Fig. 10: The influence of current I_C flowing through the tether on the motion of the satellite (satellite RHESSI [13], length of the tether $l = 1$ km – altitude versus time

Influence of the basic parameters of the tether

The influence of its length $l \approx \sqrt{S_1 S_2}$ or current I_C follows from Fig. 10 generated also for the satellite RHESSI equipped with a tether of length $l = 1$ km that carries direct current I_C . The current is changing, which results in variations of the Lorentz force F_L acting on the system (at the same time equation (6) says that the influence of the relative change of I_C is equivalent to the influence of the relative change of length l). It is clear that the change of both parameters may influence the movement of the satellite in quite a wide range.

Conclusion

The paper shows that the tether, employing the geomagnetic field, represents a prospective and technically quite real device that is able to control (within a relatively wide range) the movement of the artificial satellites of the Earth. The associated problems can successfully be solved by means of classical macroscopic electrodynamics together with utilization of the laws of the space geodesy. The facts presented and results obtained can be used for a good design of a real space system of the considered type.

Acknowledgment

The financial support of the Research Plan MSM6840770017 and grant project GA ČR 102/07/0496 is gratefully acknowledged.

REFERENCES

- [1] Sládek, J.: *Anatomy of Earth*. ALBATROS, Prague, 1995 (in Czech).
- [2] Glatzmaier, G. A., Olson, P.: *Geodynamo*. Scientific American (Czech issue), January 2006, pp. 79–85.
- [3] Bočkarov, N. G.: *Magnetic Fields in Space*. NAUKA, Moscow, 1985 (in Russian).
- [4] Kleczek, J.: *Large Encyclopedia of Space*. Academia Praha, 2002 (in Czech).
- [5] Lorenzini, E., Sanmartin, J.: *Electrodynamic Tethers*. Scientific American (Czech issue), July 2005, pp. 12–19.
- [6] Přeč, L.: *Active Experiments in the Space Plasma*. Progress of mathematics, physics & astronomy, Vol. 51, No. 3, 2006, pp. 239–258.
- [7] Ripka, P., Lewis, A.: *Eddy Current Metal Detectors – Pulse VS. CW*. Proc. MME6 (JEE Journal), in print.
- [8] Kabeláč, J., Kostecký, J.: *Geodetic Astronomy 10*. Learning text of the Czech Technical University, Faculty of Civil Engineering, Prague, 2001 (in Czech).
- [9] De Paor, A., Burke, E.: *A New Eccentric Geomagnetic Dipole to Give the Correct Dipole Locations*. AEEE, Žilina (Slovakia), Vol. 5, No. 1–2, 2006, pp. 316–318.
- [10] www.quickfield.com.
- [11] Kabeláč, J.: *Introduction to Space Geodesy – II. part*. Czech Technical University, Prague, 1991 (in Czech).
- [12] Haňka, L.: *Theory of Electromagnetic Field*. SNTL/ALFA, Prague, 1975.
- [13] <http://www.lib.cas.cz/www/space.40/2002/004A.HTM>.
- [14] <http://www.lib.cas.cz/www/space.40/2002/003A.HTM>.
- [15] *Orbital Task of the Satellite Geodesy*. Dept. of Higher Geodesy, Czech Technical University, Prague, 2002, pp. 65 (in Czech).
- [16] www.mathworks.com.
- [17] Vitásek, E.: *Numerical Methods*. SNTL, Prague, 1987 (in Czech).
- [18] Stratton, J.: *Electromagnetic Theory*. McGraw Hill Book Co., NY, 1941.

Authors

Dr. Ing. Jiří Büllow, University of West Bohemia, Faculty of Electrical Engineering, Univerzitní 26, 316 04 Plzeň, Czech Republic, E-mail: buillow@kte.zcu.cz;
 Prof. Ing. Ivo Doležel, CSc., Institute of Thermomechanics, Academy of Sciences of the Czech Republic, Dolejškova 5, 182 02 Praha 8, Czech Republic, E-mail: dolezel@jee.cas.cz;
 Prof. Ing. Josef Kabeláč, CSc., University of West Bohemia, Faculty of Electrical Engineering, Univerzitní 26, 316 04 Plzeň, Czech Republic;
 Ing. Pavel Karban, University of West Bohemia, Faculty of Electrical Engineering, Univerzitní 26, 316 04 Plzeň, Czech Republic, E-mail: karban@kte.zcu.cz;
 Doc. Ing. Bohuš Ulrych, CSc., University of West Bohemia, Faculty of Electrical Engineering, Univerzitní 26, 316 04 Plzeň, Czech Republic, E-mail: ulrych@kte.zcu.cz;

Positive discrete-time linear Lyapunov systems with delays

Abstract. The notion of positive discrete-time linear Lyapunov system with delays is introduced. Necessary and sufficient conditions for the positivity and the asymptotic stability of this system are established. The necessary and sufficient conditions for reachability are given and the Cayley-Hamilton theorem is extended for linear Lyapunov systems with delays. The considerations are illustrated on the numerical example.

Streszczenie. Praca przedstawia dodatnie dyskretne układy Lapunowa z opóźnieniami. Ustanowione są warunki konieczne i wystarczające dodatniości, asymptotycznej stabilności i osiągalności. Rozszerzone jest Twierdzenie Cayley'a-Hamiltona dla tej klasy układów. Rozważania są zilustrowane na przykładach numerycznych. (**Dodatnie dyskretne układy Lapunowa z opóźnieniem**).

Keywords: Lyapunov systems, stability, reachability, Cayley-Hamilton theorem, delays

Słowa kluczowe: układy Lyapunowa, stabilność, osiągalność, twierdzenie Cayley'a-Hamiltona, opóźnienia

Introduction

In positive systems inputs, state variables and outputs take only non-negative values. Examples of positive systems are industrial processes involving chemical reactors, heat exchangers and distillation columns, storage systems, compartmental systems, water and atmospheric pollution models. A variety of models having positive linear behavior can be found in engineering, management science, economics, social sciences, biology and medicine, etc.

Positive linear systems are defined on cones and not on linear spaces. Therefore, the theory of positive systems is more complicated and less advanced. An overview of state of the art in positive systems theory is given in the monographs [3,4]. The realization problem for positive linear systems without and with time delays has been considered in [1,4,7-10].

The reachability, controllability to zero and observability of dynamical systems have been considered in [19].

The reachability and minimum energy control of positive linear discrete-time systems was considered in [2].

The positive discrete-time systems with delays have been considered in [10,15,18].

The controllability and observability of Lyapunov systems have been investigated by Murty Apparao in the paper [20].

The positive discrete-time and continuous-time Lyapunov systems have been considered in [11,13,14].

The positive linear time-varying Lyapunov systems have been investigated in [16].

The Lyapunov cone systems have been considered in [17].

In this paper, the notion of positive discrete-time linear Lyapunov system with delays will be introduced. Necessary and sufficient conditions for the positivity and the asymptotic stability of this system will be established. The necessary and sufficient conditions for reachability are given and the Cayley-Hamilton theorem will be extended for linear Lyapunov systems with delays. The considerations will be illustrated on the numerical example.

To the best knowledge of the authors those problems for the positive Lyapunov systems has not been considered yet.

Introduction

Let $R^{n \times m}$ be the set of real $n \times m$ matrices with and $R^n = R^{n \times 1}$. The set of real $n \times m$ matrices with

nonnegative entries will be denoted by $R_+^{n \times m}$. The set of nonnegative integers will be denoted by Z_+ .

The system described by the equations:

$$(1a) \quad X_{i+1} = A_0 X_i + X_i B_0 + \sum_{k=1}^h (A_k X_{i-k} + X_{i-k} B_k) + F U_i,$$

$$(1b) \quad Y_i = C X_i + D U_i$$

with the initial conditions $X_{-k} \in R_+^{n \times m}$, $k = 0, \dots, h$, is called *the discrete-time linear Lyapunov system with h delays*.

where, $X_i \in R^{n \times m}$ is the state-space matrix, $U_i \in R^{m \times n}$ is the input matrix, $Y_i \in R^{p \times m}$ is the output matrix, $h \in Z_+$, $A_k, B_k \in R^{n \times n}$ ($k = 0, \dots, h$), $F \in R^{n \times m}$, $C \in R^{p \times n}$, $D \in R^{p \times m}$, $i \in Z_+$.

Definition 1.

The *Kronecker product* $A \otimes B$ of the matrices $A = [a_{ij}] \in R^{m \times n}$ and $B \in R^{p \times q}$ is the block matrix [5]:

$$(2) \quad A \otimes B = [a_{ij} B]_{\substack{i=1, \dots, m \\ j=1, \dots, n}} \in R^{m \times p \times n \times q}$$

Lemma 1.

Let us consider the equation:

$$(3) \quad AXB = C$$

where: $A \in R^{m \times n}$, $B \in R^{q \times p}$, $C \in R^{m \times p}$, $X \in R^{n \times q}$

The equation (3) is equivalent to the following one:

$$(4) \quad (A \otimes B^T)x = c$$

where: $x := [x_1 \ x_2 \ \dots \ x_n]^T$, $c := [c_1 \ c_2 \ \dots \ c_m]^T$,

and x_i and c_i are the i th rows of the matrices X and C respectively.

Proof: See [5]

Lemma 2.

The Lyapunov system with delays (1) can be transformed to the equivalent standard discrete-time, nm -inputs and pn -outputs, linear system in the form:

$$(5a) \quad \bar{x}_{i+1} = \bar{A}\bar{x}_i + \bar{B}\bar{u}_i$$

$$(5b) \quad \bar{y}_i = \bar{C}\bar{x}_i + \bar{D}\bar{u}_i$$

where, $\bar{x}_i \in R^{n^2}$ is the state-space vector, $\bar{u}_i \in R^{(nm)}$ is the input vector, $\bar{y}_i \in R^{(pn)}$ is the output vector and

$$\bar{A} \in R^{\bar{n} \times \bar{n}}, \bar{B} \in R^{\bar{n} \times (nm)}, \bar{C} \in R^{(pn) \times \bar{n}}, \bar{D} \in R^{(pn) \times (nm)},$$

$$\bar{n} = n^2(h+1).$$

Proof:

Using Lemma 1 we transform the system (1) into the equivalent standard system with delays:

$$(6a) \quad \tilde{x}_{i+1} = \tilde{A}_0 \tilde{x}_i + \sum_{k=1}^h \tilde{A}_k \tilde{x}_{i-k} + \tilde{F} \tilde{u}_i$$

$$(6b) \quad \tilde{y}_i = \tilde{C} \tilde{x}_i + \tilde{D} \tilde{u}_i$$

and this transformation is based on Lemma 1. The matrices X, U, Y are transformed to the vectors:

$$\tilde{x} = [X_1 \ X_2 \ \dots \ X_n]^T, \tilde{u} = [U_1 \ U_2 \ \dots \ U_m]^T,$$

$$\tilde{y} = [Y_1 \ Y_2 \ \dots \ Y_p]^T$$

where X_i, U_i, Y_i denotes the i th rows of the matrices X, U, Y , respectively.

The matrices of (6) are:

$$\tilde{A}_k = (A_k \otimes I_n + I_n \otimes A_k^T), \tilde{F} = F \otimes I_n,$$

$$(7) \quad \tilde{C} = C \otimes I_n, \tilde{D} = D \otimes I_n$$

$$k = 0, \dots, h$$

In the next step we transform the system (6) into the system (5). According to [11,13,14] the matrices of (5) are:

$$(8) \quad \bar{x} = \begin{bmatrix} \tilde{x}_i \\ \tilde{x}_i \\ \vdots \\ \tilde{x}_{i-h} \end{bmatrix}, \bar{A} = \begin{bmatrix} \tilde{A}_0 & \tilde{A}_1 & \dots & \tilde{A}_h \\ I_{n^2} & 0 & \dots & 0 \\ \vdots & \ddots & \ddots & \vdots \\ 0 & \dots & I_{n^2} & 0 \end{bmatrix}, \bar{F} = \begin{bmatrix} \tilde{F} \\ 0 \\ \vdots \\ 0 \end{bmatrix},$$

$$\bar{C} = [\tilde{C} \ 0 \ \dots \ 0], \bar{D} = \tilde{D}$$

Lemma 3.

If $\lambda_1, \lambda_2, \dots, \lambda_n$ are the eigenvalues of the matrix A and $\mu_1, \mu_2, \dots, \mu_n$ the eigenvalues of the matrix B , then $\lambda_i + \mu_j$ for $i, j = 1, 2, \dots, n$ are the eigenvalues of the matrix:

$$\bar{A} = A \otimes I_n + I_n \otimes B^T$$

Proof: See [5]

Positivity of the Lyapunov systems with delays

Definition 2.

The Lyapunov system (1) is called (*internally*) *positive* if and only if $X_i \in R_+^{nxn}$ and $Y_i \in R_+^{pxn}$ for any $X_{-k} \in R_+^{nxn}$, $k = 0, \dots, h$ and for every input $U_i \in R_+^{mxn}$, $i \in Z_+$.

Theorem 1.

The Lyapunov system (1) is positive if and only if:

$$A_k, B_k \in R_+^{n \times n} (k = 0, \dots, h), F \in R_+^{n \times m}, C \in R_+^{p \times n}, D \in R_+^{p \times m}$$

Proof:

The Lyapunov system (1) is positive if and only if, the equivalent standard system (5) is positive. It is well-known [4] that the standard system (5) is positive if and only if the matrices $\bar{A}, \bar{B}, \bar{C}, \bar{D}$ have nonnegative entries. From (7) and (8) follows the hypothesis of the Theorem 1.

Asymptotic Stability of the Lyapunov systems with delays

Consider the positive autonomous Lyapunov system with delays:

$$(9) \quad X_{i+1} = A_0 X_i + X_i B_0 + \sum_{k=1}^h (A_k X_{i-k} + X_{i-k} B_k)$$

where $X_i \in R_+^{n \times n}, i \in Z_+, A_k, B_k \in R_+^{n \times n}, k = 0, \dots, h$

Definition 3.

The Lyapunov system (9) is called *asymptotically stable* if:

$$(10) \quad \lim_{i \rightarrow \infty} X_i = 0, \text{ for every } X_{-k} \in R_+^{n \times n}, k = 0, \dots, h.$$

Theorem 2.

The positive Lyapunov system (1) is asymptotically stable if and only if one of the following equivalent conditions is met:

i. all eigenvalues $(z_1, z_2, \dots, z_{\bar{n}})$ of the matrix \bar{A} defined in

$$(8) \text{ have moduli less than 1, i.e. } |z_i| < 1, i = 1, \dots, \bar{n}.$$

ii. all coefficients $\bar{a}_i (i = 1, \dots, \bar{n} - 1)$ of the characteristic polynomial

$$w_{\bar{A}-I} = \det(I_{\bar{n}} z - \bar{A} + I_{\bar{n}}) = z^{\bar{n}} + \bar{a}_{\bar{n}-1} z^{\bar{n}-1} + \dots + \bar{a}_1 z + \bar{a}_0$$

are positive, i.e. $\bar{a}_i > 0, i = 0, 1, \dots, \bar{n} - 1$

iii. all the principal (leading) minors $\Delta_i (i = 1, 2, \dots, \bar{n})$ of the matrix $A = (I_{\bar{n}} - \bar{A})$ are positive, i.e.

$$(11) \quad |a_{11}| > 0, \begin{vmatrix} a_{11} & a_{12} \\ a_{12} & a_{22} \end{vmatrix} > 0, \dots, \det A > 0$$

where

$$(12) \quad A = (I_{\bar{n}} - \bar{A}) = \begin{bmatrix} a_{11} & a_{12} & \dots & a_{1\bar{n}} \\ a_{21} & a_{22} & \dots & a_{2\bar{n}} \\ \vdots & \vdots & \ddots & \vdots \\ a_{\bar{n}1} & a_{\bar{n}2} & \dots & a_{\bar{n}\bar{n}} \end{bmatrix}$$

Proof:

The Lyapunov system (1) is asymptotically stable if and only if, the equivalent standard system (5) is asymptotically stable. The hypothesis of the theorem 2 results directly from theorem of asymptotic stability of the standard discrete-time system [4] and Lemma 2.

Reachability of the Lyapunov systems with delays

Definition 4.

The positive Lyapunov system (1) is called *reachable* if for any given $X_f \in R_+^{n \times n}$ there exists $q \in Z_+, q > 0$ and an input sequence $U_i \in R_+^{n \times m}, i = 0, 1, \dots, q-1$ that steers the state of the system from the initial conditions $X_{-k} = 0, (k = 0, \dots, h)$ to X_f , i.e. $X_q = X_f$.

Theorem 3.

The positive system Lyapunov (1) is reachable if and only if the matrix:

$$(13) \quad R_{\bar{n}} = \begin{bmatrix} \bar{F} & \bar{A}\bar{F} & \dots & \bar{A}^{\bar{n}-1}\bar{F} \end{bmatrix}$$

contains \bar{n} linearly independent monomial columns.

The matrices \bar{A} and \bar{F} are defined by (8).

Proof:

The Lyapunov system (1) is reachable if and only if, the equivalent standard system (5) is reachable. The hypothesis of the theorem 2 results directly from theorem of reachability of the standard discrete-time system [4] and Lemma 2. \square

Extension of The Cayley-Hamilton Theorem for Lyapunov systems with delays

Let $\sigma_{V_k}(\sigma_{\tilde{A}_k})$ be the spectrum of the matrix $V_k = A_k + B_k$ ($\tilde{A}_k = A_k \otimes I_n + I_n \otimes B_k^T$) for $k = 0, \dots, h$ and

$$(14) \quad p(z) = \det(I_{\bar{n}}z - \bar{A}) = z^{\bar{n}} + a_{\bar{n}-1}z^{\bar{n}-1} + \dots + a_1z + a_0$$

$$\bar{n} = n^2(h+1)$$

be the characteristic polynomial of Lyapunov system with h delays (1).

Let

$$(15) \quad \Phi_{i+1} = V_0\Phi_i + V_1\Phi_{i-1} + \dots + V_h\Phi_{i-h}$$

and

$$(16) \quad \Phi_0 = I_n \quad \text{and} \quad \Phi_i = 0 \quad \text{for} \quad i < 0$$

Theorem 4.

If $\sigma_{V_k} \subset \sigma_{\tilde{A}_k}$ for every $k = 0, \dots, h$, then the matrices Φ_i for $i = 1, 2, \dots$ defined by (15) and (16) satisfy the equation

$$(17) \quad \Phi_{\bar{n}} + a_{\bar{n}-1}\Phi_{\bar{n}-1} + \dots + a_1\Phi_1 + \Phi_0 = 0$$

Proof:

Let $\lambda_i^{(k)}, i = 1, 2, \dots, n$ ($\mu_j^{(k)}, j = 1, 2, \dots, n$) be the eigenvalues of the matrix A_k (B_k) for $k = 0, \dots, h$. Then

by Lemma 3 ($\lambda_i^{(k)} + \mu_j^{(k)}$) for $i, j = 1, 2, \dots, n$ are the eigenvalues of the matrix \tilde{A}_k . From the Cayley-Hamilton theorem for the standard discrete-time systems with delays we have that the equation:

$$(18) \quad \tilde{\Phi}_{\bar{n}} + a_{\bar{n}-1}\tilde{\Phi}_{\bar{n}-1} + \dots + a_1\tilde{\Phi}_1 + \tilde{\Phi}_0 = 0$$

is satisfied by the matrices defined by:

$$(19) \quad \tilde{\Phi}_{i+1} = \tilde{A}_0\tilde{\Phi}_i + \tilde{A}_1\tilde{\Phi}_{i-1} + \dots + \tilde{A}_h\tilde{\Phi}_{i-h}$$

If $\sigma_{V_k} \subset \sigma_{\tilde{A}_k}$ then $\sigma_{\Phi_i} \subset \sigma_{\tilde{\Phi}_i}$ (for $i = 1, 2, \dots, \bar{n}$) and from the definition of function of a matrix we have that the equation (18) implies (17). \square

Example

Let us consider the system (1) with the matrices:

$$A_0 = \begin{bmatrix} -1 & 0 \\ 0 & -1 \end{bmatrix}, B_0 = \begin{bmatrix} -3 & 0 \\ 0 & -2 \end{bmatrix}, A_1 = \begin{bmatrix} 1 & 0 \\ 0 & 1 \end{bmatrix}, B_1 = \begin{bmatrix} 1 & 0 \\ 0 & 2 \end{bmatrix}$$

Using (7) and (8) we obtain

$$\bar{A} = \begin{bmatrix} \tilde{A}_0 & \tilde{A}_1 \\ I_{n^2} & 0 \end{bmatrix} = \begin{bmatrix} -4 & 0 & 0 & 0 & 2 & 0 & 0 & 0 \\ 0 & -3 & 0 & 0 & 0 & 3 & 0 & 0 \\ 0 & 0 & -4 & 0 & 0 & 0 & 2 & 0 \\ 0 & 0 & 0 & -3 & 0 & 0 & 0 & 3 \\ 1 & 0 & 0 & 0 & 0 & 0 & 0 & 0 \\ 0 & 1 & 0 & 0 & 0 & 0 & 0 & 0 \\ 0 & 0 & 1 & 0 & 0 & 0 & 0 & 0 \\ 0 & 0 & 0 & 1 & 0 & 0 & 0 & 0 \end{bmatrix}$$

and

$$V_0 = A_0 + B_0 = \begin{bmatrix} -4 & 0 \\ 0 & -3 \end{bmatrix}, V_1 = A_1 + B_1 = \begin{bmatrix} 2 & 0 \\ 0 & 3 \end{bmatrix}$$

The characteristic polynomial (14) is:

$$p(z) = \det(I_{\bar{n}}z - \bar{A}) = z^8 + 14z^7 + 63z^6 + 62z^5 - 191z^4 - 168z^3 + 408z^2 - 216z + 36$$

We compute the matrices $\Phi_i, i = 1, \dots, 8$ from the formula (15):

$$\Phi_0 = \begin{bmatrix} 1 & 0 \\ 0 & 1 \end{bmatrix}, \Phi_1 = \begin{bmatrix} -4 & 0 \\ 0 & -3 \end{bmatrix}, \Phi_2 = \begin{bmatrix} 12 & 0 \\ 0 & 18 \end{bmatrix},$$

$$\Phi_3 = \begin{bmatrix} -80 & 0 \\ 0 & -45 \end{bmatrix}, \Phi_4 = \begin{bmatrix} 356 & 0 \\ 0 & 171 \end{bmatrix},$$

$$\Phi_5 = \begin{bmatrix} -1584 & 0 \\ 0 & -648 \end{bmatrix}, \Phi_6 = \begin{bmatrix} 7048 & 0 \\ 0 & 2457 \end{bmatrix},$$

$$\Phi_7 = \begin{bmatrix} -31360 & 0 \\ 0 & -9315 \end{bmatrix}, \Phi_8 = \begin{bmatrix} 139536 & 0 \\ 0 & 35316 \end{bmatrix}.$$

Using (17) we obtain:

$$p(z) = \Phi_8 + 14\Phi_7 + 63\Phi_6 + 62\Phi_5 - 191\Phi_4 - 168\Phi_3 + 408\Phi_2 - 216\Phi_1 + 36\Phi_0 = \begin{bmatrix} 0 & 0 \\ 0 & 0 \end{bmatrix}$$

Conclusions

The notion of positive discrete-time linear Lyapunov system with delays has been introduced. Necessary and sufficient conditions for the positivity (Theorem 1), asymptotic stability (Theorem 2) and the reachability (Theorem 3) of this system have been established. The Cayley-Hamilton theorem has been extended for linear Lyapunov systems with delays (Theorem 4). The considerations have been illustrated on the numerical example. An extension of these considerations for positive continuous-time Lyapunov systems is an open problem.

The work was supported by the State Committee for Scientific Research of Poland under grant No. 3T11A00628.

REFERENCES

- [1] Benvenuti L. and Farina L., A tutorial on positive realization problem, IEEE Trans. Autom. Control, vol. 49, No 5, 2004, pp. 651-664.
- [2] Busłowicz M. and Kaczorek T., Reachability and minimum energy control of positive linear discrete-time systems with one delay, 12th Mediterranean Conference on Control and Automation, June 6-9, 2004, Kusadasi, Izmir, Turkey.
- [3] Farina L. and Rinaldi S., Positive Linear Systems; Theory and Applications, J. Wiley, New York 2000.
- [4] Kaczorek T., Positive 1D and 2D systems, Springer Verlag, London 2001.
- [5] Kaczorek T., Vectors and Matrices in Automation and Electrotechnics, Wydawnictwo Naukowo-Techniczne, Warszawa 1998 (in Polish).
- [6] Kaczorek T., New reachability and observability tests for positive linear discrete-time systems, Bull. Pol. Acad. Sci. Techn. vol. 55, No. 1, 2007.
- [7] Kaczorek T., Realization problem for positive discrete-time systems with delay, System Science, vol. 30, No. 4, 2004, pp.117-130.
- [8] Kaczorek T., Realization problem for positive multivariable discrete-time linear systems with delays in the state vector and inputs, Int. J. Appl. Math. Comp. Sci. 2006, vol. 16, No. 2, pp. 101-106.
- [9] Kaczorek T., A realization problem for positive continuous-time systems with reduced number of delays, Int. J. Appl. Math. Comp. Sci. 2006, vol. 16, No. 3, pp. 101-117.
- [10] Kaczorek T., Positive discrete-time linear Lyapunov systems, Submitted to The 15th Mediterranean Conference of Control and Automation – MED 2007, 27-29 June, Athens.
- [11] Kaczorek T., Stability of positive discrete-time systems with time-delay, The 8th World Multi-Conference on Systemics, Cybernetics and Informatics, July 18-21, 2004 ~ Orlando, Florida, USA.
- [12] Kaczorek T. and Busłowicz M., Minimal realization problem for positive multivariable linear systems with delay, Int. J. Appl. Math. Comp. Sci. 2004, vol. 14, No. 2, pp. 181-187.
- [13] Kaczorek T. and Busłowicz M., Recent developments in theory of positive discrete-time linear systems with delays – stability and robust stability, Pomiary, Automatyka, Kontrola, No 9, 2004, pp. 9-12
- [14] Kaczorek T. and Busłowicz M., Recent developments in theory of positive discrete-time linear systems with delays – reachability, minimum energy control and realization problem Pomiary, Automatyka, Kontrola, No 9, 2004, pp. 12-15.
- [15] Kaczorek T. and Przyborowski P., Positive continuous-time linear Lyapunov systems, Submitted to The International Conference on Computer as a Tool EUROCON 2007, 9-12 September, Warsaw.
- [16] Kaczorek T. and Przyborowski P., Positive continuous-time linear time-varying Lyapunov systems, Submitted to The XVI International Conference on Systems Science, 4-6 September, Wrocław - Poland.
- [17] Kaczorek T. and Przyborowski P., Continuous-time linear Lyapunov cone-systems, Submitted to 13th IEEE IFAC International Conference on Methods and Models in Automation and Robotics, 27 - 30 August 2007, Szczecin - Poland.
- [18] Kaczorek T. and Przyborowski P., Reachability, controllability to zero and observability of the positive discrete-time Lyapunov systems, Submitted to The Control and Cybernetics Journal, 2007.
- [19] Klamka J., Controllability of dynamical systems, Kluwer Academic Publ. Dordrecht 1991
- [20] Murty M.S.N. and Apparao B.V., Controllability and observability of Lyapunov systems, Ranchi University Mathematical Journal 2005, vol. 32, pp. 55-65.

Authors:

Prof. Tadeusz Kaczorek
Politechnika Warszawska
Instytut Sterowania i Elektroniki Przemysłowej
ul. Koszykowa 75, 00-662 Warszawa Poland,
E-mail: <mailto:Kaczorek@isep.pw.edu.pl>
Mgr. inż. Przemysław Przyborowski
Politechnika Warszawska
Instytut Sterowania i Elektroniki Przemysłowej
ul. Koszykowa 75, 00-662 Warszawa Poland,
E-mail: <mailto:Przyborp@isep.pw.edu.pl>

Finding parametric characteristics in diode-transistor circuits

Abstract. The paper is devoted to the analysis of transistor circuits having multiple DC solutions. A method for tracing multivalued parametric characteristics expressing output signals in terms of some parameters is offered. The proposed approach utilizes the previously developed method for finding all the DC solutions of circuits containing the Ebers-Moll modeled transistors and the Newton-Raphson algorithm. Unlike the SPICE which usually loses some branches or exhibits apparent hysteresis the proposed method gives complete characteristics. It is illustrated via numerical examples.

Streszczenie. W pracy przedstawiono metodę wyznaczania wielowartościowych charakterystyk parametrycznych w stałoprądowych układach tranzystorowych. Wykorzystuje ona wcześniej opracowaną metodę znajdowania wszystkich rozwiązań DC oraz algorytm Newtona-Raphsona i pozwala wyznaczyć pełne charakterystyki wyrażające sygnał wyjściowy w funkcji pewnych parametrów obwodowych. Symulator SPICE w przypadku takich charakterystyk gubi niektóre gałęzie lub daje błędną charakterystykę w postaci pętli histerezy. Przykłady numeryczne potwierdzają skuteczność zaproponowanego podejścia. (**Wyznaczanie charakterystyk parametrycznych w układach diodowo-tranzystorowych**).

Keywords: DC analysis, multiple solutions, parametric characteristics, transistor circuits.

Słowa kluczowe: Analiza stałoprądowa, wiele rozwiązań, charakterystyki parametryczne, układy tranzystorowe.

Introduction

Analysis of nonlinear transistor circuits having multiple DC solutions is a basic, still open and difficult problem of the design of electronic circuits [1]-[10]. The existing methods in this area are able to analyze only rather small-scale circuits. In the paper [6] a method is proposed, for finding all the DC solutions of transistor circuits, which significantly improves the idea of successive contraction, division, and elimination. This method can be applied to tracing multivalued or even multibranched parametric characteristic, which expresses an output signal (voltage or current) in terms of some parameter (e.g. a resistor). The characteristics are very useful in the fault diagnosis of electronic circuits, when the simulation before test approach is employed. To decrease the amount of computations, instead of using the brute-force approach based on method [6], a combination of this method and the Newton-Raphson algorithm is proposed.

Tracing parametric characteristics in diode-transistor circuits

This section is devoted to tracing characteristics expressing an output signal y (voltage or current) in terms of some parameter, e.g. resistance R , in diode-transistor circuits. If a circuit has multiple DC solutions, for the considered resistance value, the characteristic is multivalued or even multibranched. To find the characteristic $y = F(R)$ at different values of the parameter in a prescribed range we propose the algorithm based on the method for finding all the DC solutions, developed in [6]. For this purpose a mathematical representation of the circuit, explicitly depending on the parameter, is needed. To derive the representation we consider a circuit containing t Ebers-Moll modeled transistors, d diodes, linear resistors including the resistor R , and independent sources.

We extract all the transistors, diodes and the resistor R from the circuit. In this way an $(n+1)$ -port is created, where $n = 2t + d$, composed of linear resistors and independent sources. Let the port $(n+1)$ correspond to the resistor R . Using the admittance representation we obtain

$$(1) \quad \begin{bmatrix} i_1 \\ \vdots \\ i_n \\ i_{n+1} \end{bmatrix} = \begin{bmatrix} \hat{G} \\ \hline G_{n+1,1} & \cdots & G_{n+1,n} & G_{n+1,n+1} \end{bmatrix} \begin{bmatrix} v_1 \\ \vdots \\ v_n \\ v_{n+1} \end{bmatrix} = [b_1 \ \cdots \ b_n \ b_{n+1}]^T,$$

where i_1, \dots, i_n (v_1, \dots, v_n) are the port currents (voltages) corresponding to the transistors and diodes, i_{n+1} (v_{n+1}) is the port current (voltage) corresponding to the resistor R , $\hat{G} = [G_{ij}]_{n \times (n+1)}$ is the upper part of the admittance matrix, and $[b_1 \ \cdots \ b_n \ b_{n+1}]^T = [b^T \ | \ b_{n+1}]^T$ is a source vector. Using the Ebers-Moll model of transistors we write

$$\begin{bmatrix} i_1 \\ \vdots \\ i_n \end{bmatrix} = \mathbf{T} \mathbf{f}(\mathbf{v}), \quad \mathbf{v} = \begin{bmatrix} v_1 \\ \vdots \\ v_n \end{bmatrix}, \quad \mathbf{f}(\mathbf{v}) = \begin{bmatrix} f_1(v_1) \\ \vdots \\ f_n(v_n) \end{bmatrix},$$

where \mathbf{T} is a block diagonal matrix composed of the blocks $\begin{bmatrix} 1 & -\alpha_R \\ -\alpha_F & 1 \end{bmatrix}$ and a unit matrix, whereas $f_i(v_i) = K_i(e^{\lambda v_i} - 1)$. Hence, it follows

$$(2) \quad \mathbf{T} \mathbf{f}(\mathbf{v}) + \hat{G} \begin{bmatrix} \mathbf{v} \\ v_{n+1} \end{bmatrix} = \mathbf{b},$$

$$(3) \quad \frac{v_{n+1}}{R} + \sum_{j=1}^{n+1} G_{n+1,j} v_j = b_{n+1}.$$

Let

$$(4) \quad g(R) = \frac{R}{1 + R G_{n+1,n+1}},$$

then equation (3) becomes

$$(5) \quad v_{n+1} = g(R) b_{n+1} - \sum_{j=1}^n g(R) G_{n+1,j} v_j.$$

Matrix \hat{G} can be presented in the form

$$(6) \quad \hat{G} = \begin{bmatrix} \tilde{G} & G_{1,n+1} \\ & \vdots \\ & G_{n,n+1} \end{bmatrix}.$$

Multiplying both sides of equation (2) by T^{-1} we obtain

$$(7) \quad f(v) + \tilde{A}v + \tilde{d}v_{n+1} = \tilde{b},$$

where

$$\tilde{A} = [\tilde{a}_{ij}]_{n \times n} = T^{-1} \tilde{G}, \quad \tilde{d} = \begin{bmatrix} \tilde{d}_1 \\ \vdots \\ \tilde{d}_n \end{bmatrix} = T^{-1} \begin{bmatrix} G_{1,n+1} \\ \vdots \\ G_{n,n+1} \end{bmatrix},$$

$\tilde{b} = T^{-1}b$. Using (5) and (7) yields

$$(8) \quad f(v) + Av = c,$$

where $A = [a_{ij}]_{n \times n}$, $a_{ij} = \tilde{a}_{ij} - \tilde{d}_i g(R) G_{n+1,j}$, $c_i = \tilde{b}_i - \tilde{d}_i g(R) b_{n+1}$. Thus, matrix A and vector c , in equation (8) depend explicitly on R :

$$(9) \quad A = \tilde{A} - \tilde{A}g(R),$$

where $\tilde{A} = [\tilde{a}_{ij}]$, $\tilde{a}_{ij} = \tilde{d}_i G_{n+1,j}$,

$$(10) \quad c = \tilde{b} - \tilde{d}g(R),$$

where $\tilde{d} = \tilde{d}b_{n+1}$.

To find the characteristic $y = F(R)$ for $R \in [R^-, R^+]$ we formulate the circuit equation expressing the output signal y in terms of v_1, v_2, \dots, v_{n+1} , in the form

$$(11) \quad y = \sum_{j=1}^{n+1} k_j v_j + k_0.$$

We divide the interval $[R^-, R^+]$ into S_a subintervals with length ΔR_a . At each point of the division we determine A and c using (9) and (10), respectively, and perform the analysis of the circuit using the method for finding all the DC solutions developed in [6]. As a result we obtain a set of the solutions corresponding to v . Next we compute v_{n+1} for each of the solutions using (5) and substitute it into equation (11). In this way some points of the characteristic are determined. To decrease the amount of computations we choose the increment ΔR_a rather large. Therefore the obtained characteristic is incomplete and some essential information may be lost. To overcome this drawback we perform additional analyses with small increment ΔR_N (say 1% of ΔR_a) using the Newton-Raphson algorithm as described underneath. Let us consider i -th subinterval

$[(R^-)^i, (R^+)^i]$ having the length ΔR_a . For each of the solutions corresponding to $(R^-)^i$ we choose $R = (R^-)^i + \Delta R_N$ and determine A and c using (9)-(10). Next we solve equation (8) using the Newton-Raphson algorithm. As the initial guesses we pick the earlier determined solution at $(R^-)^i$. In this way we find the points of the characteristic at R . This process is continued until the end of the subinterval $(R^+)^i$ is reached, or a turning point occurs. In the first case we check if the solutions obtained using the Newton-Raphson algorithm coincides with the solutions determined by the method proposed in [6]. If this condition is satisfied we repeat the procedure for subsequent subinterval. If the number of all the solutions at $(R^+)^i$ is greater than the number of solutions obtained using the Newton-Raphson algorithm, at least one turning point occurs in the considered subinterval. In such a case we select all the solutions which have not been found by the Newton-Raphson algorithm and continue the algorithm with the initial guesses equal to these solutions, decreasing the parameter until the turning point is reached. Every time when a turning point is reached we carry out additional analyses in the neighborhood of this point using the method for finding all the DC solutions [6]. Taking into account the obtained results we control the process of tracing the characteristic.

Note. The increments ΔR_a and ΔR_N depend on the length the interval $[R^-, R^+]$ and may be different in different decades.

Numerical examples

To illustrate the approach proposed above we consider two numerical examples.

Example 1

Let us consider the transistor circuit shown in Fig. 1, composed of two Schmitt's triggers. The transistors are characterized by the Ebers-Moll model: ($\alpha_F = 0.99$, $\alpha_R = 0.5$, $\lambda = 38.67$, $K_i = 7.068$ fA ($i = 1, 3, 5, 7$), $K_i = 13.995$ fA ($i = 2, 4, 6, 8$), with additional 1 Ω emitter and collector resistors and 3 Ω base resistor. In this circuit we find the characteristics $v_{out} = F_1(R_1)$, $v_{out} = F_5(R_5)$ and $v_{out} = F_8(R_8)$ for the resistances belonging to the interval [100 Ω , 100k Ω]. We choose $\Delta R_a = 50\Omega$ in the first decade, $\Delta R_a = 500\Omega$ in the second and $\Delta R_a = 5k\Omega$ in the third. The increment ΔR_N equals one percent of ΔR_a . Using the proposed approach we obtain the characteristic plots depicted in Fig. 2. The time consumed by the proposed method, on PC Pentium IV, 3GHz, is 1.04s, 0.52s, and 0.65s, respectively. Figure 3 shows the corresponding characteristics provided by PSPICE [11] simulator, obtained by means of two DC Sweep analyses (up and down), with the step equal to 10 Ω . They exhibit apparent hysteresis and lose some branches of the real characteristics. The same characteristics as shown in Fig. 2 can be obtained using the method for finding all the DC solutions with the increment ΔR_N . This brute force method operates much slower than the proposed one. The time consumed by the brute force method is 50.46s, 73.85s, and 91.08s, respectively.

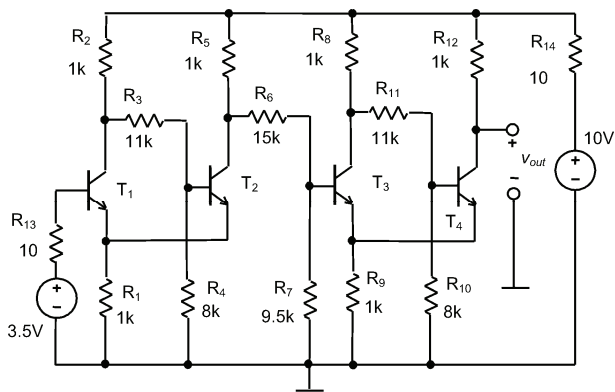


Fig. 1. The circuit composed of two Schmitt triggers

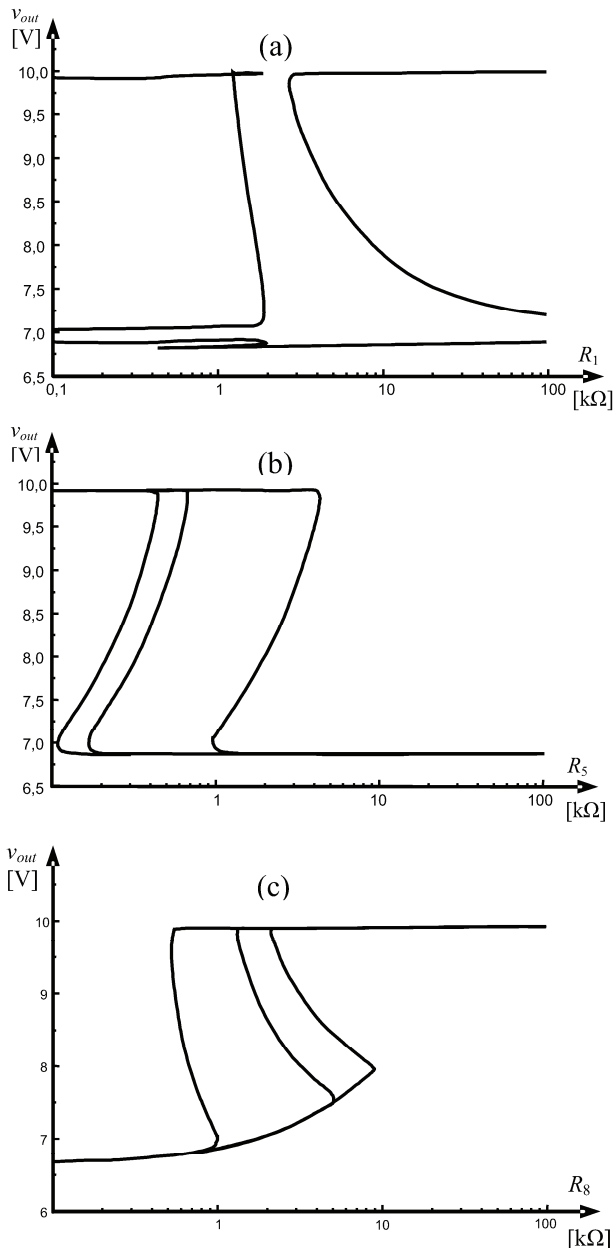


Fig. 2. The parametric characteristics obtained by the proposed method

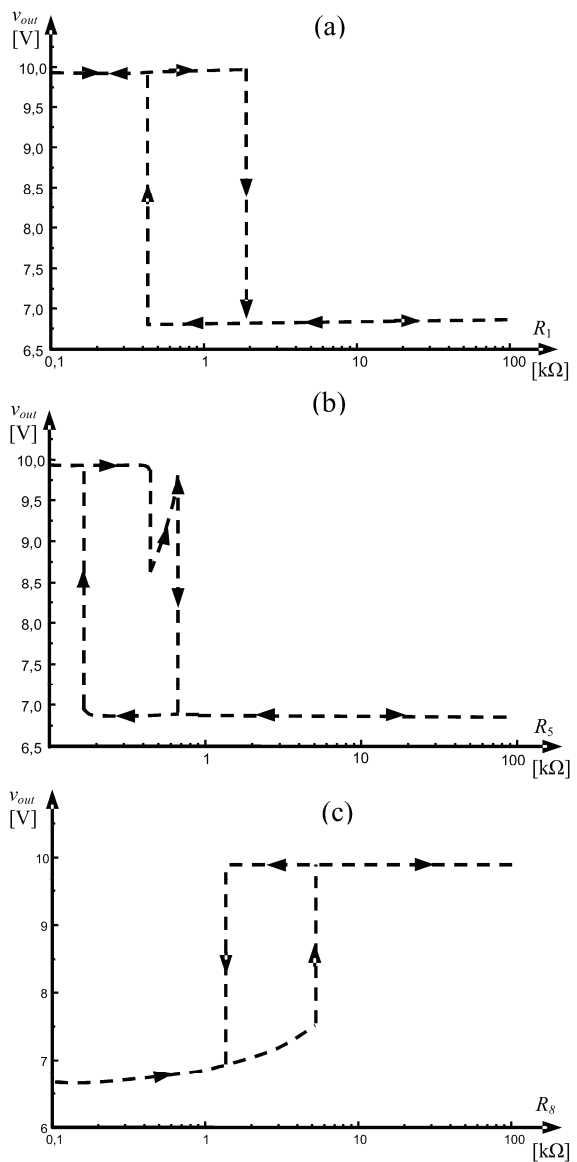


Fig. 3. The parametric characteristics provided by PSPICE

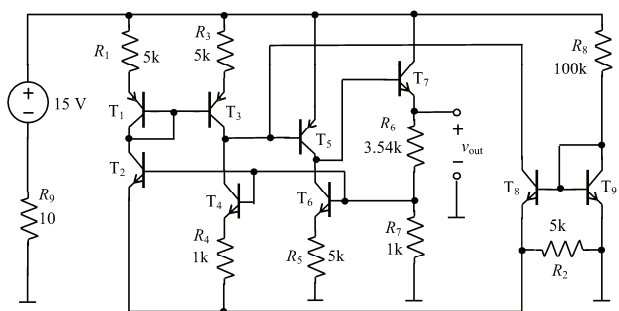


Fig. 4. The voltage regulator

Example 2

Figure 4 shows the voltage regulator analysed in [9]. The transistors are characterized by the Ebers-Moll model ($\alpha_F = 0.99$, $\alpha_R = 0.5$, $\lambda = 38.67$, $K_i = 7.068$ fA ($i = 1, 3, 5, 7, 9, 11, 13, 15, 17$), $K_i = 13.995$ fA ($i = 2, 4, 6, 10, 12, 14, 16, 18$), $K_7 = 35.34$ fA, $K_8 = 69.973$ fA), with additional 10Ω emitter and collector resistors and 3Ω base resistor.

We find the characteristics $v_{out} = F_1(R_1)$ and $v_{out} = F_3(R_3)$, for the resistances belonging to the interval [100Ω,

100kΩ] choosing the increments ΔR_a and ΔR_N similarly as in Example 1. As a result we obtain the characteristics plotted in Fig. 5. The time consumed by the method for computing the characteristics, on PC Pentium IV, 3GHz, is 28.3s, and 28.2s, respectively. The brute force method operates 96 times slower than the proposed one. Figure 6 shows the corresponding characteristics provided by PSPICE simulator, obtained by means of two DC Sweep analyses (up and down) with the step equal to 10Ω. The characteristics exhibit either apparent hysteresis or lose some branches of the real characteristics.

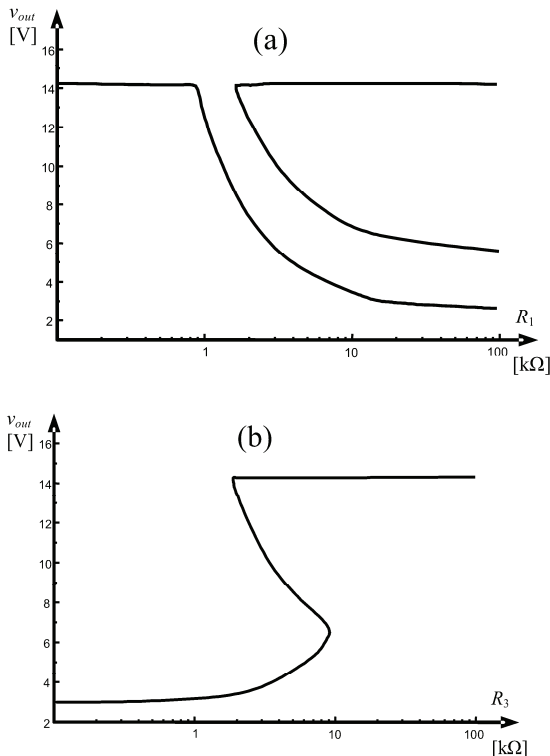


Fig. 5. The parametric characteristics obtained by the proposed method

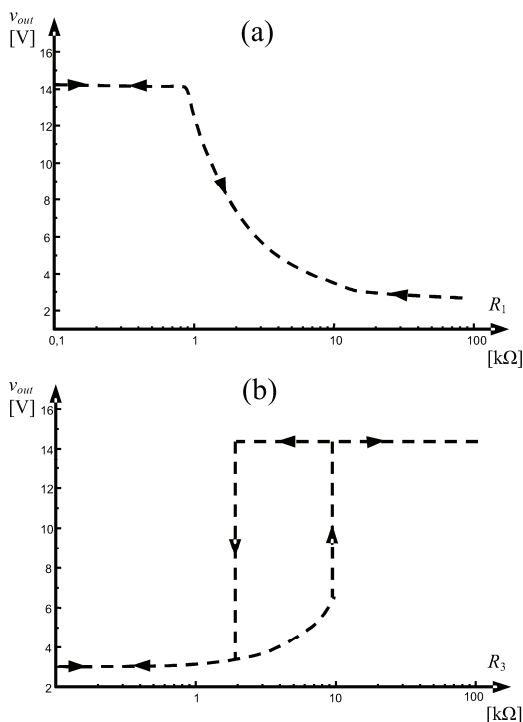


Fig. 6. The parametric characteristics provided by PSPICE

Conclusion

The proposed method enables us to efficiently trace complete multivalued and multibranching parametric characteristics in mid-sized circuits. On the other hand the characteristics provided by PSPICE are fragmentary and usually exhibit apparent hysteresis.

Acknowledgments

This work was supported by the Ministry of Science and Higher Education under Grant 3T 11B 05529.

REFERENCES

- [1] Pastore S., Premoli A., Finding all DC solutions of nonlinear resistive circuits by exploring both polyhedral and rectangular circuits, *IEE. Proc., Cir. Dev. Syst.*, 144 (1997), No. 9, 17-21
- [2] Yamamura K., Kameko R., Finding all solutions of piecewise-linear circuits using simplex method, *IEEE Tran. Cir. Syst. I*, 50 (2003), 160-165
- [3] Tadeusiewicz M., Głowienka K., A contraction algorithm for finding all the DC solutions of piecewise-linear circuits, *J. Cir. Syst. Comp.*, 4 (1994), No. 3, 319-336
- [4] Vandenberghe L., Moor B.L., Vandewalle J., The generalized linear complementarity problem applied to the complete analysis of resistive piecewise-linear circuits, *IEEE Trans. Cir. Syst.*, 36 (1989), No. 11, 1382-1391
- [5] Tadeusiewicz M., Hałgas S., A method for the analysis of transistor circuits having multiple DC solutions, *Int. J. Electron. Commun. (AEÜ)*, 60 (2006), No. 8, 582-589
- [6] Tadeusiewicz M., Hałgas S., Finding all the DC solutions in circuits containing bipolar transistors, *Proc. of Int. Conf. on Signals and Electronic Systems, ICSES'06*, (2006), 361-364
- [7] Kolev L., An interval method for global nonlinear analysis, *IEEE Tran. Cir. Syst. I*, 47 (200), 675-683
- [8] Reibiger A., Mathis W., Nähring T, Trajković Lj., Mathematical foundations of the TC-method for computing multiple DC-operating points, *Int. J. Appl. Electromagnet. Mech.*, 17 (2003), 169-191
- [9] Goldgeisser L.B., Green M.M., A method for automatically finding multiple operating points in nonlinear circuits, *IEEE Trans. Cir. Syst. I*, 52 (2005), 776-784
- [10] Yamamura K., Igarashi N., An interval algorithm for finding all solutions of non-linear resistive circuits, *Int. J. Cir. Theor. Appl.*, 32 (2004), 47-55.
- [11] Quarles T.L., Newton A.R., Pederson D.O., Sangiovanni-Vincentelli A., SPICE-3 Version 3F5 User's Manual, Berkley, CA: Dep. of EECS, Univ. California, 1994.

Authors: dr inż. Stanisław Hałgas, prof. dr hab. inż. Michał Tadeusiewicz, Politechnika Łódzka, Instytut Elektrotechniki Teoretycznej, Metrologii i Materiałoznawstwa, ul. Stefanowskiego 18/22, 90-924 Łódź, E-mail: stanislaw.halgas@p.lodz.pl, michal.tadeusiewicz@p.lodz.pl.

Economical mathematical model for Ukrainian electroenergetic complex management

Abstract. A closed model of the material and financial balance is developed for electrical energetics of Ukraine. The model is verified by the current branch information of 2003-2006. The links between consumer's income and energy payment level are investigated.

Streszczenie. W artykule przedstawiono wyprowadzenie zamkniętego modelu bilansu finansowo-materiałowego dla systemu elektroenergetycznego Ukrainy. Model został zweryfikowany przy wykorzystaniu aktualnych danych dla lat 2003-2006. Przedyskutowano powiązania pomiędzy zyskami użytkowników a poziomem cen energii elektrycznej. (**Ekonomiczny model matematyczny dla ukraińskiego systemu elektroenergetycznego**).

Keywords: Energetic complex, material and financial balance, forecasting scenarios, consumer's characteristics.

Słowa kluczowe: system elektroenergetyczny, bilans finansowy.

Introduction

The fuel energetic complex plays the leading role in the regeneration of the Ukrainian economics by providing sufficient and reliable energy supply to all parts of economics. This is the necessary condition of its normal functioning and development. The most important factors of bringing economics to efficient state are the mechanisms of financing based on efficient price, tax and investment policy of the State. The analytical basis available for forming the problem decisions of management and evaluation of their consequences in the field of energetic policy is insufficient under quickly changing conditions of market economics formation. The role of fuel-energetic complex in the State economics is of decisive importance therefore the creation of economical mathematical instruments is evidently necessary. These instruments should be able to form the main quantitative parameters of various scenario of national policy in the field of power engineering and to predict their consequences for economics both in short-term and remote period. It is also evident that the peculiarities of energetics and economics as a whole of the country for which those instruments are created should be taken into account.

The methodological basis of this instrument is an economical mathematical model constructed by the scheme of material and financial balance of the branch. The problems of indicators analysis of part of fuel-energetic complex that is related to the production, transmission and distribution of electric energy are considered here. The peculiarity of the Ukrainian fuel-energetic complex structure is in the fact that the part of nuclear energetics (NEP) within the total production of electric energy is approximately 50 %, the part of heat energetics (HEP) is 40 %, of hydro stations (HS) and the sources of other kinds of energy are 10 %. The main amount of the primary non-renewal fuel resources that are produced and consumed for electric energy production is the solid fuel (coal). Under these circumstances, the problems of fuel-energetic complex which must be promptly solved seriously affect the activity of the fuel energy generating companies. Therefore the problem of thorough analysis and short-term prediction just for this part of fuel-energetic complex is especially urgent.

The economical mathematical model of the power engineering branch is the set of balance equations of supply and demand of goods in energy and energy carrier markets, of functional relations between the amounts of energy generation and energy carrier consumption by various manufacturers, of balance equations of financial resources in the main companies of the Ukrainian fuel-energetic complex.

The difficulties of the model formation are caused by seasonal fluctuations of electric energy and energy carrier consumption volumes, by significant variations of their price conjuncture and by negative fuel-energetic complexes of tardiness of payments between energy, raw materials and equipment suppliers and consumers. The model is intended for searching appropriate tactic decisions by complex management using quantitative estimation of their consequences.

The model structure

The statistical data on fuel-energetic complex functioning in Ukraine during 2003-2006 were used as the primary data for model construction. The model is based on the data of predicted monthly electric energy demand of the main consumers and on the characteristics of specific fuel consumptions for electric energy generation. These data (with the losses in low-voltage networks and high-voltage networks taken into account) are the basis for defining electric energy output by producers and necessary fuel amount for its generation. The last-mentioned amounts are calculated on a basis of fuel expenditure characteristics for generating blocks of a HEP. As example the characteristics for block 300K of Krivorozhaska HEP is presented on Fig. 1.

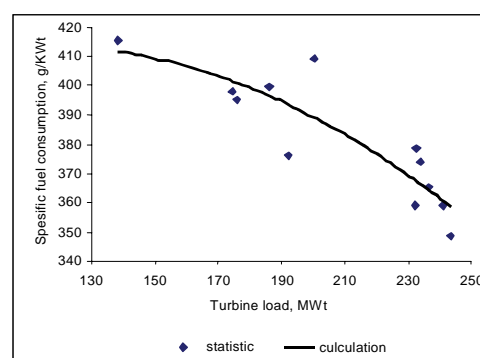


Fig. 1. Example of fuel expenditure characteristics for generating block.

The equations of material balance are formed for two kinds of natural fuel: coal and fuel oil (the accumulation of gas in underground reservoirs is not considered). The amounts of fuel in-stock balance are defined by the accepted accumulation strategy and may not be under a certain level. This is a limiting condition. If the balance for coal appears negative, the use of gas is an equilibrating factor.

The manufacturing costs of the electrical energy generated by any company $E_{Cost_{Gen}}(t)$ are defined by a prime cost $PrimeCost(t)$, which consist material costs (dominantly by fuel), a costs of wages and social payments, a costs of depreciation and other costs, and benefits of company $Profit(t)$:

$$(1) \quad E_{Cost_{Gen}}(t) = PrimeCost(t) + Profit(t).$$

The seasonal character of fuel consumption in HPS should be taken into account; it depends on the type and regime of equipment work. The fuel prices are changed in time and may be different for different companies. The costs of wages and social payments and other costs depend on inflation index.

The profit of an energy generating company is formed as a result of a competition on a wholesales market. Hence, a profitness of an individual company may be a varied volume. The wholesale price of energy $Pr E_W$, which is sailed by producers in energy market, is estimated by summary costs of all generating companies with the account of planned profit and by summary energy volume for sale V_E :

$$(2) \quad Pr E_W = \sum_{comp} E_{Cost_{Gen}}(t) / \sum_{comp} V_E,$$

where \sum_{comp} is the summary symbol for all generating companies.

In the wholesale energy market the costs of market and Ukrenergo Company operation Exp_W , the appropriate profit $Prof_W$ and investment extra charge Inv to electric energy price are added. As a result, the wholesale rate of suppliers on the market $Pr E_{sup}$ is (with the account of energy losses in high-voltage networks ΔV_{line}):

$$(3) \quad Pr E_{sup} = (V_E * Pr E_W + Exp_W + Prof_W) / (V_E - \Delta V_{line}).$$

The energy in wholesale market is purchased by the companies (oblenergo and other wholesale suppliers) which realize energy supply to consumers. The costs of these companies for energy transmission and distribution Exp_{cons} involve the costs for purchasing some energy amounts V_{cons} by wholesale price $Pr E_{cons}$, estimated costs for distributive company operation Exp_{distr} and its planned profit $Prof_{distr}$. The average energy price for consumers $Pr E_{cons}$ is determined with the account of energy losses in power transmission lines ΔV_{distr} :

$$(4) \quad Pr E_{cons} = (V_{cons} * Pr E_{cons} + Exp_{distr} + Prof_{distr}) / (V_{cons} - \Delta V_{distr}).$$

The model operates with the average price indices and payments of consumers as a whole without separating kinds of consumers.

It has been known that the consumers do not pay off for electric energy in full measure. These payments come to bank accounts of SE "Wholesale market of electric energy" (WMEE) and are distributed between market participants by a certain algorithm. The immediate payments for recoat the costs of fuel $Cost_{fuel}$, wages $Cost_{wage}$, for fuel stock replenishment $Cost_{stock}$, other costs $Cost_{other}$ are taken from the sums which come from WMEE at the account of

generating company as a realization income $Income$. These sums are expended also in order to pay for value-added tax VAT, profit tax PT , dividends Div and creditors Cr .

The net monetary flow MF for generating company is formed as follows

$$(5) \quad MF = Income - Cost_{fuel} - Cost_{wage} - Cost_{stock} - Cost_{other} - VAT - PT - Div - Cr.$$

If the monetary flow appears negative the company needs crediting for floating capital replenishment.

Thus the closed economical mathematical model is obtained. That model involves the following balance equations: energy supply and demand in market; fuel resources; financial resources of companies; the financial indices and monetary balances companies taking account the payment levels for energy consumed [1].

The model is verified by the data of statistical accounting of Ukrainian fuel-energetic complex in 2003-2004. The examples of comparison by calculated and statistical data are presented at Figs. 2 and 3. Fig. 2 shows the results of control computations of fuel purchase dynamics by Vostokenergo Company.

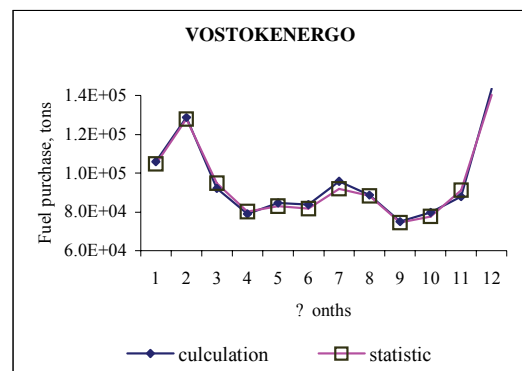


Fig. 2. Results of the fuel purchase modelling vs statistical data.

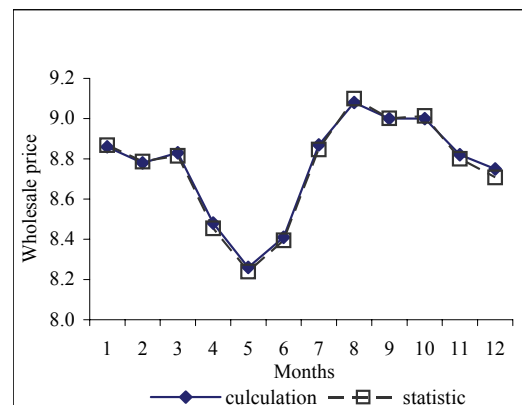


Fig. 3. The dynamics of wholesale price evaluation for electrical energy.

Fig. 3 presents the results of electric energy wholesale price dynamics. The results of comparison confirm good coincidence of statistic data and those obtained by the model computation.

The application of the model permits the study of relation between fuel price and electric energy wholesale price variation and dynamics of economic factors of functioning. The model allows also analyzing the dynamics of credit obligations of companies when economic factors of fuel-energetic complex operation are changed.

Along with the above scenario of fuel-energetic complex development prognosis for short-term prospect, the model makes possible to reach compromise between fuel-energetic complex enterprise activities (when essential deviation of situation from basic scenario is appeared). Thus the reliable and efficient electric energy generation is provided.

The model of short-term prognosis of technical economic factors in fuel energetic complex of Ukraine is realized in program medium Excel as 40 pages of interconnected electronic tables of data and formulas.

The model reproduces dynamics of technical economic factors with monthly separation of time variations. The specification of technical factors is performed for power generating blocks and separate electric plants .

The specification of economic factors is made for separate generating companies and the largest HEC such as Kiev HEC-5 and HEC-6 and Kharkov HEC-5.

The model represents dynamics of technical economic factors of NEC "Ukrenergo", State enterprise (SE) "Energorynok", SE "Ukrinterenergo" and "Oblenergo" (low-voltage distributive network) companies. The technique of processing statistical data on payment levels for the analysis of their dynamics is extended to the analysis of payment level data for electric energy by its final (generalized) consumers.

In the process of model design, special methods of statistical data processing are used for plotting approximating characteristics. These latter show dynamics of payment level for commodity production supplied by generating companies to market. The econometric analysis of factors influencing the formation of disbursing price of commodity production is made.

The above basic principles of constructing technical economic model for heat generation may be also used for constructing the models of generating companies "Energoatom", "Dneprogidroenergo" and "Dnestrogidroenergo".

Consumer analysis

The availability of consumers' debts is one of peculiarities of Ukrainian electro energetic market operation. It is evident that payment level is correlated to the payer's income level, a proportion of the cost of electrical energy consumed in those incomes, general expenditures level for different categories of consumers. It is necessary to state from statistical data the quantitative characteristics of a link between expectative electro energy consumption and payment levels for different categories of consumers. The most power-intensive categories of consumers were investigated: households, general government and such types of economical activities as coal, metallurgy, chemistry, machine building, agriculture and other industries.

General government enterprises have paid from state budget expenditures for electro energy consumed. Then general state budget expenditures must be analyzed and a part of those expenditures, which is intended for energy payment, must be estimated.

The reduced budget expenditures are subdivided into obligatory discharges (protected items) and all other $OtherExp(t)$, which involve a payment for electro energy consumed. A percent of economical value energy consumed by general government in unprotected items of reduced budget expenditures is following

$$(6) \quad EnergyPartExp(t) = \frac{EOutput(t)}{OtherExp(t)} \cdot 100\%,$$

and level of energy payment is

$$(7) \quad PayLevel(t) = \frac{EnergyExp(t)}{EOutput(t)} \cdot 100\%$$

where $EOutput(t)$ is economical value energy consumed by general government, $EnergyExp(t)$ is reduced budget expenditures on energy consumed, thousand hrn.

Then relation of payment levels and $EnergyPartExp(t)$ is obtained by statistical data 2003-2006 as following approximation function

$$(8) \quad PayLevel(t) = a_0 + a_1 \cdot EnergyPartExp(t).$$

As volume of energy supplied by general government $EGen(t)$ changes seasonally we should analyze the function $EGen(t)$ growth rates:

$$(9) \quad GrowthRateEGen(t) = \frac{EGen(t)}{EGen(t-12)} \cdot 100\%.$$

Function $GrowthRateEGen(t)$ trend is built by 2003-2006 statistical data as linear function and is used for energy consumption prognosis.

An average price of 1kWh consuming household energy $AveragePriceHousehold(t)$ was obtained for analysis of household energy consumption dynamics:

$$(10) \quad AveragePriceHousehold(t) = \frac{EConsHousehold(t)}{EnergyHousehold(t)},$$

where $EConsHousehold(t)$ is economical value of energy, which is consumed by all households; $EnergyHousehold(t)$ is natural volume of energy consumed by households on average one household is following:

$$(11) \quad EnergyOneHouse(t) = \frac{EnergyHousehold(t)}{Household(t)},$$

where $EnergyOneHouse(t)$ is energy volume consumed by all investigated households, $Household(t)$ is the average number of investigated households for a monitoring period.

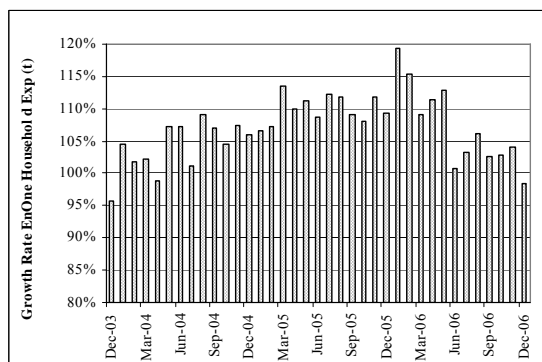


Fig.4. The growth rates function for energy consumed one household.

As volume of energy, which supplied by one household, changes seasonally we should analyze the growth rates function $GrowthRateEnergyOneHouse(t)$. The function is built by statistical data 2003-06 and is shown on the Fig. 4. In according to the trend of function

$GrowthRateEnergyOneHouse(t)$ the monthly volume of energy household consumed is determined on prognosis period:

$$(12) \quad EnergyOneHouse(t) = GrowthRateEnergyOneHouse(t) \times EnergyOneHouse(t - 12)$$

Dependence a consuming energy payment level $PayLevelHousehold(t)$ on energy payment portion $PartEConsTotalPaymentHousehold(t)$ in whole household expenses is investigated. The last-named factor as determined as following:

$$(13) \quad PartEConsTotalPaymentHousehold(t) = \frac{EConsOneHouse(t)}{TotalPaymentHousehold(t)}$$

where $EConsOneHouse(t)$ is economical value of energy consumed by one household, $TotalPaymentHousehold(t)$ is a whole household expense.

The above mentioned relation is built by statistical data 2003-2006 and is approximated by polynomial function:

$$(14) \quad PayLevelHousehold(t) = [a_0 + PartEConsTotalPaymentHousehold(t) \times (a_1 + a_2 \cdot PartEConsTotalPaymentHousehold(t))]$$

Another important factor which must be taking to account in forecasting of consuming energy payment level is significance of energy cost into housing and communal expenses. A portion of housing and communal expenses into a whole household expense are obtained as:

$$(15) \quad PartOutlayCommTotalPaymentHouse(t) = \frac{OutlayHousing(t)}{TotalPaymentHousehold(t)}$$

where $OutlayHousing(t)$ is average monthly housing and communal expenses of household. By function $PartOutlayCommTotalPaymentHouse(t)$, which is a payment characteristic, forecasting estimates of consuming energy payment for household are determined. For this purpose above mentioned function is built by statistical data 2003-2006 and is approximated by polynomial function:

$$(16) \quad PayLevelHouseholdF(t) = a_0 + PartOutlayHousingTotalPaymentHouse(t) \times (a_1 + a_2 \cdot PartOutlayHousingTotalPaymentHouse(t))$$

Volume of energy consumed by particular industry depends on its output, and payment level for energy consumed depends on the fact what part of production cost is energy consumed. For quantitative estimate determination of mentioned relations the growth dynamics for energy consumption and its payment by different industries was investigated. Coal, metallurgy, chemical, machine building, agriculture and other industries integrated in one group was considered. The designed methodology is illustrated on the example of coal industry.

The input data for coal industry output economical value definition in prognosis period $OutputBranchCoalF(t)$ is

monthly data about in prior period. From that data is determined a growth rate of natural value of coalmining production. A growth rate function is shown on Fig.5.

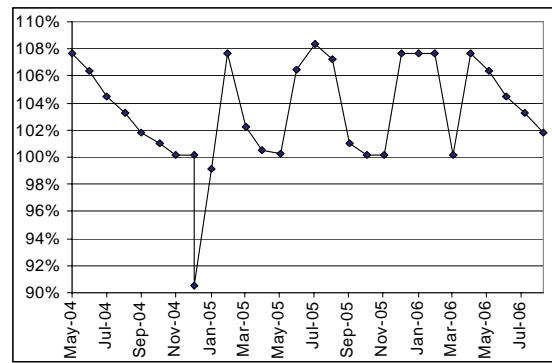


Fig.5. The growth rates function for natural value of coalmining production.

Expected monthly coal industry output economical value is determined with consideration of specified production growth rates and price growth as following:

$$(17) \quad OutputBranchCoalF(t) = GrowthRatePriceBranchCoal(t) \times GrowthRateBranchCoal(t) \cdot OutputBranchCoal(t - 12)$$

Estimate an expected production price using prior period price and specified price growth rate:

$$(18) \quad PriceBranchCoalF(t) = PriceBranchCoal(t - 12) \times GrowthRatePriceBranchCoal(t)$$

and determine a prognostic natural volume of coalmining:

$$(19) \quad BranchCoalF(t) = \frac{OutputBranchCoal(t)}{PriceBranchCoal(t)}$$

Energy volume consumed by coal industry in prognosis period is determined from relationship between changes of energy consumed and changes of production volume:

$$(20) \quad EBranchCoalF(t) = (a_0 + a_1 \times BranchCoalF(t))$$

Expected cost of energy consumed of coal industry is following:

$$(21) \quad OutputEBranchCoalF(t) = EBranchCoalF(t) \times EPriceSupply(t)$$

where $EPriceSupply(t)$ is prognosis 1kWh price Consuming energy payment level depends on a part of energy cost into economical value of coal production:

$$(22) \quad PartOutputEBranchCoal(t) = \frac{OutputEBranchCoal(t)}{OutputBranchCoal(t)}$$

Fig.6 shows a dependence of payment level elasticity vs a part of energy cost into economical value of coal production.

The changes of payment level in prognosis period are determined as approximating linear function of a part of energy cost into economical value of coal production:

$$PayLevelEBranchCoalF(t) = a_0 + a_1 PartOutputEBranchCoal(t)$$

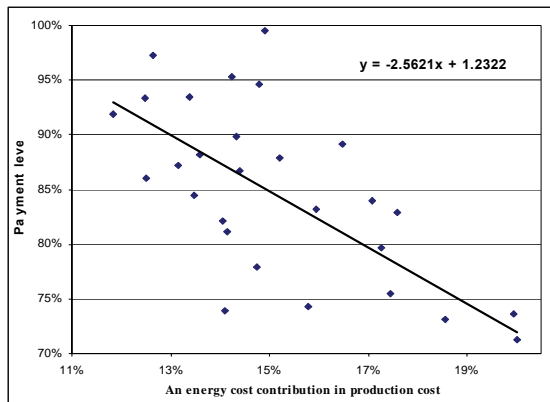


Fig.6. A dependence of payment level elasticity vs a part of energy cost into economical value of coal production.

According to this function an expected energy payment from coal industry is:

$$PaymentEBranchCoalF(t) = PayLevelEBranchCoal(t) \cdot OutputEBranchCoalF(t)$$

Prognosis indicators for other industries are determined analogically. The proposed procedure is applied in the model for short-term monthly prognosis of main technical-economical indicators of Ukrainian power industry in 2004-2007.

REFERENCES

- [1] Saukh S., Semagina E., Tverdokhle N. Commodity and monetary flows model as an instrument for making decision in electrical energy management, "Operation and evolution electrical energy and gas markets", Proceedings of the IPME NAS of Ukraine (Special issue), Kyiv, (2005), 73-85.

Author: *prof. dr hab. Sergiy Saukh, PhD Evelina Semagina, G.E.Pukhov's Institute of Modelling Problems in Energetics, NAS of Ukraine, Naumova st. 15, 03164 Kiev, E-mail: em@jpme.kiev.ua.*

Optimal electric power flow computation

Abstract. The paper proposes a comparative study of the Optimal Active Power Flow computation for a power delivery system. The main goal of the paper is to use different Security models for Optimal Power Flow analysis for the case study. Some models allow power flow computing to obtain the minimum total system generation cost. The comparative study, on the proposed power system, is done considering different restriction of the system. Power flow computation gives information about system efficiency. The economical aspect presents a great deal of interest.

Streszczenie. W artykule przedstawiono studium porównawcze wyznaczania optymalnego rozptywu mocy w systemie elektroenergetycznym. Podstawowym celem artykułu jest porównanie różnych modeli bezpieczeństwa w obliczaniu optymalnego rozptywu mocy. Niektóre z modeli umożliwiają wyznaczenie takiego rozptywu mocy, który zapewnia minimalizację całkowitych kosztów wytworzenia. Studium porównawcze proponowanego systemu uwzględnia rozmaite ograniczenia. Obliczenie rozptywu dostarcza informacji o efektywności systemu. Jest to bardzo interesujące ze względu na aspekt ekonomiczny. (**Obliczenia numeryczne optymalnego rozptywu mocy**).

Keywords: simulation, power Systems, power flow, optimization.

Słowa kluczowe: symulacja komputerowa, systemy energetyczne, rozptyw mocy, optymalizacja.

Introduction

The Optimal Active Power Flow (OAPF) program of EDSA software utilizes a linear programming model, and has two main functions:

- a. Security-constrained active load flow calculations;
- b. Security-constrained economic dispatch calculations.

The features and advantages of this program are:

- a. $N-1$ security analysis is incorporated into the program. Not only N , but also $N-1$ line security is satisfied while an active load flow or economic operating solution is obtained.
- b. Minimum load shedding is incorporated into the program. When load shedding is avoidable, an active load flow or economic operating solution without load shedding is obtained. When load shedding is indispensable due to security constraints, optimal values and bus locations of load shedding are also obtained.

Therefore, the OAPF program is a useful and powerful decision-making tool in selecting an optimal operating schedule, or a reinforcement plan for power system expansion.

Generally load flow analysis by either Newton-Raphson, Siedel Gauss or Fast Decoupled methods, estimates system power flows based on the generation and load levels specified by the user [1], [2]. When convergence is achieved, the results will satisfy the mathematical conditions of the load flow equations. The algorithm will always calculate the real load of all the branches, overloaded or not. Optimal Active Power Flow can take measures to avoid overload conditions that may be present in the system.

Furthermore, the conventional load flow methodology does not take into consideration the operating costs associated with the power system under study, but Optimal Active Power Flow can present such results. The system power generation is not a specified condition but, rather, a calculated value that will not exceed the maximum load restriction imposed on the system branches. This concept is known as branch security. Optimal Active Power Flow analysis can also be used to determine the most economic operating load flow solution, while ensuring that all the conditions for branch security are met [2]-[4]. The model gives the minimum load shedding in order to meet branch security. When load shedding is avoidable, a load flow solution will be obtained without load shedding. When load

shedding is indispensable due to security constraints, the model determines optimal values and bus locations for load shedding.

Section 1 introduces the most important and actual aspects in Optimal Active Power Flow computation. Section 2 presents the Security concepts of the Optimal Active Power Flow analysis. Section 3 gives results about the comparative study of Optimal Power Flow computation considering different restriction for the case study.

Security Concepts

In the Optimal Active Power Flow model a Line Security is considered. Line Security could be:

- a. - N Security – a network consisting of N branches, none of which is overloaded, satisfies an N branch security condition. When an N security restriction is imposed in the OAPF calculation, the program will shed load if necessary to meet this requirement.
- b. - $N-1$ Security - a network consisting of N branches satisfies $N-1$ Security requirements when all of the following conditions are met:
 - c. Only one branch trips due to overload, and
 - d. None of the remaining $N-1$ branches is overloaded.

In a load flow solution if no overload exists on all branches, it is stated that the system state satisfies N line security. No overload exists on other branches even when any one branch trips out, it is stated that the system state satisfies $N-1$ line security [3], [5]. Obviously, N security is the most fundamental requirement for a load flow solution, and $N-1$ security is a very important requirement when operating reliability is emphasized.

Active Load Flow analysis means active load flow computation, considering methods such as the Newton-Raphson or P-Q fast decoupled load flow, when the generations of all sources buses are specified by the user. The least possible reactive power is transmitted in power system operation to reduce network losses. Line security is, therefore, mainly associated with active load flow. It is possible that a load flow solution cannot satisfy line security. Overloads might exist on some branches. Conventional load flow programs cannot solve the problem of how to alleviate these overloads. In the Optimal Active Power Flow model the generations of all sources are not specified, but, are calculated under the condition that line security must be met [6], [7].

In order to conduct an Active Optimal Power Flow using EDSA the single line diagram and the equipments data

have to be introduced. The following data are required for branches and generation points:

- Branches: kW Rating of the Branch;
- Generators: Generator Cost (Euro/kWh), Maximum and Minimum Power Limit (kW).

Specifying different generations for each source bus leads to different load flow solutions. The paper proposes a comparative study of the following OAPF models:

- Active Load Flow / N Security of All Branches (Case A);
- Economic Dispatch Load Flow / N Security of All Branches (Case B);
- Economic Dispatch Load Flow / N & N-1 Security of All Branches (Case C);
- Economic Dispatch Load Flow / N Security of All Branches & N-1 Security of Crucial Branches (Case D).

Security-Constrained Economic Dispatch model [5], [8] is used to find a set of generations for all sources to minimize the total generating cost (economic operating solution). The load flow obtained by conventional economic dispatch may lead to overloads on some branches, so Optimal Active Power Flow model provides an N security- constrained, or N and $N-1$ security-constrained, economic dispatch solution depending on the user's choice.

The security-constrained economic active load flow is calculated using the following main equations [9]:

$$(1) \quad F(0) = A(0) \cdot (P + C - L)$$

$$(2) \quad F(l) = A(l) \cdot (P + C - L), \quad l = 1, NL$$

where: P - active power generation vector, C - load shedding vector; L - active power load vector; $F(0)$ - active power branch flow vector when no branch trips out; $F(l)$ - active power branch flow vector when the l th branch trips out; $A(0)$ - relation matrix between active power branch flows and

active power injections when no branch trips out; $A(l)$ - relation matrix between active power branch flows and active power injections when the l th branch trips out; NL - set of branches

The security-constrained active load flow, or economic dispatch, is a very large scale problem. For example, for a system of 500 buses and 1,000 branches, the number of elements in Matrix $A(0)$ is 500,000. If $N-1$ security of all branches is considered, there will be 1,000 $A(l)$ matrices and each has the same size as $A(0)$. The number of the relative security constraints in the calculation model is 1,000,000. The model utilizes the following techniques to reduce the time and memory storage:

- only sparse bus admittance matrix is stored;
- the sparsity technique and the bus order optimization technique are used;
- the linear programming relaxation technique is applied.

The Optimal Active Power Flow program can solve a system of 500 buses and 1,000 branches on a micro-computer. $N-1$ security analysis is associated with much more numerous calculations compared to N security analysis. It is, therefore, important, that, in the case of a relatively large system, " $N-1$ security of crucial branches" be chosen instead of " $N-1$ security of all branches".

Comparative Study of Optimal Power Flow Computation

The power system from Fig. 1 was modeled and simulated using the Optimal Active Power Flow program from EDSA Technical 2000. The case study consists of 3 Generators (1 swing bus, 2 PV Generators), and 35 Branches (13 power lines, 19 breakers, 3 transformers).

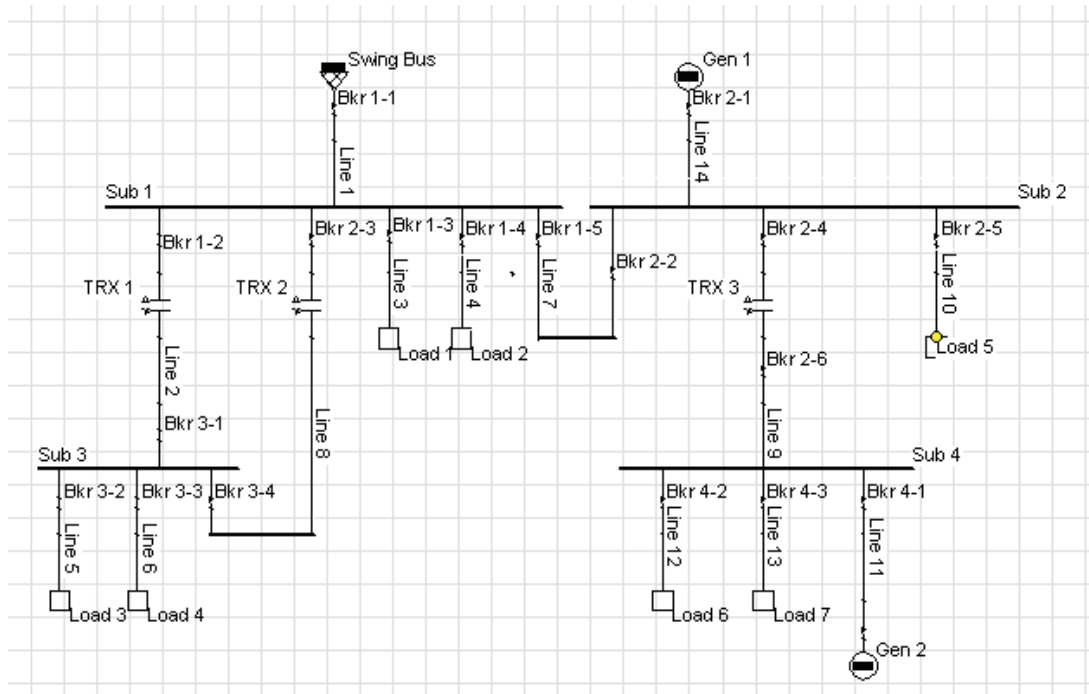


Fig. 1. Single line diagram for case study system

The original data for the test systems are given in per unit, and the transformer data are given in the form of transformer equivalent circuits. The actual unit data of the system were obtained by assuming base values of VA capacity and bus voltages.

The system was calculated in terms of actual unit and transformer input data. The data for the analyzed power systems and the data associated with reactive load flow distributions, which are not required by the optimal active power flow, are also given. The additional data for Optimal Active Power Flow are the kW ratings of all lines and transformer windings, the upper and lower limits of generations for all generators, and the generation cost coefficients of all generators.

A comparative optimal active power flow study of the analyzed power system will be presented. The system is simulated in cases A, B, C, D. The input data are the same in all the cases, see table 1.

The results of the computation in four different cases Active Load Flow / N Security of All Branches (Case A), Economic Dispatch Load Flow / N Security of All Branches (Case B), Economic Dispatch Load Flow / N & N-1 Security of All Branches (Case C), Economic Dispatch Load Flow / N Security of All Branches & N-1 Security of Crucial Branches (Case D) are presented in tables 2-4. The branches and the generators output results are presented in tables 2 and 3. The buses at which load must be shed along with the estimated load shedding in kW are presented in table 4.

In case A a load shedding is necessary in order to maintain the N security constraint for the Active Power Flow. Total Load Shedding is 80,018 kW and all generators are set at maximum output.

In case B an Economic Dispatch Load Flow / N Security of all branches is realized. Since we have maintained the N security constraint on the system, the same load shedding scheme calculated in case A is still required.

Table 1. Initial OAPF data associated with the system

| Component | P Rating [kW] | Cost [E/kWh] | Min P [kW] | Max P [kW] |
|---------------|---------------|--------------|------------|------------|
| Generators | | | | |
| Swing Bus | - | 0,01 | 50,000 | 150,000 |
| Gen 1 | - | 0,035 | 10,000 | 50,000 |
| Gen 2 | - | 0,035 | 5,000 | 10,000 |
| Lines | | | | |
| 01 | 300,000 | - | - | - |
| 02 | 200,000 | - | - | - |
| 03 | 50,000 | - | - | - |
| 04 | 50,000 | - | - | - |
| 05 | 200,000 | - | - | - |
| 06 | 60,000 | - | - | - |
| 07 | 100,000 | - | - | - |
| 08 | 50,000 | - | - | - |
| 09 | 50,000 | - | - | - |
| 10 | 100,000 | - | - | - |
| 11 | 100,000 | - | - | - |
| 12 | 12,200 | - | - | - |
| 13 | 12,200 | - | - | - |
| 14 | 10,000 | - | - | - |
| Transformers | | | | |
| Trx 1 | 75,000 | - | - | - |
| Trx 2 | 75,000 | - | - | - |
| Trx 3 | 50,000 | - | - | - |
| Breakers | | | | |
| Brk 1-1...4-4 | 200,000 | - | - | - |

Table 2 Branches output results

| No | Initial bus | Terminal bus | Rating [kW] | Active power [kW] | Loading [%] | Active power [kW] | Loading [%] | Active power [kW] | Loading [%] |
|----|-------------|--------------|-------------|-------------------|-------------|-------------------|-------------|-------------------|-------------|
| | | | | Case A | | Case C | | Case D | |
| 1 | 001 | 002 | 300000 | 150000 | 50 | 113973 | 37.99 | 140058 | 46.69 |
| 2 | 002 | 003 | 300000 | 149000 | 49.99 | 113973 | 37.99 | 139988 | 46.58 |
| 3 | 003 | 004 | 200000 | 30565 | 15.28 | 23666 | 11.83 | 25978 | 12.99 |
| 4 | 005 | 006 | 50000 | 30565 | 61.13 | 23666 | 47.33 | 25978 | 51.96 |
| 5 | 006 | 007 | 200000 | 30404 | 15.20 | 23565 | 11.78 | 25844 | 12.92 |
| 6 | 007 | 012 | 200000 | 59796 | 29.9 | 49661 | 24.83 | 51181 | 25.59 |
| 7 | 012 | 014 | 60000 | 60000 | 100 | 49775 | 82.96 | 51181 | 85.22 |
| 8 | 007 | 013 | 200000 | 0 | 0 | 0 | 0 | 0 | 0 |
| 9 | 013 | 015 | 60000 | 0 | 0 | 0 | 0 | 0 | 0 |
| 10 | 007 | 026 | 200000 | -28884 | 14.44 | -25590 | 14.8 | -24830 | 12.42 |
| 11 | 003 | 008 | 200000 | 47000 | 23.50 | 47000 | 23.5 | 47000 | 23.5 |
| 12 | 008 | 010 | 50000 | 47000 | 94 | 47000 | 94 | 47000 | 94 |
| 13 | 003 | 009 | 200000 | 42518 | 21.26 | 42518 | 21.26 | 42518 | 21.26 |
| 14 | 009 | 011 | 50000 | 42518 | 85 | 42518 | 85 | 42518 | 85 |
| 15 | 003 | 016 | 200000 | 29281 | 14.64 | 277 | 0.14 | 23975 | 12 |
| 16 | 016 | 020 | 200000 | 29281 | 29.28 | 277 | 0.28 | 23975 | 23 |
| 17 | 017 | 018 | 200000 | 49920 | 24.99 | 30000 | 15 | 30000 | 15 |
| 18 | 018 | 019 | 100000 | 49920 | 50 | 30000 | 30 | 30000 | 30 |
| 19 | 019 | 020 | 200000 | -29208 | 14.6 | -277 | 0.14 | -23929 | 12 |
| 20 | 019 | 021 | 200000 | 7742 | 3.87 | 4705 | 2.35 | 4750 | 2.38 |
| 21 | 022 | 023 | 200000 | 7745 | 3.86 | 4704 | 2.35 | 4708 | 2.35 |
| 22 | 023 | 027 | 50000 | 7706 | 15.41 | 4703 | 9.41 | 4704 | 9.41 |
| 23 | 027 | 028 | 200000 | 12202 | 6.1 | 12202 | 6.1 | 12202 | 6.1 |
| 24 | 028 | 030 | 12200 | 12202 | 100 | 12202 | 100 | 12202 | 100 |
| 25 | 027 | 029 | 200000 | 5503 | 2.75 | 0 | 0 | 0 | 0 |
| 26 | 029 | 031 | 12200 | 5503 | 40.36 | 0 | 0 | 0 | 0 |
| 27 | 027 | 034 | 200000 | -9993 | 5 | -7494 | 3.75 | -7494 | 3.75 |
| 28 | 034 | 035 | 100000 | -9993 | 10 | -7494 | 7.5 | -7494 | 7.5 |
| 29 | 035 | 033 | 100000 | -10003 | 10 | -7403 | 3.75 | -7499 | 3.75 |
| 30 | 019 | 024 | 200000 | 28856 | 14.43 | 25570 | 12.79 | 24633 | 12.31 |
| 31 | 025 | 026 | 50000 | 28747 | 59.49 | 25573 | 52.15 | 24633 | 49.12 |
| 32 | 019 | 032 | 200000 | 42756 | 21.38 | 0 | 0 | 24600 | 12.3 |
| 33 | 032 | 036 | 100000 | 7709 | 15.42 | 4704 | 9.41 | 4706 | 9.41 |
| 34 | 004 | 005 | 75000 | 28743 | 38.32 | 25572 | 34 | 24565 | 32.75 |

Table 3 Generators output results

| No | Bus no | Generation [kW] | Generation [kW] | Total Cost [E/h] | Generation [kW] | Total Cost [E/h] | Generation [kW] | Total Cost [E/h] |
|-------|--------|-----------------|-----------------|------------------|-----------------|------------------|-----------------|------------------|
| | | Case A | Case B | | Case C | | Case D | |
| 1 | 001 | 150000 | 150000 | 150 | 113994 | 113.99 | 140017 | 140.0117 |
| 2 | 017 | 50000 | 50000 | 1750 | 30000 | 1050 | 30000 | 1050 |
| 3 | 033 | 10000 | 10000 | 350 | 75000 | 262.5 | 75000 | 262.5 |
| TOTAL | | | | 2250 | | 1426.49 | | 1452.52 |

All generators are also set at maximum output.

In case C we will apply the N & N-1 branch security. As seen from these results, the N & N-1 security conditions are more restrictive in terms of guaranteeing a reliable supply of power. In this case we see that the load shedding required to maintain the constraints is the highest so far 139,024 kW. The generators are not set at maximum output.

In case D we will apply N security to all branches & N-1 security to two crucial branches in the system. The two branches considered as crucial for this exercise are:

- line 7: From node 0016 to node 0020 (the line between Sub 1 and Sub 2)
- line 8: From node 0025 to node 0026 (the line between Sub 3 and Transformer TRX 3)

As seen from the results the N security for all branches & N-1 security for crucial branches also result in a more restrictive scenario (although not as much as the previous case C) in terms of how much energy can be transferred if either of the crucial links trips out. In this case we see that the load shedding required to maintain the constraints is: 113,003 kW. The generators are not set at maximum output.

Table 4. Load shedding required

| Bus | Load | Shedding [kW] | | |
|-------|------|---------------|--------|--------|
| | | Case A | Case C | Case D |
| 14 | 3 | 5000 | 15224 | 13868 |
| 15 | 4 | 42000 | 42500 | 42500 |
| 30 | 6 | 800 | 800 | 800 |
| 31 | 7 | - | 5500 | 5500 |
| 36 | 5 | 32218 | 75000 | 50335 |
| TOTAL | | 80018 | 139024 | 113003 |

The branches output results demonstrate that no overload occurs on any of the branches, in all the analyzed cases A, B, C, D.

Because the kW rating of the generation the total generation cost in the Case B is increased to 2250Euro/h, as compared with 1426.49 Euro/h for Case C, or 1452.52Euro/h for Case D.

Conclusion

The Optimal Active Power Flow model is an adequate one when we are interested to quantify the generation of all sources for a power delivery system. The reliability of the analyzed system is very important, so N Line Security and/or N-1 Line Security are considered.

Power Systems efficiency is another important meter when economical aspects are involved. So the Security-Constrained Economic Dispatch model solves the

economical problems of the active power flow. We can find a set of generations for all sources to minimize the total generating cost and to improve power system efficiency. Different models are used on a proposed power delivery system. The simulation is done on four cases, considering different restrictions in the system Security. The economical aspect of power delivery is affected on an important meter of the imposed restrictions, so the power system efficiency has variations.

REFERENCES

- [1] M.M. Saied, "Measures for the supply efficiency in distribution network", *INT.J.Elect. Power Energy Systems*, vol 23, pp. 427-434, 2001.
- [2] D. Niebur, C. Nwankpa, R. Fischl, "Identification of generation for sources on a complex system", *IEEE Trans. Power Delivery*, vol. 14 1368-1373, Oct.1999.
- [3] M. M. Saied, "Analysis and Proposed Technique for Identifying Active Load Flow", *IEEE Trans. Power Delivery*, vol. 19 759-765, April 2004.
- [4] M. Dumitrescu, "Power Systems", edited on Didactica and Pedagogica Bucuresti 2002, ISBN 973-30-2139-3, pp. 270-295.
- [5] El. Hawary, "Electrical Power Systems", edited on IEEE Press, N.J 1997, pp. 356-369.
- [6] M. Dumitrescu, "Efficiency and Reliability on Power Systems", edited on Didactica and Pedagogica" Bucuresti 2003, ISBN 973-30-2187-3, pp. 150-161.
- [7] M. Dumitrescu and T. Munteanu, Power System Safety. *Lecture Notes in Computer Science*, Vol. 2206. Springer-Verlag, Berlin Heidelberg (2001), 886-889.
- [8] M. Dumitrescu, T. Munteanu and D. Florica, A Software for Electric-Power Critical Analysis. *IEEE International Conference on Power Systems*, Hungary Budapest 25-29 July 2004, pp. 168-172.
- [9] M.Dumitrescu, Power Delivery System Modeling and Simulation. *First International Symposium on Electrical and Electronics Engineering – ISEEE-2006*, Electric and electronic Faculty Galati, Romania, 13-14 Septembrie 2006, pp.128-131.

Authors: professor Mariana Dumitrescu, Electrical Engineering Department, University "Dunarea de Jos" of Galati, Stiintei Street, No.2, Galati-800146, Romania, Ph/Fax: (40-236) 470905, E-mail: Mariana.Dumitrescu@ugal.ro; professor Toader Munteanu, Electrical Engineering Department, University "Dunarea de Jos" of Galati, Stiintei Street, No.2, Galati-800146, Romania, Ph/Fax: (40-236) 470905, E-mail: Toader.Munteanu@ugal.ro; professor Dan Florica, Politehnica University Bucharest, Splaiul Independentei 133, Bucharest Romania, danfi2005@yahoo.com

Eddy currents induced in the screen of a non-coaxial cable

Abstract. Expanding the logarithmic vector potential into Fourier series we determine the source magnetic field generated in the screened non-coaxial cable as a function of two variables r and Θ of the cylindrical co-ordinate system. In the non-conducting areas, internal and external, the electric field is described by Laplace equation, while in the conducting area by Helmholtz equation for two variables. These equations are solved using the separation of variables method. From the classic boundary conditions, taking into account the reciprocal interaction of eddy currents, we determine the density of eddy currents induced in the screen.

Streszczenie. Poprzez rozwinięcie logarymicznego potencjału wektorowego w szereg Fouriera wyznaczono źródłowe pole magnetyczne generowane w ekranowanym układzie niewspółosiowym jako funkcję dwóch zmiennych r oraz Θ walcowego układu współrzędnych. W nieprzewodzących obszarach wewnętrznym i zewnętrznym pole elektryczne opisano równaniem Laplace'a zaś w obszarze przewodzącym równaniem Helmholtza dla dwóch zmiennych. Równania te rozwiązano stosując metodę rozdzielnie zmiennych. Z klasycznych warunków brzegowych, uwzględniając przy tym także oddziaływanie zwrotne prądów wirowych, wyznaczono gęstość prądów wirowych indukowanych w ekranie. (**Prądy wirowe indukowane w ekranie kabla niewspółosiowego**)

Keywords: cable, electromagnetic screens, eddy currents, electromagnetic field.

Słowa kluczowe: kabel, ekran elektromagnetyczny, prądy wirowe, pole elektromagnetyczne.

Introduction

An important question in the determination of the losses in the screens and the impedances of the systems of screened conductors is the determination of eddy currents induced in the screens by the alternating magnetic field of the currents in the conductors. [1, 2, 3, 5, 6, 10].

Let us consider a stationary conductor C with conductivity γ in the proximity of the source Z of harmonic electromagnetic field \underline{H}^w , induced by the source.

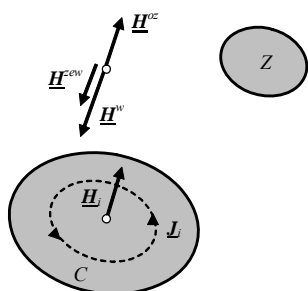


Fig.1. Conductor C in external magnetic field \underline{H}^{zeW}

This external, alternating magnetic field induces, in the conductor, the induction electric field \underline{E}_i defined by the second Maxwell equation. The electric field \underline{E}_i causes the appearance of eddy currents in the conductor, whose density $\underline{J}_i = \gamma \underline{E}_i$, called Foucault currents. These currents, due to the principle of Biot-Savart law, generate the induction magnetic field \underline{H}_i whose sense, according to

the Lenz rule, is inverse to the field \underline{H}^w .

In the external area, in reference to the conductor, the so-called magnetic field of reciprocal interaction will appear [4], which is vectorially added to the field \underline{H}^w thus creating the resultant magnetic field

$$(1) \quad \underline{H}^{zeW} = \underline{H}^w + \underline{H}^{oz}$$

The phenomenon of inducing eddy currents in the conductor under consideration by the external magnetic field deriving from the currents in the neighboring conductors is called the Foucault's effect [4]. If moreover

there is its own source current \underline{J}_0 in the considered conductor, the resultant current in this conductor $\underline{J} = \underline{J}_0 + \underline{J}_i$ and such change in the distribution of the conductor's own current \underline{J}_0 is called the proximity effect [7-9].

Source magnetic field

Let us consider the proximity effect in the system of a tubular conductor with conductivity γ_1 , with internal radius R_1 and external radius R_2 parallel to a non-coaxial internal tubular conductor with conductivity γ_2 and radius R with sinusoidal current of complex efficient magnitude \underline{I}_2 . The distance between the axes of the conductors is d - fig.2.

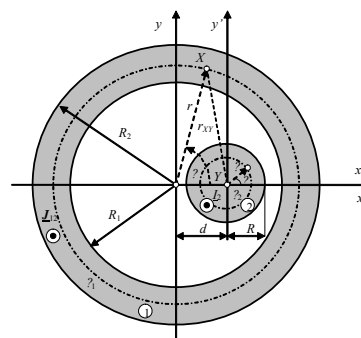


Fig.2. Tubular conductor with an internal non-coaxial cylindrical screen

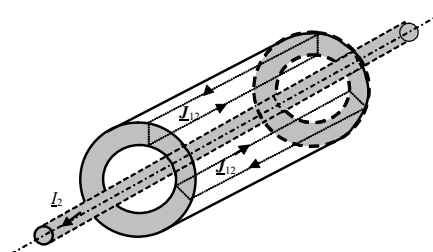


Fig.3. Eddy currents induced in the screen

The proximity effect in the system of conductors shown in fig.1. consists of inducing eddy currents $\underline{J}_{12}(r, \theta) = \mathbf{1}_z \underline{J}_{12}(r, \theta)$ in the tubular conductor (the screen) by the sinusoidal alternating magnetic field $\underline{H}^w(r_{XY})$ generated by the current \underline{I}_2 in the second internal conductor – fig.3.

The vector magnetic potential generated by the current \underline{I}_2 has only one component along the Oz axis and it is the source potential referring to the first conductor, defined in the local co-ordinate system (r, θ) of the screen under consideration by the formula

$$(2) \quad \underline{A}^w(r, \theta) = \frac{\mu_0 \underline{I}_2}{2\pi} \ln \frac{1}{\sqrt{r^2 + d^2 - 2rd \cos \theta}} + \underline{A}_0$$

Inside the screen $r > d$, thus

$$(2b) \quad \ln \frac{r_{XY}}{r} = \frac{1}{2} \ln \left[1 + \left(\frac{d}{r} \right)^2 - 2 \frac{d}{r} \cos \theta \right]$$

and in the expansion of the left-hand side of the equation (2b) into a Fourier series [9] we obtain for $n \in N$, the vector magnetic potential at point $X(r, \theta)$, such that $r > d$

$$(3) \quad \underline{A}^w(r, \theta) = \frac{\mu_0 \underline{I}_2}{2\pi} \left[\ln \frac{1}{r} + \sum_{n=1}^{\infty} \frac{1}{n} \left(\frac{d}{r} \right)^n \cos n\theta \right] + \underline{A}_0$$

The magnetic field strength vector is determined from the definition of the vector magnetic potential $\underline{H}^w(r, \theta) = \frac{1}{\mu_0} \text{rot} \underline{A}^w(r, \theta)$ with the following components

$$(4) \quad \underline{H}_r^w(r, \theta) = -\frac{\underline{I}_2}{2\pi r} \sum_{n=0}^{\infty} \left(\frac{d}{r} \right)^n \sin n\theta$$

$$(4a) \quad \underline{H}_\theta^w(r, \theta) = \sum_{n=0}^{\infty} \frac{\underline{I}_2}{2\pi r} \left(\frac{d}{r} \right)^n \cos n\theta$$

The magnetic field \underline{H}^w is a source field so it exists both inside and outside the screen, as well as in its external area.

Magnetic field inside the screen

The magnetic field $\underline{H}^{wew}(r, \theta)$ in the internal area ($r \leq R_1$) of the screen

$$(5) \quad \underline{H}^{wew}(r, \theta) = \underline{H}^w(r, \theta) + \underline{H}^{ozw}(r, \theta)$$

where $\underline{H}^{ozw}(r, \theta)$ is the magnetic field of reciprocal interaction inside the screen and is generated by eddy currents $\underline{J}_{12}(r, \theta) = \mathbf{1}_z \underline{J}_{12}(r, \theta)$ induced in the screen by the source magnetic field $\underline{H}^w(r, \theta)$. The strength of the electric field $\underline{E}^{ozw}(r, \theta)$ accompanying the magnetic field

$\underline{H}^{ozw}(r, \theta)$ in this area also fulfills the Laplace equation with the solution

$$(6) \quad \underline{E}^{ozw}(r, \theta) = f_1(r) f_2(\theta)$$

where

$$(6a) \quad f_1(r) = C_1 r^\beta + \frac{C_2}{r^\beta}$$

$$(6b) \quad f_2(\theta) = C_3 \cos \beta\theta + C_4 \sin \beta\theta$$

while β is the separation of variables constant, and C_1, C_2, C_3 i C_4 are integration constants.

The electric field has to be limited to $r=0$, which leads to the conclusion that the constant $C_2=0$. Moreover, when the angle value changes from $+\theta$ to $-\theta$ the electric field strength cannot change its sign so the constant $C_4=0$. As we know [9], the constant β has to be an integer because from the solutions (6b) one should chose the ones fulfilling the condition $f_2(\theta) = f_2(\theta + 2\pi)$. The general solution of the Laplace equation in this area has then the form

$$(6c) \quad \underline{E}^{ozw}(r, \theta) = \sum_{n=1}^{\infty} \underline{E}_n^{ozw}(r, \theta) = \sum_{n=1}^{\infty} \underline{F}_n r^n \cos n\theta$$

where \underline{F}_n is the constant determined from the boundary conditions, which will be done later.

From the second Maxwell equation we get the magnetic field of reciprocal interaction $\underline{H}^{ozw}(r, \theta)$ having two components

$$(7) \quad \underline{H}_r^{ozw}(r, \theta) = \sum_{n=1}^{\infty} \frac{n \underline{F}_n r^{n-1}}{j\omega\mu_0} \sin n\theta$$

$$(7a) \quad \underline{H}_\theta^{ozw}(r, \theta) = \sum_{n=1}^{\infty} \frac{n \underline{F}_n r^{n-1}}{j\omega\mu_0} \cos n\theta$$

Taking into account the above solutions we can define the magnetic field $\underline{H}^{wew}(r, \theta)$ in the internal area ($r \leq R_1$) of the screen with the following components

$$(8) \quad \underline{H}_r^{wew}(r, \theta) = -\sum_{n=0}^{\infty} \left[\frac{\underline{I}_2}{2\pi r} \left(\frac{d}{r} \right)^n - \frac{n \underline{F}_n r^{n-1}}{j\omega\mu_0} \right] \sin n\theta$$

$$(8a) \quad \underline{H}_\theta^{wew}(r, \theta) = \sum_{n=0}^{\infty} \left[\frac{\underline{I}_2}{2\pi r} \left(\frac{d}{r} \right)^n + \frac{n \underline{F}_n r^{n-1}}{j\omega\mu_0} \right] \cos n\theta$$

Magnetic field in the screen

In the screen ($R_1 \leq r \leq R_2$) the density of induced currents $\underline{J}_{12}(r, \theta) = \mathbf{1}_z \underline{J}_{12}(r, \theta)$ fulfills the scalar Helmholtz equation with the following solution

$$(9) \quad \underline{J}_{12}(r, \theta) = \sum_{n=0}^{\infty} [C_n I_n(\Gamma_1 r) + D_n K_n(\Gamma_1 r)] \cos n\theta = \underline{J}_{120}(r) + \sum_{n=1}^{\infty} \underline{J}_{12n}(r, \theta)$$

where

$$(9a) \quad \underline{J}_{120} = \underline{C}_0 I_0(\underline{\Gamma}_1 r) + \underline{D}_0 K_0(\underline{\Gamma}_1 r)$$

$$(9b) \quad \underline{J}_{12n} = [\underline{C}_n I_n(\underline{\Gamma}_1 r) + \underline{D}_n K_n(\underline{\Gamma}_1 r)] \cos n\theta$$

From the second Maxwell equation we obtain the magnetic field $\underline{H}_{12}(r, \theta)$ in the screen under consideration, whose components are

$$(10) \quad \underline{H}_{12r}(r, \theta) = \frac{1}{\underline{\Gamma}_1^2} \sum_{n=0}^{\infty} n [\underline{C}_n I_n(\underline{\Gamma}_1 r) + \underline{D}_n K_n(\underline{\Gamma}_1 r)] \sin n\theta$$

(10a)

$$\underline{H}_{12\theta}(r, \theta) = -\frac{1}{\underline{\Gamma}_1^2} \sum_{n=0}^{\infty} \left\{ \begin{array}{l} \underline{C}_n [n I_n(\underline{\Gamma}_1 r) - \underline{\Gamma}_1 r I_{n-1}(\underline{\Gamma}_1 r)] + \\ + \underline{D}_n [n K_n(\underline{\Gamma}_1 r) + \underline{\Gamma}_1 r K_{n-1}(\underline{\Gamma}_1 r)] \end{array} \right\} \cos n\theta$$

Magnetic field outside the screen

Outside the considered screen, i.e. for $r \geq R_2$ the magnetic field

$$(11) \quad \underline{H}^{zew}(r, \theta) = \underline{H}^w(r, \theta) + \underline{H}^{ozz}(r, \theta)$$

where $\underline{H}^{ozz}(r, \theta)$ is the magnetic field of reciprocal interaction outside the screen and it is generated by eddy currents $\underline{J}_{12}(r, \theta) = \underline{1}_z \underline{J}_{12}(r, \theta)$ induced in the screen by

the source magnetic field $\underline{H}^w(r, \theta)$.

The strength of the electric field $\underline{E}^{ozz}(r, \theta)$ accompanying the magnetic field $\underline{H}^{ozz}(r, \theta)$ in this area is defined by the formula (2.60), i.e.

$$(12) \quad \underline{E}^{ozz}(r, \theta) = \sum_{n=1}^{\infty} \underline{E}_n^{ozz}(r, \theta) = \sum_{n=1}^{\infty} \underline{B}_n \frac{1}{r^n} \cos n\theta$$

where \underline{B}_n is the constant determined from the boundary conditions, which will be done later.

Applying the second Maxwell equation to the formula (12) we obtain the complex form of the magnetic field of reciprocal interaction outside the screen $\underline{H}^{ozz}(r, \theta)$ whose components are

$$(13) \quad \underline{H}_r^{ozz}(r, \theta) = \sum_{n=1}^{\infty} \frac{n \underline{B}_n}{j \omega \mu_0 r^{n+1}} \sin n\theta$$

$$(13a) \quad \underline{H}_\theta^{ozz}(r, \theta) = -\sum_{n=1}^{\infty} \frac{n \underline{B}_n}{j \omega \mu_0 r^{n+1}} \cos n\theta$$

Taking into account the above reasoning we can define the magnetic field in the external area ($r \geq R_2$) of the screen $\underline{H}^{zew}(r, \theta)$ with the following components

$$(14) \quad \underline{H}_r^{zew}(r, \theta) = -\sum_{n=0}^{\infty} \left[\frac{\underline{I}_2}{2 \pi r} \left(\frac{d}{r} \right)^n - \frac{n \underline{B}_n}{j \omega \mu_0 r^{n+1}} \right] \sin n\theta$$

$$(14a) \quad \underline{H}_\theta^{zew}(r, \theta) = \sum_{n=0}^{\infty} \left[\frac{\underline{I}_2}{2 \pi r} \left(\frac{d}{r} \right)^n - \frac{n \underline{B}_n}{j \omega \mu_0 r^{n+1}} \right] \cos n\theta$$

If we assume that the magnetic permittivity of the screen under consideration $\mu_1 = \mu_0$, we can write the following boundary conditions for the magnetic field strength:

- for $r = R_1$

$$(15) \quad \underline{H}^{zew}(r = R_1, \theta) = \underline{H}_{12}(r = R_1, \theta)$$

- for $r = R_2$

$$(15a) \quad \underline{H}^{zew}(r = R_2, \theta) = \underline{H}_{12}(r = R_2, \theta)$$

The above conditions imply the equality of the tangent and ordinary components of the magnetic field on the boundary of two mediums. Therefore, in the general case we obtain a system of four equations with the unknown quantities \underline{B}_n , \underline{C}_n , \underline{D}_n i \underline{F}_n .

However, one should pay attention to the fact that for $n=0$ the condition for the continuity of the radial components of the magnetic field strength does not imply the equality of the terms placed next to the factor $\sin n\theta$ in equations (15) and (15a). That is why the above system of equations is solved for two cases: $n=0$ and $n \geq 1$.

Current density in the screen

For $n=0$ the current density

$$(16) \quad \underline{J}_{120}(r) = \frac{\underline{\Gamma}_1 \underline{I}_2}{2 \pi R_1} \frac{b_0 I_0(\underline{\Gamma}_1 r) + c_0 K_0(\underline{\Gamma}_1 r)}{d_0}$$

where

$$(16a) \quad d_0 = I_1(\underline{\Gamma}_1 R_2) K_1(\underline{\Gamma}_1 R_1) - I_1(\underline{\Gamma}_1 R_1) K_1(\underline{\Gamma}_1 R_2)$$

$$(16b) \quad b_0 = \beta K_1(\underline{\Gamma}_1 R_1) - K_1(\underline{\Gamma}_1 R_2)$$

$$(16c) \quad c_0 = \beta I_1(\underline{\Gamma}_1 R_1) - I_1(\underline{\Gamma}_1 R_2)$$

$$(16d) \quad \beta = \frac{R_1}{R_2}, \quad (0 \leq \beta \leq 1)$$

For $n \geq 1$ and any values of the angle θ from the system of equations (15) i (15a) we obtain the density of the current induced in the tubular conductor in the following form:

$$(17) \quad \underline{J}_{12n}(r, \theta) = \frac{\underline{\Gamma}_1 \underline{I}_2}{\pi R_1} \underline{g}_n(r) \cos n\theta$$

where the function

$$(17a) \quad \underline{g}_n(r) = \left(\frac{d}{R_1} \right)^n \frac{K_{n-1}(\underline{\Gamma}_1 R_2) I_n(\underline{\Gamma}_1 r) + I_{n-1}(\underline{\Gamma}_1 R_2) K_n(\underline{\Gamma}_1 r)}{d_n}$$

$$(17b) \quad d_n = I_{n-1}(\underline{\Gamma}_1 R_2) K_{n+1}(\underline{\Gamma}_1 R_1) - I_{n+1}(\underline{\Gamma}_1 R_1) K_{n-1}(\underline{\Gamma}_1 R_2)$$

In fig.4. we show the distribution of this current density in relative units i.e. referring to the relation of the current in the phase conductor to the area of the cross-section of the screen. Moreover we assume a relative radius

$$\rho = \frac{r}{R_2}, \quad \beta \leq \rho \leq 1 \quad \text{and a parameter } \alpha = \frac{R_2}{\delta_2} = k_1 R_2,$$

where δ_2 is the equivalent skin thickness in the screen. The distance between the axes of the conductor and of the screen is given in relative units as the parameter $\lambda = \frac{d}{R_1}$, $0 \leq \lambda < 1$.

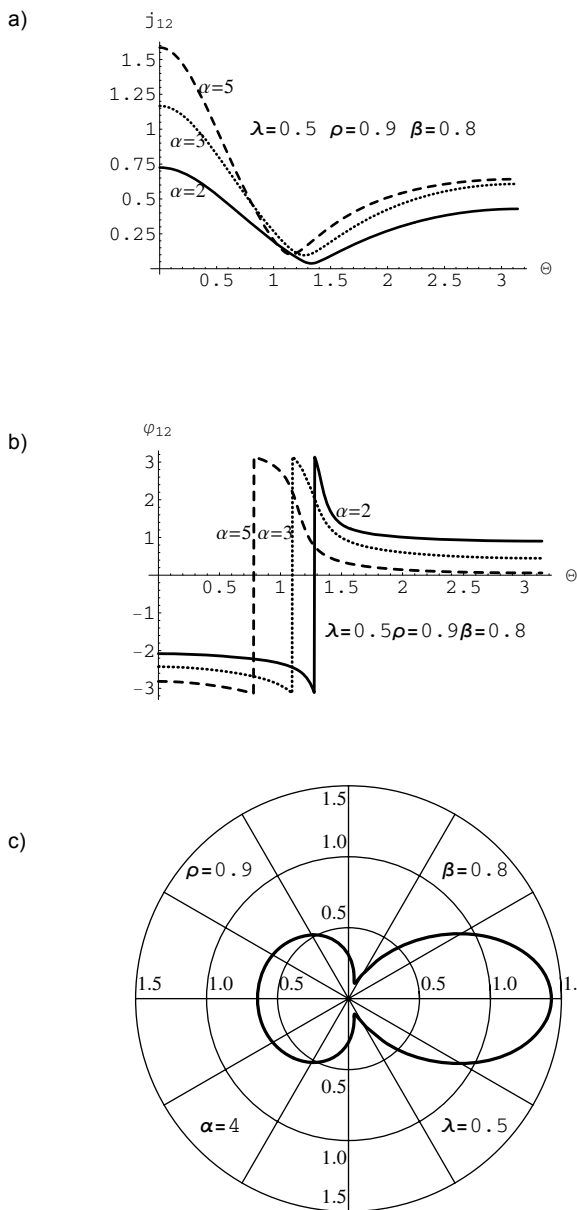


Fig.4. Density of the current induced in the tubular screen; a) distribution of the current density module, b) distribution of the current density argument, c) distribution of the current density module in polar coordinates.

Final remarks

If a cylindrical conductor is placed to the left of the screen axis the solution for the current density is given by the formulas (16) and (17), while the latter is multiplied by $(-1)^n$ and then the distribution of the current density module is shown in fig. 5.

Inducing currents in the screen by the alternating magnetic field of the current in the cylindrical conductor considered here influences the total impedance of the screened cable [7, 8].

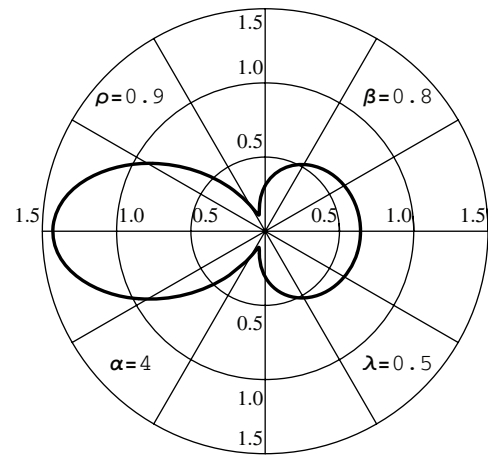


Fig.5. Distribution of the density module of the induced current for the case of a phase conductor placed to the left of the screen axis.

The solution for $n = 0$ in the form of the formula (16) defines the eddy currents induced in the screen for the case of a coaxial concentric cable [7, 8]. The solution (17) disappears for $d = 0$. The determined constants \underline{B}_n , \underline{C}_n , \underline{D}_n i \underline{F}_n also allow to determine the magnetic field in all the areas of the non-coaxial concentric cable considered here.

REFERENCES

- [1] Dokopoulos P., Tampakis D.: *Eddy Currents in a System of Tubular Conductor*. IEEE Trans. on Magnetics, Vol. MAG-20, No 5, September 1984, pp. 1971-1973.
- [2] Ferkal K., Poloujadoff M., Dorison E.: *Proximity Effect and Eddy Current Losses in Insulated Cables*. IEEE Trans. on Power Delivery, Vol. 11, No 3, July 1996, pp. 1171-1178.
- [3] Imai T.: *Exact Equation for Calculation of Sheath Proximity Loss of Single-Conductor Cables*. IEEE Proc., Vol. 56, No 7, July 1968, pp. 1172-1180.
- [4] Jouguet M.: *Traité d'électricité théorique*. Gauthier-Villars, Paris, 1968.
- [5] Kane M., Ahmad A., Auriol Ph.: *Multiwire Shielded Cable Parameter Computation*. IEEE Trans. on Magnetics, Vol. 31, No 3, May 1995, pp. 1646-1649.
- [6] Kreizis E. E., Chrissoulidis D. P., Georgadis L. G.: *Generalized Solution of Field Distribution in Cylindrical Shells of Finite Length and Thickness due to Axial Currents*. IEEE Proc., Vol. 129, Pt. A., 1982, pp. 56-61.
- [7] Piątek Z.: *Impedances of Single-Pole Gas-Insulated Transmission Line*. Archives of Electrical Engineering, Vol. XLVIII, No. 1-2, 1999, pp. 181-197.
- [8] Piątek Z.: *Self and mutual impedances of a finite length gas-insulated transmission line (GIL)*. Electric Power Systems Research 77, 2007, pp. 191-203.
- [9] Piątek Z.: *Method of Calculating Eddy Currents Induced in Pipe-Sheathings of the Three-Phase Flat Line*. Electrimacs'96, Saint-Nazaire, September 17-19, 1996, pp. 1011-1015.
- [10] Tegopoulos J. A., Kriezis E. E.: *Eddy Current Distribution in Cylindrical Shells of Infinite Length Due to Axial Currents. Part II: Shells of Finite Thickness*. IEEE Trans., Vol. PAS-90, 1971, pp. 1287-1294.

Author: Ph.D., D.Sc., Professor Zygmunt Piątek, Czestochowa University of Technology, Faculty of Electrical Engineering, Chair of Electrotechnics, Aleja Armii Krajowej 17, 42-200 Czestochowa, E-mail: zpiatek@el.pcz.czest.pl;

Automatic cell counting in neuroblastoma

Abstract. The paper presents a method of automatic cell counting on the basis of the pathology images. The evaluated images are microscope slides of neuroblastoma disease in Ki-67 (MIB-1) staining. This disease is recognized as the fourth in frequency of appearance of the malignant tumours for people under 15 years old. This evaluation was introduced by Shimada and it is important factor in the stroma-poor tumors for classification into favorable and unfavorable prognosis subgroups. To make an evaluation, the expert must count 5000 cells in few areas of view. We use the images of the magnification 400x, of the size 320x240 μm with resolution 768x576 pixels. The main aim of this evaluation is counting the cells in the considered area, for recognition of immunopositive and immunonegative types of cells. The nuclei or the whole cells of the immunonegative type are stained on blue color and a basic problem is the segmentation of the image because cells are not well separated and very often overlap. In the case of immunopositive cell its nuclei is stained in brown colour. After segmentation we make a classification of cells counting them into two groups on the basis of their relation to the brown colour with the help of Support Vector Machine. In high packed area (many cells in limited region) the algorithm counts about 1500 cells in 100 seconds (PC 2.4GHz, 512 Mb RAM). The system error is less than 5% for both types of cells and this accuracy is acceptable for medical need.

Streszczenie. Artykuł prezentuje system do automatycznego zliczania komórek w barwieniu immunohistochemicznym Ki-67(MIB-1) preparatów mikroskopowych z rozpoznaniem nowotworem neuroblastoma. Wyznaczany na tej podstawie wskaźnik mitotyczno-apoptyczny jest kluczowym w prognozowaniu przeżycia i jest oznaczony na podstawie występowania dodatniego odczynu wśród 5000 komórek nowotworowych. System bazując na operacjach morfologii matematycznej i Support Vector Machine jest w stanie wyznaczyć go w błędem poniżej 5% w czasie wielokrotnie krótszym od tego, w którym jest w stanie wykonać to człowiek. (**Automatyczne zliczanie komórek w barwieniu immunohistochemicznym.**)

Keywords: cell counting, mathematical morphology, neuroblastoma, Support Vector Machine.

Słowa kluczowe: zliczanie komórek, morfologia matematyczna, neuroblastoma, Support Vector Machine.

Introduction

Neuroblastoma is the small blue cell tumour of childhood, and ranks fourth in frequency of malignant tumours under 15 years old with incidence rate 9.6 per 1 million in the white population [1,2,3,4,5]. The mean survival rate of people suffering this illness is only 55% with differentiation for 5 prognosis subgroups of survival from 100% to only 4.5%. About 80% of neuroblastoma patients are classified for stroma-poor tumours subgroup and the most significant immunohistology indicator is mitosis-karyorrhexis index, introduced in classification by Shimada et al. [3]. This index is calculated for Ki-67 (MIB-1) staining slides by counting number of immunopositive cells in 5000 tumour cells in few areas of view. This process is a very tedious and time-consuming for human expert. Recently there exist some programs for automatic counting the cells in immunohistochemical stains [6,7,8,9]. The authors associate the main problems with high touching rate of cells and high number of them in the analyzed images.

The main new idea of the paper is based on the sequential thresholding connected with the differentiation of the immunopositive/ immunonegative state using artificial neural network [10,11]. The first stage is the determination of the difference between blue colour and other colours in the RGB image representation. In practice it is calculated as a difference between the blue and green components. The next stage is the step threshold operation performed on the converted colour image and then the application of the watershed method. In each step the algorithm adds the next cells to the cell mask, separate them from the rest, and checks the selected size restriction. In this way the cells are segmented and then separated from the other cells on the basis of the border formed by the lighter pixels. The additional process relies on the segmentation of the rest of cell nuclei area. It is obtained using the threshold method on the grey scale image. In all steps of segmentation we use the reference value for the area of the cell.

Image preparation and standardization

The images are obtained from the Olympus BX50 microscope with help of the Sony 3CCD COLOR VIDEO CAMERA Model DXC-950P. The settings of a microscope were as following: achromat 0.62, LD and ND6 filters on,

with focus lens, light for camera sign, and the magnification 400x. The images were stored with the help of AnalySIS 3.0 Soft Imaging System GmbH software in *tif* format and after cutting a frame they have resolution of 759x572 pixels. The automatic counting system was written in the Matlab language as a stand-alone application. Before analysing the images they are normalized by the linear extension of the histogram to the white colour. There are numerous immunonegative cells stained in blue colour and some number of the immunopositive brown cells. Many cells are touching or overlapping. Generally they have good coloured nuclei and not well coloured cytoplasm. In many cases cytoplasm is hardly recognizable. The difficult problem of the recognition of the neuroblastoma cells is large variety of images. They differ by the intensity of colour, density of cell compaction, shape and the background colour. Fig. 1 a and b present two images, both typical to neuroblastoma. Fig. 1a is a specific Homer-Wright rosette in immature type and Fig. 1b is a mature type of neuroblastoma.

Procedure of cell extraction

The algorithm is based on the mathematical morphology methods and is supported by the Support Vector Machine. The first stage is the determination of the difference between blue colour and the other colours in the RGB image, represented in a grey scale. In practice the first step is to determine the difference between blue and green components. The next stage is the step threshold operations performed sequentially on the grey scale image, defined as [10]

$$(1) \quad T_{[t_1, t_2]}[f(x)] = \begin{cases} 1 & \text{if } t_1 \leq f(x) \leq t_2 \\ 0 & \text{else} \end{cases}$$

with selected lower threshold value t_1 and usually without higher limit t_2 . In this step the algorithm adds the next cells to the cell mask. They are separated from the rest, and fulfil a selected size restriction. The algorithm starts from the minimal value of threshold and checks if they are objects full separated from the other objects and fulfil a selected size restriction. If yes, they are added to cell mask. In this process the threshold is changing from the minimal value to

the maximal one equal to the most dark pixel in the image. It is done in 100 linear steps. We note that if the object was separated in just one step and had some darker pixels, then in the next few steps these pixels create an object. It doesn't change the mask, because is already fully included in the object, just before this step of segmentation. This property can be described by the following relation [10]

$$(2) \quad T_{[t_{\max}, t_{\max}]}(f) \subseteq T_{[t_{\max-1}, t_{\max}]}(f) \subseteq \dots \subseteq T_{[t_0, t_{\max}]}(f)$$

In the described above process the cells are segmented and then separated from the other cells by the lighter pixels or partly bordered (to some degree). The additional tool of segmentation of the extracted bordered cells is the watershed method. A map of pixels distance from the border of object area in this method is built by sequential erosion using a structuring element in the form of disk shape of radius equal 1 pixel. The binary mask of segmented cell nuclei corresponding to the image of Fig. 1a is presented in Fig. 2.

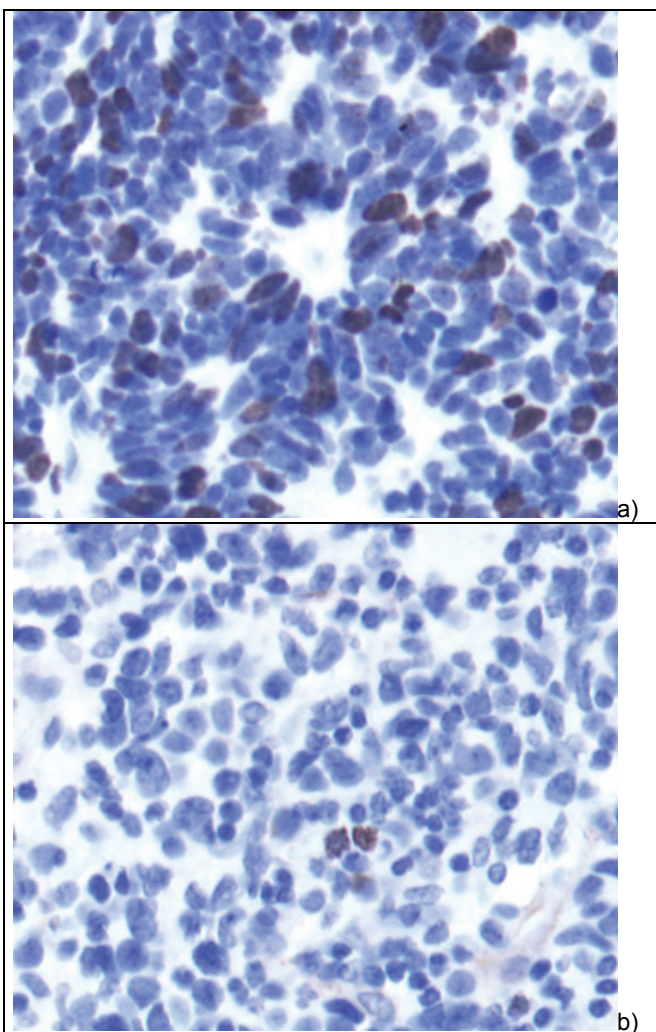


Fig.1. An example of the tissue image a) specific Homer-Wright rosette in immature type, b) mature type of neuroblastoma (Ki-67, 400x)

Because some nuclei of cells are not separated from the other cells by the light pixels of cytoplasm, it is necessary to apply the additional process. It is the segmentation of the rest of cell nuclei area, obtained by applying using the thresholding of the grey scale image. The threshold value is obtained automatically by using the Otsu method [12]. In

this thresholding process the cells are selected by processing also a brown (immunopositive) cells. From the mask of nuclei we subtract the mask being the result of the previous segmentation. This difference is once again segmented with the use of the watershed method. The additional cells of the image, returned in this step are presented in Fig. 3.

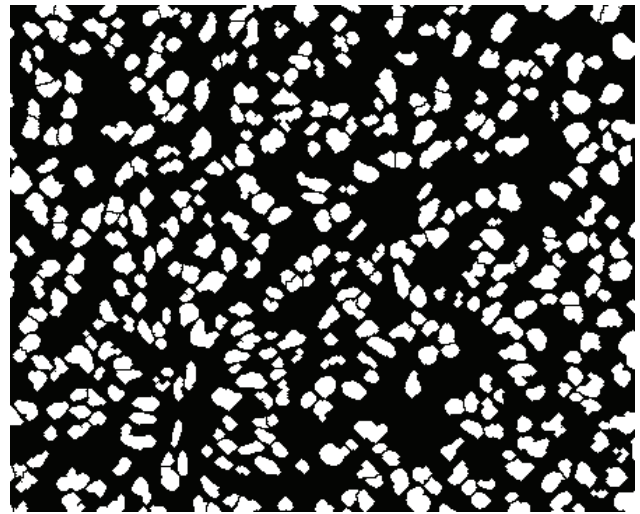


Fig.2. The binary mask of nuclei corresponding to the image of Fig. 1a.

These two masks are combined together and create a mask of all extracted cells (or their nuclei). However there is still no distinguished immunopositive cells and some problems with the accurate extraction of them, because some of them are not coloured in a monotonous way. In some cases it is possible, that part of the cell is more blue than brown and is extracted in the process of the segmentation of the blue (immunonegative) cells. The rest if that cell is segmented in the second processing stage. In this case we obtain two cells from one not monotonous immunopositive item (in the sense of colour). Of course in the medical sense this cell is immunopositive.

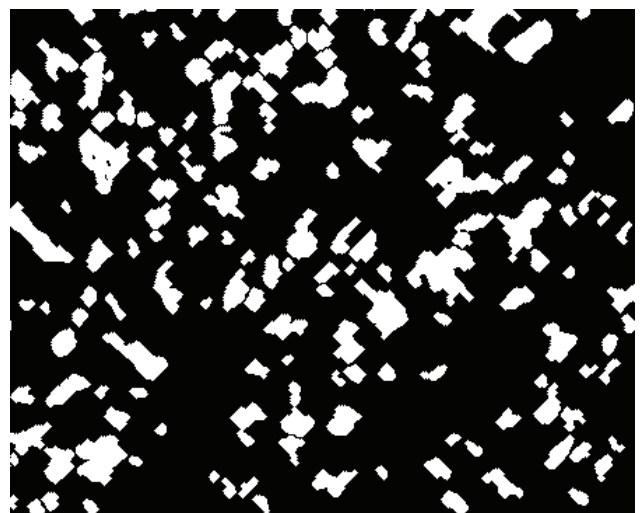


Fig.3. The binary mask of additional cells

For the recognition of immunopositive/immunonegative cells we have used the Support Vector Machine working in a classification mode [11]. The main idea of this classifier is create a hiperplane, that will separate both classes with the maximal margin. The input vector for this network is created

by three colour components representing the RGB standard. The output signal of the network with linear kernel function is defined in the form

$$(3) \quad \begin{aligned} y &= \mathbf{w}^T \mathbf{x} + b \geq +1 \quad \text{for first class or} \\ y &= \mathbf{w}^T \mathbf{x} + b \leq -1 \quad \text{for second class} \end{aligned}$$

where: y – output signal, \mathbf{w} – vector of weights, \mathbf{x} – input vector, b – bias.

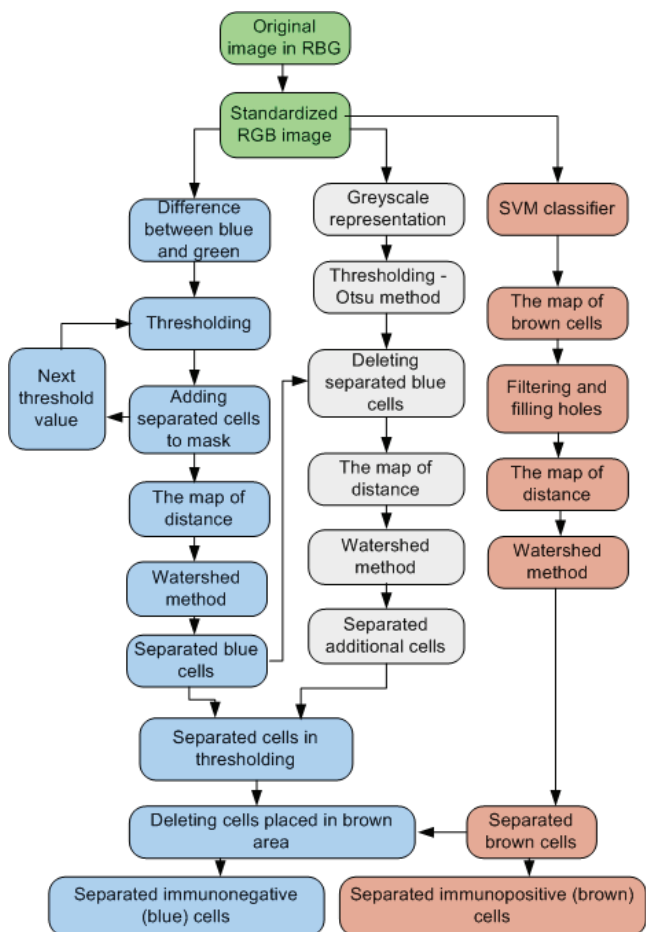


Fig.4. The scheme of the algorithm for counting immunopositive and immunonegative cells

The SVM network of linear kernel function is used to classify the pixels of the image into two classes: immunopositive cells and other. As a result we obtain a mask dividing the image regions into two classes – one class includes the pixels of the immunopositive cells and the second class the other pixels. This mask is subsequently filtered and segmented with the use of the watershed method. The result of this process is the set of the immunopositive separated cells. The final step is deleting cells that have the area representation in the set of immunopositive cells from the set of all extracted cells using morphological methods. The remaining cells create the set of immunonegative cells. The illustration of the presented above algorithm is depicted in Fig. 4.

Results of the automatic evaluation of the image

For the evaluation of the accuracy of the developed automatic system of the cells we present the results produced by our system and compare it with the human expert score. Fig. 5 presents the graphical results of cell

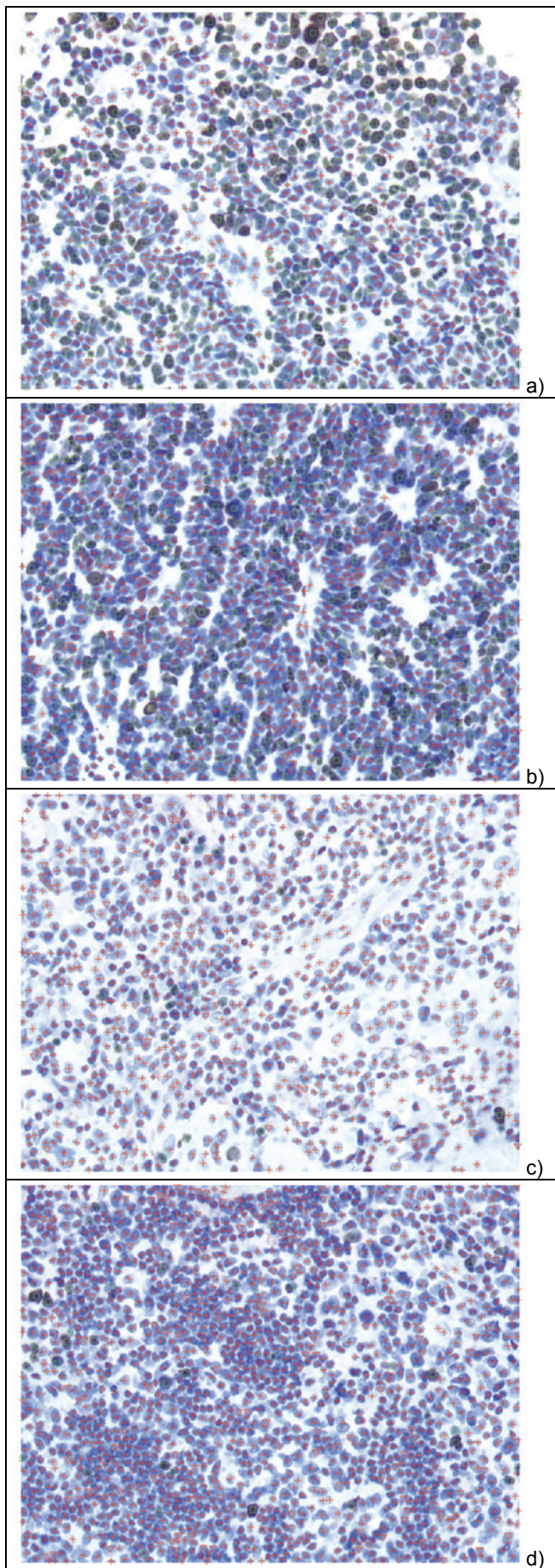


Fig.5. The results of automatic cell counting in the four sample images of neuroblastoma (Ki-67, 400x)

recognition for four samples of images under evaluation. Two images (Fig. 5a,b) belong to the type of high MKI index and the other two (Fig. 5c,d) of low index. The immunonegative cells obtained in the first processing are signed by "+" (red colour), the cells obtained in the additional segmentation are signed by "∇" (red colour) and the immunopositive cells obtained from SVM classification are signed by "□" (green colour). The comparison of the results of our automatic system evaluation and the human expert are collected in Table 1. The notation HE means the human expert results, AS – the score of our automatic system. The cut values of the mitosis-karyorrhexis index (MKI) are 100 or 200 immunopositive cells for 5000 counted cells depended on age and type of the differentiation. In the currently WHO classification [1] these values are presented usually as the relative values if percentage.

Table 1. The results of the automatic system of counting and recognition of the cells compared with evaluation by the human expert

| Nr of figure | Number from AS | Nr of missing | Nr of too much | Nr of different classes | MKI value [%] |
|----------------|----------------|---------------|----------------|-------------------------|----------------------|
| Fig. 5a | | | | | AS 41.22 HE 39.42 |
| negative cells | 686 | 33 | 13 | 7 | |
| positive cells | 481 | 39 | 11 | 37 | |
| Fig. 5b | | | | | AS 30.32 HE 30.88 |
| negative cells | 956 | 37 | 28 | 11 | |
| positive cells | 416 | 44 | 23 | 15 | |
| Fig. 5c | | | | | AS 2.09 HE 2.24 |
| negative cells | 1027 | 16 | 38 | 1 | |
| positive cells | 22 | 0 | 0 | 0 | |
| Fig. 5d | | | | | AS 2.53 HE 2.69 |
| negative cells | 1500 | 54 | 28 | 3 | |
| positive cells | 39 | 0 | 0 | 1 | |

Conclusion

The results of the automatic counting system are in very good agreement with the results of human experts. The differences between the scores of AS and human experts are negligible and below 5% in the worst case. The main advantage of AS is its speed and repeatability of results. The results of score of the same human experts may be different and depend on his actual mental concentration and mood. The same image may result in different MKI value even by the same expert. This will never happen in an automatic system. The results produced for the same image are always the same.

Acknowledgments

This work is supported by grant of The Polish Ministry of Science and Higher Education.

REFERENCES

- [1] Schwab M., Shimada H., Joshi V., Brodeur G.M., Neuroblastic tumours of adrenal gland and sympathetic nervous system (in "Pathology and Genetics of Tumours of the Nervous System, Paul Kleihues and Webster K. Cavense eds.), World Health Organization Classification of Tumours, International Agency for Research on Cancer (IARC), Lyon, 2000
- [2] Silvenberg S.G., DeLellis R.A., Frable W.J., Principles and practice of surgical pathology and cytopathology, Churchill Livingstone, New York, 1997
- [3] Shimada H., Chatten J., Newton W.A.Jr., et al., Histopathologic prognostic factors in neuroblastic tumors: definition of subtypes of ganglioneuroblastoma and age-linked classification of neuroblastomas, J Natl Cancer Inst, 73 (1984), 405:416
- [4] McLendon R.E., Bigner D.D., Bigner S.H., Provenzale J.M., Pathology of Tumours of the Central Nervous System, Arnold, London, 2000
- [5] Stachura J., Domagała W, Patologia znaczy słowo o chorobie, Polska Akademia Umiejętności, Kraków, 2003
- [6] Markiewicz T., Osowski S., Patera J., Kozłowski W., Image processing for accurate recognition and counting of cells of the histological slides, Anal. & Quant. Cytol. & Histol., 26 (2006), 281:292
- [7] Osowski S., Markiewicz T., Support Vector Machine for Recognition of White blood Cells of Leukaemia (in Camps-Valls G., Rojo-Alvarez J.L., Martinez-Ramon M. eds., Kernel Methods in Bioengineering, Signal and Image Processing), Idea Group, Hershey, 2007, 93:122
- [8] Hamilton P.W., Bartels P.H., Montironi R., Anderson N.H., Thompson D., Diamond J., Trewin S., Bharucha H., Automated histometry in quantitative prostate pathology, Anal. & Quant. Cytol. & Histol., 20 (1998), 443:460
- [9] Lezoray O., Elmoataz A., Cardot H., Gougeon G., Lecluse M., Elie H., Revenu M., Segmentation of color images from serous cytology for automated cell classification, Anal. & Quant. Cytol. & Histol., 22 (2000), 311:322
- [10] Soille P., Morphological image analysis, principles and application, Springer, Berlin, 2003
- [11] Scholkopf B., Smola A., Learning with kernels, MIT Press, Cambridge, 2002
- [12] Otsu N., A threshold selection method from gray-level histograms, IEEE Trans. SMC, 9 (1979), 62:66

Authors: dr inż. Tomasz Markiewicz, Politechnika Warszawska, Instytut Elektrotechniki Teoretycznej i Systemów Informacyjno-Pomiarowych, ul. Koszykowa 75, 00-661 Warszawa, and Wojskowy Instytut Medyczny, Zakład Patomorfologii, ul. Szaserów 128, 00-909 Warszawa, E-mail: markiewt@nov.iem.pw.edu.pl; dr Piotr Wiśniewski, prof. dr hab. Wojciech Kozłowski and dr Janusz Patera, Wojskowy Instytut Medyczny, Zakład Patomorfologii, ul. Szaserów 128, 00-909 Warszawa.

Fading channels modelation in digital communication systems

Abstract. In this paper, a MATLAB based approach for mobile radio channels modeling is presented. Specifically, the paper introduces the basic concepts for modeling flat fading channels in MATLAB by means of user-defined m-files. Typical small-scale fading channel models are derived such as uncorrelated Rician fading channel and Rayleigh fading channel with Doppler shift. Further, simple and useful MATLAB constructions for approximation of cumulative distribution functions (CDFs) and probability density functions (PDFs) are also given.

Streszczenie. Referat przedstawia metodę modelowania kanału dla łączności radiowej mobilnej przy wykorzystaniu programu Matlab. W szczególności wprowadzono podstawowe pojęcia dotyczące modelowania fali płasko zanikającej. Rozważono typowe kanały małowymiarowe z zanikaniem zgodnie z rozkładem Rice i Raleigh z uwzględnieniem przesunięcia Dopplerowskiego. Zaprezentowano proste i użyteczne funkcje w postaci m-plików aproksymujące dystrybuantę i funkcje gęstości prawdopodobieństwa. (**Modelowanie zanikania fali w systemach komunikacji cyfrowej**).

Keywords: fading, Rician fading, Rayleigh fading, flat fading.

Słowa kluczowe: modelowanie kanału łączności radiowej mobilnej, rozpraszanie Rayleigha i Rice.

Introduction

In digital communication theory the most frequently assumed model for a transmission channel is the additive white Gaussian noise (AWGN) channel. Using MATLAB for digital communication systems simulation one has the advantage of exploiting the powerful features of its Communications Toolbox along with a nice programming language.

The paper is organized as follows. In Section I, a brief introduction to mobile radio channel is given. The basic concepts for modeling flat fading channels in MATLAB are presented in Section II. In this section, example m-files are proposed to model different types of flat fading channels. Finally, the concluding remarks are given in Section III.

I. The mobile radio channel

The mobile radio channel is characterized by two types of fading effects: large-scale fading and small scale fading [1], [2]. Large-scale fading is the slow variation of the mean (distant-dependent) signal power over time. This depends on the presence of obstacles in the signal path and on the position of the mobile unit. The large-scale fading is assumed to be a slow process and is commonly modeled as having lognormal statistics. Small-scale fading is also called Rayleigh or Rician fading because if a large number of reflective paths is encountered the received signal envelope is described by a Rayleigh or a Rician probability density function (PDF) [3]. The small-scale fading under consideration is assumed to be a flat fading (i.e., there is no intersymbol interference). It is also assumed that the fading level remains approximately constant for (at least) one signaling interval. With this model of fading channel the main difference with respect to an AWGN channel resides in the fact that fading amplitudes are now Rayleigh or Rician-distributed random variables, whose values affect the signal amplitude (and, hence, the power) of the received signal.

The fading amplitudes can be modeled by a Rician or a Rayleigh distribution, depending on the presence or absence of specular signal component. Fading is Rayleigh if the multiple reflective paths are large in number and there is no dominant line-of-sight (LOS) propagation path. If there is also a dominant LOS path, then the fading is Rician-distributed. The fading amplitude r_i at the i th time instant can be represented as

$$(1) \quad r_i = \sqrt{(x_i + \beta)^2 + y_i^2}$$

where β is the amplitude of the specular component and x i, y i are samples of zero-mean stationary Gaussian random processes each with variance σ_0^2 . The ratio of specular to defuse energy defines the so-called Rician K-factor, which is given by

$$(2) \quad K = \beta^2 / 2\sigma_0^2$$

The best and worst-case Rician fading channels associated with K-factors of $K = \infty$ and $K = 0$ are the Gaussian and Rayleigh channels with strong LOS and no LOS path, respectively. So, the Rayleigh fading channel can be considered as a special case of a Rician fading channel with $K = 0$. The Rician PDF is given by [3]

$$(3) \quad f_{Rice}(r) = \frac{r}{\sigma_0^2} \exp\left[-(r^2 + \beta^2)/2\sigma_0^2\right] I_0\left[\frac{r\beta}{\sigma_0^2}\right] r \geq 0$$

where $I_0[\cdot]$ is the zero-order modified Bessel function of the first kind. Now, if there is no dominant propagation path, $K = 0$ and $I_0[\cdot] = 1$ yielding the worst-case Rayleigh PDF

$$(4) \quad f_{Rayleigh}(r) = \frac{r}{\sigma_0^2} \exp\left[-r^2/2\sigma_0^2\right] r \geq 0$$

The Rician cumulative distribution function (CDF) takes the shape of [3]

$$(5) \quad C_{Rice}(r) = 1 - \exp(-\gamma) \sum_{m=0}^{\infty} \left[\frac{\beta}{r}\right]^m I_m\left[\frac{r\beta}{\sigma_0^2}\right]$$

where $\gamma = (K + r^2 / 2\sigma_0^2)$. Clearly, this formula is more difficult to evaluate than the PDF of (3) due to the summation of an infinite number of terms. However, in practical terms it is sufficient to increase m to the value, where the last terms contribution becomes less than 0.1 percent.

Having described the main fading statistics let us consider the effects of the Doppler frequency shift. Doppler shift from the carrier frequency f_c occurs when the distance between the mobile receiver and the transmitter is changing. The magnitude of the Doppler frequency shift f_m is determined by

$$(6) \quad f_m = \frac{vf_c}{c}$$

where v is the mobile station velocity and $c = 3 \cdot 10^8$ m/s is the speed of light. The Doppler frequency f_m is often called fading bandwidth or fading rate of the channel. The relationship between f_m and the coherence time T_m of the channel (i.e., the time over which the channel's response to a sinusoid is essentially invariant) is given by [1]

$$(7) \quad T_m \approx \frac{0.5}{f_m}$$

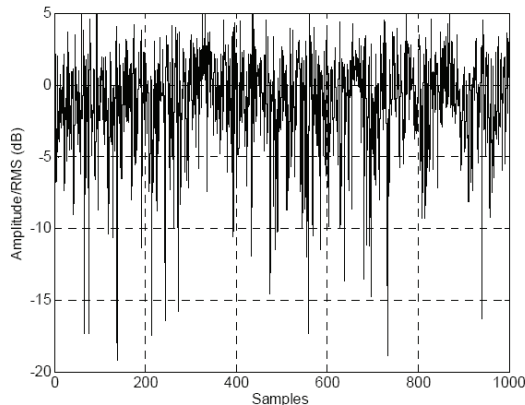


Fig. 1. A typical Rician fading envelope for $K = 5$ dB.

The Doppler power spectral density $S(f)$ of the mobile channel is often expressed as [4], [5]

$$(8) \quad S(f) = \frac{1}{\pi f_m \sqrt{1 - (f/f_m)^2}}$$

The above equality holds for frequency shifts of f in the range $\pm f_m$ about the carrier frequency f_c .

Some important notes are in order here. First, the primary factor, which affects the performance of digital communication systems in a mobile environment, is the smallscale fading. So, we will consider Rayleigh and Rician fading channels from now on. Second, uncorrelated Rayleigh or Rician-distributed fading sequences can be obtained directly by exploiting (1). Third, correlated fading sequences can be obtained by means of "colored" Gaussian noise processes. A well-known approach is the so-called sum-of-sinusoids method in which a "colored" Gaussian noise is approximated by a finite sum of weighted and properly designed sinusoids [5]-[8]. In this paper we opt on the modified sum-of-sinusoids method as described in [8], because of its improved statistical properties and simple software realization.

II. Fading generation in Matlab

Let us first consider the generation of uncorrelated Rician-distributed fading sequences in MATLAB. The mean-squared value of the Rician distribution is known to be $2\sigma_0^2 (K + 1)$, where σ_0^2 is the variance of the component Gaussian noise processes in (1). Further, it is often required a Rician distribution with unit mean-squared value, i.e., $E\{r^2\} = 1$, so that the signal power and the signal-to-noise ratio (SNR) coincide. In order to meet the requirement $E\{r^2\} = 1$, the equation (1) can be written in the form

$$(9) \quad r_i = \sqrt{\frac{(x_i + \sqrt{2K})^2 + y_i^2}{2(K+1)}}$$

where now x_i, y_i are samples of zero-mean stationary Gaussian random processes each with variance $\sigma_0^2 = 1$. So, the desired Rician fading sequences can be generated according to (9) by using the MATLAB random number generator `randn`, which produces normally distributed random numbers. The following MATLAB m-file `rice_fading` does the task.

```
function r = rice_fading(Kdb, N, Mi)
K = 10^(Kdb/10); const = 1/(2*(K+1));
x = randn(1,N); y = randn(1,N);
r = sqrt(const*((x + sqrt(2*K)).^2 + y.^2));
rt = zeros(1,Mi*length(r)); ki = 1
for i=1:length(r)
rt(ki:i*Mi) = r(i); ki = ki+Mi;
end
r = rt;
```

With this MATLAB code one can obtain both the "symbol-level" and "block-level" Rician fading channels for a proper chosen interpolation factor M_i . Also, Rayleigh fading samples can be obtained for $Kdb = -\infty$. A typical Rician fading envelope is shown in Fig.1, where the fading amplitudes are plotted in decibels (about the root-mean-squared (RMS) value).

Now, we will consider a MATLAB based approximation of the Rician CDF. In the MATLAB code below, the Rician CDF is approximated from the derived fading samples according to the m-file `rice_fading`.

```
Kdb=7; N=100000; Mi=1; r=rice_fading(Kdb,N,Mi);
RdB = 20*log10(r);
Rt = [min(RdB):max(RdB)];
for m = 1:length(Rt)
fade = find(RdB < Rt(m)); Nm = length(fade); AF(m) = Nm/N;
end
semilogy(Rt,AF,'k-o'); grid;
```

In this example the Rician CDF is derived by means of an iterative construction, where at each iteration the MATLAB functions `find` and `length` are used to obtain the number of fades, which are below the specified threshold value. The obtained CDF is plotted in Fig. 2.

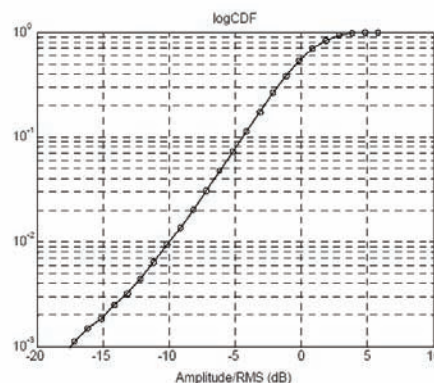


Fig. 2. An approximated Rician CDF for $K = 7$ dB.

The Rician CDF in Fig.2 is plotted on a logarithmic probability scale, which allows us to expand the tail of the CDF, where for example the 10 dB fading margin overload probability is seen to be approximately 10^{-2} .

The next MATLAB code is an example construction for comparing an approximated Rayleigh PDF with the corresponding analytical PDF given by (4). The obtained result is shown in Fig. 3.

```
N = 100000;
x = randn(1, N); y = randn(1, N); r = sqrt(0.5*(x.^2 + y.^2));
step = 0.1; range = 0:step:3; h = hist(r, range);
fr_approx = h/(step*sum(h)); fr = (range/0.5).*exp(-range.^2);
plot(range, fr_approx,'ko', range, fr,'k');
grid;
```

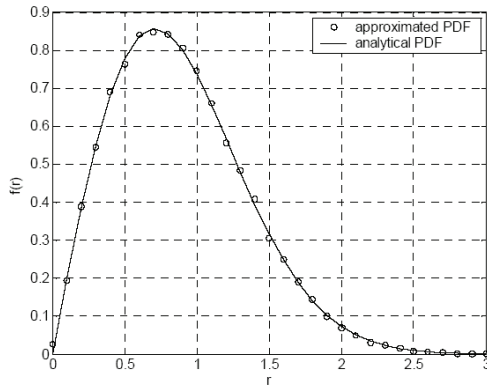


Fig. 3. The approximated and analytical Rayleigh PDF for $\sigma_{02} = 0.5$.

In the above code the approximated Rayleigh PDF (denoted as `fr_approx`) is derived in MATLAB by means of the useful function `hist` (the histogram function). Then, a two-dimensional plot is used (by means of the MATLAB function `plot`) to compare the approximated PDF with the analytical PDF (denoted as `fr`) over a range of interest.

Finally, we will consider the generation of correlated Rayleigh-distributed fading samples by using the modified sum-of-sinusoids method as described in [8]. The quadrature components of Rayleigh fading process are given by

$$(10) \quad x(t) = \sqrt{\frac{2}{M}} \sum_{n=1}^M \cos(\omega_d t \cos \alpha_n + \phi_n)$$

$$(11) \quad y(t) = \sqrt{\frac{2}{M}} \sum_{n=1}^M \cos(\omega_d t \sin \alpha_n + \phi_n)$$

with

$$(12) \quad \alpha_n = \frac{2\pi n - \pi + \theta_n}{4M}, \quad n = 1, 2, \dots, M$$

where ω_d is the maximum angular Doppler frequency, ϕ_n , α_n and θ_n are statistically independent and uniformly distributed on $[-\pi, \pi]$ for all n . The following m-file, named `ray_doppler`, exploits equations (9)-(12) for correlated Rayleigh-distributed fading samples generation in MATLAB.

```
function r = ray_doppler(fm, M, dt, N)
T = N*dt-dt; t = 0:dt:T;
c = sqrt(2/M); w = 2*pi*fm; x = 0; y = 0;
for n = 1:M
alpha = (2*pi*n-pi+(2*pi*rand-pi))/(4*M);
ph1 = 2*pi*rand - pi;
ph2 = 2*pi*rand - pi;
x = x + c*cos(w*t*cos(alpha) + ph1);
y = y + c*cos(w*t*sin(alpha) + ph2);
end
r = sqrt(x.^2 + y.^2)/sqrt(2);
```

Input arguments of the m-file `ray_doppler` are the maximum Doppler frequency (denoted as f_m) in Hz, the number of sinusoids (denoted as M), the time step (denoted as dt) and the desired fading sequence length (denoted as N). All

values of ϕ_n , α_n and θ_n are obtained by means of the MATLAB random number generator `rand`, which produces uniformly distributed random numbers. Using proper values for M (M should be not less than eight [8]), N and dt , one can obtain the desired Doppler spread. The considered approach can be extended with minor additions for correlated Rician fading samples generation.

III. Conclusions

In this paper, an approach to demonstrate mobile radio channels modeling in MATLAB is presented. The basic types of small-scale fading channel models are derived and simulated using MATLAB. The developed channel models can be extended with minor additions to model other types of fading channels (for example, a correlated Rician fading channel). Further, simple and useful MATLAB constructions for approximation of CDFs and PDFs are also given.

REFERENCES

- [1] Sklar, B. Rayleigh fading channels in mobile digital communication systems, Part I: Characterization. IEEE Communications Magazine, 1997, vol. 35, no. 7, p. 90 - 100.
- [2] Suzuki, H. A statistical model for urban radio propagation. IEEE Transactions on Communications, 1977, vol. COM-25, no. 7, p. 673 to 680.
- [3] Proakis, J. G. Digital communications. 2nd ed. New York: McGraw-Hill, 1989.
- [4] Clarke, R. H. A statistical theory of mobile-radio reception. Bell Systems Technical Journal, 1968, vol. 47, no. 6, p. 957 - 1000.
- [5] Jakes, W. C. Microwave mobile communications. New York: Wiley, 1974.
- [6] Patzold, M., Killat, U., Laue, F., Li, Y. On the statistical properties of deterministic simulation models for mobile fading channels. IEEE Transactions on Vehicular Technology, 1998, vol. 47, no. 1, p. 254 - 269.
- [7] Hoehner, P. A statistical discrete-time model for the WSSUS multi-path channel. IEEE Transactions on Vehicular Technology, 1992, vol. 41, no. 4, p. 461 - 468.
- [8] Zheng, Y., R., Xiao, C. Improved models for the generation of multiple uncorrelated Rayleigh fading waveforms. IEEE Communications Letters, 2002, vol. 6, no. 6, p. 256 - 258.

Authors: Lect. drd eng Sorin Popa University of Oradea: Electronics Department, Faculty of Electrical Engineering and Information Technology, Universitatii street 1, 410087 Oradea, Romania, E-Mail: sorin2popa@yahoo.co.uk.
Lect. drd eng Morgos Lucian University of Oradea: Electronics Department, Faculty of Electrical Engineering and Information Technology, Universitatii street 1, 410087 Oradea, Romania, E-Mail: lmorgos@uoradea.ro.
Conf. dr eng Simona Castrase University of Oradea: Electronics Department, Faculty of Electrical Engineering and Information Technology, Universitatii street 1, 410087 Oradea, Romania, E-Mail: s.castrase@uoradea.ro.
Prof. drd eng Draghiciu Nicolae University of Oradea: Electronics Department, Faculty of Electrical Engineering and Information Technology, Universitatii street 1, 410087 Oradea, Romania, E-Mail: n.draghiciu@uoradea.ro.

Modeling of high currents dismantable contacts

Abstract. The paper presents an electro-thermal numerical model which can be used for the modelling and optimization of dismantable contacts of high currents by neglecting the skin effect (by taking into account of the very large ratio, near to 10, of the dimensions of cross-section of the current lead for which the skin effect is very weak). The numerical model is obtained by the coupling of the electrokinetic field problem with the thermal field problem. The coupling is carried out by the source term of the differential equation which describes the thermal field. The source term depends on the electric conductivity which varies according to the temperature. The model allows the calculation of the distribution in the space of the electric quantities (electric potential, the gradient of potential and the current density) and of the thermal quantities (the temperature, the temperature gradient, the Joule losses and heat flow). In the contact zone, it appears a heating larger than that of the current lead caused by the contact resistance. The additional heating, caused by the contact resistance, is simulated by an additional source injected on the surface of contact. For an imposed limiting value of the temperature, using the model, one can determine the optimal geometry of dismantable contact.

Streszczenie. Praca przedstawia model numeryczny procesów ciepło-elektrycznych w wyłącznikach silnoprądowych dla potrzeb ich modelowania i optymalizacji. Model numeryczny otrzymuje się przez sprzężenie pola elektrokinetycznego z polem termicznym. Sprzężenie realizowane jest poprzez źródło opisywane poprzez równania różniczkowe modelujące pole termiczne. Wartość źródła zależy od konduktywności elektrycznej zależnej od temperatury. Model umożliwia wyznaczenie rozkładu przestrzennego wielkości elektrycznych (potencjał, gradient potencjału, gęstość prądowa) oraz termicznych (temperatura, gradient temperatury, straty Joule'a i przepływ ciepła). Na bazie tego modelu możliwe jest zaprojektowanie optymalnej geometrii kontaktów. (Modelowanie wyłączników wysokoprądowych).

Keywords: numerical modelling, dismantable contacts, coupled problems, optimization.

Słowa kluczowe: modelowanie numeryczne, pola sprzężone, optymalizacja.

Introduction

The optimization of the dismantable contacts (figure 1) for high currents (1250 – 6000 A), used in the design of electrical equipment in metal envelope, is possible by solution of a coupled problem, electrical and thermal. The dismantable contact of a system of bus bars has a non-uniform distribution of current density (figure 2) on the cross-section of the current leads. The non-uniform distribution of the current density implies a non-uniform distribution of source term in the thermal conduction equation.

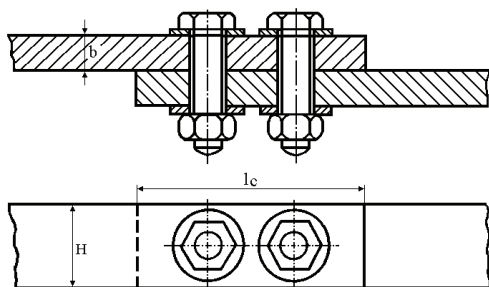


Fig. 1. Typical dismantable contacts

The distribution of the electric quantities can be obtained by solving of Laplace equation for electric potential. The solution of this equation depends on the temperature by electric conductivity. In its turn the electric conductivity influences the source term in the thermal conduction equation and thus the value and the distribution of the temperature of electrical contact.

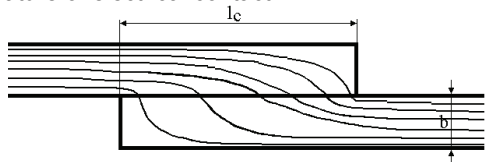


Fig. 2. Current density distribution

Obtaining the correct distributions for the electric quantities (potential, intensity of the electric field, current density and losses by Joule effect) and thermic (the temperature, the gradient of temperature, density of the heat flow, the convection flow on the contact surface, etc) is possible by the coupling of the two problems, electrical and thermal.

The numerical model allows the calculation of the constriction resistance (caused by the variation of the cross section of the current lead). The tightening force influences the contact resistance and consequently the heating of the contact.

Mathematical model

The mathematical model used for obtaining the numerical model has two components, the electrical model and the thermal model, coupled by the electric conductivity, which varies according to the temperature, $\sigma(T)$ and the source term $S(T) = \sigma(T)E^2 = \rho(T)J^2$.

The electrical model is governed by a 2D model described by the Laplace equation for the electric potential:

$$(1) \quad \frac{\partial}{\partial x} \left(\sigma(T) \frac{\partial V}{\partial x} \right) + \frac{\partial}{\partial y} \left(\sigma(T) \frac{\partial V}{\partial y} \right) = 0$$

where electric conductivity and thus the electrical resistance vary according to the temperature as:

$$(2) \quad \rho(T) = \rho_{20} (1 + \alpha_R (T - 20))$$

By knowing the electric potential, one can obtain the intensity of the electric field $\vec{E} = -\overrightarrow{grad}(V)$ and the current density $\vec{J} = \sigma \vec{E}$ (law of electric conduction).

The Joule losses (by the unit of volume) which represents the source term in the thermal conduction equation are calculated by the following relation:

$$(3) \quad S(T) = \vec{J} \cdot \vec{E} = \rho(T)J^2 = \sigma(T)E^2$$

The thermal model is governed by the thermal conduction equation in steady state:

$$(4) \quad \frac{\partial}{\partial x} \left(\lambda(T) \frac{\partial T}{\partial x} \right) + \frac{\partial}{\partial y} \left(\lambda(T) \frac{\partial T}{\partial y} \right) + S = 0$$

where: λ - the thermal conductivity which is considered constant in the temperature range of the current lead (below 200 °C).

Domain of analysis and boundary conditions

One considers a simplified analysis domain which is presented in figures 3 and 4 where one neglects the existence of the fastening bolts.

The boundary conditions of the electrical model are presented in figure 3. In the general case, one knows the current I carrying the current lead and which determines a voltage drop V_1-V_2 . In this model, one initializes a voltage drop for which one calculates the current which corresponds to it (at each iteration) and then in a iteration loop one modifies the voltage drop to obtain the desired value of the current.

The current which passes any section of the current lead is calculated by the following relation:

$$(5) \quad I = \int_S (\vec{J} \cdot \vec{n}) dS$$

where: \vec{n} - the normal at S which is the cross-section of the current lead.

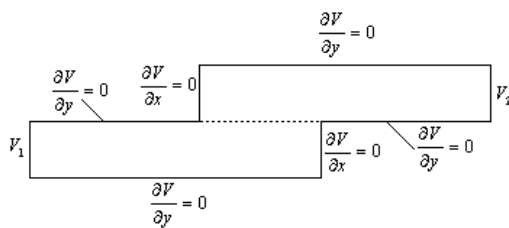


Fig. 3. Analysis domain and boundary conditions for electrical model

The two assembled bars are considered sufficiently long to set, on the boundaries AB and CD (figure 4) the boundary conditions of Neumann homogeneous type.

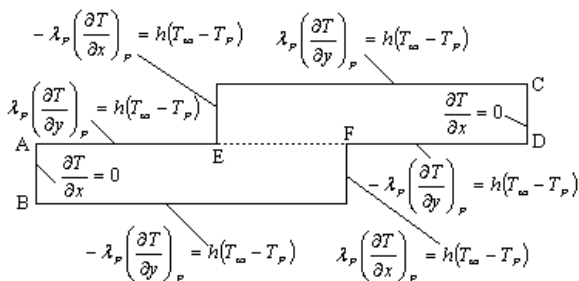


Fig. 4. Analysis domain and boundary conditions for thermal model

On the other borders, one sets boundary conditions of the convection type, with a global heat exchange coefficient h (by convection and radiation, $h=20 \text{ W/m}^2\text{K}$) to the environment having the temperature T_∞ [3].

Numerical algorithm

The numerical model is obtained by the discretization of the differential equations (1) and (4) by using the finite volumes method [1].

The coupled model is of alternate type [2] where the equations are solved separately and coupling is realized by the transfer of the data of one problem to the other. The two problems (electric and thermal) are integrated in the same source code and thus use the same mesh. The numerical algorithm is shown in figure 5.

The criterion of convergence of the coupled model was selected the value of the current, through the current lead, calculated using the relation (5). One used a mesh having

4293 nodes (with $\Delta x = \Delta y = 0.002m$). The imposed error, for the electric model, was $\varepsilon_E = 10^{-7}$ and for thermal model $\varepsilon_T = 10^{-5}$. The error imposed for the coupled model was $\varepsilon_C = 10^{-4}$. The convergence of the coupled model is very fast, as we see in table 1 (for $l_c = 100mm$).

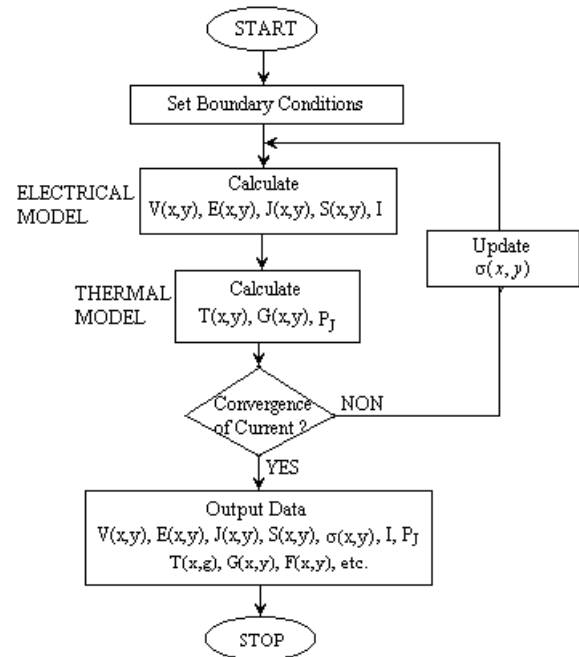


Fig. 5. Simplified diagram of numerical algorithm

Table 1. Convergence of the iterative process for coupled model and current.

| Iterations (coupled model) | Iterations (electrical model) | Iterations (thermal model) | Current [A] |
|----------------------------|-------------------------------|----------------------------|-------------|
| 1 | 388104 | 171986 | 1405.05 |
| 2 | 61053 | 45277 | 1262.67 |
| 3 | 26832 | 1 | 1264.66 |
| 4 | 1 | 1 | 1264.65 |

Numerical results

The figures 6, 7, 8, 9 and 10 present some numerical results. The dimensions of the analysis domain are those of figure 6. The principal difficulty, in modelling and simulation the temperature distribution of a dismountable contact, is to take into account the resistance of contact (especially disturbance resistance because the resistance of constriction can be calculated by the model).

The optimization of the contact design supposes to determine the value of dimension l_c such that the maximum temperature, in the contact region, remains lower than the acceptable limiting value allowed by standards.

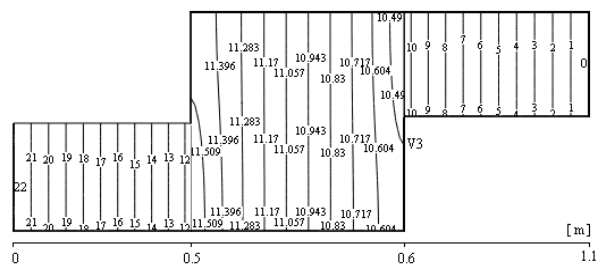


Fig. 6. Potential distribution (in mV)

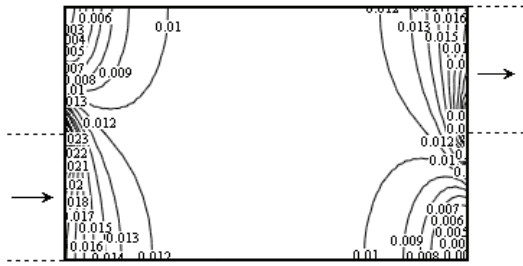


Fig. 7. Electrical field distribution in the contact region (in V/m)

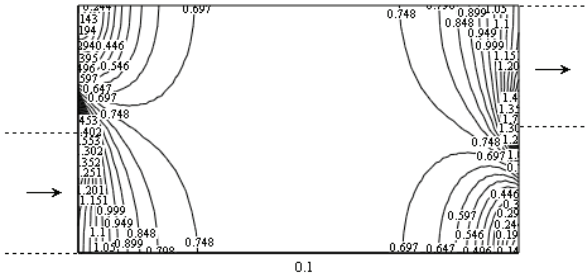


Fig. 8. Current density distribution in the contact region (in A/mm²)

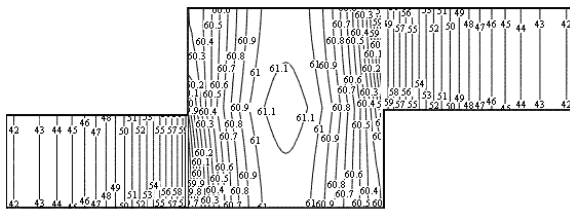


Fig. 9. Temperature distribution (in °C)

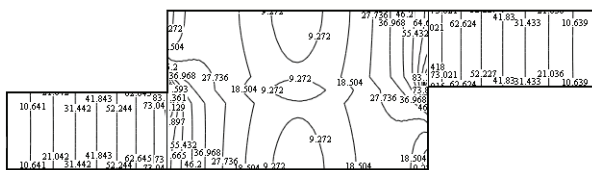


Fig. 10. Temperature gradient distribution (in °C/m)

For the case presented in table 1 ($l_c=100\text{mm}$ and $I=1264.65\text{ A}$) the calculated losses by Joule effect are 28.89 W, while calculated ohmic losses are 24.91 W. The difference is due to the constriction resistance of the current lead.

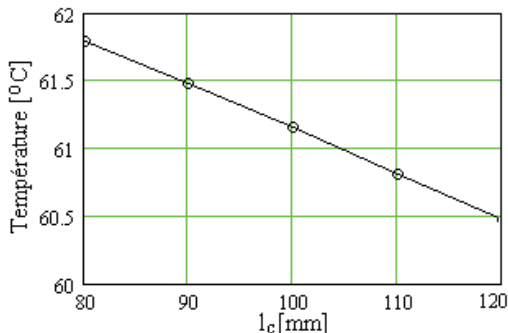


Fig. 11. Maximum temperature of contact versus length of contact (for $S_c = 1.01\text{ kW}$).

Model validation

The numerical validation of the model was made using a simplified analysis domain, by using a current lead with variable cross-section. The analysis domain and the boundary conditions are presented at figures 12 and 13, [3].

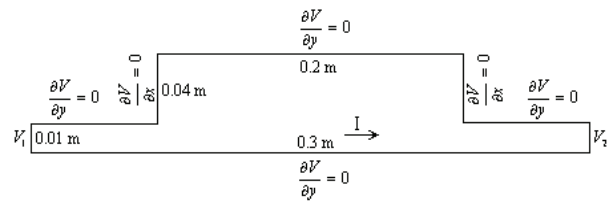


Fig. 12. Electrical model and boundary conditions for numerical validation

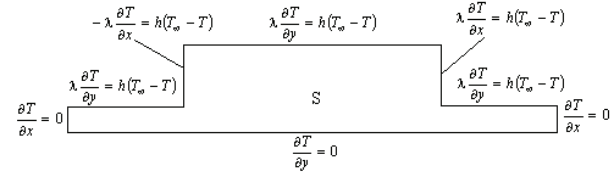


Fig. 13. Thermal model and boundary conditions for numerical validation

The numerical results obtained in this case are presented in figures 14, and 15.

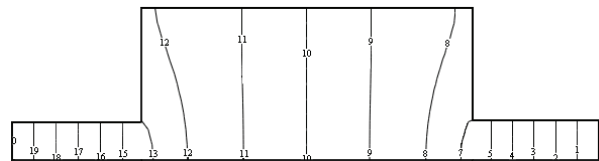


Fig. 14. Electric potential distribution

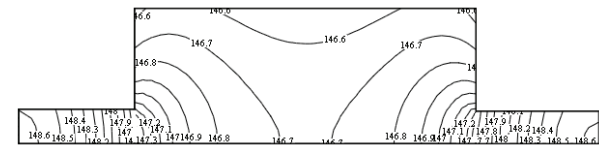


Fig. 15. Temperature distribution

The results presented in figures 14 and 15 were obtained for a current $I=965.22\text{ A}$ what corresponds to a voltage drop $V_1-V_2=0.02\text{ V}$ (the thickness of the current lead was considered 0.01m).

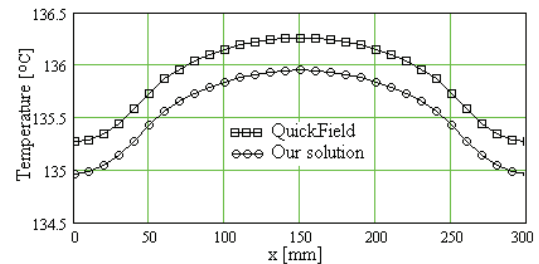


Fig. 16. Temperature distribution ($y=0$)

The numerical validation of the results of this model was made by using the software QuickField for the electrical model and the software Mirage (FEMM) for the thermal model. In figure 16, one presents the temperature distribution on the symmetry axis of the current lead. One notes a very good agreement between our results and the results obtained using the Mirage software.

Contact resistance model

The source term determined by the contact resistance is calculated by the following relation:

$$(6) \quad S_c = \frac{R_c I^2}{(nc - 1) \Delta x \Delta y H}$$

where: Δx and Δy - the dimensions of the control volume, nc - the number of mesh points in the contact region (see fig. 17), H - the bus bar height (see fig. 1). The contact resistance R_c is calculated with the following relation [9]:

$$(7) \quad R_c = \frac{\rho}{\pi n a n} \arctg \frac{\sqrt{d^2 - a^2}}{a} - 1.2 \frac{\rho \sqrt{d^2 - a^2}}{A_a} + \frac{R_{ss}}{n \pi a^2}$$

where: ρ - the electric resistivity, n - the number of contact points, $A_a = 8(2d)^2$ - the total area of contact (see fig. 18) and R_{ss} (in Ωm^2) - the specific resistance of oxide film of contact point.

The radius of contact surface a is calculated from Holm's relation:

$$(8) \quad a = \sqrt{\frac{F}{\pi n \xi H_a}}$$

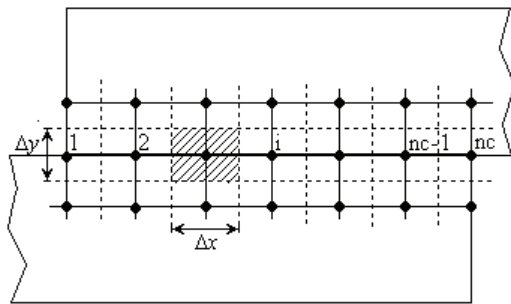


Fig. 17. The mesh in contact region

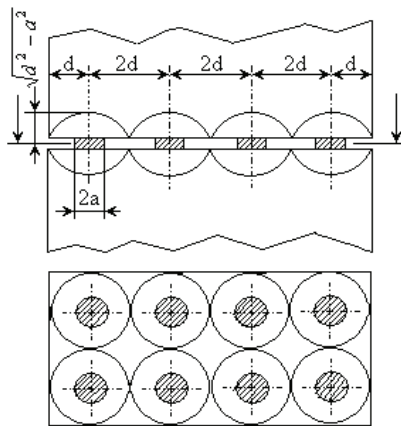


Fig. 18. Physical model of contact region

The relation (7) does not take into account the variation of contact resistance with temperature. To take it into account one can use the relation [5]:

$$(9) \quad R_c(T) = R_c(20) \left(1 + \frac{2}{3} \alpha_R (T - 20) \right)$$

where: α_R - the variation coefficient of electric resistivity with temperature.

The contact resistance model was implemented in numerical model of dismantable contact. For a constant value of the current ($I = 2275 A$), varying the tightening

force of the screws one can get the variation of the maximum temperature versus tightening force (see fig. 19)

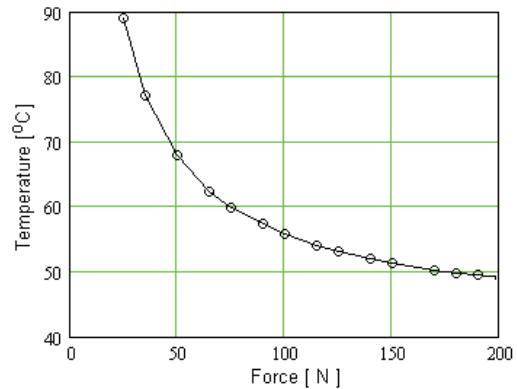


Fig. 19. Maximum temperature in contact area versus tightening force (for $I = 2275 A$)

Conclusions

The elaborated model can be used for the optimization of the current leads of high currents with variable cross-section, such as the dismantable contacts. The model allows the calculation of the constriction resistance of current lead, the constriction resistance of contact region and takes into account the specific resistance of oxide film of contact point which is an important component of the contact resistance.

The results presented in figure 11 shows that it is possible to optimize the geometry and to reduce the mass of the contact. Numerical model elaborated allows determination of the maximum temperature in the contact area as a function of the tightening force of the dismantable contact (see fig.19). However an experimental validation of the numerical results is absolutely necessary.

REFERENCES

- [1] Popa I., Modélisation numérique du transfert thermique. Méthode des volumes finis, *Édition Universitaria*, Craiova, 2002.
- [2] Meunier G., Electromagnétisme et problèmes couplés, *Hermes Science*, Paris, 2002.
- [3] Popa I., Cautil I., Electro-Thermal Model for Optimization of Current Leads with Variable Cross-Section, *International Conference on Scientific Computing in Electrical Engineering (SCEE 2006)*, Sinaia 17-22 September 2006, Romania, Book of Abstract, 125 -126.
- [4] Kogut L., Komvopoulos K., Electrical Contact resistance theory for conductive rough surface separated by a thin insulating film, *Journal of Applied Physics*, Vol. 95, No. 2 January 2004, 576-584.
- [5] Hortopan G., Electrical Apparatus of Switching (in romanian), vol. 1. *Editura Tehnica*, Bucharest 1993.
- [6] Lee S., Song S., Moran K. P., Yovanovich M. M., Analytical Modeling of Thermal Resistance in Bolted Joints, *HTD-Vol., 263, Enhanced Cooling Technique for Electronics Applications*, ASME 1993, 115 - 122.

Authors: prof. dr. ing. Ioan Popa, University of Craiova, Faculty of Electrical Engineering, Bd. Decebal 107, 200440 Craiova, E-mail: ipopa@elth.ucv.ro; assoc. prof. dr ing. Ioan Cautil, University of Craiova, E-mail: icautil@elth.ucv.ro; prof. dr. ing. Dan Floricau, Politehnica University of Bucharest, Faculty of Electrical Engineering, E-mail: floricau@stat.conv.pub.ro; assist. ing. Florin OCOLEANU, University of Craiova, Faculty of Electrical Engineering, E-mail focoleanu@elth.ucv.ro.

Characterization of particular circuit elements requisite for studying the electrochemical processes

Abstract. Electrochemical Impedance Spectroscopy (EIS) is reported to equivalent circuit models which fit the data obtained for some chemical processes. EIS data and the equivalent circuit model provide a useful approach for effective studies of electrochemical problems. Equivalent circuit models are not limited to "classical" electrical components (resistors, capacitors, and inductors) but need of a few specialized electrochemical elements such as Warburg diffusion and constant phase elements. They match in the best possible form the model's and measured impedances.

Streszczenie. Metoda Elektrochemicznej Spektroskopii Impedancyjnej (MESI) została wykorzystana do przedstawienia pewnych procesów chemicznych za pomocą zjawisk w obwodzie elektrycznym. Możliwość porównania wyników pomiarów MESI z tymi, które otrzymuje się z analizy modelu obwodowego, pozwala efektywnie oceniać procesy elektrochemiczne. Jednakże elementy stosowanych wówczas modeli obwodowych nie mogą być ograniczone tylko do „klasycznych” elementów (oporniki, kondensatory i cewki), lecz muszą być uzupełnione o takie specyficzne elementy, jak impedancja Warburga i elementy o stałej fazie. Włączając takie specyficzne elementy do modelu obwodowego uzyskuje się dobrą zgodność wyników pomiarów MESI z uzyskiwanymi za pomocą obwodowej impedancji. (Wykorzystanie Metody Elektrochemicznej Spektroskopii Impedancyjnej (MESI) do przedstawienia pewnych procesów chemicznych za pomocą zjawisk w obwodzie elektrycznym).

Keywords: electrochemical processes, equivalent circuit models, Warburg impedance, constant phase element.

Słowa kluczowe: procesy elektrochemiczne, modele obwodowe, impedancja Warburga, element stało-fazowy.

Introduction

Electrochemistry is the study of reactions in which charged particles (ions or electrons) cross the interface between two phases of matter, typically a metallic phase (the *electrode*) and a conductive solution, or *electrolyte*. A process of this kind can always be represented as a chemical reaction and is known generally as an *electrode process*. Electrode processes (also called *electrode reactions*) take place within the double layer and produce a slight unbalance in the electric charges of the electrode and the solution. Much of the importance of electrochemistry lies in the ways that these potential differences can be related to the thermodynamics and kinetics of electrode reactions. In particular, manipulation of the interfacial potential difference affords an important way of exerting external control on an electrode reaction.

Presently, electrochemistry is recognized as the basis for corrosion, and a number of electrochemical techniques are under development, specifically for corrosion measurement. These are generally referred to as "DC Techniques" and they are quite similar one to other. Among these techniques are Polarization Resistance, Tafel Plots, Potentiodynamic Plots, Cyclic Polarization, and Electrochemical Potentiokinetic Reactivation.

On the other hand the Electrochemical Impedance Spectroscopy (EIS) can be a very useful tool to help the formulation of hypotheses, particularly when EIS data is fit to equivalent circuit models. Often, an equivalent circuit model which fits the data will suggest some chemical model, process, or mechanism which can be proposed and tested. EIS data and the equivalent circuit model provide a useful approach for effective studies of electrochemical problems. Analyzing EIS data by fitting it to equivalent circuit models can be a valid and rewarding approach, particularly in the early stages of an investigation. Most of the circuit elements in the model are common electrical elements such as resistors, capacitors, and inductors. The choice of which model applies to a given process is made from knowledge of the physical characteristics. The model is chosen to give the best possible match between the model's impedance and the measured impedance.

Examinations of electrochemical corrosion behaviors by the method of impedance spectroscopy and evaluations of the total energy absorbed by the investigated specimen appear as very effective approaches for estimations of the

actual states of many practical devices. By monitoring the rate of corrosion and determining the degree of corrosion we can predict metal fatigue. EIS data accompanied by equivalent circuit models provide a useful approach for effective studies of electrochemical problems.

The most correct approach to match EIS spectra to equivalent circuit model needs few specialized electrochemical elements such as Warburg diffusion elements and constant phase elements. To be useful, these elements in the model should have a basis in the physical electrochemistry of the system.

Characterization of corrosion mechanisms

Corrosion can be defined as the deterioration of materials by chemical processes. Of these, the most important by far is electrochemical corrosion of metals, in which the oxidation process $M \rightarrow M^+ + e^-$ is facilitated by the presence of a suitable electron acceptor, sometimes referred to in corrosion science as a depolarizer. Oxygen is the most common depolarizer [2].

In practice, almost all processes involving oxidation and reduction can be regarded as driven exclusively by the entropy increase of the system. In any spontaneous macroscopic change, the entropy of the system with surrounding increases; it never decreases.

In the above sense, corrosion can be viewed as the spontaneous return of metals to their ores; the huge quantities of energy that were consumed in mining, refining, and manufacturing metals into useful objects is dissipated by a variety of different routes to corrosion.

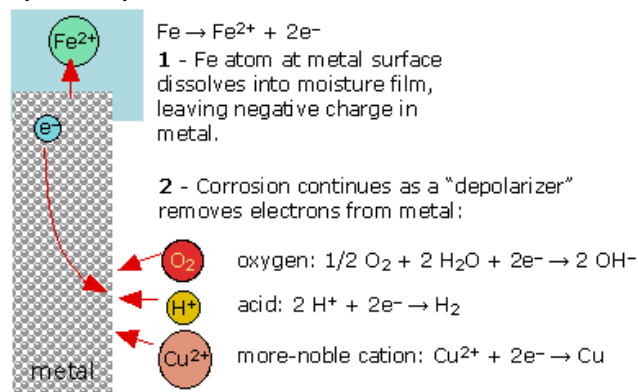


Fig. 1. Electrochemical processes leading to the corrosion of iron

The special characteristic of most corrosion processes is that the oxidation and reduction steps occur at separate locations on the metal. This is possible because metals are conductive, so the electrons can flow through the metal from the anodic to the cathodic regions. Oxidation-reduction reactions proceed in a direction that allows the electron to fall (in free energy) from a source to a sink. The presence of water is necessary in order to transport ions to and from the metal, but a thin film of adsorbed moisture can be sufficient.

When an electrode is polarized, it can cause current to flow via electrochemical reactions that occur at the electrode surface. The amount of current is controlled by the kinetics of the reactions and the diffusion of reactants both towards and away from the electrode.

In cells where an electrode undergoes uniform corrosion at open circuit, the open circuit potential is controlled by the equilibrium between two different electrochemical reactions. One of the reactions generates cathodic current and the other anodic current. The open circuit potential ends up at the potential where the cathodic and anodic currents are equal. It is referred to as a mixed potential. The value of the current for either of the reactions is known as the corrosion current. Under small amplitude excitations the studied materials exhibit linear properties and their corrosion resistances are expressed in terms of driving point impedances depending on the total internal energies and their degrees of disorder. Equivalent circuits are fitted to the measurement data and can suggest some chemical model, process, or mechanism which can be proposed and tested.

An electrical double layer exists at the interface between an electrode and its surrounding electrolyte. This double layer is formed as ions from the solution "stick on" the electrode surface. Charges in the electrode are separated, on the order of angstroms, from the charges of these ions.

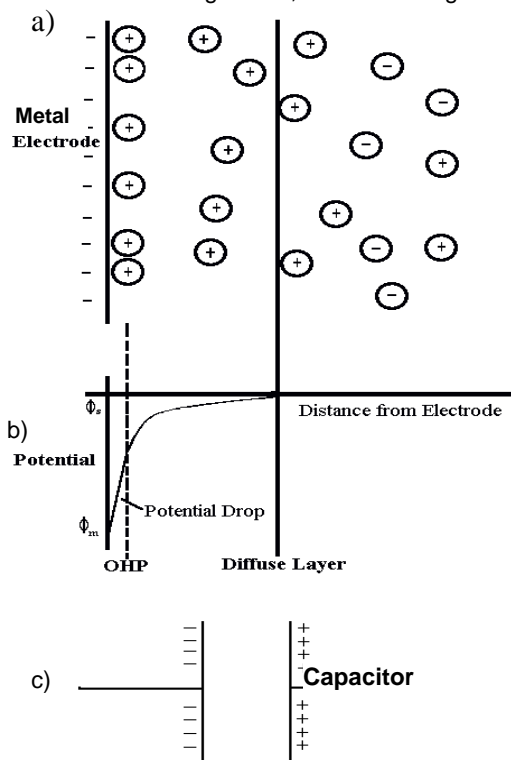


Fig. 2. Charge and potential distributions within a double layer

Charges separated by an insulator form a capacitor. The value of the double layer capacitance depends on many variables including electrode potential, temperature, ionic concentrations, types of ions, oxide layers, electrode

roughness, impurity adsorption, etc. On a bare metal immersed in an electrolyte, an estimate indicates that there will be approximately 30 μF of capacitance for every $\text{cm} \times \text{cm}$ of electrode area.

Electrochemical Impedance Spectroscopy and Circuit Models

Monitoring of metallic corrosion assumes greater importance because of the huge loss caused by material deterioration [1-3]. Among the various electrochemical methods suitable for measurements of corrosion rate of metals, the harmonic current analysis method is highly useful since the corrosion current can be obtained without the usage of Tafel constants at corrosion potential [6]. Recently, the emphasis in electrochemistry has consequently shifted from a time-concentration dependency to frequency related phenomena, a trend toward small-signal alternating current studies. They are now extended to the study of mass transport and stress corrosion cracking as well as to noise analysis suitable for the study of localized corrosion, stress corrosion cracking and the blistering of coatings. In particular, impedance measurements have been adopted to determine the different elementary steps involved in overall process, thus providing a better knowledge of the mechanisms of corrosion and corrosion protection [5]-[7]. They may be used to investigate the dynamics of bound or mobile charge in the bulk or interfacial regions of any kind of solid or liquid material: ionic, semiconducting, mixed electronic-ionic, and even dielectrics. The electrical output of a heterogeneous device can vary substantially depending on the species of charge present, the microstructure of the electrolyte, and the texture and nature of the electrodes. Electrical double layers and their inherent capacitive reactances are characterized by their relaxation times, or more realistically by the distribution of their relaxation times.

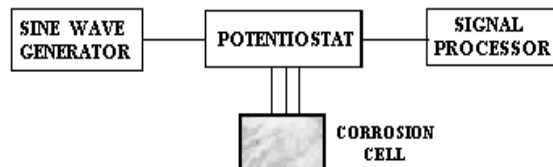


Fig. 3. Basic instrumentation for corrosion investigations

In order to investigate the values of the various parameters controlling the electrochemical reaction it is often necessary to perturb the system in some way. Their application to real problems lies in making the optimum assumptions, and in recognizing when these assumptions are starting to break down. This includes all techniques that are designed and analyzed on the assumption that the electrochemical system can be treated as a combination of *linear* circuit elements (e.g. resistors, capacitors etc.). This is almost invariably an approximation to reality, but by restricting ourselves to small changes of potential (of the order of 10 mV or less) we generally obtain a reasonable approximation to linear behavior.

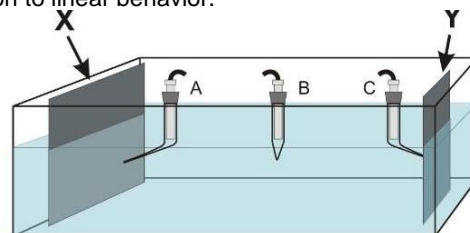


Fig. 4. Typical electrolytic cell: X - electrode from studied material, Y - passive electrode, B - reference electrode, A, C - Youdin's capillaries

Electrical measurements performed to evaluate the electrochemical behavior of electrode and/or electrolyte materials are usually made with cells shown in Fig.4.

Impedance spectroscopy has firmly established itself as one of the most informative and irreplaceable investigation methods in fundamental and applied electrochemistry and materials science. The development of the electrochemical theory of corrosion has caused a growing importance of electrochemical techniques in the study of corrosion and corrosion protection. In a number of view-points it is the method of choice for characterizing the corrosion behavior of devices in which the overall device state is determined by a number of strongly coupled processes, each proceeding at a different rate.

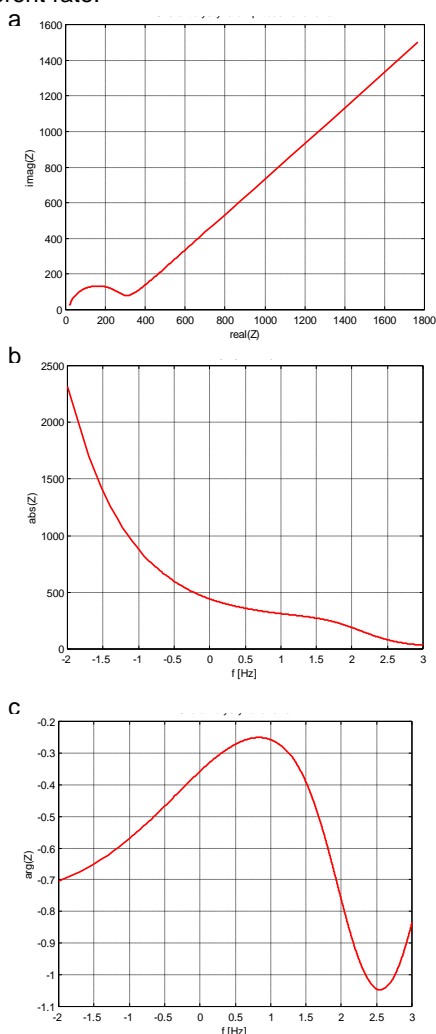


Fig.5. Spectral characteristics of an electrochemical process: a) Nyquist plot, b) magnitude plot, c) phase plot

Particular Circuit Elements

A detailed physicoelectrical model of all processes which may occur in investigations on an electrode-material system may be unavailable, premature, or perhaps too complicated to warrant its initial use. Thus it is important to approximate the experimental impedance data $Z_{exp}(j\omega)$ by the impedance $Z_{ec}(j\omega)$ of an equivalent circuit made up of appropriate elements. It should be pointed out that ordinary circuit elements such as resistors and capacitors are always considered as lumped-constant quantities which involve ideal properties. But to be able well interpreting most impedance spectra of investigated electrochemical systems all essential properties of the nonlocal processes must be taken into account. They are related in different ways to the finite spatial extension of any real system. This means that

such processes as diffusion which can occur even in a completely homogeneous material, and charge mobility as well as microscopic material properties influence importantly the composition of an equivalent circuit model.

Warburg diffusion element

Diffusion can create impedance known as the Warburg impedance. This impedance depends on the frequency of the potential perturbation. At high frequencies the Warburg impedance is small since diffusing reactants don't have to move very far. At low frequencies the reactants have to diffuse farther, thereby increasing the Warburg impedance.

The Nyquist plot (Fig. 5a) shows a depressed semi-circle, typical of a Randles element. At low frequency, the plot shows a well-developed diagonal line at an angle of 45°, indicative of a Warburg impedance (Fig.6). The phase angle of a Warburg impedance is 45°.



Fig. 6. Symbol of the Warburg diffusion element

The equation for the "infinite" Warburg impedance is:

$$(1) \quad Z = \sigma \cdot (\omega)^{-1/2} (1 - j)$$

On a Nyquist plot the infinite Warburg impedance appears as a diagonal line with a slope of 0.5. On a Bode plot, the Warburg impedance exhibits a phase shift of 45°.

In equation (1), σ is the Warburg coefficient defined as:

$$(2) \quad \sigma = \frac{RT}{n^2 F^2 A \sqrt{2}} \left(\frac{1}{C_0^* \sqrt{D_0}} + \frac{1}{C_R^* \sqrt{D_R}} \right)$$

in which ω = angular frequency, D_0 = diffusion coefficient of the oxidant, D_R = diffusion coefficient of the reductant, A = surface area of the electrode, n = number of electrons transferred, C^* = bulk concentration of the diffusing species (moles/cm³).

This form of the Warburg impedance is only valid if the diffusion layer has an infinite thickness. Quite often this is not the case. If the diffusion layer is bounded, the impedance at lower frequencies no longer obeys the equation above. Instead, we get the form:

$$(3) \quad Z_0 = \sigma \omega^{-1/2} (1 - j) \tanh\left(\delta \left(\frac{j\omega}{D}\right)^{1/2}\right)$$

with δ = Nernst diffusion layer thickness, D = an average value of the diffusion coefficients of the diffusing species.

This more general equation is called the "finite" Warburg impedance. For high frequencies where $\omega \rightarrow \infty$, or for an infinite thickness of the diffusion layer where $d \rightarrow \infty$, equation (3) simplifies to the "infinite" Warburg impedance.

Constant Phase Element

Capacitors in EIS experiments often do not behave ideally. Instead, they act like a constant phase element (CPE) as defined below. The impedance of a capacitor is

$$(4) \quad Z = A(j\omega)^{-\alpha}$$

When this equation describes a capacitor, the constant $A=1/C$ (the inverse of the capacitance) and the exponent $\alpha=1$. For a constant phase element, the exponent α is less than one. The Constant Phase Element (CPE) is a non-intuitive circuit element that is given by

$$(5) \quad 1 / Z = Y = Q^\circ (j\omega)^n$$

where Q° has the numerical value of the admittance ($1/|Z|$) at $\omega=1$ rad/s. The CPE name is given by this fact that the phase angle of the CPE impedance is independent of the frequency. The constant A in equation (4) depends on the relaxation time τ as follows

$$(6) \quad A = \tau_0^{1-\alpha} (\epsilon_s - \epsilon_\infty)^{-1}$$

where ϵ_s and ϵ_∞ denote static and high-frequency limiting dielectric constant, respectively, and τ_0 is the mean relaxation time.

The behavior of a CPE depends directly on an exponential distribution of activation energies and an exponential form for τ . The CPE exhibits no transition from intensive to extensive behavior as the frequency decreases. In fact, the CPE cannot be applied for all frequencies and becomes physically unrealizable for sufficiently low or high frequencies.

The "double layer capacitor" on real cells often behaves like a CPE instead of like a capacitor. Several theories have been proposed to account for the non-ideal behavior of the double layer but none has been universally accepted. In most cases, we can safely treat α as an empirical constant and not worry about its physical basis.

The symbol of a constant phase element is usually presented in the form shown in Fig.7

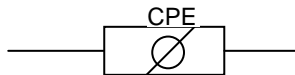


Fig.7. Symbol of a constant phase element

There are three important subcircuits, shown in Fig.8, which consist of the CPE in conjunction with other circuit elements. Their wide use as combined elements justifies involving as compound circuit elements. However, the CPE is frequently used separately and not directly in any of the above compounds. Its presence is quite valuable for interpretation of a wide variety of EIS data on dielectric and conduction materials, underlying its wide usefulness. -

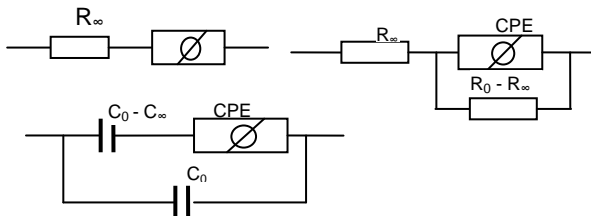


Fig. 8. Three compound circuits containing CPE

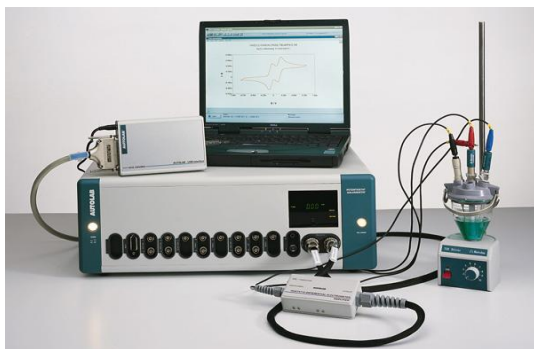


Fig. 9. Set-up of experimental appliances

Experiments

Now we can proceed in what follows to applications of circuit element models to identification of corrosion

resistances of chosen systems. Experiments have been realized by using a set up of appliances shown in Fig. 9.

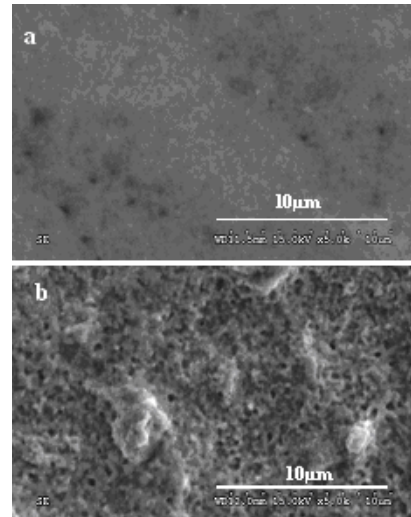


Figure 10. Nano-crystalline structure of the copper: a) layer surface without corrosion, b) layer surface after corrosion

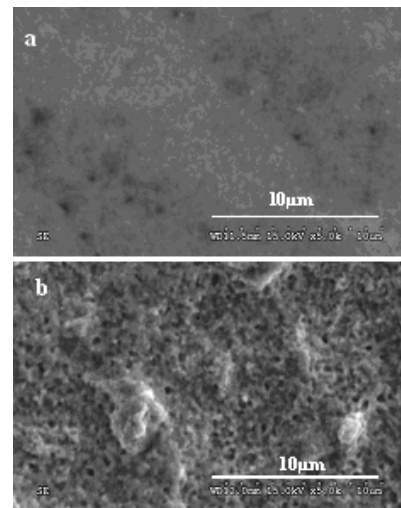


Figure 11. Microcrystalline structure of the copper layer: a) surface without corrosion, b) surface after corrosion

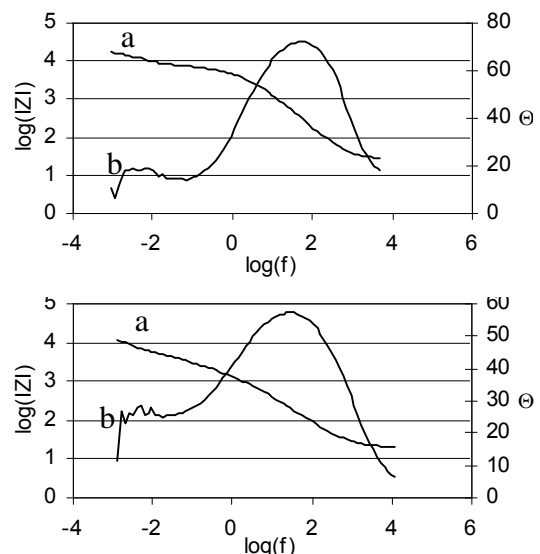


Fig.12. EIS data for copper thin layers: a) nano-, b) micro-structure

The best case is a sample of nano- and micro-structural copper thin layers (Figs. 10,11) which were subjected to corrosion tests. The obtained EIS data are given in Fig. 12.

Table I. Parameters of Equivalent Circuit Elements

| Copper structure | C_d [$\mu\text{F}/\text{cm}^2$] | R_t [$\text{k}\Omega\text{cm}^2$] | C_c [$\mu\text{F}/\text{cm}^2$] | R_c [$\text{k}\Omega\text{cm}^2$] | R_e [$\text{k}\Omega\text{cm}^2$] |
|------------------|--|--|--|--|--|
| μm | 10.0 | 8.8 | 1.29 | 58.0 | 7.28 |
| nm | 13.0 | 7.9 | 3.45 | 77.0 | 7.47 |

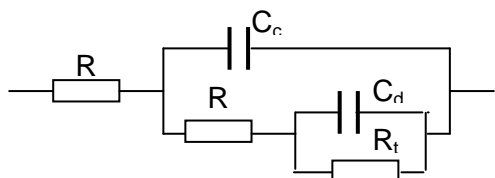


Fig.13. Circuit model of copper thin layers: R_e - resistance of electrolyte, R_c - polarisation resistance, R_t - resistance of charge transfer, C_c - polarisation capacitance, C_d - double layer capacitance

The second case of EIS data is reported to the corrosion of a metal plate covered by a thin layer isolator. The measured EIS data are represented by spectral characteristics shown in Fig.14.

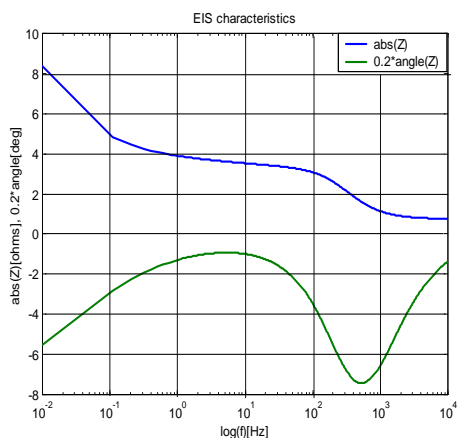


Fig. 14. EIS characteristics for a copper plate coated by an isolator

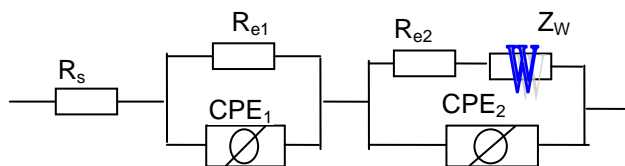


Fig.15. Equivalent circuit model with CPE and Z_w elements

The values of identified element parameters are given in Table II.

Table II. Parameters of Equivalent Circuit Elements

| R_s [Ω] | R_{e1} [Ω] | R_{e2} [Ω] | $\sigma(Z_w)$ [$\Omega\text{s}^{-0.5}$] | CPE ₁ | | CPE ₂ | |
|-----------------------|--------------------------|--------------------------|--|------------------|-----------|------------------|-----------|
| | | | | A[Ω] | $-\alpha$ | A[Ω] | $-\alpha$ |
| 0.71 | 0.59 | 2.24 | 0.91 | 2.836 | 2.482 | 2337.9 | 1.542 |

The above element parameters match in a best as possible manner the obtained EIS data.

Discussion and Conclusion

It has been our intent in this article to outline the fundamentals of a newly introduced concept in modeling of

electrochemical corrosion processes with appropriate elements widely applied in electric circuits. Moreover, we have found that this concept must be thoroughly mastered before more advanced topics can be understood. In our experience, we can measure the EIS characteristics for the studied corrosion samples and using such specific circuit elements as the Warburg diffusion impedance and constant phase element we are able identify the corrosion resistance of investigated materials.

The main feature of the presented approach lies in involving two types of non-intuitive circuit elements leading to the best possible match between the model's impedance and the measured impedance of a corrosion specimen. Results from the EIS measurements can be easily interpreted in terms of circuit elements parameters.

REFERENCES

- [1] Bala H., Korozja materialów –Teoria i praktyka. Wyd. WIPMiFS, Polit. Częstoch, Częstochowa, 2002
- [2] Baszkiewicz J., Kamiński M., Korozja materialów. Ofic. Wyd. PW, Warszawa, 2006
- [3] Zajt T., Metody woltoamperometryczne i elektrochemiczna spektroskopia impedancyjna. Wyd. Politechn. Gdańskiej, Gdańsk, 2001
- [4] Barsoukov E., Macdonald J.R., Impedance Spectroscopy; Theory, Experiment, and Applications, 2nd ed., Wiley Interscience Publications, N.Y., 2005
- [5] Bard A.J., Faulkner L.R., Electrochemical Methods: Fundamentals and Applications, Wiley Interscience Publications, N.Y., 2000.
- [6] Scully J.R., Silverman D.C., and Kendig M.W., (eds), Electrochemical Impedance: Analysis and Interpretation, ASTM, N.Y., 1993.
- [7] Mansfeld, F., Electrochemical Impedance Spectroscopy (EIS) as a New Tool for Investigation Methods of Corrosion Protection, Electrochimica Acta, 35 (1990), 1533.
- [8] Walter, G.W., A Review of Impedance Plot Methods Used for Corrosion Performance Analysis of Painted Metals", Corrosion Science, 26 (1986) 681.
- [9] Kendig, M., J. Scully, Basic Aspects of Electrochemical Impedance Application for the Life Prediction of Organic Coatings on Metals", Corrosion, 46 (1990) 22.
- [10] Cottis R. and Turgoose S., Electrochemical Impedance and Noise, NACE International, 1440 South Creek Drive, Houston, Electrochemical Methods; Fundamentals and Applications, A.J. Bard, L.R. Faulkner, Wiley Interscience Publications 2000.
- [11] Atkins P.W., Physical Chemistry, Oxford University Press, 1990.
- [12] Dobbelaar J.A.L., The Use of Impedance Measurements in Corrosion Research; The Corrosion Behavior of Chromium and Iron Chromium Alloys, PhD thesis TU-Delft, 1990.
- [13] Geenen F., Characterization of Organic Coatings with Impedance Measurements; A Study of Coating Structure, Adhesion and Underfilm Corrosion, , PhD thesis, TU-Delft, 1990.
- [14] Gabrielle C., Identification of Electrochemical Processes by Frequency Response Analysis, Solartron Instrumentation Group, 1980.
- [15] Trzaska M., Trzaska Z., Control of Copper Thin-layer Coatings with Electrochemical Impedance Spectroscopy. Proc. Amer. Control Conference (ACC'2007), New York, 11-13 July 2007, Paper ThC19.4.
- [16] Yeager E., Bockris J.O'M., Conway B.E., Sarangapani S., AC Techniques, in M. Sluyters-Rehbach, J.H. Sluyters (eds), Comprehensive Treatise of Electrochemistry; Vo. 9, Electrode: Experimental Techniques; Chapter 4, Plenum Press, 1984.

Author: prof. dr hab. inż. Zdzisław Trzaska, Politechnika Warszawska, Instytut Elektrotechniki Teoretycznej i Systemów Informacyjno-Pomiarowych, Plac Politechniki 1, 00-661 Warszawa, E-mail: zdzislaw.trzaska@netlandia.pl.

Using Stochastic Petri Nets for power system dependability computation

Abstract. Combining the Generalized Stochastic Petri nets (GSPN) properties and high level Petri nets facilities, a structural simplified model Logical Explicit Stochastic Petri Nets (LESPN), having the same modeling power as GSPN, is built. LESP primitive architectural modules are used in repairable power systems dependability modeling. The paper presents a dependability comparative analysis, used in electric ship power plant study. Three Electrical Generators-Main Switchboard (EG-MS) coupling alternatives, for the electric ship power plant, are proposed and analyzed.

Streszczenie. Przez połączenie uogólnionych, stochastycznych Sieci Petriego (GSPN) i sieci Petriego wyższego rzędu utworzono Logiczną Prosta Sieć Petriego (LESPN), która posiada podobne zalety w zakresie modelowania, jak sieci GSPN. Podstawowe moduły LESPN wykorzystano do symulacji zależności w reperowanym systemie elektroenergetycznym. Artykuł przedstawia porównawczą analizę zależności w symulacji zasilania statku elektrycznego. Zaproponowano i przeanalizowano trzy alternatywne sposoby połączenia głównej tablicy przełączników dla elektrowni statku elektrycznego. (**Wykorzystanie Sieci Petriego do analizy niezawodności sieci energetycznych**).

Keywords: high level Petri nets, dependability, electric ship power plant.

Słowa kluczowe: Sieci Petriego wyższego rzędu, analiza zależności, zasilanie statku elektrycznego.

Introduction

Reliability uses several model types, such as reliability block diagrams, fault trees and Markov chains, to evaluate various dependability metrics [1], [2]. These model types differ from one another, not only in the ease of use in a particular application, but in terms of modeling power. Modeling power of a model type is determined by the kinds of dependencies within subsystem to be modeled and the kind of dependability measures to be computed.

Scientific works as [1], [2] established a hierarchy, among the most commonly used types of dependability models, according to their modeling power. The Markov (state-space) model types (continuous-time Markov chains, Generalized Stochastic Petri Nets) are more powerful than combinatorial-model types, in that they can capture dependencies, such as a shared repair facility between system components. Markov models are capable of handling phased missions, state dependent failure rates, common mode failures, physical interconnection dependencies, time dependent transitions, maintenance policies. But to describe the Markov chain (MC) for a complex system, became a very difficult task. In this case a stochastic Petri net (SPN) equivalent to MC, is usually used in modeling power system failure-repair behavior. The GSPN model is the most commonly used because it's ability to use in events modeling both kinds of transitions, timed and immediate transition.

This paper uses a power system dependability model based on GSPN model, but having a simplified structure. Logical Explicit Stochastic Petri Nets (LESPN) model is used for a dependability comparative study of Electrical Generators-Main Switchboard (EG-MS) coupling alternatives. A computerized tool, Stochastic Petri Nets Evaluation (SPNE) using Visual basic software, for 586 PC, predicting dependability metrics of complex repairable power system, was developed. Given input data in the form of Petri net structure, elements failure and repair rates and availability logical conditions, for candidate architectures during conceptual design of power system, the computation of the dependability metrics is straight forward.

Section 2 briefly introduces Generalized Stochastic, Logical Explicit Stochastic Petri Nets. Section 3 describes the LESP simplified models for the EG-MS coupling alternatives. Section 4 gives the dependability metrics of the EG-MS coupling alternatives and makes the safety comparative study.

Petri nets in dependability modeling

The dynamic behavior of a system, according to Petri net theory, is determined by the movement of tokens based on the firing of transition. A transition is enabled to fire if the number of tokens in each of its input places is at least equal to the multiplicity of the corresponding input arc from that place.

A marking of a Petri net is the distribution of the tokens in the set of places of Petri net. Each marking defines a state of the system. A marking is reachable from an original marking, if there is a sequence of transition firings starting from the original marking which results in that marking. The reachability graph (RG) of a Petri net is the set of all markings that are reachable from the initial marking. Most important firing times can be associated with transitions. When the distribution of firing times for all transitions is exponential, the net is a stochastic Petri net (SPN). Ajmone-Marsan [3] proposed in 1984 generalized stochastic Petri nets (GSPN) which allow transitions to have 0 firing time (immediate transitions) or exponentially distributed firing times (timed transitions). SPN and GSPN are equivalent to continuous time Markov chain (CTMC). There are two types of markings for a GSPN: vanishing (at least one immediate transition is enabled in that marking) and tangible (otherwise).

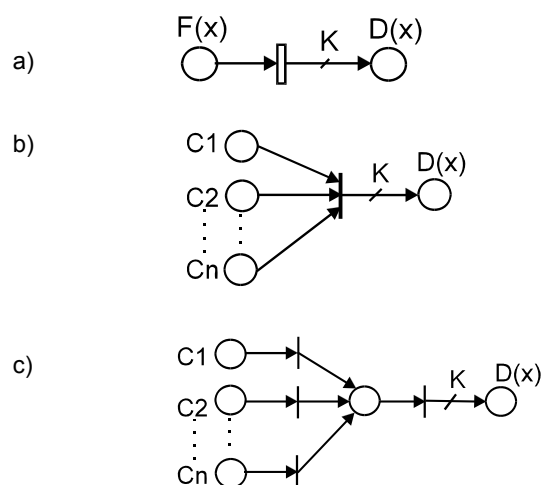


Fig. 1. GSPN subnets modeling: a stochastic failure (repair) event (a), AND logical condition (b), OR logical condition (c)

According to [1], GSPN dependability models consist of two subnets: the subnets modeling the stochastic failure-repair events (Fig. 1.a) and the logical subnets modeling AND or OR logical conditions of system performances Fig. 1.b,c).

This paper uses the new simplified LESP model [4], extracting from inside GSPN model the logical subnets. The GSPN properties and the colored Petri net facilities are combined, to create the set of primitive architectural modules. Primitive architectural modules are used to construct a modular architecture for this structural simplified model, named logical explicit stochastic Petri nets (LESPN), because the logical conditions of system performance are explained outside the SPN model. Including predicate/transitions nets facilities, a great structural simplification of the model is obtained. The arc label of the colored Petri net dictates how many and which kinds of "colored" tokens will be removed from or added to the places.

In Fig. 2, for G1, G2 power system, are presented the primitive architectural modules of redundancy modeling alternatives: ideal switch- cold redundancy Fig. 2a. hybrid switch- active redundancy Fig. 2b.

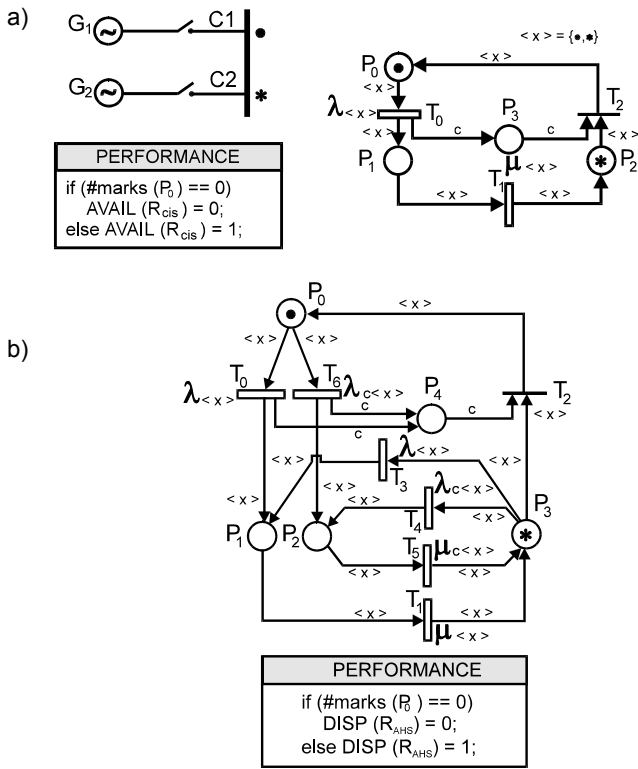


Fig. 2. Primitive architectural modules of LESP model for redundant system modeling alternatives, ideal switch- cold redundancy (a) hybrid switch- active redundancy (b.)

The LESP primitive module for a cold redundant system (G_1, G_2), having ideal switches (C_1, C_2 , without fail) and unlimited repairs R_{cis} is shown in Fig. 2.a. Generators operational/ stand-by/ fail/ state is modeled by the places $P_0/P_2/P_1$. Generator fail/repair event is modeled by the stochastic transitions T_0/T_1 . The stand-by commutation is modeled by immediate transition T_2 . Fig. 2b. presents the LESP primitive module for an active redundant system (G_1, G_2), having hybrid switches (C_1, C_2 , fail before and after the commutation) and unlimited repairs R_{AHS} .

The LESP primitive module for a repairable series system (transformer T , switches S_1, S_2) is presented in Fig. 3. System operational state and components (S_1, T, S_2) fail states are modeled by the places P_0, P_1, P_2 , respectively

P_3 . Components fail (repair) events are modeled by the stochastic transitions $T_0, T_2, T_4, (T_1, T_3, T_5)$. The system performance logical conditions are shown for each model in the PN associated table (system availability logical condition).

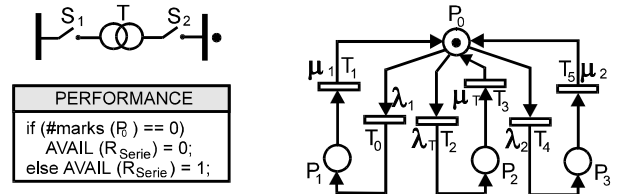


Fig. 3. Primitive architectural modules of LESP model for series system

Dependability models of EG-MS coupling alternatives

Naval power plant is an isolated system, usually having a single sectioned bus bar system. The fault tolerant power system has automatically coupled Diesel generators to different bus bar sections, improving the system availability. The Diesel generators are coupled to the MS, according to the three coupling alternatives presented in Fig. 4.

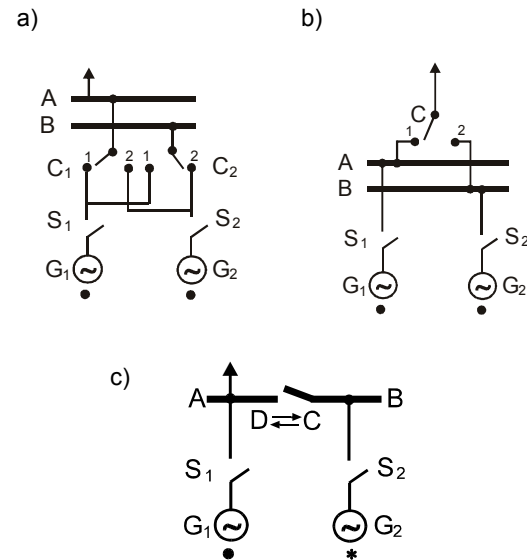


Fig. 4. EG-MS coupling alternative A (a), alternative B (b), alternative C (c)

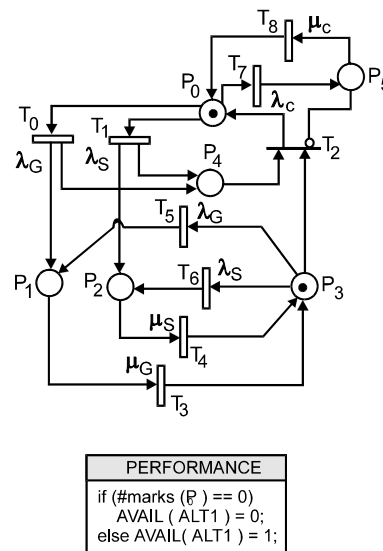


Fig. 5. LESP model for EG-MS, alternative 1.

The behavior, on reliability criteria, of each proposed alternatives 1, 2 and 3 is modeled, in the paper, using the LESP model, as we can see in Fig. 5., Fig. 6., respectively Fig. 7. For all analyzed alternatives, the logical availability conditions are described in the "PERFORMANCE" table associated to the LESP model.

The LESP model for EG-MS alternative1 (Fig. 5.) uses a set of locations modeling: $P_0/P_1/P_3$ - the working /the failed/the stand-by generators number, P_4 - the failed S switches number, P_5 the fail state of C separator, P_6 the stand-by generator command. The LESP transitions mean: $T_0, T_5/T_1, T_6/T_7$ -the generator/ S switch/ C separator failure event (conditioned by the good working of a generator), $T_3/T_4/T_8$ -the generator/ S switch/ C separator repair event, T_2 the stand-by generator coupling event (conditioned by the good working of the C separator).

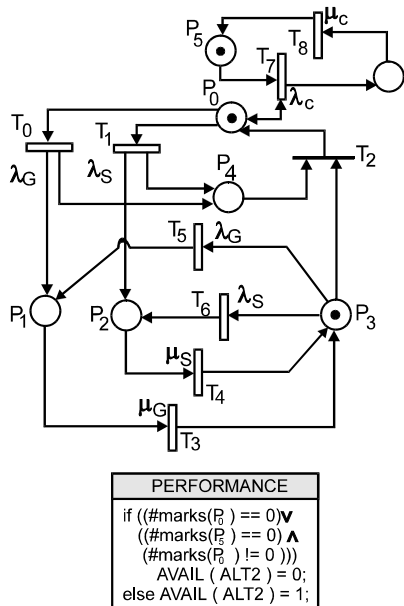


Fig. 6. LESP model for EG-MS, alternative 2.

The LESP model for EG-MS alternative 2 (Fig. 6.) uses a set of locations modeling: $P_0/P_1/P_3$ - the working /the failed/the stand-by generators number, P_4 - the failed S switches number, P_5 the working state of C separator, P_6 the fail state of C separator, P_4 the stand-by generator command. The LESP transitions mean: $T_0, T_5/T_1, T_7$ -the generator/ S switch/ C separator failure event (conditioned by the good working of a generator), $T_3/T_4/T_8$ - the generator/ S switch/ C separator repair event, T_2 the stand-by generator coupling event (not conditioned by the good working of the C separator).

The LESP model for EG-MS alternative 3 (Fig. 7.) uses a set of four colors (*, •, D, C), a set of predicates/ transition $\langle x \rangle$, $\langle y \rangle$, $\langle z \rangle$ and a set of locations modeling: $P_0/P_1/P_2$ - the working G-S drives and the C separator state (C- connected, D- disconnected)/the failed generators number /the failed S switches number, P_3 the fail state of C separator. The LESP transitions mean: $T_0/T_2/T_6$ -the generator/ S switch/ C separator failure event (conditioned by the good working of a generator), $T_1/T_3/T_7$ -the generator/ S switch/ C separator repair event, T_4 the C separator connecting event (conditioned by the failure of a

generator), T_5 the C separator disconnecting event (conditioned by the good working of both the generators).

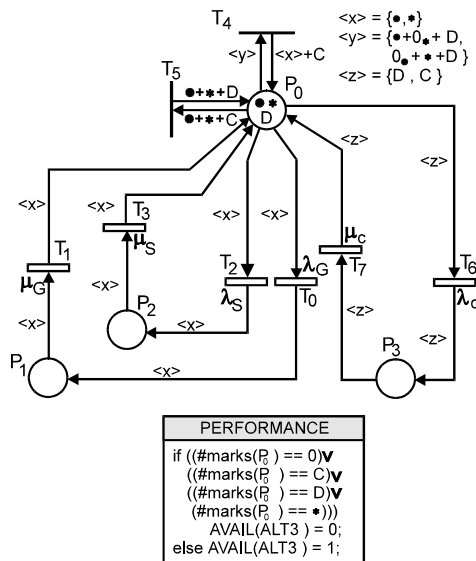


Fig. 7. LESP model for EG-MS, alternative 3

Dependability comparative study

According to [5] dependability metrics for the EM-MS coupling alternatives, computed with the SPNE tool (considering a planned operational time $T_p = 80000$ h) are the following: general availability indices as system success probability P_s , system failure probability; and power system availability specific indices (PE 013/ 1994) as, the average of failure total time $M[\alpha(T_p)]$, the average of success total time $M[\beta(T_p)]$, the average of failure interruptions total number $M[v(T_p)]$, the average of maneuver interruptions total number $M[v'(T_p)]$ (table 1).

For the dependability metrics evaluation purpose, SPNE tool [6] constructs the reachability graph (RG) of the bounded SPN, the reduced RG (obtained by reducing the vanishing markings), and the MC isomorphic to reduced RG, both modeling the failure-repair behavior of power system design alternative. The SPNE tool constructs the subset: success states, failure states.

Table 1 also presents the number of total / reduced states (NT/N), of success /failure states (NS/NR) associated to the EM-MS coupling alternatives.

For the EM-MS coupling alternative 2, two cases are studied: the complex case, with $NR=16$ states and $N=12$ states, considering the consumer availability (conditioned by the good working of the C separator) and the simple case of the MS availability, only. Obviously the complex case in EM-MS alternative2 must be compared with all the other alternatives, because the important task of the analyzed systems is the consumer power supply.

Comparative study results leads to the conclusion that the EM-MS alternative 3 has the best availability indices. To achieve this goal a very large number of maneuvers, compared to the other alternatives, must be done. But an important increase of the electric ship power supply system safety is obtained.

Table 1. Dependability metrics of EM-MS coupling alternatives

| | NT/N | NS/NR | P_s | $M[v(T_P)]$ | $M[v'(T_P)]$ | $M[\alpha(T_P)] \times E+04$ | $M[\beta(T_P)]$ |
|---------------|-------|-------|------------|-------------|--------------|------------------------------|-----------------|
| Alternative 1 | 11/9 | 3/6 | 0.99814648 | 8.38414 | 53.1243 | 7.98517 | 148.2808 |
| Alternative 2 | 16/12 | 3/9 | 0.99814644 | 8.38415 | 53.2193 | 7.98517 | 148.284 |
| | 3/3 | 1/2 | 0.99008135 | 16.7231 | 0 | 5.4312 | 255.37 |
| Alternative 3 | 32/27 | 11/16 | 0.99984377 | 1.41449 | 216.072 | 7.99874 | 12.5377 |

5. Conclusions

The structural simplified model (LESPN), having the same modeling power as GSPN is more practical for engineering applications, more easy to understand and also very adequate in power system dependability modeling.

Extracting the logical subnets from inside the GSPN model, the vanish markings and the immediate transitions associate to logical conditions does not appear in the reachability graph RG. Obviously the states number N, modeling the behavior of the analyzed system is very small, compared to GSPN model. This leads to a smaller computational effort and also to the possibility of increasing the complexity of the analyzed systems.

Different dependability metrics may be evaluated using LESP model and on this purpose specialized software is created. In the designing phase this model and the associated tool can be easily used for dependability comparative study. The computed availability indices are used in techno-economical comparative study, for choosing the proper alternative system design.

The comparative study may has two different stages: a simplified stage using simplified LESP models for design alternatives and a complex stage using complex LESP models for the vital areas power supply of the chosen system. The simplified stage purpose is to choose an adequate alternative and the complex stage purpose is to compare the dependability metrics for the system vital areas and to propose maintenance policies.

For the electric ship power plant dependability studies are very important in the design stage but also in working stage of the system. This electric power system is isolated and a very high availability is necessary including also proper maintenance politics.

REFERENCES

- [1] Malhotra M, and Trivedi K. S., "Power-Hierarchy for Dependability- Model Types". *IEEE Trans. Reliability*, no 3, Sept.(1994), 34-42
- [2] Malhotra M, and Trivedi K. S., "Dependability modeling using Petri nets", *IEEE Trans. Reliability*, no 3, Sept. (1995), 29-36
- [3] M. Ajmone-Marsan et. al. (1984), A class of generalized stochastic Petri nets for the performance evaluation of multiprocessor systems", *ACM Trans. Computer Systems*, vol. 2, Apr. (1984), 93-122
- [4] Dumitrescu M., - Stochastic Petri Nets Architectural Modules for Power System Availability, *The 9-th IEEE International Conference on Electronic, Circuit and Systems, ICECS'2002 - Dubrovnik - Croatia*, 15-18 september (2002), 745-748
- [5] M. Dumitrescu. "Contribution to the structure configuration and control of naval power system, on reliability criteria", *Physics theses -Dunarea de Jos- University of Galati*, (1997)
- [6] JohnsonA. and Malek M., "Survey of software tools for evaluating reliability, availability, and serviceability", *ACM Computing Surveys*, vol. 2, Apr. (1988), 227-269

Authors: professor Mariana Dumitrescu, Mariana.Dumitrescu@uqal.ro; Electrical Engineering Department, University "Dunarea de Jos" of Galati, Stiintei Street, No.2, Galati-800146, Romania.:

Comparison between classical and fuzzy optimization in one-phase electrical circuits

Abstract. In the paper a comparison between classical and fuzzy optimization in relation to electrical circuits is presented. It is considered one-phase system with linear load and non-ideal voltage source with a sinusoidal waveform. The fuzziness of the system is represented by RMS values of the voltage source described as fuzzy numbers. The solution of this problem is based on the frequency domain. This solution (an active current) is received as a crisp one (real numbers) in a numerical way. After optimization the source current has minimal RMS values in fuzzy sense.

Streszczenie. W artykule przedstawiono porównanie optymalizacji klasycznej i rozmytej w odniesieniu do obwodów elektrycznych. Rozpatrywany jest układ jednofazowy złożony z liniowego odbiornika i nieidealnego źródła napięcia sinusoidalnego. Rozmycie w układzie reprezentowane jest przez wartość skuteczną napięcia zapisaną jako liczba rozmyta. Rozwiązanie uzyskiwane jest w dziedzinie częstotliwości na drodze numerycznej. (Porównanie optymalizacji klasycznej i rozmytej w odniesieniu do obwodów elektrycznych).

Keywords: optimization, fuzzy sets, active current.

Słowa kluczowe: optymalizacja, zbiory rozmyte, prąd aktywny.

Introduction

This paper is a continuation author's papers presented before concerning application of fuzzy sets in electrical circuits [1,2,3]. In contrast to classical optimization in the paper a fuzzy optimization has been considered, in particular a comparison between classical and fuzzy optimization has been presented. The optimization approach used in fuzzy systems is applied to achieve the optimal current (active current) of the electrical circuit. This technique allows to obtain the solution of the optimization problem taking into account a range of changes of the voltage source. The solution of this problem is based on the frequency domain.

Fuzzy time functions

The presented problems concerning an application of fuzzy sets in optimization of electrical systems making use of fuzzy functions. In publications presented before there are considered different types of fuzzy functions [4,5,6]. In the paper are considered periodical fuzzy time functions where the amplitudes of functions are fuzzy numbers. In particular, the voltage source is described as a fuzzy time function:

$$(1) \quad \tilde{u}(t) = \sqrt{2}|\tilde{U}| \sin \omega t ,$$

where: $|\tilde{U}|$ - the RMS value of the voltage source being not a real (crisp) but a fuzzy number.

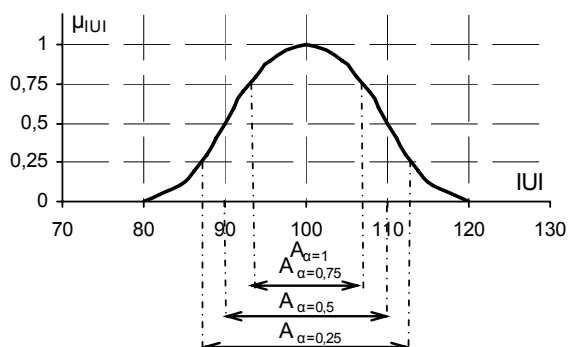


Fig.1. The RMS value of the voltage source as the fuzzy number with marked α -cuts

For example, the RMS value $|\tilde{U}| = 100V$ as a fuzzy number with membership function $\mu_{|U|}$ of class s with the fuzzy set carrier described as: $B_{|U|} = |U| \pm 0,2|U|$, is presented in Fig.1. Then the waveform (1) of the voltage source can be presented in graphical form as in Fig.2.

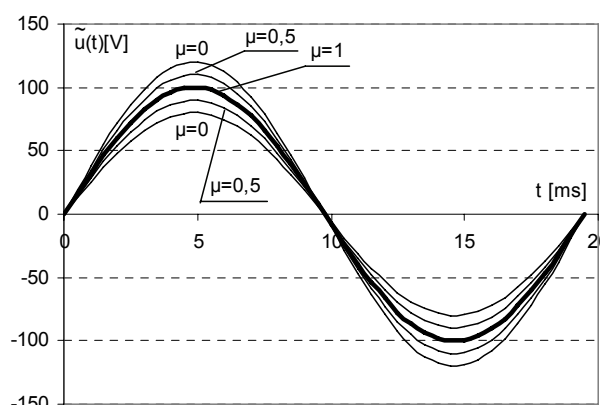


Fig.2. The $\tilde{u}(t)$ waveform

Decision making under fuzzy conditions

The choice of the optimal solution in fuzzy systems is called as decision making under fuzzy conditions. It was considered in many publications presented before [4,5,6,7]. In this paper optimal decision is considered as a compromise between membership functions of a fuzzy goal and a fuzzy constraint. Generally, it is considered optimization problem (2) under fuzzy constraint (3):

$$(2) \quad \min_{x \in X} f(x),$$

$$(3) \quad \tilde{C}(x) \subset X ,$$

where: $\tilde{C}(x)$ - the fuzzy constraint.

This fuzzy constraint is described by its membership function:

$$(4) \quad \mu_{\tilde{C}(x)}(x) : C(x) \rightarrow [0,1], \mu_{\tilde{C}(x)}(x) \in [0,1].$$

The shape of this membership function is known. Process of decision making under fuzzy constraints requires knowledge about the shape of membership function $\mu_{f(x)}(x)$. Although the form of the $f(x)$ is given, its membership function $\mu_{f(x)}(x)$ is not known. When values of the function $f(x)$ are limited: $f(x) \leq L$, the membership function $\mu_{f(x)}(x)$ of the function $f(x)$ can be determined as:

$$(5) \quad \mu_{f(x)}(x) = 1 - \frac{f(x)}{L}.$$

And then the optimal point can be determined as the intersection point of $\mu_{f(x)}(x)$ and $\mu_{C(x)}(x)$ (Fig.3).

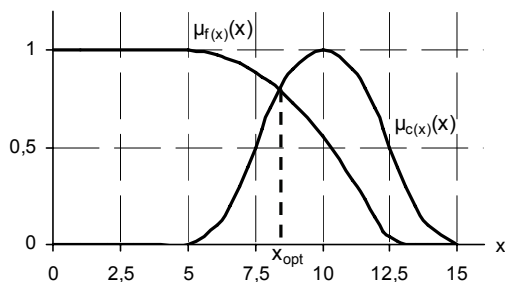


Fig.3. The method of selection of the optimal solution

This technique can be applied in the considered one-phase electrical circuit. This circuit, shown in Fig.4, is composed of linear load and non-ideal voltage source with periodical sinusoidal waveforms. The considered problem of optimization of the electrical circuit can be described as following crisp (not fuzzy) minimization:

$$(6) \quad \min J = \min_i \|i\|^2,$$

under fuzzy constraint:

$$(7) \quad \operatorname{Re}\{\tilde{E}I^* - IZI^*\} \approx \tilde{P},$$

where: P – the active power consumed by the load before optimization as fuzzy number; \approx - equals sign in fuzzy sense described by membership functions; $Z = R + jX$ - the complex inner impedance of the voltage source; $Z_o = R_o + jX_o$ - the complex impedance of the load; I - the complex RMS value of the current; $I = I_a + jI_b$; \tilde{E} - the complex RMS value of the source voltages; $\tilde{E} = |\tilde{E}|e^{i\alpha}$

where $|\tilde{E}_h|$ is not a real but a fuzzy number.

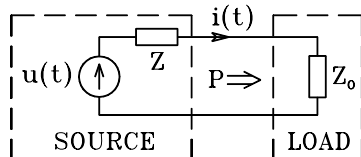


Fig.4. The considered one-phase system

The calculations of algebraic operations on fuzzy numbers [8] are based on using the α -cuts concept of the fuzzy number (Fig.1). The optimal current $_{opt}I$, as the solution of the problem, can be determined in a numerical

way according to method presented in Fig.3. In order to receive the solution, for the optimization problem (2),(3), the following algorithm can be used [4]:

1. It is assumed that the α -cut:

$$(8) \quad \alpha_k = I, k=1.$$

2. Next, it is calculated:

$$(9) \quad f_k = \bigvee_{x \in C_{\alpha_k}} \mu_{f(x)}(x) = \max_{x \in C_{\alpha_k}} \mu_{f(x)}(x).$$

3. Next it is calculated the following difference:

$$(10) \quad \varepsilon_k = \alpha_k f_k.$$

If $|\varepsilon_k| > \varepsilon$ then follow to point 4, otherwise follow to point 5 (where: ε - a tolerance factor).

4. New α -cut is equal to:

$$(11) \quad \alpha_{k+1} = \alpha_k - r_k \varepsilon_k$$

and follow to point 2 assuming $k=k+1$. The value of the parameter k should be selected in such way that $r_k \geq 0$; $0 \leq \alpha_k \leq I$.

5. The solution is: $\alpha_* = \alpha_k$ and optimal point x_* can be determined from relationship:

$$(12) \quad \mu_{f(x)}(x_*) = \bigvee_{x \in C_{\alpha_*}} \mu_{f(x)}(x).$$

When functions $\mu_{f(x)}(x)$ and $\mu_{C(x)}(x)$ have convex shapes:

$$(13) \quad \mu(\lambda x_1 + (1-\lambda)x_2) > \mu(x_1) \wedge \mu(x_2), \text{ i.e.}$$

$$(14) \quad \mu(\lambda x_1 + (1-\lambda)x_2) > \min(\mu(x_1), \mu(x_2)), \forall \lambda \in [0,1],$$

the determined solution is the unique one. Functions $\mu_{f(x)}(x)$ and $\mu_{C(x)}(x)$ considered in the paper have convex shapes. After optimization the source current has minimal RMS value with reference to fuzzy constraint.

Classical optimization

The problem of optimization (6) under constraint (7) in crisp (not fuzzy) version can be determined as classical approach, for example by means of Lagrange's multipliers method [9,10].

It is taken into account minimization as follows:

$$(15) \quad \min J = \min_i \|i\|^2,$$

under power constraint:

$$(16) \quad \operatorname{Re}\{\tilde{E}I^* - IZI^*\} = P.$$

Then the Lagrange's functional has the form:

$$(17) \quad L(I, \lambda) = \|I\|^2 + \lambda \left[P - \operatorname{Re}\{\tilde{E}I^* - IZI^*\} \right].$$

Minimization of the Lagrange's functional (17) allows to obtain the optimal current (active current) described as:

$$(18) \quad \text{opt } \underline{I} = \frac{\lambda}{2(1 + \lambda R_Z)} \underline{E} = \left(1 - \sqrt{\frac{|E|^2 - 4R_Z P}{|E|^2}} \right) \frac{\underline{E}}{2R_Z}$$

where the Lagrange's multiplier λ can be determined as:

$$(19) \quad \lambda = \frac{1}{R} \left[\sqrt{\frac{|E|^2}{|E|^2 - 4R_Z P}} - 1 \right]$$

In case of considered minimization for the system presented in Fig.4 the classical optimization allows to obtain the solution in analytical form (18). After optimization the source current (18) has minimal RMS value with reference to the constraint (16).

Example

It is considered a system presented in Fig. 4 with parameters:

$$(20) \quad \underline{Z} = R + jX = 2 + j4\Omega; \quad \underline{Z}_o = R_o + jX_o = 8 + j6\Omega;$$

$$(21) \quad \tilde{E} = |\tilde{E}| e^{i\alpha} = \tilde{100} e^{i0} = \tilde{100} V.$$

The active power consumed by the load is equal $P=400W$, and the RMS value of the current of the system before optimization is equal to $||_{\text{init}}=7,07A$. The active current (optimal current), as a solution of optimization problem, determined in classical way is equal to $\text{opt } I = \text{opt } I_a = 4,38A$.

With fuzzy approach the shape of membership function $f(x)=f(\underline{I})=||i||^2$ is equal:

$$(22) \quad \mu_f(\underline{I}) = 1 - \frac{||i||^2}{|I|_B^2}.$$

This membership function is presented in Fig.5.

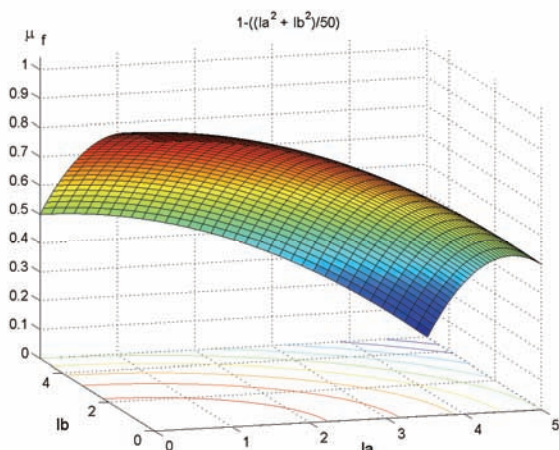


Fig.5. The shape of membership function μ_f

When RMS value of the voltage source is not fuzzy but the crisp one, the membership function of the constraint can be determined as:

$$(23) \quad \mu_C(\underline{I}) = \frac{1}{1 + \left[\text{Re}\{E I^* - |Z I^* - P\} \right]^2} = \frac{1}{1 + \left[|E| I_a - R(I_a^2 + I_b^2) - P \right]^2}$$

This membership function μ_C is presented in Fig.6.

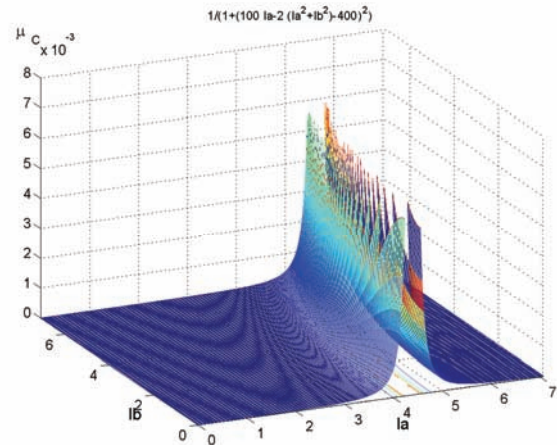


Fig.6. The shape of membership function μ_C for $|E|=100V$

It can be noticed from Fig.6, that the solution considered as intersection point between mf and μ_C will be very close to $\text{opt } || = \text{opt } I_a = 4,38A$. That is, if optimized function and considered constraint are described as a crisp (not fuzzy) functions the solution in fuzzy optimization will be equal to solution obtained in classical optimization.

If $|E|$ of the RMS value of the voltage source is not a crisp but the fuzzy number the membership function μ_C will be dependent on three parameters: real and imaginary part of the current (I_a, I_b) and $|\tilde{E}|$.

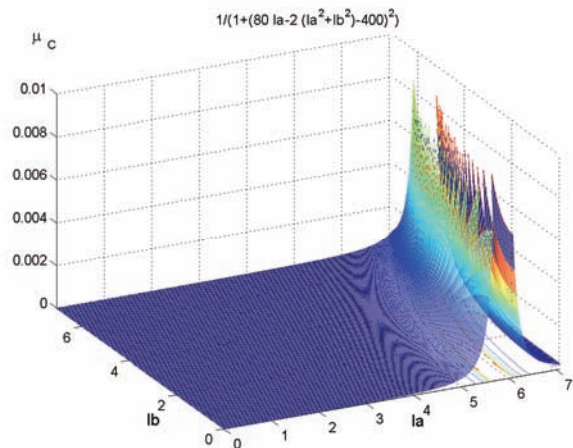


Fig.7. The shape of membership function μ_C for $|E|=80V$

Because it is difficult to present it in three-dimensional version in figures 7 and 8 have been presented shapes of μ_C for $|E|=80V$ and $|E|=120V$. From these figures it could be noticed that the solution of the problem – the active current – has always the imaginary part $I_b=0$.

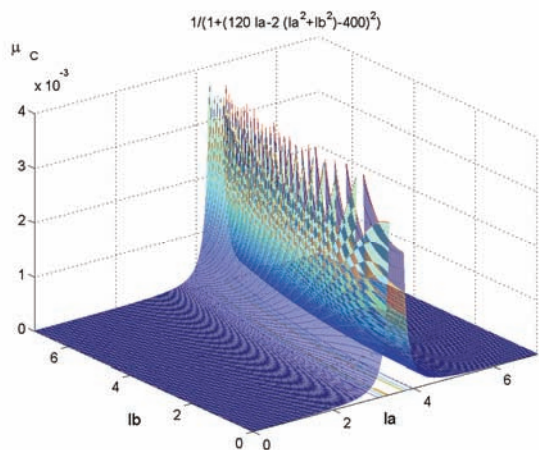


Fig.8. The shape of membership function μ_C for $|E|=120V$

It is agreed with solutions obtained in classical ways. In case of consideration of the fuzzy problem the solution of the problem is determined by means of numerical algorithm presented in the paper.

Conclusions

The approaches to optimization problem in classical and fuzzy way are completely different. The classical approach leads to creation of certain functional and to minimize their values under considered constraints. This minimization is realized by determination of first and second order derivatives of the functional. For simple problems this technique allows to obtain the solution in closed form. For more complicated problems a solution in the classical optimization is obtained in a numerical way. The fuzzy optimization is based on knowledge of the membership functions of optimized function and considered constraints. For simple problems this technique allows to present the solution graphically. Generally, the solution is determined in a numerical way. Then the optimal point can be determined as the intersection point between a membership function of the optimized function and membership function of constraints. If optimized function and considered constraint are described as a crisp (not fuzzy) functions the solution in fuzzy optimization will be

equal to solution obtained in classical optimization. Moreover, the fuzzy optimization allows to solve the optimization problems based on not crisp but fuzzy constraints. Then this optimization takes into account the membership function of the constraint. In this case the determined solutions can be different with relation to the solution obtained in classical optimization.

REFERENCES

- [1] Dębowski K., Zastosowanie zbiorów rozmytych w teorii mocy z przebiegami okresowymi odkształconymi, *XXIX Międzynarodowa Konferencja Z Podstaw Elektrotechniki I Teorii Obwodów IC-SPETO*, Gliwice-Ustroń, 2006, 361-364
- [2] Dębowski K., About possibility of the application of fuzzy sets in modeling of one-phase circuits with nonlinear loads, *XIX Symposium Electromagnetic Phenomena in Nonlinear Circuits*, Maribor, Slovenia, 2006, 137-138
- [3] Dębowski K., Fuzzy optimization in one-phase electrical circuits, *XXX IC-Speto - International Conference on Fundamentals of Electrotechnics and Circuit Theory*, Gliwice-Ustroń, 2007, 177-178
- [4] Kacprzyk L., *Zbiory rozmyte w analizie systemowej*, PWN, Warszawa, 1986
- [5] Zimmermann H.-J., *Fuzzy set theory - and its applications*, Kluwer Academic Publishers, 1991
- [6] Cox E., *The fuzzy systems, Handbook*, Academic Press Limited, London, 1994
- [7] Bellman R.E., Zadeh L.A., Decision-making in a fuzzy-environment, *Manag. Sci.*, 1970, vol. 17, 141-164
- [8] Dębowski K., Algorytmizacja algebry liczb rozmytych oparta na α -przekrojach, *XI Konferencja Zastosowania Komputerów w Elektrotechnice ZKwE*, Poznań, 2006, 71-72
- [9] Walczak J.: Optymalizacja energetyczno-jakościowych właściwości obwodów elektrycznych w przestrzeniach Hiberna. *Zeszyty Naukowe Politechniki Śląskiej*, z.125 (monografia habilitacyjna), Gliwice, 1992
- [10] Pasko M.: Dobór kompensatorów optymalizujących warunki pracy źródeł napięć jednofazowych i wielofazowych z przebiegami okresowymi odkształconymi. *Zeszyty Naukowe Politechniki Śląskiej*, z.135 (monografia habilitacyjna), Gliwice, 1994

Author: dr inż. Krzysztof Dębowski, Politechnika Śląska, Instytut Elektrotechniki Przemysłowej i Informatyki, ul. Akademicka 10, 44-100 Gliwice, E-mail: Krzysztof.Debowski@polsl.pl

Estimation of transients' parameters in wind converter systems using advanced signal processing algorithms

Abstract. The impact of wind generation on the electrical system should be assessed to figure out potential hazards to system operation and deterioration of power quality indicia. In this paper signal processing algorithms has been applied to analyze switching transients within wind generation units. A Prony model of the signal and a nonlinear regression method were applied to determine transients' parameters for various operation modes of the wind generator. Both methods delivered quite satisfactory results, but the regression method was prone to local minima.

Streszczenie. Oszacowanie wpływu elektrownii wiatrowych na system elektroenergetyczny jest pomocne w określeniu stopnia zagrożenia bezawaryjnej pracy systemu oraz odchyłek wskaźników jakości energii elektrycznej. W artykule zaprezentowano zastosowanie metody Prony'ego i regresji nieliniowej do wyznaczania parametrów zakłóceń łączeniowych w elektrowni wiatrowej. Obie metody okazują się skuteczne, niemniej algorytm wykorzystujący regresję nieliniową jest mało odporny na minima lokalne. (Oszacowanie składowych przejściowych elektrowni wiatrowych przy wykorzystaniu algorytmów przetwarzania sygnału).

Keywords: wind generation, transients, Prony method, nonlinear regression

Słowa kluczowe: energetyka wiatrowa, składowe przejściowe, algorytm Prony'ego, regresja nieliniowa

Introduction

The widespread implementation of wind energy conversion systems is a reality. Wind is seen as clean and renewable energy source, so the development of wind generation technologies is welcomed and supported by ecologists and governments. In the next years we will have even more generator units connected to the grid [1].

Besides distinctive merits, the connection of wind generators leads to many disturbances, such as: voltage fluctuation, flickers, harmonics, instability, blind power regulation problems, and transients [2]. Those disturbances affect power quality. Power quality issues connected with wind generation are not only important because of technical aspects, they are also crucial on the free energy market.

There are at least three main wind generators structures, which can be pointed out [3]. The simplest one, but certainly not advanced technologically, is the squirrel-cage induction generator connected directly to the grid.

Many of the wind energy converters installed today still have a squirrel-cage induction machine connected directly to the grid [4, 5]. This type of the generator cannot perform voltage control and it absorbs reactive power from the grid. Compensating capacitors are often directly connected. That type of installation is cost saving, and therefore widely used, but from the system analysis point of view it can be considered as a potential source of disturbances [3].

During the switching of capacitors transients occur, which are devastating for sensitive equipment, protection relays and insulation. The impact of transients on power quality indices cannot be neglected [2]. Transient overvoltages can theoretically reach peak values up to 2.0 pu. High current transients can reach values up to ten times the nominal capacitor current with duration of several milliseconds [6].

The purpose of this paper is the assessment of transients in electrical system with asynchronous wind generator. The analysis was carried out for real measured signals and for different operation conditions of the wind converter simulated in Matlab in SimPowerSystem Toolbox [9].

Presented below, the nonlinear regression method and the Prony method were considered as appropriate tools for parameters estimation of transients. Further, the simulation model and analyses of simulated and measured signals are presented.

Nonlinear regression

Nonlinear regression is a general technique to fit a curve through data. It fits data to any equation that defines Y as a function of X and one or more parameters. It finds the values of those parameters that generate the curve that comes closest to the data (minimizes the sum of the squares of the vertical distances between data points and curve). That technique requires a model of the analyzed signal. In the case of capacitor bank switching, the signal model of transient component can be defined as

$$(1) \quad x(t) = A_1 \sin(\omega_1 t + \varphi_1) + A_2 e^{-\alpha t} \sin(\omega_2 t + \varphi_2)$$

where A - amplitudes, α - damping factor and ω - angular velocities are unknown and should be estimated.

Practically, the signal is observed (or measured) during a finite duration of time and N samples of this signal are available. The measured discrete time signal $y(nT_p)$ can be specified as

$$(2) \quad \begin{aligned} y(nT_p) &= A_1 \sin(\omega_1 nT_p + \varphi_1) + \\ &+ A_2 e^{(-\alpha nT_p)} \sin(\omega_2 nT_p + \varphi_2) + e(nT_p) = \\ x(nT_p) &+ e(nT_p) \end{aligned}$$

for $n=1,2,3,\dots,N$.

As previously T_p - is the sampling period, N - the number of samples and e the estimation error correlated with each sample, which includes random noise and other distortions.

The problem of nonlinear regression can be formulated as an optimization problem, where the goal is to minimize the difference between the physical observation and the prediction from the mathematical model. More precisely, the goal is to determine the best values of the unknown parameters A , α , ω , φ in order to minimize the squared errors between the measured values of the signal and the computed ones.

Thus, the optimization problem can be formulated as follows:

Find a vector $\mathbf{w} = [A_1, A_2, \alpha, \omega_1, \omega_2, \varphi_1, \varphi_2]^T$ which minimizes the objective function

$$(3) \quad E(\mathbf{w}) = \sum_{n=1}^N e^2(nT_p) = \sum_{n=1}^N [y(nT_p) - x(nT_p)]^2$$

That is a well known standard least squares problem. To solve that problem, the Quasi-Newton method was applied [12]. At each iteration, the problem is to find a new iterate \mathbf{w}_{k+1} of the form:

$$(4) \quad \mathbf{w}_{k+1} = \mathbf{w}_k + \tau \mathbf{d}$$

where τ is a scalar step length parameter and \mathbf{d} is the search direction. Using the quasi-Newton method, a line search is performed in the direction

$$(5) \quad \mathbf{d} = -\mathbf{H}_k^{-1} \cdot \nabla E(\mathbf{w}_k)$$

where \mathbf{H}^{-1} is an approximation of the inverse Hessian matrix.

The DFP formula was used for approximation of the inverse of Hessian matrix

$$(6) \quad \mathbf{H}_{k+1}^{-1} = \mathbf{H}_k^{-1} + \frac{\mathbf{s}^k (\mathbf{s}^k)^T}{(\mathbf{q}^k)^T \mathbf{s}^k} - \frac{(\mathbf{H}_k^{-1} \mathbf{q}^k) (\mathbf{H}_k^{-1} \mathbf{q}^k)^T}{(\mathbf{q}^k)^T \mathbf{H}_k^{-1} \mathbf{q}^k}$$

where $\mathbf{q}_k = \nabla E(\mathbf{w}_{k+1}) - \nabla E(\mathbf{w}_k)$ is gradient increment and $\mathbf{s}_k = \mathbf{w}_{k+1} - \mathbf{w}_k$ is variable increment.

Prony Method

The Prony method is a technique for modelling sampled data as a linear combination of exponential functions [8]. Although it is not a spectral estimation technique, the Prony method has a close relationship to the least squares linear prediction algorithms used for AR and ARMA parameter estimation. Prony method seeks to fit a deterministic exponential model to the data in contrast to AR and ARMA methods that seek to fit a random model to the second-order data statistics.

Assuming N complex data samples the investigated function can be approximated by p exponential functions:

$$(7) \quad y[n] = \sum_{k=1}^p A_k e^{(\alpha_k + j\omega_k)(n-1)T_p + j\psi_k}$$

where $n=1,2,3,\dots,N$, T_p - sampling period, A_k - amplitude, α_k - damping factor, ω_k - angular velocity, ψ_k - initial phase. The discrete-time function may be concisely expressed in the form

$$(8) \quad y[n] = \sum_{k=1}^p h_k z_k^{n-1}$$

where $h_k = A_k e^{j\psi_k}$ and $z_k = e^{(\alpha_k + j\omega_k)T_p}$.

The estimation problem is based on the minimization of the squared error over the N data values

$$(9) \quad \delta = \sum_{n=1}^N |\varepsilon[n]|^2$$

where

$$(10) \quad \varepsilon[n] = x[n] - y[n] = x[n] - \sum_{k=1}^p h_k z_k^{n-1}$$

This turns out to be a difficult nonlinear problem. It can be solved using the Prony method that utilizes linear equation solutions.

If as many data samples are used as there are exponential parameters, then an exact exponential fit to the data can be made.

Consider the p -exponent discrete-time function:

$$(11) \quad x[n] = \sum_{k=1}^p h_k z_k^{n-1}$$

The p equations of (11) may be expressed in matrix form as

$$(12) \quad \begin{bmatrix} z_1^0 & z_2^0 & \dots & z_p^0 \\ z_1^1 & z_2^1 & \dots & z_p^1 \\ \vdots & \vdots & \dots & \vdots \\ z_1^{p-1} & z_2^{p-1} & \dots & z_p^{p-1} \end{bmatrix} \begin{bmatrix} h_1 \\ h_2 \\ \vdots \\ h_p \end{bmatrix} = \begin{bmatrix} x[1] \\ x[2] \\ \vdots \\ x[p] \end{bmatrix}$$

The matrix equation represents a set of linear equations that can be solved for the unknown vector of amplitudes.

Prony proposed to define the polynomial that has the exponents as its roots:

$$(13) \quad F(z) = \prod_{k=1}^p (z - z_k) = (z - z_1)(z - z_2) \dots (z - z_p)$$

The polynomial may be represented as the sum:

$$(14) \quad \begin{aligned} F(z) &= \sum_{m=0}^p a[m] z^{p-m} = \\ &= a[0] z^p + a[1] z^{p-1} + \dots + a[p-1] z + a[p] \end{aligned}$$

Shifting the index on (11) from n to $n-m$ and multiplying by the parameter $a[m]$ yield

$$(15) \quad a[m] x[n-m] = a[m] \sum_{k=1}^p h_k z_k^{n-m-1}$$

Equation (14) can be modified into:

$$(16) \quad \begin{aligned} \sum_{m=0}^p a[m] x[n-m] &= \\ &= \sum_{k=1}^p h_k z_k^{n-p} \left\{ \sum_{m=0}^p a[m] z_k^{p-m-1} \right\} \end{aligned}$$

The right-hand summation in (16) may be recognized as a polynomial defined by (14), evaluated at each of its roots yielding the zero result:

$$(17) \quad \sum_{m=0}^p a[m] x[n-m] = 0$$

The equation can be solved for the polynomial coefficients. In the second step the roots of the polynomial defined by (14) can be calculated. The damping factors and sinusoidal frequencies may be determined from the roots z_k .

For practical situations, the number of data points N usually exceeds the minimum number needed to fit a model of exponentials, i.e. $N > 2p$. In the overdetermined data case, the linear equation (17) should be modified to:

$$(18) \quad \sum_{m=0}^p a[m]x[n-m] = e[n]$$

The estimation problem is based on the minimization of the total squared error

$$(19) \quad E = \sum_{n=p+1}^r |e[n]|^2$$

Asynchronous wind generator with compensating capacitors

The wind generator with compensating capacitors is shown in Fig.1. The simulation was done in Matlab using the SimPowerSystem Toolbox [9].

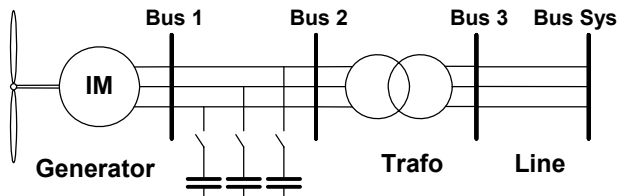


Fig. 1. Induction generator with compensating capacitors

A wind turbine generates power accordingly to mechanical torque on the rotating shaft of the turbine. Produced power depends on rotor speed and pitch angle and is often given in a table form [10].

The pitch control dynamic can be neglected in power system transient analysis [4]. The simulated generator is a 150 kW, 400 V, 1487 rpm, induction machine. It is connected to the grid through a Dyg 25/0.4 kV distribution transformer which nominal power was varied during the research process and other parameters were set with accordance to [11]. A typical 5 km overhead line [11] connected the generator to a system. The system was represented by equivalent source with short circuit capacity of 100 MVA and X/R ratio of 7. The induction generator reactive power demand varies with the produced real power [2]. During the research different compensation levels were simulated. Simulation results correlate with measured values.

Estimation of transients' parameters

Analysis of simulated signals

For variable wind speeds the exact compensation of reactive power using a capacitor bank is difficult [10]. The reactive power variation should be taken into account even if additional capacitors are switched on and off during the operation [7].

Assuming, theoretically, full reactive power compensation at freely chosen wind speed implies capacitance adjustment of the compensating capacitor for every particular case.

Three wind speeds were chosen – 8 m/s, 10 m/s, 12 m/s. For these wind speeds the capacitor was adjusted to fully compensate reactive power. Fig. 1 shows the current during the switching and Fig. 3 the FFT of that signal.

Table 1 shows the estimated parameters of signal components of fourth order Prony model (PRO) and obtained using nonlinear regression (NLR). In every case described in this chapter the sampling frequency was 5 kHz. Two signal frequencies in the current waveform (Fig. 2) were assumed and estimated. The main 50 Hz frequency component was named as "No. 2" and an additional capacitor bank switching transient as "No. 1".

The influence of a capacitor change on transient parameters is clear (Table 1). For higher wind speeds and therefore greater capacitance value, the amplitude of the transients was higher and the transients' frequency lower. Time constant did not change significantly.

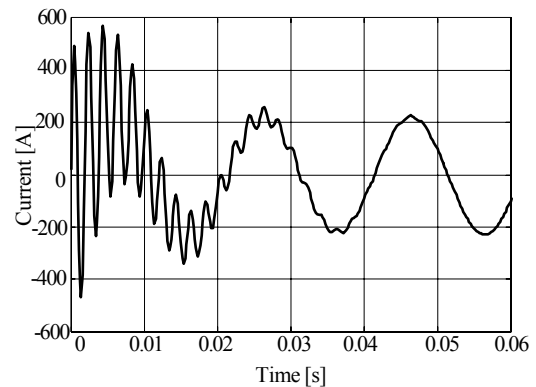


Fig. 2 Current during capacitor bank switching, wind speed 10 m/s

Table 1. Transients' parameters by different wind speed

| SignalCom./ Method [No. -Mth.] | I [A] | τ [s] | f [Hz] | ψ [rd] |
|--------------------------------|-------|------------|--------|-------------|
| wind speed 8 m/s | | | | |
| 1.-PRO | 579.4 | 0.0095 | 526.6 | -0.15 |
| 1.-NLR | 579.7 | 0.0095 | 526.5 | -0.14 |
| 2.-PRO | 105.7 | | 49.66 | -2.37 |
| 2.-NLR | 107.2 | | 49.64 | -2.36 |
| wind speed 10 m/s | | | | |
| 1.-PRO | 624.8 | 0.0095 | 501.6 | -0.15 |
| 1.-NLR | 625.2 | 0.0095 | 501.6 | -0.15 |
| 2.-PRO | 231.1 | | 49.82 | -2.47 |
| 2.-NLR | 233.3 | | 49.81 | -2.47 |
| wind speed 12 m/s | | | | |
| 1.-PRO | 710.6 | 0.0095 | 456.5 | -0.16 |
| 1.-NLR | 711.1 | 0.0095 | 456.5 | -0.16 |
| 2.-PRO | 394.4 | | 49.86 | -2.49 |
| 2.-NLR | 396.7 | | 49.86 | -2.48 |

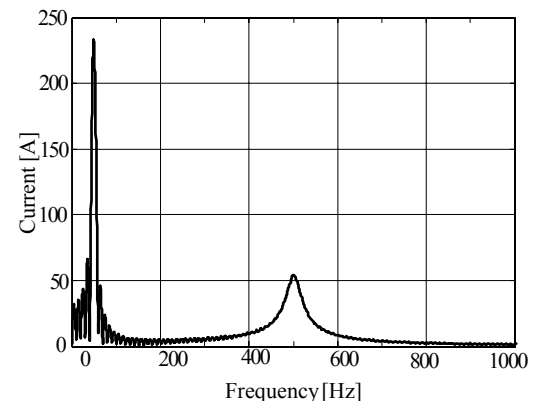


Fig. 3. Fourier transform of the capacitor switching current

Analysis of measured signals

Nonlinear regression and the Prony model were also applied to estimate the parameters of the measured signals. The measurements were done on a system described in extend in [7, 13]. The wind park consisted of two 225 kW pitch-controlled wind turbines connected with cables to a 500 kVA transformer. In this practical case two-stage phase-compensating capacitors were connected at the wind turbines. One small ($C_1=0.5$ mF), for low rotor speed and both ($C_1+ C_2=1.7$ mF), when the wind turbines operated at higher rotor speed [7].

The current measured during the switching operation of both capacitors is shown in Fig. 4. The sampling frequency was 6250 Hz.

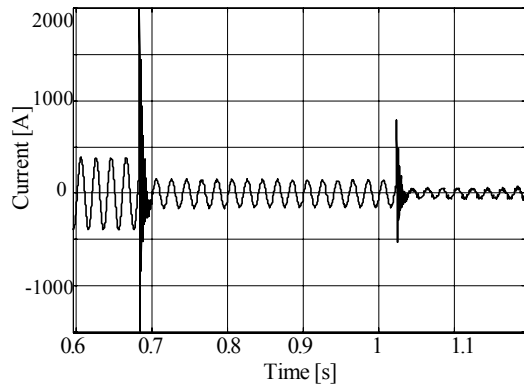


Fig. 4. Current waveform measured during switching of two capacitors

The transients resulting from the both switching operations were analyzed (Table 2).

Table 2. Transients' parameters computed for switching of two capacitors

| SignalCom./ Method [No. -Mth.] | I [A] | τ [s] | f [Hz] | ψ [rd] |
|--------------------------------------|----------|---------------|-----------|----------------|
| first capacitor switching | | | | |
| 1.-PRO | 2225.2 | 0.0039 | 592.2 | 0.07 |
| 1.-NLR | 2278.9 | 0.0037 | 592.2 | 0.07 |
| 2.-PRO | 162.9 | | 49.9 | 0.70 |
| 2.-NLR | 155.8 | | 49.8 | 0.71 |
| second capacitor switching | | | | |
| 1.-PRO | 831.0 | 0.0040 | 519.2 | -0.34 |
| 1.-NLR | 849.9 | 0.0039 | 508.4 | -0.22 |
| 2.-PRO | 51.2 | | 50.9 | 0.83 |
| 2.-NLR | 54.2 | | 50.5 | 0.95 |

Table 2 contains the same symbols and descriptions as Table 1. The windowed and zoomed current waveform during the first switching is shown in Fig. 5.

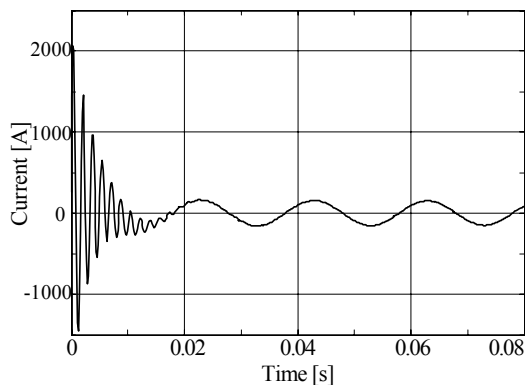


Fig. 5. Current waveform during switching of the first capacitor

Conclusion

The research results show, that nonlinear regression and the Prony model are useful for transient estimation in systems with wind generators and compensating capacitors. These methods enabled accurate estimation of amplitude, time constant, phase and frequency of transients' components of simulated and measured signals. The current waveform and its parameters depend on

system elements and its operating mode. These dependences could be observed during simulation of various cases.

Application of both Prony model and nonlinear regression required a signal model. Fourier transform, as non parametric method, did not require a signal model or even the number of components, but could not compute signal parameters besides frequency. Using nonlinear regression, the problem of local minima was observed. Unconsidered setting of the initial parameters can lead to local minimum and inadequate results. Additionally, two signal components were predefined, so the rest was considered noise. Application of the Prony method did not show the problem of local minima. The order of the signal model could be easily extended to detect additional components. Both methods delivered similar results, however, application of Prony model seems more suitable for estimation of transients' parameters.

REFERENCES

- [1] Hammons T.: Status of Integrating renewable electricity production in Europe into the grids. Proceedings of Universities Power Engineering Conference, Cork (Ireland), 2005, p.73
- [2] Hanzelka Z., Mroz M., Pawelek R., Pitek K.: Quality Parameters of 15kV supply voltage after connection of wind farms-case study. Proceedings of Conference on Harmonics and Quality of Power, Cascais (Portugal), September 2006, on CD, paper ID 124
- [3] Quinonez-Varela G., Cruden A., Grant A. D., Castaneda A.: Electrical Integration Assessment of Wind Turbines into Industrial Power System: The Case of a Mining Unit. Proceedings IEEE Power Tech Conference, Porto (Portugal), September 2001, paper ID DRS3-292
- [4] Chompoo-inwai Ch., Wei-Jen L., Fuangfoo P., Williams M., Liao J. R.: System Impact Study for the Interconnection of Wind Generation and Utility System. IEEE Trnas. on Industry Applications, vol. 41, January 2005, pp 163-168
- [5] Shulz, D., Moutawakkil, K., Hanitsh, R., Saniter, C: Power Quality Behaviour of Large Wind Parks with variable speed wind energy converters. CIRED, 17th International Conference on Electricity Distribution, Barcelona, Spain, 12-15 Mai 2003, CD
- [6] Tabesh A., Irvani R.: Transient Behavior of Fixed-Speed Grid-Connected Wind Farm. Transactions of International Conference on Power Systems Transients, Montreal (Canada), June 2005, Paper No. IPST05-068
- [7] Thiringer T.: Power Quality Measurements Performed on a Low-Voltage Grid Equipped with Two Wind Turbines. IEEE Trans. on Energy Conversion, vol. 11, September 1996, pp. 601-606
- [8] Lobos T., Rezmer J., Kolin H.-J.: Analysis of Power System Transients using Wavelets and Prony Method. Proceedings IEEE Power Tech Conference, Porto (Portugal), September 2001, paper ID EMT-103
- [9] The Mathworks: SimPowerSystems User's Guide. The Math Works Inc., 2006
- [10] Lubosny Z.: Wind Turbine Operation in Electric Power Systems. Springer Verlag, Berlin Heidelberg (Germany), 2003
- [11] SIEMENS: Electrical Engineering Handbook, 1987
- [12] Bhatti A. M.: Practical Optimization Methods. Springer Verlag, New York (USA), 2000, pp. 288-302
- [13] Larsson A., Thiringer T.: Measurement on and Modelling of Capacitor-Connecting Transients on a Low-voltage Grid Equipped with Two Wind Turbines. Proceedings IPST Conference, Lisbon (Portugal), 1995

Authors: (1) Wrocław University of Technology, Faculty of Electrical Engineering, Institute of Electrical Engineering Fundamentals, Wyb. Wyspińskiego 27, 50-370 Wrocław, Poland, e-mail: jacek.rezmer@pwr.wroc.pl
 (2) Chalmers University of Technology, Department of Energy and Environment, Division of Electric Power Engineering, SE-412 96 Göteborg, Sweden
 email: torbjorn.thiringer@chalmers.se

Electromagnetic torque, power losses analysis for spherical electromechanical converters with anisotropy rotor

Abstract. The paper deals with the problem of electromagnetic field analysis for the electromechanical converter with anisotropic rotor. Field distribution is evaluated analytically with the help of non-standard separation method. The electromagnetic torque are calculated and power balance is checked. Power losses and electromagnetic torque are evaluated. The results obtained can be used as test tasks for both electromagnetic field numerical analysis and torque calculation.

Streszczenie. Artykuł przedstawia analityczne określenie rozkładu pola elektromagnetycznego dla przetwornika elektromechanicznego z anizotropowym wirnikiem. Obliczenia dokonano za pomocą zaproponowanej niestandardowej separacji zmiennych dla wektorowego potencjału magnetycznego. Sformułowano warunki brzegowe. Dokonano analizy składowych momentu elektromagnetycznego, strat mocy czynnej w wirniku sprawdzono bilans mocy. (Analiza momentu elektromagnetycznego i strat mocy przetwornika elektromechanicznego z anizotropowym wirnikiem).

Keywords: przetwornik elektromechaniczny, wirnik anizotropowy, moment elektromagnetyczny.

Słowa kluczowe: electromechanical converter, anisotropic rotor, electromagnetic torque.

Introduction

The paper deals with the problem of electromagnetic field analysis for spherical electromechanical converters taking into account magnetic anisotropy. The electromagnetic field is evaluated analytically with the help of proposed separation method for magnetic vector potential. The boundary conditions are formulated for electromechanical converters spherically shaped. Power losses, electromagnetic torque are calculated and power balance is checked. The results obtained can be used as test tasks for electromagnetic field numerical analysis and torque calculations, power balance.

Electromagnetic field analysis

The electromagnetic field problems can be solved in analytical way. The analytical solution gives better ideas about the influence of various parameters on device operation than the numerical solution. One of the most commonly used methods is the separation of variable [2], [5], [6], [10]. The way of separation proposed leads to the analytical solution for the spherical symmetry problem considering anisotropy. The solution obtained can be applied for analysis of electromechanical converters work [7]. For electromechanical converter with magnetic field dominate as follows

$$(1) \quad \frac{1}{2} \nu_o B^2 \gg \frac{1}{2} \epsilon_o E^2$$

the magnetic flux density can be calculated by means of vector magnetic potential as follows

$$(2) \quad \vec{B} = \text{curl}(\vec{A})$$

\vec{B} : magnetic flux density vector, \vec{A} : magnetic vector potential.

The Eqn (2) leads to the following relation for spherical coordinate system

$$(3) \quad \vec{B} = \frac{\vec{I}_r}{r \sin \theta} \left\{ \frac{\partial A_\theta}{\partial \varphi} - \frac{\partial(A_\varphi \sin \theta)}{\partial \theta} \right\} - \frac{\vec{I}_\varphi}{r} \left\{ \frac{\partial(rA_\theta)}{\partial r} - \frac{\partial A_r}{\partial \theta} \right\} + \frac{\vec{I}_\theta}{r \sin \theta} \left\{ \frac{\partial}{\partial r} r A_\varphi \sin \theta - \frac{\partial A_r}{\partial \varphi} \right\}$$

where $\vec{I}_r, \vec{I}_\varphi, \vec{I}_\theta$ denote the unit vectors for spherical coordinate system that satisfy the relation $\vec{I}_r \times \vec{I}_\varphi = \vec{I}_\theta$

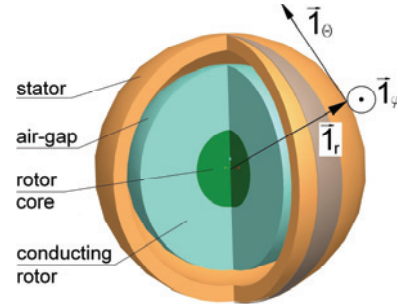


Fig.1. Spherical co-ordinate system

For simplification (assumption for stator windings construction) electromagnetic field is calculated for \vec{A}_θ component in spherical coordinate system Fig.1 [11].

$$(4) \quad \vec{A} = \vec{A}_\theta = A_\theta \vec{I}_\theta = A \vec{I}_\theta$$

According to Eqn (5) the above written assumption leads to the magnetic field density in the form

$$(5) \quad \vec{B} = \frac{\vec{I}_r}{r \sin \theta} \left\{ \frac{\partial A_\theta}{\partial \varphi} \right\} - \frac{\vec{I}_\varphi}{r} \left\{ \frac{\partial(rA_\theta)}{\partial r} \right\}$$

$$(6) \quad \vec{B}_\theta = 0$$

The current density for magnetic anisotropy area can be written from the Maxwell equation

$$(7) \quad \text{curl}(\vec{H}) = \vec{j}$$

\vec{H} magnetic field strength vector, \vec{j} : current density vector and constitutive relation for anisotropic magnetic medium

$$(8) \quad \begin{bmatrix} H_r \\ H_\varphi \\ H_\theta \end{bmatrix} = \begin{bmatrix} \nu_{rr} & \nu_{r\varphi} & 0 \\ \nu_{\varphi r} & \nu_{\varphi\varphi} & 0 \\ 0 & 0 & \nu_{\theta\theta} \end{bmatrix} \cdot \begin{bmatrix} B_r \\ B_\varphi \\ 0 \end{bmatrix} = \begin{bmatrix} \nu_{rr} B_r + \nu_{r\varphi} B_\varphi \\ \nu_{\varphi r} B_r + \nu_{\varphi\varphi} B_\varphi \\ 0 \end{bmatrix}$$

where ν matrix of rotor magnetic reluctivities lead to the following equation

$$(9) \quad -\frac{\bar{I}_r}{r \sin \theta} \left\{ \frac{\partial H_\varphi \sin \theta}{\partial \theta} \right\} + \frac{\bar{I}_\varphi}{r} \left\{ \frac{\partial H_r}{\partial \theta} \right\} + \frac{\bar{I}_\theta}{r \sin \theta} \left\{ \frac{\partial}{\partial r} r H_\varphi \sin \theta - \frac{\partial H_r}{\partial \varphi} \right\} = \bar{j}$$

Due to the assumption that currents flow only in θ -direction, the θ -component of current density (9) is as follows

$$(10) \quad \frac{1}{r \sin \theta} \left\{ \frac{\partial}{\partial r} r H_\varphi \sin \theta - \frac{\partial H_r}{\partial \varphi} \right\} = j_\theta = \gamma E_\theta = -\gamma \dot{A}_\theta$$

where γ stands for electric conductivity of rotor layer. Taking into account Eqns (8) and (10) it can be written

$$(11) \quad \frac{1}{r} \frac{\partial}{\partial r} r \left(\frac{\nu_{\varphi r}}{r \sin \theta} \left\{ \frac{\partial A_\theta}{\partial \varphi} \right\} - \frac{\nu_{\varphi \varphi}}{r} \left\{ \frac{\partial r A_\theta}{\partial r} \right\} \right) - \frac{1}{r \sin \theta} \frac{\partial}{\partial \varphi} \left(\frac{\nu_{r r}}{r \sin \theta} \left\{ \frac{\partial A_\theta}{\partial \varphi} \right\} - \frac{\nu_{r \varphi}}{r} \left\{ \frac{\partial r A_\theta}{\partial r} \right\} \right) = j_\theta$$

Now, a non-standard separation variable is proposed in the form given below [4]

$$(12) \quad A = A_\theta = R(r, \theta) F(\varphi) = R \cdot F$$

For complex analysis of magnetic vector potential the time-partial derivative of magnetic vector component A is given by multiplication of the operand $i\omega$ (i means imaginary unit, ω is field pulsation) and the complex vector magnetic potential A at the steady state (for time-sinusoidal varying field). Thus Eqn (9) takes the following form

$$(13) \quad \frac{\nu_{\varphi r}}{r R F \sin \theta} \frac{\partial^2 R F}{\partial r \partial \varphi} - \frac{\nu_{\varphi \varphi}}{r R} \frac{\partial^2 r R}{\partial r^2} - \frac{\nu_{r r}}{r^2 F \sin^2 \theta} \frac{\partial^2 F}{\partial \varphi^2} + \frac{\nu_{r \varphi}}{r^2 R F \sin \theta} \frac{\partial^2 r R F}{\partial \varphi \partial r} = \frac{i \omega \gamma}{R F}$$

γ : rotor conductivity.

For $\theta \in (0, \pi)$, and subsequently

$$(14) \quad \frac{\nu_{\varphi \varphi}}{r R} \frac{\partial^2 r R}{\partial r^2} + \frac{\nu_{r r}}{r^2 F \sin^2 \theta} \frac{\partial^2 F}{\partial \varphi^2} - \left(\frac{\nu_{\varphi r}}{r R} \frac{\partial R}{\partial r} + \frac{\nu_{r \varphi}}{r^2 R} \frac{\partial r R}{\partial r} \right) \frac{1}{F \sin \theta} \frac{\partial F}{\partial \varphi} = i \omega \gamma$$

For the function $F(\varphi)$ it is assumed that separation constant equals to p^2 for the first mmf space harmonic $h = 1$ (for higher space harmonics of mmf $p \rightarrow ph$) in the form of [10]

$$(15) \quad \frac{1}{F} \frac{\partial^2 F}{\partial \varphi^2} = -p^2$$

with the general solution as follows

$$(16) \quad F = C \exp(ip\varphi) + D \exp(-ip\varphi)$$

C_1, C_2 : constants

The Eqns (15) and (16) are adequate for rotating magnetic field exerted by stator mmf (p denotes the pair-pole number for stator mmf). The angular frequency ω is determined in relevancy to mmf harmonic angular speed equal to $\pm 2\pi f_1/ph$. The solution (16) for unidirectional rotating field (constant $D = 0$) leads to equation

$$(17) \quad \frac{\partial^2 R}{\partial r^2} + 2(1-h(\theta)) \frac{\partial R}{\partial r} + R \left(-\beta^2 - \frac{p^2 \nu_{r r} + ip \sin \theta \nu_{r \varphi}}{r^2 \nu_{\varphi \varphi} \sin^2 \theta} \right) = 0$$

with the analytical solution for anisotropic region as follows [1], [3]

$$(18) \quad R(r, \theta) = (\beta r)^{\lambda(\theta) - \frac{1}{2}} (C_1 I_{\lambda(\theta)}(\beta r) + C_2 K_{\lambda(\theta)}(\beta r))$$

C_1, C_2 : constants, I_λ, K_λ : Bessel function, β : Bessel equation parameter, λ : order of a function where it was denoted

(19a,b,c)

$$\lambda(\theta) = \pm \sqrt{(h(\theta) - \frac{1}{2})^2 + \frac{p^2 \nu_{r r} + ip \sin \theta \nu_{r \varphi}}{r^2 \nu_{\varphi \varphi} \sin^2 \theta}}$$

$$h(\theta) = \frac{\nu_{r \varphi} + \nu_{\varphi r}}{2 \nu_{\varphi \varphi} \sin \theta} ip, \quad \beta^2 = \frac{i \gamma \omega}{\nu_{\varphi \varphi}}$$

The solution in the form of (18) confirms that the proposed non-standard separation (12) is correct. The Eqn (14) for non-conducting region (e.g. the gap $\gamma=0, \nu_{r\varphi}=\nu_{\varphi r}=0$) takes the simpler form as written below

$$(20) \quad \frac{\partial^2 r R}{\partial r^2} - (\kappa(\theta) + 1) \kappa(\theta) \frac{R}{r} = 0$$

where

$$(21) \quad \kappa(\kappa + 1) = \frac{\nu_{r \delta} p^2}{\nu_{\varphi \delta}}$$

and $\nu_{r\delta}, \nu_{\varphi\delta}$ mean radial and tangential (latitudinal) reluctivities for the gap. The solution of Eqn (20) is as follows

$$(22) \quad R = R(r, \theta) = a_\delta r^{\kappa_1(\theta)} + b_\delta r^{\kappa_2(\theta)}$$

a, b : constants, κ_1, κ_2 : solution of an equation on the end domain.

The analytical solution for electromagnetic field equation for the vector magnetic potential in the anisotropic conducting area (rotor) and non-conducting (air gap) the motor can be in terms of separated function $R(r, \theta)$ and $F(\varphi)$ obtained with the help of separation proposed.

Boundary condition

There are defined four conditions for electromagnetic field vectors. It enables to calculate the four unknown constants [14]:

a) The magnetic field strength disappears at the inner layer surface ($r=R-a$)

$$(23) \quad H_\varphi = \nu_{\varphi r} B_r + \nu_{\varphi \varphi} B_\varphi = 0$$

that results from the fact that magnetic reluctivity of rotor core is zero.

b) The continuity for normal (radial) magnetic flux density ($r=R$)

$$(24) \quad B_{r\delta} = B_{ra}$$

c) for tangential (longitudinal) component of magnetic field strength ($r=R$)

$$(25) \quad v_{\varphi\delta} B_{\varphi\delta} = v_{\varphi\varphi} B_{\varphi\alpha} + v_{\varphi r} B_{ra}$$

d) The magnetomotive force induced by converter currents leads to the condition for tangential (longitudinal) component of magnetic field strength at the stator surface as follows ($r=R+g$)

$$(26) \quad v_{\varphi\delta} B_{\varphi\delta} = -\frac{\partial \Theta_s}{R_g \sin \theta \partial \varphi}$$

which is derived under the assumption that the magnetic field strength vanishes on the outer side of winding surface (infinitely magnetic reluctivity) [7]. The electromagnetic field problem can be solved in analytical way. The exemplary spherical induction motor with anisotropic and spherical rotor is considered and shown in Figure 2. The coils are spread on part of spherical surface. The data for exemplary analysis are specified in Table 1.

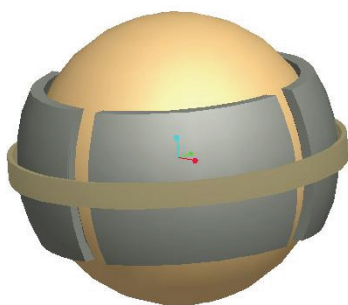


Fig.2. Spherical induction motor-view

Table 1 Exemplary spherical motor data

| Dane | Wartość |
|--|--|
| stator mmf Θ_s | 350 A ($h=1$) 70 A ($h=-5$) 50 A ($h=7$) |
| rotor radius R | 0.055 m |
| solid rotor (conductive) layer width a | 0.006 m |
| radial reluctivity $v_r = v_r$ | $v_o/20$ |
| tangential (longitudinal) reluctivity $v_{\varphi\varphi} = v_{\varphi}$ | $v_o/15$ |
| solid rotor conductivity γ | $7 \cdot 10^6$ S/m |
| gap width g | 0.0012 m |
| angles interval of stator mmf | |
| longitudinal width $\theta_1 \div \theta_2$ | $\pi/4 \div 3\pi/4$ |

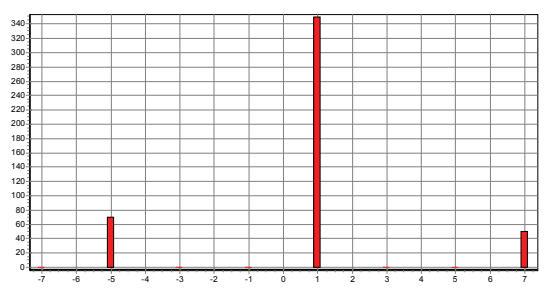


Fig.3. Amplitude mmf harmonics for stator windings

The amplitude mmf harmonics of stator windings for three phase motor are presented in Fig.3. Stator winding mmf/magnetomotive force(for all harmonics) are presented in Fig.4.

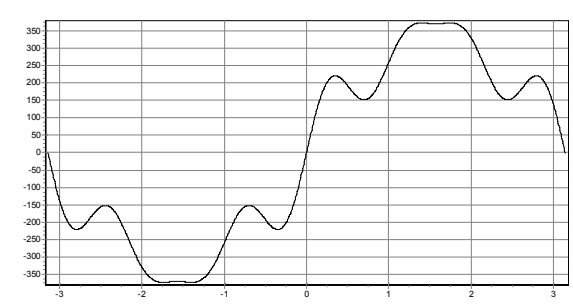


Fig.4. Stator winding mmf/magnetomotive force(for all harmonics)

Energy balance

For checking the correctness of the obtained electromagnetic field distribution the power balance has been checked. The complex power is calculated with the help of Poynting vector as follows

$$(27) \quad S_c = -i\omega v_{\varphi\delta} \int_S B_{\varphi\delta} A_{\theta} dS$$

where S_c : Poynting vector

The fulfilment of electromagnetic field power balance ensures us that the analytical solutions are correct. Moreover, the power analysis leads to the power losses value in solid rotor

$$(28) \quad P_q = \gamma \int_V E_{\theta}^2 dV$$

P_q power losses that are very important from thermal point of view.

Electromagnetic torque calculation in electromechanical spherical converter

Knowledge of the calculating magnetic field vector component in rotor conducting area ($\gamma \neq 0$) and air gap area ($\gamma = 0$) enables to calculate electromagnetic torques components for hypothetical spherical induction motor with anisotropic rotor Fig.2. There are presented the electromagnetic torque two components: Lorentz T_{eL} and material T_{eFe} that together constitute the total electromagnetic torque T_e [12],[13].

The Maxwell torque as follow

$$(29) \quad T_e = \int_0^{2\pi} \int_{\theta_1}^{\theta_2} H_{\varphi} B_r r^3 \sin^2 \theta d\theta d\varphi$$

The electromagnetic torque component forced by rotor currents can be evaluated with the help of Lorentz force density as follows

$$(30) \quad T_{eL} = \int_0^{2\pi} \int_{R_o}^R \int_{\theta_1}^{\theta_2} j_{\theta} \frac{\partial A_{\theta}}{\partial \varphi} r^2 \sin \theta d\theta dr d\varphi$$

The both torques values are equal

$$(31) \quad T_e = T_{eL}$$

Exemplary torque-speed curves for both torques are presented Fig.5.

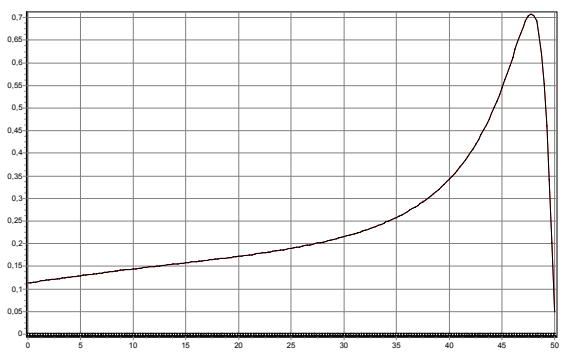


Fig.5. Exemplary torque-speed curve

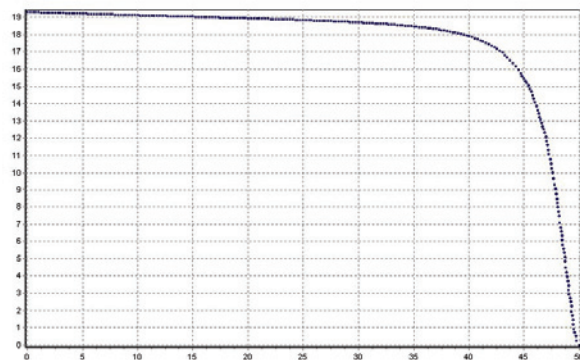


Fig.6. Power losses curves for conducting layers (for all harmonics)

Power losses

Knowledge of the calculating magnetic field vector component in rotor enables to calculate power losses in rotor layer. The conductive layer power losses are evaluated by means of:

1. Poynting vector surface integral

$$(32) \quad S = s\pi v_{\delta} \int_{\theta_1}^{\theta_2} R(r, \theta) \frac{\partial}{\partial r} (rR^*(r, \theta)) \sin(\theta) d\theta$$

2. Joule power losses volume density (volume integral)

$$(33) \quad P_L = \gamma\pi |s|^2 \int_{\theta_1}^{\theta_2} \int_{R-a}^R |R(r, \theta)|^2 r^2 dr \sin(\theta) d\theta$$

The both above mentioned method lead to the same power losses values. Exemplary power losses curves (for all harmonic) in conducting layer are presented Fig.6.

REFERENCES

- [1] Tolstow G., Fourier series. *PWN, Warszawa* 1954 (wyd.1).
- [2] Sikora R., Electromagnetic field theory, *WNT Warszawa* 1998 (Wyd.3).
- [3] Gradsztajn I. S., Ryzik I. M., Tables of integrals, sums, series and derivatives, Moscow 1962 (in Russian).
- [4] Kački E., Partial differential equation in electrotechnics, *WNT Warszawa* 1971.
- [5] Suffczyński M., Elektrodynamics, *PWN Warszawa* 1980 (wyd. IV).
- [6] Spalek D.: Electromechanical converter linear, cylindrical and spherical. (Part I - Electromagnetic field analysis, Part II – Force and torque calculation), *ZN Politechnika Śląska Elektryka*, Gliwice 2004.
- [7] Spalek D., Analytical electromagnetic field and forces calculation for linear, cylindrical and spherical electromechanical converter, *Bulletin of The Polish Academy of Sciences*, Vol. 52, No. 3, 2004
- [8] Purczyński J., Kaszycki L., Power losses and electromagnetic torque of spherical induction motor, *Rozprawy Elektrotechniczne* 34, No. 3, pp. 819–838 (1988) (in Polish).
- [9] Spalek D., Waleczek K., Electromechanical converter with anisotropic spherical rotor-analytical solution for electromagnetic field, torques and power losses, *Acta techn. CSAV* 49, 329-344 (2004)
- [10] Spalek D., Waleczek K.: Non-standard variable separation for magnetic field spherical problems, *XXVII Seminar on Fundamentals of Electrotechnics and Circuit Theory IC-SPETO, Gliwice-Niedzica* Proc. Vol. I, pp. 121-124, 2004.
- [11] Spalek D., Waleczek K., Application of non-standard variable separation for electromagnetic torque calculation for electromechanical converter with spherical anisotropic rotor, *XXVIII Seminar on Fundamentals of Electrotechnics and Circuit Theory IC-SPETO, Gliwice-Ustroń* Proc. Vol. I, pp. 167-170, 2005.
- [12] Spalek D., Waleczek K., Analytical analysis of electromagnetic field power balance and electromagnetic torques for electromechanical converter with spherical anisotropic rotor, *XXIX Seminar on Fundamentals of Electrotechnics and Circuit Theory IC-SPETO, Gliwice-Ustroń* Proc. Vol. I, pp. 183-186, 2006
- [13] Spalek D., Waleczek K., Power balance for electromagnetic field for electromechanical converter with anisotropy rotor, *XXX Seminar on Fundamentals of Electrotechnics and Circuit Theory IC-SPETO, Gliwice-Ustroń* Proc.29-30 2007.
- [14] Jackson J., Classical elektrodynamics., *PWN, Warszawa* 1982.
- [15] Engineers handbook-Mathematics, *WNT. Warszawa* 1986.

Autorzy. Dr hab. inż. Dariusz SPĄŁEK, prof. Pol. Śl., Politechnika Śląska, Wydział Elektryczny, Instytut Elektrotechniki Teoretycznej i Przemysłowej, 44-100 Gliwice ul. Akademicka 10, email: Dariusz.Spalek@polsl.pl; mgr inż. Krzysztof Waleczek, Kontakt-Simon S.A., 43-500 Czechowice-Dziedzice ul. Bestwińska 21, Email: kwalecz@interia.pl

Finding operating points of the diode-transistor circuits via homotopy approach

Abstract. The paper is devoted to DC analysis of circuits containing diodes and the Ebers-Moll modelled transistors. The basic question, how to find efficiently the operating points is considered. For this purpose a method is developed, based on the homotopy idea and the Padé approximation of the diodes characteristics. Two numerical examples are given confirming efficiency of the method.

Streszczenie. W artykule rozważany jest podstawowy problem analizy i projektowania układów elektronicznych, dotyczący wyznaczania punktów pracy obwodów diodowo-tranzystorowych. Zaproponowano metodę opartą na idei homotopii oraz aproksymacji Padego charakterystyk diod. Przytoczono dwa przykłady numeryczne potwierdzające efektywność tej metody. **(Obliczanie punktów pracy układów diodowo-tranzystorowych z użyciem metody homotopii.)**

Keywords: DC analysis, diode-transistor circuits, homotopy approach.

Słowa kluczowe: analiza stałoprądowa, układy diodowo-tranzystorowe, metoda homotopii.

Introduction

The basic question of the analysis and design of electronic circuits is finding the operating points. Even though there is a wide variety of nonlinear circuits, the diode-transistor ones occupy a special place, in electronic. To find a unique operating point of a circuit the Newton-Raphson method [1,2] is commonly used. Unfortunately, in some cases the method fails or is inefficient, due to specific nonlinearities of the transistor models. The method may be divergent or oscillating when the initial guess is not sufficiently close to the solution [2]. Also the overflow problem can occur. Even if the method gives the solution the rate of convergence may be low. To make the method convergent some modifications have been proposed [2-8]. Different concepts and techniques improving the convergence have been implemented in the computer program for the analysis and design of electronic circuits SPICE [9, 10]. In some cases the modifications are not efficient, especially in large-size circuits.

In this paper DC circuits consisting of bipolar transistors, diodes, resistors and sources are considered. The transistors are characterized by the Ebers-Moll model composed of two diodes and two current controlled current sources. All the diodes, originally specified by the exponential function, are represented by the Padé approximation [11]. To find the operating points a method based on the homotopy idea [12] is developed, with the discrete homotopy parameter introduced inside the Padé formula. For each value of the homotopy parameter the corresponding equations have been solved using a proposed algorithm, including the Newton-Raphson iteration formula as the main tool.

The offered method based on the homotopy concept and the Padé approximation has been implemented and tested on a set of representative diode-transistor circuits. The numerical experiments show that it significantly improves the Newton-Raphson method and leads to the solutions in all the cases, even when the Newton-Raphson method fails. Thus, the method allows efficient and robust computation of the operating points of the diode-transistor circuits.

Let us consider a circuit containing n_t bipolar transistors, n_d diodes, linear resistors, and independent DC sources. The transistors are represented by the Ebers-Moll model composed of two diode - controlled source combinations. Also small resistors R_E, R_C, R_B are included in the model. To describe the circuit we extract all the diodes, as shown in Fig.1.

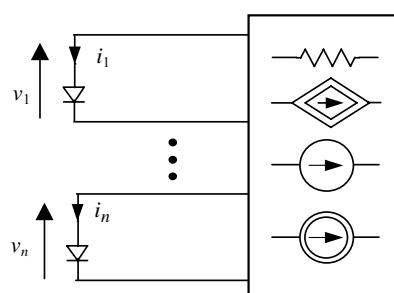


Fig.1. A circuit with the extracted diodes

In this manner a linear resistive n -port ($n = 2n_t + n_d$) is created, consisting of linear resistors, independent and controlled sources. The circuit can be described by the Sandberg-Willson equation [13]

$$(1) \quad \mathbf{f}(\mathbf{v}) + \mathbf{A}\mathbf{v} - \mathbf{b} = \mathbf{0}$$

where

$$\mathbf{v} = [v_1 \dots v_n]^T, \quad \mathbf{f}(\mathbf{v}) = [f_1(v_1) \dots f_n(v_n)]^T,$$

$$(2) \quad f_i(v_i) = K_i (e^{\lambda v_i} - 1),$$

$$\mathbf{A} = [a_{ij}]_{n \times n}, \quad \mathbf{b} = [b_1 \dots b_n]^T.$$

Thus, each function $f_i(v_i)$, $i = 1, \dots, n$, contains the exponential function $e^{\lambda v_i}$. It will be rewritten in the form

$$(3) \quad e^{\lambda v_i} = (e^{0.1v_i})^{10\lambda}$$

and the function $e^{0.1v_i}$, will be represented by the Padé approximation [11]:

$$(4) \quad p(0.1v_i) = \frac{2 + 0.1v_i}{2 - 0.1v_i}, \quad 0.1v_i < 1.$$

We use the Padé approximation of $e^{0.1v_i}$ for $0 \leq v_i \leq 0.8$ and replace the function $f_i(v_i)$ specified by (2) with $g_i(v_i)$, defined as follows

$$(5) \quad g_i(v_i) = \begin{cases} 0 & \text{for } v_i < 0 \\ K_i \left((p(0.1v_i))^{10\lambda} - 1 \right) & \text{for } 0 \leq v_i \leq 0.8 \\ K_i \left((p(0.08))^{10\lambda} - 1 \right) + \\ + 10\lambda K_i (p_i(0.08))^{(10\lambda-1)} \frac{dp}{dv_i} \Big|_{v_i=0.8} (v_i - 0.8) & \text{for } v_i > 0.8 \end{cases}$$

As a result the equation describing the circuit becomes

$$(6) \quad \mathbf{g}(\mathbf{v}) + \mathbf{A}\mathbf{v} - \mathbf{b} = \mathbf{0},$$

where $\mathbf{g}(\mathbf{v}) = [g_1(v_1) \dots g_n(v_n)]^T$.

Solving equation (6) using the homotopy approach

The homotopy method to obtain a solution \mathbf{x}^* of equation $\mathbf{r}(\mathbf{x}) = \mathbf{0}$, where $\mathbf{x} = [x_1 \dots x_n]^T$, $\mathbf{r}(\mathbf{x}) = [r_1(\mathbf{x}) \dots r_n(\mathbf{x})]^T$ is as follows [12]. We define a special function, called the homotopy function $\mathbf{h}(\mathbf{x}, \alpha)$ which has the n variables x_1, \dots, x_n and an additional variable α . The homotopy function has to be created so that $\mathbf{h}(\mathbf{x}, 0)$ has a solution which can be easily determined, whereas $\mathbf{h}(\mathbf{x}, 1)$ has the solution \mathbf{x}^* which we seek.

To solve equation (6) using the homotopy approach we create the homotopy equation

$$(7) \quad \mathbf{h}(\mathbf{v}, \alpha) = \mathbf{0},$$

where

$$(8) \quad \mathbf{h}(\mathbf{v}, \alpha) = \hat{\mathbf{g}}(\mathbf{v}, \alpha) + \mathbf{A}\mathbf{v} - \mathbf{b},$$

$\hat{\mathbf{g}}(\mathbf{v}, \alpha) = [\hat{g}_1(v_1, \alpha) \dots \hat{g}_n(v_n, \alpha)]^T$ with i -th component ($i = 1, \dots, n$) of $\hat{\mathbf{g}}(\mathbf{v}, \alpha)$ specified by the relationship

$$(9) \quad \hat{g}_i(v_i, \alpha) = \begin{cases} 0 & \text{for } v_i < 0 \\ K_i \left((\hat{p}(0.1v_i, \alpha))^{10\lambda} - 1 \right) & \text{for } 0 \leq v_i \leq 0.8 \\ K_i \left((\hat{p}(0.08, \alpha))^{10\lambda} - 1 \right) + \\ + 10\lambda K_i (\hat{p}_i(0.08, \alpha))^{(10\lambda-1)} \frac{d\hat{p}}{dv_i} \Big|_{v_i=0.8} (v_i - 0.8) & \text{for } v_i > 0.8 \end{cases}$$

where

$$(10) \quad \hat{p}(0.1v_i, \alpha) = \frac{2 + 0.1v_i}{2 - \frac{0.1v_i}{2} - \alpha \frac{0.1v_i}{2}}.$$

For $\alpha = 0$: $\hat{p}(0.1v_i, 0) = \frac{2 + 0.1v_i}{2 - \frac{0.1v_i}{2}}$. This is a smooth

function for $0 \leq v_i \leq 0.8$, which does not grows rapidly. Consequently, $\hat{g}_i(v_i, 0)$ is also a smooth function and the equation

$$(11) \quad \mathbf{h}(\mathbf{v}, 0) = \mathbf{0},$$

can be efficiently solved. For $\alpha = 1$, $\hat{p}(0.1v_i, 1) = p(0.1v_i)$ is the Padé approximation of the function $e^{0.1v_i}$.

According to the homotopy idea we find the solution $\mathbf{v}^{(k)}$ to equation (7) at $\alpha = \alpha_k$ and next employ it to find the solution $\mathbf{v}^{(k+1)}$ of this equation at $\alpha = \alpha_{k+1}$. Underneath it is listed the proposed algorithm for finding $\mathbf{v}^{(k+1)}$.

Step 1

Denote $(\hat{\mathbf{v}}^{(k+1)})^{(0)} = \mathbf{v}^{(k)}$ and set $l = 0$.

Step 2

Let $y_j = (\hat{v}_j^{(k+1)})^{(l)}$ for $j = 1, \dots, n$. Compute

$$z_i = b_i - \sum_{j=1}^n a_{ij} y_j \quad \text{for } i = 1, \dots, n.$$

If $z_i > \eta$, where η is a small positive number, then solve the equation $g_i(x_i, \alpha_{k+1}) = z_i$ for x_i , otherwise set $x_i = 0$.

Step 3

Denote

$$(\hat{v}_i^{(k+1)})^{(l)} = \begin{cases} y_i & \text{if } x_i \leq 0.5 \\ x_i & \text{if } x_i > 0.5 \end{cases} \quad i = 1, \dots, n, \text{ next from}$$

the vector $(\mathbf{v}^{(k+1)})^{(l)} = [(\hat{v}_1^{(k+1)})^{(l)} \dots (\hat{v}_n^{(k+1)})^{(l)}]^T$ and

perform one iteration of the Newton-Raphson method

$$(\hat{\mathbf{v}}^{(k+1)})^{(l+1)} = (\mathbf{v}^{(k+1)})^{(l)} - \left[\frac{\partial \hat{\mathbf{g}}}{\partial \mathbf{v}} \left((\mathbf{v}^{(k+1)})^{(l)}, \alpha_{k+1} \right) + \mathbf{A} \right]^{-1} \mathbf{h} \left((\mathbf{v}^{(k+1)})^{(l)}, \alpha_{k+1} \right).$$

If $\|(\hat{\mathbf{v}}^{(k+1)})^{(l+1)} - (\mathbf{v}^{(k+1)})^{(l)}\| < \varepsilon$, where ε is a tolerance,

then assume that $(\mathbf{v}^{(k+1)}) = (\hat{\mathbf{v}}^{(k+1)})^{(l+1)}$ is the solution to equation $\mathbf{h}(\mathbf{v}, \alpha_{k+1}) = \mathbf{0}$. Otherwise, set $l := l + 1$, and go to Step 2.

The developed homotopy method has been implemented in PC Pentium Core 2 Duo and tested using several practical transistor circuits. In all the cases the method considerably reduces the number of the Newton-Raphson iterations. Furthermore, the method gives a solution also in the cases where the Newton-Raphson method fails. To illustrate the approach and show its efficiency we consider two numerical examples.

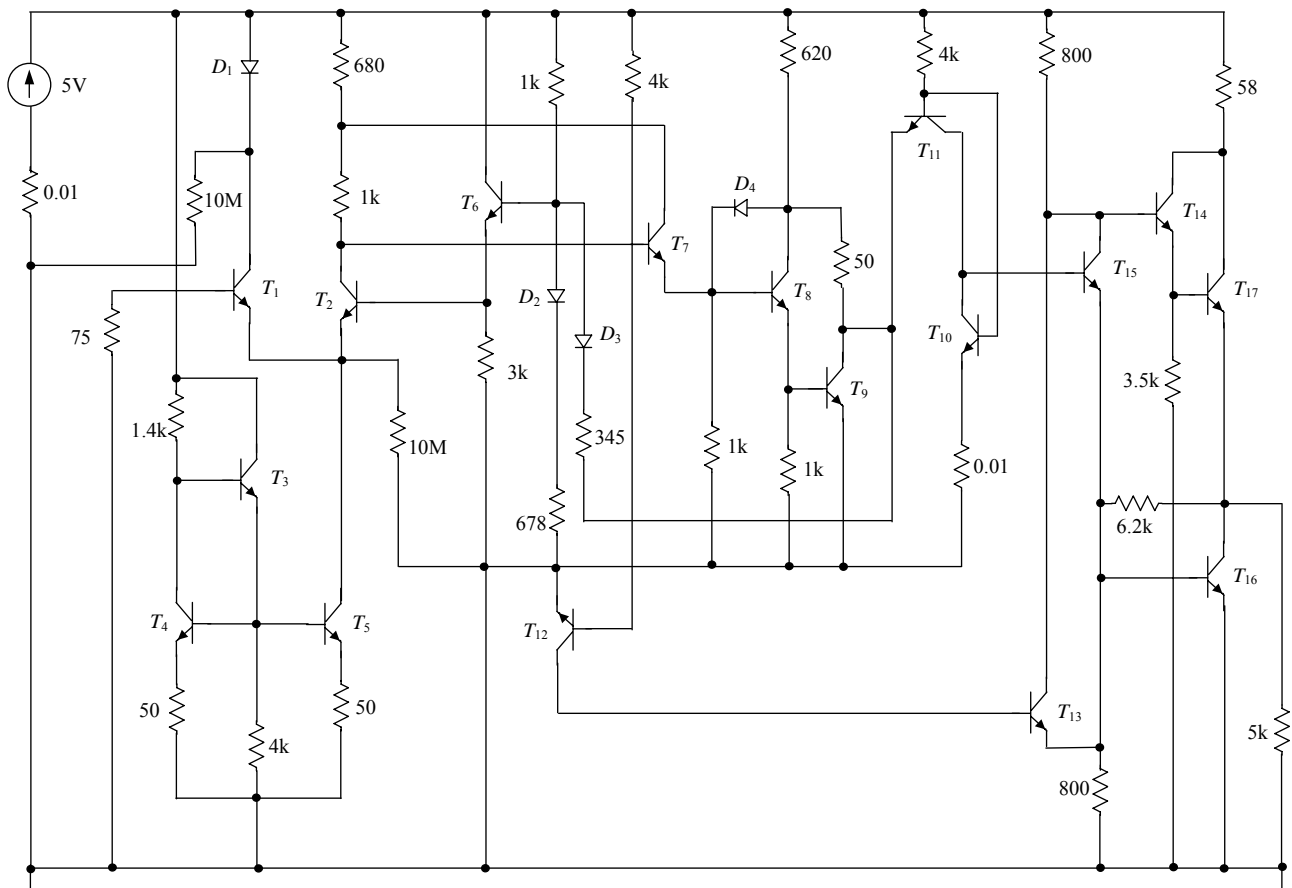


Fig. 2. The circuit for Example 1

Numerical examples

Example 1

Figure 2 shows the line receiver SN 75122 (high-level output voltage) which contains 17 bipolar transistors and 4 diodes. The transistors are represented by the Ebers-Moll model with the following parameters: $\alpha_F = 0.9975$, $\alpha_R = 0.8$, $I_{SE} = 8.02 \text{ fA}$, $I_{SC} = 10 \text{ fA}$, $R_E = R_C = 1 \Omega$, $R_B = 3 \Omega$, $\lambda = 38.67 \text{ V}^{-1}$. The diodes parameters are $I_S = 8 \text{ fA}$, $R_S = 1 \Omega$, $\lambda = 38.67 \text{ V}^{-1}$. The circuit has been described by the Sandberg-Willson equation consisting of 38 scalar equations.

The Newton-Raphson method with the zero initial guess gives the solution

$$v = [-1.065 \quad -4.538 \quad 0.692 \quad 0.657 \quad 0.621 \quad -3.564 \quad 0.685 \\ -0.619 \quad 0.685 \quad -0.248 \quad 0.655 \quad -2.582 \quad -0.206 \quad -2.318 \\ 0.650 \quad -0.668 \quad 0.660 \quad -1.174 \quad 0.704 \quad 0.682 \quad -1.127 \\ 0.678 \quad 0.704 \quad 0.698 \quad -0.412 \quad -4.991 \quad 0.666 \quad 0.143 \\ -0.392 \quad -4.970 \quad 0.419 \quad -3.244 \quad 0.666 \quad -0.524 \quad 0.462 \\ 0.685 \quad 0.570 \quad 0.668]^T$$

in 47ms (Intel Core 2 Duo 6400) performing 67 iterations. The method developed in this paper with the homotopy parameter assuming the discrete values: 0, 0.2, 0.6, 0.8, 1, gives the same solution in 18 iterations consuming 15ms.

Example 2

Let us consider the inverting amplifier based on $\mu\text{A} 741$ composed of 20 bipolar transistors. The transistors are characterised by the Ebers-Moll model with the following parameters: $\alpha_F = 0.99$, $\alpha_R = 0.5$, $I_{SE} = 0.808 \text{ fA}$, $I_{SC} = 1.6 \text{ fA}$, $R_E = R_C = 1 \Omega$, $R_B = 3 \Omega$, $\lambda = 38.67 \text{ V}^{-1}$. The circuit has been described using the Sandberg-Willson equation consisting of 40 scalar equations.

The Newton-Raphson method with the zero initial guess is not convergent to the solution in 1000 iterations. The proposed method gives the solution

$$v = [0.597 \quad -14.369 \quad 0.598 \quad -14.368 \quad 0.617 \quad 0.000 \quad 0.598 \\ -12.570 \quad 0.598 \quad -12.419 \quad 0.606 \quad -28.750 \quad 0.601 \quad -0.606 \\ 0.601 \quad -0.757 \quad 0.617 \quad -15.563 \quad 0.617 \quad -13.075 \quad 0.712 \\ 0.001 \quad 0.711 \quad 0.001 \quad 0.035 \quad -1.333 \quad 0.621 \quad -8.928 \\ 0.711 \quad -9.548 \quad 0.708 \quad -0.452 \quad 0.711 \quad -17.798 \quad 0.000 \\ -0.473 \quad 0.473 \quad -18.511 \quad 0.678 \quad -10.295]^T$$

performing 36 iterations in 63ms (Intel Core 2 Duo 6400). To improve the efficiency of this method we propose to pick the initial guess as the solution of the linear circuit obtained after replacing all the diodes by very large ($10 \text{ M}\Omega$) resistors. In such a case the method leads to the solution in 21 iterations consuming 31ms. The Newton-Raphson method with the same initial guess is not convergent to the solution in 1000 iterations.

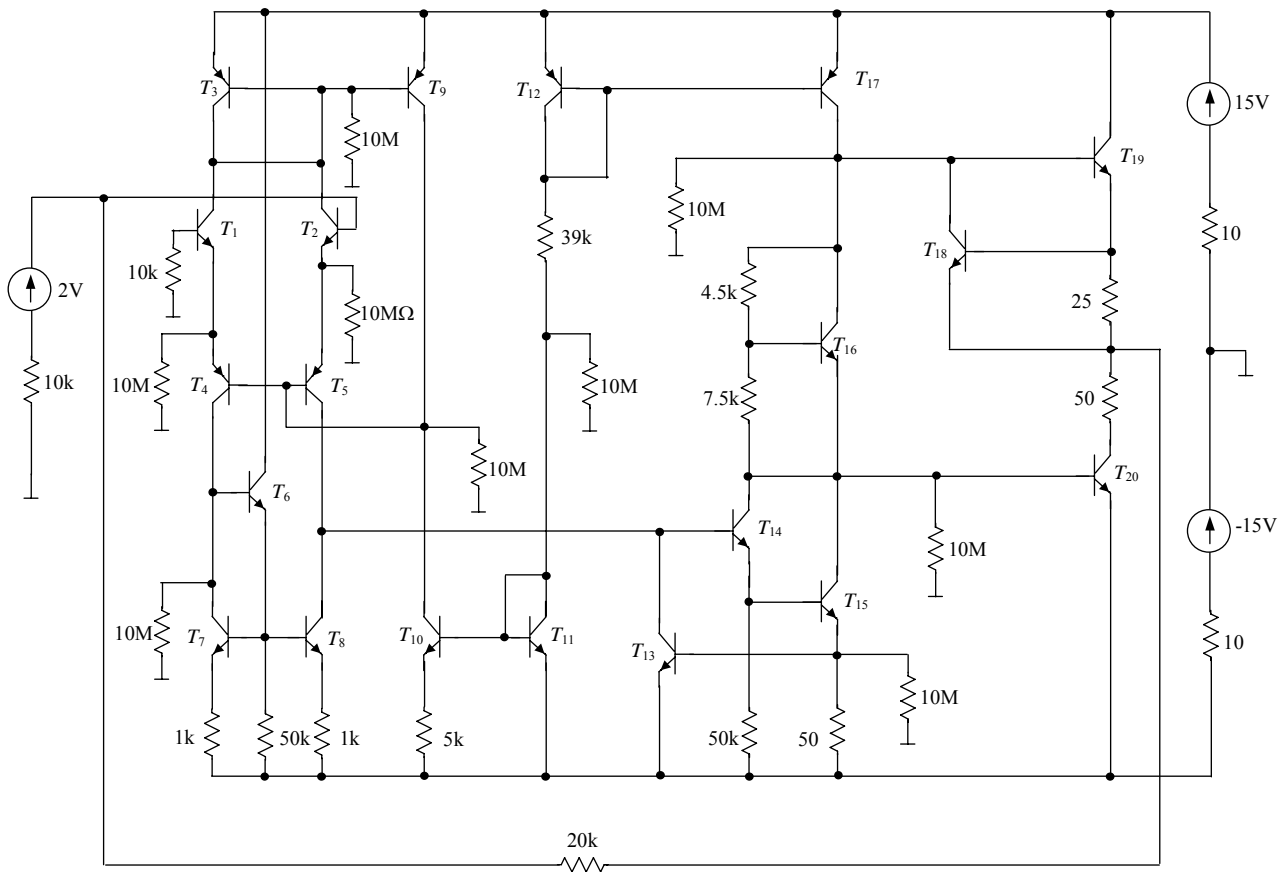


Fig. 3. The circuit for Example 2

Conclusion

The method developed in this paper, based on the homotopy idea and the Padé approximation, enables us to efficiently find the operating points of electronic circuits containing diodes and the Ebers-Moll modelled bipolar transistors. Numerical experiments show that the offered method allows robust computation and considerably improves the DC analysis of the diode-transistor circuits based on the Newton-Raphson method.

REFERENCES

- [1] Ortega J.M., Rheinboldt W.C., Iterative solution of nonlinear equation in several variables, Academic Press, (1970), New York-London
- [2] Chua L.O., Lin P.M., Computer aided analysis of electronic circuits. Algorithm and computational techniques, (1975), Prentice-Hall
- [3] Chua L.O., Wang N.N., A new approach to overcome the overflow problem in computer aided analysis of nonlinear resistive circuits, *Int. Journal of Cir. Theor. Appl.*, (1975), vol 3, 261-284
- [4] Shichman H., Computation of DC solutions for bipolar transistor networks, *IEEE Trans. on Cir. Theor.*, (1969), vol. 16, 460-466
- [5] Melville R.C., Trajković L., Fang S.C., Watson L.T., Artificial parameter homotopy methods for the DC operating point problem, *IEEE Trans. on Computer-Aided Design of Integrated Circuits and Systems*, (1993), vol. 12, 861-877
- [6] Tadeusiewicz M., DC analysis of circuits with idealized diodes considering reverse bias breakdown phenomenon, *IEEE Trans. on Cir. and Syst.-I*, (1997), vol. 44, 312-326
- [7] Tadeusiewicz M., Pawlak K., Hałgas S., DC analysis of diode transistor circuits, *Proc. XIII Int. Symp. on Theoret. Electr. Eng.*, (2005), 392-392
- [8] Tadeusiewicz M., Hałgas S., Computing multivalued input-output characteristics in the circuits containing bipolar transistors, *IEEE Trans. on Cir. and Syst.-I*, (2004), vol. 51, 1859-1867
- [9] Quarles T.L., Newton A.R., Pederson D.O., Sangiovanni-Vincentelli A., SPICE-3. Version 3F5 User's Manual, (1994), Berkeley, CA: Dep. of EECs, Univ. California
- [10] Kielkowski R.M., Inside SPICE, (1998), McGraw-Hill
- [11] <http://mathworld.wolfram.com/PadéApproximant.html>
- [12] Garcia C.B., Zangwill W.I., Pathways to solutions, fixed points, and equilibria, (1981), Prentice-Hill, Inc. Englewood Cliffs, N.J.
- [13] Sandberg I.W., Willson A.N., Some network-theoretic properties of nonlinear DC transistor networks, *Bell Syst. Tech. Journal*, (1969), vol. 48, 1293-1311

Authors: The authors are with the Department of Electrical, Electronic, Computer and Control Engineering of the Technical University of Lodz, ul. Stefanowskiego 18/22, 90-924 Lodz, Poland, e-mail: michal.tadeusiewicz@p.lodz.pl

Mathematical model for M-phases switched reluctance motor

Abstract. The constructive schemes of switched reluctance motor and basic electrical scheme of a commutator with capacity buffers of energy are circumscribed. Is explained a mathematical model to a research of electromechanical processes in electric drives with switched reluctance motor with buffers of an energy.

Streszczenie. Artykuł prezentuje schematy konstrukcyjne silnika o przełączanej reluktancji i podstawowy schemat elektryczny komutatora z pojemnościowymi buforami energii. Omówiony jest również model matematyczny do badania procesów elektromechanicznych w silnikach elektrycznych z przełączaną reluktancją i z buforami energii. (**Model matematyczny M-fazowego silnika o przełączanej reluktancji**).

Keywords: switched reluctance motor, electromechanical converters, construction, mathematical model, electronic commutator.

Słowa kluczowe: silnik z przełączaną reluktancją, konwertery elektromechaniczne, konstrukcja, model matematyczny.

Introduction

The switched reluctance motor (SRM) with explicitly poles on the stator and concentrated coils its winding and toothed passive rotor is one of elementary by a construction, technological and reliable.

From the whole varieties inductors electromechanical converters (EMC) most expedient for use in SRM are constructions with salient poles on the stator, in which it is possible to provide magnetic isolation of separate sections. The most known of them is a classic construction.

Construction EMC of SRM

On the basis of a construction EMC of SRM it is possible to define stator, which permits to use waste less steel cutting, to reduce expenditure of cooper and better used volume the machine active part (fig. 1). Let's name such construction as stator with T-similar elements.

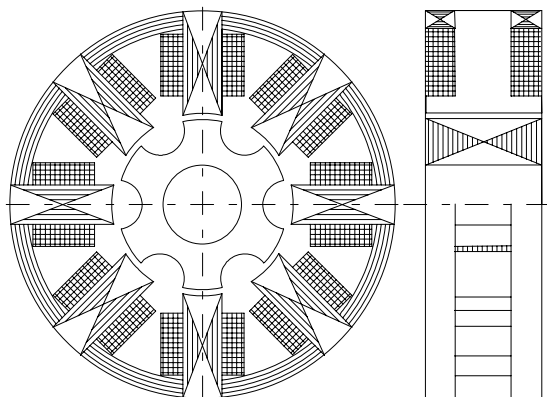


Fig. 1. EMC with the T-similar elements of stator

One more construction, which completely uses axial length of the machine as an active part given in a fig. 2. Let's name it as EMC with C-similar elements or with an axial magnetic flux. It is expedient to use in case when is necessary to receive minimum axial length of the machine (for example, in a lift drive of a glass in automobiles doors) and full magnetic isolation of sections of a stator's winding.

he construction of EMC with U-similar elements isffered in [1] which, as well as the above mentioned construction with C-similar elements ensures full magnetic isolation of sections of SRM. To disadvantage of U-similar construction it is possible to refer it's non technology and low repair ability stipulated that separately made stator elements are necessary composing in a completed construction of stator with help of additional technological elements and fixing materials.

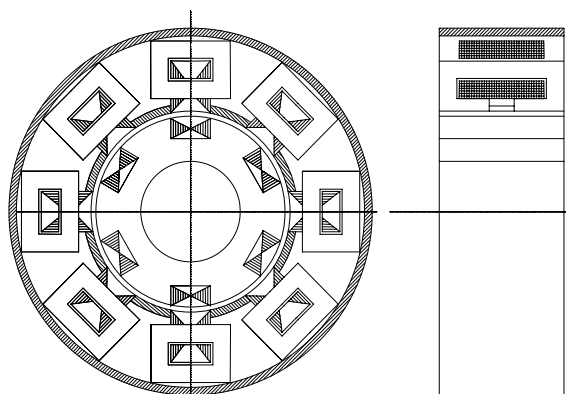


Fig.2. EMC with an axial magnetic flux of stator

This disadvantage haven't the construction of stator, which given in a fig. 3. Let's name it as pseudo-U-similar. In this construction the stator core is laminated in axial direction from isolated plate of electrotechnical steel, then on teeth superimpose frame or unframed concentrated coils of a stator winding, which fix with help of wedges between parallel or others teeth. On the base of this stator it is possible to build EMC without tank. The place for tightening bolts is between nonparallel teeth.

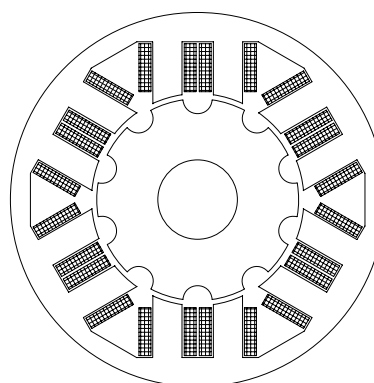


Fig. 3. Pseudo U-similar construction of EMC of SRM

Described construction is expedient to use during design SRM of rather large diameter with a many teeth on a rotor, as it permits considerably reduce, in a comparison with a classical construction, length of magnetic force lines, so also the steel losses.

Transistor commutators with capacity accumulators

The wide use SRM is braked by their low power indexes, that is stipulated by necessity of dissemination, during commutation of a current in sections by transistor keys accumulated in an electromagnetic field with the purpose of a guard them from high voltages. Brightly it exhibit in SRM with an one-semiperiodic commutator with stabilitron receiver of a magnetic field energy.

So, the task of creation switched drive on the base of simple, cheap and technological inductor machine is largely reduced to necessity of creation of new schemes solutions, which will permit to use the energy accumulated in a magnetic field armature winding section to execute the useful work. During a solution of this task, on chair of electrical machines were developed structural and principle schemes of electronic commutator, which have the raised reliability and ensure recuperation of magnetic field energy of sections, which are commutating. [2, 3].

One of the schemes of transistor commutators with sequential capacity accumulators is given in a fig. 4 [3]. The principle of its work based on the following: if the rotor will take a position of an angle of switching β (fig.5), the signals K1 - K4 RPS will open VT1 and VT4, which will remain in open state during the angle of commutation γ . The armature winding section EMC w1 receives a feed from source and sequentially agrees with it connected condenser C1, charged in a preceding cycle through these keys. The diode VD1 will be switched off by applied to it in opposite direction voltage of the condenser C1. The section current w1 forced increase, the condenser C1 is discharged and then the it voltage on it will zero, the diode VD1 will switch on, section w1 connect to the energy source on a circuit: the diode VD1, transistor VT1. Under the influence of electromagnetic moment rotor turn and then a value of an commutation angle is reaching VT1 and VT4 are switch off.

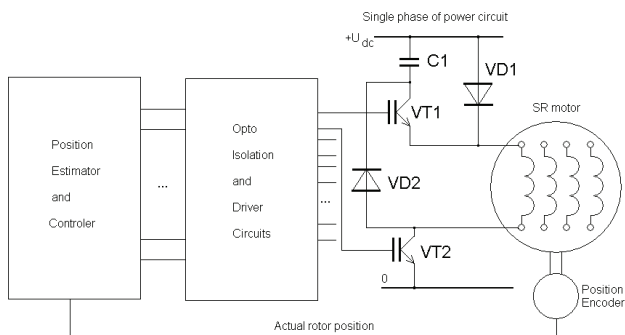


Fig. 4. The principle electrical scheme of a transistor commutator with sequential capacity accumulators in each section

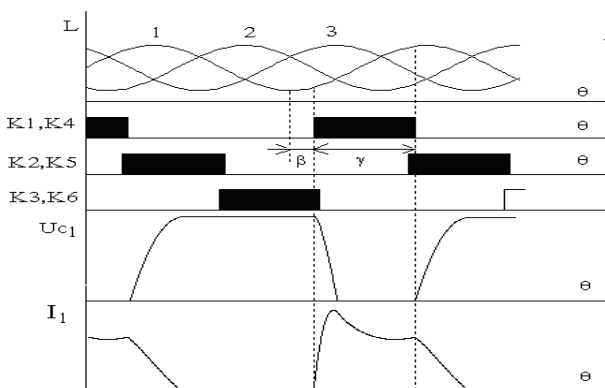


Fig. 5. Inductance and current of section, diagram of work of transistor and voltage on the storage capacity

Under the action of self-inductions EMF the section current $w1$ will begin to flow on a circuit: the diode $VD4$, condenser $C1$, diode $VD1$. The condenser $C1$ is charged, the current of section is forced decreases. For others sections this process will repeat through an angle $2 \cdot \pi / m$, where m - amount of sections. Thus three tasks are solve: at first, utilized the energy accumulated in an electromagnetic field of armature of EMC; secondly, the increase of voltage on collector-emitter passage of a transistor of a commutator to a level supposed is limited; thirdly, for the score of almost instant interception of reenergizing current of the transistor by a circle of a charge of the condenser dynamic losses on switching the transistor of commutator considerably decrease. Calculation and the experimental researches show, that the application of the schemes with CBE in SRM is improved it coefficient of a response in 1.7 - 1.8 in a comparison with the scheme with stabilitron safe from high voltage power keys of a commutator.

Mathematical model switched reluctance motor

The tasks of creation of new types of electrical machines, in which it is possible to refer salient pole switched reluctance motors with and energy buffers can be successfully solve only with presence of rather exact tools of computation their static and dynamic characteristics.

Present time is developed many theories and that permit to calculate periodic processes in electromechanical devices, in other words when the currents, interlinkage, voltages, linear and angular shifting are periodic functions of time.

The power method offers two modes for an evaluation of an electromagnetic force, which operates in the given direction on chosen volume of a nonlinear system. With the first mode the electromagnetic force expresses through an increase of magnetic energy stipulated by small shifting of chosen volume in conditions of flux constancy. With second - the electromagnetic force express through an increase magnetic kou-energy, which is carried out with small shifting of chosen volume in conditions of a constancy of excitation current circuit.

Admissible behind precision results can be received with the help of power approach only in those cases, if an increase of an energy or kou-energy in a nonlinear magnetic system is given analytically.

Interlinkage of a winding phase of an armature of EMC with a passive rotor is unique nonlinear function, which can be approximated by analytical expression. Thus it is necessary that the mode of approximation ensured coincidence of real and approximated of dependence as in function of rotor and stator mutual position angle, and in and function of current, possibility of integration and differentiation in analytical form and didn't require complicated and bulky evaluations of coefficients.

Equations (1) suit mentioned conditions:

$$(1) \quad \psi(\theta, i) = [\psi_{10} - \psi_{1t} \sin(\theta / 2)]i + \psi_y \sin(\theta / 2) [1 - e^{-a \cdot i \cdot \sin(\theta / 2)}]$$

where: θ - electrical angle between an axes of rotor slot and axes of stator tooth; i - phase excitation current; ψ_{10} , ψ_{1t} , ψ_y , a - coefficients.

The offered analytical expression for an evaluation EMC of interlinkage with passive rotor gives possibility to note the equations of voltages for magneto insulated phase of SRM and calculate electromagnetic moment, which can form the basis for creation of mathematical models of SRM.

Electromagnetic moment it is possible to note as:

$$(2) \quad M(\theta, i) = \frac{\partial W_k}{\partial \theta} = \frac{Z_r \cdot \psi_y}{2} I \cdot \cos(\theta / 2) \times \left\{ I - e^{-aI \sin(\theta / 2)} - \frac{\psi_{II} I}{2} \right\}$$

where: $\theta_M = \theta / Z_r$ - geometric angle of a rotor position; Z_r - amount of rotor teeth.

The equation (2) enables to calculate electromagnetic moment in a function of current and angle of a rotor and stator mutual position.

For design of a mathematical model of this switched drive we shall accept the following assumptions:

- The drive feed from voltage source, which internal resistance is equal zero;
- The magnetic connections between sections are absent (absolutely fairly for T-, C- and U- similar constructions of stator and does not bring in significant errors for "classical" constructions);
- Power keys of a commutator - electronic keys without inertia, for which it is possible to accept that at first - transients process, well the commutation of sections of EMC of SRM passes practically instantly; secondly - the inverse resistance of closed key is equaled infinity;
- Diodes in a conducting condition represented by a mathematical model of the diode, in the closed condition their resistance is equaled infinity;
- Stator is concentrated of winding parameters.

The modelling of power transistor keys is realized in view of assumption that the transient's process of their turning on and turning off happen instantly, the resistance of closed key is leveled infinity; the volt-ampere performance of a saturated key is described equations

$$(3) \quad \Delta U_T = U_{KE} = U_{KE.0} + R_{KE.HAC} \cdot i,$$

where: $\Delta U_{KE.0}$ & $R_{KE.HAC}$ define from the passport of transistor.

Condition of transistor EC caused by a mutual position of rotor and stator, that is they are controlled by signals of rotor position sensors. Let's assume in the correspondence with a condition of these keys formal coefficients K_j , which receive a value "1" - if a key open, and "0" - if a key closed; j - number of a key.

Value of formal coefficients K_j depend on a rotor position and calculate according to the following switching function:

$$(4) \quad K_j = 1 \text{ if } \beta + 2(N_j - 1)\pi + (j+1)2\frac{\pi}{m} < \theta \leq \beta + 2(N_j - 1)\pi + (j+1)2\frac{\pi}{m} + \gamma$$

$$K_j = 0 \text{ for all other values,}$$

where: $N_j = \frac{\theta + \pi + (j-1) \cdot 2 \cdot \frac{\pi}{m}}{2 \cdot \pi} + 1$ - number of period for appropriate section.

The scheme of EC contains the nonlinear element - diode, which volt-ampere characteristic can be approximated by expression

$$(5) \quad i_\Delta = I_0 \left(e^{b \cdot \Delta U_\Delta} - 1 \right),$$

and then voltage drop on the diode can be noted as:

$$(6) \quad \Delta U_\Delta = \ln \frac{i_\Delta + I_0}{I_0} / b,$$

where: I_0 and b - current of the diode and coefficient of a temperature potential.

Is known that losses in steel - is loss on hysteresis and losses from Fuko currents. In SRM with a passive rotor the basic magnetic flux doesn't change the direction, but only pulses behind magnitude in separate parts of magnetic circuit from the maximum value to minimum without a polarity change. Such magnetization equivalent normal magnetization by a variable magnetic-motion force of sold which already magnetized up to some magnetic condition constantly affixed to it magnetic-motion force and hysteresis loop enough narrow, that, as shows experience, caused insignificant magnitude dsgouls losses from a magnetic aftereffect. That means in a common part of losses in steel a main occupied losses from eddy currents, and that losses from a hysteresis can didn't take into consideration.

The variable magnetic flux, close on the steel core, creates in it electromotive force, which is by reason of Fuko currents in steel, which caused losses in it. The intersection of magnetic circuit can be considered as such, that consists of elementary closed loops, which organize short-circuit turn, which are penetrated by a variable magnetic flux. Let's present them in the circuit of section of SRM - as a branch L_σ and R_σ , which is connected in a parallel to a branch magnetization.

Resistance of steel Fuko currents with sufficient for engineering practice precession it is possible to define by equations

$$(7) \quad R_s = \frac{E^2}{\Delta P_s},$$

where:

$$E = 4.44 \cdot f \cdot w_z \cdot B \cdot s, \quad \Delta P_s = P_0 \cdot \gamma_s \cdot s \cdot l_m \cdot B^2 \cdot (f / f_0)^2.$$

Substitute values E and ΔP_s in (7), we receive equations for evaluation R_s of one section:

$$(8) \quad R_s = 4,9 \cdot 10^4 \cdot \frac{w_z^2 \cdot S \cdot q}{P_0 \cdot \gamma_s \cdot l_m},$$

where: $p_0, \gamma_s, S, l_m, w_z, q$ - specific losses in steel, denseness of a material magnetic circuit, length of a magnetic force line, amount of winding coils of a winding on one tooth, amount of stator teeth on one section accordingly.

The leakage inductance of Fuko currents circuits L_σ is insignificant and its magnitude it would be possible dose not calculate. However for ensuring stability of a differential equations solution by the numerical methods propose values L_σ to accept, following,

$$(9) \quad L_\sigma \cong \frac{\Delta t}{12} \cdot R_s,$$

where: Δt - integration step of the differential equations.

Taking into account given higher, and also considering that SRM feet from a source with a zero internal resistance, for m-sectional EMC with a passive rotor, magnetic insulated sections and EC with sequential CBE in each phase the unrolled equations after transformations can be given form, as:

$$\begin{cases} \frac{di_j}{dt} = \left[u_j + R \cdot i_j + \frac{A_j}{L_\sigma} (u_j - R \cdot i_j + R_S \cdot i_{Sj}) - B_j \omega \right] / A_j \\ \frac{di_{Sj}}{dt} = -(R_S i_{Sj} + u_j - R \cdot i_j) / L_\sigma \\ \frac{du_{Cj}}{dt} = (1 - K_j - K_{j+m}) \frac{i_j}{C} \\ \frac{d\omega}{dt} = \left\{ \sum_{j=1}^m \left[\frac{Z_r}{2} (i_j + i_{Sj}) \cos \theta_{pj} \cdot \psi_y \times \right. \right. \\ \left. \left. \times (1 - e^{-a(i_j + i_{Sj}) \sin \theta_{pj}} - \frac{\psi_{Ll}(i_j + i_{Sj})}{2\psi_y}) \right] - M_C \right\} \frac{Z_r}{J} \\ \frac{d\theta}{dt} = \omega \end{cases}$$

where:

$$u_j = (U + \Delta U_\partial) \cdot (K_j - K_{j+m}) + u_C (K_j + K_{j+m} - 1) - \Delta U_T (K_j + K_{j+m}) - \Delta U_\partial (3 - K_j - K_{j+m})$$

$$A_j = \psi_{10} - \psi_{Ll} \sin \theta_{pj} + \psi_y \cdot a \cdot \sin^2 \theta_{pj} \cdot e^{-a(i_j + i_{Sj}) \sin \theta_{pj}}$$

$$B_j = \frac{\cos \theta_{pj}}{2} \left[\psi_y - \psi_{Ll} (i_j + i_{Sj}) - \psi_y \cdot e^{-a(i_j + i_{Sj}) \sin \theta_{pj}} \times \right. \\ \left. \times (1 - a(i_j + i_{Sj}) \sin \theta_{pj}) \right]$$

$$\theta_{pj} = \frac{\theta}{2} - (j-1) \frac{2\pi}{m}$$

$j = 1, 2, \dots, m$; J - moment of inertia; M_C - moment of load resistance

Computing of instantaneous values starting and quasisteady state regimes of operations of the electric drive on the basis of three-phase SRM with sequential CBE

The reduced mathematical model is base for creation of numerical models of electric drives with a SRM with buffers of energy and permits to realize a research of dynamic and quasisteady state regimes of operations, to receive instantaneous values of currents, moment, rotation frequency, voltage on an accumulator, and also integrated values of these magnitudes and separate composite losses (in copper, in steel, on the force electronic elements of a commutator etc.). For a numerical solution of a differential equations system the method of Runge - Kutti of the fourth order with a fixed integration step is used.

The method of inverting differential equations behind an angle of a turn of rotor, current of section or voltage on the accumulative condenser is applied for the exact definition of instants turning on (turning of) of power keys EC, diminution of a current in any of section to zero, full discharge of condensers. In a fig.6 given the example of computing of instantaneous values starting and quasisteady state regimes of operations of the electric drive on the basis of three-phase SRM with sequential CBE in each section - current of section, current, which equivalent to losses in steel, voltage on accumulative condensers, electromagnetic moment and rotation frequency.

Conclusion

Comparison of outcomes of calculation with research times responses, and also average values of a moment, rotation frequency and composite losses for market exemplar of SRM with nominal moment from 0.05 up to

20 Nm have shown, that a divergence do not exceed 5%, that confirm the adequacy of mathematical model to physical sample.

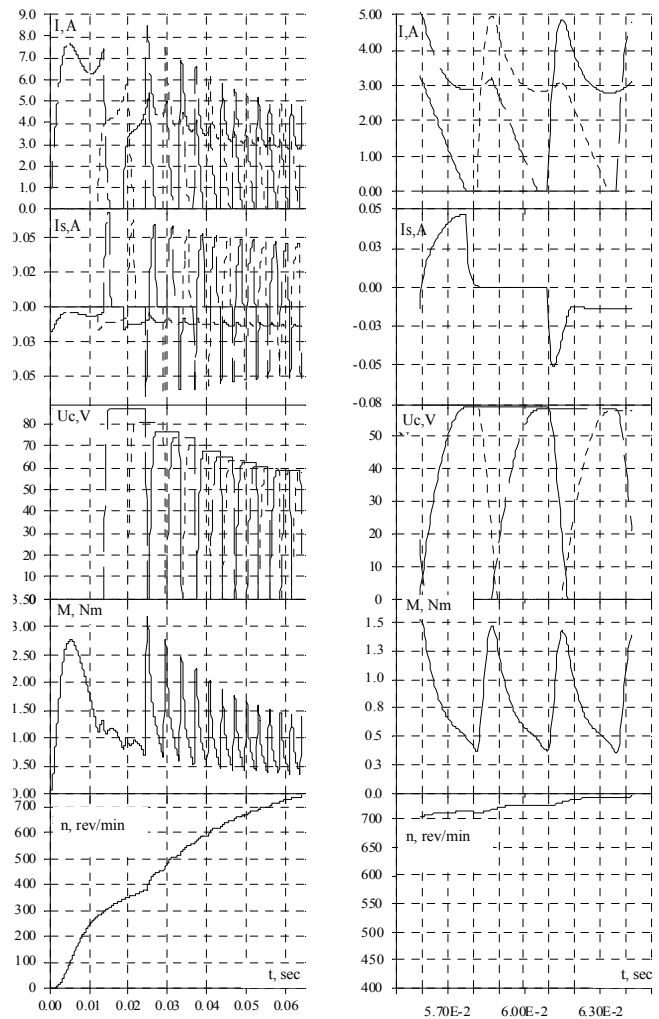


Fig. 6. Simulation result of starting and quasisteady state regimes of operations of three-phase SRM with sequential CBE

REFERENCES

- [1] Osidach Y.V., Tkachuk V.I. Switched m-phase reluctance motor, *The copyright certificate 1561162 USSR №4394816/24-07; Req. 21.03.88. Publ. 30.04.90. Bulletin №16.*
- [2] Osidach Y.V., Tkachuk V.I. Switched reluctance motor, *The copyright certificate 1246265 USSR №3814427/24-07; Req. 19.11.84. Publ. 23.07.86. Bulletin №27.*
- [3] Tkachuk V.I. Capacity of energy in switched reluctance motor, *Electroenergetics and electromechanics systems. Publishing by SU "Lvivska politehnika", 1997, № 334, pp. 125 - 131.*
- [4] Tkachuk V.I., Osidach Y.V. Transistor commutators with capacity buffers of energy. *Electroenergetics and electromechanics systems. Publishing by SU "Lvivska politehnika", 1996, № 301, pp. 115 - 122.*

Authors: Chief of the chair "Electrical machines and devices", prof., doctor of sciences Vasyl Tkachuk, Lviv Polytechnic National University, Institute of Power Engineering and Control System, 12'St.Bandery str., 79013 Lviv, Ukraine (e-mail: tkachuk@polynet.lviv.ua); research assistant Kasha Lidiya, Lviv Polytechnic National University, chair of electrical machines and devices, 12'St.Bandery str., 79013 Lviv, Ukraine (e-mail: kasha.lidiya@mail.ru);

Mathematical models for wave propagation analysis in distributed and lumped parameter networks

Abstract. The approach to wave processes modelling is proposed for power networks. Propagation of overvoltages and current peaks is simulated at the network lines switching and at emergency regimes.

Streszczenie. Artykuł prezentuje modelowanie propagacji fal w sieciach zasilających. Przedstawiona jest symulacja modelu propagacji przepięć i szczytów w liniach sieci powstających w przypadkach przełączeń i zwarc. (Model matematyczny propagacji fal w sieciach zasilających w przypadkach przełączeń i zwarc).

Keywords: power networks, wave propagation, overvoltage.

Słowa kluczowe: sieci energetyczne, propagacja fali, przepięcia w sieciach energetycznych.

Introduction

Simulation of switching overvoltages appearance and propagation in multipathed structure of network is a complex problem. The replacement of real transmission line either by lossless line or by lumped resistors is well-known calculation practice [1]. Another approach to mentioned problem solving is proposed by authors [2].

The use of Duhamel integral (contrary to the well-known methods) allows one to obtain mathematical model which provides a general approach for transients description for the circuits with components both lumped and distributed parameters. This approach has some advantages, which are inherent integral models and Volterra equations in particular. The main advantage of these equations is the convenience and compactness in dynamic system description. In this case the relation between input $u(t)$ and output $i(t)$ values is represented by integral operators

$$(1) \quad i(t) = \frac{d}{dt} \int_0^t g(t-\tau)u(\tau)d\tau.$$

The relation (1) was used by J.R.Carson [3] for description of transients in a single distributed parameter line, which is represented by two-port.

The Carson's approach is suitable for line network modelling. It allows the creating a qualitatively new mathematical model of dynamic processes in power networks, which considers the distributed losses and transient wave character. In proposed model the elements of different kinds (distributed lines and lumped loads) are described the same Volterra integral equations (1). Just a kernel $g(t-\tau)$ represents the main properties of the element.

Element integral equations are united in the system similarly a node voltages method.

Integral mathematical model of power network

For obtaining of whole network mathematical model the functions of all elements transient conductivities $g(t-\tau)$ must be determined. The transient conductivities of lumped elements are invariant expressions on the all modelling interval. They are obtained once in the beginning of the research. In this case the same expressions describe the eigen and mutual transient conductivities of load. Unlike for lines the functions representing transient conductivities are discontinuous because of wave reflection in the lines [4]. The next expressions for the eigen g_{ii} and mutual g_{ij} transient conductivities of long line are used in the model:

$$(2) \quad g_{ii}(t) = \frac{1}{R_0 l} \left(1 - e^{-\lambda t} + D e^{-\frac{\lambda t}{2}} \frac{\pi}{2} \left(2i + 1 - \frac{t}{\tau} \right) \right);$$

$$(3) \quad g_{ij}(t) = \frac{1}{R_0 l} \left(1 - e^{-\lambda t} + D e^{-\frac{\lambda t}{2}} \frac{\pi}{2} \left(2i - \frac{t}{\tau} \right) \right),$$

where $\lambda = R_0/L_0$, $D = \frac{2R_0 l \sqrt{C_0/L_0}}{\pi}$, $\tau = l\sqrt{L_0 C_0}$.

The formation of a transient conductivity matrix is main stage of the network modelling as in node voltages method for circuits. Due to a discontinuity of transient conductivity function that matrix must be recout for each reflection in every line. Thus wave propagation in the network is simulated by series of equivalent circuits, in which any next circuit differ from previous one by added parallel branches.

For example, network Fig. 1 is simulated by equivalent circuit Fig. 2 for the time interval not exceeding minimal τ (for the shortest line in the network).

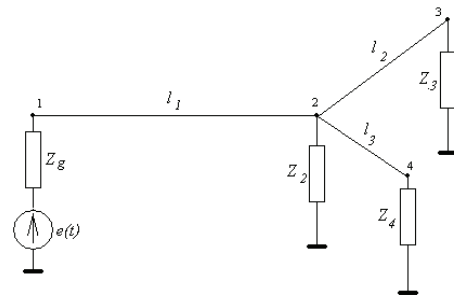


Fig. 1. An example of network

An equivalent circuit for the i -th calculation step is shown at Fig. 3 after k -th reflection in the first line, m -th reflection in the second line and n -th reflection in the third line. Including the designation $g \otimes u$ for operation

$$\frac{d}{dt} \int_0^t g(t-\tau)u(\tau)d\tau, \text{ equation (1) transform to } i(t) = g \otimes u.$$

The equation system for equivalent circuit Fig. 2 is a following:

$$\begin{aligned} & (g_{11}^{I1} + g_g) \otimes u_1 - g_{12}^{I1} \otimes u_2 = g_g \otimes e_g; \\ & -g_{21}^{I1} \otimes u_1 + (g_{22}^{I1} + g_{L2} + g_{22}^{I2} + g_{22}^{I3}) \otimes u_2 - g_{23}^{I2} \otimes u_3 - g_{24}^{I2} \otimes u_4 = 0; \\ & -g_{32}^{I2} \otimes u_2 + (g_{33}^{I2} + g_{L3}) \otimes u_3 = 0; \\ & -g_{42}^{I3} \otimes u_2 + (g_{44}^{I3} + g_{L4}) \otimes u_4 = 0. \end{aligned}$$

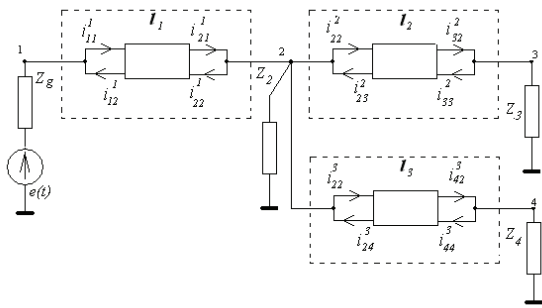


Fig. 2. Initial equivalent circuit.

The integral equation system for equivalent circuit Fig. 3 is following:

$$\begin{aligned} & \left(g_{11}^{l1} + \sum_{i=1}^k \Delta_i g_{11}^{l1} + g_g \right) \otimes u_1 - \left(g_{12}^{l1} + \sum_{i=1}^k \Delta_i g_{12}^{l1} \right) \otimes u_2 = g_g \otimes e_g ; \\ & - \left(g_{21}^{l1} + \sum_{i=1}^k \Delta_i g_{21}^{l1} \right) \otimes u_1 + \\ & \left(g_{22}^{l1} + \sum_{i=1}^k \Delta_i g_{22}^{l1} + g_{L2} + g_{22}^{l2} + \sum_{i=1}^m \Delta_i g_{22}^{l2} + g_{22}^{l3} + \sum_{i=1}^n \Delta_i g_{22}^{l3} \right) \otimes u_2 - \\ & - \left(g_{23}^{l2} + \sum_{i=1}^m \Delta_i g_{23}^{l2} \right) \otimes u_3 - \left(g_{24}^{l3} + \sum_{i=1}^n \Delta_i g_{24}^{l3} \right) \otimes u_4 = 0 ; \\ & - \left(g_{32}^{l2} + \sum_{i=1}^m \Delta_i g_{32}^{l2} \right) \otimes u_2 + \left(g_{33}^{l2} + g_{L3} + \sum_{i=1}^m \Delta_i g_{33}^{l2} \right) \otimes u_3 = 0 ; \\ & - \left(g_{42}^{l3} + \sum_{i=1}^n \Delta_i g_{42}^{l3} \right) \otimes u_2 + \left(g_{44}^{l3} + g_{L4} + \sum_{i=1}^m \Delta_i g_{44}^{l3} \right) \otimes u_4 = 0 . \end{aligned}$$

Instead of an equivalent circuit complication with a transient time increasing, dimensionality of equation system does not change. Network nodal equation system in matrix form is following:

$$\begin{bmatrix} i_1 \\ i_2 \\ i_3 \\ i_4 \end{bmatrix} = \begin{bmatrix} g_{11} & g_{12} & 0 & 0 \\ g_{21} & g_{22} & g_{23} & g_{24} \\ 0 & g_{32} & g_{33} & 0 \\ 0 & g_{42} & 0 & g_{44} \end{bmatrix} \otimes \begin{bmatrix} u_1 \\ u_2 \\ u_3 \\ u_4 \end{bmatrix} ,$$

where eigen nodal transient conductivities are following:

$$\begin{aligned} g_{11} &= g_{11}^{l1} + \sum_{i=1}^k \Delta_i g_{11}^{l1} + g_g ; \\ g_{22} &= g_{22}^{l1} + \sum_{i=1}^k \Delta_i g_{22}^{l1} + g_{L2} + g_{22}^{l2} + \\ & + \sum_{i=1}^m \Delta_i g_{22}^{l2} + g_{22}^{l3} + \sum_{i=1}^n \Delta_i g_{22}^{l3} ; \\ g_{33} &= g_{33}^{l2} + g_{L3} + \sum_{i=1}^m \Delta_i g_{33}^{l2} ; g_{44} = g_{44}^{l3} + g_{L4} + \sum_{i=1}^n \Delta_i g_{44}^{l3} ; \end{aligned}$$

and mutual nodal transient conductivities are

$$g_{ij} = g_{ij}^l + \sum_{i=1}^r \Delta_i g_{ij}^l .$$

Then generalized integral equation system for network in matrix form may be obtained:

$$(4) \quad \frac{d}{dt} \int_0^t G(t-\tau) U(\tau) d\tau = I(t) ,$$

where G is network transient conductivity matrix; U is nodal voltages vector; I is nodal current vector.

Analogue of step-by-step procedure for Volterra integral equations

Model (4) analyses assumes the solution of Volterra integral equations on the integrating interval $(0:t)$. Due to specialities of the the functions, which form kernel matrix, systeme (4) must be solving on successive subintervals with H step. Procedure of this kind for integral equations differs from well-known step-by-step procedure for differential equations.

We propose analogue of step-by-step procedure for Volterra integral equations. Let's consider it for kernel takes the form

$$(5) \quad g(t-\tau) = A e^{\lambda(t-\tau)} .$$

Just kernel (5) has a peak incidence for electrical circuit transient analyses.

Substitute (5) in eq. (1) and differentiate integral expression, one obtains

$$(6) \quad i(t) = g(0)u(t) + \int_0^t A \lambda e^{\lambda(t-\tau)} u(\tau) d\tau .$$

Represent (6) for two subintervals:

$$i(t) = g(0)u(t) + \int_0^{t_i} A \lambda e^{\lambda(t-\tau)} u(\tau) d\tau + \int_{t_i}^t A \lambda e^{\lambda(t-\tau)} u(\tau) d\tau .$$

Assume that solution is known at the point $t=t_i$:

$$(7) \quad i(t_i) = g(0)u(t_i) + \int_0^{t_i} A \lambda e^{\lambda(t_i-\tau)} u(\tau) d\tau .$$

The problem implies that expression (7) must be used to get the solution at the point $t=t_i+H$.

Since $\int_0^{t_i} A \lambda e^{\lambda(t-\tau)} u(\tau) d\tau \neq \int_0^{t_i} A \lambda e^{\lambda(t_i-\tau)} u(\tau) d\tau$ the

integral value in (7) must be corrected. The way of correction depends on kernel function kind. For exponential kernel a multiplicate correction as a factor ξ is the most suitable:

$$\begin{aligned} (8) \quad i(t_i + H) &= g(0)u(t_i + H) + \int_0^{t_i+H} A \lambda e^{\lambda(t_i+H-\tau)} u(\tau) d\tau = \\ &= g(0)u(t_i + H) + \xi \int_0^{t_i} A \lambda e^{\lambda(t_i-\tau)} u(\tau) d\tau + \\ & + \int_{t_i}^{t_i+H} A \lambda e^{\lambda(t_i+H-\tau)} u(\tau) d\tau . \end{aligned}$$

According to (8) an expression for ξ is following:

$$\xi = \frac{A\lambda e^{\lambda(t_i+H)} \left(\int_0^{t_i+H} e^{-\tau\lambda} u(\tau) d\tau - \int_{t_i}^{t_i+H} e^{-\tau\lambda} u(\tau) d\tau \right)}{A\lambda e^{\lambda t_i} \int_0^{t_i} e^{-\tau\lambda} u(\tau) d\tau} = e^{\lambda H}.$$

Thus relationship (8) corresponds to an algorithm of step-by-step procedure for Volterra integral equations.

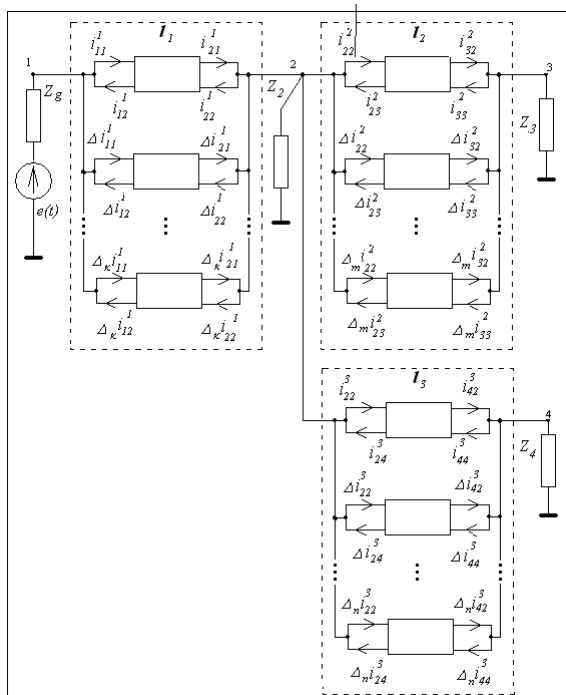


Fig. 3. An equivalent circuit for the i -th calculation step.

This adaptation procedure of a model with discontinuities to DT-transform usage based on general function theory is proposed by authors in [2].

Numerical algorithm for transient network analysis

After forming a complete network equation set it may be solved by the known numerical methods substituting the integrals for finite sums and the derivatives are substituted for finite differences. We have developed more efficient algorithm using differential Taylor (DT) transforms [2]. DT-transforms are based on the function representation by Taylor series. The function-original $x(t)$ and the function-image $X(k)$ are connected by expressions of direct and inverse transforms:

$$x(t) = \sum_{k=0}^{\infty} X(k) \left(\frac{t-t_i}{H} \right)^k \quad \text{and} \quad X(k) = \frac{H^k}{k!} \left[\frac{\partial^k x(t)}{\partial t^k} \right]_{t=t_i}$$

where $k=0,1,2,\dots,\infty$.

Note that the immediate application of DT-transforms to integral equations of network model involves some difficulties due to the discontinuity of the functions representing transient conductivities. If $g(t)$ is the

discontinuous function, which is typical of the lines with distributed parameters, then the differentiation is not correct. Using of proposed approach (step-by-step procedure) allows to apply DT-transforms to network transient analyses correctly.

In the DT-images domain the network integral model is represented by the system of algebraic equations:

$$\begin{aligned} (g_{11}^l(0) + g_g(0))U_1 + \sum_{j=1}^N \left(U_j \sum_{i=1}^k \Delta_i G_{ij} + J_{ij} \right) &= g_g(0)E + J_g; \\ (g_{22}(0) + g_{L2}(0))U_2 + \sum_{j=1}^N \left(U_j \sum_{i=1}^m \Delta_i G_{ij} + J_{ij} \right) &= 0; \\ (g_{33}(0) + g_{L3}(0))U_3 + \sum_{j=1}^N \left(U_j \sum_{i=1}^m \Delta_i G_{ij} + J_{ij} \right) &= 0; \\ (g_{44}(0) + g_{L4}(0))U_4 + \sum_{j=1}^N \left(U_j \sum_{i=1}^n \Delta_i G_{ij} + J_{ij} \right) &= 0; \end{aligned}$$

where E , U_j are the DT-images of emf source and voltages in the nodes of the network Fig. 3 obtained at the moment $t=t_i$ respectively; J_{ij} and J_g are the DT-images of integrals in network integral model, respectively [4].

Conclusion

The method proposed for forming of the network mathematical model is similar to nodal method in circuit theory. With its using the block matrices are obtained for the typical networks structures suitable for building of the models of the complex networks.

The method of transient process calculation proposed for transmission lines networks bases on DT-transforms and allows one to represent analytically the solution within continuity intervals in the form of Taylor series. The proposed DT-method more precisely simulates the processes in line and allows us to modify the solution accuracy without algorithm complication owing to the control of the discretization step numerical scheme order.

REFERENCES

- [1] Bazutkin V., Dmokhovskaya L., Transient and overvoltages calculations, *Energoatomizdat*, Moscow, 1983 (in Russian).
- [2] Semagina E.P., Beznosova O.I., Transmission line analysis via Taylor series, *International Journal of Circuit Theory and Application*, V.20, (1992),371-386.
- [3] Carson J.R., Transient Electrical Phenomena and Operation Calculus, *Gosnauchtechnizdat*, Kiev, 1937 (in Russian).
- [4] Beznosova O., Semagina E., Integral models in analysis of circuits with distributed and lumped parameters, *ISTET'03 Conference Proceedings*, Vol.1, Warsaw, (2003), 53-56.
- [5] G.E.Pukhov, Differential Transforms of Functions and Equations, *Nauk.Dumka*, Kiev, 1980 (in Russian).

Authors: PhD Olga Beznosova, PhD Evelina Semagina, G.E.Pukhov's Institute of Modelling Problems in Energetics, NAS of Ukraine, Naumova st. 15, 03164 Kiev, E-mail: em@ipme.kiev.ua.

Development in power quality specification using Time-Frequency Analysis

Abstract. In the era of technological development power quality issues have more and more crucial meaning. An example can be the scope of actual research concerning influence of dispersed energy sources on power quality, especially including wind power plants. This paper proposes time-frequency analysis as complex method for investigations of transient states in wind power plants. Investigated phenomena concern power distortion caused by faults in accordance with the influence of wind speed on instantaneous character of appearing power distortions.

Streszczenie. W dobie rozwoju technologicznego jakość energii nabiera coraz większego znaczenia. Przykładem może być zakres prac prowadzonych w zakresie oceny wpływu generacji rozproszonej na jakość energii, zwłaszcza w systemach zawierających elektrownie wiatrowe. Niniejszy artykuł proponuje wykorzystanie analizy czasowo-częstotliwościowej na potrzeby oceny zjawisk przejściowych w systemach elektrowni wiatrowych. W obszarze zainteresowania znalazły się zakłócenia mocy wywołane zwarciem w układzie przy różnych prędkościach wiatru. (Rozwój zagadnień oceny jakości energii elektrycznej z wykorzystaniem analizy czasowo-częstotliwościowej)

Keywords: power quality, system distortions, system harmonics, time-frequency analysis, wind power plants.

Słowa kluczowe: jakość energii, zakłócenia mocy, harmoniczne, analiza czasowo-częstotliwościowa, elektrownie wiatrowe.

Introduction

In the era of technological development power quality issues have more and more crucial meaning. In spite of achieved experience in specification of distortions, including IEC norms, some cases and accompanying phenomena require individual approach. In author's opinion there is still significant need to extend power quality specification, e.g. by applying advanced signal processing methods. An example can be the scope of actual research concerning influence of dispersed energy sources on power quality, especially including wind power plants.

Wind turbines become nowadays regular element of power systems with all its desirable as well as undesirable influences. Behind the undisputed significance of wind power plants for searching the renewable energy sources there are some aspects which have impact on power quality. One of them is natural result of variable weather conditions. Another comes from mechanical construction of power plant and power electronic equipment. Recognizing sources and symptoms of mentioned impacts it can be detailed: influence of stochastic wind variation on output torque, power, voltage and current fluctuation, periodical drop of output torque when the mill blade passes the tower (shadow effect), complex, nonlinear oscillation of the tower and wind turbine which can be transferred to turbine shaft (the frequency of generated oscillation can attain value from tenth to few Hz), and finally wide spectrum of harmonics in current and voltage caused by present of power converters [2,4,15].

Mentioned above mechanical oscillations as well as present of power converters manifest itself in influence on grid. The main symptom concerns deterioration of power quality. Recognized phenomena include voltage sags and flickers, main voltage drops caused by reactive power consumption, power oscillation in electrical transmission line, wide spectrum of harmonics [15].

The most significant meaning have the oscillations of generated power. This problem accompanies wind power plant both under normal and transient conditions. However, under transient conditions, such as faults, the range of oscillations is prominent. It must be emphasised that the range of power oscillations depends on construction of applied generator and load conditions. Wind power plant, working under load conditions below nominal value, are characterized by considerably higher level of power oscillations than in case of nominal-load operation. Furthermore, wind power plant fitted using asynchronous

slip-ring generator (with controlled resistance in rotor circuit or double-fed) and synchronous generator connected to grid by power converters, minimize power oscillations in comparison with asynchronous squirrel-cage induction machines [2,15].

Selection of proper method for analysis of power distortion in wind turbine system is still actual and crucial. In [14] we can find an idea which apply classical Fourier spectrum in order to investigate and classify power distortion. In this paper the authors propose to apply two-dimensional time-frequency analysis in order to obtain comprehensive analysis of power distortion. One of the contributions of this paper is developing a new qualitative method for analysis of transient phenomena in wind turbine systems. Particularly, the investigations are aimed at revealing the instantaneous character of power distortion under transient conditions. In order to explore the effects, grid connected wind turbine system was modelled using Matlab SimPowerSystemToolbox [13]. Selected wind generator structure is squirrel-cage induction machine, connected directly to the grid. Many of the wind power plants installed today have such configuration [12,14]. This type of the generator can not perform voltage control and it absorbs reactive power from the grid. Phase compensating capacitors are usually directly connected. That type of wind turbine is cheap and robust and therefore popular, but from the system analysis point of view it has some drawbacks [4,15].

Methods of analysis

The standard method for study time-varying signals is the short-time Fourier transform (STFT) that is based on the assumption that for a short-time basis signal can be considered as stationary. The spectrogram utilizes a short-time window $h(\tau)$, whose length is chosen so that over the length of the window signal is stationary. Then, the Fourier transform of this windowed signal is calculated to obtain the energy distribution along the frequency direction at the time corresponding to the centre of the window [11]:

$$(1) \quad \text{STFT}_x(t, \omega) = \int_{-\infty}^{+\infty} x(\tau) h(\tau - t) e^{-j\omega\tau} d\tau$$

where: t – time, ω – angular frequency, τ – time lag.

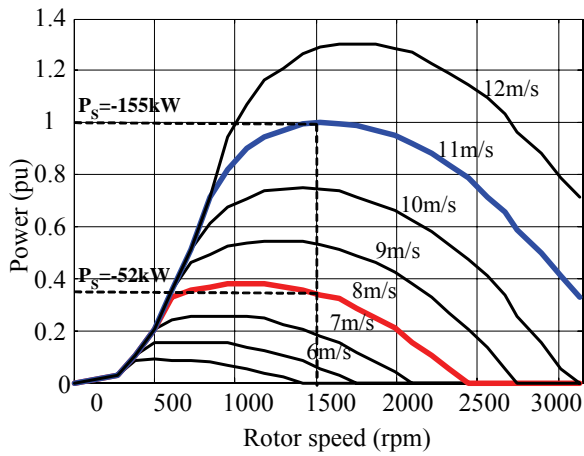


Fig. 1. Characteristic of simulated wind turbine

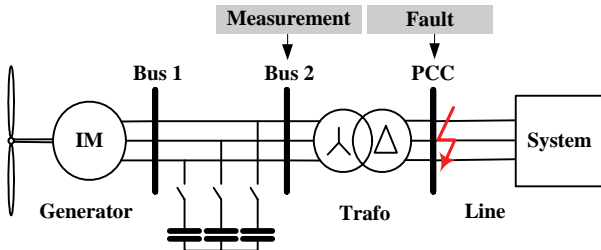


Fig. 2. Diagram of simulated grid-connected wind turbine system

The crucial drawback of this method is that the length of the window is related to the frequency resolution. Increasing the window length leads to improving frequency resolution but it means that the nonstationarities occurring during this interval will be smeared in time and frequency [8,11]. This inherent relationship between time and frequency resolution becomes more important when one is dealing with signals whose frequency content is changing rapidly. A time-frequency characterization that would overcome above drawback became a major goal for alternative development based on non-parametric, bilinear transformations.

The first suggestions for designing non-parametric, bilinear transformations were introduced by Wigner, Ville and Moyal at the beginning of nineteen-forties in the context of quantum mechanics area. Next two decades beard fruit of significant works by Page, Rihaczek, Levin, Mark, Choi and Williams [3], Born and Jordan, who provided unique ideas for time-frequency representations, especially reintroduced to signal analysis [6,7]. Finally in nineteen-eighties Leon Cohen employed concept of kernel function and operator theory to derive a general class of joint time-frequency representation. It can be shown that many bilinear representations can be written in one general form that is traditionally named Cohen's class. Cohen defined a general class of bilinear transformation (TFC) introducing kernel function $\psi_{\omega t}(\theta, \tau)$ [5,6,7]:

$$(2) \quad \text{TFC}_x(t, \omega) = \int_{-\infty}^{+\infty} \int_{-\infty}^{+\infty} \int_{-\infty}^{+\infty} x\left(u + \frac{\tau}{2}\right) x^*\left(u - \frac{\tau}{2}\right) \cdot \psi_{\omega t}(\theta, \tau) e^{j\theta t} e^{-j\omega \tau} e^{-j\theta u} du d\tau d\theta$$

where: t – time, ω – angular frequency, τ – time lag, θ – angular frequency lag, u – additional integral time variable.

Performing the transformations brings two dimensional planes which represent the changes of frequency component, here called auto-terms (a-t). Unfortunately, bilinear nature of discussed transformations manifests itself

in existing of undesirable components, called cross-terms (c-t). Cross-terms are located between the auto-terms and have an oscillating nature. It reduces auto-components resolution, obscures the true signal features and make interpretation of the distribution difficult. One crucial matter of kernel function is smoothing the cross-terms with preservation of useful properties of designed distribution. Applying Gaussian kernel in general Cohen's equation leads to Choi-Williams Distribution (CWD) which brings mentioned smoothing effect [3,7]:

$$(3) \quad \text{CWD}_x(t, \omega) = \int_{-\infty}^{+\infty} \int_{-\infty}^{+\infty} \sqrt{\frac{\sigma}{4\pi|\tau|}} e^{-\left[\frac{\sigma}{4}\left(\frac{t-u}{\tau}\right)^2\right]} \cdot x\left(u + \frac{\tau}{2}\right) x^*\left(u - \frac{\tau}{2}\right) e^{-j\omega \tau} du d\tau$$

Table 1. Power conditions of the wind turbine in steady state according to the wind speed

| Wind | Generated active power | Capacitor |
|--------|------------------------|-----------|
| 8 m/s | -52 kW | 67.2 kVar |
| 11 m/s | -155 kW | 80.4 kVar |

The main novel fields of application consist speech processing, seismic, economic and biomedical data analysis [1,10,11]. Recently some efforts was also made to introduce time-frequency analysis in electrical engineering area. The authors perceive a crucial need for better estimation of distorted electrical signal that can be achieved by applying the time-frequency analysis [1,9,10].

Model of the wind-turbine power system

A wind turbine generates power and accordingly a mechanical torque on the rotating shaft, while the electrical machine produce an opposing electromagnetic torque [4]. In steady state operation, the mechanical torque is converted to real electrical power and delivered to the grid. The power P and torque T generated by the wind turbine is [4,12,15]:

$$(4) \quad P = \frac{1}{2} \rho A C_p V^3 \quad \text{and} \quad T = \frac{P}{\omega_s}$$

where: ρ - density of air, A - swept area of the blade, C_p - performance coefficient, V - wind speed, T - mechanical torque, P - output power of the turbine, ω_s - rotor speed of the turbine.

At the constant wind speed, the C_p coefficient depends on the rotor speed ω_s and pitch angle. The pitch control dynamic can be neglected in power system transient analysis [12]. The turbine characteristic used in simulation is shown in Fig. 1. The simulation was done in Matlab using the SimPowerSystem Toolbox [13]. Fig. 2. presents the diagram of simulated wind generator system. Applied generator is a squirrel-cage induction machine rated at 150 kW, 400 V, 1487 rpm. It is connected to the grid through a Dyg 25/0.4 kV distribution transformer which nominal power equals 1 MVA. Point of common coupling is connected with the system via typical 5km overhead line, represented by positive, negative and zero-sequence of impedance. The system was simulated by equivalent source with short circuit capacity of 100 MVA and X/R ratio of 7. Capacitor banks realizes compensation of absorbed reactive power and are directly connected.

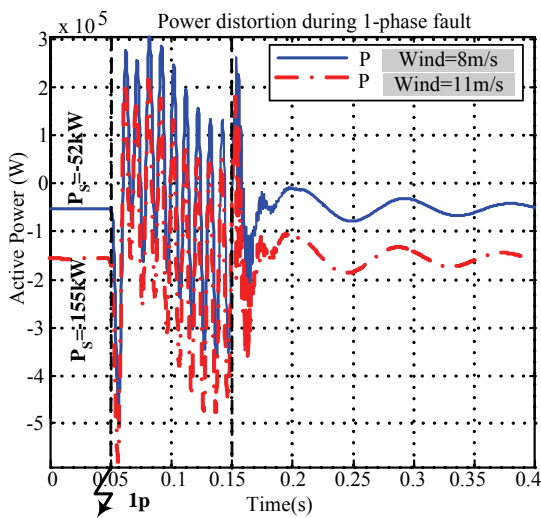


Fig. 3. Total 3-phase active power distortion during 1-phase fault in phase A for low (8m/s) and nominal (11m/s) wind speed

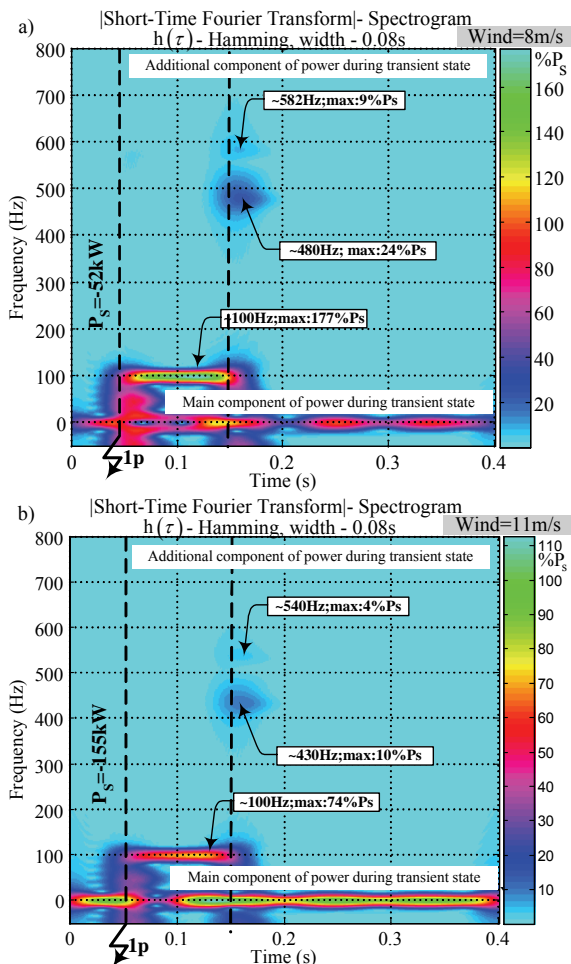


Fig. 4. Time-frequency plane of power distortion (P from Fig. 3) during 1-phase fault in phase A obtained using STFT: (a) low wind speed 8m/s, (b) nominal wind speed 11m/s

Power quality affected by faults

The aim of carried out investigations is to study the distortion of power generated by wind turbine under transient states caused faults. Fault conditions was modelled as 1-phase with ground in point of common coupling. Simulations of the fault were carried out twice, corresponding to two different wind speeds: low-speed 8m/s

and nominal speed 11m/s. Coming back to characteristic of the wind turbine, presented in Fig. 1, it corresponds to the non-nominal, $P_S = -52\text{kW}$, and nominal, $P_S = -155\text{kW}$, value of generated power. Additionally, in carried out investigations we have assumed that fault appears in steady state with full compensation. Table 1 provides details about power conditions of investigated wind turbine in steady state as well as values of capacitors, according to selected wind speed. The duration time of the fault was 100ms. Fig. 3. presents an example of total 3-phase power behaviour under fault condition for two selected wind speeds. In the next step obtained power distortion were investigated using time-frequency methods. In Fig. 4 we can observe the effects of analysis when Short-Time Fourier Transform were applied. Comparing Fig. 4a, corresponding to low-speed wind, with Fig. 4b, represented nominal condition of wind turbine work, we can reveal some influence of wind speed on character of transient states. Carried out time-frequency analysis allowed to detect visible drift of the frequency of transient components in direction of smaller frequency value, when the wind turbine works in nominal conditions. For wind speed equals 8m/s, Fig. 4a, we can observe main component as well as transient components: 100Hz, which exist during the fault, and 480Hz, 582Hz which accompany the operation of switching of the fault. The same fault, occurring for wind speed equals 11m/s, Fig. 4b, generates transient components which frequency concentration is shifted to 430Hz and 540Hz, respectively. Moreover, the percentage power contribution of the transient components also decrease. For better perception of discovered relations between character of appearing transient components and wind speed we have also group the parameters of detected component in Table 2.

Table 2. Additional component of power distortion and its contribution in 1-phase fault referring to wind speed

| Wind (Power) | Frequency component (instantaneous max. power corresponding to P_S) | | |
|----------------------------------|--|-----------------------|----------------------|
| 8 m/s ($P_S = -52\text{kW}$) | f1=100Hz (177% P_S) | f2=480Hz (24% P_S) | f3=581Hz (9% P_S) |
| 11 m/s ($P_S = -155\text{kW}$) | f1=100Hz (74% P_S) | f2=430Hz (10% P_S) | f3=540Hz (4% P_S) |

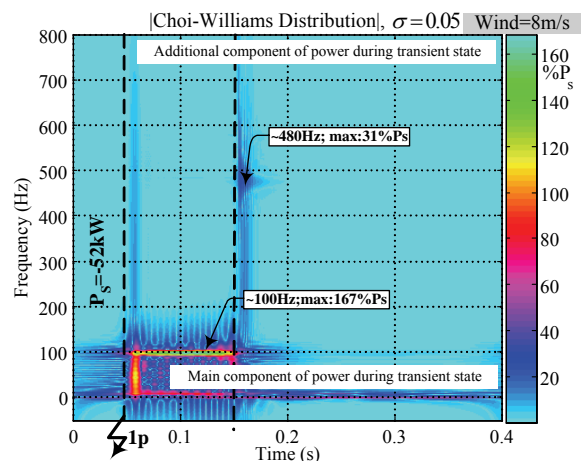


Fig. 5. Time-frequency plane of power distortion (P from Fig. 3) during 1-phase fault in phase A obtained using CWD for low wind speed

In Fig. 5 the effect of applying Choi-Williams Distribution can be observed. Sharp detection of transient components in comparison with classical spectrogram is visible. Additionally, problem with recognition of components which are modulated by peak values is exposed.

Conclusions

Visualization of power distortion using joint time-frequency planes allowed to find out some relations between transient components of power distortion and the wind speed. For low wind speed transient components are concentrated around higher frequency regions. Moreover, its percentage contribution in power distortion, comparing to generated power in steady state, is higher. Reaction of wind turbine working in nominal conditions to faults are characterized by transient components which are localized in lower frequency regions. The contribution of these components in power distortion decreases. Comparison of power during transient state only in time domain is not sufficient and do not provide complex information of appearing power quality affection. Joint time-frequency analysis develops novel tool for power quality area.

This paper introduce also some comparison between classical spectrogram and Choi-Williams Distribution with Gaussian kernel. Short-Time Fourier Transform, which is naturally weighted by sliding window, is characterized by smeared localization of instantaneous components. Choi-Williams Distribution represents high-resolution group of transformation, which through appropriate selection of kernel function can be adapted to investigated phenomena. Obtained results confirm sharp detection of transient states but also indicate problem of separation for components localized in near time-frequency regions or modulated by peak value.

This work was supported by the State Committee for Scientific Research, KBN (Poland,) under grant 3 T10A 040 30.

REFERENCES

- [1] Boashash B.: *Time-frequency signal analysis. Methods and applications*, Longman Cheshire, Melbourne or Willey Halsted Press, New York 1992.
- [2] Chen Z., Spooner E.: *Grid Power Quality with Variable Speed Wind Turbine*, IEEE Transaction on Energy Conversion, vol. 16, No. 2, pp. 148-154, 2001.
- [3] Choi H. I., Williams W. J.: *Improved time-frequency representation of multicomponent signals using exponential kernel*, IEEE Trans. on Acoustics Speech and Sig. Processing, 1989, vol. 37, no.6, pp. 862-971.
- [4] Chompoo-inwai Ch., Wei-Jen L., Fuangfoo P., Williams M., Liao J. R.: *System Impact Study for the Interconnection of Wind Generation and Utility System*. IEEE Trnas. on Industry Applications, vol. 41, January 2005, pp 163-168.
- [5] Cohen L.: *Time - Frequency distribution – a review*, Proceedings of the IEEE, 1989, vol. 77, no. 7, pp. 941-981.
- [6] Hahn S. L.: *A review of methods for time-frequency analysis with extension for signal plane-frequency plane analysis*, Kleinheubacher Berichte, 2001, Band 44, pp. 163-182.
- [7] Hlawatsch F.: *Linear and quadratic time-frequency signal representations*, IEEE Signal Processing Magazine, 1992, pp. 21-67.
- [8] Jones D. L., Parks T. W.: *A resolution comparison of several time-frequency representations*, IEEE Trans. on Acoustics Speech and Sig. Processing, 1992, vol. 40, no.2, pp. 413-420.
- [9] Lobos T., Sikorski T., Schegner P.: *Cohen's class of transformation for analysis of nonstationary phenomena in electrical power systems*, in Proc. 13-th Power System Computation Conf., Liege, 2005, CD supplies.
- [10] Papandreou-Suppappola A.: *Application in time-frequency signal processing*, CRC Press, Boca Raton, Florida 2003.
- [11] Quian S., Chen D.: *Joint time-frequency analysis. Methods and applications*, Prentice Hall, Upper Saddle River, New Jersey 1996.
- [12] Tabesh A., Iravani R.: *Transient Behavior of Fixed-Speed Grid-Connected Wind Farm*. Transactions of International Conference on Power Systems Transients, Montreal (Canada), June 2005, Paper No. IPST05-068.
- [13] The Matworks: *SimPowerSystems User's Guide*. The Math Works Inc., 2006.
- [14] Thiringer T.: *Power Quality Measurements Performed on a Low-Voltage Grid Equipped with Two Wind Turbines*. IEEE Trans. on Energy Conversion, vol. 11, September 1996, pp. 601-606.
- [15] Lubosny Z.: *Wind Turbine Operation in Electrical Power Systems*, Springer-Verlag Berlin Heidelberg 2003.

Authors: prof. dr hab. inż. Tadeusz Łobos, Politechnika Wroclawska, Instytut Podstaw Elektrotechniki i Elektrotechnologii, ul. Wybrzeże Wyspiańskiego 27, 50-370 Wrocław, E-mail: tadeusz.lobos@pwr.wroc.pl; dr inż. Jacek Rezmer, E-mail: jacek.rezmer@pwr.wroc.pl; dr inż. Piotr Ruczewski, E-mail: piotr.ruczewski@pwr.wroc.pl; dr inż. Tomasz Sikorski, E-mail: tomasz.sikorski@pwr.wroc.pl.

Dynamic system decomposition for diagnosis of mechatronic systems

Abstract. The paper proposes a unified methodology for fault diagnosis of mechatronic systems. System models including electronic, mechanical and coupling subparts are developed. A diagnosis algorithm originally introduced for electronic circuits, is extended to mechatronic systems. Differences of the application are also pointed out: large spread in time constants, different levels of measurement noise in different subparts.

Streszczenie: Artykuł przedstawia jednolitą metodologię dla diagnostyki systemów mechatronicznych. Model systemów łączy elektroniczną, mechaniczną połączoną część. Diagnostyczny algorytm opracowany dla części elektronicznej jest rozszerzony dla mechatronicznego podsystemu. Przedstawiono różnicę stałych czasowych, zróżnicowany poziom pomiarowego szumu w różnych podsystemach. (**Dekompozycja systemu dynamicznego dla diagnozy systemów mechatroniki**)

Keywords: mechatronic systems, diagnosis, noisy systems.

Słowa kluczowe: system mechatroniczny, diagnostyka, system zaszumiony.

Introduction

The paper investigates modeling and testing of multiphenomena systems. Mechatronic and microelectromechanics systems (MEMS) are examples of such objects of growing importance [1].

The steps of diagnosis of mechatronic systems are:

- development of system models and their computer simulation;
- measurement of "nominal" modules under test, development of the parameter extraction method based on measurements and computer simulations;
- fault diagnosis of the actual systems using computer simulation of the developed model and measurement of the actual system.

We consider soft faults in analog, possibly nonlinear systems. The diagnosis algorithm for noisy data, developed for electronic circuits [2], is extended to cover mechatronic system. The test example is a robot arm.

Description of mechatronic system

Let us consider a mechatronic system under test (MSUT). For simplicity sake, we assume that it contains only electronic, mechanical and coupling subsystems. Modified nodal equations are used for simulation of electronic subsystem [4]:

$$(1) \quad \mathbf{C}(\mathbf{P}_e) \dot{\mathbf{V}}(t, \mathbf{P}_e) + \mathbf{G}(\mathbf{P}_e) \mathbf{V}(t, \mathbf{P}_e) + \mathbf{N}(\mathbf{P}_e, \mathbf{V}) = \mathbf{I}(t),$$

\mathbf{V} - vector of nodal voltages and selected branch currents, \mathbf{G} , \mathbf{C} - matrices of resistive and reactive elements, \mathbf{I} - excitation vector; $\mathbf{N}(\mathbf{P}_e)$ - vector collecting all nonlinearities, and \mathbf{P}_e is the vector of diagnosable parameters of the electronic system.

State equations are used to describe the mechanical part:

$$(2) \quad \mathbf{J} \dot{\mathbf{z}}(t, \mathbf{P}_m) + \mathbf{A}(\mathbf{P}_m) \mathbf{z}(t, \mathbf{P}_m) + \mathbf{B}(\mathbf{P}_m, \mathbf{z}) = \mathbf{r}(t),$$

\mathbf{J} - inertia matrix; \mathbf{A} - matrix of damping coefficients; \mathbf{B} - vector of nonlinear functions including gravity force and friction; \mathbf{z} - vector of state variables, i.e. positions, velocities, accelerations; $\mathbf{r}(t)$ - vector of torques. \mathbf{P}_m is the vector of diagnosable parameters of the mechanical subsystems.

In the sequel we consider linear equations coupling electronic and mechanical subsystems:

$$(3) \quad [\mathbf{L}_1, \mathbf{L}_2] \begin{bmatrix} \dot{\mathbf{V}} \\ \dot{\mathbf{z}} \end{bmatrix} + [\mathbf{K}_1, \mathbf{K}_2] \begin{bmatrix} \mathbf{V} \\ \mathbf{z} \end{bmatrix} + \mathbf{F}(\mathbf{P}_{em}, \mathbf{V}, \mathbf{z}) = \mathbf{g}(t),$$

$\mathbf{L}_1, \mathbf{L}_2$, and $\mathbf{K}_1, \mathbf{K}_2$ are matrices relating electrical and mechanical variables, depending on coupling parameters \mathbf{P}_{em} ; \mathbf{F} - nonlinearity of the coupling part.

Vectors of unknowns and of diagnosable parameters of the whole system are: $\mathbf{V}_m = [\mathbf{V}^T, \mathbf{z}^T]^T$, $\mathbf{P} = [\mathbf{P}_e^T, \mathbf{P}_{em}^T, \mathbf{P}_m^T]^T$.

Combining (1), (2) and (3), we can write equations of the system:

$$(4) \quad \mathbf{C}_m \dot{\mathbf{V}}_m(t) + \mathbf{G}_m \mathbf{V}_m(t) + \mathbf{N}_m(\mathbf{P}, \mathbf{V}_m) = \mathbf{E}_m(t),$$

where

$$\mathbf{C}_m = \begin{bmatrix} \mathbf{C} & \mathbf{0} \\ \mathbf{L}_1 & \mathbf{L}_2 \\ \mathbf{0} & \mathbf{J} \end{bmatrix}, \quad \mathbf{G}_m = \begin{bmatrix} \mathbf{G} & \mathbf{0} \\ \mathbf{K}_1 & \mathbf{K}_2 \\ \mathbf{0} & \mathbf{A} \end{bmatrix}, \quad \mathbf{E}_m(t) = \begin{bmatrix} \mathbf{I}(t) \\ \mathbf{g}(t) \\ \mathbf{r}(t) \end{bmatrix}.$$

and $\mathbf{N}_m = [\mathbf{N}^T \mathbf{F}^T \mathbf{B}^T]^T$ is a nonlinear function of nodal voltages, state variables and diagnosable parameters.

Equation (4), when used for diagnostics of mechatronic systems, brings some challenges:

- time constants of electronic, mechanic and coupling parts, differ by orders;
- there is a spread of measurement precision in different subsystems, resulting in different levels of noise;
- ambiguity groups may appear in each subpart;
- feedback loops make the problem of diagnostic hard.

Method of diagnosis

System can be accessed at certain points. In electronic circuits by "points" we mean nodes. We divide nodes of the electronic subsystem into three groups: accessible (at which we apply excitations and measure responses), partially accessible (we only measure responses) and not accessible. Similarly we divide points of the mechanical part into accessible "nodes" (where excitation, e.g. force, energy, is applied and response measured), partly accessible "nodes", (output values, e.g. position, velocity, acceleration, can be measured), and inaccessible "nodes". The numbers of tests performed and measurements obtained for each of them is much larger than the number of parameters to be identified.

We use the sensitivity method of diagnosis developed for electronic circuits [2]. Differential sensitivity is susceptible to errors of a system model and noise of input data, and reduces accuracy and stability of the testing procedure. Integral sensitivity tends to reduce zero mean noise, and this effect is

amplified when time intervals are properly selected. As seminormalized integral sensitivity of V_{mj} w.r.t P_i on the time interval $[t_a, t_b]$ we understand:

$$(5) \quad W_{ji}[t_a, t_b] = \int_{t_a}^{t_b} S_{ji}(t) P_i dt, \quad S_{ij} = \frac{\partial V_{mj}(t)}{\partial P_i}.$$

Choice of the interval $[t_a, t_b]$ influences effectiveness of this technique in reducing noise [2,3]. We will also use integrated values $U_j[t_a, t_b]$ of the unknowns $V_{mj}(t)$ appearing in (4):

$$(6) \quad U_j[t_a, t_b] = \int_{t_a}^{t_b} V_j(t) dt.$$

Expanding of diagnosis method (2) to mechatronic systems has a trouble presented above a) -d). In this article we concentrate on solving of a) and b) problems.

A. Dynamic system decomposition: Most mechatronic systems exhibit temporal sparseness or latency, i.e., most of the subsystem are inactive most of the time. Traditionally mechatronic system characterized by different time constants for different subparts, and has the numerical stability problems associated with "stiff" systems. Traditionally simulation the integration algorithms constrain all the variables of the system to use the same step size, necessarily the smallest one required to maintain truncation errors within limits. This approach is time and computing consumption.

We propose dynamic system decomposition of mechatronic system. By dynamic system decomposition we mean the independent time-domain analysis of the subsystem of a given system. Matrices C_m, G_m have a border-block diagonal (BBD) structure or block diagonal (BD) structure (case of open loop system). For simplicity in the future we use BD structure. Each block represents of sub-system and characterized time constants $\tau_e, \tau_{em}, \tau_m$ respectively. Fig.1.a shows of structure of matrices.

Note that each component of the dynamic decomposition is processed for the entire time evolution individually and in a fixed sequence. The components which drive the component being processed, as well as the component which load this component, are handled by storing the temporal waveforms computed for those components on their most resent iteration. Then, when it is required to know how these components drive or load the component being processed, the necessary information can be obtained by interpolation on the stored waveforms of the adjacent components. This permits the possibility of choosing different time steps for each subsystem, allowing the sluggish subsystem to take large steps independently of the rapidly changing subsystems. Therefore, each subsystems has to be scheduled for analysis at different time points and synchronization problems arise. For synchronization of mechatronic system we connect time discretization T_1, T_2 of electronic and mechanical subpart, respectively, with time discretization of testing equipment T_0 :

$$T_1 = k_1 T_0, T_2 = k_2 T_0, \text{ where } k_1, k_2 = f(\tau_e, \tau_{em}, \tau_m);$$

B. Formulation and solving of diagnosis equations

Let us consider structure of differential sensitivity of mechatronic system at instant point t_k :

$$(7) \quad S(t_k) = \begin{bmatrix} \frac{\partial V(t_k)}{\partial P_e} & \frac{\partial V(t_k)}{\partial P_{em}} & \frac{\partial V(t_k)}{\partial P_m} \\ \frac{\partial Z(t_k)}{\partial P_e} & \frac{\partial Z(t_k)}{\partial P_{em}} & \frac{\partial Z(t_k)}{\partial P_m} \end{bmatrix}.$$

As we suppose that system is diagnosed with open feedback loop than $\partial V(t_k)/\partial P_m = \varepsilon(0), \partial Z(t_k)/\partial P_e = \varepsilon(0)$ is on level of calculation errors. We also can write:

$$S_e = \begin{bmatrix} \frac{\partial V(t_k)}{\partial P_e} & \frac{\partial V(t_k)}{\partial P_{em}} \end{bmatrix}, S_m = \begin{bmatrix} \frac{\partial Z(t_k)}{\partial P_{em}} & \frac{\partial Z(t_k)}{\partial P_m} \end{bmatrix}.$$

More generally the structure of diagnosis equations at time point t_k and for one test can be written like in Fig.1.b.

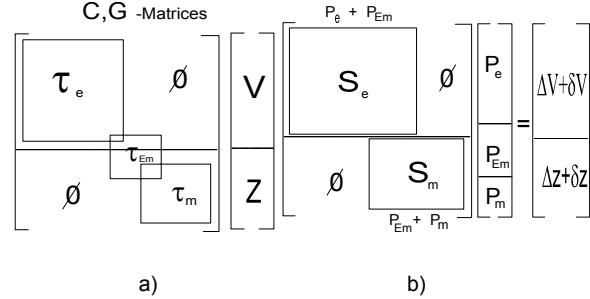


Fig.1. Structure of C_m, G_m matrices (a). The structure of diagnosis equations (one time point and one test) (b)

Diagnosis equations are obtained using integral sensitivity (5), and replacing infinitesimally small changes by finite increments:

$$(8) \quad \mathbf{W}[t_{k-N}, t_k] \delta \mathbf{P} = \Delta \mathbf{U}[t_{k-N}, t_k],$$

entries $\delta P_i = \Delta P_i / P_i$ of $\delta \mathbf{P}$ are the relative deviations of parameters from the current vector \mathbf{P} ; $\Delta \mathbf{U}$ is the difference of U_j calculated for the values of variables $V_{mj}(t)$ obtained for the tested and simulated nominal systems.

Diagnosis equations are usually overdetermined. We use this property to provide stability and a good convergence rate of the solving procedure. The regularization technique [4] was designed for solving equations with noisy data. Tikhonov's functional is defined as:

$$(9) \quad \mathbf{M}[\delta \mathbf{P}(\alpha)] = \|\mathbf{W} \delta \mathbf{P}(\alpha) - \Delta \mathbf{U}\|^2 + \alpha \|\delta \mathbf{P}(\alpha)\|^2$$

$\alpha \geq 0$ is the regularization coefficient. The first term is the standard least square (LS) term, the second is added to improve stability and convergence of the iterative procedure. When $\alpha \rightarrow 0$ then $\delta \mathbf{P}$ solves the LS problem. The solution of diagnosis equations is obtained by minimizing the functional:

$$(10) \quad \min \mathbf{M}[\delta \mathbf{P}(\alpha)] \text{ w.r.t. } \delta \mathbf{P}$$

To improve accuracy, (10) is solved iteratively. At the beginning we simulate a fault free system and calculate the required data for the nominal set of parameters $\mathbf{P}^{(1)} = \mathbf{P}^n$. A new approximation is calculated as: $\mathbf{P}^{(q+1)} = \mathbf{P}^{(q)}(I + \delta \mathbf{P}^{(q)})$, and all simulation vectors and matrices are updated. The iterative algorithm stops when: $\delta P_i^{(q)} \leq \text{TOL}_i \wedge \|\Delta \mathbf{U}\| \leq \varepsilon$,

TOL_i - the acceptable tolerance of \mathbf{P} , ε - is the level of noise characteristics of the measurement system. The decision whether the diagnosed parameter P_i is faulty is made by checking the value of $(P_i^n - P_i^{(q)}) / P_i^n$ against TOL_i . Numerical effectiveness of solving (10) depends on

the values of α . The optimal value of α for the q th iteration is found by solving the equation of generalized discrepancy [4].

The discussed algorithm covers linear systems, but it can be extended to nonlinear systems as well, using an approach similar to [2].

The values $\delta V \approx 10^{-5}$, $\delta Z \approx 10^{-3}$ characterized of precision of measurement of electronic and electromechanical parts. Differences between precision of electronic and mechanical parts demands applying of special approach for calculation of regularization coefficient. This problem is shown in the Fig.3. After performing n diagnosis tests on selected time intervals [2] the matrix \mathbf{W} and vector $\Delta \mathbf{U}$ has structure as shown in Fig.3a. Matrix \mathbf{W} has a same structure as matrix \mathbf{S} , that means what submatrices have $P_e + P_{em}$ and $P_{em} + P_m$ columns respectively.

Vector $\Delta \mathbf{U}$ include values with different level of noise $\Delta U_v = \Delta U + \delta V$ and $\Delta U_z = \Delta U + \delta Z$. When regularization procedure (10) is applied to solving diagnosis equation with structure shown in Fig.3a than regularization coefficient must be a calculated as function of $\alpha_0 = f_0(\delta V, \delta Z)$. Taking to account that values $\delta V \approx 10^{-5}$, $\delta Z \approx 10^{-3}$ has a different range, the regularization procedure has a grate trouble with convergence.

We applied sorting algorithm for reforming of matrix \mathbf{W} and vector $\Delta \mathbf{U}$. As result we achieved structure as shown in Fig.3b. We can calculate two regularization coefficient $\alpha_1 = f_1(\delta V)$, $\alpha_2 = f_2(\delta Z)$ and forming two functionals (9) $\mathbf{M}_1[\delta \mathbf{P}(\alpha_1)]$, $\mathbf{M}_2[\delta \mathbf{P}(\alpha_2)]$ for $\mathbf{W}_e, \Delta \mathbf{U}_e$ and $\mathbf{W}_m, \Delta \mathbf{U}_m$ subparts of diagnosis equations (8).

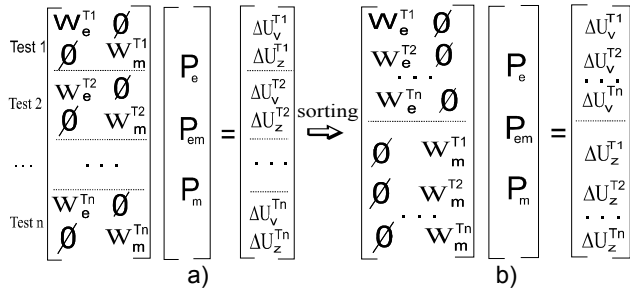


Fig 2. The structure of diagnosis equations before (a) and after (b) sorting

The solution of diagnosis equation (8) for mechatronic system is obtained by minimizing the fuctionals

$$(11) \quad \min \mathbf{M}_1[\delta \mathbf{P}(\alpha_1)], \mathbf{M}_2[\delta \mathbf{P}(\alpha_2)] \\ w.r.t. \delta \mathbf{P}$$

Test example

Consider a model of one axis of the robot. Functionally, it can be divided into three parts: electronic control, coupling DC motor, and mechanical manipulator (Fig. 4).

Part I: Controller of a reverse DC motor is a power cascade of MOSFET bridge (Fig.5). Model of a single MOSFET transistor is: $J(V_{zi}) = \beta_s (V_{zi} - V_T)^2$ where $P_e + P_{em}$ - coefficient of the nonlinear current source, V_z - voltages across resistance R_z , V_T - the threshold voltage.

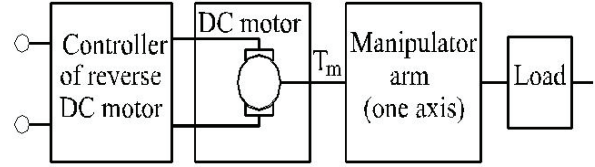


Fig. 3. Block-diagram of robot arm(one axis)

Modified nodal equations for the electronic part have the form of (1).

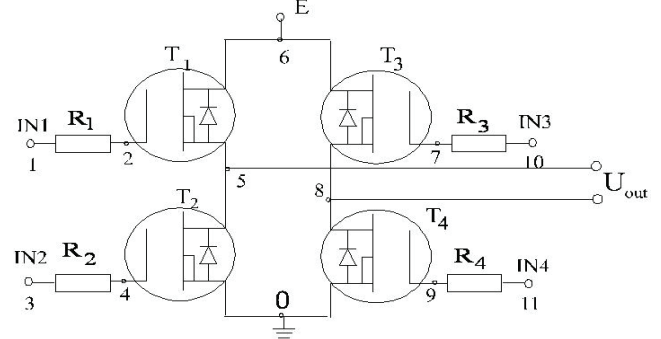


Fig.4. Power cascade of controller

Electrically, inputs IN_1 and IN_4 are coupled so are IN_2 and IN_3 . Different combinations of input signals arrange for forward, reverse and stop operating regime of DC motor. Excitation vector is: $\mathbf{I} = [I_{IN_1} g_{01} \ 0 \ I_{IN_2} g_{02} \ 0 \ 0 \ E_g \ 0 \ 0 \ 0 \ I_{IN_3} g_{03} \ I_{IN_4} g_{04}]^T$.

Diagnosis vector of the controller is set to: $\mathbf{P}_e = [C_{z1} \ C_{z2} \ C_{z3} \ C_{z4} \ G_{si1} \ G_{si2} \ G_{si3} \ G_{si4}]$, where C_z -snubber capacitance, G_{si} - MOSFET conductance. We take nonlinear parameters β_s into consideration in simulation of the power cascade, but diagnosis of these parameters is a task for the future research.

Part II: DC motor has a nominal excitation voltage 50V and nominal current 5A. The parameters of the motor are: rotation velocity $T = 75 \text{ rad/s}$; moment of inertia $J_e = 5.0 \times 10^{-4} \text{ kgm}^2$; resistance and induction of rotor $R = 0.465 \ \Omega$ and $L = 15.4 \text{ mH}$, respectively. The friction force is $D_m \omega$ and rotor movement is restrained by the spring with constant K_s , developing torque $F_s = K_s \phi$. Electrical torque is $F_e = K_e i$ and voltage induced in the coil is $K_m \omega$. Two controlled sources couple the electrical and mechanical parts.

The coupling matrices have the form:

$$[\mathbf{L}_1 \ \mathbf{L}_2] = \begin{bmatrix} L & 0 & 0 \\ 0 & J_m & 0 \\ 0 & 0 & 1 \end{bmatrix}, [\mathbf{K}_1 \ \mathbf{K}_2] = \begin{bmatrix} r_0 + R & K_m & 0 \\ -K_e & D_m & K_s \\ 0 & 0 & 0 \end{bmatrix}, [\mathbf{V} \ \mathbf{z}]^T = [i \ \omega \ \phi]^T \\ \mathbf{g}(t) = [V_{out} \ T_m \ 0]^T.$$

The diagnosis parameters of the DC motor are $\mathbf{P}_{em} = [R \ L \ D_m \ K_s \ J_m]$. Coefficients K_e , K_m , connecting electrical and mechanical parts are assumed to be constant.

Part III: State variables for the mechanical part (one axis manipulator) are \mathcal{G}, ψ angular velocity and angle of rotation, respectively. Describing equations have the form of (2) with:

$$\mathbf{J} = \begin{bmatrix} J_a & 0 \\ 0 & 1 \end{bmatrix}, \mathbf{A} = \begin{bmatrix} D_a & K_a \\ 0 & 0 \end{bmatrix}, \mathbf{z} = \begin{bmatrix} \mathcal{G} \\ \psi \end{bmatrix}, \mathbf{r}(t) = \begin{bmatrix} k_p T_m \\ 0 \end{bmatrix},$$

where J_a, D_a, K_a - are the inertia moment, friction damping and spring constant of the manipulator arm; k_p - transmission coefficient (constant). Diagnosable parameters of the manipulator arm are: $\mathbf{P}_m = [J_a \ D_a \ K_a]$.

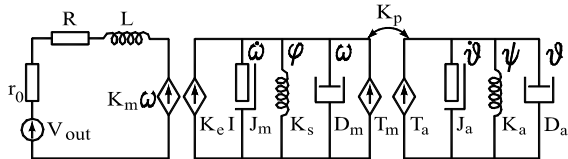


Fig.5. Equivalent circuit model of DC motor and manipulator arm

Sensitivity matrix \mathbf{S} and vector $\Delta\mathbf{U}$ have a next structure: $\mathbf{S} = \text{size}[16 \times 16]$, where number of columns is size of vector $\mathbf{P} = \mathbf{P}_e + \mathbf{P}_{em} + \mathbf{P}_m$ and number of rows is size of $\Delta\mathbf{U}$. Submatrices have a next sizes: $\mathbf{S}_e = \text{size}[13 \times 12]$, $\mathbf{S}_m = \text{size}[8 \times 4]$, $\partial\mathcal{M}(t_k)/\partial\mathbf{P}_m = \text{size}[3 \times 12]$, $\partial\mathcal{Z}(t_k)/\partial\mathbf{P}_e = \text{size}[8 \times 4]$. Vector $\Delta\mathbf{U}$ consists with: $\Delta\mathbf{U}_e = [\Delta V_1, \dots, \Delta V_{11}, \Delta i]$, $\Delta\mathbf{U}_m = [\Delta\omega, \Delta\varphi, \Delta\theta, \Delta\psi]$. As shown simulating the values of $\partial V(t_k)/\partial P_m$ $\partial Z(t_k)/\partial P_e$ matrices was in order $10^{-6} \div 10^{-8}$.

We modeled measure noise as error of quantization and random noise of least significant bit (LSB) of 16 bits ADC for electronic and 10 bits ADC for electromechanical subparts. As the simulating result the values of variances of measuring noise for electronic and electromechanical parts was $\delta V = 4.6 \cdot 10^{-5}$ and $\delta Z = 7 \cdot 10^{-3}$, respectively.

Solving minimization task (11) iteratively we must calculate

$$\delta P'(\alpha_1) = ((W_e)^* W_e + \alpha_1 I)^{-1} (W_e)^* \Delta U_v$$

$$\delta P''(\alpha_2) = ((W_m)^* W_m + \alpha_2 I)^{-1} (W_m)^* \Delta U_z$$

where $(W_e)^*$, $(W_m)^*$ conjugate matrices, and vectors $\delta P'(\alpha_1) = [\delta P_e, \delta P_{em}, 0]$, $\delta P''(\alpha_2) = [0, \delta P''_m, \delta P''_m]$.

For next iteration simulating is constructed vector: $\mathbf{P}^{(q+1)} = \mathbf{P}^{(q)}(I + \delta\mathbf{P}^{(q)})$, where $\delta\mathbf{P}^{(q)} = [\delta P_e, \delta P_{em}, \delta P_m]$ is constructed from two vectors $\delta P', \delta P''$. We apply empirical method of selecting the values δP_{em} . We take changes of electronic parameters $\delta L, \delta R$ from $\delta P'_e$ and changes of mechanical parameters $\delta D_m, \delta K_s, \delta J_m$ from $\delta P''_m$, because electronic parameters and mechanical parameter of DC motors more sensitive to vector ΔU_v to ΔU_z , respectively.

Nominal values of diagnosable parameters are collected in vector \mathbf{P}^n (Table 1). Values of K_e, K_m are fixed at 1.23 and k_p is 5. The results of identification are in Table 1: $\mathbf{P}^f, \mathbf{P}^d$ are faulted and diagnosed vectors of parameters, respectively. As it is shown in the third column the values of faulted parameters \mathbf{P}^f deviate 5% to 30% from their nominal values \mathbf{P}^n . The diagnosis procedure which started from

nominal parameters has been completed after 43 iterations. The quality of identification (column five) was better then 5%

Table 1. Values of parameters of the nominal, faulty and diagnosed elements.

| | \mathbf{P}^n | \mathbf{P}^f | $\frac{\mathbf{P}^f - \mathbf{P}^n}{\mathbf{P}^n}$ | \mathbf{P}^d | $\frac{\mathbf{P}^d - \mathbf{P}^n}{\mathbf{P}^n}$ |
|-----------|----------------|----------------|--|----------------|--|
| C_{z1} | 3.18e-7 | 3.81e-7 | 24% | 3.96e-7 | -3.8% |
| C_{z2} | 4.22e-7 | 3.46e-7 | -18% | 3.39e-7 | 2.1% |
| C_{z3} | 4.50e-7 | 4.50e-7 | 0% | 4.50e-7 | 0% |
| C_{z4} | 3.67e-7 | 4.11e-7 | 12% | 3.94e-7 | -4% |
| G_{si1} | 2.33e+4 | 2.56e+4 | 10% | 2.65e+4 | -3.4% |
| G_{si2} | 3,21e+4 | 3,21e+4 | 0% | 3,21e+4 | 0% |
| G_{si3} | 2.41e+4 | 2.26e+4 | 6% | 2.16e+4 | 4.5% |
| G_{si4} | 3.03e+4 | 3.03e+4 | 0% | 3.03e+4 | 0% |
| R | 4.65e-1 | 5.34e-1 | 15% | 5.54e-1 | -3.6% |
| L | 1.54e-2 | 1.54e-2 | 0% | 1.54e-2 | 0% |
| J_m | 5.00e-4 | 3.60e-4 | -28% | 3.75e-4 | -4.2% |
| D_m | 4.93e-5 | 5.27e-5 | 7% | 5.11e-5 | 3.1% |
| K_s | 3.34e+0 | 3.34e+0 | 0% | 3.34e+0 | 0% |
| J_a | 2.60e-5 | 2.86e-5 | 10% | 2.99e-5 | 4.5% |
| D_a | 5.50e-4 | 5.50e-4 | 0% | 5.50e-4 | 0% |
| K_a | 6.21e+0 | 5.46e+0 | -12% | 5.59e+0 | -2.4% |

Conclusions

In the paper, the method for fault diagnosis in dynamic mechatronic (nonlinear) systems has been presented. From the mathematical point of view the method handles, in a uniform manner, equations obtained using various methods of formulation, e.g. nodal modified, state. Differences in diagnosis of purely electronic circuits and mechatronic systems have been pointed out. The problem of different noise levels has been resolved by applying integral sensitivity and regularization technique with different regularization coefficients. Soft faults have been detected in the robot manipulator model, using the proposed method with a satisfactory accuracy.

REFERENCES

- [1] R.Rosing, A.Richardson, A.Dorey&A.Peyton, "Test Support Strategies for MEMS", *IEEE Int. Mixed Signal Test Workshop*, Whistler, Canada, June 1999.
- [2] V.Brygilewicz, J.Wojciechowski, "Time-domain fault diagnosis of analogue circuits in the presence of noise," *IEE Proc. Circuit Devices and Systems*, Vol. 145, 1998, pp.125-131.
- [3] B.Blagitko, W.Brygilewicz, I.Jarmolowskyj. Wieloparametryczna diagnostyka systemu mechatronicznego w obecności szumu // *Przegląd elektrotechniczny*, 2005, № 2, pp. 90-94
- [4] A.Tikhonov, V.Arsenin, "Methods for solving incorrect tasks," Nauka, Moscow 1979

Authors: Bogdan Blagitko Lviv National University named I.Franko, Electronics Faculty, Tarnavskogo str, 107, Lviv 79005, UKRAINE, E-mail: blagitko@electronics.wups.lviv.ua; Volodymyr Bryhilevych, Lviv National University named I.Franko, Electronics Faculty, Tarnavskogo str, 107, Lviv 79005, UKRAINE, E-mail: brygil@electronics.wups.lviv.ua; Igor Yarmolovskiy, Lviv National University named I.Franko, Electronics Faculty, Tarnavskogo str, 107, Lviv 79005, UKRAINE, E-mail: yarmolovskiy@electronics.wups.lviv.ua;

Analysis of reliability of power supply system on the basis of macro-modeling

Abstract. Parametrical macromodel of voltage stabilizer was synthesized. The model allows determining the area of workability in the space of model parameters.

Abstract. Przedstawiono syntezę parametrycznego makromodelu stabilizatora napięcia. Proponowany model umożliwia określenie obszaru pracy przy uwzględnieniu założonych parametrów. (Analiza niezawodności systemów zasilania bazująca na modelowaniu w skali makro).

Keywords: analysis of reliability; power supply system; macro-modeling.

Słowa kluczowe: analiza niezawodności, systemy zasilania, makro-model.

Introduction

Engineering tools advancing, their functions are growing more complicated and requirements for adequate implementation are rising. Therefore, the issue of ensuring high reliability performance of the modern radio-electronic devices (RED) is one of the most challenging.

The issue is a system of scientific, engineering and organizational systematic means aimed at providing the set reliability of RED at the stages of design, manufacture and operation. The peculiarity of the issue is that every next stage causes a drop/decay in reliability performance. At the manufacture stage, technological defects appear, while at the operation stage, marginal values of destabilizing factors (temperature, humidity, radiation, etc.) can be exceeded. Therefore, it is extremely important to ensure high reliability level at the design stage, which is achieved by development of reliability design of RED as a complex of interlinked design problems targeting assessment and efficient management of reliability performance of the design object (DO) in order to ensure the set reliability level, thereby preserving the set functional parameters and characteristics.

The principal text

Reliability design embraces a multi-stage design process, including functional and constructive technological design, since on the one hand, reliability performance depends on structural, schematic and constructive technological solutions in the design process; on the other, reliability influences structural, schematic and constructive technological solutions. Therefore, problems of reliability design should be solved concurrently with the problems of functional and constructive technological design [1].

At the stage of developing performance specification (PS), DO can be presented by a mathematical model reflecting the law of DO functioning:

$$(1) \quad Y = \Phi(Q),$$

where Y – vector of DO initial parameters; Q – vector of external influences (input signals, interference and ambient conditions: temperature); Φ – operator which describes DO functioning under the external influences.

DO functions adequately if the initial parameters are within the set limits:

$$(2) \quad Y_{i \min} \leq Y_i \leq Y_{i \max}, \quad i = \overline{1, n}.$$

The inequalities (2) determine the area of admissible values D_Y , n -dimensional vector of initial parameters Y :

$$(3) \quad Y \in D_Y$$

Most frequently, quantitative characteristic of DO is reliability index, which is reliability probability $P(T)$ on the time interval $[0, T]$ [1]. $P(T)$ value is limited by the design performance specification:

$$(4) \quad P(T) = P\{Y(t) \in D_Y; \forall t \in [0, T]\} \geq P^*$$

where P^* – lower admissible limit of $P(T)$. $Y(t)$ is a random function which depends on the changes of parameters of RED elements in the course of operation.

The form of this function at the stage of developing PS is unknown and is refined during the design process.

It should be noted that the factor (4) characterizes also productability of DO since at $T=0$ it defines workability probability at the components' parameters spread.

In the process of structural synthesis of RED in the chosen elemental basis, dimension and composition of vector X of elements' parameters and vector of phase variables V characterizing physical and informational state of DO become defined.

$$i. \quad V = F_1(X, Q).$$

Vector of initial variables Y depends on vector of phase variables V :

$$b. \quad Y = F_2(V) = F_2(F_1(X, Q)).$$

Operators F_1 and F_2 can be set analytically, in the form of algorithms for solving differential equations, simulation programs, etc.

Expressions (5) and (6) are mathematical models of DO and are used for assessing reliability performance.

Reliability schematic design consists in choosing vector of parameters of elements X , which would best meet the condition (4), i.e., it is a problem of parametrical optimization. To solve this problem, workability area D_Y from the space of initial parameters should be mapped into the area D_X in the space of elements' parameters. Then, condition (4) assumes the following form:

$$c. \quad P(T) = P\{X(t) \in D_X; \forall t \in [0, T]\} \geq P^*.$$

In a more general case, search for area D_X is a complicated task and demands considerable developer's calculation volume and creative efforts. Efficiency of the solution depends on the right choice of the DO mathematical model and methods of its analysis [1].

Designing the area of parameters D_x based on the workability area D_Y can be substantially simplified by using macromodels of RED being designed with dependencies of elements' parameters and initial parameters. This approach will be illustrated below using compensation voltage stabilizer.

Fig.1 shows electrical circuits of the stabilizer and its macromodel in the system MicroCap-7.0, built without parametrical dependency by the method of non-linear statics and low-signal dynamics [2].

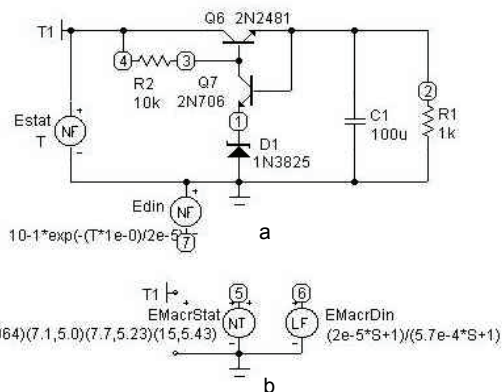


Fig. 1. Electrical circuits of the stabilizer a) and its mathematical macromodel b) without parametrical dependency

The macromodel consists of two sequential subsystems: non-linear non-inertial one and linear dynamic one. According to the method of non-linear statics and low-signal dynamics, first, the static characteristic of the stabilizer was identified. Piecewise-linear approximation (EMacStat used as a power source) quite satisfactorily recreates the static characteristic, which is shown in Fig.2. Thereat, static coefficient of transfer of the model's linear subsystem is considered to be equal one [2].

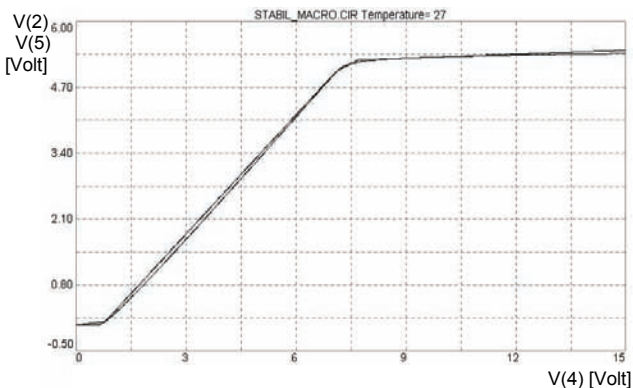


Fig. 2. Static characteristics of the stabilizer and its mathematical macromodel without parametrical dependency

The dynamic characteristic (Fig.3) is identified based on the transient of the stabilizer (voltage at node 2). The transient process excites a rapid surge of the input voltage from 9 to 10V (Edin used as a power source instead of Estat in Fig. 1). The linear dynamic subsystem is identified by the transient from the input source Edin. Applying least square method, the problem of identifying first-order dynamic system with transfer function $W(\lambda) = (1 + b\lambda) / (1 + a\lambda)$ is solved:

$$(8) \quad \min_{a,b} \sum_{k=1}^{200} (y(t_k) - (u(t_k) + bu'(t_k)) + ay'(t_k))^2$$

where $y(t_k)$, $u(t_k)$ – output (voltage at node 2) and input (voltage at node 5) signals of the linear subsystem at moment t_k , and $y'(t_k)$ and $u'(t_k)$ are their differentials.

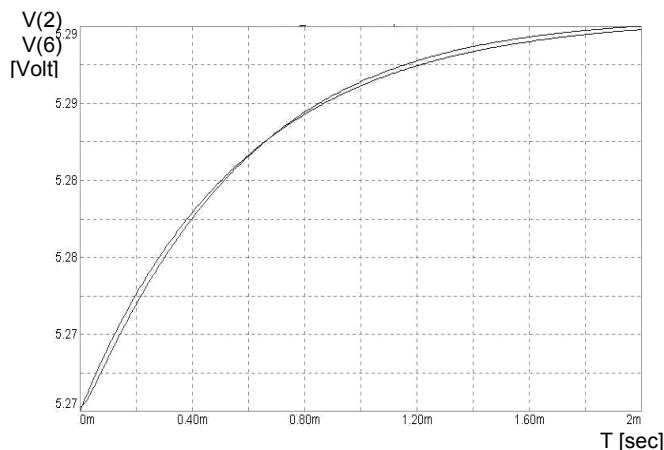


Fig 3. Dynamic characteristics of the stabilizer and its mathematical macromodel without parametrical dependency

In the circuit of the macromodel in Fig.1, the linear subsystem is presented by power source EMacDin with complex transfer function.

Differential equation of the model will be the following:

$$(9) \quad a \cdot dy/dt + y = b \cdot df(v)/dt + f(v)$$

where: y – output signal (voltage at node 6 in Fig. 1,b); v – input signal (voltage at node T1); $a = 5.7 \cdot 10^{-4}$; $b = 2 \cdot 10^{-5}$; $f(v)$ – approximation of the static characteristic (power source EMacStat in Fig. 1,b).

Let us introduce parametric dependence into the stabilizer macromodel.

Load resistance $R1 = R_n$ was chosen as a parameter of influence on initial characteristics. It was noticed that the effect of this resistance on the initial characteristics can be modelled by non-linear variation of input voltage without changing the determined characteristics of the static and dynamic subsystems of the model. It is proposed to introduce the dependency of initial voltage vs. load resistance R_n : $c_1 + c_2 \cdot \exp(c_3 \cdot R_n + c_4) + c_5 \cdot R_n$.

Coefficients of the non-linear approximation calculated with the help of the appropriate MATLAB program for non-linear optimization are shown in the functional dependency of amplification of controlled power E1 in Fig.4.

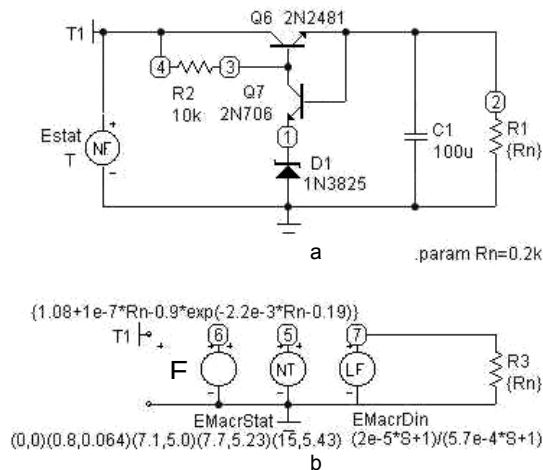


Fig.4. Electric circuits of the stabilizer a) and its parametrical macromodel b) with dependency on load resistance R_n

Equations of the parametric macromodel are as follows:

$$(10) \quad a \cdot dy/dt + y = b \cdot df(v \cdot w)/dt + f(v \cdot w);$$

$$w = 1.08 + 1 \cdot 10^{-7} \cdot R_n - 0.9 \cdot \exp(-0.0022 \cdot R_n - 0.19);$$

where: y – output signal (voltage at node 7 in Fig. 4,b); v – input signal (voltage at node T1); $a=5.7 \cdot 10^{-4}$; $b=2 \cdot 10^{-5}$; w – input signal factor determined by parameter R_n (i.e., coefficient of transfer of controlled power source E1 in Fig.4,b); $f(v \cdot w)$ – piecewise linear approximation of the static characteristics (power source EMacrStat in Fig.4,b).

In Fig.5, static characteristics of the stabilizer and its parametrical macromodel are shown for two values of resistance R_n . These characteristics agree fairly well.

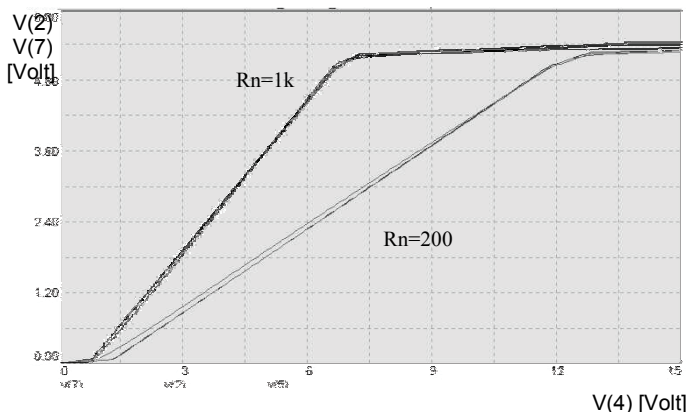
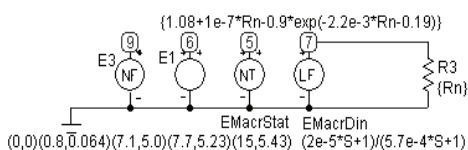


Fig.5. Static characteristics of the stabilizer and its macromodel defined by resistance R_n

The synthesized parametric macromodel satisfactorily recreates the influence of load resistance on static characteristics. Relative error of reproduction does not exceed 5%, voltage range being from 6 to 15V. However, the macromodel is far simpler than the original, due to which the problem of recalculation of the workability area D_Y into admissible area of parameters D_X can be solved much more efficiently.



$$E3 = T + 0.005 * (TEMP - 27) - 0.01 * (TEMP - 27) * (T - (7 + 0.01 * (TEMP - 27))) * (T > 7 + 0.01 * (TEMP - 27))$$

Fig.6. Mathematical macromodel of the stabilizer with dependencies on resistance R_n and temperature $TEMP$

Let us assume that, load resistance changing by up to 1k Ω , permissible variations of output voltage do not exceed $\pm 0.5\%$ (the D_Y area is set). By designing parametrical macromodel in Fig.4,b, the respective variations in load resistance can be found to be $\pm 500\%$ (D_X area is determined).

Parametric dependency on temperature can also be incorporated into the macromodel. The corresponding macromodel is shown in Fig.6, where non-linear power source E3 recreates temperature dependency of output voltage.

By designing this simple macromodel one can determine workability area for the stabilizer concerning variations of two parameters – temperature and load resistance (Fig.7).

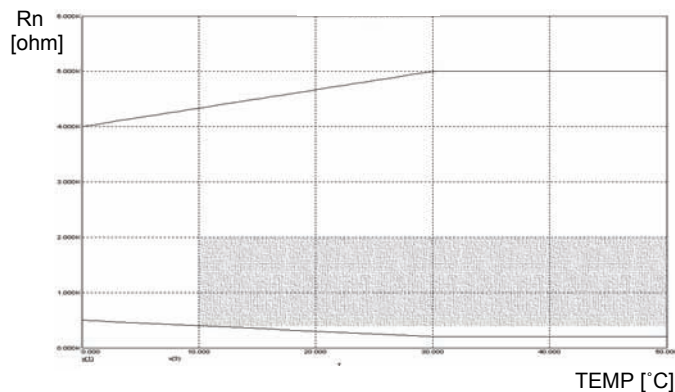


Fig.7. Area of 0.5% variation of output voltage vs. temperature and load resistance

Conclusions

Workability area enables estimation of stabilizer design quality and conclusions as to further development of the device. For instance, if it is needed to ensure workability of voltage stabilizer in the range of temperatures from $+10^\circ\text{C}$ to $+50^\circ\text{C}$ at possible variations of load resistance $R_n \pm 80\%$ of the nominal value (10000), in this case workability area is limited by the highlighted rectangle (Fig.7). Within this rectangle, there is a point corresponding to the nominal values of the parameters ($R_n=10000$; $T=20^\circ\text{C}$).

REFERENCES

- [1] Yu. Ya. Bobalo, B. O. Kapustiy, B. A. Mandziy. Functional reliability of digital devices. Lviv Polytechnic State University Publishing House, 1997. –160p.
- [2] Ya. M. Matviychuk. Mathematical macromodeling of dynamic systems: theory and practice. Lviv Ivan Franko National University Publishing Center, 2000. –215p.

Authors: prof. dr hab. Iuri Bobalo, Politechnika Lvovska, rektor; prof. dr hab. Bogdan Mandziy, College of Computer Science, Lodz; prof. dr hab. Yaroslav Matviychuk, Politechnika Lvovska, E-mail: matv@ua.fm.

GA optimization of wavelet analysis of dynamic current supply applied to fault diagnosis

Abstract. A wavelet transform based dynamic supply current analysis technique for detecting catastrophic faults in analog circuits is described in the paper. Some methods for improving fault detection sensitivity are proposed and verified. A special goal function for GA optimization has been formulated and tested. An algorithm for choosing the best set of continuous wavelet transform (CWT) parameters was illustrated by the representative computational example.

Streszczenie. W pracy przedstawiono możliwości poprawy selektywności metody diagnostyki obwodów opartej na analizie dynamicznej prądu zasilania. Zaproponowano algorytm optymalizacji współczynników transformacji falkowej i parametrów sygnałów testowych wykorzystujący techniki ewolucyjne. (Optymalizacja metody falkowej zastosowanej do diagnostyki obwodów).

Keywords: wavelet transform, fault diagnosis, genetic algorithms (GA), dynamic current supply.

Słowa kluczowe: transformacja falkowa, diagnostyka uszkodzeń, algorytmy genetyczne (GA).

Introduction

There is no doubt, that fault diagnosis is crucial for the process of both modelling and designing analogue electric devices. The main and most significant achievement in the field of fault diagnosis is an ability to verify the system during preparation to the production process and production itself, as well as when it comes to repair services. Digital circuits have some normalised diagnostic systems. In opposition to that, analogue circuits are much more difficult to deal with. It is known that development of test procedures depends on engineers' knowledge and expertise. The main reason behind the difficulty of analogue testing is the effect of parametric variations which can cause the behaviour of the fault-free device to deviate significantly from nominal values, masking the effect of the fault. In order to be efficient enough, test algorithm has to be as sensitive as it is needed to identify the deviations beyond the tolerance limit. Moreover the cost of the test increases in proportion to the required precision. The specification testing (SDT) is slow and expensive, hence the researchers are rather interested in structural or fault-based tests for analog circuits like voltage measurements or IDDQ tests. The first mentioned method cannot access some internal nodes and has poor fault coverage. The IDDQ method (validating circuits by measuring and observing their quiescent supply current) has high fault coverage but has problems with very high steady state currents in many analog circuits [1]. Measurements of dynamic power supply investigated by many authors [2,3], are useful for testing analog circuits because of its potential to detect large class of manufacturing defects, especially when the direct access to internal nodes is limited or impossible. However, the mentioned above methods, based on statistical or spectral properties of current waveform passing through the VDD or ground pin, are effective for catastrophic faults but not for parametric faults. In this paper, we discussed some further modification [4,7,8] of the algorithms using wavelet based dynamic current analysis. The set of tested parameters was enlarged and performance review concerning improving sensitivity of the fault detection is presented.

Basic ideas: Wavelet transform

Morlet-Grossman [5] definition of the continuous wavelet transform (CWT) of the one-dimensional signal $f(x) \in L^2(\mathfrak{R})$ is of the form:

$$(1) \quad W_{CT}(a,t) = \int_{-\infty}^{\infty} f(\tau) \Psi^*(a,t,\tau) d\tau,$$

where (*) denotes conjugate number, $a > 0$ is a scale parameter, t is a shift coefficient and $\Psi(a,t,\tau)$ denotes wavelet belonging to the family of wavelets obtained from the basic form (called mother-wavelet) according to the following formula:

$$(2) \quad \Psi(a,t,\tau) = \frac{1}{\sqrt{a}} \Psi\left(\frac{\tau-t}{a}\right),$$

Wavelet Transform (WT) is a mathematical tool applied to the signal analysis. Using this transformation the decomposition of an investigated signal is done as well in time domain as in frequency domain. It simplifies the analysis of the circuit properties improving the effectiveness of the fault detections. For a given value of a parameter a (scale), wavelet $\Psi(a,t,\tau)$ is shifted by time t in relation to $\Psi(a,0,\tau)$.

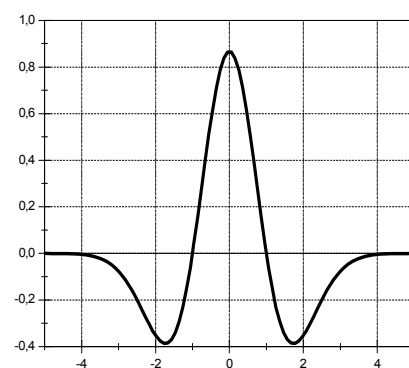


Fig.2. Wavelet "Mexican hat"

Wavelet transform values are the measure of the input signal approximation in relation to shifted and scaled mother wavelet. Popular, commonly used mother wavelet called mexican hat is shown in Fig.1. It is defined by Murenzi [5] as follows:

$$(3) \quad \Psi(\tau) = \left(\frac{2}{\sqrt{3}} \pi^{-\frac{1}{4}} \right) (1 - \tau^2) e^{-\frac{\tau}{2}}$$

Basic ideas: Current supply analysis (IDD)

The concept of using current supply analysis for the fault detection is generally based on the comparison between some individual features of the current supply for the tested circuit (faulty) and the standard one (unfaulty, golden circuit). In early works, transient responses of the devices were directly compared. Later, some authors introduced discrete transforms of the signals (FFT) [2]. The most recent achievements are concerned with wavelet transformations of the compared current signals [4,6] ensuring distinctly better fault detection.

Supply current response is obtained as an answer to a step change of DC supply. Series of the wavelet coefficients calculated for the faulty (tested) device are compared to the analogue series obtained for the standard device. The measure of this difference is commonly calculated from the following formula:

$$(4) \quad R_{RMS} = \sqrt{\frac{1}{N} \sum_1^N (F_i - G_i)^2}$$

where N denotes a number of wavelet samples, G_i are coefficients for golden circuit, F_i for the tested one.

Basic ideas: GA Optimization

Genetic Algorithms (GAs) are adaptive heuristic search algorithms premised on the evolutionary ideas of natural selection and genetic. They are modeled loosely on the principles of the evolution (first laid down by Charles Darwin) via natural selection, employing a population of individuals that undergo selection in the presence of variation-inducing operators such as mutation, selection and recombination (crossover). GAs represent an intelligent exploitation of a random search within a defined search space to solve a problem. Hence, Genetic Algorithms have been used in a wide variety of optimization tasks, including numerical optimization, and combinatorial optimization problems, circuit analysis and design, video and sound quality optimization and many, many more. GAs are useful and efficient especially when the search space is large, complex or poorly understood and traditional search methods fail.

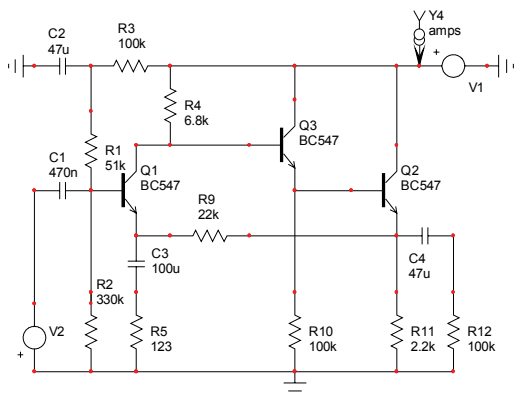


Fig.2 An exemplary device under test.

Results of numerical experiments concerned with proper selection of wavelet types and coefficients used for fault detection [7] showed, that multiparameter optimization may

improve significantly effectiveness of the diagnostic algorithms.

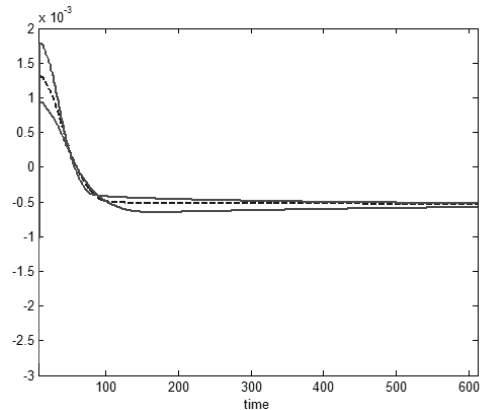


Fig.3 Typical current supply time responses of standard device with nominal values of elements(dotted line), faulty device (upper line) and unfaulty device with tolerance included (lower line)

The methods of improving sensitivity of the diagnostic algorithm

Let us consider typical exemplary nonlinear circuit (see Fig.2) to illustrate the main problem of improving effectiveness of the IDD methods. Transient supply current responses to the step change of DC supply for golden (dotted line), tested circuit and unfaulty circuit with tolerance of elements included are shown in Fig. 3. Corresponding wavelet transform coefficients curves are presented in Fig.4. Supply current time response curve for faulty circuit is closer to the golden circuit curve than to the curve for circuit with tolerance included (see Fig.3). Comparing corresponding wavelet components curves (see Fig.4), it can be stated that distance between faulty circuit curve and golden circuit curve is larger than distance between curve for circuit with tolerance included and "golden" one.

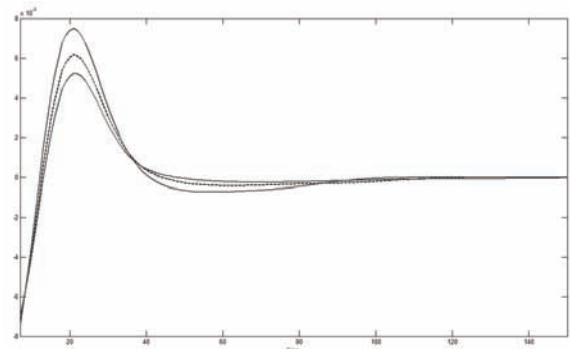


Fig.4 Wavelet transform coefficients of typical current supply time response of standard device (dotted line), faulty device (upper line) and unfaulty device with tolerance included (lower line)

The distance between them is greater, as in all of the investigated circuits. Unfortunately, for the most catastrophic faults the difference between wavelet coefficients curves for golden circuit and tested circuit is still too small and does not guarantee fault detection. Taking into consideration tolerance of the elements, we deepen the problem.

In the previous works we solved the sensitivity problem by use of the multistage selection of input testing signals [7]. Better results the authors have obtained applying multiparameter optimization for the selection of the wavelet scale [8]. Maximized goal function is of the form:

$$(5) \quad k_{(TF)}(a) = \frac{R_{RMS_F}}{R_{RMS_T}} = \frac{\sqrt{\frac{1}{N} \sum_1^N (F_i(a) - G_i(a))^2}}{\sqrt{\frac{1}{N} \sum_1^N (T_i(a) - G_i(a))^2}}$$

where G_i denotes i -th sample of the wavelet transform of the current supply of the standard circuit, F_i denotes analogue sample of the faulty circuit, and T_i i -th sample for the standard (unfaulty) circuit analyzed with taking into consideration tolerance of the elements (the worst case), Parameter a is the wavelet scale factor we are looking for and TF denotes wavelet type.

Function $k_{(TF)}(a)$ (called detection coefficient) proposed by authors is a relative measure of the difference between wavelet transforms of golden and faulty circuit including tolerance of elements. It enables use of different scale for different faults and enables comparison of the results.

The farthest research concentrated on the observation time (length of wavelet transform interval) and the type of test signals. Numerical experiments proved uniquely, that sensitivity of the IDD tests depends strongly on the observation time. If the time interval is close to the time of the dynamic state the results are the best.

A distinct improvement of method's sensitivity has been obtained by enlarging DC supply voltage change causing dynamic state. The value of the voltage change may be even greater than nominal value of DC supply. Moreover, investigation of a sequence of dynamic states improves effectiveness of the diagnosis. Results of exemplary test are presented in Table 1. Dynamic state was a result of DC supply step change from the value of 12V to 5V. Applying wavelet "mexican hat" and scale parameter GA optimization almost all the catastrophic faults (short-circuit) were detected. Catastrophic faults are indicated by the value of detection coefficient (greater than 1), hence, only short-circuit of the C4 capacitor can not be detected by the proposed test. For the C4 fault detection DC supply step change from the value of 12V to -12V was applied and investigation of four dynamic states (one by one) was performed.

Table 1. Results of the diagnostic test

| No | Element | $k_{(TF)}(a)$ |
|----|---------|---------------|
| 1 | C1 | 476 |
| 2 | C2 | 476 |
| 3 | C3 | 476 |
| 4 | C4 | 0.32 |
| 5 | R1 | 4.7e+4 |
| 6 | R2 | 476 |
| 7 | R3 | 4.7e+4 |
| 8 | R4 | 10.6 |
| 9 | R5 | 471 |
| 10 | R10 | 484 |
| 11 | R11 | 2.9e+4 |
| 12 | R12 | 4.98 |

For the better selection of wavelets it is possible to use linear combination of the wavelets having the best individual results:

$$\Psi(\mathbf{w}, \mathbf{a}, t, \tau) = \sum_{j=1}^{nw} w_j \Psi|_{TF_j}(a, t, \tau),$$

$$(6) \quad \mathbf{a} = [a_1 \ a_2 \ \dots \ a_{nw}]^T$$

$$\mathbf{w} = [w_1 \ w_2 \ \dots \ w_{nw}]^T, \quad \sum_{i=j}^{nw} w_j = 1$$

where nw is the number of considered wavelets and TF_j denotes the j -th wavelet type.

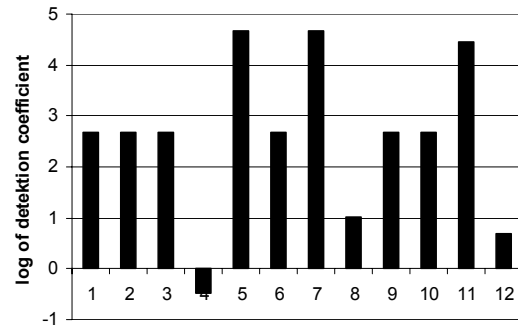


Fig.5 Graphical interpretation of the detection test.

Testing algorithm

Taking into account results of many computer simulations we introduce multiparameter definition of the continuous wavelet transform:

$$(7) \quad W_{CT}(\mathbf{w}, \mathbf{a}, t) = \int_{-\infty}^{\infty} f(\tau) \Psi^*(\mathbf{w}, \mathbf{a}, t, \tau) d\tau$$

Let us denote current supply time response of the standard circuit with nominal values of elements by $i_G(\tau)$, current supply response of faulty (DUT) circuit (fault free) by $i_F(\tau)$ and dynamic current supply of the circuit with taking tolerance into account (worst case) by $i_T(\tau)$. Hence, wavelet transform of the current $i_G(\tau)$ is defined by the following formula:

$$(8) \quad G(\mathbf{w}, \mathbf{a}, t) = \int_{-\infty}^{\infty} i_G(\tau) \Psi^*(\mathbf{w}, \mathbf{a}, t, \tau) d\tau$$

Similarly, we may define wavelet transforms of the currents $i_F(\tau)$ and $i_T(\tau)$:

$$(9) \quad F(\mathbf{w}, \mathbf{a}, t) = \int_{-\infty}^{\infty} i_F(\tau) \Psi^*(\mathbf{w}, \mathbf{a}, t, \tau) d\tau$$

$$(10) \quad T(\mathbf{w}, \mathbf{a}, t) = \int_{-\infty}^{\infty} i_T(\tau) \Psi^*(\mathbf{w}, \mathbf{a}, t, \tau) d\tau$$

Modified detection function (1) has the form:

$$(11) \quad k_{(TF)}(\mathbf{w}, \mathbf{a}) = \frac{\sqrt{\frac{1}{N} \sum_1^N (F_i(\mathbf{w}, \mathbf{a}) - G_i(\mathbf{w}, \mathbf{a}))^2}}{\sqrt{\frac{1}{N} \sum_1^N (T_i(\mathbf{w}, \mathbf{a}) - G_i(\mathbf{w}, \mathbf{a}))^2}}$$

where $G_i(\mathbf{w}, \mathbf{a})$, $T_i(\mathbf{w}, \mathbf{a})$, $F_i(\mathbf{w}, \mathbf{a})$, denote i -th sample of the corresponding wavelet transform.

Assuming that the main aim of the detection process is to define all the parameters of dynamic current supply wavelet analysis ensuring detection of all chosen catastrophic faults, the following algorithm is formulated:

ALGORITHM

1. Define initial variation of supply voltage.
2. Calculate dynamic supply current responses for:
 - a) standard circuit with nominal values of elements (golden) $\rightarrow i_G(\tau)$
 - b) circuit having values of elements differ from nominal but beneath the tolerance limits (worst case) $\rightarrow i_T(\tau)$
 - c) faulty circuit (device under) $\rightarrow i_F(\tau)$
3. Perform full GA optimization procedure to obtain maximal sensitivity of the method
 - ◆ function $k_{(TF)}(\mathbf{w}, \mathbf{a})$ is the fitness function
 - ◆ final (maximized) value of $k_{(TF)}(\mathbf{w}, \mathbf{a})$ enables to detect fault (for $k_{(TF)}(\cdot)$ greater then 1).

Numerical tests have shown, that algorithm presented above ensure detection of almost all the assumed catastrophic faults. However, sometimes appears the situation listed in Table 1 – short-circuit of the capacitor C_4 is not detected. Defining another variation of supply voltage or changing the set of wavelets we may solve this problem. The following preliminary algorithm enables to find optimal set of parameters (\mathbf{w} , \mathbf{a} , type of supply voltage variation):

PRELIMINARY ALGORITHM

STEP 0. Define initial variation of supply voltage.

STEP 1. Calculate dynamic supply current responses for:

- a) standard circuit with nominal values of elements (golden) $\rightarrow i_G(\tau)$
- b) circuit having values of elements differ from nominal but beneath the tolerance limits (worst case) $\rightarrow i_T(\tau)$

for $j=1$ to NL (number of potentially faulty elements) **do begin**

calculate dynamic supply current responses for faulty circuit (catastrophic fault for j -th element) $\rightarrow i_{F(j)}(\tau)$

perform full GA optimization procedure to obtain maximal sensitivity of the method and calculate maximized value of $k_{(TF)(j)}(\mathbf{w}_{(j)}, \mathbf{a}_{(j)})$

end

if $\min_{j=1 \dots NL} k_{(TF)(j)}(\cdot) > 1$ **then STOP** (variation of supply voltage ensures detection of all the catastrophic faults))
else change variation of supply voltage and **go to STEP 1**

To perform preliminary procedure we need to complete a list of possible variation of supply voltages. If the preliminary algorithm fails, it is possible to formulate the similar one using new sets of wavelets instead of supply variation.

Conclusions

The main goal of the paper was to describe the methods of improving the effectiveness of the fault detection algorithm based on wavelet transform of the dynamic supply current. The method does not request an access to the internal nodes and is not sensitive to measurement noises, hence it seems to be a practical tool for fault diagnosis.

The new approach to the detection coefficient was presented and some compact algorithms were described. It was experimentally confirmed, that it is possible to improve the sensitivity of the method by extending the observation time, introducing GA optimization of the wavelet scale and selection of the test signals type.

Assuming that we are looking for simple diagnostic method ensuring detection of the specified catastrophic faults of the circuits having limited access to the internal nodes we may expect that proposed procedure based on wavelet transform of the supply current response optimized by Genetic Algorithms will be good enough.

Acknowledgments:

This work was supported by the Ministry of Education and Science under Grant 3 T11B 055 29.

REFERENCES

- [1] Baturone I., Lhuertas J., Sanchez Solano S., Richardson A.M., Testing Analog Circuits by Supply Voltage and Supply Current Monitoring, Proc. *IEEE Customs Integrated Circuit Conference*, 1999, pp.155-158.
- [2] Vinnakota B., Monitoring Power Dissipation for Fault Detection, *Journal of Electric Testing.: Theory and Application* 11, pp.173-181.
- [3] Gilen G., Wang Z., Sansen W., Fault Detection and Input Stimulus Determination for the Testing of Analog Integrated Circuits Based on Power Supply Current Monitoring, *IEEE/ACM International Conference on CAD*, 1994, pp.495-499.
- [4] Bhunia S., Roy K., A Novel Wavelet Transform-Based Transient Current Analysis for Fault Detection and Localization, *IEEE Transactions on VLSI Systems*, vol.13, no.4, April 2005, pp. 503-507, 2003.
- [5] Graps A., An Introduction to Wavelets, *IEEE Computational Science and Engineering*, Summer 1995, vol.2, no.2., Los Alamitos, USA.
- [6] Frenzel J., Marinos P., Power supply Current Signature (PSCS) Analysis: A New Approach to System Testing, *International Test Conference*, pp.125-135.
- [7] Kuczyński A., Ossowski M., Wavelet Analysis for Defect Oriented Testing of Analog Circuits Containing Bipolar Transistors, *Proceedings of the International Conference on Signals and Electronic Systems*, September 2006, pp. 557-560, Łódź, Polska.

Authors: dr inż. Andrzej Kuczyński, Politechnika Łódzka, Instytut Elektrotechniki Teoretycznej, Metrologii i Materiałoznawstwa, ul. Stefanowskiego 18/22, E-mail: akuczyn@p.lodz.pl, dr inż. Marek Ossowski, Politechnika Łódzka, Instytut Elektrotechniki Teoretycznej, Metrologii i Materiałoznawstwa, ul. Stefanowskiego 18/22, E-mail: marek.ossowski@p.lodz.pl

Electrodes modeling in the copper electrocrystallization process

Abstract: In the article will be presented usefulness of the computer-aided modeling of electrochemical technologies. Modeling of the electrolytic surface deposits needs solutions of problems connected with current distribution in the electrolyte, with electrodes shape and composition of electrochemical environments in which the process takes place. Adapted methodology is used to analyze the coating layer structure and its surface topography. Classification of properties of the presented methods makes possibility of its valuation in the case of elasticity, usefulness in the galvanic process and conforming in practice.

Streszczenie: W artykule przedstawiona zostanie przydatność komputerowego wspomaganie w modelowaniu procesów występujących w technologiach elektrochemicznych. Modelowanie powłok elektrolitycznych wymaga rozwiązania problemów związanych, między innymi, z rozkładem prądu w elektrolicie, kształtem elektrod i składem elektrochemicznym środowiska, w którym zachodzi proces. Zastosowaną metodologię wykorzystuje się do analizy wewnętrznej struktury osadzonej powłoki i jej struktury oraz topografii powierzchni. Klasyfikacja własności tej metody umożliwi jej ocenę pod względem elastyczności i przydatności w procesie galwanizacji oraz możliwości późniejszego jej zastosowania w praktyce. **(Elektrody modelujące w procesie elektrokryształizacji miedzi).**

Keywords: electrocrystallization, electrode processes, copper surface layer.

Słowa kluczowe: elektrokryształizacja, procesy elektrodowe, powierzchniowa warstwa miedzi.

Introduction

Improvement of continual demand for the different industrial products and improvement of consumption character of our present life takes a great role in intensive acceleration of the contemporary technology development. It is associated with increasing demands, which put people in present time in the face of products. People acquire them for applying in industry and for the daily application. Presently, the goods are in better quality and have the best properties. This is connected with the durability and infallibility of final products. In many cases the usefulness of an applied product during the time is determined by the state of its surface layer. This layer is subjected to influence of external factors, many times of extreme levels and it also mediates between the inner structure of the product and its environment. Today is used the surface deposits on metal products in the aim, among other reasons, to improving their mechanical proprieties, as well as to offer appropriate resistances for the influence of electrical and magnetic fields. In the surface layer deposition process very important role plays the electrocrystallization method. On this way it is possible to produce a great variety of surface layers. Pure metallic layers and metallic alloy layers, as well as composite structures or multilayers can be produced by the electrocrystallization method.

The aim of the researches presented in this paper is a characterization of a method which is suitable for producing copper surface layers and influencing on their outer and inner proprieties. The researches are focused on an innovative method of situating additional electrodes in neighboring of a cathode for effective modifications of the electrochemical system into forms suitable for real electrochemical processes.

Electrocrystallization process of the copper

Electrocrystallization process of the layer deposition on the product surface is carried out in the system which is consisting of an electrolyzer fulfilled with an electrolyte, where suitable electrodes are immersed (Fig.1). The studied system is connected with an external source of energy which excites an electric current flowing through liquid environment of the electrolyte solution. Surface layer is deposited on the cathode. Second electrode i.e. anode is build from metal which is deposited on the product surface. The deposition process is usually realized at the current density taking a constant level.

The current flow causes many physical and chemical reactions. A potential difference between electrodes constituting the basis of each electrochemical system produces regular movements of ions and coupled reactions of reduction and oxidation occurring on the interfaces between the solution and the cathode, and the anode, respectively.

The current density distribution influences on final effects of the process through the induction on potential distribution in the process environment.



Fig.1. Set-up for electrochemical experiments

In the case of layer depositions on the cathode surface takes place the reduction reaction of the two-positive copper ions Cu^{2+} to the atomic copper Cu^0 . On the second electrode surface – anode surface – an opposite process occurs. It is an oxidation reaction of atomic copper Cu^0 to copper ion Cu^{2+} . Processes on the both electrodes are coupled with each other. They take place with the same velocity and they are the cause of dynamic stability state in the electrochemical environment. As the result of the oxidation and reduction reactions the copper deposition on the cathode and the anode dissolution evolve.

On the electrocrystallization effect have an influence two fundamental processes. The crystalline structure of the deposited layer depends mainly on how fast crystallites grow and new nuclei form. The course of processes determines the transport of metal ions from electrolyte

interior to cathode surface and then reduction of the ions to atomic forms. These in turn depend on the parameters of the fabrication process itself. Where crystallites grow much faster than the new nuclei form the layer exhibits coarse grain structure. Where new nuclei form faster than crystallites grow slowly and a fine grain structure is obtained. Then the deposit surface is fine-grained and its level of smoothness is higher.

In the time of electrocrystallization process could be happened situation when only the part of crystals grows in the anode direction. Then are forming the dendrite structures of crystals or in the shape of needles. This kind of structure eliminates the products from putting them into technical using.

On this stage of the electrocrystallization process important role play controls like: kind of crystal phase, kind of electrolyte, kind of substrate material, its structure, and parameters of the process realization such as current density, temperature of the electrolyte solution, as well as its pH.

The electrolytic process found wide application in the process of the fabrication of moulds. The metal form shaping using the electrolysis process relies on a suitable deposition of a thick metal layer during the production of the mould surface layer, which is an exact copy of the final product. This layer after the mould dismissing presents the form to manufacturing the raw material products in the technological processes.

To make possible the fulfillment of the above requirements appropriate conditions as well as electric and physical parameters in the time of deposition processes must be guaranteed. Very important aim is the assurance of the mould fit and at the same time homogenous thickness of the mould form. In consequence of an increase in considerable way of its mechanical strength, the moulds find applications in the industry of manufacturing of raw material products. Uniformity of the layer deposits produced in an electrochemical way could be in some cases deformed in result of edge effects. Cathode regions subjected to these effect actions are the sharp edges of the covered products and especially their complicated shapes may appear.

Application of modifying electrodes

During the electrocrystallization process in the electrochemical system the potential ϕ and its distribution are strictly determined by dependences between appropriate quantities. When the potential distribution is known, we could determine the value of electric field intensity given by the formula: $E = -grad\phi$.

According to the electrical field theory, great differences in potential values between neighboring field points cause important potential gradients being responsible for values of electrical field intensity. It is very important question in the case of metal depositions, especially when surface layers are deposited on the products exhibiting sharp edges. These edges play an important role during the producing of the moulds for the industry of plastic material processing.

Studying a situation from the point of view of the electrical field theory the fundamental problem amounts to suitable shaping of the distribution (and uniformity) of the vector field intensity in the electrochemical system. Taking into account the rectangular system of coordinates (X, Y, Z) we locate it in the following way, that covered surface is situated in plane XY and direction Z is perpendicular to it. Two functions were taken as the performance index:

1. getting the greatest value of the component Z of the electrical field intensity:

$$(1) \quad \|E_{XY}\|_2 = \min|E_{XY}| = \min \sum_{i=1}^I \sqrt{E_{XB,i}^2 + E_{YB,i}^2}$$

2. getting the smallest value of the component XY module of the electrical field intensity:

$$(2) \quad \|E_Z\|_1 = \max|E_Z|$$

Two components of the performance index have one together task to do. They must helping in shaping of the electrical field distribution in order that the vector field intensity must be directed perpendicularly to covered surface in all points of it. In result the copper layer should be evenly deposited on the given product surface. The thickness of the deposited layer is described by:

$$(3) \quad d = \frac{m}{s \cdot \rho_{Cu}}$$

where: m – metal mass deposited on cathode [g]; s – surface of covered cathode [cm²]; ρ_{Cu} – copper density [gcm⁻³].

Above-mentioned guidelines will be realized by additional electrodes modifying the electrical field distribution. These electrodes will be suitably arranged into the electrochemical system and subjected to the cathode potential.

Methods of investigations

The ground of the proposed method is elaborated and provisionally verified on a physical model of the electrochemical system. In the time of experimental researches were determined parts of the system where the electrical field must to be suitably formed. The sensitive regions are the edges of the product and for this reason the modifying electrodes are immersed near the sensible places.

Composition and arrangement of the modifying electrodes were elaborated due to simulating method by using the American Simulation Program E.M.R.C. NISA/EMAG (Fig2.). It works on the basis differential Laplace equation.

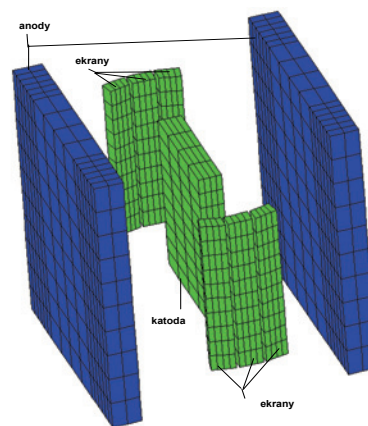


Fig.2. The image of the numerical model of the electrochemical arrangement

The two dimensional model of the electrochemical arrangement was applied in the analysis. This type of the model allows to shortening time, which is needed for analysis of successive variants of the electrolytic cell. Initial calculation is realized on the base of 2D model formed as XY cross-section of the cell (Fig.3).

The computation of the elaborated 2D model of the electroplating cell was carried out by helping of the professional software Emag. A special program was written for the acceleration of the obtained results. This program co-operated with NISA and calculated many compositions of modifying electrodes. At the end it gives the results corresponding to the performance index expressed by (1) and (2). Based on these results could be pointed out the composition of the modifying electrodes.

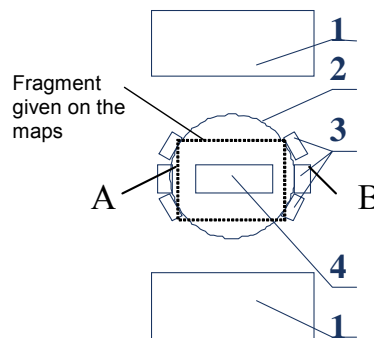


Fig.3. View of the XY cross-section of the electrochemical system: 1-anodes, 2-isolated ring, 3-modifying electrodes, 4-cathode

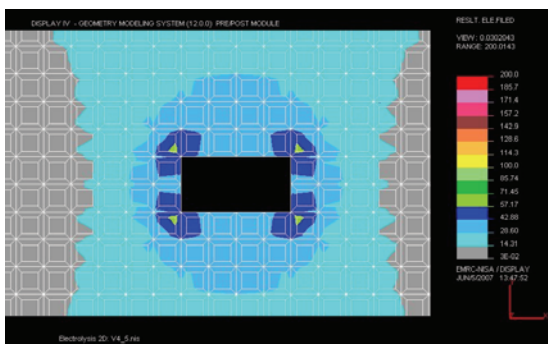


Fig.4. Map of the electrical field intensity distribution (arrangement with six modifying electrodes immersed near the cathode)

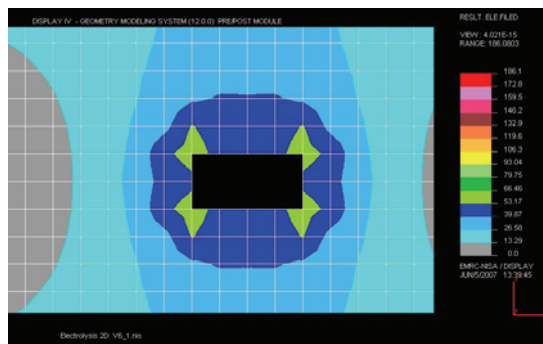


Fig.5. Map of the electrical field intensity distribution (arrangement with six modifying electrodes immersed near the cathode)

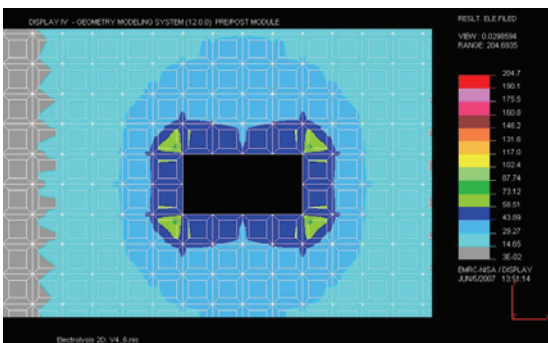


Fig.6. Map of the electrical field intensity distribution (arrangement with four modifying electrodes immersed near the cathode)

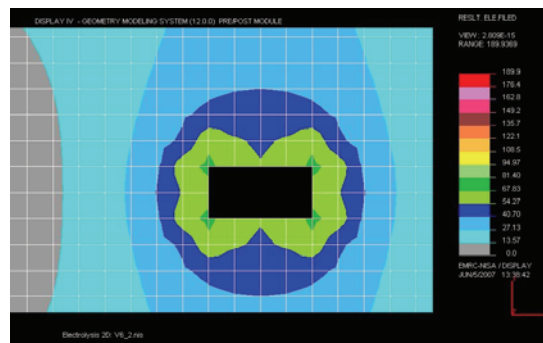


Fig.7. Map of the electrical field intensity distribution (arrangement with four modifying electrodes immersed near the cathode)

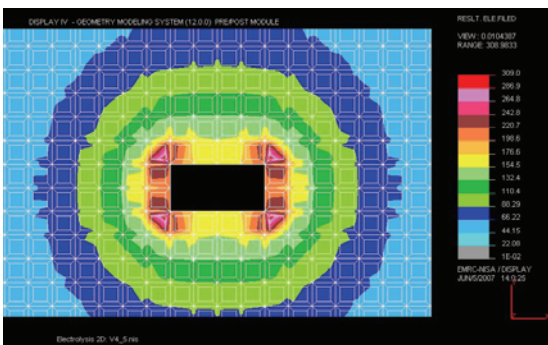


Fig.8. Map of the electrical field distribution (arrangement without modifying electrodes immersed near the cathode)

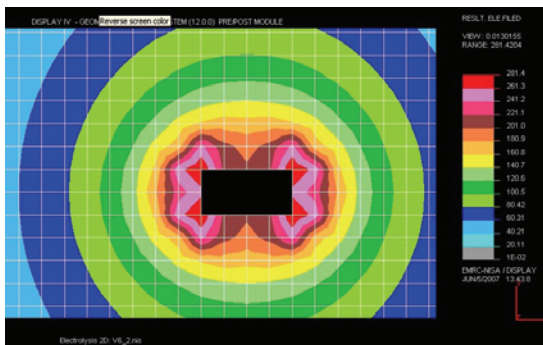


Fig.9. Map of the electrical field intensity distribution (arrangement without modifying electrodes immersed near the cathode)

The real electrochemical studies of copper layers deposition were carried out in an electrolyte bath. It included:

- sulphate(VI) of the copper(II) (CuSO_4) 200g/l,
- sulphate(VI) acid (H_2SO_4) 50g/l,
- hydrochloric acid (HCl) 0,07g/l.

In this environment was realized the studied process. It was related on moving the modifying electrodes within the electrochemical system. The electrode system was supplied by direct current with density 5 A/dm².

Structure of deposited copper layers was analyzed by the HITACHI S-3500N electronic scanning microscope (SEM). Surface microgeometry of deposited layers was examined by profilometer Taylor Hobson- μ ltra-[NP4N-1].

Results of investigation and their analysis

The configuration taken into considerations after computations was the background to conduct the electrocrystallization process in a basic bath. Deposition process was realized by using direct current and the value of the cathodes current density was equal to 5 A/dm². All produced copper layers are characterized by a polycrystalline structure with great sizes of grains.

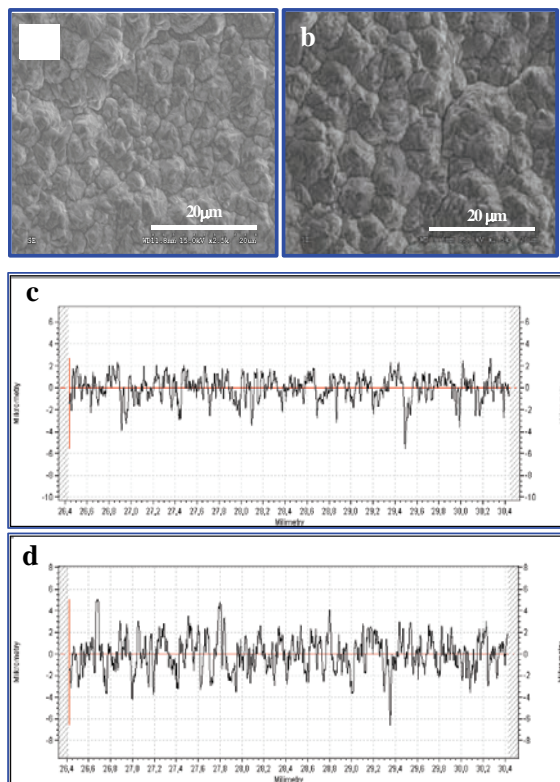


Fig.10. Surface structures and profiles of deposited copper layers made by electrocrystallization method: a), c) fine grains, b), d) coarse grains

During the realized studies it was made modifications of electrodes compositions. There were two compositions of the modifying electrodes. First of them: six modifying electrodes (Fig.3.), the second: four modifying electrodes (Fig.3. – without modifying electrodes number A and B). The results of the computations are given on the figures (Fig.4. to Fig.9.). After applications of the modifying electrodes. There are the differences in the electric field intensity distribution, which are the results of different kinds of the computing cells applied during the computations. Figures 4, 6, 8 show the distributions which are due to first

kind of the cells. Figures 5, 7, 9 show the distributions which due to second kind of the cells.

Summary

During the performed experiments the metal layers were deposited on the silver ground (artificial very thin layer produced by silver paint SCP 003). In the case when in the electrochemical arrangement weren't put any modifying electrodes the structure of obtained layers was characterized by smaller crystals then in the case with modifying electrodes arrangement. Profiles of the deposited layers differ as a result of values of crystal variations.

Profiles of the layers deposited without the modifying electrodes arrangement exhibited regular peaks with great differences in value which appear very frequently. Profiles of the layers deposited with the modifying electrodes arrangement are characterized by greater stability what is shown by smaller frequency and smaller value of peaks differences. Applications of the modifying electrodes have a positive influence on the deposited metal layer. It was obligatory to carry out the suitable researches, which were supported by computations. The first kind of the cells gives the better distribution the electrical field intensities and values of them on the lower level. In the near future will be carried out the researches and computations which will help us on the way of the electrochemical system optimization. The metal deposited layers will be more regular and will find more frequent applications in the industry.

REFERENCES

- [1] Wong K. P., Chan K. C., Yue T. M., Modeling of electrocrystallization for pulse current electroforming of nickel, *Applied Surface Science*, 178 (2001), nr 2, 178-180
- [2] Trzaska M., Struktura i twardość warstw Ni, Cu i Co wytwarzanych elektrochemicznie (in Polish), *Inżynieria Materiałowa*, 147, (2005), nr 5, 698-700
- [3] Kostin N. A., Kubłanowski W. S., Impulsnyj elektroliz spławow, *Naukowa Dumka*, Kijew 1996
- [4] Socha J., Weber J. A., Podstawy elektrolitycznego osadzania stopów metali (in Polish), *IMP*, Warszawa (2001)
- [5] Gellings P. J., Bouwmeester H. J. M. (ed.), Solid state electrochemistry, *CRC Press*, Boca Raton, 1997
- [6] Pauleau Y. (ed.): Chemical Physics of Thin Film Deposition Processes for Micro- and Nano-Technologies, *NATO Science Series, Kluwer Academic Publishers*, Dordrecht 2002
- [7] Trzaska M., Elektrokrystalizacja metal (in Polish).i, *Przegląd Elektrotechniczny*, (2004), nr 11, 1166-1169
- [8] Nalwa H. S. (ed.), Nanostructured Materials and Nanotechnology, *Academic Press*, San Diego, (2002)
- [9] Trzaska M., Właściwości elektryczne, cieplne i mechaniczne nanokrystalicznej miedzi (in Polish), *Elektronika*, (2006), nr 1, 11-13
- [10] Trzaska M., Trzaska Z., Model Development of High-frequency Phenomena in Nanocrystalline Copper Conductors. *Proceedings of the IASTED International Conference on Modelling, Identification, and Control - MIC 2006*, Lanzarote, Spain, (2006), 332-337
- [11] Białostocka A. M., Walendziuk W., Bolkowski S., Komputerowy pomiar rozkładu potencjału podczas trwania procesu galwanizacji (in Polish)., *VIII Konferencja Naukowo – Techniczna ZKwE'2003, Poznań/Kiekrz*, (2003), Tom I, 195-198

This work is supported by the Polish Scientific Committee, under the project S/WE/3/03, Białystok Technical University.

Authors: prof. dr hab. inż. Maria Trzaska, Politechnika Warszawska, Wydział Inżynierii Materiałowej, Zakład Inżynierii Powierzchni, ul. Narbuta 85, Warszawa, e-mail: matrz@inmat.pw.edu.pl; mgr inż. Anna Maria Białostocka, Politechnika Białostocka, Wydział Elektryczny, Katedra Elektrotechniki Teoretycznej i Metrologii, ul. Wiejska 45d (pokój 259), 15-351 Białystok, e-mail: bianal@pb.edu.pl

Investigations of influence on power quality of superconducting fault current limiter

Abstract. Waveforms obtained from a superconducting Fault Current Limiter are investigated using the Prony modelling technique. Comparable measurements with the use of standard tools of spectral analysis (like FFT) fail because of short data available and low levels of higher spectral components.

Streszczenie. W pracy przedstawiono wyniki analizy widmowej prądów i napięć zarejestrowanych w obwodach z nadprzewodzącym dławikiem przetężeniowym. Zastosowano metodę parametrycznego modelowania za pomocą metody Prony. Klasyczne metody oparte na FFT zawodzą w tym przypadku z powodu krótkich sekwencji danych, niestacjonarności przebiegów i niskiego poziomu wyższych harmonicznych. **(Badanie wpływu nadprzewodzącego dławika przetężeniowego na jakość energii elektrycznej).**

Keywords: Prony method, superconducting fault current limiter, harmonic analysis, power quality.

Słowa kluczowe: metoda Prony, nadprzewodzący dławik przetężeniowy, analiza widmowa, jakość energii.

Introduction

The quality of voltage waveforms is nowadays an issue of the utmost importance for power utilities, electric energy consumers and also for the manufactures of electric and electronic equipment. The voltage waveform is expected to be a pure sinusoidal with a given frequency and amplitude. Modern electric apparatus generate a wide spectrum of components which can deteriorate the quality of the delivered energy, increase the energy losses as well as decrease the reliability of a power system. Investigated signals contain multiple harmonic components and present often non-stationary behaviour [1].

The standard method for studying time-varying signals is short-time Fourier transform (STFT) where the Fourier transform is applied to a windowed signal to obtain the energy distribution along the frequency direction at the time corresponding to the centre of the window. The crucial drawback of this method is that the length of the window is related to the frequency resolution. Increasing the window length leads to improving frequency resolution but it means that the non-stationarities occurring during this interval will be smeared in time and frequency. This inherent relationship between time and frequency resolution becomes more important when one is dealing with signals whose frequency content is changing. [2]

In this paper the time-varying characteristics of power system signal components are estimated using the Prony model [3].

Prony method is a technique for modeling sampled data as a linear combination of exponentials [4]. Although it is not a spectral estimation technique, Prony method has a close relationship to the least squares linear prediction algorithms used for AR and ARMA parameter estimation. Prony method seeks to fit a deterministic exponential model to the data in contrast to AR and ARMA methods that seek to fit a random model to the second-order data statistics. The paper [3] presents a new method of real-time measurement of power system frequency based on Prony model.

The paper contains detailed analysis of the fundamental component waveforms of the currents and higher harmonic analysis of the voltages recorded at the test setup with a superconducting Fault Current Limiter (FCL) using the Prony method, recalled below.

Fault Current Limiter

For the large-scale power system, the development of FCLs for suppressing the over fault currents is strongly desired. FCLs with diverse principles, which apply superconducting techniques, have been proposed, such as: resistive, inductive, magnetic shielding and saturated core FCLs, etc

[5]. The structure of a prototype saturated core FCL incorporating the DC HTS (High Temperature Superconductor) bias winding is shown in Fig. 1.

Because of the nonlinear influence of the saturated magnetic core, it is expected that the currents and voltages measured from the testing circuit shown in Fig. 2 can show a certain level of harmonic and interharmonics components as well as non-characteristic components.

The DC bias winding for FCL is expected to use HT superconductors, which will drive the core into saturation with a low DC power supply voltage. In this case of investigated Saturated Core High Temperature Superconducting Fault Current Limiter (FCL) [5] the spectral contents of the currents and voltages and, therefore, periodicity intervals are unknown. Detection of additional frequency components can be used for assessment of the impact of such devices on the quality of energy and for fault identification.

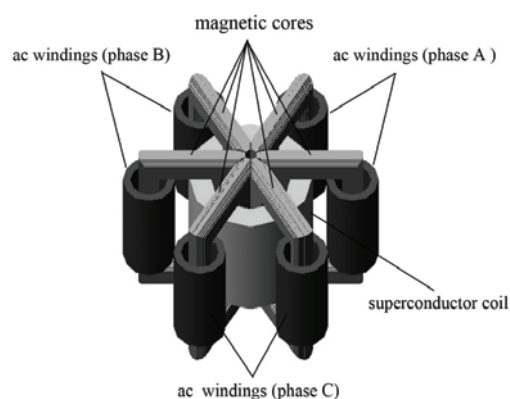


Fig. 1. Schematic view of the structure of HTS current limiter.

The frequencies of signal components are estimated using the Prony model. Prony method is a technique for modelling sampled data as a linear combination of exponentials. Although it is not a spectral estimation technique, Prony method has a close relationship to the least squares linear prediction algorithms used for AR and ARMA parameter estimation. Prony method seeks to fit a deterministic exponential model to the data in contrast to AR and ARMA methods that seek to fit a random model to the second-order data statistics [6].

Prony Method

Assuming the M data samples $[x_1, x_2, \dots, x_M]$ the investigated function can be approximated by p exponential functions:

$$(1) \quad y[n] = \sum_{k=1}^p A_k e^{(\alpha_k + j\omega_k)(n-1)T_s + j\psi_k}$$

where: $n = 1, 2, \dots, M$; T_s – sampling period, A_k – amplitude, α_k – damping factor, ω_k – angular velocity, ψ_k initial phase.

The following vectors can be defined :

$$(2) \quad \mathbf{x}_{w0} = [x_p, x_{p-1} \dots x_1]$$

$$(3) \quad \mathbf{x}_{k0} = [x_p, x_{p+1} \dots x_{M-1}]^T$$

$$(4) \quad \mathbf{x}_{k1} = [-x_{p+1}, -x_{p+2} \dots -x_M]^T$$

$$(5) \quad \mathbf{x}_{k2} = [x_1, x_2 \dots x_p]^T$$

where p is the assumed number of exponential components, which can approximate the investigated signal.

The Toeplitz matrix:

$$(6) \quad \mathbf{t} = \begin{bmatrix} x_p & x_{p-1} & \dots & x_1 \\ x_{p+1} & x_p & \dots & x_2 \\ \vdots & \vdots & & \vdots \\ x_{M-1} & x_{M-2} & \dots & x_{M-p} \end{bmatrix}$$

created from (2) and (3), makes it possible to determine the vector of coefficients \mathbf{a} of the characteristic polynomial:

$$(7) \quad \mathbf{t} \cdot \mathbf{a} = \mathbf{x}_{k1}$$

where:

$$(8) \quad \mathbf{a} = [a_1 \ a_2 \ \dots \ a_p]^T$$

The roots of the characteristic polynomial:

$$(9) \quad z^p + a_1 z^{p-1} + \dots + a_{p-1} z + a_p = 0$$

written in a vector form:

$$(10) \quad \mathbf{z} = [z_1 \ z_2 \ \dots \ z_p]^T$$

define a Vandermonde matrix:

$$(11) \quad \mathbf{v} = \begin{bmatrix} z_1^0 & \dots & z_{p-1}^0 & z_p^0 \\ z_1^1 & \dots & z_{p-1}^1 & z_p^1 \\ \vdots & & \vdots & \vdots \\ z_1^{p-1} & \dots & z_{p-1}^{p-1} & z_p^{p-1} \end{bmatrix}$$

Vector of complex values \mathbf{h} can be calculated from (5) and (11) solving the system of equations:

$$(12) \quad \mathbf{v} \cdot \mathbf{h} = \mathbf{x}_{k2}$$

where:

$$(13) \quad \mathbf{h} = [h_1 \ h_2 \ \dots \ h_p]^T$$

Using the equations (10) and (13), parameters of exponential components for $k=1, 2, \dots, p$ can be calculated from:

$$(14) \quad A_k = |\mathbf{h}_k| \quad \text{amplitude,}$$

$$(15) \quad \phi_k = \arg(\mathbf{h}_k) \quad \text{initial phase,}$$

$$(16) \quad \alpha_k = f_p \cdot \ln|z_k| \quad \text{damping factor,}$$

$$(17) \quad \omega_k = f_p \cdot \arg|z_k| \quad \text{angular velocity.}$$

Investigation results and discussion

Because of the short data records available (two periods of the fundamental component of 50 Hz), only limited extent of investigations was possible. The measurement setup is shown in Fig. 2. The signals under investigation were phase load currents sampled at the frequency of 5 kHz.

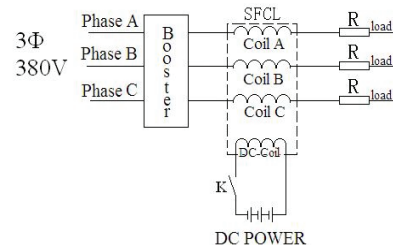


Fig. 2. Test measurement setup with FCL.

Initial investigations included the computation of current spectra using classical Welch spectrum. As expected, the presence of 3rd, 5th and 11th harmonic was detected. Some additional basic results are presented in Table 1.

Table 1. Parameters of phase currents

| | without FCL | | | with FCL | | |
|---------------|-------------|------|------|----------|------|------|
| phase | A | B | C | A | B | C |
| I_{RMS} [A] | 39,7 | 35,0 | 34,7 | 38,3 | 34,3 | 33,9 |
| THD % | 9,87 | 6,20 | 5,65 | 10,69 | 5,94 | 5,66 |

Above presented results suggest a slight increase of harmonic distortion in the circuit with FCL and quite strong asymmetry between phases.

In the next step the analysis of fundamental frequency (50 Hz) was performed using the Prony method.

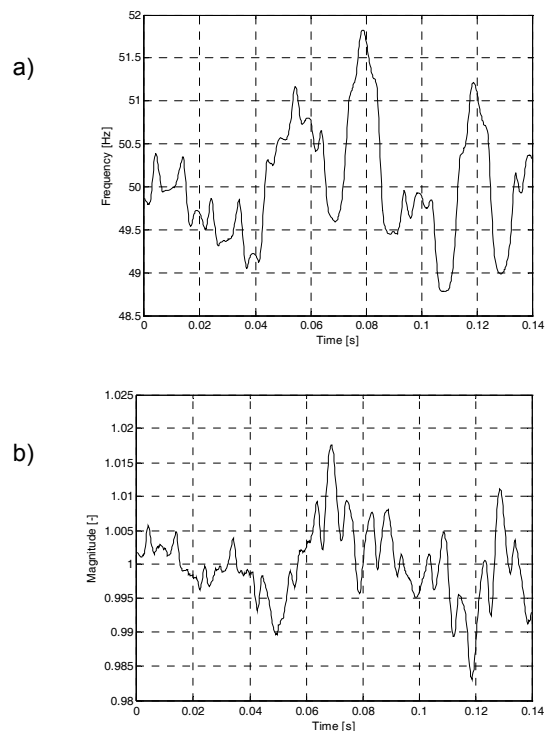


Fig. 3. Analysis of fundamental frequency of the current without FCL (50 Hz) using Prony method. (a – frequency, b – magnitude).

Fig. 3 shows the current in the circuit without FCL and Fig. 4. – current with FCL. Figures represent the fluctuations in time of frequency and of amplitude of the fundamental component of the current.

There is quite a strong evidence that FCL causes important fluctuations of parameters of the fundamental component. Nature of these fluctuations is periodical (when comparing results without FCL where fluctuations are lower and of stochastic nature with results with FCL- where fluctuations are much stronger and periodical).

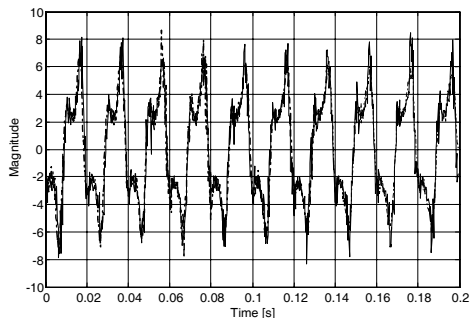


Fig. 4. Original (black) and approximated (using Prony method) (red) waveform of the voltage in phase B.

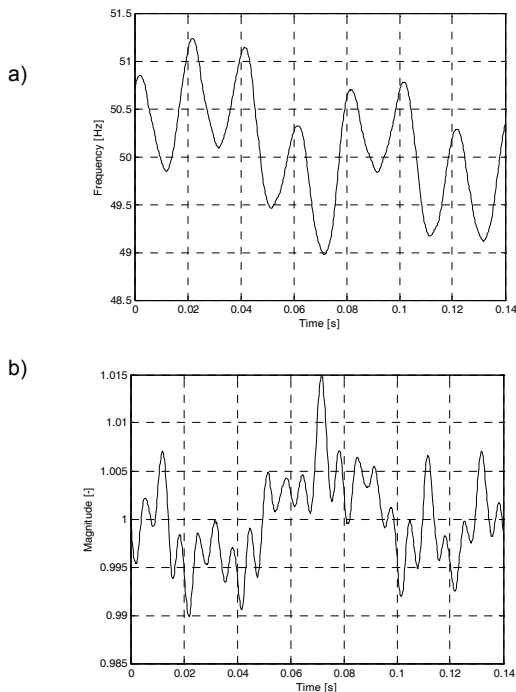


Fig. 5. Analysis of fundamental frequency of the current with FCL (50 Hz) using Prony method. (a –frequency, b- Magnitude).

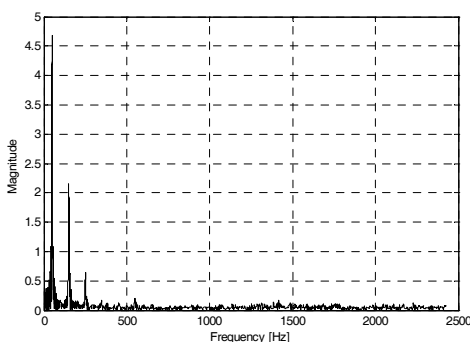


Fig. 6. Spectrum FFT of the voltage waveform.

When roughly comparing the fluctuations (over 2 periods) it appears that FCL causes 2.2 Hz and 1.016 (pu) of fluctuations compared to 1.3 Hz and 1.0086 pu without FCL. Results based on shorter data sequences (not reported in this paper) show higher values although these results can be less accurate and more affected more by noise.

In the next step the voltages recorded during tests with FCL were investigated. The Fig. 5 shows the voltage waveform in phase B with superposed approximated waveform using parameters obtained using the Prony method.

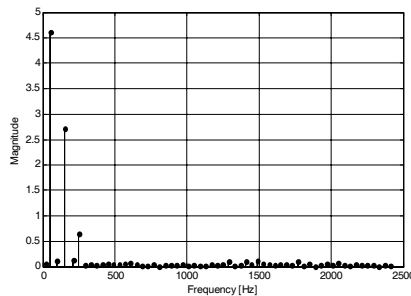


Fig. 7. Estimated spectral components of the voltage using Prony method.

The spectra of voltage waveforms are shown in Figs. 6 and 7. The FFT spectrum shows the presence of 3 harmonic components (fundamental, third and fifth harmonic) which is confirmed by Prony parameter estimation which yields the values of main spectral components as: 49,95Hz, 149,8Hz and 248,4Hz. It was also observed an expressed asymmetry between phases which needs further investigations.

Conclusions

Higher harmonics generated within the circuits with non-linear devices (such as Fault Current Limiter) can affect the power quality and disturb the function of connected apparatus. Therefore it is important to accurately know the spectral contents of investigated waveforms. The investigations show the advantages of parametric modelling using the Prony model, which delivers highly accurate results, even for short data records.

This work was supported in part by the Ministry of Science under Grant No. 3T10A 04030.

REFERENCES

- [1] Bollen M. H. J., What is power quality, *Electric Power System Research*, 66 (2003), 5-14.
- [2] Kay S.M., *Modern spectral estimation: theory and application* (Englewood Cliffs, NJ: Prentice-Hall, 1988).
- [3] Lobos T., Rezmer J., Real Time Determination of Power System Frequency, *IEEE Trans. on Instrumentation and Measurement*, (1997), 46, No. 4, 877-881.
- [4] Lobos T., Rezmer J., Schegner P., Parameter estimation of distorted signals using Prony method. *2003 IEEE Bologna PowerTech Proceedings*. (2003), ref. BPT03-45.
- [5] Zhao C., Wang S., Qiu J., Guo Z., Guo Y., Gong W., Cao Z., Transient Simulation and Analysis for Saturated Core High Temperature Superconducting Fault Current Limiter, *12th Biennial IEEE Conference on Electromagnetic Field Computation*, (2006), 503 – 503.
- [6] Meunier M., Brouage F., Fourier transform, wavelets, Prony analysis: tools for harmonics and quality of power, *Proc. 8th Int. Conf. on Harmonics and Quality of Power*, Athens, Greece, (1998), 71-76.

Authors: Dr Ying Xin Zhengjian Cao, Yang Wang, Innopower Superconductor Cable Co., Ltd., Beijing, 100176, China, E-mail: yingxin@innopower.com, dr inż. Zbigniew Leonowicz i dr inż. Jacek Rezmer, Politechnika Wroclawska, Instytut Podstaw Elektrotechniki i Elektrotechnologii, Wyb. Wyspińskiego 27, 50-370 Wrocław, E-mail: leonowicz@iee.org, jacek.rezmer@pwr.wroc.pl.

Optimization of time delays in Active Power Filter control algorithm

Abstract. In this paper influence of processing delays in active power filter control system on its performance and comparison of the experimental results with different processing delay time have been presented. Delays in control unit may cause incorrect work of current controller and shifting of compensating currents. Shortening of processing time by control algorithm optimization resulted in an improvement of supply current THD from 27% to 17% (from 121% before APF using). The experimental results were obtained in the laboratory.

Streszczenie. W pracy przedstawiono wpływ opóźnień w układzie sterowania energetycznego filtru aktywnego na poprawność jego działania. Zaprezentowano porównanie wyników laboratoryjnych dla różnych opóźnień. Opóźnienia te powodować mogą nieprawidłowe działanie nadającego regulatora prądu oraz przesunięcie generowanych prądów kompensujących. Skrócenie czasu przetwarzania poprzez optymalizację algorytmu sterowania spowodowało poprawienie współczynnika THD prądu sieci z 27% do 17% (dla 121% przed użyciem EFA). (Optymalizacja opóźnień w algorytmie sterowania energetycznego filtru aktywnego).

Keywords: nonsinusoidal waveforms, higher harmonics, digital signal processing, active power filters

Słowa kluczowe: przebiegi odkształcone, wyższe harmoniczne, cyfrowe przetwarzanie sygnałów, energetyczne filtry aktywne

Introduction

One of the methods for high harmonic reduction, reactive power compensation or symmetrization in three phase system is using active power filter (APF) [2, 3]. APF connected to power system, depending on control strategy and configuration, can realize all of these functions or only selected ones. An example of active power filter configuration (shunt) has been presented in fig. 1. The active filter injects i_c currents required to compensate the higher harmonics and reactive components of the source currents (i_s). The three-phase voltage source PWM converter with L_c inductors performs the execution devices function. Reference compensating currents in such devices are usually calculated by using theory of instantaneous power (p-q) and its generalization [1, 2, 3]. This type of control algorithm allows setting the requested compensating current in only few mathematical operations. For the sake of the control algorithm characteristics the control system is usually realized by a digital signal processor (DSP). Despite of so many advantages, the digital signal processors have a finite computing time which may influence the active power filter performance. Additionally fixed-point errors as well as inaccuracy of analog to digital conversion may influence APF operating. Shortening of processing delays may be achieved by using more efficient digital signal processor or by control algorithm optimization.

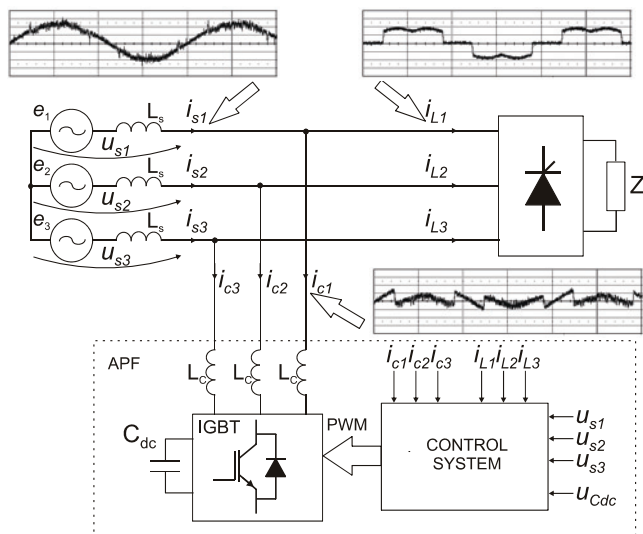


Fig. 1. Shunt Active Power Filter - principle of working

Shunt Active Power Filter

A three-phase active power filter based on a digital signal processor - TMS320F2812 has been presented in the earlier authors' paper [5].

Implementation of control algorithm can be divided into two major sections – the first one implements device initialization, whereas the second one is responsible for requiring of interrupt service. PWM interrupts have been used in this case [10]. Diagram of interrupt service routine has been presented in fig. 2

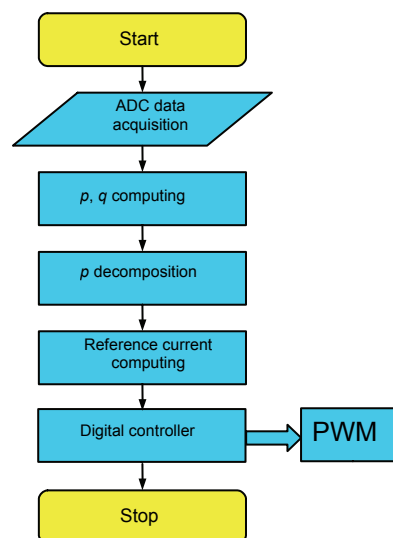


Fig. 2. Diagram of PWM interrupt service routine

Reference compensating currents, in this case, have been calculated by using theory of instantaneous power (p-q) [1, 6, 7]. At first source currents are measured and transformed from abc coordinate to $\alpha\beta$ coordinate [1] (Clarke transformation):

$$(1) \quad \begin{bmatrix} F_\alpha \\ F_\beta \end{bmatrix} = \sqrt{\frac{2}{3}} \begin{bmatrix} 1 & -\frac{1}{2} & -\frac{1}{2} \\ 0 & \frac{\sqrt{3}}{2} & -\frac{\sqrt{3}}{2} \end{bmatrix} \begin{bmatrix} F_{L1} \\ F_{L2} \\ F_{L3} \end{bmatrix},$$

then the instantaneous real power and instantaneous imaginary power is calculated according to Akagi [1, 2]:

$$(2) \quad \begin{bmatrix} p \\ q \end{bmatrix} = \begin{bmatrix} u_\alpha & u_\beta \\ -u_\beta & u_\alpha \end{bmatrix} \begin{bmatrix} i_\alpha \\ i_\beta \end{bmatrix}$$

Next the instantaneous real power (p) is being decomposed on dc and ac components by using IIR digital filter (low-pass). DC component of p (active power P) corresponds to the fundamental active component of current. The rest components should be excluded. After the decomposition reference compensating currents are being calculated:

$$(3) \quad \begin{bmatrix} i_{ac} \\ i_{bc} \end{bmatrix} = \frac{1}{u_\alpha^2 + u_\beta^2} \begin{bmatrix} u_\alpha & -u_\beta \\ u_\beta & u_\alpha \end{bmatrix} \begin{bmatrix} \tilde{p} \\ q \end{bmatrix}$$

and processed through inverse Clarke transformation:

$$(4) \quad \begin{bmatrix} i_{c1} \\ i_{c2} \\ i_{c3} \end{bmatrix} = \sqrt{\frac{2}{3}} \begin{bmatrix} 1 & 0 \\ -\frac{1}{2} & \frac{\sqrt{3}}{2} \\ -\frac{1}{2} & -\frac{\sqrt{3}}{2} \end{bmatrix} \begin{bmatrix} i_{ac} \\ i_{bc} \end{bmatrix}$$

Those reference compensating currents are put between power system and nonlinear load through a voltage source inverter. This kind of algorithm is a fundamental one and has some disadvantages [7, 8, 9], but it proved to be sufficiently effective in this case.

The active power filter was built (Fig. 3) and used for tests. The results of those tests have been presented in this paper.

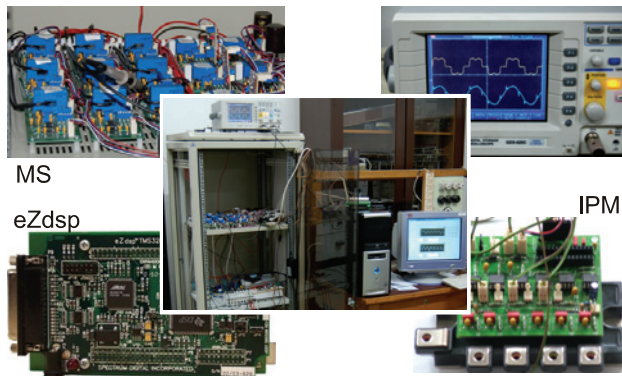


Fig. 3 Experimental system in our laboratory. MS – measurement system, IPM – IGBT module

The experimental results obtained in the laboratory were attained with following values of system components:

- Supply voltage $|E_{1,2,3}| = 30$ V (symmetrical THD_u < 4%)
- Supply line inductance $L_s = 0.2$ mH
- Compensator inductance $L_c = 1.2$ mH
- IGBT switching frequency $f_s = 18$ kHz
- Inverter dc-bus capacitance $C_{dc} = 3300$ μ F
- DC-bus voltage $U_{dc} = 180$ V

Processing delays

Regardless of the control algorithm the cycle of DSP processing consists of the following steps (Fig. 4):

- Currents and voltages measurement.
- Compensating currents reference computing.
- Compensator currents measurement.
- PWM width computing.

Setting out of a compensating current reference analog signal for external PWM controller may substitute the last two steps. The length of the whole cycle has to be shorter than PWM period.

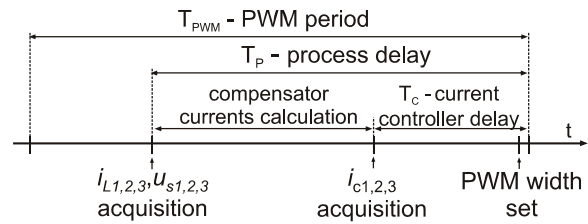


Fig. 4. Illustration of the control process cycle

In the process cycle two types of delay can be distinguished:

- T_C – current controller delay which influences current controller performance,
- T_P – processing delay which causes shift of the compensator current. The time of compensating current reference computing has a primary impact on the length of T_P delay.

Both of the delay types have influence on the whole active power filter working.

The current controller delay has fundamental influence on APF working. Effect of the finite controller computing time and delays of analog to digital converters is putting out PWM signal after a definite time. If compensator currents change much during this time, the current controller will work incorrectly.

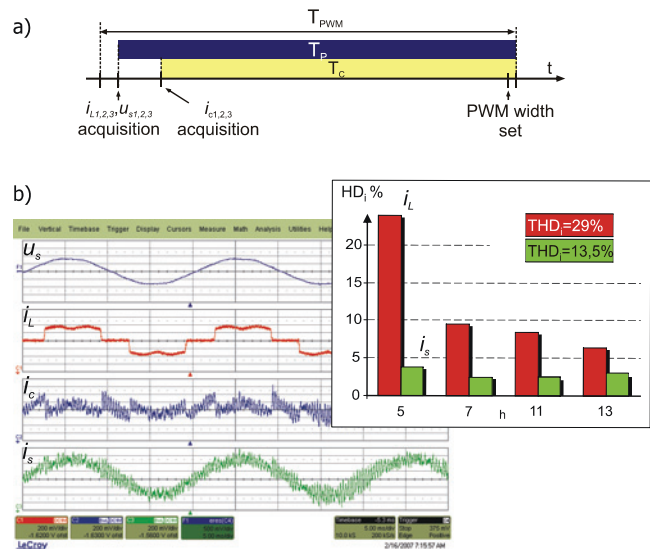


Fig. 5. a) Illustration of the processing delays $T_P = 55 \mu$ s, $T_C = 52 \mu$ s b) APF voltage, current waveforms and harmonic distortion for i_s and i_L current. The experimental results for a six-pulse bridge rectifier with R load

Experimental results for current controller delay $T_C = 52 \mu$ s has been presented in the fig. 5. The incorrect working of current controller is visible in this case. There is a high frequency oscillation (about 30 harmonic) in compensator currents which causes increase of its RMS value.

After shortening current controller delay to $T_C = 12 \mu$ s, the controller worked correctly and RMS compensator currents value decreased almost three times. The experimental results for this case have been presented in fig. 6. Additionally decrease of total harmonic distortion (THD) is visible here.

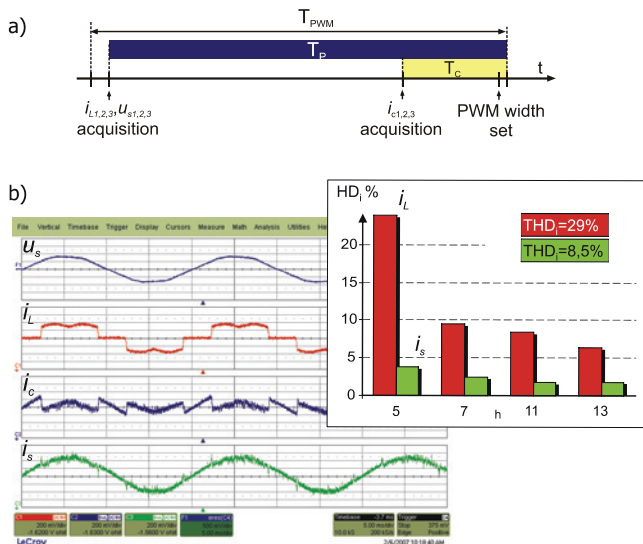


Fig. 6. a) Illustration of the processing delays $T_P=55 \mu s$, $T_C=12 \mu s$ b) APF voltage, current waveforms and harmonic distortion for i_s and i_L current. The experimental results for a six-pulse bridge rectifier with R load

Effects of the T_P process delay are particularly visible in case of compensating of supply current with large total harmonic distortion. Experimental results for the six-pulse bridge rectifier with RC load when $T_P=T_{PWM}=55 \mu s$ have been presented in fig. 7. Despite of a correct shape of the compensator current, i_s current distortion is plainly visible here.

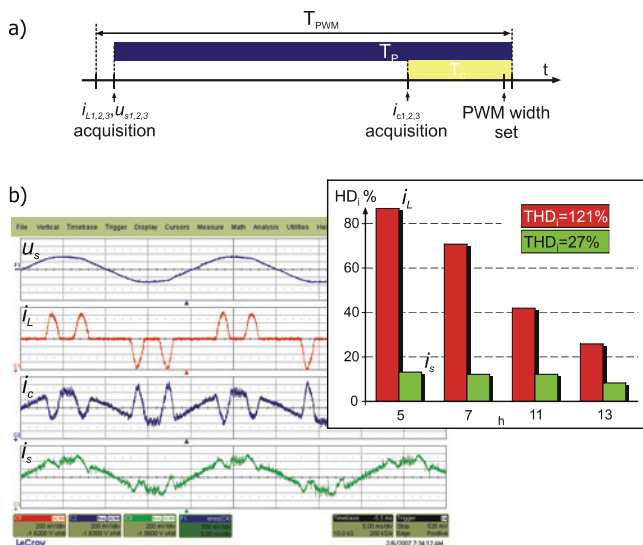


Fig. 7. a) Illustration of the processing delays $T_P=55 \mu s$, $T_C=12 \mu s$ b) APF voltage, current waveforms and harmonic distortion for i_s and i_L current. The experimental results for a six-pulse bridge rectifier with RC load

After control algorithm optimization and correcting T_P time to $17 \mu s$, a considerable improvement of APF performance has been achieved. Experimental results for this case have been presented in Fig. 8.

A floating-point unit is not available in TMS320F2812 processor [10]. Because there is no hardware system to perform floating point, it has to be emulated in software. These operations are very slow, because in case of floating-point numbers, the numbers have to be converted, operated on, and then converted back into their format. An alternative to the floating-point emulation libraries is using fixed-point routines.

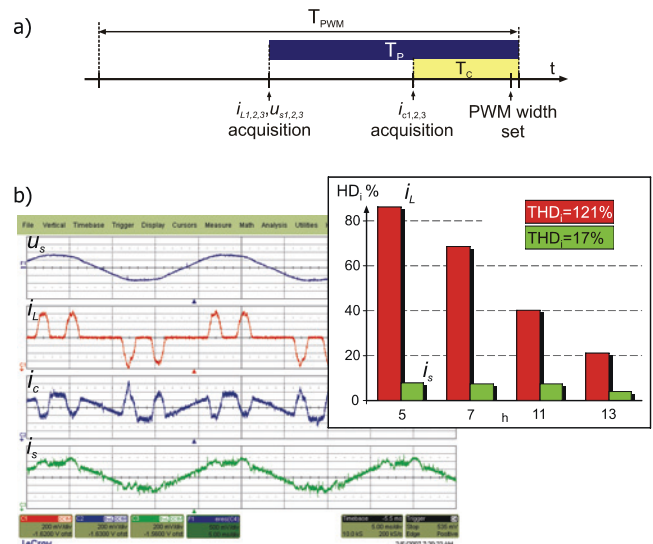


Fig. 8. a) Illustration of the processing delays $T_P=17 \mu s$, $T_C=12 \mu s$ b) APF voltage, current waveforms and harmonic distortion for i_s and i_L current. The experimental results for a six-pulse bridge rectifier with RC load

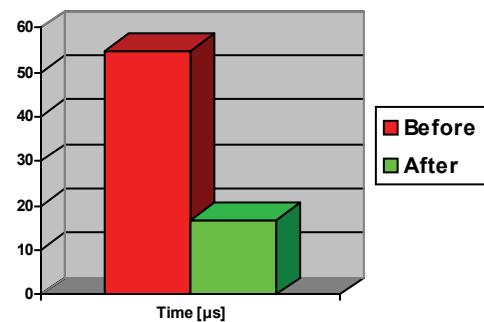


Fig. 9. Illustration of the execution run time before and after optimization

Table1. Example of optimization

| Before optimization |
|--|
| $Ic = \text{AdcRegs.ADCRESULT0} \gg 4;$ |
| $Uc = \text{AdcRegs.ADCRESULT3} \gg 4;$ |
| $Ib = \text{AdcRegs.ADCRESULT2} \gg 4;$ |
| $Ub = \text{AdcRegs.ADCRESULT5} \gg 4;$ |
| $Ia = \text{AdcRegs.ADCRESULT4} \gg 4;$ |
| $Ua = \text{AdcRegs.ADCRESULT7} \gg 4;$ |
| $Uaf = -(0.03663 * (\text{float})Ua - 80.25);$ |
| $Ubf = -(0.03663 * (\text{float})Ub - 80.25);$ |
| $Ucf = -(0.03663 * (\text{float})Uc - 80.25);$ |
| $Iaf = (0.003663 * (\text{float})Ia - 8.25);$ |
| $Ibf = (0.003663 * (\text{float})Ib - 8.25);$ |
| $Icf = (0.003663 * (\text{float})Ic - 8.25);$ |
| $Ualfa = 0.81649658 * (\text{float})Uaf$ |
| $\quad - 0.40824829 * (\text{float})(Ubf + Ucf);$ |
| $Ubeta = 0.707106781 * (\text{float})(Ubf - Ucf);$ |
| After optimization and conversion |
| $Ic = \text{AdcRegs.ADCRESULT0} \gg 4;$ |
| $Uc = \text{AdcRegs.ADCRESULT3} \gg 4;$ |
| $Ib = \text{AdcRegs.ADCRESULT2} \gg 4;$ |
| $Ub = \text{AdcRegs.ADCRESULT5} \gg 4;$ |
| $Ia = \text{AdcRegs.ADCRESULT4} \gg 4;$ |
| $Ua = \text{AdcRegs.ADCRESULT7} \gg 4;$ |
| $Ualfa = ((31363 * (\text{long})Ua - 15680 * (\text{long})(Ub + Uc)) \gg 16);$ |
| $Ubeta = (27158 * (\text{long})(Ub - Uc)) \gg 16;$ |
| $Ialfa = ((50181 * (\text{long})Ia - 25089 * (\text{long})(Ib + Ic)) \gg 16);$ |
| $Ibeta = (43453 * (\text{long})(Ib - Ic)) \gg 16;$ |

A global refactoring and source code optimization was made to improve the execution run time. An example of the optimization has been shown in Table 1.

This execution improvement is noticeable as it has been presented by the experimental results (Fig.9).

Conclusions

The experimental results presented in this paper show that even very short delays in control processing cause worsening of the active power filter performance. Shortening of the processing time by using a more efficient digital signal processor or control algorithm optimization may considerably improve APF performance. Applying of a parallel processing or constructing a controller as an analog circuit [4] may be an interesting solution. Unavoidable are deviations which come from finite transistors switching frequency or errors in method of reference compensating currents assigning (e.g. supply voltage distortion).

REFERENCES

- [1] Akagi H., Kanazawa Y., Nabae A.: Generalized theory of the instantaneous reactive power in three-phase circuits. *Proc. of the Int. Power Electron. Conf., (IIEE IPEC)*, 1983, 1375–1386
- [2] Akagi H., Kanazawa Y., Nabae A.: Instantaneous Reactive Power Compensators Comprising Switching Devices without Energy Storage Components. *IEEE Transactions on Industry Applications*, Vol. 1A-20, No. 3, May/June 1984, 625-630.
- [3] Akagi H., Nabae A.: The p-q Theory in Three-Phase Systems under Non-Sinusoidal Conditions. *ETEP* Vol.3, No. 1, January/February 1993, 27-31.

- [4] Buła D.: Conception of an analog controller of active power filter. *VIII OWD, Wiśła*, October 2006, 225-230
- [5] Buła D., Maciążek M., Pasierbek A., Pasko M.: Three-phase active power filter based on TMS320F2812 processor. *XXIX IC-SPEO, Ustroń*, May 2006. 372-376.
- [6] Maciążek M., Pasko M.: The control algorithm of active power filter based on instantaneous power theory (p-q). *ZN. Pol. Śl. „Elektryka”*, Nr 182, Gliwice 2002, 69-87.
- [7] Maciążek M., Pasko M.: Wybrane zastosowania algorytmów numerycznych w optymalizacji warunków pracy źródeł napięcia. *Monografia (pod patronatem Komitetu Elektrotechniki PAN)*, Gliwice 2007.
- [8] Pasko M., Maciążek M.: Teoria mocy p-q poprawna teoria czy użyteczny algorytm sterowania kompensatorów kluczujących. *Przegląd Elektrotechniczny*, Nr 6, 2006, 34-39.
- [9] Pasko M., Maciążek M.: Teoria mocy p-q poprawna teoria czy użyteczny algorytm sterowania kompensatorów kluczujących – podsumowanie. *Przegląd Elektrotechniczny*, Nr 10, 2006, 73-76.
- [10] Digital Signal Processors - TMS320F2812, Data Manual - SPRS174N, *Texas Instruments*, (2001).

Authors:

prof. dr hab. inż. Marian Pasko, e-mail: marian.pasko@polsl.pl,
dr inż. Marcin Maciążek, e-mail: marcin.maciazek@polsl.pl,
mgr inż. Dawid Buła, e-mail: dawid.bula@polsl.pl, *Instytut Elektrotechniki Przemysłowej i Informatyki, Zakład Elektrotechniki Teoretycznej, Informatyki i Telekomunikacji, ul. Akademicka 10, 44-100 Gliwice.*

Analysis of second order LTV section with exponentially varying parameters

Abstract. In this paper the model of second order parametric section with exponential varying parameters has been presented. The effect of analyze is the formula describing the section response to any excitation with finite average power. The physical implementation of section has also been showed. The results have been illustrated by simulation example.

Streszczenie. W artykule zaproponowano model sekcji parametrycznej drugiego rzędu o parametrach zmiennych eksponencjalnie. Przeprowadzona analiza doprowadziła do zależności określających odpowiedź sekcji na wymuszenie w postaci dowolnego sygnału o skończonej mocy. Pokazano również fizyczną implementację rozpatrywanej sekcji parametrycznej. Uzyskane wyniki zilustrowano przykładem symulacyjnym. (Analiza sekcji parametrycznych z parametrami zmiennymi eksponencjalnie)

Keywords: parametric section, LTV filter

Słowa kluczowe: sekcje parametryczne, filtry o zmiennych parametrach

Introduction

The universal sections is of great importance in linear electric circuits LLS (Linear, Lumped, Stationary) synthesis in particular first and second order sections [1]. Those sections are elementary blocks which enable to build more complex filters including filters with different properties. Parametric filters can be used in measurement chains of signal processing, stochastic signals analysis and synthesis, speech and image signal processing, in automatic control [4,5] and other branches.

The model of the linear time-varying (LTV) section is further referred to simply as the parametric section. One can get the model of parametric section by varying parameters in differential equation describing stationary section. Depending on the time waveform of the varying coefficient parametric systems can be divided into two basic groups:

- sections for which the waveform is a periodic or almost periodic function [3,6],
- sections for which the waveform is a linear combination of a constant and limited energy functions [4,6,7,8].

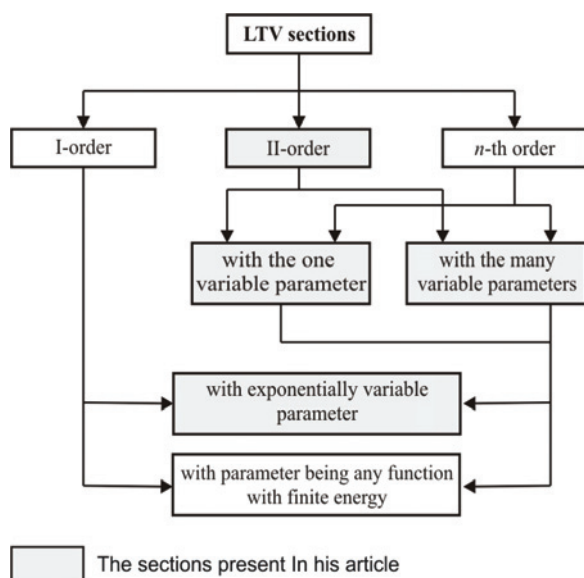


Fig. 1. The classification of the LTV section with non-periodic varying parameters.

This paper concerns systems belonging to the second of mentioned earlier groups. Further classification of this group has been shown in Fig. 1.

Analysis of first order parametric section has been presented in papers: [7,8]. In the paper [7] a model of the first order parametric section with exponentially variable parameter has been described, whereas in the paper [8] a section with parameter $\alpha(t)$ being any function with finite energy has been presented. Parametric function has been expressed there by its generalized Fourier series. The basis of the series is a set of linear combination of exponential functions. Both papers mentioned above show how to calculate system response to any excitation with finite average power. The continuation of analysis LTV sections has been included in works [9,10,11] and this article in which the responses to the any excitation of the second order LTV section with exponentially varying parameters has been carried out.

1. Analysis of the second order LTV section

Model of second order LTV section is described by the differential equation with varying parameters:

$$(1) \quad y''(t) + 2\sigma(t)\omega_0 y'(t) + \omega_0^2(t)y(t) = kx(t),$$

$x(t)$ – input signal of section (excitation); $y(t)$ – output signal of section (section response); k – gain coefficient for constant component; ω_0 – angular limit frequency (cut-off frequency); σ_0 – attenuation ratio.

In order to analyze dynamic properties of the second-order parametric section one ought to consider the following cases:

- I. Second order LTV section with varying coefficient $\omega_0^2(t)$
- II. Second order LTV section with varying coefficient $2\sigma(t)$
- III. Second order LTV section with simultaneous variation of both coefficients: $\omega_0^2(t)$ and $2\sigma(t)$.

Variability of parametric functions

Processes in parametric systems are described by differential equations where coefficients depend on time. Solutions to these equations are not always known therefore exact analysis is possible only for special cases of function variability of parameters. In this paper equation of LTV section with variability of parameters described by equations (2) and (3) has been considered. Coefficient γ describes the time in which the stationary value is reached and is the same for both parametric functions.

$$(2) \quad 2\sigma(t) = \sigma_0 + De^{-\gamma t}; \quad D \in [-\sigma_0, \infty); \quad \gamma > 0; \quad \sigma_0 > 0,$$

$$(3) \quad \omega_0^2(t) = \omega_0 + Ce^{-\gamma t}; \quad C \in [-\omega_0, \infty); \quad \gamma > 0; \quad \omega_0 > 0.$$

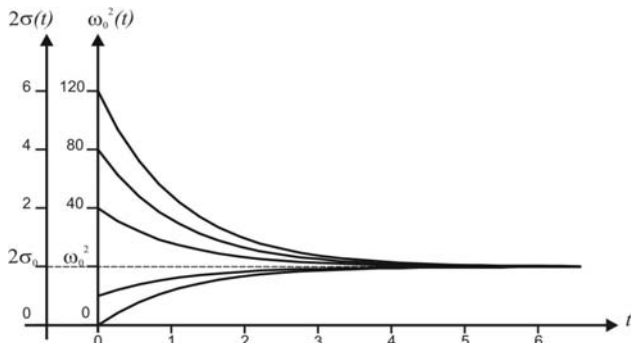


Fig. 2. Examples of waveform of the parametric functions.

Assumed variability of the coefficients makes both parametric functions strictly positive.

1.1 Filter response to any excitation $x(t)$

Particularly analysis in time domain for three cases mentioned before has been carried out in works [9,10,11] and in this article. This analysis show how to determine the section responses to any excitation $x(t)$. The response for section with zero initial conditions is given by formula (4) [6,9,10,11]:

$$(4) \quad y(t) = A \left[\int_0^t [q_2(t)q_1(\tau)x(\tau) - q_1(t)q_2(\tau)x(\tau)] e^{-a(\tau)} d\tau \right] e^{a(t)}.$$

The coefficients and functions in equations (4) are defined as: A – constant coefficient for every cases [9,10,11].

For case I ($\omega_0^2(t)$ –var, σ_0 –const)

$$(5) \quad a(t) = -\sigma_0 \omega_0 t,$$

$$(6) \quad q_1(t) = J_\nu \left(-\frac{2}{\gamma} \sqrt{C} e^{-\frac{\gamma}{2}t} \right),$$

$$(7) \quad q_2(t) = Y_\nu \left(-\frac{2}{\gamma} \sqrt{C} e^{-\frac{\gamma}{2}t} \right),$$

$$(8) \quad \nu = -\frac{2}{\gamma} \sqrt{\omega_0^2(\sigma_0 - 1)},$$

where: $J_\nu(\cdot)$ –First kind Bessel function of non-integral order ν [5]; $Y_\nu(\cdot)$ - Second kind Bessel function of non-integral order ν [5].

For case II ($2\sigma_0$ –var, $\omega_0^2(t)$ –const)

$$(9) \quad q_1(t) = e^{-\frac{\omega_0 D}{2\gamma} e^{-\gamma t} - \frac{-\omega_0 \sqrt{\sigma_0^2 - 4}}{2} t} {}_1F_1(\alpha, \beta; z),$$

$$(10) \quad q_2(t) = e^{-\frac{\omega_0 D}{2\gamma} e^{-\gamma t} - \frac{-\omega_0 \sqrt{\sigma_0^2 - 4}}{2} t} {}_1F_1(\alpha - \beta + 1, 2 - \beta; z),$$

where:

$$(11) \quad a(t) = \frac{\omega_0}{2} \left(\frac{D}{\gamma} e^{-\gamma t} - \sigma_0 t \right),$$

$$(12) \quad \alpha = \frac{\omega_0 \sigma_0}{2\gamma} + \frac{\omega_0 \sqrt{\sigma_0^2 - 4}}{2\gamma},$$

$$(13) \quad \beta = 1 + \frac{\omega_0 \sqrt{\sigma_0^2 - 4}}{\gamma},$$

$$(14) \quad z = \frac{\omega_0 D}{\gamma} e^{-\gamma t},$$

${}_1F_1(\alpha, \beta; z)$ –confluent hypergeometric function [5].

For case III ($2\sigma_0$ –var, $\omega_0^2(t)$ –var)

$$(15) \quad a(t) = \frac{\omega_0}{2} \left(\frac{D}{\gamma} e^{-\gamma t} - \sigma_0 t \right),$$

$$(16) \quad q_1(t) = e^{-\frac{\omega_0 D}{2\gamma} e^{-\gamma t} - \frac{-\omega_0 \sqrt{\sigma_0^2 - 4}}{2} t} {}_1F_1(\alpha, \beta; z),$$

$$(17) \quad q_2(t) = e^{-\frac{\omega_0 D}{2\gamma} e^{-\gamma t} - \frac{-\omega_0 \sqrt{\sigma_0^2 - 4}}{2} t} {}_1F_1(\alpha - \beta + 1, 2 - \beta; z),$$

thus:

$$(18) \quad \alpha = \frac{1}{4\gamma} \left(2C + \gamma(D\omega_0 - 2) - \omega_0(4\sqrt{\sigma_0^2 - 4} + D\sigma_0\omega_0) \right),$$

$$(19) \quad \beta = 1 + \frac{\omega_0 \sqrt{\sigma_0^2 - 4}}{\gamma},$$

$$(20) \quad z = \frac{\omega_0 D}{\gamma} e^{-\gamma t}.$$

The equation (4) determines in a closed form the filter response to any signal $x(t)$ with finite average power.

If the input signal $x(t)$ is represented by the generalized Fourier series:

$$(21) \quad x_1(t) = \sum_{n=0}^{\infty} X_n e_n(t),$$

where: X_n – series coefficients, $e_n(t)$ – set of basis function

and analytical formula determining integrals of products of functions $q_1(t)$, $q_2(t)$ and basic functions $e_n(\cdot)$ exist, then the solution to equation (4) exists in a closed form. Otherwise, the integrals should be computed using numerical methods.

2. Realization of the second order low pass LTV filter

Structure of the universal filter has been presented in Fig. 3. The transfer function which is determined in the output indicated by U_2 is the transfer function of the low-pass filter and is given by [1]:

$$(22) \quad H_{LP} = \frac{U_2}{U_1} = \frac{1}{s^2 + \frac{1}{R_1 C_1} s + \frac{R_2 R_4 C_1 C_2}{R_2 R_3 R_5 C_1 C_2}}.$$

In the time domain transfer function (22) is equivalent to the differential equation:

$$(23) \quad u_2''(t) + \frac{u_2'(t)}{R_1 C_1} + \frac{R_6 u_2(t)}{R_2 R_3 R_5 C_1 C_2} = \frac{u_1(t)}{R_2 R_4 C_1 C_2}.$$

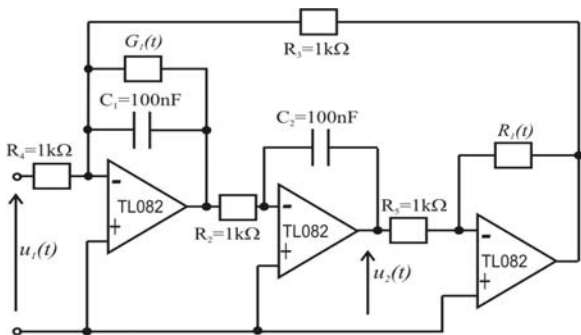


Fig. 3. Structure of the LTV second order filter with variable parameters

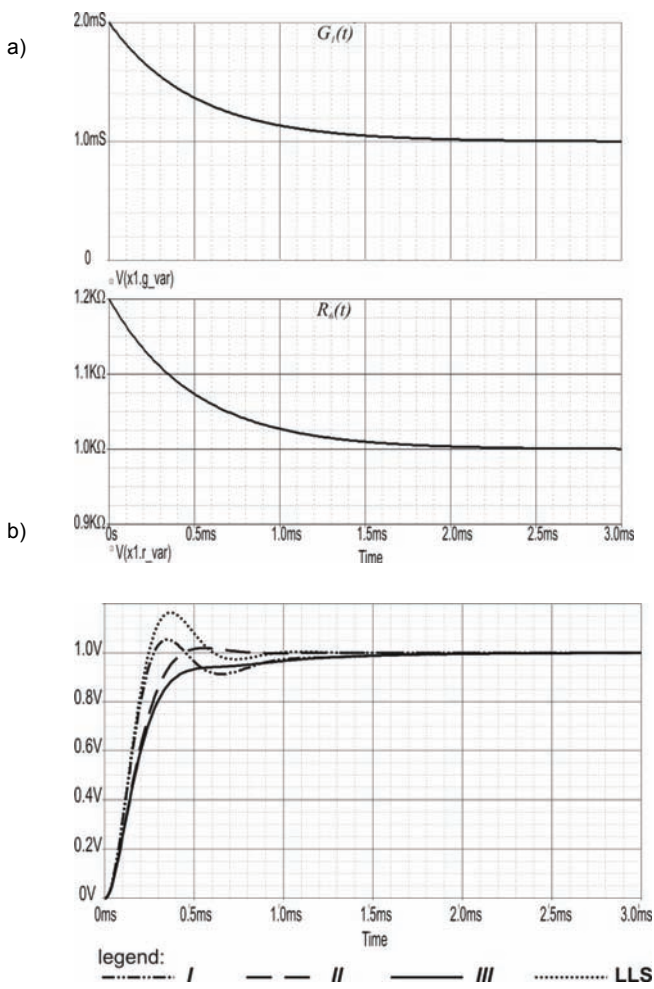


Fig. 4. Results of PSpice simulation No. 1
a). waveforms of the conductance $G_1(t)$ and resistance $R_6(t)$, variability
b). step responses of the filters

It is easy to notice, that varying the parameters $G_1(t)=1/R_1$ and $R_6(t)$ varies the coefficient of the equation located by the functions $u_2'(t)$ and $u_2(t)$ thus it becomes the equation analyzed in this article (24):

$$(24) \quad u_2''(t) + \frac{G_1(t)u_2'(t)}{C_1} + \frac{R_6(t)u_2(t)}{R_2 R_3 R_5 C_1 C_2} = \frac{u_1(t)}{R_2 R_4 C_1 C_2}.$$

Methods of realization of variable resistance and conductance are known from literature e.g. [2]. The circuit shown in Fig 5 has been analyzed for few sets of the functions $G_1(t)$ and $R_6(t)$. The waveforms of those functions have been presented in Fig. 4a, 5a, 6a. Results of simulations are comparisons in one graph the step responses of three cases LTV filters analyzed in this article: with one varying parameter $G_1(t)=var$ and $R_6=const$, with one varying parameter $G_1=const$ and $R_6(t)=var$, and with simultaneous variation of both parameters $G_1(t)=var$ and $R_6(t)=var$ (Fig. 4b, 5b, 6b).

In order to present the influence of the parametric function variability on LTV filter dynamic properties the step responses have been compared with step response of classical LLS filter with constants parameters.

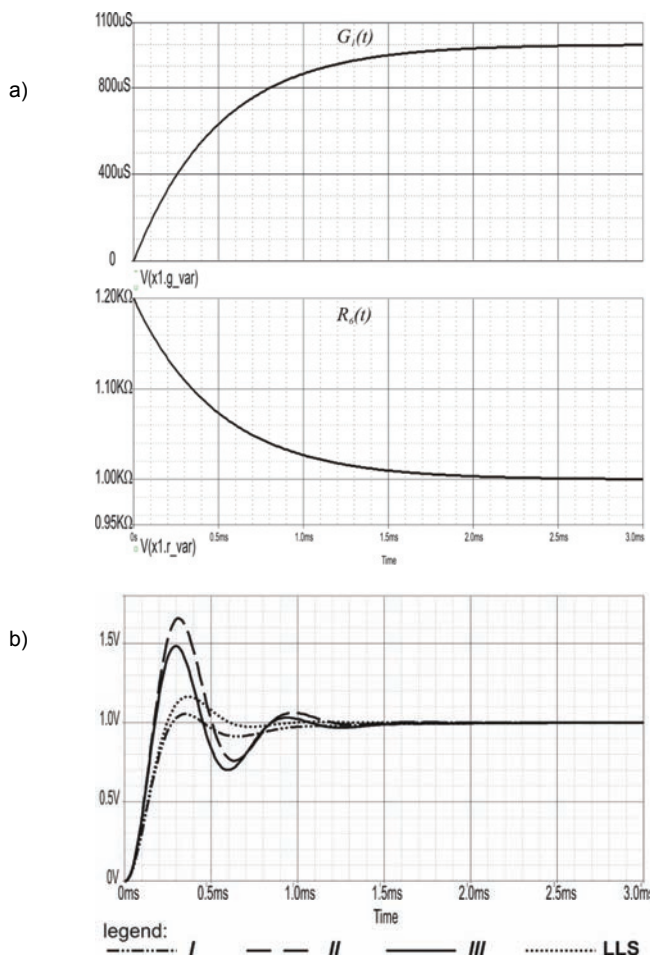


Fig. 5. Results of PSpice simulation No. 2
a). waveforms of the conductance $G_1(t)$ and resistance $R_6(t)$, variability
b). step responses of the filters

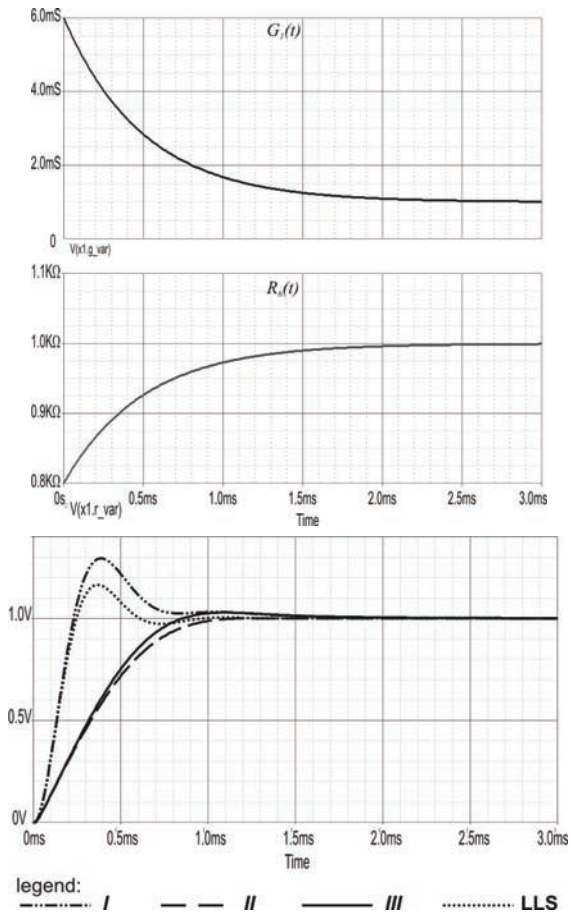


Fig. 6. Results of PSpice simulation No. 3
a). waveforms of the conductance $G_I(t)$ and resistance $R_o(t)$, variability
b). step responses of the filters

3. Conclusions:

Results of presented analysis and simulations shown that changes in the character of the function variation result in modification of dynamic properties of the system.

It allows to find optimal structures and determine values of parameters for expected filter properties (e.g. dynamic characteristic, noise reduction etc.) In the stationary state the sections with variable parameters are equivalent to LLS sections.

If the coefficients of equation are varying, the responses will be different for different time moments of switching on the signal to the system input. The mentioned effect is typical for nonstationary systems and does not exist in LLS systems.

REFERENCES

1. Chen W. K.: *The Circuits and Filters Handbook* IEEE Press, New York, 1995.
2. Czarnul Z.: *Novel MOS Resistive Circuit for Synthesis of Fully Integrated Continuous – Time Filters* IEEE Trans. on Circuits and Systems, Vol. 3, Issue 7, 1986, s. 718-721.
3. D'Angelo H.: *Linear Time-Varying Systems. Analysis and Synthesis*, Allyn and Bacon, Inc. Boston 1970.
4. Kaszyński R.: *Low-pass and signal constant component filters with time varying parameters*, No.569, Wyd. Naukowe Pol. Szczecińskiej, Szczecin 2001 (in polish).
5. Polyanin, A. D., Zaitsev, V. F.: *Handbook of Exact Solutions for Ordinary Differential Equations*, 2nd Edition, Chapman & Hall/CRC, Boca Raton, 2003.
6. Richards J. A.: *Modelling Parametric Processes—A Tutorial Review*, IEEE Proc., 1977, No 65, s. 1549-1557.
7. Walczak J. Romanowska A.: *First order parametric sections*, Conf. ZKwE'2006, April 2006, pp. 97-98.
8. Walczak J. Romanowska A.: *Generalized first order parametric sections*, Conf. ICSPETO'2006, May 2006, pp. 293-296.
9. Walczak J., Romanowska A.: *Second order parametric sections* ZKwE'2006 Monograph, Poznań 2006.
10. Walczak J., Romanowska A.: *Second order parametric sections with a time-varying attenuation radio* Zeszyty Elektryka, Gliwice 2007, (in polish) (in reprint).
11. Walczak J., Romanowska A.: *Second order parametric sections with both varying parameters* Conf. ICSPETO'2007, May 2006, pp. 107-109 (short text), CD No. 054 (full text).

Authors: prof. dr hab. inż. Janusz Walczak, mgr inż. Anna Romanowska; Politechnika Śląska, Wydział Elektryczny, Instytut Elektrotechniki Przemysłowej, Informatyki i Telekomunikacji; ul. Akademicka 10, 44-100 Gliwice. E-mail: Janusz.Walczak@polsl.pl, Anna.Romanowska@polsl.pl.

Parallel computations of transient processes in the electric circuits in cluster systems

Abstract. A parallel process of computation of transient processes in the electric circuits is based on a diakoptic theory of the portioning of the circuit into the sub-circuits, that are computed independent of each other, in the fixed time intervals. Every process is defined by the complexity of computation. This complexity is changed in the time of process of computations. These properties are utilized to implement computation in cluster systems. Currently the growth of cluster systems has been observed for several years. In this article, advantages and disadvantages of the cluster system in computations of transient processes in the electric circuits are presented. An example of the algorithm, that ensures optimal automatic control of the process of computations in the cluster system is shown. The method of dynamic creations of tasks to reach the minimum summary waiting time is received.

Streszczenie. Równoległa realizacja obliczeń analizy stanów dynamicznych obwodów elektrycznych bazuje na diakopcyjnym podziale obwodu na pod-obwody, które w określonych krokach czasowych obliczane są niezależnie od siebie. Każdy taki proces charakteryzuje się dużą złożonością obliczeniową, która w trakcie procesu obliczeniowego może ulegać zmianie. Właściwości te pozwalają na zastosowanie do obliczeń systemów klastrowych, których dynamiczny rozwój jest obserwowany od kilku lat. W artykule przedstawiono krótką charakterystykę systemów klastrowych i omówiono wady i zalety stosowania ich do obliczeń stanów dynamicznych obwodów elektrycznych. Zaprezentowano przykład algorytmu realizującego automatyczne sterowanie klastrem, zapewniające optymalne rozłożenie procesu obliczeniowego na poszczególne węzły klastra. Dzięki temu otrzymano sposób dynamicznego tworzenia zadań w celu minimalizacji sumarycznego czasu oczekiwania. (Równoległe obliczenia w modelowaniu stanów nieustalonych w obwodach elektrycznych przy pomocy systemów klastrowych)

Keywords: transient analyze, parallel computation, cluster systems, diakoptic.

Słowa kluczowe: analiza stanów przejściowych, obliczenia równoległe, systemy klastrowe, diakoptyka.

Introduction

Computation of complex systems is always connected with necessity of making a large number of step by step mind-numbing calculations. Firstly, it causes a huge waste of time, secondly, the possibility that mistakes and inaccuracies will appear is increasing very fast. Moreover, existing novel computer technologies do not eliminate factors mentioned above. Therefore, it is necessary to look for possible variants of changing a particular serial complicated process of computation for a few independent simplest procedures of calculation, which would enable to get the same solution in several computational stages. Mathematical theory which is needed to get this attitude is known and was created and systematized in Kron's work. [1]. This mechanism was adapted to a specificity of theory of the circuit's tasks in works [5,4]. In this chapter an idea of diakoptical attitude to implementation parallel computation of transient processes of electric circuit will be presented. We assume that particular electric circuit will be replaced with three sub-circuits, as we can see in the picture 1. Each of separate pieces of chart include a number of variables which contain a set of internal and external variables.

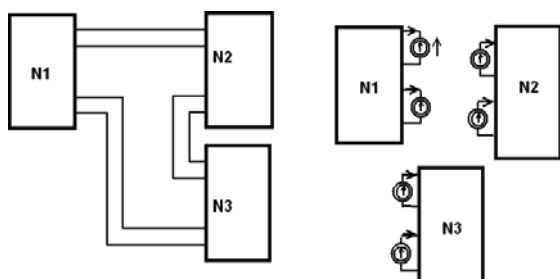


Fig.1. Diakoptic method of division of electric circuit

Internal variables in this case are currents and voltages on the elements inside sub-circuits N_1 , N_2 , N_3 , while external variables are independent currents and voltages ($\{i_1, i_2, i_3, i_4\}, \{u_{12}, u_{23}, u_{34}, u_{25}\}$), on external nodes of these sub-circuits. A rule of diakoptic attitude according to concept of the circuit theory is as follows:

We assume that values of variables are known (it can be calculated because the initial conditions are known). Assuming that values of external variables are fixed we

increase a time-variable to a particular value and we calculate new values of internal variables.

Using calculated earlier internal variables we find new values of external variables for each particular external nodes of sub-circuit. As the new values of external variables will not suit to the conditions of their sub-circuits connections, we have to do a correction according to the location of a particular connection. Afterwards we go to the first point and we repeat the whole procedure. As we can see in a sequence that was shown above the process mentioned in the second point is executed independently for each particular sub-circuit N_1 , N_2 , N_3 . It enables to run a parallel procedure of calculation for every sub-circuit, which can be shown with the help of the block graph below. It is noticeable that these processes of computation take most of the time, so it may be useful to implement these methods to parallel processing.

So algorithm of computation of transient states of electric circuit according to diakoptic attitude is shown in a general outline (fig. 2).

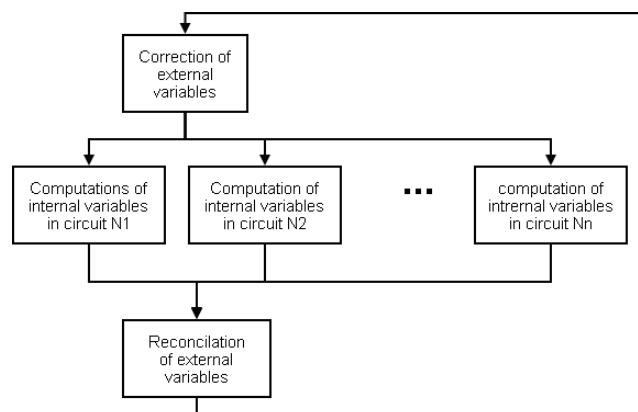


Fig. 2. Schema of diakoptic computations of electric circuit.

As you can see this algorithm has two parts of computation. One of them is a group of independent parallel processes, the second is a procedure of agreement of external variables. The time of computation of one parallel task is much longer than a time of correction of external variables. In all parallel tasks we must resolve a set of

integral equations, in the second part only a set of algebraic equations is resolved.

The process of numerical computation of integral equation is asynchronous. The values of external variables come from the previous step of computation. In consequence, a method of explicit integration must be used. In theory this method is computationally unstable. In the correction step the problem of stability must be estimated. At this moment the methods of estimations of stability are known. If instability is found, the process of computation is stopped, the step of integration is changed and the process of computations starts from the beginning. It means that the total time of computation will be increased.

In this article a problem of computation of transient processes realized in cluster system was presented. In the next part of the article cluster systems are presented.

Cluster systems

One of the methods of parallel computations is the usage of cluster systems. A cluster is kind of parallel or distributed system, which consists of a set of connected computers and it is used as one computer system. Differences between SMP parallel systems (*Symmetric Multi-Processor*) and cluster systems are clear.

Firstly, the scalability of the system. The rebuilding of cluster is very easy. Whenever it is needed we can connect or disconnect every node of the cluster. A node is a full computer with memory and system of input – output. SMP systems are closed. We cannot add many processors without rebuilding other parts of the SMP system.

Secondly, availability of a breakage of one processor in SMP system means stopping all system. If the node is damaged the cluster does not stop working. Only tasks from this node must be relocated.

Thirdly, the management of SMP system is easier than distributed system such as a cluster system. Cluster systems are divided into two groups according to their usage:

- Systems with a main task of reliability in accidents of failure of one or more nodes.
- Systems oriented on parallel computation.

In the next paragraph elements of operating system of cluster are discussed.

Environment of cluster systems

A cluster system consists of modules that ensure functionality of the system:

Cluster System Management (CSM) is designed to minimize the cost and complexity of administering clustered and partitioned systems by enabling comprehensive management and monitoring of the entire environment from a single point of control. CSM provides:

- Software distribution, installation and update (operating system and applications)
- Comprehensive system monitoring with customizable automated responses
- Distributed command execution
- Hardware control
- Diagnostic tools
- Management by group
- Both a graphical interface and a fully scriptable command line interface

In addition to providing all the key functions for administration and maintenance of distributed systems, CSM is designed to deliver the parallel execution required to manage clustered computing environments effectively.

General Parallel File System (GPFS) is a high-performance cluster file system that provides users with shared access to files spanning multiple disk drives. By

dividing individual files into blocks and reading/writing these blocks in parallel across multiple disks, GPFS provides very high bandwidth; in fact, GPFS has won awards and set world records for performance. In addition, GPFS's multiple data paths can also eliminate single points of failure, making GPFS extremely reliable. GPFS currently powers many of the world's largest scientific supercomputers and is increasingly used in commercial applications requiring high-speed access to large volumes of data such as digital media, engineering design, business intelligence, financial analysis and geographic information systems. GPFS is based on a shared disk model, providing lower overhead access to disks not directly attached to the application nodes, and using a distributed protocol to provide data coherence for access from any node.

Job scheduling is used for dynamic workload scheduling, Workload Scheduler is a distributed network-wide job management facility designed to dynamically schedule work such as maximize resource utilization and minimize job completion time. Jobs are scheduled based on job priority, job requirements, resource availability and user-defined rules to match processing needs with resources.

High Performance Math Libraries. This scientific subroutine library is a collection of state-of-the-art mathematical subroutines specifically tuned to hardware and offering significant performance improvement to any math-intensive scientific or engineering applications. Parallel subroutines extend the function of library to support parallel applications. Math and Parallel libraries support C, C++ and Fortran applications.

Parallel application development is a comprehensive development and execution environment for parallel applications (distributed-memory, message-passing applications running across multiple nodes). It is designed to help organizations develop, test, debug, tune and run high-performance parallel applications in C, C++ and Fortran on clusters.

Geographic clustering and disaster extends high availability capabilities across geographic sites with remote data mirroring (replication) and failover using this mirrored data. This combination can maintain application and data availability even if an entire site is disabled by a disaster.

Computational problems of diakoptic method of analysis of electric circuits

Partitioning of electric circuit into sub-circuits is executed on the level of electric schema. Mathematical models of sub-circuits consist of different numbers of integral equations. It means that every sub-circuit needs different computational resources. Necessity of correction of external data needs synchronicity of computational task.

Another problem is estimation of computational stability after all points of correction.

Estimation of stability bases on analysis of changes of values of external variables of sub-circuits. At this point of computation all variables must be known. It means that all mathematical models of sub-circuits must be resolved to the point of correction. A set of algebraic equations must be resolved so as to correct the values of external variables. It means that computations of sub-circuits must be stopped, external variables must be corrected and stability ratio must be estimated. If stability ratio is fulfilled, computations are resumed. In case of instability the step of integration must be reduced, and computations must be restarted. It means that the total time of computations must be increased by the time of repeated computations.

Rules of cluster systems for diakoptic computation.

A cluster system consists of defined number of nodes. All nodes are described by computational power and speed

of communication. The number of nodes can be changed during computations. In this approach a restriction is assumed, that the mathematical model of sub-circuit is an independent and indivisible computational process. This limitation reduces the exchange of information between nodes. The transfer of data is reduced to sending of input and receiving output data, and intermediate results of computations.

Speed of parallel diakoptic computations depends on optimal organization of tasks and good job scheduling used for dynamic management of computational tasks.

Special algorithm for optimal scheduling of tasks is proposed in the next section.

Algorithm of tasks distribution in cluster system

A new algorithm of task scheduling was created. It is optimised for diakoptic model of computations. The algorithm is presented on the diagram shown in figure 3.

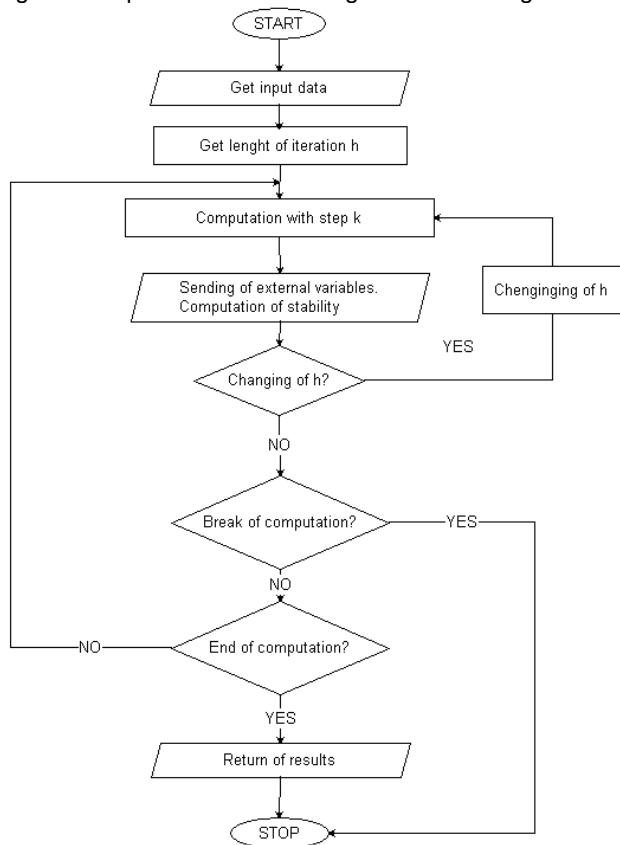


Fig.3. Algorithm of computation in node of the cluster

In this algorithm a case of stopping of computations after every iteration is implemented. Management system can stop computations in every moment and move it into a new node. It depends on the system of job scheduling. For example: computations of one sub-circuit will be started on a few nodes with different steps of integrations and after correction and estimation of stability, system management stops unnecessary tasks. This problem occurs in one large schema consisting of one big sub-circuit and all little sub-circuits.

The algorithm of distributions of tasks is shown in figure 3. The cluster system management, after distribution of tasks, collects output data. With a full set of results it runs a task of computation of correction and estimation stability. After the procedure of optimisation, system management redistributes tasks between nodes and waits for results of the next step of computations.

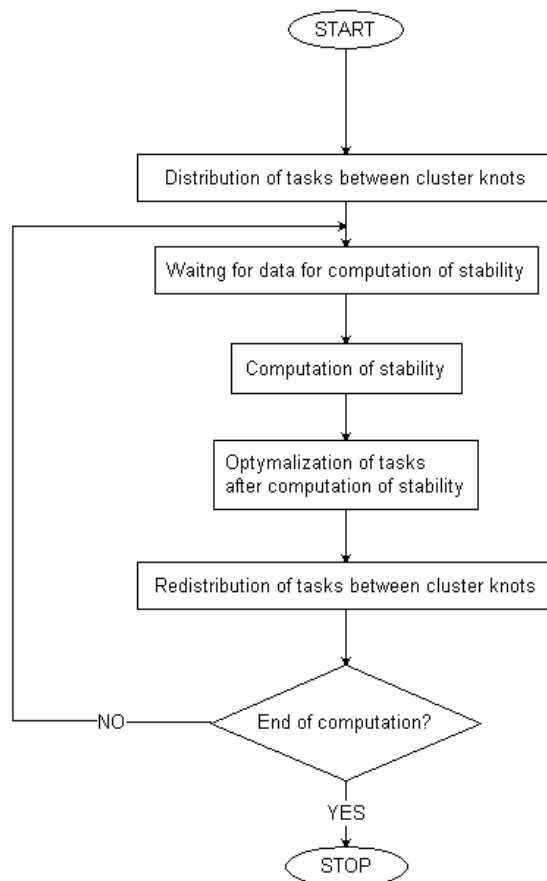


Fig.4. Algorithm of tasks distribution

Conclusion

In this article the model of computations in cluster system is presented, which is optimized for parallel execution of tasks of analyses of transient states in electric circuits. The rules of distributions of tasks and steering of processes were shown. The problem of synchronous computations of stability of diakoptic method was taken into account.

REFERENCES

- [1] [1] G. Kron, A set of principles to interconnect the solution of physical systems, *Journal of applied Physics*, vol 24, no. 8, August 1953, page. 980
- [2] [2] H. H. Happ., Diakoptics and Piecewise Methods, *IEEE Transactions on Power Apparatus and Systems*, vol 89, no. 7, September/October 1970, page 1373
- [3] [3] BM., IBM System Cluster 1350, *IBM Corporation*, CLD00221USEN-15, 2006.
- [4] P. Stakhiv, Анализ динамических режимов в электронных схемах с многополюсниками, Lviv 1988.
- [5] H. H. Happ, Diakoptics and Networks. New York: Academic Press, 1971
- [6] P. Stakhiv, S. Rendzinyak, B. Krupskyy, Parallelization of Diakoptic Methods for Multiprocessor Computing Systems, *BULLETIN OF THE POLISH ACADEMY OF SCIENCES TECHNICAL SCIENCES Vol. 51, No. 4, 2003*
- [7] P.M. Petkovic, S. Dordevic, V. Litovski, A new approach to symbolic analysis of large circuits, *Proc 22nd International Conference on Microelectronics (MIEL 2000)*, vol 2, Serbia 14-17 MAY, 2000

Authors: prof. dr hab. inż. Liliana Byczkowska-Lipińska, Politechnika Łódzka, Instytut informatyki, ul. Wólczańska 215, 93-005 Łódź, E-mail: spg@ics.p.lodz.pl; mgr inż. Marcin Cegielski, Politechnika Łódzka, Instytut informatyki, ul. Wólczańska 215, 93-005 Łódź, E-mail: mceg@ics.p.lodz.pl.

2.5D tomographic imaging for ultrasonic investigations

Abstract. Tomography image is obtained on the basis of measurements (of the average value) got during projections, using reconstruction algorithm based on Radon transform. For this reason the geometry of tomography measurements plays an important part during reconstruction of the object. In presented case an algorithm using algebraic reconstruction techniques (based on function approximation through finite series) was used. The image is constructed with the help of algorithm which digitize the diagnosed area to the quadratic cells, which geometric centers are handled like pixels in the image. Imaging multipath system with different sets of emitters and receivers placed in the same plane (2,5D reconstruction) have been used. This is the way leading to the real 3D.

Streszczenie. Do tworzenia tomograficznych obrazów wykorzystywane są często algorytmy bazujące na transformacie Radona, które przetwarzają dane uzyskiwane w poszczególnych projekcjach z pomiarów średnich wartości czasów przebiegów fal ultradźwiękowych w badanym środowisku. Z tego powodu geometria pomiarów tomograficznych ma istotny wpływ na rekonstrukcję obrazów badanych obiektów. W przedstawionym przypadku zastosowano algorytmy z grupy metod algebraicznych, bazujących na metodologii aproksymacji funkcji przez szeregi o skończonej długości. Obraz odtwarzany jest przy pomocy algorytmu dyskretyzującego badany obszar do postaci kwadratowych komórek, których środki geometryczne traktowane są jako piksele w odtwarzanym obrazie. System obrazowania wielościeżkowego z różnymi konfiguracjami nadajników i odbiorników umiejscowionych w jednej płaszczyźnie (rekonstrukcja 2,5 D) został zastosowany w omawianym przypadku. Jest to metoda, która umożliwi tworzenie obrazów tomograficznych w przestrzeni 3D. (Tomograficzne obrazowanie z wykorzystaniem przestrzeni 2,5D w badaniach ultradźwiękowych).

Keywords: multipath flowmeters, tomographic imaging, ultrasonic tomography

Słowa kluczowe: tomografia ultradźwiękowa, obrazowanie tomograficzne, wielościeżkowy przepływomierz ultradźwiękowy.

Introduction

The ultrasonic flowmeters using transit time or time of flight method are widely used for industrial flow velocity measurement [9].

Multipath systems with different sets of emitters and receivers are used in order to enlarge the accuracy of measurement. In described system an equally spaced sensors around the pipe perimeter were placed in perpendicular (Fig. 2) or coaxial (Fig. 1) surfaces of the pipe's axis.

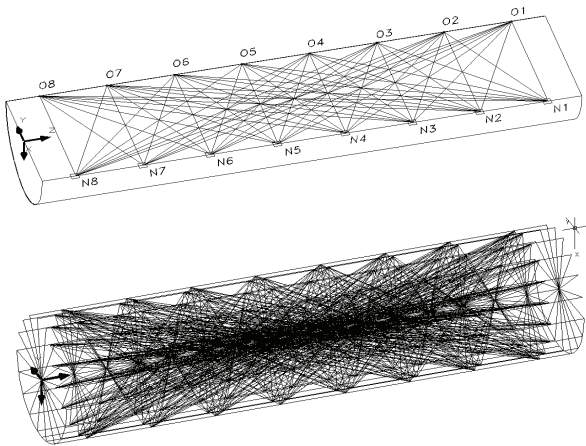


Fig. 1. Measuring paths between all transmitters (N) and all receivers (O) placed in coaxial surfaces to pipe's axis

If we assume that the transmitters emit ultrasound waves of not too high frequencies, than the angle of spreading groups of waves is big enough to allow them to reach all of the receivers placed in pipe's perimeter (Fig. 2).

In analyzed system the transmitters one by one generates ultrasound impulses, which with different delays reach all receivers. The time duration of these waves are the basis to calculate the average value of measured flow's speed. The average value of flow's

speed is insufficient to define correctly the flow velocity profile in whole pipe's cross section [4].

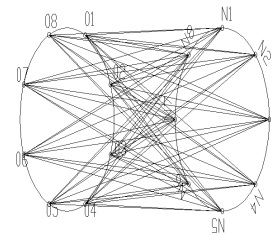


Fig. 2. Measuring paths between all transmitters (N) and all receivers (O) placed in perpendicular surface to the pipe's axis [7]

The image of all vectors of speed which appeared in examined pipe's cross section is required in order to reconstruct the velocity profile.

Such algorithm, called in the literature 2,5D imaging is leading to the full 3D tomographic imaging.

The inverse problem solution

In presented case an algorithm from algebraic reconstruction techniques (based on function approximation through finite series) was used [4]. The image is constructed with the help of algorithm which digitize the diagnosed area to the quadratic cells, which geometric centers are the pixels in the image.

Velocity profile image construction in a plane of receivers means estimation of a set of unknown values, which we can denote as $f(x,y)$. Let us assume, that in each cell of the square grid, the function $f(x,y)$ is constant. The relationship between the f_j 's and s_i 's may be expressed as [1,2]:

$$(1) \quad \sum_{j=1}^n w_{ij} f_j = s_i, \quad i = 1, 2, \dots, m$$

We are looking for set of solutions of $[s_1, s_2, \dots, s_m]^T$ which equally well satisfy all of equations (1), but

every measured value is determined with an error. So, in order to solve this problem we have to look for a global minimum in an n -dimensional space.

The iterative methods, based on the “method of projections” as first proposed by Kaczmarz are very useful for solving this problem. One of them is named ART (ang. *Algebraic Reconstruction Technique*) [2].

Problem of image construction in case of the ultrasonic flowmeters very often leads to the overdetermined algebraic set of equations, which in matrix form can be expressed [7, 8]:

$$(2) \quad Wf = s$$

where: W is the matrix of dimensions $m \times n$ and $m > n$, $s = [s_1, s_2, \dots, s_m]^T$ – right hand side vector, and $f = [f_1, f_2, \dots, f_m]^T$ – the solution vector.

One of the ways of the solution of the problem (1) is to find the vector f , which minimize Euclidean norm of residual vector r for the known matrix W and vector s [11]. This is Linear Least Squares Problem (LSP) [1, 3, 5].

In order to calculate the solution of the Problem LS and analyzing the influence of data errors, we have used the Singular Value Decomposition (SVD) theorem.

To select the proper candidate solution the compromise between the smallest residual and solution norm have to be selected. In the literature this criterion is known as L curve – criterion [3].

A numerical experiment was carried out on synthetic data without noise (Fig. 4b). Unfortunately (among the others) an immanent feature of the tomography is the fact, that the coefficient matrix is a rectangular and very often pseudo – rank deficient one. Therefore it is necessary to consider the candidate solutions [1, 3] and choose one of them using L curve – criterion.

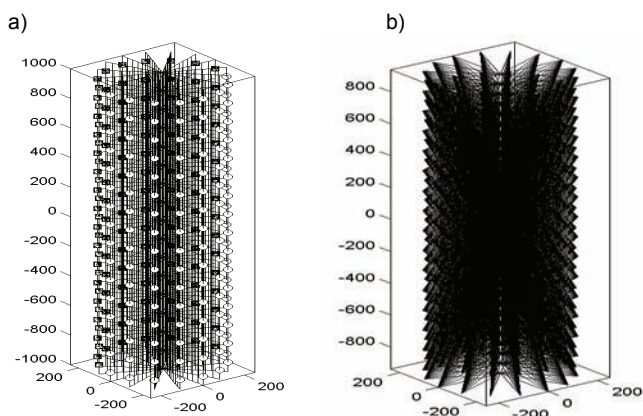


Fig. 3. Measurement area: a) 2,5D imaging of the measurement area; b) Measuring paths between all transmitters and all receivers placed in one coaxial surface

Numerical experiment

In the Fig. 3 measurement area was presented. 2,5D modeling of space was achieved by rotation of the measurement surface around the vertical axis (Fig. 3a).

In this paper the 2,5D technique which allows to get 3D solutions in much easier way, was used.

The difficulty in solving the space problem lies in the necessity of calculation of points which arise by the punctuation of space element called voksel (showed in Fig. 4) with the ray (the line connecting transmitter and receiver).

Technique 2,5D simplifies the solution of this issue to the problem of calculating the points of intersection with the flat element (rectangular pixel).

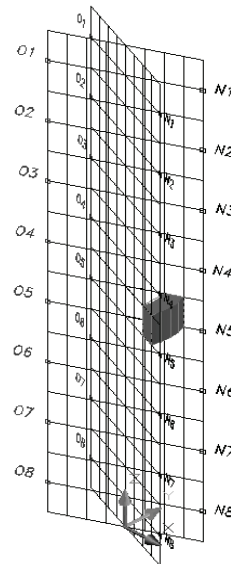


Fig. 4. Voksel in the measurement area

In this model, the simplified flow's speed distribution changing linearly from the smallest values at the walls to the highest values in the axis of flow (Fig. 5b), was imposed.

The suggested measurement system does not assure the sufficient precision in the whole measurement range, what has to be taken into consideration. To this end the window which limits the measurement area to it's central part in the simulated system (Fig 5a) was introduced. For such a window the solution of flow's speed was obtained. The results are shown in Fig. 6a and 6b.

In the Fig. 6c there is a chart of distribution of singular values, which could help to select the proper candidate solution if the L – shaped curve criterion is not calculated.

The diagram (Fig. 6b) shows some differences between the obtained results and assumed data. The character of flow's changes has been kept but shows some discrepancies in relation to linearity. It is probably caused by this, that the coefficient matrix W was solved with the simplified method.

Obtained results confirm the fact, that the method based on SVD and in particular the choice of candidate's solution is effective method to achieve a real image [5, 6].

Theoretical and experimental researches carried out in this work prove that by increasing the number of radiuses which cross a measurement area we increase the size of column vector s and the number of rows in the matrix of W factors from $Wf = s$ equation.

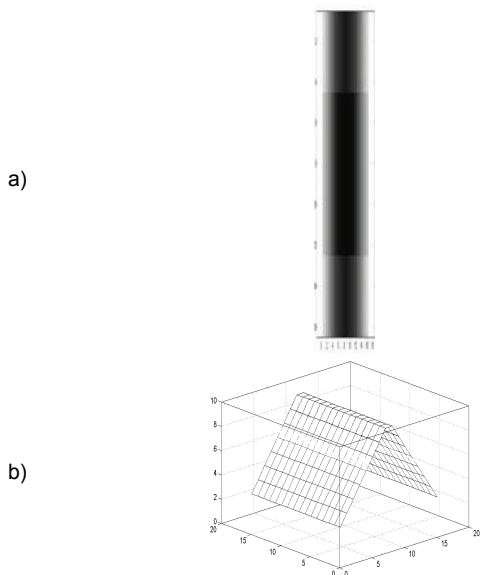


Fig. 5. The window in measurement area; a) the image, b) the relief plot

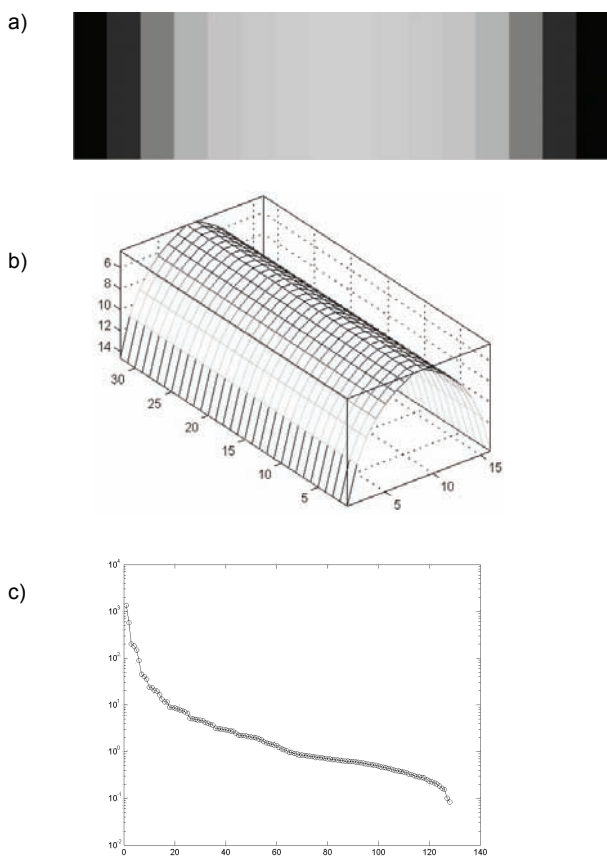


Fig. 6. Results of calculations; a) the image, b) the relief plot, c) distribution of singular values

The number of rays should be selected in reasonable and considered way, thinking about image's quality and algorithm's execution time. By increasing the size of the resolution of the square grid (increase number of pixel) we cause a rise of the number of columns in coefficient matrix of \mathbf{W} factors. On the other hand, the higher resolution of the square grid, the projected object has more

details and it is more similar to the pattern. We should notice that with growth of the resolution of the square grid, the number of used rays has to be increase proportionally.

Conclusions

2,5D calculations, give a chance to get results which reflect the phenomenon in the analyzed 3D area, very accurately. The obtained results are quite satisfying and further work should give the answer on the question, if the proposed method will find practical application.

The simplification of calculations with assuring the sufficient accuracy in making tomography images of analyzed physical phenomenon should succeed in faster imaging.

This issue is important because the contemporary tomography is expected to bring real time, tomography images of dynamically changing environment.

REFERENCES

1. Guziak T., Kamińska A., Pańczyk B., Sikora J.: *Metody numeryczne w elektrotechnice*, Wydawnictwa Politechniki Lubelskiej, Lublin, wyd. III (2002)
2. Kak A. C., Slaney M.: *Principles of Computerized Tomographic Imaging*, IEEE Press, (1999)
3. Lawson C. L., Hanson R. J.: *Solving Least Squares Problems*, Classics in Applied Mathematics 15, SIAM (1995)
4. Opielński K.: *Analiza możliwości zobrazowania struktury wewnętrznej obiektów metodą ultradźwiękowej tomografii transmisyjnej*. Praca doktorska, Instytut Telekomunikacji i Akustyki Politechniki Wrocławskiej, Wrocław (1998).
5. Polakowski K., Sikora J., Filipowicz S. F.: *Linear Least Squares Problem for Image Forming of Multipath Ultrasound Tomography*, 7th International Workshop "Computational Problems of Electrical Engineering", Odessa, Ukraina, (August 28–30, 2006), pp. 5–9
6. Polakowski K., Sikora J., Filipowicz S. F.: *Ultrasound Tomography Imaging based on linear Least Squares Problem*, 4rd International Symposium on Process Tomography In Poland, Warszawa, Sep. 14–15 2006, pp. 79–84
7. Polakowski K., Sikora J., Kaczorowski P., Kaźmierczak J., Filipowicz S. F.: *Liniowe zadanie najmniejszych kwadratów w konstrukcji obrazów wielościeżkowej tomografii ultradźwiękowej*, Przegląd Elektrotechniczny, R. LXXXII (10/2006), pp. 18–24
8. Sikora J.: *Numeryczne algorytmy w tomografii impedancyjnej i wiropądowej*, Oficyna Wydawnicza Politechniki Warszawskiej Warszawa (2000)
9. Sikora J., Zacharopoulos A., Douiri A., Schweiger M., Horesh L., Arridge S.R. and Ripoll J.: *Diffuse photon propagation in multilayered geometries*. Physics in Medicine and Biology, vol. 51, (2006), pp. 497-516
10. Śliwiński A.: *Ultradźwięki i ich zastosowania*, WNT, Warszawa (1993).

Krzysztof Polakowski, Warsaw University of Technology, Institute of Electrical Machines, Pl. Politechniki 1, 00-661 Warszawa, E-mail: kp@zkue.ime.pw.edu.pl;

Jan Sikora, Warsaw University of Technology, Institute of the Theory of Electrical Engineering, Measurement and Information Systems, Pl. Politechniki 1, 00-661 Warszawa, E-mail: sik@nov.iem.pw.edu.pl;

Stefan F. Filipowicz, Warsaw University of Technology, Institute of the Theory of Electrical Engineering, Measurement and Information Systems, Pl. Politechniki 1, 00-661 Warszawa, E-mail: 2xf@nov.iem.pw.edu.pl

Stability of parallel computations of transient processes in the electric circuits

Abstract. A diakoptic method of the analysis of transient processes in the electric circuits shows a certain lack of asynchrony of the process of computation. External variables are computed with a delay in relation to internal variables. It means that implicit methods of integration are used in computation. The main disadvantage of implicit methods is potential instability that may be controlled in the phase of fitting external variables. Nowadays, the methods of improving stability and the methods of predicting instability are known. The main problem of the estimation of instability in its high cost, which directly influences the total cost of computation. In this article new criteria of estimation of stability based on features of the electric circuits were proposed, such as voltage or impedance. This feature was used to optimize the partitioning of circuits and selection of the step of computation to secure the computation process. The effectiveness of the selection of these parameters will be confirmed by computer experiments.

Streszczenie. Analiza stanów dynamicznych obwodów elektrycznych za pomocą podejścia diakoptycznego wykazuje pewną niesynchronizację procesu obliczeń, która polega na tym, że zmienne zewnętrzne są obliczane z pewnym opóźnieniem w stosunku do zmiennych wewnętrznych. To oznacza, że koniecznym staje się użycie jawnych metod numerycznego całkowania, których wadą jest potencjalna niestabilność. W danej chwili znane są sposoby, które pozwalają zdecydowanie polepszyć stabilność obliczeń jak i również pozwalają ją przewidzieć. W artykule zostały zaproponowane nowe kryteria oceny stabilności, bazą, których są parametry obwodów elektrycznych. Skuteczność doboru tych elementów została potwierdzona za pomocą eksperymentów komputerowych. (Stabilność obliczeń równoległych w symulacji stanów nieustalonych w obwodach elektrycznych)

Keywords: transient analyse, parallel computation, diakoptic.

Słowa kluczowe: analiza stanów przejściowych, obliczenia równoległe, diakptyka.

Introduction

Analysing of transient processes in the electric circuits requires a lot of complex computations. It is connected with the necessity of the solution of the differential equations. A number of differential equations depends on the size and complexity of electric circuit. The analysis of the electric circuit means solving a set of differential equations. The time of computations is directly conditioned by the size of circuits. The main idea of increasing computation process is the diakoptic method of division of the circuit into sub-circuits and their independent computation. The division of the circuit is achieved on the level of electric schema. Sub-circuits are extracted from the main schema and the nodes of the division are replaced with controlled voltage or current sources. This method of division of the circuit is shown in figure 1.

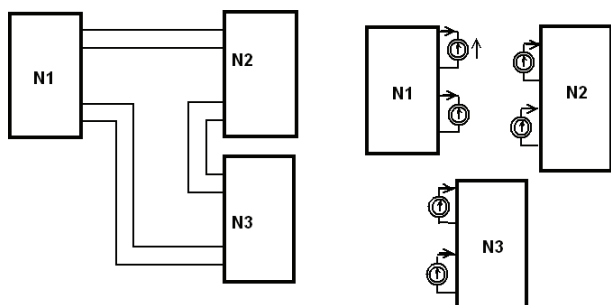


Fig.1. Diakoptic method of division of the electric circuit

Mathematical models of sub-circuits can be computed independently. All sub-circuits consist of internal variables, that represent currents and voltages inside the model and external variables that represent currents and voltages of controlled sources. We can say that connections between the parts of the circuit are modelled by the controlled sources in the sub-circuits. This approach involves the procedure of agreement of external variables between successive steps of computations. Since transient values of external variables come from the previous results of the step of computations of the

mathematical model, we must use explicit methods of integrations. The disadvantage of this method of numerical integration is potential instability of the processes of computation. The main important element of computations is the problem of stability estimation. In this article a new criteria of estimation stability were proposed, based on the parameters of electric circuits, such as voltage or impedance. The efficacy of selection of these criteria is confirmed by computer experiments.

Mathematical model of the diakoptic method

The diakoptic model of the circuit gives a set of the following equations:

$$(1) \quad F_i(X_i, V, Y) = 0 \quad i = 1, 2, \dots, N$$

$$(2) \quad G(X, V, Y) = 0$$

where X_i is a vector of internal variables of the i -th circuit; $X = X_1, X_2, \dots, X_n)^T$; V, Y are vectors of additional input and output variables; $F_i(\cdot)$ is a set of differential equations that describe dynamic processes in the i -th sub-circuits; $G(\cdot)$ is a set of algebraic equations that represents the separate sub-circuits interaction.

The essence of the diakoptic approach is an independent solution (numerical integration) of each equation (1), and sequential matching of obtained results by solving equations (2). It is possible to solve equations (1) both in particular time intervals and in separate iterations. The integration process of these equations in time domain is known as waveform relaxation method and as the practice has shown is the most effective.

Each iteration of waveform integration algorithm contains three stages of evaluations:

- 1) integration of the separate sub-circuit during one forward step;
- 2) estimations of stability and corrections of constraint variables and selection of corrections step;
- 3) integration of all sub-circuits to a point of corrections.

Example of making of the diakoptic model

Look at the schema of electric circuit shown in figure 2.

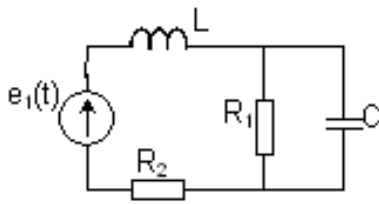


Fig.2. Schema of electric circuit

This circuit is divided into two independent sub-circuits. The nodes of division are replaced with the equivalent controlled sources, as shown in figure 3.

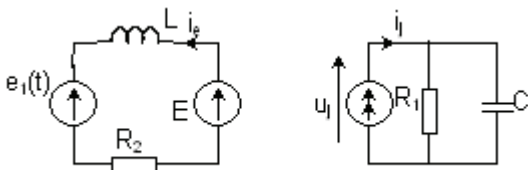


Fig.3. Schema of electric sub-circuits

Mathematical model of the first circuit is represented by the set of equations (3) and second sub-circuit (4).

$$(3a) \quad -e_1 + E - L \frac{di_E}{dt} - i_E R_2 = 0$$

$$(3b) \quad i_E = x_1$$

$$(4a) \quad I - \frac{u_j}{R_1} - C \frac{du_j}{dt} = 0$$

$$(4b) \quad u_j = x_2$$

Values of the external variables between the sub-circuits, that have to agree with each other, are shown in (5) and (6).

$$(5) \quad E = u_j$$

$$(6) \quad -I = i_E$$

By substituting equations (5) to (3), and (6) to (4) we receive equations of models of sub-circuits (7) and equations (8).

$$(7a) \quad \frac{dx_1}{dt} = \frac{R_2}{L} x_1 - e_1 + E$$

$$(7b) \quad \frac{dx_2}{dt} = -\frac{x_2}{R_1 C} + I$$

$$(8) \quad \begin{cases} E = x_1 \\ -I = x_2 \end{cases}$$

The values of external variables E and I are unknown and values have to be taken from the previous step of numerical integration. It means that we must use explicit methods of numerical integration to solve (7). The explicit methods are known as unstable. Stability of computation is equivalent to value of the step of numerical integration h . The value of h is equivalent to the cost of computation and it influences sub-divisional error indirectly, but on the other hand, it minimizes probability of instability of computations. Therefore optimal selection of h is so important.

The method of estimation of computational stability of numerical integration is testing of external values of mathematical models of sub-circuits, which are corrected after each particular step of integration.

We can see, if the differences between equivalent external variables are less then these values in previous step, then probability of instability is less.

New methods of estimations of stability are presented in the next section.

Estimation stability of computations

The first method proposed of stability estimation bases on the analysis of changes of values of external variables. We assume, we must correct currents i_1 and i_2 , in sub-circuits, as shown in figure 4.

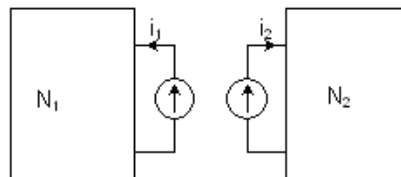


Fig.4. Schema of electric comparable circuits

The Kirchoff Law tells, that values of currents i_1 and i_2 should be equivalent. In the diakoptik method this currents are computed independently and their values can be different. It is shown in equation (9).

$$(9) \quad |i_1 + i_2| = \varepsilon$$

where ε is a difference in one step of computation.

If the difference ε will grow in the next step, it means that process of computations can be unstable.

As a result of experiments, a new method of stability estimation was proposed. This coefficient is a ratio between changes of currents or voltages in sub-circuits. It is illustrated in formula (10a, 10b).

$$(10a, 10b) \quad K_1 = \frac{\Delta i_1}{\Delta i_2} \quad K_2 = \frac{\Delta u_1}{\Delta u_2}$$

In the next method we can check changes of signs of currents or voltages in sub-circuits. If changes of current's directions are not synchronized, it means instability.

The method from formula (10) can be modified by values of computation steps of sub-circuits. We can say that changes of i_1 and i_2 are normalized to each other. It is shown on formulas (11) for currents:

$$(11a, 11b) \quad K_2 = \frac{h_2 \Delta i_2^{(1)}}{h_1 \Delta i_1^{(2)}} \quad \bar{K}_2 = \frac{h_2 \Delta i_1^{(1)}}{h_1 \Delta i_2^{(2)}}$$

and formulas (12) for voltages

$$(12a, 12b) \quad K_2 = \frac{h_2 \Delta u_2^{(1)}}{h_1 \Delta u_1^{(2)}} \quad \bar{K}_2 = \frac{h_2 \Delta u_1^{(1)}}{h_1 \Delta u_2^{(2)}}$$

In the next case, external nodes of sub-circuits are modelled by different types of sources. The coefficients of estimations of computation probability are modified. We are interested in finding changes of equivalents of currents or voltages in sub-circuits.

The next case of circuit division bases on heterogeneous types of sources. We are interested in analyses of changes of current and voltage in sub-circuits. It is shown in figure 5.

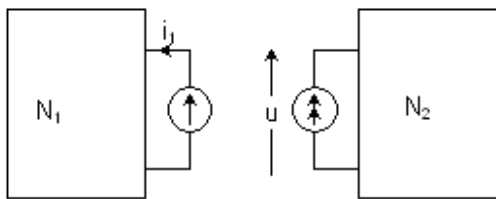


Fig.5. Schema of electric circuits with heterogeneous sources

Coefficient K_i in formulas (10)...(12), is divided by its current or voltage. This values from different sub-circuits we can compare to each other. Equivalent formula in (10a) is converted to (13).

$$(13a, 13b) \quad K_1 = \frac{\Delta i_1}{i_1} \quad K_1 = \frac{\Delta u_2}{u_2}$$

Formula (14) is a proposition of estimation stability in two neighbor steps of numerical integration.

$$(14a, 14b) \quad K_2 = \frac{\frac{\Delta u_1^{(1)}}{u_1^{(1)}}}{\frac{\Delta i_2^{(2)}}{i_2^{(2)}}} \quad K_2 = \frac{\frac{\Delta i_1^{(1)}}{i_1^{(1)}}}{\frac{\Delta u_2^{(2)}}{u_2^{(2)}}}$$

Results of computer experiments

Coefficient K was computed from the mathematical model RLC circuit from figure 1 and 2, where integrations step of sub-circuits were equal to $h_1=h_2=h$.

In these experiments coefficient K was estimated from equation (10). The value $K_i < 1,7$ means that the process of computation is stable and the value $K_i > 2,3$ means unstable process of computation. Changing of directions of currents or voltages has 85% efficacy of stability detection.

Analogical results of experiments were obtained for models with different controlled sources (fig. 5).

The value $K_2 < 1,7$ means stable process and the value $K_2 > 2,2$ means unstable. Changes of directions of currents or voltages were similar as for homogeneous sources and accounted for 85% probability of instability occurring.

Conclusion

From these analyses, estimation of computation stability can be divided into stages. Stability can be estimated after the first step of integration without any complicated computations (formula 10, 13). If the condition of stability is satisfied then the process of computations starts with the next step. After this step, the ratio of stability is computed by all formulas. If the condition of stability are fitful in formulas (10), (13), then it is computed by formula (12) or (14), which should strengthen the evaluation results.

The method of estimation stability needs a few computations of coefficients and results can be reached after first step iteration. The total time of computation of mathematical model can be reduced,

REFERENCES

- [1] H. H. Happ., Diakoptics and Piecewise Methods, IEEE Transactions on Power Apparatus and Systems, vol 89, no. 7, September/October 1970, page 1373
- [2] K. Strunz., E. Carlson, Nested Fast and Simultaneous Solution for Time-Domain Simulation of Integrative Power-Electric and Electronic Systems, IEEE Transactions on Power Delivery, vol 22, no. 1, January 2007, page 277
- [3] P. Stakhiv, S. Rendzinyak, B. Krupskyy, Parallelization of Diacoptic Methods for Multiprocessor Computing Systems, BULLETIN OF THE POLISH ACADEMY OF SCIENCES TECHNICAL SCIENCES Vol. 51, No. 4, 2003
- [4] L. Chua, L. Chen, IEEE Transactions on Circuits and Systems, vol cas-23, no. 12, December 1976, page 694
- [5] P.M. Petkovic, S. Dordevic, V. Litovski, A new approach to symbolic analysis of large circuits, Proc 22nd International Conference on Microelectronics (MIEL 2000), vol 2, Serbia 14-17 MAY,2000

Authors: prof. dr hab. inż. Petro Stakhiv, Politechnika Łódzka, Instytut informatyki, ul. Wólczańska 215, 93-005 Łódź, E-mail: spg@ics.p.lodz.pl; mgr inż. Marcin Cegielski, Politechnika Łódzka, Instytut informatyki, ul. Wólczańska 215, 93-005 Łódź, E-mail: mceg@ics.p.lodz.pl.

A time-varying capacitance: control function of active power filters

Abstract. This paper proposes new fixed switching frequency control techniques for power active filters. The method is based on an auxiliary capacitance function. This function is equivalent to time-varying capacitance. Such capacitance function can be computed when reference signal is known. The fixed switching frequency control techniques for PWM voltage source inverter can be easily obtained when the auxiliary capacitance function is known. Auxiliary capacitance functions have been derived for single phase and three-phase structure. The simulation of the circuit with two time-varying capacitances shows that such circuit generates required harmonics.

Streszczenie. Praca zawiera nowy algorytm obliczania chwil przełączeń aktywnego filtra mocy o stałej częstotliwości przełączania. Metoda wykorzystuje pomocniczą funkcję pojemności równoważną pojemności zmiennej w czasie. Funkcję tę można wyznaczyć, korzystając z wzorcowego przebiegu prądu. Pokazano sposób wyznaczania funkcji pojemności dla układu trójfazowego. Symulacje wykonane dla układu trójfazowego z filtrem mocy zawierającym dwa kondensatory pokazały, że układ generuje pożądane harmoniczne. (**Zmienna pojemność – funkcja sterowania aktywnych filtrów mocy**).

Keywords: power active filters, control techniques, current harmonics generation.

Słowa kluczowe: filtr aktywny mocy, algorytm sterowania, generowanie harmonicznego prądu.

Introduction

The active filtering is one of the most challenging applications for digital current controls [1,2,3]. There are many methods and algorithms for current control of voltage source converter generating desired current waveforms. The hysteresis band controller is a most popular current controller in active filters. By using hysteresis band controller, it is not possible to control the switching frequency [4,5]. To ensure the fixed switching frequency control other techniques should be developed. In this paper a new algorithm of constant switching frequency control in stationary periodical state is considered. The method is based on a time-varying capacitance function. Such function can be computed if the reference signal, which should be traced, is known. The reference signal for a current controlled compensator can be worked out from the distorted current [2,4] of identified load or from distorted voltage when a nonlinear load is unidentified [6].

Time-varying model of voltage source converter

The single-phase topology of the voltage source converter generating desired current waveform is shown in Fig.1.

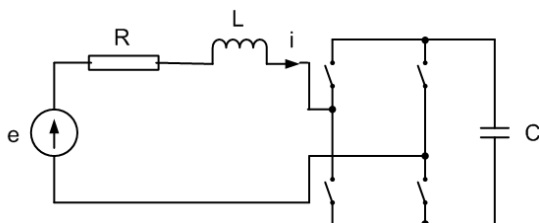


Fig. 1. Switched circuit generating harmonics

The properly switched circuit should generate such current i which is as close to reference signal as possible. Now, we assume that this signal is known and circuit in Fig. 1 is switched in such way, that current i has desired waveform.

For averaged signal the switched circuit shown in Fig. 1 can be replaced by model containing time-varying capacitance, as shown in Fig. 2 [7, 8].

The problem can be stated as follows: determine time function $C(t)$ which causes that system current has desired

waveform $i(t)$. For given parameters R and L of the supplying system the problem can be solved solving the following equations

$$(1) \quad v(t) = e(t) - L \frac{di(t)}{dt} - Ri(t)$$

$$(2) \quad q(t) = \int_0^t [i(\tau) - Gv(\tau)] d\tau + q(0)$$

$$(3) \quad K(t) = \frac{1}{C(t)} = \frac{v(t)}{q(t)}$$

where $v(t)$ - capacitor voltage, $q(t)$ - capacitor electrical charge, $C(t)$ - time-varying capacitance. The inverse of time-varying capacitance $K(t)$ will be further called an auxiliary capacitance function. Initial charge $q(0)$ should be properly chosen in order to fulfill the following condition

$$(4) \quad q(t) > 0$$

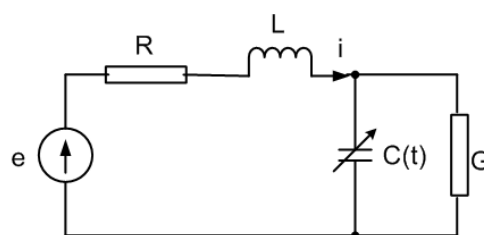


Fig.2. Time-varying circuit modeling the switched circuit of Fig. 1

Such auxiliary function enables one to generate the required current waveform. It is difficult to realize a capacitor whose capacitance is a continuous time function. An approximation of such function can be obtained in the well known switched circuit shown in Fig. 1. The current i in both circuits shown in Fig. 1 and Fig. 2 differs only by high frequency pulsation appearing in the switched circuit. The switched circuit of Fig. 1 is equivalent to the circuit shown in Fig. 3a. The time varying capacitance $C_s(t)$ is changing like this shown in Fig. 3b.

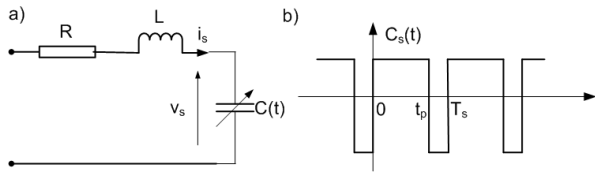


Fig. 3. Model of the circuit containing the switched capacitor : a) structure of the circuit, b) waveform of the capacitance

Current i_s in Fig. 3a is

$$(5) \quad i_s(t) = \frac{dq_s(t)}{dt} = \frac{d[C_s(t)v_s(t)]}{dt}$$

The example waveforms of capacitor charge $q_s(t)$ and capacitor voltage $v_s(t)$ for fixed switching period T_s smaller then time-constant L/R are shown in Fig. 4.

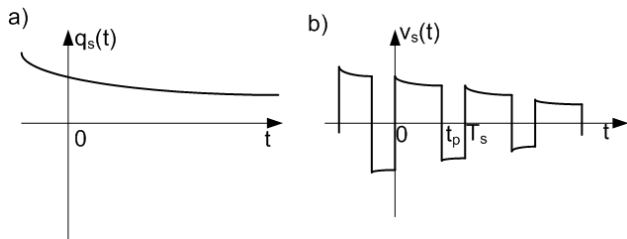


Fig. 4. Waveforms in the circuit shown in Fig. 3b: a) electric charge, b) capacitor voltage

Current i_s can be controlled if the capacitor charge remains positive, $q_s(t) > 0$. With such assumption, it is more suitable to operate with the inverse of capacitance $K_s(t) = 1/C_s(t)$ instead of capacitance $C_s(t)$. Let function $K_s(t)$ has the form of the rectangular wave like $C_s(t)$ shown in Fig. 3b. To synthesize desired current with the use of the auxiliary function $K(t)$, the average function $\overline{K_s(t)}$ can be defined

$$(6) \quad \overline{K_s(t)} = \left(2 \frac{t_p(t)}{T_s} - 1\right) K_m$$

where K_m is the amplitude of the rectangular wave.

Comparing average function $\overline{K_s(t)}$ to $K(t)$ defined in (3) it is possible to compute switching time $t_p(t)$ when capacitance function $K(t)$ is known

$$(7) \quad t_p(t) = \left(1 + \frac{K(t)}{K_m}\right) \frac{T_s}{2}$$

Using formula (7) the example of third harmonic generation is presented.

Example – third harmonic generation in the switched circuit

Assume that third current harmonic should be generated in the switched circuit shown in Fig. 1. The results presented in Fig. 5, 6 and 7 have been obtained for the following circuit parameters: $e = 600 \sin(314t)$, $L = 10 \text{ mH}$, $R = 0.08 \text{ } \Omega$, $C = 128.2 \text{ } \mu\text{F}$, switching losses modeled by additional conductance shunted the capacitor $G = 0.00013 \text{ } 1/\Omega$. The assumed current to be generated is $i(t) = 20 \sin(3 \cdot 314t) + 0.116 \sin(314t)$. The fundamental current harmonic must be added in order to ensure the

energy balance. The constant switching period was chosen equal $T_s = 0.5 \text{ ms}$.

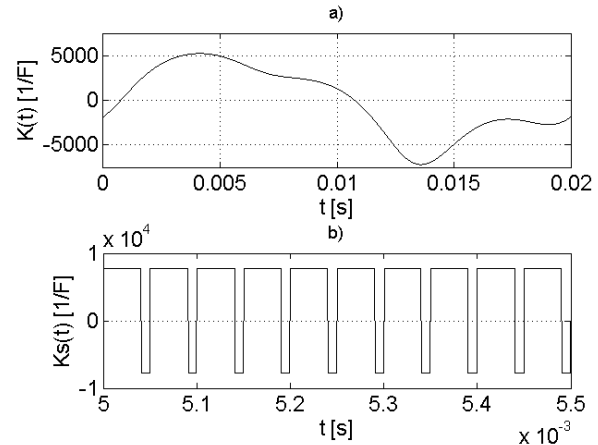


Fig. 5. Auxiliary capacitance functions: a) periodical continuous time function of the capacitance inverse, b) switching capacitor function within short time interval

Fig.5a shows the waveform of the auxiliary capacitance function. This continuous periodical function enables one to compute the switching time $t_p(t)$ according to equation (7). This sequence of switching times determines the switching capacitor function shown in Fig. 5b. The waveform of current $i(t)$ observed in short time interval is shown in Fig. 6a and the respected capacitor voltage is shown in Fig. 6b.

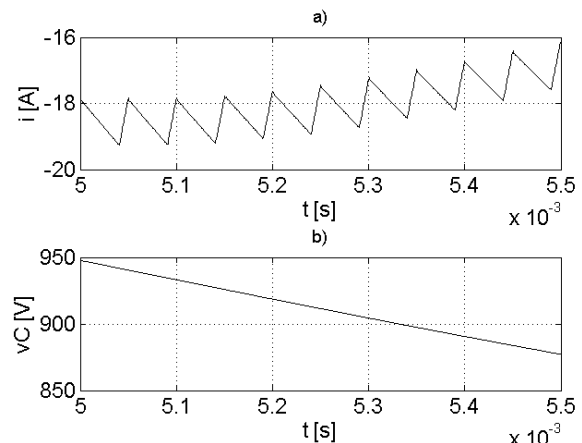


Fig. 6. Waveforms in the circuits shown in Fig. 1 within short time interval: a) compensator current, b) capacitor voltage

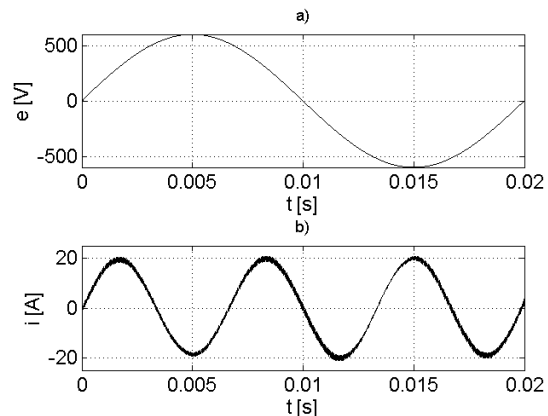


Fig. 7. Waveforms obtained in the circuit shown in Fig. 1: a) source voltage, b) current generated

Fig. 7b presents final solution of the generated current when voltage is sinusoidal as shown in Fig. 7a. The required third harmonic current has been generated with fixed switching frequency.

Three-phase circuit

Practically, mainly three-phase structures are employed. Such structure for a three-wire system is shown in Fig. 8.

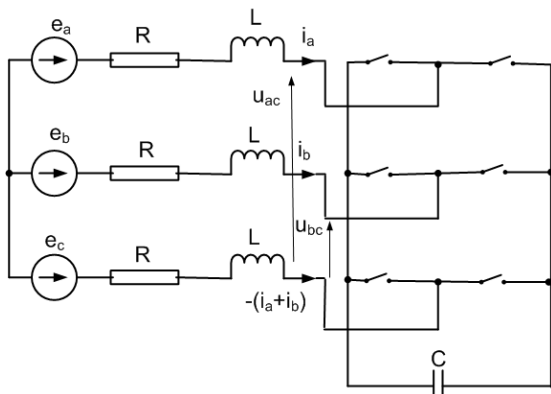


Fig. 8. Voltage source topology of the three-phase compensator

This structure is widely used, because it has many advantages. It needs minimal number of switches and only one capacitor. But such circuit with minimal number of elements cannot ensure the optimal current waveforms and constant switching frequency. The three-wire circuit has two independent currents, but only one capacitor is available. There are possible six switching modes in Fig. 8. The equivalent circuit shown in Fig. 9 is adequate for one chosen switching mode, when the left switch in phase *a* and the right switches in phases *b* and *c* are closed. Second switching mode is equivalent to the circuit shown in Fig. 9 with changed polarity of voltage source v_C .

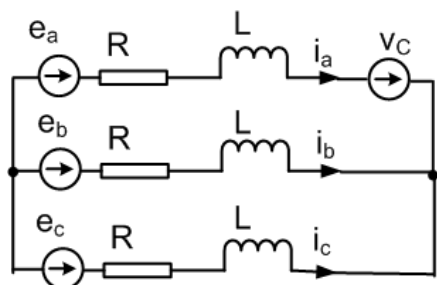


Fig. 9. Equivalent circuit model for one of six possible switches states

In the next four modes the voltage source v_C appears in the phase *b* and *c*. Let for simplicity resistance R in Fig. 9 is equal to zero, then differential equations (8) describes currents of this circuit. Two of them are independent, third is linearly dependent, because of current Kirchhoff law.

$$(8) \quad \begin{aligned} L \frac{di_a}{dt} &= e_a \pm \frac{2}{3} v_C \\ L \frac{di_b}{dt} &= e_b \mp \frac{1}{3} v_C \\ L \frac{di_c}{dt} &= e_c \mp \frac{1}{3} v_C \end{aligned}$$

It is seen that current derivative di_i/dt is unequivocally determined if di_a/dt is forced according to the first equation

(8). Always when capacitor voltage $2v_C/3$ in phase *a* has positive polarity then capacitor voltage $v_C/3$ in phase *b* has negative polarity. It means that the independent control of current waveforms in three phases is impossible. Such limitation causes that the switching needed for tracing the current waveform in one phase can have negative influence on waveforms in the remaining phases.

When hysteresis controller is used then switchings are performed rather chaotically. To avoid such disadvantage it is necessary to use at least two capacitors and more switches. The example of such structure with two capacitors and eight switches is shown in Fig. 10. The equivalent averaged model of this circuit is shown in Fig. 11. This circuit contains two time-varying capacitors. Two capacitance functions can be computed similarly as presented above for single-phase circuit.

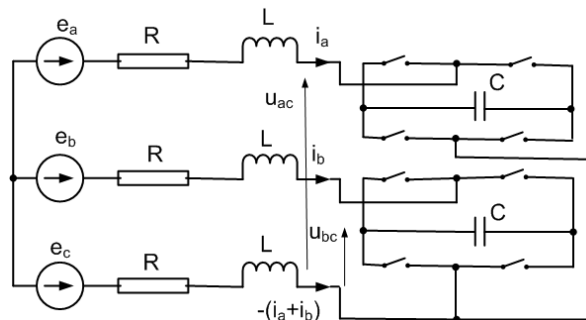


Fig. 10. Structure with two capacitors and eight switches

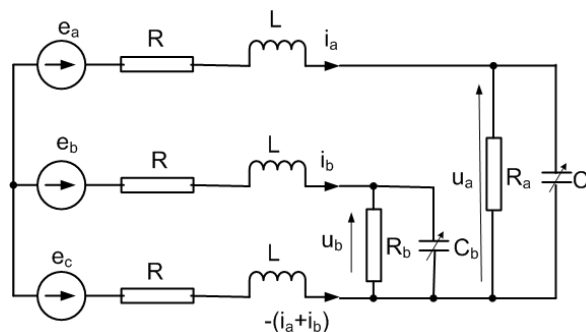


Fig. 11. Time-varying model of the switched circuit

The following equations are valid for circuit of Fig. 11

$$(9) \quad u_a = e_a - e_c - R_a(2i_a + i_b) - L \frac{d}{dt}(2i_a + i_b)$$

$$(10) \quad u_b = e_b - e_c - R_b(i_a + 2i_b) - L \frac{d}{dt}(i_a + 2i_b)$$

$$(11) \quad q_a(t) = \int_0^t [i_a(\tau) - G_a v_a(\tau)] d\tau + q_a(0)$$

$$(12) \quad q_b(t) = \int_0^t [i_b(\tau) - G_b v_b(\tau)] d\tau + q_b(0)$$

$$(13) \quad K_a(t) = \frac{1}{C_a(t)} = \frac{v_a(t)}{q_a(t)}$$

$$(14) \quad K_b(t) = \frac{1}{C_b(t)} = \frac{v_b(t)}{q_b(t)}$$

Example – fifth harmonic generation in the three-phase circuit

Assume that fifth current harmonic should be generated in the circuit shown in Fig. 11. The results presented in Fig. 12 and 13 have been obtained for the following circuit parameters:

generator is symmetrical and $e_a=600\sin(314t)$, $L=10\text{ mH}$, $R=0.08\ \Omega$, $C=128.2\ \mu\text{F}$, conductance shunted the capacitor $G=0.0001\ 1/\Omega$, initial electric charges $q_a(0)=0.5C$, $q_b(0)=0.5C$. The assumed currents to be generated are

$$i_a(t) = 20\sin(5 \cdot 314t) + 0.3\sin(314t)$$

$$i_b(t) = 20\sin(5 \cdot 314t + 2\pi/3) + 0.3\sin(314t - 2\pi/3)$$

$$i_c(t) = 20\sin(5 \cdot 314t - 2\pi/3) + 0.3\sin(314t + 2\pi/3)$$

The first harmonic had to be added in order to ensure the energy balance.

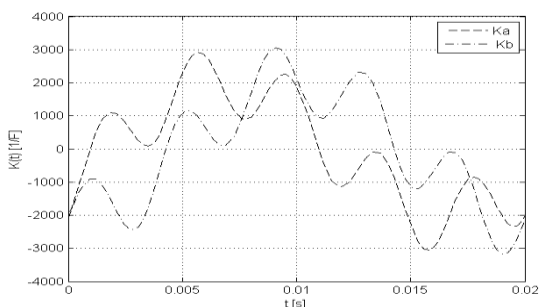


Fig. 12. Capacitance functions K_a and K_b

The time varying capacitance functions obtained according to equations (9)-(14) are shown in Fig. 12.

The simulation of the circuit shown in Fig. 11 with capacitance functions shown in Fig. 12 gives currents presented in Fig. 13.

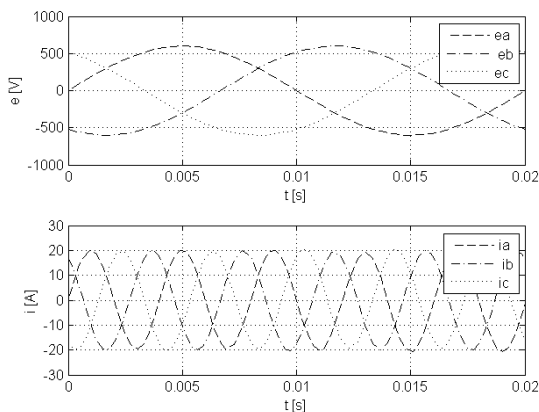


Fig. 13. Currents generated by circuit shown in Fig. 11: a) source voltages, b) generated currents

Having capacitance functions K_a and K_b , it is possible to obtain sequence of switching instance for circuit shown in Fig. 10. Two independent switching bridges should be switched according to formula (7) presented for the single-phase case.

Conclusions

When the reference signal is given, the harmonic compensator should trace this signal. It means that current generated by inverter is known. For such state of work, knowing parameters of supplying system, auxiliary capacitance function can be computed. From this function the sequence of switching time instants can be obtained. Such sequence of switching instants guaranties the generation of desired current waveform. The switching frequency remains fixed.

REFERENCES

- [1] Singh B., K. Al-Haddad K., A Review of Active Filters for Power Quality Improvement, *IEEE Trans. Industrial Electronics*, 46 (1999), No. 5, 960-971
- [2] Akagi H., Modern Active Filters and Traditional Passive Filters, Int. Conf. PELINCEC, Warsaw, 2005.
- [3] De Heredia A.L., H. Gaztanga H., Etxeberria-Otadui I., Bacha S., Reyero R., A Coparative Study of Stationary Frame and Fixed Switching Frequency Digital Current Control Techniques for Power Active Filters, Int. Conf. PELINCEC, Warsaw, 2005.
- [4] Strzelecki R., Supronowicz H., Power Factor in Power Systems and Methods of Its Improvement, (in Polish), *Warsaw University of Technology*, 2000.
- [5] Shen D., Lehn P.W., Fixed-frequency space-vector modulation control for three-phase four-leg active power filters, *IEE Proc. Electr. Power Appl.* 149 (2002), No. 4, 268-274.
- [6] Kwiczak S., Mikołajuk K., Iterative and optimization algorithms for current harmonics estimation, *Archives of Electrical Engineering*, 55 (2006), No. 1, 91-108.
- [7] Siwczynski M., Jaraczewski M., Synthesis of optimal compensation circuits, (in Polish), *JUEE*, 7 (2001), 77-86.
- [8] Mikołajuk K., Tobała A., Switched Circuits for Harmonic Generation, VII Int. Workshop Computational Problems of Electrical Engineering, Odessa, Ukraine, 2006, 111-114.

Authors: prof. dr hab. inż. Kazimierz Mikołajuk, Warsaw University of Technology, ul. Koszykowa 75, 00-661 Warsaw, E-mail: mik@iem.pw.edu.pl; mgr inż. Andrzej Tobała, E-mail: ato@iem.pw.edu.pl

Multistage filtration via blind signal separation for prediction improvement

Abstract. In this paper we present a new method for prediction result improvement when many models are tested. In the multivariate variable of models results we identify the latent components with constructive and destructive impact on prediction results. The filtration of those destructive components by blind signal separation methods leads to improvement of final prediction. The basis filtration step can be extended to nonlinear and multistage process. The validity and high performance of our concept is presented on the real problem of energy load prediction.

Streszczenie. W artykule przedstawiamy nową metodę dla poprawy dokładności prognozy przy wykorzystaniu integracji rezultatów pochodzących z wielu modeli. W podejściu tym identyfikujemy ukryte komponenty, mające konstruktywny lub destrukcyjny wpływ na rezultatu prognozowania. Zastosowanie metod ślepej separacji dla filtracji komponentów destrukcyjnych, prowadzi do poprawy końcowej dokładności predykcji. Omówiony sposób filtracji może zostać rozszerzony na proces wieloetapowe pozwalający eliminować komponenty destrukcyjne o różnej charakterystyce. Zasadność stosowania prezentowanego rozwiązania została potwierdzona na problemie predykcji obciążeń systemu elektroenergetycznego. (Poprawa dokładności prognozowania przy wykorzystaniu wieloetapowej filtracji z pośrednictwem ślepej separacji sygnałów).

Keywords: ensemble methods, blind signal separation, prediction, load forecasting

Słowa kluczowe: ślepa separacja sygnałów, predykcja, prognozowanie obciążeń w systemie elektroenergetycznym

Introduction

The development of the ensemble methods is motivated by existence of the many models adequate for analysed problem [7]. This motivation is especially visible in neural network modelling. The neural networks, as well as the other regression models, try to represent the dependency between input data and target [3,7]. Typically, in real problems many different types and structures of neural networks are tested and optimised according to chosen cost function. Having many models, it seems natural to integrate them and to use the information generated by many neural networks what leads us to wide area of ensemble methods. Usually solutions propose the combination of a few models by mixing their results or parameters [2,8,21].

In this paper we propose an alternative concept of ensemble methods for prediction improvement. Our concept is based on the assumption that prediction results contain the latent destructive and constructive components common to all the model results [19]. The elimination of the destructive ones should improve final results.

The estimation of the latent components we make via multivariate decompositions from blind signal separation methods. Due to fact that the particular latent components can have different properties we apply multistage decomposition technique where in each stage different signal features are analysed.

2 Prediction results model

We assume that after the learning process each prediction result includes two types of components: constructive associated with the target and destructive associated with the inaccurate learning data, individual properties of models, missing data, not precise parameter estimation, distribution assumptions etc. Now we collect particular model results x_i together and treat them as multivariate variable $\mathbf{X} = [x_1, x_2, \dots, x_m]^T$, $\mathbf{X} \in R^{m \times N}$ where N means the number of observations. We describe that the set of latent components as $\mathbf{S} = [\hat{s}_1, \hat{s}_2, \dots, \hat{s}_k, s_{k+1}, s_m]^T$, $\mathbf{S} \in R^{m \times N}$ where \hat{s}_j denote constructive component and s_i is destructive one [3]. We assume the relation between observed prediction results and latent components as linear transformation

$$(1) \quad \mathbf{X} = \mathbf{A}\mathbf{S}$$

where matrix $\mathbf{A} \in R^{m \times m}$ represents the mixing system. The (1) means matrix \mathbf{X} factorisation by latent components matrix \mathbf{S} and mixing matrix \mathbf{A} .

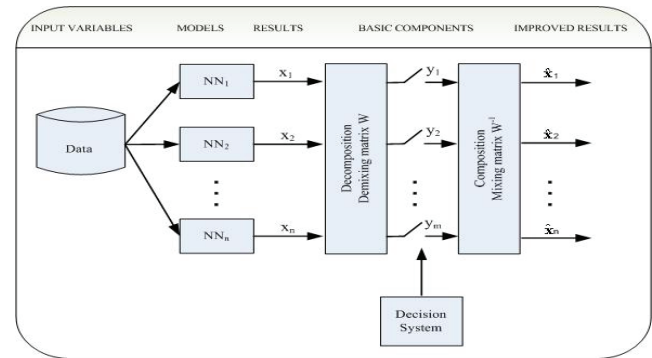


Fig.1. The scheme of modelling improvement method by multivariate decomposition.

Our aim is to find the latent components and reject the destructive ones (replace them with zero) and next mix the constructive components back to obtain improved prediction results as

$$(2) \quad \hat{\mathbf{X}} = \hat{\mathbf{A}}\hat{\mathbf{S}} = \mathbf{A}[\hat{s}_1, \hat{s}_2, \dots, \hat{s}_k, \mathbf{0}_{k+1}, \mathbf{0}_n]^T$$

The replacement of destructive signal by zero is equivalent to putting zero in the corresponding column of \mathbf{A} . If we express the mixing matrix as $\mathbf{A} = [\mathbf{a}_1, \mathbf{a}_2, \dots, \mathbf{a}_n]$ the purified results can be described as

$$(3) \quad \hat{\mathbf{X}} = \hat{\mathbf{A}}\hat{\mathbf{S}} = [\mathbf{a}_1, \mathbf{a}_2, \dots, \mathbf{a}_k, \mathbf{0}_{k+1}, \dots, \mathbf{0}_n]\mathbf{S}$$

3 Blind Signal Separation and decomposition algorithms

Blind signals separation (BSS) methods aim at identification of the unknown signals mixed in the unknown system [5,10,18]. There are many different methods and algorithms used in BSS task. They explore different properties of data like: independence [4], decorrelation [5], sparsity [14], smoothness [5], non-negativity [13] etc. In our case, we are not looking for specific real signals but rather for interesting analytical data representation of the form (2).

To find the latent variables \mathbf{A} and \mathbf{S} we can use a transformation defined by separation matrix $\mathbf{W} \in R^{m \times m}$, such that

$$(4) \quad \mathbf{Y} = \mathbf{W}\mathbf{X}$$

where \mathbf{Y} is related to \mathbf{S} and satisfies the following relation

$$(5) \quad \mathbf{Y} = \mathbf{P}\mathbf{D}\mathbf{S}$$

where \mathbf{P} is a permutation matrix and \mathbf{D} is a diagonal matrix [5,10]. The relation (6) means that estimated signals can be rescaled and reordered in comparison to the original sources. These properties are not crucial in our case, therefore \mathbf{Y} can be treated directly as estimated version of sources \mathbf{S} . There are some additional assumptions depending on particular BSS method. We focus on methods based on decorrelation, independent component analysis and smoothness.

Decorrelation is one of the most popular statistical procedures for the elimination of the linear statistical dependencies existing in the data [20]. It can be performed by diagonalization of the correlation matrix $\mathbf{R}_{xx} = E\{\mathbf{X}\mathbf{X}^T\}$. It means that matrix \mathbf{W} should satisfy the following relation

$$(6) \quad \mathbf{R}_{yy} = \mathbf{W}\mathbf{R}_{xx}\mathbf{W}^T = \mathbf{E}$$

where \mathbf{E} is any diagonal matrix. From many methods leading to the decorrelation matrix \mathbf{W} (Table 1) the most popular is the principal component analysis due to its interesting statistical and algebraic properties [11].

Table 1. Methods of decorrelation possible for models decomposition

| Method ^a | Form correlation | EIG (PCA) |
|---------------------|---|---|
| Factorisation | $\mathbf{R}_{xx} = \mathbf{R}_{xx}^{1/2} \mathbf{R}_{xx}^{1/2}$ | $\mathbf{R}_{xx} = \mathbf{U}\mathbf{\Sigma}\mathbf{U}^T$ |
| Decorrelation | $\mathbf{W} = \mathbf{R}_{xx}^{-1/2}$ | $\mathbf{W} = \mathbf{U}^T$ |

^aDefinition and characteristic of the particular methods can be found in [6].

Independent component analysis (ICA) is a statistical tool, which allows decomposition of observed variable \mathbf{X} into independent components $\mathbf{Y} = [\mathbf{y}_1, \mathbf{y}_2, \dots, \mathbf{y}_m]^T$ [4,5,10].

Typical algorithms for ICA explore higher order statistical dependencies in a dataset, so after ICA decomposition we have got signals (variables) without any linear and non-linear statistical dependencies. To obtain independent components we explore the fact that the joint probability of independent variables can be factorized by the product of the marginal probabilities

$$(7) \quad \overbrace{p_1(\mathbf{y}_1)p_2(\mathbf{y}_2)\dots p_n(\mathbf{y}_n)}^{q_y(\mathbf{Y})} = \overbrace{p_{1\dots n}(\mathbf{y}_1, \mathbf{y}_2, \dots, \mathbf{y}_n)}^{p_y(\mathbf{Y})}$$

One of the most popular method to obtain (8) is to find such \mathbf{W} that minimize the Kullback-Leibler divergence between $p_y(\mathbf{Y})$ and $q_y(\mathbf{Y})$ [5]

$$(8) \quad \mathbf{W}_{opt} = \min_{\mathbf{W}} \int_{-\infty}^{+\infty} p_y(\mathbf{Y}) \log \frac{p_y(\mathbf{Y})}{q_y(\mathbf{Y})} d\mathbf{Y}$$

There are many numerical algorithms estimating independent components like Natural Gradient, FOBI, JADE or FASTICA [4,5,10,18].

Smooth Component Analysis (SmCA) is a method of finding the smooth components in a multivariate variable with temporal structure [5]. We propose a new smoothness measure as

$$(9) \quad P_1(\mathbf{y}_i) = \frac{\frac{1}{N} \sum_{k=2}^N |y_i(k) - y_i(k-1)|}{R_i + \delta(R_i)}$$

where $R_i = \max(\mathbf{y}_i) - \min(\mathbf{y}_i)$ means range and symbol $\delta(\cdot)$ means Kronecker Delta. The measure $P_1(\mathbf{y}_i)$ has simple interpretation: it is maximal when changes of \mathbf{y}_i in each step are equal to range (maximal), and it is minimal, when data are constant. The possible values vary from zero to one. Our aim is to find such $\mathbf{W} = [\mathbf{w}_1, \mathbf{w}_2, \dots, \mathbf{w}_m]$ that for $\mathbf{Y} = \mathbf{W}\mathbf{X}$ we obtain $\mathbf{Y} = [\mathbf{y}_1, \mathbf{y}_2, \dots, \mathbf{y}_n]^T$ where $\mathbf{y}_1 = \mathbf{w}_1^T \mathbf{X}$ maximizes

$$(10) \quad \mathbf{w}_1 = \arg \max_{\|\mathbf{w}\|=1} (P(\mathbf{w}^T \mathbf{X}))$$

Having estimated the first $k-1$ smooth components the next one is calculated as the smoothest combination of the residual signals

$$(11) \quad \mathbf{w}_k = \arg \max_{\|\mathbf{w}\|=1} (P(\mathbf{w}^T (\mathbf{x} - \sum_{i=1}^{k-1} \mathbf{w}_i \mathbf{w}_i^T \mathbf{x})))$$

Finding of the vector \mathbf{w} in (11) can be performed by the Newton method. In many cases the SmCA give results similar to ICA or other BSS methods but in contradistinction to them it is focused on temporal structure of data, what can be important for problems described by time series.

4 Generalized Mixing and Multistage Filtration

Presented method assumes basis components classification as constructive or destructive. The possible solution is the analysis of the basis components statistical characteristics and removing the random signals interpreted as the noises. It can be made by utilizing R/S analysis where randomness of signals is characterised by the Hurst exponent [9,17]. This can be good indicator for primary classification but not optimal because obtained components might be not pure constructive or destructive due to many reasons like improper linear transformation assumption or other statistic characteristics than explored by chosen BSS methods. Therefore particular component can have constructive impact on one model and destructive on the other or there may exist components destructive as a single but constructive in a group. It means that components classified as destructive should have weight other than 0 and we can try to find the better mixing system than described by $\hat{\mathbf{A}}$. The new mixing system can be formulated more general than linear, e.g. we can take MLP neural network as the mixing system

$$(12) \quad \hat{\mathbf{X}} = \mathbf{g}^{(2)}(\mathbf{B}^{(2)}[\mathbf{g}^{(1)}(\mathbf{B}^{(1)}\mathbf{S} + \mathbf{b}^{(1)})] + \mathbf{b}^{(2)})$$

where $\mathbf{g}^{(i)}(\cdot)$ is a vector of nonlinearities, $\mathbf{B}^{(i)}$ is a weight matrix and $\mathbf{b}^{(i)}$ is a bias vector respectively for i th layer, $i=1,2$. The first weight layer will produce results related to (4) if we take $\mathbf{B}^{(1)} = \hat{\mathbf{A}}$. But we employ also some nonlinearities and the second layer, so comparing to the linear form the mixing system gains some flexibility. If we learn the whole structure starting from system described by $\hat{\mathbf{A}}$ with initial weights of $\mathbf{B}^{(1)}(0) = \hat{\mathbf{A}}$, we can expect the results will be better.

Now we extend the presented methodology exploring many decompositions at once. Such approach is motivated by assumption that there may exist different latent components with different statistical properties so different decompositions can be used. In this extension we perform the full methodology for each type of transformation. Let's assume we have K decompositions with separation \mathbf{W}_i and

remixing $\hat{\mathbf{A}}_i$ matrices respectively, $i=1, \dots, K$. If we employ the transformations one by one we can describe the full filtration process as

$$(13) \quad \hat{\mathbf{X}} = \mathbf{W}_K \hat{\mathbf{A}}_K \dots \mathbf{W}_2 \hat{\mathbf{A}}_2 \mathbf{W}_1 \hat{\mathbf{A}}_1 \mathbf{X} = \mathbf{C} \mathbf{X}$$

where \mathbf{C} means global filtration matrix. When we apply in each remixing stage the generalised mixing we obtain improved results as

$$\hat{\mathbf{X}} = F_K(\hat{\mathbf{A}}_K, \mathbf{W}_K F_{K-1}(\dots F_2(\hat{\mathbf{A}}_2, \mathbf{W}_2 F_1(\hat{\mathbf{A}}_1, \mathbf{W}_1 \mathbf{X})))$$

where

$$F_i(\hat{\mathbf{A}}_i, \mathbf{S}_i) = \mathbf{g}_i^{(2)}(\mathbf{B}_i^{(1)}[\mathbf{g}_i^{(2)}(\mathbf{B}_i^{(1)}\mathbf{S}_i + \mathbf{b}_i^{(1)})] + \mathbf{b}_i^{(2)}),$$

$$\mathbf{B}_i^{(1)}(0) = \hat{\mathbf{A}}_i$$

5 Practical experiment

To prove the validity of our concept, the real problem – energy load forecasting was analyzed [12,16]. Forecast of hourly energy consumption in Poland for 24 hours ahead was based on energy demand from last 24 hours and calendar variables: month, day of the month, day of the week, and holiday indicator. The training data set included observations from 1988-1997 and the test was performed on 1998.

Table 2 The results on MAPE for primary models and after particular filtrations

| | MLP 12 | MLP 18 | MLP 24 | MLP 27 | MLP 30 | MLP 33 |
|---------|--------|--------|--------|--------|--------|--------|
| Primary | 2.3933 | 2.3556 | 2.3676 | 2.3975 | 2.4027 | 2.3589 |
| ICA | 2.4112 | 2.2372 | 2.3886 | 2.4034 | 2.4202 | 2.3777 |
| PCA | 2.2990 | 2.2467 | 2.2821 | 2.2664 | 2.2492 | 2.2315 |
| SmCA | 2.3490 | 2.2906 | 2.2686 | 2.3297 | 2.3204 | 2.2302 |
| ICA_PCA | 2.3518 | 2.2170 | 2.3167 | 2.2866 | 2.2800 | 2.2841 |

We trained a hundred MLP neural networks with one hidden layer and we chose the best six as our primary models. The error measures were MAPE and MSE. For one-stage ensemble (filtration) process we used PCA, ICA, SmCA decompositions. The two-stage filtration was performed with various pairs of decompositions.

In Tables 2-5 we present the results. For multistage filtration we show only the best combination, ICA-PCA (the others achieved the level of one-stage processes).

Table 3 The percentage improvements on MAPE after particular filtrations

| | MLP 12 | MLP 18 | MLP 24 | MLP 27 | MLP 30 | MLP 33 |
|---------|---------|--------|---------|---------|---------|---------|
| ICA | -0.7462 | 5.0272 | -0.8866 | -0.2483 | -0.7248 | -0.7972 |
| PCA | 3.9389 | 4.6233 | 3.6102 | 5.4685 | 6.3898 | 5.4004 |
| SmCA | 1.8531 | 2.7581 | 4.1798 | 2.8257 | 3.4261 | 5.4541 |
| ICA_PCA | 1.7343 | 5.8861 | 2.1495 | 4.6245 | 5.1102 | 3.1694 |

Table 4 The results on MSE for primary models and after particular filtrations

| 10^{-3} | MLP 12 | MLP 18 | MLP 24 | MLP 27 | MLP 30 | MLP 33 |
|-----------|--------|--------|--------|--------|--------|--------|
| Primary | 1.1285 | 1.1106 | 1.1151 | 1.1319 | 1.1464 | 1.1080 |
| ICA | 1.1434 | 1.0278 | 1.1285 | 1.1393 | 1.1593 | 1.1234 |
| PCA | 1.0239 | 1.0262 | 1.0240 | 1.0191 | 1.0271 | 1.0179 |
| SmCA | 1.1326 | 1.1083 | 1.0484 | 1.1347 | 1.0962 | 1.1110 |
| ICA_PCA | 1.1055 | 1.0135 | 1.0780 | 1.0532 | 1.0488 | 1.0516 |

Table 5 The percentage improvements on MSE after particular filtrations

| | MLP 12 | MLP 18 | MLP 24 | MLP 27 | MLP 30 | MLP 33 |
|---------|---------|--------|---------|---------|---------|---------|
| ICA | -1.3209 | 7.4500 | -1.1990 | -0.6552 | -1.1283 | -1.3933 |
| PCA | 9.2678 | 7.6006 | 8.1670 | 9.9656 | 10.4016 | 8.1270 |
| Samca | -0.3701 | 0.2089 | 5.9846 | -0.2476 | 4.3769 | -0.2747 |
| ICA_PCA | 2.0400 | 8.7416 | 3.3264 | 6.9556 | 8.5129 | 5.0936 |

Note, that the proposed method improves each primary model by a few percent. We observe good effects especially for PCA and ICA-PCA decompositions (3-5% in MAPE and 4-10% in MSE). The most important result includes Table 6 summarizing comparison of the best primary model with the best models after decomposition stage. We can conclude that each decomposition enables improvement by 5% in MAPE and 5-8% in MSE.

Table 6 The percentage improvements on MAPE and MSE after particular filtrations

| | MAPE | MSE |
|---------|--------|--------|
| ICA | 5.0272 | 7.2336 |
| PCA | 5.2699 | 8.1270 |
| SmCA | 5.3237 | 5.3805 |
| ICA_PCA | 5.8861 | 8.5282 |

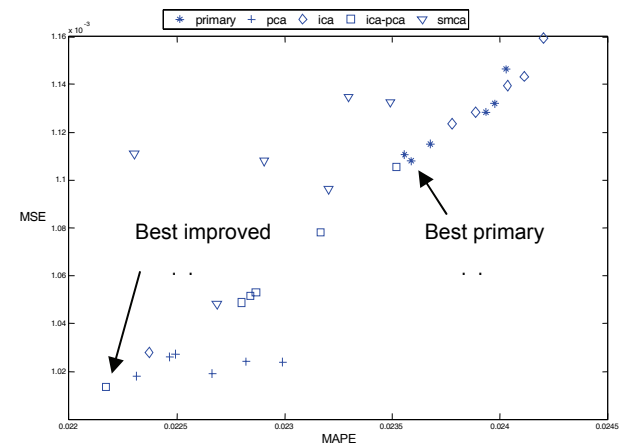


Fig.2. Quality of the primary and improved models in terms of MAPE and MSE.

The visualisation of models quality in Figure 2 helps to analyse the properties of the proposed method. The most important conclusion is, that actually the decompositions enable to improve the quality of most models on most criteria, It is especially notable for PCA and ICA-PCA, which moved the whole "cloud" of the results left-down.

Conclusions

The presented method enables to perform an efficient integration of the information generated by different models. The practical experiment with the energy load forecasting confirmed the validity of our method.

The results achieved in one filtration system can be improved in further multistage filtration process. In case of multistage filtration system, each stage is realized by different transformation and therefore a variety of destructive components can be eliminated. It is an open question the way of choosing the optimal succession. In this particular experiment we only took into the consideration the filtration based on PCA, ICA, SmCA types of decomposition and as a result it was possible to investigate all of the combinations. In case of greater number of proposed decomposition methods such research can be difficult in terms of computational power. The results from the experiment confirm the rationality of searching for and eliminating of common destructive components. Those fundamental factors possess a physical character and therefore the elimination should improve the quality of models results in general, what can be observed on many different error criteria.

REFERENCES

- [1] Amari, S., Natural gradient works efficiently in learning, *Neural Computation* 10 (1998) 271-276.
- [2] Breiman, L., Bagging predictors. *Machine Learning* 24 (1996) 123-140.
- [3] Bishop, C.M., *Neural networks for pattern recognition*, Oxford Univ. Press, Oxford UK (1996).
- [4] Cardoso, J.F., High-order contrasts for independent component analysis, *Neural Computation* 11 (1999) 157-192.
- [5] Cichocki, A., Amari, S., *Adaptive Blind Signal and Image Processing*, John Wiley, Chichester (2002).
- [6] Golub, G.H., Van-Loan, C.F., *Matrix Computations*, [Johns Hopkins (1996).
- [7] Haykin, S., *Neural networks: a comprehensive foundation*, Macmillan, New York (1994).
- [8] Hoeting, J., Mdigian, D., Raftery, A., Volinsky, C., Bayesian model averaging: a tutorial, *Statistical Science* 14 (1999), pp. 382-417.
- [9] Hurst, H.E., Long term storage capacity of reservoirs, *Trans. Am. Soc. Civil Engineers* 116.
- [10] Hyvärinen, A., Karhunen, J., Oja, E., *Independent Component Analysis*, John Wiley (2001).
- [11] Jolliffe, T.: *Principal Component Analysis*, Springer-Verlag (1986).
- [12] Lendasse, A., Cottrell, M., Wertz, V., Verdleysen, M., Prediction of Electric Load using Kohonen Maps – Application to the Polish Electricity Consumption, *Proc. Am. Control Conf., Anchorage AK* (2002) 3684-3689.
- [13] Lee, D.D., Seung, H.S., Learning of the parts of objects by non-negative matrix factorization, *Nature* 401 (1999).
- Li, Y., Cichocki, A., Amari S., Sparse component analysis for blind source separation with less sensors than sources, *Fourth Int. Symp. on ICA and Blind Signal Separation, Nara, Japan* (2003) 89-94.
- [14] Mitchell, T.: *Machine Learning*. McGraw-Hill, Boston (1997).
- [15] Osowski, S., Siwek, K.: Regularization of neural networks for improved load forecasting in the power system. *IEE Proc. Generation, Transmission and Distribution* 149(3) (2002) 340-344.
- [16] Samorodnitskij, G., Taqqu, M.: *Stable non-Gaussian random processes: stochastic models with infinite variance*. NY, London, Chapman & Hall (1994)
- [17] Stone, J.V.: Blind Source Separation Using Temporal Predictability. *Neural Computation* 13(7) (2001) 1559-1574.
- [18] Szupiluk, R., Wojewnik, P., Zabkowski, T.: Model Improvement by the Statistical Decomposition. *Artificial Intelligence and Soft Computing Proceedings. LNCS*, Springer-Verlag Heidelberg (2004) 1199-1204.
- [19] Therrien, C.W.: *Discrete Random Signals and Statistical Signal Processing*. Prentice Hall, New Jersey (1992).
- [20] Yang Y.: Adaptive regression by mixing. *Journal of American Statistical Association* 96 (2001).

Authors: dr inż. Ryszard Szupiluk, Piotr Wojewnik, Warsaw School of Economics, Tomasz Zabkowski, Polska Telefonia Cyfrowa, Poland, dr inż. Krzysztof Siwek, Warsaw University of Technology, ul. Koszykowa 75, 00-661 Warsaw, Poland, E-mail: rszupi@sgh.waw.pl, ksiwek@iem.pw.edu.pl

Level Set Method for capacitor optimization problem

Abstract. The optimal shape design of capacitor with Laplace equation of state using level set method is presented in the paper. The inverse problem solution provides the positions of the capacitor plates, which was optimized to achieve required potential distribution. The forward problem was approximated by Boundary Elements Method.

Streszczenie. W pracy przedstawiono rozwiązanie zadania odwrotnego dla problemu opisanego równaniem różniczkowym Laplace'a. Poszukiwano wartości promienia kondensatora, dla którego przebieg napięcia między okładkami będzie zbliżony do zadanego. Do optymalizacji kształtu zastosowano metodę zbiorów poziomicowych. (**Metoda zbiorów poziomicowych w optymalizacji kształtu kondensatora**)

Keywords: level set method, boundary elements method, optimal shape design.

Słowa kluczowe: metoda zbiorów poziomicowych, metoda elementów brzegowych, optymalne projektowanie kształtu.

Introduction

Optimal shape design methods of electromagnetic equipment have been used to achieve some special features of this equipment. The optimization problem solution deals with minimizing the objective function of the problem [1, 2]. There are many different algorithms for minimizing the objective function: deterministic methods (e.g. back-projection, perturbation, and Newton-Raphson, Conjugate Gradient method), stochastic methods (e.g. Genetic Algorithms, Monte-Carlo method, Simulated Annealing), and also Artificial Neural Network (ANN). The results of inverse problem solution using deterministic methods strictly depend on approximation of forward model with boundary or finite element. In our case, the Boundary Element Method (BEM) was used. This method is an interesting alternative to more commonly used numerical methods such as Finite Element Method (FEM). The main advantages of using BEM are: discretization only a boundary of analyzed domain, resulting reduction of the dimension and number of unknowns from $O(N^2)$ to $O(N)$, finding the unknown function in the inside points is possible, without necessity of discretization of this domain [3, 4]. In the numerical realization of BEM the form of boundary elements depend on the problem dimension. For the 1D problem – the boundary elements are reduced to points, for 2D problem are the form of rectilinear or curved segments, and for 3D problem the boundary elements are triangular or quadrangular parts of a surface [3, 4].

In order to solve inverse problem using iterative optimization method it is necessary to repeat forward problem solution many times – to determine the distribution of potential.

The pioneering work using set level method for the shape optimization was presented by Osher and Santosa [5]. This method is a powerful technique for describing and tracking propagating boundaries and for locating static boundaries. It can be used for inverse boundary problem solution of recovering the interfaces between two materials.

The level set methods approach in optimal shape design involving partial differential equation has received little attention up till now. The combination level set formulation to describe the shapes of the domains with essentially nonoscillatory schemes to solve the Hamilton-Jacobi equation is efficient method for wide class of shape optimization problems involving partial differential equation [6, 7].

There are two different parts in the paper. One of both deals with the forward problem solution – Laplace equation by BEM. Second part of the paper is connected with level set method approach in the inverse problem solution. The

solution provides the position of the capacitor plate, which was optimized to achieve required potential distribution.

Problem description

The cylindrical capacitor (Fig. 1) with potential distribution described by Laplace equation (1) was considered [8, 9]:

$$(1) \quad \frac{1}{r} \frac{\partial}{\partial r} \left(r \frac{\partial u}{\partial r} \right) = 0$$

with boundary conditions:

$$(2) \quad \begin{aligned} u(a) &= 1 \\ u(b) &= 0 \end{aligned}$$

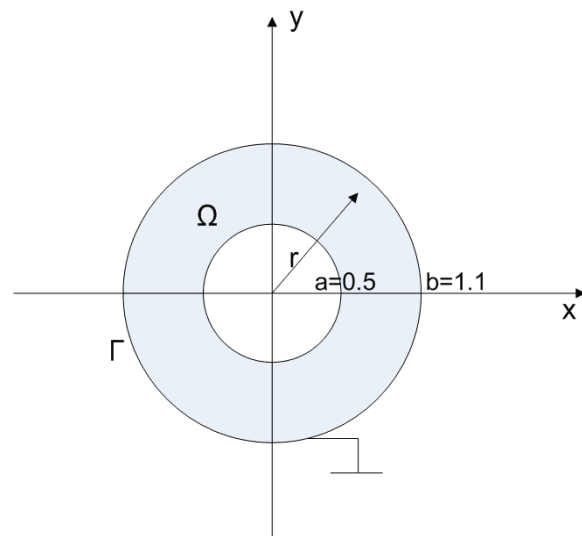


Fig.1. Cross-section of the capacitor

The potential distribution is known in original region Ω and defined as $u_0(r) = -0.721348 \ln(0.714286r)$.

The solution of considered problem is finding the region Ω_0 , where the function u_0 is the solution of Laplace equation with boundary conditions (2).

The conjugate equation for Laplace equation is defined as:

$$(3) \quad \Delta q = \ln r \left(\frac{1}{\ln \frac{a_0}{b_0}} - \frac{1}{\ln \frac{a}{b}} \right) + \left(\frac{\ln b}{\ln \frac{a}{b}} - \frac{\ln b_0}{\ln \frac{a_0}{b_0}} \right)$$

Numerical methods

BEM

Integral equations are used to solution to the forward problems (analysis) and the inverse problems (synthesis and identification) [3, 4]. To the transformation of the integral equations, the function and Green's formulas are used.

The Green's function satisfies the Laplace's equation:

$$(4) \quad \nabla^2 G = 0$$

and for 2D domain is:

$$(5) \quad G(M, P) = -\frac{1}{2\pi} \ln(r)$$

where: r – the distance between M and P

$$(6) \quad r(M, P) = \sqrt{(x_M - x_P)^2 + (y_M - y_P)^2}$$

The second Green's identity (symmetrical), which was used in transformation of the integral equation, is described as follows:

$$(7) \quad \int_{\Omega} (u \nabla^2 G - G \nabla^2 u) d\Omega = \oint_S \left(u \frac{\partial G}{\partial n} - G \frac{\partial u}{\partial n} \right) dS$$

where: u - potential in 2D domain Ω

Let consider the Laplace equation in the three-dimensional domain:

$$(8) \quad \nabla^2 u(r) = 0 \quad \forall_{r \in \Omega}$$

for the Dirichlet boundary conditions on the surface of the volume.

Using equation (7) – second Green's identity we get:

$$(9) \quad u(M) + \int_{\Gamma} K_1(M, P) u(P) d\Gamma(P) = \int_{\Gamma} K_2(M, P) \frac{\partial u}{\partial n} d\Gamma(P)$$

where functions K_1 and K_2 are kernels of integral transformation, which are defined as follows [3, 4]:

$$(10) \quad K_1(M, P) = \frac{\partial G(M, P)}{\partial n}$$

$$(11) \quad K_2(M, P) = G(M, P)$$

Let move the interior load point M to the boundary which results in the following equation:

$$(12) \quad \begin{aligned} & C(P_0) u(P_0) + \int_{\Gamma} K_1(P_0, P) u(P) d\Gamma(P) = \\ & = \int_{\Gamma} K_2(P_0, P) \frac{\partial u(P)}{\partial n} d\Gamma(P) \end{aligned}$$

The coefficients in equation (12) are identified with inside point of Ω domain or boundary point $C(P_0)$. In the case, when the point P is located in the within Ω domain, $C(P_0) = 1$, and $C(P_0) = 0.5$ for boundary points, on the assumption that boundary is smooth.

To calculate the first kernel $K_1(M, P)$, the Green's function is differentiated with respect to unit normal at the point P , as follows [3, 4]:

$$(13) \quad \frac{\partial G(M, P)}{\partial n} = \frac{\partial G}{\partial r} \left(\frac{\partial r}{\partial n} \right) = \frac{\partial G}{\partial r} \left[\frac{\partial r}{\partial x} \left(\frac{\partial x}{\partial n} \right) + \frac{\partial r}{\partial y} \left(\frac{\partial y}{\partial n} \right) \right]$$

where the derivatives of the coordinates x, y, z with respect to the unit outward normal n in point P are the components of the outward normal as follows:

$$(14) \quad n_x = \frac{\partial x}{\partial n}, \quad n_y = \frac{\partial y}{\partial n},$$

and

$$(15) \quad \begin{aligned} \frac{\partial r(M, P)}{\partial x} &= \frac{x_P - x_M}{r(M, P)} \\ \frac{\partial r(M, P)}{\partial y} &= \frac{y_P - y_M}{r(M, P)} \end{aligned}$$

To solve the three-dimensional problem numerically, the surface has to be discretized into elements. The element, which was modeled as a constant value have been used in this case.

Level Set Method

Level set methods were proposed as a versatile tool for representing moving fronts in a variety of physical processes, involving flow phenomena, crystal growth and phase changes among others. The use level set methods for shape optimization involving partial differential equations apparently received little attention so far [9].

Given an interface Γ and region Ω was analyzed and computed its subsequent motion under a velocity field. The level set function φ has the following properties (see Fig. 2) [6, 7, 10]:

$$(16) \quad \begin{aligned} \varphi(x, t) &> 0 & x \in \Omega_1 \\ \varphi(x, t) &< 0 & x \in \Omega_2 \\ \varphi(x, t) &= 0 & x \in \partial\Omega \end{aligned}$$

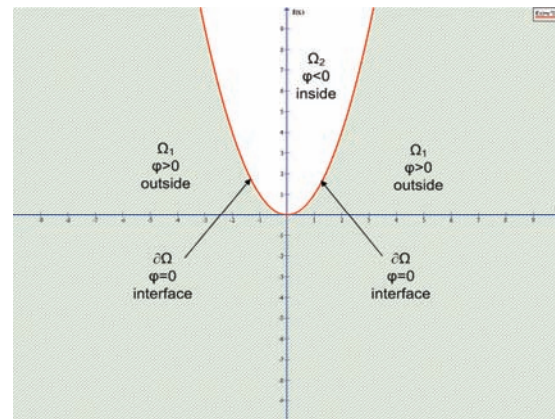


Fig.2. Considered regions

The level set method allows to move the interface Γ along the direction \vec{V} within a neighborhood of Γ . To derive the equation for level set function, let $\varphi(t, \cdot)$ denote a family of functions from R^2 to R . If $x \rightarrow \varphi(t, x)$ is perturbed to $x \rightarrow \varphi(t, x + th(x))$ then differentiating level contours $\{x: \varphi(t, x + th(x)) = const\}$ with respect to t we obtain [11]:

$$(17) \quad \varphi_t + h \nabla \varphi = 0$$

This leads to the Hamilton-Jacobi equation for level set function.

The updating of level set is possible using Hamilton-Jacobi equation (18) in which velocity field is the function of the direction of the unit normal [7, 11]:

$$(18) \quad \frac{\partial \varphi}{\partial t} + \vec{V} \nabla \varphi = 0, \text{ where } \vec{V}_N = \vec{V} \frac{\nabla \varphi}{|\nabla \varphi|}$$

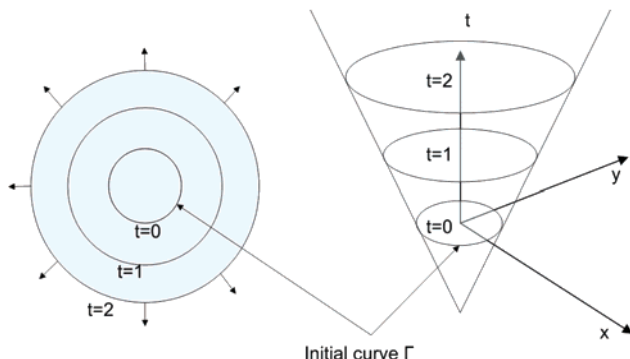


Fig.3. Zero-level set

The first step in the solution of a problem using set level method is determination of zero-level set $\Gamma_0 = \varphi(x,0)$ for $t=0$ [6].

The following steps in the numerical algorithm until its convergence:

- solve the Laplace equation (1) with boundary conditions (2);
- determine the potential distribution u_0 [6];
- compute the difference of the observed value and expected value $u - u_0$;
- solve the Poisson equation:

$$(19) \quad -\Delta p = u - u_0$$

- evaluate the normal velocity:

$$(20) \quad v_k = \nabla p_k \cdot \nabla u_k,$$

- update the level set function $\varphi(x,t)$ by solving the Hamilton-Jacobi equation:

$$(21) \quad \varphi_t^k + v_k |\nabla \varphi^k| = 0$$

$$(22) \quad \varphi_t^{k+1} = \varphi_t^k - \Delta t v_k |\nabla \varphi^k|$$

- check convergence; options include repeating the process, stopping if convergence criteria are satisfied [6].

The stability of received solution is guaranteed by Courant-Friedrichs-Levy's condition, which asserts that the numerical waves should propagate at least as fast as the physical waves. The CFL time step restriction is described as:

$$(23) \quad \Delta t < \frac{\Delta x}{\max\{|u|\}}$$

Equation is usually enforced by choosing a CFL number α with [6]:

$$(24) \quad \Delta t \left(\frac{\max\{|u|\}}{\Delta x} \right) = \alpha \text{ and } 0 < \alpha < 1$$

An optimum value of α is 0.9, and a common conservative choice is $\alpha = 0.5$.

Hamilton-Jacobi ENO

The scheme ENO – essentially nonoscillatory polynomial interpolation was used to the determination of the function of level set gradient $|\nabla \varphi^k|$ in the following iterations. As a standard with Newton polynomial interpolation, the zeroth divided differences of φ are defined at the grid nodes and defined by [6]:

$$(25) \quad D_i^0 \varphi = \varphi_i$$

at each grid node i . The first divided differences of defined midway between grid nodes as:

$$(26) \quad D_{i+1/2}^1 \varphi = \frac{D_{i+1}^0 \varphi - D_i^0 \varphi}{\Delta x}$$

The divided differences are used to reconstruct a polynomial of the form:

$$(27) \quad \varphi(x) = Q_0(x) + Q_1(x)$$

that can be differentiated and evaluated at x_i to find $(\varphi_x^+)_i$ and $(\varphi_x^-)_i$. That is, we use

$$(28) \quad \varphi_x(x_i) = Q_0'(x) + Q_1'(x)$$

to define $(\varphi_x^+)_i$ and $(\varphi_x^-)_i$.

Results

The solution of considered problem was finding the positions of the capacitor plates (the region Ω_0), with boundary conditions (2).

Figures 4 – 7 presents the iteration process for two different values of α . For $\alpha=0.8$ we got the radii values of capacitor plates $a=0.35$ and $b=1.40$ in 29 iterations (Fig. 4 and 5). Whereas for $\alpha=0.9$ the function u_0 is the solution of Laplace equation for the radii values $a=0.349$ and $b=1.401$ (Fig. 6 and 7) in 48 iterations. Our experiments confirm that in this case, the selection of α value is very important.

The gradient of state equation was used to calculating of velocity of propagating boundary.

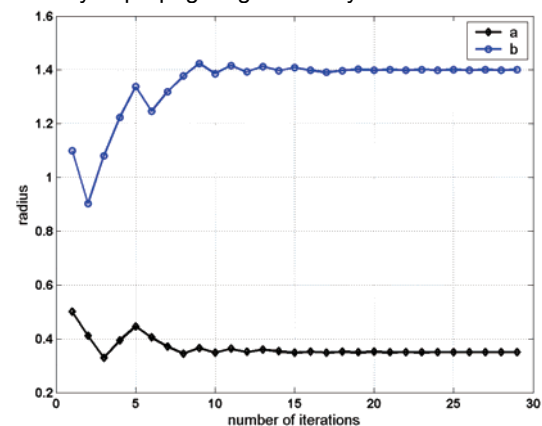


Fig.4. Iterations process for $\alpha=0.8$

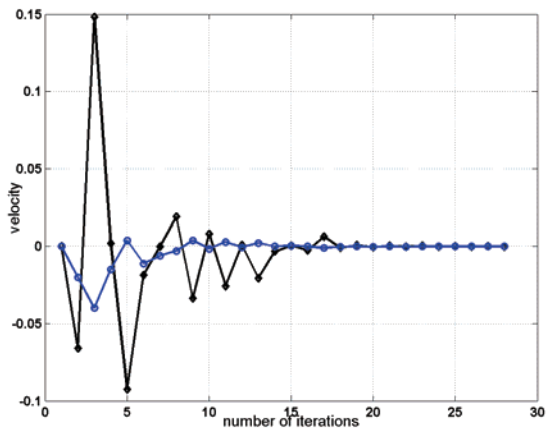


Fig.5. The normal velocity in following iterations for $\alpha=0.8$

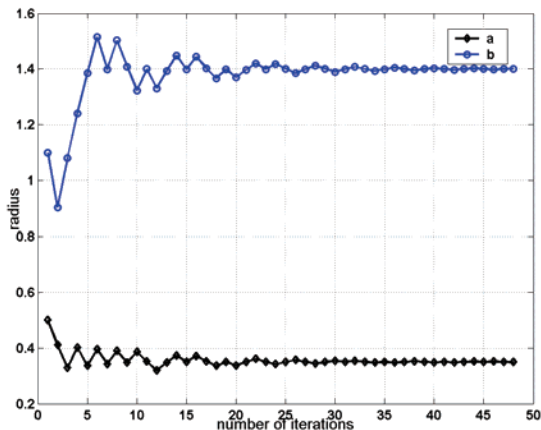


Fig.6. Iterations process for $\alpha=0.9$

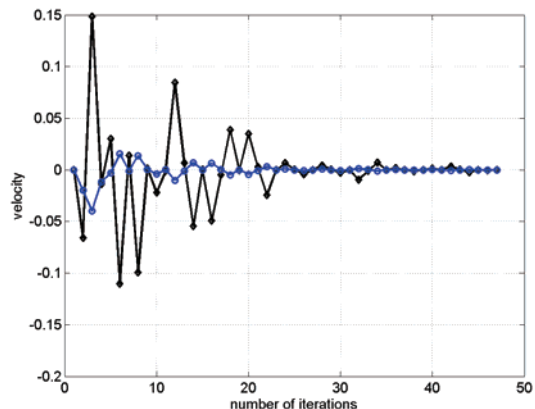


Fig.7. The normal velocity in following iterations for $\alpha=0.9$

Conclusion

These presented experiments indicated efficiency of combination level set method with BEM to the solution forward and inverse problem. Level set formulation to describe the shapes of the domains combined with essentially nonoscillatory schemes to solve the Hamilton-Jacobi equation is efficient method for optimal shape design involving partial differential equation.

This suggested method can be used in the inverse problem solution of electromagnetic fields (e.g. image reconstruction in impedance, optical tomography).

In the next experiments we are going to use WENO (weighted essentially nonoscillatory polynomial interpolation) instead of ENO and solve Poisson equation by BEM.

REFERENCES

- [1] Sokolowski J., Zalesio J.P., Introduction to Shape Optimization, *Springer-Verlag*, 1992
- [2] Kwiatkowska A., Krawczyk A., Sikora J., Material Derivative Technique In Optimal Design, *Journal of Technical Physics*, 43, pp. 427-431, 2002
- [3] Aliabadi M.H., The Boundary Element Method, Volume 2, John Wiley & Sons, LTD, 2002
- [4] Sikora J., 3D BEM for Impedance and Optical Tomography, Internal Report, Department of Computer Science, UCL, 2003
- [5] Osher S., Santosa F., Level set methods for optimization problems involving geometry and constraints, *Journal of Comput. Physics* 171, pp.272-288, 2001
- [6] Osher S., Fedkiw R., Level Set Methods and Dynamic Implicit Surfaces, *Springer-Verlag New York*, 2003
- [7] Sthian J.A., Level Set Methods and Fast Marching Methods. *Cambridge University Press*, 1999
- [8] Berowski P., Stasiak M., Sikora J., Zastosowanie zbiorów poziomowych w optymalnym projektowaniu kształtu, XII Conference Computer Applications in Electrical Engineering, pp. 61-62, Poznan 2007
- [9] Berowski P., Kwiatkowska A., Stasiak M., Sikora J., Optymalne projektowanie kształtu metodą zbiorów poziomowych, *Elektrotechnika 2006*, Warszawa 2006
- [10] Bertsekas D.P., Nedic A, Ozdaglar A.E., Convex Analysis and Optimization, *Athena Scientific*, Belmont, 2003
- [11] Ito K., Kunisch K., Li Z., Level-Set Function Approach to an Inverse Interface Problem, *Inverse Problems* 17, pp. 1225-1242, 2001

Authors:

Magdalena Stasiak, Institute of Electrical Apparatus, Technical University of Lodz, Stefanowskiego 18/22, 90-924 Lodz, E-mail: stasiak@p.lodz.pl, Przemysław Berowski, Electrotechnical Institute, Pozaryskiego 28, 04-703 Warsaw, E-mail: p.berowski@iel.waw.pl
 Jan Sikora, Institute of Theory of Electrical Engineering, Measurement and Information Systems, Warsaw University of Technology, Koszykowa 75, 00-661 Warsaw, E-mail: sik@iem.pw.edu.pl

Calculus of total losses in three-levels voltage source converters

Abstract. Static converters design has to guarantee that in all specific operating conditions the junction temperature of power devices does not exceed admitted limits. The temperature of different components depends on losses distribution and on the number of switches in IGBT modules. This paper investigates the losses balancing in the most popular 3L conversion structures: 3L-Stacked Cells, 3L-Neutral Point Clamped (NPC) and 3L-Active NPC. The 3L-Active NPC concepts accomplish a two independent stages conversion which leads to a better equilibration of losses.

Abstract. Projekty statycznych konwerterów muszą gwarantować, że we wszystkich warunkach pracy temperatura złącza urządzenia nie przekracza określonego limitu. Temperatura poszczególnych komponentów jest uzależniona od rozkładu strat oraz od liczby przełączników w modułach IGBT. W artykule przedstawiono analizę bilansowania strat w najpopularniejszych strukturach konwerterów 3L: 3L- Stacked Cells, 3L – Neutral Point Clamped (NPC) oraz 3L – Active NPC. W przypadku rozwiązania 3L-Active NPC zapewnia dwa niezależne poziomy konwersji co prowadzi do lepszego równoważenia strat. (**Wyznaczanie całkowitych strat w trzypoziomowych konwerterach źródeł napięcia**)

Keywords: multilevel converters, Voltage Source Converter (VSC), Voltage Source Inverter (VSI), Pulse Width Modulation (PWM).

Słowa kluczowe: konwertery wielopoziomowe, przetwornik typu źródło napięciowe, modulacja szerokości impulsu

Introduction

Multilevel structures have been studied for over 25 years and they represent an intelligent solution to connect serial switches [1]. There is a limited number of converters suitable for medium voltage applications which deliver multilevel voltages. The first developed topology has consisted in a serial connection of single-phase inverters with DC separate sources [2]. This structure was followed by a study concerning the stacked commutation cells in order to obtain a multilevel conversion (SC – Stacked Cells) [3]. The main source was made of many secondary sources serially connected. The first experimental results were published 18 years later [4]. Fig.1a shows a 3L-SC structure, which is also called “three-pole cell” [5].

Following the SC concept study, a new multilevel NPC (Neutral Point Clamped) structure was developed [6], [7]. This is the most popular multilevel conversion structure. The 3L-NPC inverters (Fig.1.b) are considered a particular way of implementing 3L-SC topology [5]. The role of the middle side in the 3L-SC structure is taken by the inner switches and by the two clamp diodes.

Later, another invention [8] introduced the concept of the multilevel converter with flying capacitors (FC – Flying Capacitor, Fig.1.c). In the field of low and moderate frequencies (200 Hz - 1 kHz) the NPC structure is more advantageous than the FC structure because of the required flying-capacitor size, which is inversely proportional to the switching frequency.

Recently, the 3L-NPC structure performances were improved by developing the 3L-ANPC (Active NPC) converter [9], [10] (Fig.1.d). It allows a significant increase of the output power and improves performances at “zero” speed.

This paper calculates and compares losses in power devices between three popular topologies: 3L-SC, 3L-NPC and 3L-ANPC. The commutation cells are composed by IGBT modules type Eupec FF200R33KF2C, and the clamp diodes are equivalent to the IGBT modules’ diodes. The analysis made on the 3L-SC and 3L-NPC topologies proved that the losses in middle side power devices (3L-SC) and the losses in clamp diodes (3L-NPC) increase simultaneously with the reducing of the modulation index. This leads to the increase of the junction temperature in power devices which limits the converters output power, especially at “zero” speed operation. The paper shows that 3L-ANPC structure leads to the best losses balancing in power devices.

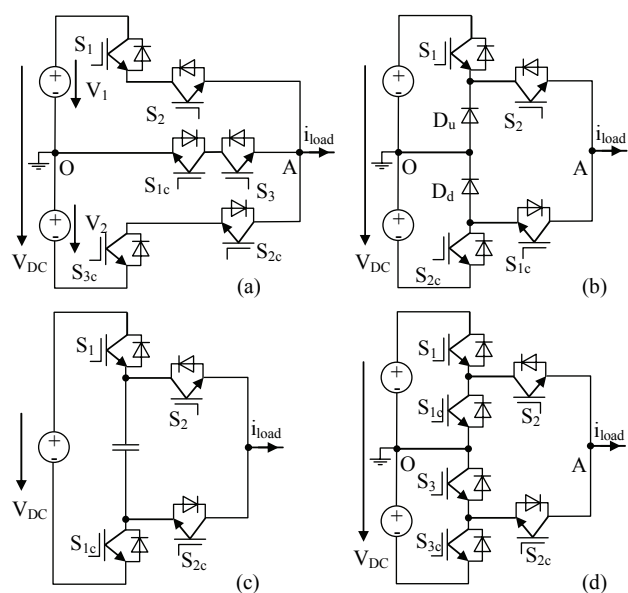


Fig.1. Popular 3L structures: (a) 3L-SC, (b) 3L-NPC, (c) 3L-FC, (d) 3L-ANPC

3L-Stacked Cells Structure

The 3L-SC structure is made of 6 switches disposed on three sides (Fig.1a). Each switch is capable to support a voltage equal to $V_{DC}/2$. The exterior sides are made of two switches serially connected and the middle side is composed by two switches opposite connected. The middle point of the two serial voltage supplies is defined as neutral point. The switches form 3 commutation cells controlled with α_1 , α_2 and α_3 duty cycles: cell 1 (S_1 - S_{1c}), cell 2 (S_2 - S_{2c}) and cell 3 (S_3 - S_{3c}). A sinusoidal PWM strategy was used in order to emphasize the constraints applied to 3L-SC converter (Fig.2).

The PWM strategy has four switching states (Table 1). The output voltage (v_{AO}) has three states: $V_{DC}/2$, 0 and $-V_{DC}/2$. Two switching states (P and N) correspond to direct connection of the load at DC voltage and the others states correspond to obtain “0” voltage level (O_1^- and O_2^+). For $V_{DC}/2$ voltage level (P) the switches S_1 , S_2 and S_3 must be turned on. For $-V_{DC}/2$ level (N) the switches S_{1c} , S_{2c} and S_{3c} must be turned on.

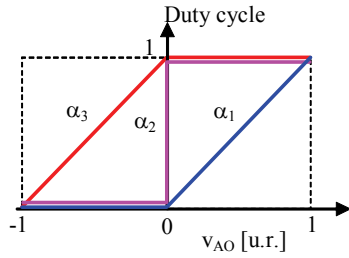


Fig.2. Duty cycles for 3L-SC and 3L-ANPC topologies

The O_1^- state is obtained when the reference output voltage is negative. In this case the S_{1c} , S_{2c} and S_3 are turned on. The O_2^+ state is obtained when the reference output voltage is positive. For this switch sequence the S_{1c} , S_2 and S_3 must be turned on.

Table 1. Output voltage for the switching sequences of 3L-SC

| Output Voltage (v_{AO}) | Switching State | Switch Sequence | | | | | |
|-----------------------------|-----------------|-----------------|----------|-------|----------|-------|----------|
| | | S_1 | S_{1c} | S_2 | S_{2c} | S_3 | S_{3c} |
| $-V_{DC}/2$ | N | 0 | 1 | 0 | 1 | 0 | 1 |
| 0 | O_1^- | 0 | 1 | 0 | 1 | 1 | 0 |
| | O_2^+ | 0 | 1 | 1 | 0 | 1 | 0 |
| $V_{DC}/2$ | P | 1 | 0 | 1 | 0 | 1 | 0 |

The energy conversion is based on two partial uncoupled stages and this represents a disadvantage for the structure. The middle side is common for the both energy conversion stages. This leads to the increase of conduction losses in S_{1c} and S_3 switches, which limit the load current, especially at low modulation index.

3L-Neutral Point Clamped Structure

A three-level neutral point clamped structure (NPC) is shown in Fig.1b. The four switches form two commutation cells controlled by α_1 and α_2 duty cycles: cell 1 (S_1 - S_{1c}) and cell 2 (S_2 - S_{2c}). The duty cycles (Fig.3) are obtained by following a sinusoidal PWM strategy. The clamp diodes D_u and D_d are the distinct elements of this circuit. Compared to the 3L-SC topology, this structure use only three switching states (P, O and N) to obtain the three voltage levels (Table 2). "O" switching state is obtained by turning on the inner switches (S_{1c} and S_2). In this case the load inductive current can pass through two different paths. If the load current is positive, it passes through the D_u clamp diode and the S_2 switch. If the load current is negative, the path is through the D_d clamp diode and the S_{1c} switch.

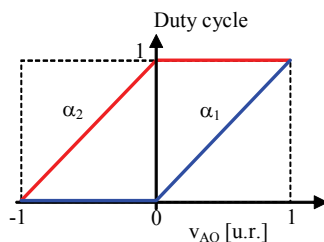


Fig.3. Duty cycles for 3L-NPC topology

Table 2. Output voltage for the switching sequences of 3L-NPC

| Output Voltage (v_{AO}) | Switching State | Switch Sequence | | | |
|-----------------------------|-----------------|-----------------|----------|-------|----------|
| | | S_1 | S_{1c} | S_2 | S_{2c} |
| $-V_{DC}/2$ | N | 0 | 1 | 0 | 1 |
| 0 | O | 0 | 1 | 1 | 0 |
| $V_{DC}/2$ | P | 1 | 0 | 1 | 0 |

3L-Active NPC Structure

The 3L-ANPC structure was developed in order to obtain a better balancing of losses in power devices [8]. An active switch is anti-parallel connected with clamp diodes from NPC structure (Fig.1d). The three commutation cells are controlled by α_1 , α_2 and α_3 duty cycles: cell 1 (S_1 - S_{1c}), cell 2 (S_2 - S_{2c}) and cell 3 (S_3 - S_{3c}).

The modification of duty cycles is made similarly to the 3L-SC topology (Fig.2) following a sinusoidal PWM strategy.

The switches are disposed on two independent stages: stage 1 (S_1 , S_{1c} and S_2) and stage 2 (S_{2c} , S_3 and S_{3c}). The cell 1 and cell 3 switch at a high frequency while the cell 2 switches at a low frequency. Similarly to the 3L-SC structure, the PWM strategy for 3L-ANPC has four switching states (Table 3).

Table 3. Output voltage for the switching sequences of 3L-ANPC

| Output Voltage (v_{AO}) | Switching State | Switch Sequence | | | | | |
|-----------------------------|-----------------|-----------------|----------|-------|----------|-------|----------|
| | | S_1 | S_{1c} | S_2 | S_{2c} | S_3 | S_{3c} |
| $-V_{DC}/2$ | N | 0 | 0 | 0 | 1 | 0 | 1 |
| 0 | O_1^- | 0 | 0 | 0 | 1 | 1 | 0 |
| | O_2^+ | 0 | 1 | 1 | 0 | 0 | 0 |
| $V_{DC}/2$ | P | 1 | 0 | 1 | 0 | 0 | 0 |

The "0" voltage level is obtained by two switching states (O_1^- and O_2^+): Thus the load current can pass in both directions only through stage 1 (paths: S_1 - S_2 or S_{1c} - S_2) or only through stage 2 (paths: S_{3c} - S_{2c} or S_3 - S_{2c}).

Analytic expressions to calculate the losses

The evolution of temperature in IGBT modules is a direct consequence of the total losses and imposes the maximum power that can be delivered by power switches.

The following hypotheses were considered to calculate the losses in power devices:

- all semiconductor devices switch at the same voltage, equal to $V_{DC}/2$;
- the load is considered linearly;
- the load current is sinusoidal;
- the current and voltage ripples are neglected;
- the phase-shift θ between the load current (i_{load}) and the output voltage (v_{AO}) is included in $[0, \pi]$ interval;
- the dead times of the IGBT modules are neglected.

The total losses (P_X) are made up of conduction losses (P_{condX}) and switching losses (P_{swX}) [11]:

$$(1) \quad P_X = P_{condX} + P_{swX}$$

A) Conduction losses

The conduction losses are obtained as a sum of all conduction losses in transistors (P_{condT}) and diodes (P_{condD}):

$$(2) \quad P_{condX} = P_{condT} + P_{condD}$$

$$(3) \quad P_{condT} = v_{CE0} \cdot I_{avg}^{condT} + r_{dT} \cdot (I_{rms}^{condT})^2$$

$$(4) \quad P_{condD} = v_{D0} \cdot I_{avg}^{condD} + r_{dD} \cdot (I_{rms}^{condD})^2$$

where: v_{CE0} , r_{dT} , v_{D0} and r_{dD} – parameters of the transistors and diodes, I_{avg}^{condX} and I_{rms}^{condX} – average and RMS values of the conduction current through X semiconductor.

The expressions for conduction losses depend on the RMS load current (I). The paper presents an example to calculate the conduction losses in T_1 transistor from the S_1 switch (3L-SC, 3L-NPC and 3L-ANPC).

The modulation function for T_1 is sinusoidal:

$$(5) \quad f_{T1}(x) = M \cdot \sin x, \quad x \in [0, \pi]$$

The T_1 transistor is in conduction during $[\theta, \pi]$ interval. As a result, the average and RMS values of the conduction current through T_1 semiconductor can be written:

$$(6) \quad \begin{aligned} I_{avg}^{condT1} &= \frac{1}{2\pi} \int_{\theta}^{\pi} \sqrt{2} \cdot I \cdot \sin(x-\theta) \cdot f_{T1}(x) \cdot dx = \\ &= \frac{I \cdot \sqrt{2} \cdot M}{4 \cdot \pi} \cdot [(\pi - \theta) \cdot \cos \theta + \sin \theta] \end{aligned}$$

$$(7) \quad \begin{aligned} I_{rms}^{condT1} &= \sqrt{\frac{1}{2\pi} \int_{\theta}^{\pi} (\sqrt{2} \cdot I \cdot \sin(x-\theta))^2 \cdot f_{T1}(x) \cdot dx =} \\ &= I \cdot \sqrt{\frac{M}{2\pi} \cdot \left[1 + \frac{4}{3} \cdot \cos \theta + \frac{1}{3} \cdot \cos(2 \cdot \theta) \right]} \end{aligned}$$

For the other switches, the losses are similarly calculated but the modulation functions and the conduction intervals differ from a switch to another for each structure.

B) Switching losses

The IGBTs designers deliver characteristics for the consumed energy at the turning off $E_{off}(I_C)$ and the consumed energy at the turning on $E_{on}(I_C)$. These characteristics depend on the switched voltage (v_{def}) and on the switched current. For an entire switching period, the total energy absorbed by a semiconductor device at v_{def} corresponds to the sum of these energies:

$$(8) \quad E_{vdef}(I_C) = E_{on}(I_C) + E_{off}(I_C)$$

This sum (8) can be approximated with a parabola with A_{swX} , B_{swX} and C_{swX} coefficients:

$$(9) \quad E_{vdef}(I^{swX}) = A_{swX} + B_{swX} \cdot I_{avg}^{swX} + C_{swX} \cdot (I_{rms}^{swX})^2$$

The following proportionality law is used to take into consideration the real commutation voltage (v_{sw}) for transistors [13]:

$$(10) \quad E_{vdef}(v_{sw}, I^{swX}) = \frac{v_{sw}}{v_{def}} \cdot E_{vdef}(I^{swX})$$

For a semiconductor device which switch at f_{sw} on Δ_{sw} interval the losses in commutation can be written as follows:

$$(11) \quad \begin{aligned} P_{swX} &= f_{sw} \cdot \frac{v_{sw}}{v_{def}} \cdot \left(A_{swX} \cdot \Delta_{sw} + B_{swX} \cdot I_{avg}^{swX} + \right. \\ &\left. + C_{swX} \cdot (I_{rms}^{swX})^2 \right) \end{aligned}$$

where, A_{swX} , B_{swX} , C_{swX} and v_{def} – constants taken from the IGBT's characteristics, Δ_{sw} – ratio between the switching interval and the switching period for semiconductor device, I_{avg}^{swX} and I_{rms}^{swX} – average and RMS values of the

switched current through X semiconductor, f_{sw} – switching frequency and v_{sw} – switched voltage.

The expressions for switching currents also depend on the commutation intervals and on the RMS load current (I). The paper presents an example to calculate the switching losses in T_1 transistor from the S_1 switch (3L-SC, 3L-NPC and 3L-ANPC). This transistor switches on $[\theta, \pi]$ interval. As a result, the average and RMS values of the switching current through T_1 semiconductor can be written as follows:

$$(12) \quad I_{avg}^{swT1} = \frac{1}{2\pi} \int_{\theta}^{\pi} \sqrt{2} I \sin(x-\theta) dx = \frac{I\sqrt{2}}{2\pi} (1 + \cos(\theta))$$

$$(13) \quad \begin{aligned} I_{rms}^{swT1} &= \sqrt{\frac{1}{2\pi} \int_{\theta}^{\pi} (\sqrt{2} I \sin(x-\theta))^2 \cdot dx =} \\ &= I \sqrt{\frac{1}{2\pi} \cdot \left(\pi - \theta + \frac{\sin(2\theta)}{2} \right)} \end{aligned}$$

This paper compares the losses in power devices between three popular topologies 3L-SC, 3L-NPC and 3L-ANPC. The commutation cells are composed by IGBT modules type Eupec FF200R33KF2C, and the clamp diodes are equivalent to the IGBT module diodes.

Loss distribution in power devices

The losses in power devices depend on the PWM strategy. In the case of analysed converters, there are commutation cells that switch at a low frequency and others that switch at a high frequency. The last ones were controlled by sinusoidal duty cycles. The PWM strategies used to control the popular 3L structures are equivalent and lead to the same output voltages v_{AO} . The critical points are located at the boundaries of the converter's operating area, being maximum and minimum modulation index (M), at power factor of PF=1 and PF=-1. In these points the loss distribution presents the biggest lack of balance. All the other operation points are less critical.

Fig.4 shows the loss distribution in switches for 3L-SC, 3L-NPC and 3L-ANPC structures. They were considered two extreme values of modulation index ($M=0.05$ and $M=0.95$) and six values for power factor (PF=1; 0.86; 0.707; 0.5; 0 and -1). The next were observed:

- the middle stage switches (S_{1c} and S_3) from 3L-SC topology limit the maximum phase current at low modulation indexes;
- in the case of 3L-NPC operation mode, at higher modulation index, total losses in switches are not very different from 3L-SC structure;
- for high values of modulation index, the devices that limit the switching frequency and the maximum phase current are the outer ones, as follow: for 3L-SC – S_1 and S_{3c} , for 3L-NPC – S_1 and S_{2c} and for 3L ANPC – S_1 and S_{3c} ; this leads to the increase of the junction temperature in power devices which limits the converters output power;
- in the case of low modulation index, the losses distribution in switches is more uniform in 3L-NPC and 3L-ANPC than in 3L-SC;
- at high modulation index and low power factor/rectifier operation mode the losses distribution in switches is more uniform in 3L-ANPC than 3L-NPC or 3L-SC;

A better loss-balancing ensures that the operating junction temperatures of all devices do not exceed their limits under all specified operation conditions.

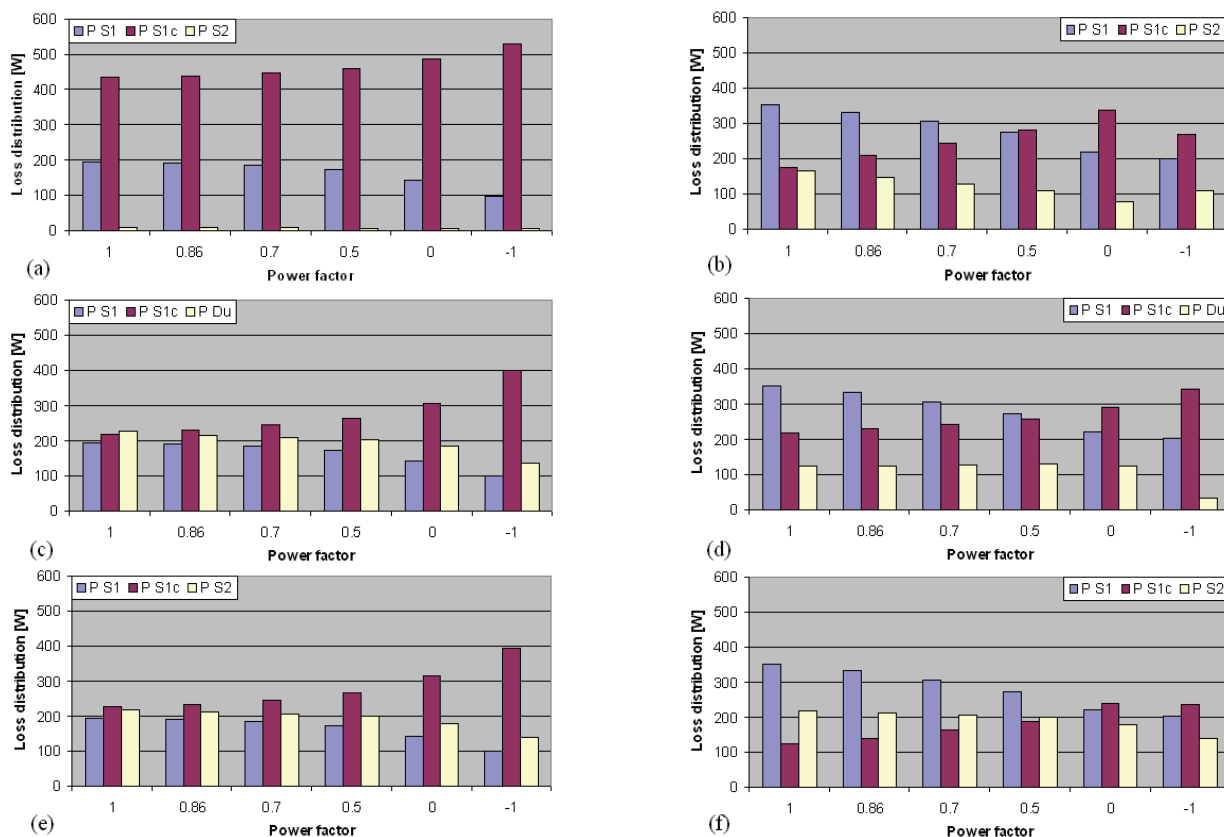


Fig.4: Simulated loss distribution in popular 3L topologies (Eupec FF200R33KF2C IGBTs, $I=130A$, $V_{DC}=3000V$, $f_{sw}=1000Hz$): (a) 3L-SC ($M=0.05$), (b) 3L-SC ($M=0.95$), (c) 3L-NPC ($M=0.05$), (d) 3L-NPC ($M=0.95$), (e) 3L-ANPC ($M=0.05$), (f) 3L-ANPC ($M=0.95$)

Conclusion

In this paper the states and commutation sequences for three of the most popular 3L topologies (3L-SC, 3L-NPC and 3L-ANPC) were analysed. Only two of these topologies (3L-SC and 3L-ANPC) are made of two conversion stages. In the case of 3L-SC structure these stages are not completely decoupled, while in the 3L-ANPC one the conversion stages are completely decoupled. This advantage confers to the 3L-ANPC topology more degrees of freedom, which can be used to develop some PWM control strategies with high performances. PWM sinusoidal strategies were used to control the structures in order to obtain the same output voltages.

It is also presented an analytic method to calculate the total losses in power devices and it is investigated the loss distribution among the semiconductor devices. This analysis shows that the total losses in studied converters are not different, but the loss distribution in switches is unequal and it depends on the type of structure, the modulation index and the power factor. The losses in the most stressed switches limit the operation frequency and the maximum phase current of the entire converter.

Between the studied structures, the 3L-ANPC topology allows a better loss balancing in switches, both at low and high values of modulation index, for any power factor.

REFERENCES

- [1] Rodriguez J., Lai J.-S., Peng F.Z., Multilevel Inverters: A Survey of Topologies, Controls, and Applications, *IEEE Trans. on Ind. Electronics*, Vol.49 (2002), 724-738
- [2] Baker R.H.: Electric Power Converter, U.S.Patent 3 867 643, Feb.1975
- [3] Bhagwat P., Stefanovic V.R., Generalized structure of a multilevel PWM inverter, *IEEE Industry Applications Society Annual Meeting* (1980), pp.761-76

- [4] Brumsickle W.E., Divan D.M., Lipo T.A., Reduced Switching Stress in High-Voltage IGBT Inverters via a Three-Level Structure, *Applied Power Electronics Conference and Exposition APEC'98*, Vol.2 (1998), pp.544-550
- [5] Meynard T.A., Foch H., Forest F., Turpin C., Richardeau F., Multicell Converters, Derived Topologies, *IEEE Trans. on Ind. Electronics*, Vol.49 (2002), pp.978-986
- [6] Nabae A., Takahashi I., Akagi H., A new neutral-point-clamped PWM inverter, *IEEE Trans.Industry Applications*, Vol.IA-17 (1981), pp.518-523
- [7] Baker R.H., Bridge converter circuit, U.S.Patent 4 270 163, May 1981
- [8] Meynard T.A., Foch H., Multi-level Conversion: High Voltage Choppers and Voltage-Source-Inverters, *IEEE Power Electronics Specialist Conference* (1992), pp.397-403
- [9] Brückner T., Bernet S., Loss balancing in three-level voltage source inverters applying active NPC switches, *Proc.IEEE PESC*, Vancouver (2001), pp.1135-1140
- [10] Brückner T., Bernet S., Güldner H., The Active NPC Converter and Its Loss-Balancing Control, *IEEE Trans.Ind.Electronics*, Vol.52 (2005), pp.855-868
- [11] Lienhardt A.-M., Etude de la Commande et de l'Observation d'une Nouvelle Structure de Conversion d'Energie de type SMC (Stacked Multicell Converters), Phd. Thesis (2006), INPT Toulouse, France

Authors: prof.dr.ing. Dan Florica, "Politehnica" University of Bucharest, Faculty of Electrical Engineering, 313 Spl. Independentei, 060042 Bucharest, E-mail: danfi2005@yahoo.com; prof.assoc.dr.ing. Guillaume Gateau, Institute National Polytechnic of Toulouse, ENSEEIHT-LAPLACE, 2 Camichel, 31071, Toulouse Cedex 7, E-mail: gateau@laplace.univ-tlse.fr; prof.dr.ing. Mircea Covrig, Politehnica University of Bucharest, Faculty of Electrical Engineering, 313 Spl.Independentei, 060042 Bucharest, E-mail: m_covrig@amotion.pub.ro; prof.dr.ing. Ioan Popa, University of Craiova, Faculty of Electrical Engineering, Electrical Apparatus and Technologies Department, 107 Bd. Decebal, 200440 Craiova, E-mail: ipopa@elth.ucv.ro; prof.dr.ing. Mariana Dumitrescu, "Dunarea de Jos" University of Galati, 111 Domneasca, 6200 Galati, E-mail: mariana.dumitrescu@ugal.ro.

The design of electrical system with microcontroller for the measurement of electrical parameters

Abstract. The paper presents an experimental monitoring system, developed by the authors, using a micro-controller within the 8051 family. This micro-system has two main parts: the acquiring and transfer module and the user interface developed using the facilities specific to Graphic User Interface of Matlab®. The possible functions of the system are related to the acquiring of the six signals specific to the tri-phased equipments, three voltages and three currents end store the number of the commutations performed by the installation.

Abstract. Artykuł przedstawia, opracowany przez autorów, eksperymentalny system monitoringu wykorzystujący mikrokontroler z rodziny 8051. Przedstawiony mikrosystem składa się z dwóch części: modułu akwizycji i transferu oraz interfejsu użytkownika zaimplementowanego przy wykorzystaniu specyficznych funkcji biblioteki Graphic User Interface of Matlab®. Systemu ma możliwość akwizycji sześciu określonych sygnałów systemu elektrycznego z mikrokontrolerem do pomiaru parametrów).

Keywords: micro-controller, monitoring, assembler programming, user interface.

Słowa kluczowe: mikrokontroler, monitoring, programowanie w języku assembler, interfejs użytkownika.

Introduction

The modern electric equipments include performant monitoring systems based on microcontrollers. The electrical equipments, being characterised by small time constants and high risk, impose major efforts in order to develop competitive monitoring systems.

The paper deals with experimental monitoring system, developed by the authors, by using a microcontroller within the 8051 family.

This micro-system has two main parts: the acquiring and transfer module and the user interface developed using the facilities specific to Graphic User Interface (GUI) of Matlab®. The user interface has as aim to establish an on-line link between the acquiring and transfer module and the user.

For the fastest and efficient behaviour to the user's demanded functions, the acquiring and transfer module was programmed in assembler, by using the complex interrupting system of the controller.

The possible functions of the system are related to the acquiring of the six signals specific to the tri-phased equipments, three voltages and three currents. The interface displays, at demand, the number of commutations of the equipment, stored in the non volatile serial RAM memory of the acquiring and transfer module.

The domain of the possible input signals reaches 830V for the voltages, 8.2A for the current respectively. We mention that in what concern the current domain, it corresponds to the 5A connection of the transducers and can be easily extended to 12.3A or 24.6A with different connections. In order to extend the measure domains, it is also possible to have external voltage and/or current transformers.

As such monitoring systems implies two main subsystems: hardware (sensors, transducers, A/DC, serial transmission) and software (field module programming, transmission protocols, user interface), the two parts must interact without conflicts, achieving the expected performances.

The hardware architecture

The hardware part of the monitoring system is centred on the Dallas micro-controller DS87C550. This type of micro-controller is code fully compatible with the 8051 family micro-controllers, being equipped with many integrated peripherals that make it suitable for embedded applications. More than that, being equipped with the high

speed core specific to the Dallas micro-controllers, the performances achieved by the hardware subsystem based on this module make it very suitable for the on-line monitoring of the high speed electrical equipments.

The acquiring and transfer module consists of the blocks: Sources, Controller, Local console, Inputs, Outputs and Serial communication interface. By the way of three precise voltage regulators, the Sources block supplies the regulated voltages to the micro system.

The Controller block is the core of the module and consists of the controller itself, the full duplex RS485 serial interface, connector to the 7 digits display, digital open collector output, that can be used for commanding a power element (relay), non-volatile serial EEPROM with 32 bytes, for saving adjusting parameters or essential events, 8 micro switches for possible changes of the system's functionality, LED for signalling the state of the system.

The Fig. 1 depicts the bloc diagram of the acquiring and transfer module.

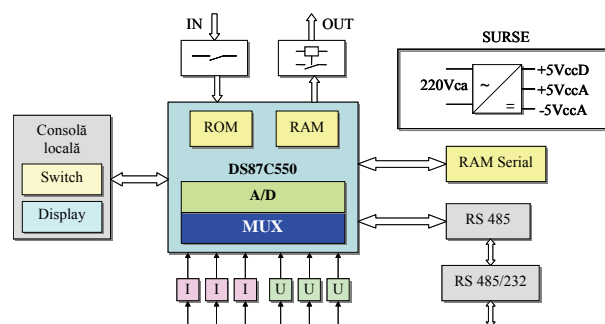


Fig.1. The acquiring and transfer module

In order to integrate the mentioned component in the hardware subsystem of the monitoring structure, specific to the electrical equipments, special transducers must be used.

The system was designed to acquire all the three phase currents and voltages. As current sensors, LEM transducers LTS15-NP are used, special adapted to the integration with the micro-controller [1].

The voltages are measured by using three precise voltage dividers, built with 1% resistors. These dividers were designed in such manner to obtain, at the rated voltage, a trip by $\pm 0.5V$. The 1% tolerance is quite enough,

but more important is the thermal stability. For this reason, for building these dividers were used resistors with identical thermal factor.

The software subsystem

For the fastest and efficient behaviour to the user's demanded functions, the acquiring and transfer module was programmed in assembler, by using the complex interrupting system of the controller [2].

The compensation of the possible offset both of the current transducers and of the resistive dividers is performed a single time, at the system setting, by using the calibration routine. This task is achieved only in local-mode control, by proper configuring the micro switches. The obtained values are stored in the non volatile serial EEPROM RAM [3]. At each start of the system, the values of the offsets are read from the serial non volatile RAM and further used for the correction of the acquired samples.

Experimental tests were performed both for calibrating the six transducers and for checking their linearity. The RMS values of the currents and voltages as inputs and the peak values of the corresponding outputs were measured.

Due to the limitations of the internal RAM memory of the micro-controller, the acquisition strategy was fixed to get all the time 120 samples within 20ms. Depending on the option of the user, the following types of acquisitions can be performed: one channel (phase voltage or current) with 175 μ s sampling period; two channels (phase current and voltage of the same phase) with 350 μ s sampling period; three channels (phases currents or voltages of the three phases) with 500 μ s sampling period; six channels (all phases currents and voltages of the three phases) with 1ms sampling period. The equidistance between the acquired data packages is achieved by a proper programming of one

Timer of the controller, which will generate an interruption at specified intervals. Immediately after the acquisition of the first sample, the transmission routine is started and consequently, the acquisition and the transmission work in parallel, on the same bank of data [4].

By using the interruption system of the micro-controller, the code, written in assembly, is quite compact and efficient. The whole acquisition process is started by the serial port interruption that receives a command generated by the user interface (on-line).

Depending on the structure of the channels to be acquired, the sampling period is programmed within a Timer, in order to have equidistant samples. At each Timer interruption, all the programmed channels are sampled consecutively, based on using the interruption system of the micro-controller.

User Interface

As medium for the development of the user interface, the Graphic User Interface (GUI) of Matlab® was chosen.

It allows the bi-directional communication with the hardware subsystem. Thus, on one hand, based on the channels chosen within the interface, it sends the proper command to the hardware subsystem which configures the proper sampling period. On the other hand, the user interface receives the sampled data and reconstitutes the signals on each sampled channel.

The user interface was conceived in such way to be intuitive and easy to use. In the same time, more inter-blockings were inserted, in order to avoid the transmission of wrong commands, keeping always the high versatility of the module's programming.

The user can choose what to be displayed: instantaneous values of the signals (currents or voltages) of one, two, three or all the six channels, or the synthetic

values of the signals (RMS, phases, powers) of one or all the three phases respectively.

No matter of the displaying mode, for all the commands configurations, the user interface is able to demand acquisition and conditioning in a continuous manner, with the rate of refresh of about 1 second, or on a single period. The user interface is launched within Matlab®, with the command "inter". Consequently, the application is initiated and a window is opened.

Fig. 2 depicts an example, when the command is to display the instantaneous values of the currents and voltages on the all three phases.

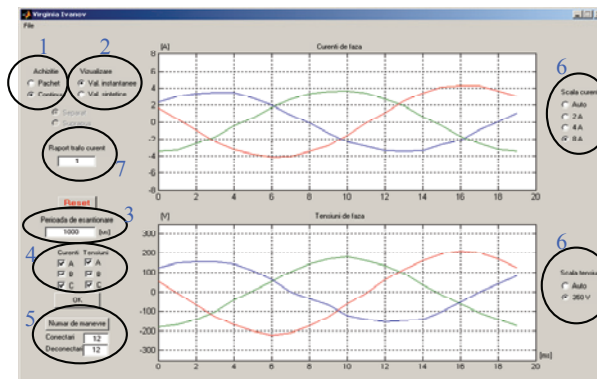


Fig.2. User interface window

The rated current of the employed current transducers is 5A. If we have to monitor equipments whose rated current I_N is much greater, it is necessary to use external current transformers having the ratio $I_N/5$.

The user interface offer the possibility to specify the value of the ratio of the external current transformers and takes into account then this value when scaling the axes. For a correct displaying of the values, at the start-up of the application, the user must specify the value of the ratio of the external current transformers (zone 7). The default value of the ratio is 1 (without external transformers).

Then, the displaying type is selected from the buttons within the zone „Visualization”: instantaneous or synthetic values (zone 2).

If the continuous acquisition is preferred, this must be chosen with the buttons within the zone „Acquisition”. The default selection is of type „Packet” that corresponds to one period acquisition (zone 1).

Then, the channels to be acquired and displayed are selected. In the same time, the value of the sampling period is updated automatically, depending on the number of selected channels (zone 3).

Depending on the user's demand, can be displayed on one hand, the instantaneous values of the signals (currents or voltages) on one, two, three or all the six channels, or on the other hand, the synthetic values (RMS values, powers, phases) on a selected phase or on all the three (zone 4).

The interface displays, at demand, the number of commutations of the equipment, stored in the non volatile serial RAM memory of the acquiring and transfer module (zone 5).

If two channels are selected to be displayed as instantaneous values, the buttons for the selection of the type of representation become active. From here, can be selected the representation in different axes or in the same axes, with the automatic adaptation of the scales, in order to be easily readable. For the option of representation in different axes, the buttons for selecting the scales of the two systems become active (zone 6).

Experimental results

The described hardware subsystem and user interface were used to monitor two types of loads: a resistive one and a high inductive one.

The results obtained with the experimental micro-system are compared with the information found with industrial measurement equipment, the Tektronix power scope.

In the following, some results will be presented.

Fig.3 depicts the instantaneous values of voltages obtained with the user interface of the micro-system for the three phases of a resistive load.

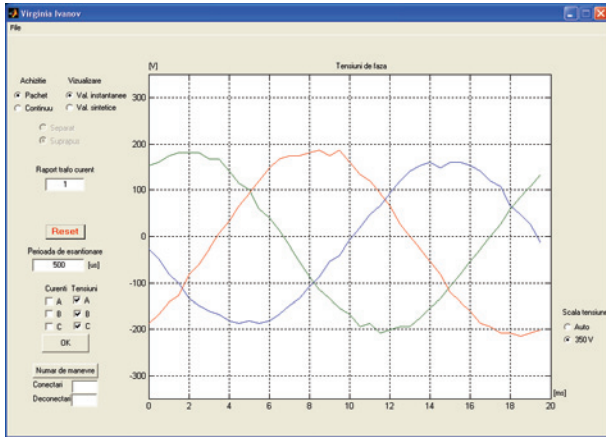


Fig.3. Experimental results with micro-system

For the same load, Fig. 4 contains the plots of the screen of the Tektronix scope.

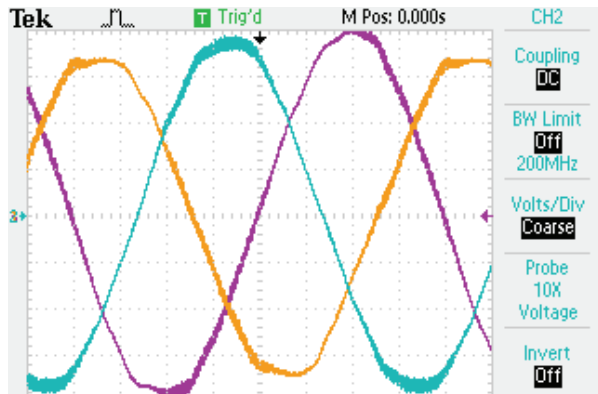


Fig.4. Experimental results with Tektronix

It can be noticed the high similitude of the values obtained with the two measurement systems.

The synthetic values are computed based on the instantaneous values sampled on one period by using the following expressions:

- rms values:

$$(1) \quad U = \sqrt{\frac{1}{N \cdot \Delta t} \cdot \sum_{k=1}^N u_k^2 \cdot \Delta t}$$

where: N – number of samples per period, Δt – sampling period, u_k – the sampled values of the voltage

- the angle between the two signals of the same phase is computed by using the Mann-Morrison algorithm that computes the phase angle depending on three successive sampled values [5]:

$$(2) \quad \varphi = \arctg \frac{2\omega\tau u_2}{u_3 - u_1} - \arctg \frac{2\omega\tau i_2}{i_3 - i_1}$$

where: τ – sampling period, ω – frequency expressed in rad/sec, u_1, u_2, u_3 – three successive sampled values of one phase voltage, i_1, i_2, i_3 – three successive sampled values of the corresponding phase current.

Fig.5 depicts the instantaneous values obtained with the micro-system for the phase A of an inductive load and Fig.6 presents the synthetic values for the same load.

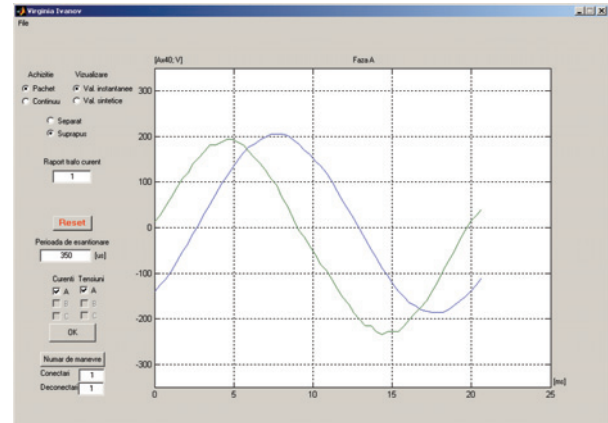


Fig.5. Instantaneous values for the phase A of an inductive load with micro-system



Fig.6. Synthetic values for the phase A of an inductive load with micro-system

The results obtained with the experimental micro-system are compared with the information found with the industrial measurement equipment, Fluke 196 power scope.

Fig.7. contains the plots of the screen of the Fluke 196 scope.

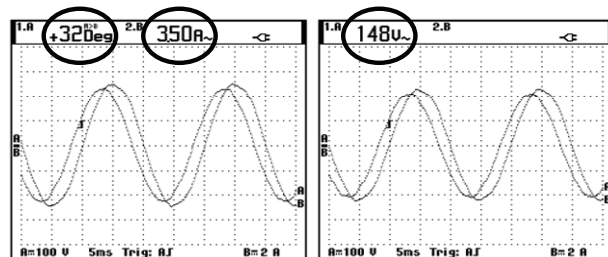


Fig.7. Experimental results with the Fluke 196 power scope

The micro-system presented in this paper allows the acquisition and display of six independent signals (but having common ground), respectively the voltages and the currents, or the synthetic values (active power, reactive power, power factor), on all the three phases. This facility could be considered as an important advantage comparing with the two industrial measurement devices, the scopes Tektronix and Fluke mentioned in the paper.

The Fig. 8 and Fig.9 depict an example of such data set.

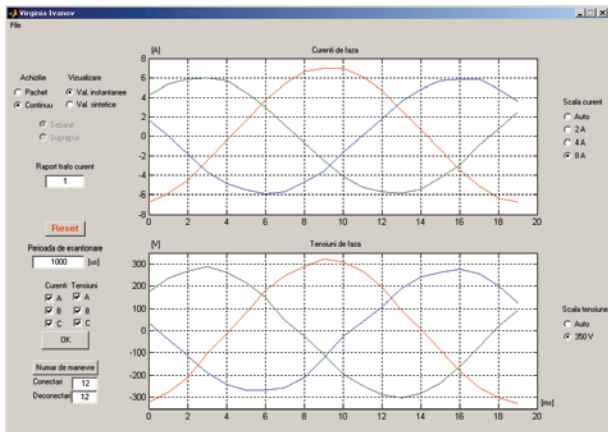


Fig.8. Instantaneous values for the three phases with micro-system

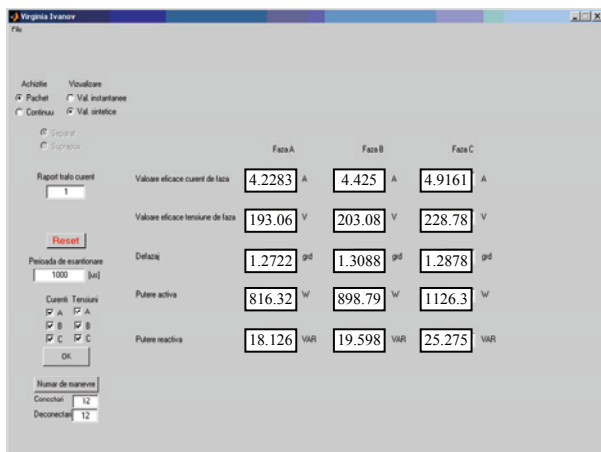


Fig.9. The synthetic values obtained with micro-system

Fig.8 depicts the acquired signals for a pure resistive load, when all six channels were selected with continuous acquisition and Fig.9 presents synthetic values obtained with the micro-system.

Conclusions

A simple, experimental model of a monitoring system of the electric equipments was presented. It consists of a hardware subsystem and a software one, both developed by the authors. Due to the small time constants and high risk specific to the considered applications, the whole structure was designed in order to respond fast and efficient to the specified demands.

The experimental results, compared with the indications of classical measurement devices confirm the correctness, both of the micro-controller programming and of the algorithms specific to the user interface.

REFERENCES

- [1] *** LEM Components, Current Transducer LTS 15-NP (1999)
- [2] *** DALLAS Semiconductor, High-Speed Microcontroller User Guide (1999)
- [3] *** DALLAS Semiconductor, DS87C550 EPROM High-Speed Micro with A/D and PWM (1999)
- [4] Guo Y., Lee H. C., Wang X., A Multiprocessor Digital Signal Processing System for Real-time Converter Applications, *IEEE Transactions on Power Systems*, 7(1992), No.2.
- [5] Cârțină G., Artificial neuronal networks and expert systems for energetics, *Editura Gh.Asachi* (1994).

Authors: lecturer dr. eng. Virginia Ivanov, University of Craiova, Faculty for Electrical Engineering, 107 Decebal Blv., 200440 Craiova, E-mail: vivanov@elth.ucv.ro; prof. dr. eng. Sergiu Ivanov, University of Craiova, Faculty for Electromechanical Engineering, 107 Decebal Blv., 200440 Craiova, E-mail: sivanov@em.ucv.ro; prof. dr. eng. Maria Brojboiu, University of Craiova, Faculty for Electrical Engineering, 107 Decebal Blv., 200440 Craiova, E-mail: mbrojboiu@elth.ucv.ro; prof. dr. eng. Silvia Maria Digă, University of Craiova, Faculty for Electrical Engineering, 107 Decebal Blv., 200440 Craiova, E-mail: sdiga@elth.ucv.ro.

Output power characteristics of the GaInAs lasers emitting in the spectral range of 1.0 μm

Abstract. Luminescence spectra of the quantum-well heterolasers in the GaInAs–GaAs–AlGaAs system are measured, polarization properties of the radiation are analyzed and theoretical description of the emission characteristics is given.

Streszczenie. Przedstawiono pomiary spektrum luminescencji studni kwantowej w systemie GaInAs–GaAs–AlGaAs. Przeanalizowano właściwości polaryzacji promieniowania oraz przedstawiono teoretyczny opis charakterystyki emisji. (Charakterystyki mocy laserów GaInAs, emitujących w zakresie 1 mikrometra)

Keywords: quantum well, luminescence, polarization of radiation, amplification.

Słowa kluczowe: studnia kwantowa, luminescencja, polaryzacja promieniowania, wzmacnianie.

1. Introduction

Lasers and superluminescence diodes emitting at the wavelength diapason of 1.0–1.3 μm are intensively developed and widely used in fiber-optical systems, free atmosphere lines of communications, and also for pumping of solid-state lasers [1, 2]. Powerful superluminescence diodes having wide emission spectra are applied as optimal sources for optical coherent tomography [3]. However out power characteristics of heterostructure lasers and superluminescence diodes operating at the diapason of wavelengths 1.0–1.3 μm are not studied in detail and influence of the component composition of the heterostructure layers on the emission spectra and efficiency of injection is not examined.

In the paper, optical model of quantum-well heterostructures with active layers of GaInAs, which emit in the spectral range of 1 μm is suggested and observed experimental spectra of amplified luminescence including effects of polarization of radiation are explained.

2. Optical model of laser heterostructures

Studied laser heterostructures contain two quantum wells of GaInAs with width of 6 nm. Barrier layers are made from GaAs. These layers and the quantum wells are not doped. Change in the mole fraction x of InAs from 0 to 0.4 in the active layers of GaInAs results in the varying of the wavelength of emission λ_{1h} which corresponds to the initial optical transitions between the first (ground) states of the electron and heavy hole subbands in the quantum wells. Knowledge of such a value gives possibility to predict maximum in the amplified luminescence spectrum at quite enough level of excitation of the heterostructure (Fig. 1).

Comparison of results of measured luminescence spectra of the laser heterostructures under pump current near the threshold with calculated spectra shows that good agreement occurs if in the active region the material of the quantum wells corresponds to the ternary compound of $\text{Ga}_{0.78}\text{In}_{0.22}\text{As}$. In this case the wavelength connected with the initial optical transitions through the ground subbands of electrons and heavy holes is 1.041 μm .

Physical parameters used at modeling of spectral characteristics of the laser heterostructures are given in Table 1. Values of the effective masses of carriers are determined through the Luttinger parameters for the appropriate compounds. Here, m_c , m_{vh} , and m_{vl} are the longitudinal components of the effective masses of electrons, heavy holes, and light holes in the active layer and they determine quantum-size levels. Quantities m_{vht} and m_{vlt} are the transverse components of the effective masses of heavy holes and light holes in the active layer

and they determine the density of states in the respective subbands. In the GaAs barrier layers the effective masses of electrons, heavy holes, and light holes are m_{cb} , m_{vhb} , and m_{vlb} . The $\text{Ga}_{0.78}\text{In}_{0.22}\text{As}$ active layer is characterized by the energy band gap E_{g0} at temperature $T = 300$ K and in conditions of thermal equilibrium (with no pump current). For the examined $\text{Ga}_{0.78}\text{In}_{0.22}\text{As}$ –GaAs system the heights of the potential barriers in the conduction band and valence band are equal to ΔE_c and ΔE_v , respectively.

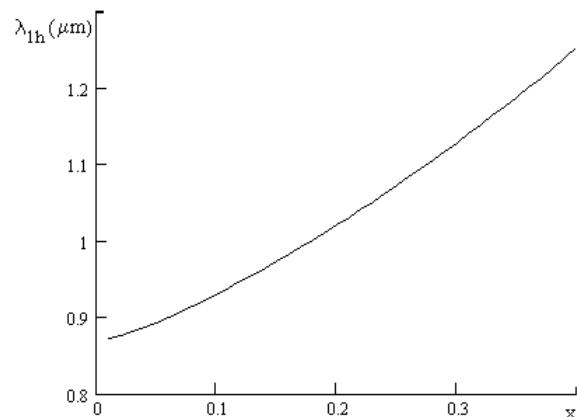


Fig. 1. Dependence of the wavelength of emission corresponding to initial optical transitions in the $\text{Ga}_{1-x}\text{In}_x\text{As}$ –GaAs system on the In mole fraction x in the active region

Table 1. Values of physical parameters

| T , K | E_{g0} , eV | ΔE_c , eV | ΔE_v , eV | m_c/m_e | m_{vh}/m_e |
|--------------|---------------|-------------------|-------------------|---------------|---------------|
| 300 | 1.105 | 0.279 | 0.037 | 0.056 | 0.346 |
| m_{vl}/m_e | m_{vht}/m_e | m_{vlt}/m_e | m_{cb}/m_e | m_{vhb}/m_e | m_{vlb}/m_e |
| 0.060 | 0.075 | 0.157 | 0.067 | 0.350 | 0.090 |

Accomplished calculations of the quantum-size levels show that in the quantum wells two subbands of electrons, two subbands of heavy holes, and one subband of light holes are realized. In a model of direct optical transitions the initial transitions through the ground subbands of electrons and heavy and light holes correspond to the quantum energies (the wavelengths), respectively, $h\nu_{1h} = 1.191$ eV ($\lambda_{1h} = 1.041$ μm), $h\nu_{1l} = 1.202$ eV ($\lambda_{1l} = 1.031$ μm), and $h\nu_{2h} = 1.396$ eV ($\lambda_{2h} = 0.888$ μm). Energy diagram of the quantum-well heterostructure in the $\text{Ga}_{0.78}\text{In}_{0.22}\text{As}$ –GaAs system and possible optical transitions are schematically demonstrated in Fig. 2.

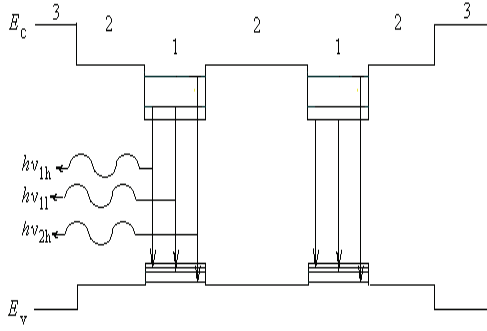


Fig. 2. Band diagram of the heterostructure and optical transitions. (1) Ga_{0.78}In_{0.22}As, (2) GaAs, (3) Al_{0.2}Ga_{0.8}As

3. Spectral characteristics of emission

Spectrum of emission is determined by the rate of spontaneous recombination $r_{sp}(h\nu)$ which depends on mechanism of radiative recombination, probability of optical transitions, level of excitation of the active region, and character of spectral broadening. Generally it takes into account through the density of states in the subbands and the function of spectral broadening [4]. Expression for the rate of spontaneous recombination has the form

$$(1) \quad r_{sp}(h\nu) = r_0 \frac{1}{d} \sum_{n,i} \frac{m_{ni}}{m_e} \int f_e(E_{cni}) f_h(E_{vni}) \times L_{ni}(h\nu - E_{cv}, \Delta F) \alpha_{ni}(\alpha, \theta_{ni}) H_{ni}(E_{cv} - h\nu_{ni}) dE_{cv}$$

where $r_0 = A_{cv} m_e / \pi \hbar^2$, A_{cv} is the Einstein coefficient for spontaneous transitions, $n = 1, 2$ is the number of the subband in the quantum well, $i = h, l$ is the index corresponding to heavy and light holes, m_{ni} is the reduced mass, $E_{cv} = E_{cni} - E_{vni}$ is the energy of optical transitions, $f_e(E_{cni})$ and $f_h(E_{vni})$ are the Fermi-Dirac functions for electrons and holes, $L_{ni}(h\nu - E_{cv}, \Delta F)$ is the function of spectral broadening, $\Delta F = F_e - F_h$ is the difference of quasi-Fermi levels for electrons and holes, $H_{ni}(E_{cv} - h\nu_{ni})$ is the Heaviside function. Value of the normalization coefficient r_0 is $4.722 \times 10^{23} \text{ cm}^{-2} \text{ s}^{-1} \text{ eV}^{-1}$.

The polarization factor $\alpha_{ni}(\alpha, \theta_{ni})$ depends on the orientation of the polarization vector (angle α) and on the wave vector of holes (angle θ_{ni}) relative to the axis of quantization $\langle 100 \rangle$ [4]. For the TE-mode it is $\alpha = \pi/2$, and for the TM-mode $\alpha = 0$. At calculations, the narrowing of the band gap E_g of a material of the quantum well GaInAs is taken into account with increasing the concentration of carriers under growth of the pump current, i. e.,

$$(2) \quad E_g = E_{g0} - k_g (n^{1/3} + p^{1/3}),$$

where n and p are the concentrations of electrons and holes in the active layer of GaInAs, $k_g = 1.0 \times 10^{-8} \text{ eV cm}$.

Integration in (1) is carried out over the energy of optical transitions E_{cv} starting at the energy of the initial transitions $h\nu_{1h} = E_g + E_{c1} + E_{v1h}$, where E_g is the energy band gap of Ga_{0.78}In_{0.22}As at the temperature T , and it is finished at reaching the potential barrier height. The function of spectral broadening is taken as the Lorentzian function, i. e.,

$$(3) \quad L_{ni}(h\nu - E_{cv}, \Delta F) = \frac{1}{\pi} \frac{\Gamma_{ni}(\Delta F)}{(h\nu - E_{cv})^2 + \Gamma_{ni}^2(\Delta F)},$$

where the parameter $\Gamma_{ni}(\Delta F)$ increases with the pump level growth and varies for optical transitions between the electron subbands and subbands of heavy and light holes according to $\Gamma_{ni}(\Delta F) \approx (4^{1/3} - 1)^{1/2} \gamma_{ni}(\Delta F)$. The parameter γ_{ni} is determined as [5]

$$(4) \quad \gamma_{ni}^2 = 2,05 \text{ Ry} \frac{\sqrt{m_c m_{vit}}}{m_e \epsilon^2} kT \exp\left(\frac{\Delta F - h\nu_{ni}}{2kT}\right),$$

where $\epsilon = 12.96$ is the dielectric constant of the active layer. Dependence of the parameter Γ_{ni} on the difference of the quasi-Fermi levels ΔF is represented in Fig. 3.

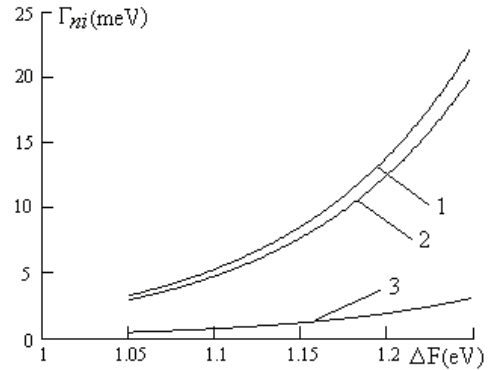


Fig. 3. Dependence of the spectral broadening parameter Γ_{ni} on the excitation level ΔF for different channels of recombination. (1) $n = 1, i = h$, (2) $n = 1, i = l$, (3) $n = 2, i = h$

The gain spectrum $k(\nu)$ with taking into account the spectral broadening is defined by the universal relation. Mode gain includes also the waveguide parameter Γ^j . Calculated values of the optical confinement factor are $\Gamma^{TE} = 7.83 \times 10^{-3}$ and $\Gamma^{TM} = 5.23 \times 10^{-3}$.

Spectral intensity of the amplified luminescence is described by the expression [6]

$$(5) \quad S_1(h\nu) = \frac{h\nu r_{sp}(h\nu)}{k_{tr} - \Gamma^j k(\nu)}.$$

Here $j = \text{TE, TM}$ is the polarization index, k_{tr} is the coefficient of losses of the trapped radiation in the active region averaged over volume and directions of distribution of the radiation. The coefficient of trapped radiation losses is inversely proportional to the square root of the surface area of the laser active layer [6]. Analysis of changes in the amplified luminescence spectra at varying the losses k_{tr} shows that at smaller values of k_{tr} the intensity of luminescence is larger and its spectrum is narrower at the same pump current density in the heterostructure. At below consideration it is supposed $k_{tr} = 20 \text{ cm}^{-1}$.

Spectra of the amplified luminescence at different pump levels are shown in Fig. 4. Maximum of the calculated spectra of the amplified luminescence with the pump current growth shifts slightly to the short-wavelength region due to the effect of filling the high lying energy states by current carriers that results in increasing the rate of optical transitions through the light hole subband. Thus, for explanation of shifting the maximum to the long-wavelength region in the experimental spectra it is required to take into account, together with the narrowing of the energy band gap in the active layer of GaInAs, the effect of heating the laser diode.

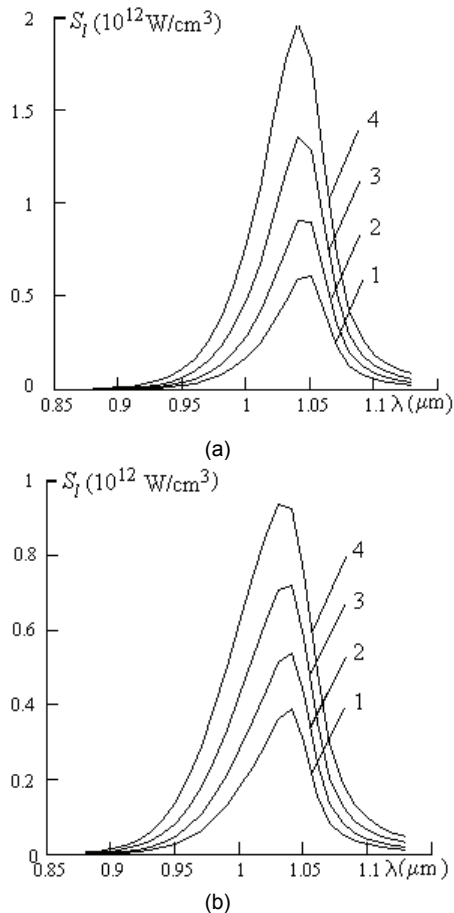


Fig. 4. Spectra of amplified luminescence at various differences of quasi-Fermi levels ΔF for (a) TE- and (b) TM-mode of radiation. (1) $\Delta F = 1.18$ eV, (2) $\Delta F = 1.20$ eV, (3) $\Delta F = 1.22$ eV, (4) $\Delta F = 1.23$ eV

4. Degree of polarization

The degree of polarization of the amplified luminescence is determined by the expression $P = (S_1^{TE} - S_1^{TM}) / (S_1^{TE} + S_1^{TM})$, where S_1^{TE} is the intensity of the TE-mode radiation, S_1^{TM} is the intensity of the TM-mode radiation. Change in the degree of radiation polarization within the band of emission is presented in Fig. 5.

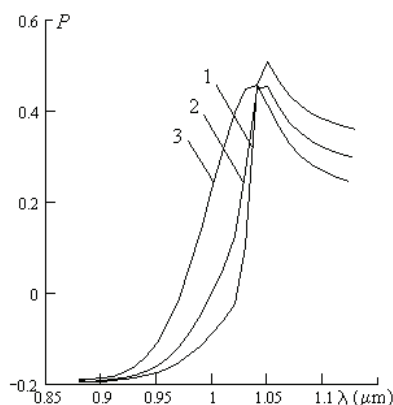


Fig. 5. Degree of polarization of the amplified luminescence at different excitation levels. (1) $\Delta F = 1.20$ eV, (2) $\Delta F = 1.25$ eV, (3) $\Delta F = 1.30$ eV

In the long-wavelength region of the spectrum, radiation has TE-polarization, and in the short-wavelength region role of TM-modes in radiation increases. It is related with difference in probabilities of optical transitions between different subbands of electrons and holes for the TE- and TM-modes. For radiation of the TE-polarization main role have transitions through the heavy hole subband, and for the TM-modes it increases relative contribution of transitions through the light hole subband. Transitions through the second subband of heavy holes give negligibly small contribution into the luminescence spectrum. Polarization of radiation depends also on the orientation and sizes of the quantum well, possible stresses at the heterostructure interfaces, and on the waveguide properties of the laser active region. So, difference in the degree of polarization obtained in experiment can be explained by polarization characteristics of transmission at the cavity ends, non-uniformities and mechanical strains in the heterostructure.

5. Conclusion

Out put power characteristics were studied for quantum-well heterostructure laser diodes in the $\text{Ga}_{0.78}\text{In}_{0.22}\text{As}-\text{GaAs}$ system. In the framework of direct optical transitions the effects of spectral broadening have been included and the dependence of the energy band gap of semiconductor in the active region on the excitation level of the diode has been taking into account. For more detail description of the spectral characteristics of the sources it is required to account effects of the strained state in the heterostructure layers and their heating under high current of pumping.

REFERENCES

- [1] Zhuravleva O.V., Kurnosov V.D., Kurnosov K.V., Lobintsov A.V., Romantsevich V.I., Simakov V.A., Chernov R.V., Study of the spectral and power characteristics of superluminescent diodes, *Quantum Electron.*, 34 (2004), 15–19
- [2] Duraev V.P., Marmalyuk A.A., Padalitsa A.A., Petrovskii A.V., Ryaboshtan Yu.L., Sumarov M.A., Sukharev A.V., Effect of GaAsP barrier layers on the parameters of InGaAs/AlGaAs laser diodes emitting in the 1050–1100-nm spectral range, *Quantum Electron.*, 35 (2005), 909–911
- [3] Lapin P.I., Mamedov D.S., Marmalyuk A.A., Padalitsa A.A., Yakubovich S.D., High-power broadband superluminescent diodes emitting in the 1000–1100-nm spectral range, *Quantum Electron.*, 36 (2006), 315–318
- [4] Kononenko V.K., Nalivko S.V., Spectral characteristics of asymmetric quantum-well heterostructure laser sources, *Proc. SPIE*, 2693 (1996), 760–767
- [5] Afonenko A.A., Kononenko V.K., Spectral line broadening in quantum wells due to Coulomb interaction of current carriers, *Physica E: Low-dimensional Systems and Nanostructures*, 28 (2005), 556–567
- [6] Gribkovskii V.P., Kononenko V.K., Ryabtsev G.I., Samoilyukovich V.A., Trapped radiation in injection lasers, *IEEE J. Quantum Electron.*, QE-12 (1976), 322–326

Authors: student Alexander V. Ivanov, Belarussian state University, Independence Ave., 4, 220050 Minsk, E-mail: Ivanov_A13ks@tut.by; prof. Dr. Sc. Valerii K. Kononenko, Stepanov Institute of Physics, National Academy of Sciences of Belarus, Independence Ave., 70, 220072 Minsk, E-mail: lavik@dragon.bas-net.by; associate prof. Ph. D. Ivan S. Manak, Belarussian state University, Independence Ave., 4, 220050 Minsk, E-mail: manak@bsu.by.

Analysis of electromagnetic processes in power system elements on the basis of unique-flux methodology

Abstract. The paper deals with analysis of electromagnetic processes in power system elements based on unique-flux methodology. The said methodology allows avoiding the complicated task of definition of boundary conditions that is essential in field models as well as applying of simplifying assumptions concerning the field distribution what serves as an utmost cause of circuit models' inaccuracy. The developed algorithms are to be used in further research for analysis of transient phenomena of transmission lines.

Abstract. Artykuł przedstawia analizę zjawisk elektromagnetycznych w elementach systemów zasilających bazującą na metodologii unikalnego strumienia (ang. unique-flux). Wspomniana metodologia pozwala pominąć skomplikowane zadanie definicji warunków brzegowych, które są niezbędne w modelach polowych oraz zastosować założenia upraszczające związane z rozkładem pola co jest przyczyną niedokładności większości modeli obwodowych. Opracowane algorytmy zostaną wykorzystane w przyszłych badaniach związanych ze zjawiskiem przełączania w liniach przesyłowych. (Analiza procesów elektromagnetycznych w elementach systemów zasilających bazującą na metodologii unikalnego strumienia)

Keywords: unique-flux technique; differential electromagnetic parameter; synchronous turbo-generator; differential reluctivity.

Słowa kluczowe: technika unikalnego strumienia, różniczkowy parametr elektromagnetyczny, generatory synchroniczne, reluktancja różniczkowa

Introduction

The unique-flux methodology was proposed [1] to overcome the limitations of both circuit and field models of electromagnetic apparatus (EMA). It is well known that due to high complicity of electromagnetic relations the circuit models of EMA imply the existence of a great number of assumptions and simplifications [2, 3] which preclude from obtaining high-accuracy results, e.g. the assumption of harmonic distribution of magnetizing force leads to employment of transformation formulas what considerably reduces the effectiveness of the models in question. On the other hand, the difficulties concerning precise evaluation of boundary conditions are the predominant reason precluding field models from high adequacy. The offered technique attempts to combine the assets of circuit and field approaches and to minimize their drawbacks.

Underlying concepts

The mathematical model of EMA based on the unique-flux technique has been constructed with help of the following concepts:

- 1) magnetic parts of an electromagnetic apparatus are divided into elementary volumes that are small enough to satisfy the assumption of uniform (homogeneous) field distribution inside each volume. In such case every elementary volume is represented in the form of a lumped reluctivity;
- 2) power waste in a stacked magnetic circuit are represented by an ohmic element hooked up in parallel to windings' resistances;
- 3) displacement currents and current push effect in windings are neglectable;
- 4) the influence of temperature on electrical conductivity and magnetic permeance is neglectable;
- 5) hysteresis is not taken into account; nonlinear dependency of magnetic induction from magnetic field intensity is represented by a main magnetic curve.

Representation of magnetic parts

Let us use a synchronous turbo-generator as first example. The magnetic circuit of the turbo-generator has been divided into elementary volumes using coaxial cylindrical surfaces as well as planes which are normal to the axis. Magnetic fluxes flowing through the elementary volumes consist of tangential and radial components.

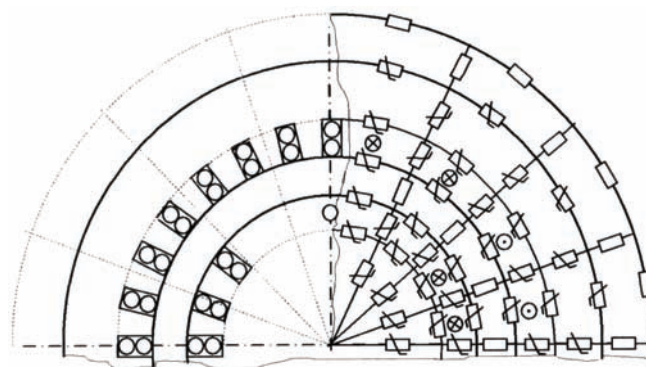


Fig. 1. Model of the magnetic circuit of a turbo-generator.

As a result, the magnetic system of the turbo-generator can be approximated with a ringed planar magnetic circuit shown on Fig. 1. The elementary volumes obtained by those means constitute mainly the sectors of thin-shelled cylinders and include parts with different magnetic characteristics. Magnetic reluctivity R_m and Ampere-Weber characteristic of each elementary volume are obtained in accordance with its geometric parameters and appropriate saturation curve and approximated by cubic splines.

Average Ampere-Weber characteristics $F(\Phi)$ of elementary volumes with heterogeneous parts are replaced by elements connected in parallel, in series, etc. For instance, the scheme shown on Fig. 2 was used for calculation of radial (normal) component of the magnetic flux in a rotor tooth-zone. It is worth to remind that this very component of magnetic flux is instrumental for computing of electromagnetic torque of an electric machine.

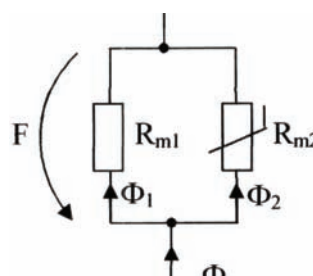


Fig. 2. Modeling of an elementary volume in a tooth-zone.

Let us use an autotransformer as second example. Taking into account certain symmetry of magnetic field with respect to legs bearing windings, the magnetic circuit of the autotransformer has been divided into elementary volumes using coaxial cylindrical surfaces (their axes coincide with legs' axes) as well as planes which are normal to the axis. Such a division is shown on the Fig. 3.

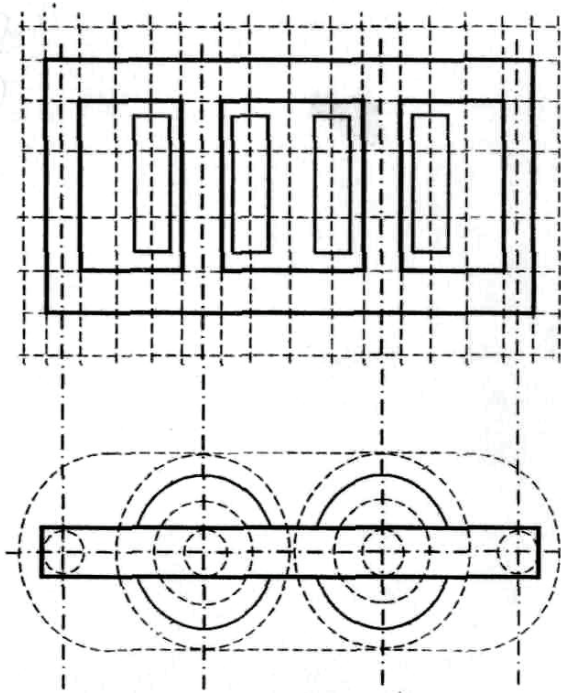


Fig. 3. Space division of autotransformer.

The elementary volumes obtained by those means constitute mainly the sectors of thin-shelled half-cylinders shown on Fig. 4 and include parts with different magnetic characteristic.

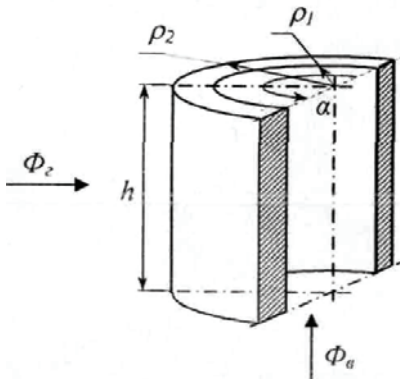


Fig. 4. Elementary volume of autotransformer.

Sections of a magnetic core and sectors of a case have non-linear characteristic; air, oil and windings have linear characteristics. If an elementary volume contains both ferromagnetic and non-ferromagnetic parts, an equivalent Ampere-Weber characteristic $F(\Phi)$ is obtained in accordance with its geometric parameters and appropriate saturation curves. As a result, the magnetic system of the autotransformer can be approximated with the planar magnetic circuit shown on Fig. 4.

Let us use a typical three-leg transformer as third example. Taking into account certain symmetry of magnetic field with respect to legs, the magnetic circuit of the trans-

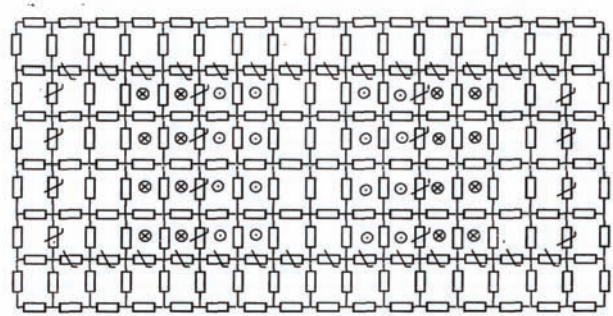


Fig. 5. Planar magnetic circuit of autotransformer.

former has been divided into elementary volumes using mainly coaxial cylindrical surfaces (their axes coincide with legs' axes) as well as planes which are normal to the axis. Such a division is shown on the Fig. 6.

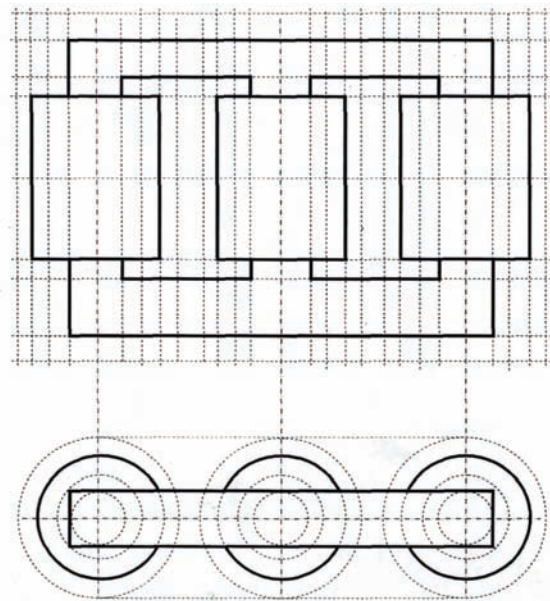


Fig. 6. Space division of three-leg transformer.

The obtained thin-shelled cylinders are divided in halves by vertical planes. Sections of a magnetic core and sectors of a case have non-linear characteristic; air, oil and windings have linear characteristics. If an elementary volume contains both ferromagnetic and non-ferromagnetic parts, an equivalent Ampere-Weber characteristic $F(\Phi)$ is obtained in accordance with its geometric parameters and appropriate saturation curves. As a result, the magnetic system of the transformer can be approximated with the planar magnetic circuit shown on Fig. 7.

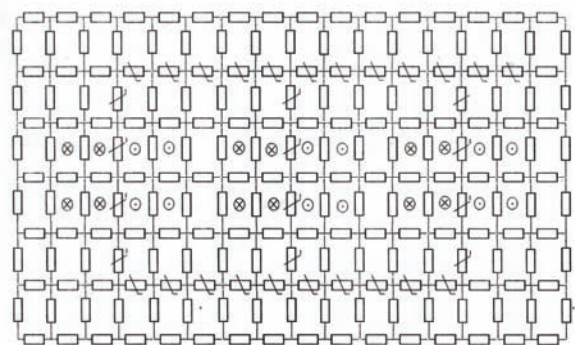


Fig. 7. Planar magnetic circuit of transformer.

After completion of such approximation, the magnetic state of the electromagnetic apparatus in question is described by a system of algebraic non-linear equations:

$$(1) \quad \Gamma_m \vec{F}(\vec{\Phi}_k) = \vec{T}_k,$$

where Γ_m is a three-dimensional second incidence matrix of a magnetic circuit of $q \times s \times p_m$ size ($q \times s$ is the size of the grid of the planar magnetic circuit; p_m is the number of lines of magnetic circuit graph); \vec{F} is p_m -sized vector-column of magnetic voltages of the said magnetic circuit; $\vec{\Phi}_k$ is a vector-column of contour magnetic fluxes; \vec{T}_k is a vector-column of contour magnetizing forces.

Representation of electrical parts

The next group of equations complementing the system (1) consists of Kirchhoff's equations and equations describing the relationship between electrical (a current and a flux linkage) and magnetic (a magnetizing force and a magnetic flux) variables:

$$(2) \quad \Pi_e \vec{i} = 0;$$

$$(3) \quad \Gamma_e(d\vec{\Psi}/dt + L_s d\vec{i}/dt + R\vec{i}) = \Gamma_e \vec{u};$$

$$(4) \quad \vec{\Psi} = W\vec{\Phi}_k;$$

$$(5) \quad \vec{T}_k = W_t \vec{i},$$

where Π_e and Γ_e are the first and the second incidence matrixes of the electric circuit; \vec{i} is a vector-column of electrical currents; in case of a turbogenerator these are currents of stator phases a, b, c , an excitation current, a direct-axis current, and a quadrature-axis current, i. e. $\vec{i} = (i_a, i_b, i_c, i_f, i_d, i_q)$; in case of an autotransformer these are currents of a serial, common and transformer windings, i. e. $\vec{i} = (i_1, i_2, i_3)$; $\vec{\Psi}$ is a vector-column of flux linkages; in case of a turbogenerator these are the flux linkages of stator phases a, b, c , of an excitation winding, a direct-axis rotor contour, and a quadrature-axis rotor contour, i.e. $\vec{\Psi} = (\Psi_a, \Psi_b, \Psi_c, \Psi_f, \Psi_d, \Psi_q)$; in case of an auto-transformer these are flux linkages s of a serial, common and transformer windings, in case of a turbo-generator $L_s = \text{diag}(L_{sa}, L_{sb}, L_{sc}, L_{sf}, 0, 0)$ is a diagonal matrix of inductivities of flank dispersion; R is a diagonal matrix of resistances; in case of a turbogenerator these are the resistances of stator phases a, b, c , of an excitation winding, a direct-axis rotor contour, and a quadrature-axis rotor contour, i. e. $R = \text{diag}(r_a, r_b, r_c, r_f, r_d, r_q)$; in case of an autotransformer these are resistances of a serial, common and transformer windings, i. e. $R = \text{diag}(r_1, r_2, r_3)$, \vec{u} is a vector-column of electrical voltages; in case of a turbogenerator these are the voltages of stator phases a, b, c , and of an excitation winding, i. e. $\vec{u} = (u_a, u_b, u_c, u_f, 0, 0)$; in case of an autotransformer these are the voltages of the high, middle and low sides, i. e. $\vec{u} = (u_H, u_M, u_L)$; W is the matrix of windings of elementary magnetic contours.

In case of a turbogenerator the matrix W is a dynamic one. Taking into consideration the fact that magnetizing

forces' distribution is of trapezium-stepped form, an algorithm for calculation the matrix W elements on each step of integration procedure has been developed [4]. The elements are dependent on a rotation co-ordinate γ .

Representation of mechanic movement

An electromagnetic torque M_E must be determined on each step of integration procedure on the basis of branch currents and contour magnetic fluxes [5]. It can be calculated as the sum of single torques produced by forces impressed upon rotor conductors and computed according to Ampere formula:

$$(6) \quad M_E = R_e l_r \sum_{j=1}^s (\Phi_{n,j} / S_{n,j} w_{r,j} i_r),$$

where R_e is equivalent radius of a rotor tooth-zone; l_r is an active rotor length; $\Phi_{n,j}$ is a normal component of the magnetic flux through the j -th sector of the rotor tooth-zone; $S_{n,j}$ is an equivalent slot surface of the j -th sector of the rotor tooth-zone; $w_{r,j}$ is the number of rotor winding turns in the j -th sector of the rotor tooth-zone; i_r ($r=f, d, g$) is the current of an applicable rotor winding. For example [5], the normal component $\Phi_{n,j}$ of the magnetic flux coincides with the magnetic flux Φ_1 on the Fig.2 and can be obtained as follows:

$$(7) \quad \Phi_{n,j} = F / R_{m1} = F \mu_0 S_{n,j} / l_r,$$

where μ_0 is the magnetic permittivity of vacuum.

The equation of mechanical movement is written down in the form of the second Newton's law for rotating elements:

$$(8) \quad J d\omega / dt + M_E - M_t = 0,$$

where J is a moment of inertia of the rotating part; ω is an instant angle velocity; M_t is a turbine torque.

After complementing the system (1)-(5), (8) with the equation

$$(9) \quad d\gamma / dt = \omega,$$

the full system of algebraic-differential equations comprising the sought model of the electromagnetic apparatus and describing the electrical, magnetic and mechanical phenomena in the apparatus in question has been received. This system is solved by means of back-differentiation formulas and Newton's method.

Results of transformer and turbo-generator simulation

The mathematical model of a transformer has been obtained by combination of equations (1)-(5) in the form

$$(10) \quad \Gamma_m \vec{F}(\vec{\Phi}_k) - W_t \vec{i} = 0;$$

$$(11) \quad \Gamma_e (W d\vec{\Phi}_k / dt + R\vec{i}) - \vec{u} = 0.$$

For the integration of the received system of differential equations the method of back integration formulas (BIF) was used and for solving of nonlinear equations Newton's method was used. The discrete model of electrical and magnetic circuits of the transformer applying differential magnetic parameters was written in the following form:

$$(12) \quad \left\| \begin{array}{c} \Gamma_m \left(\frac{\partial \vec{F}}{\partial \vec{\Phi}} \right)_{k+1} \Gamma_{m,t} \quad W_{t,k+1} \\ a_0 h^{-1} \Gamma_e W_{k+1} \quad \Gamma_e R \end{array} \right\| \times \left\| \begin{array}{c} \Delta \vec{\Phi}_{\kappa,k+1} \\ \Delta \vec{i}_{k+1} \end{array} \right\| =$$

$$\left\| \begin{array}{c} \Gamma_m \vec{F} \left(\vec{\Phi}_{\kappa,k+1} \right) - W_t \vec{i}_{k+1} \\ \Gamma_e \left(a_0 h^{-1} W_{k+1} \vec{\Phi}_{\kappa,k+1} \right) + R \vec{i}_{k+1} + \\ + h^{-1} \sum_{s=1}^p a_s \left(W_{k+1-s} \vec{\Phi}_{\kappa,k+1-s} \right) - \vec{u}_{k+1} \end{array} \right\|$$

where a_0, a_s are coefficients of the BIF method; h is the integration step; p is the order of BIF method; l is current iteration step number of Newton's method.

New approximations were calculated as:

$$\left(\vec{\Phi}_{\kappa,k+1}^{(l+1)}, \vec{i}_{k+1}^{(l+1)} \right)_t = \left(\vec{\Phi}_{\kappa,k+1}^{(l)}, \vec{i}_{k+1}^{(l+1)} \right)_t - \left(\vec{\Phi}_{\kappa,k+1}^{(l)}, \Delta \vec{i}_{k+1}^{(l+1)} \right)_t.$$

On the basis of the presented algorithm its software implementation has been developed, with a separate module for differential electromagnetic parameters computation. It was used for analysis of various regimes of EMA.

Below the time diagrams of currents of the transformer ТДТН-110/35/10 are produced; they are given for the cases of connection of the transformer to input steady voltage in idling conditions and short-circuit conditions.

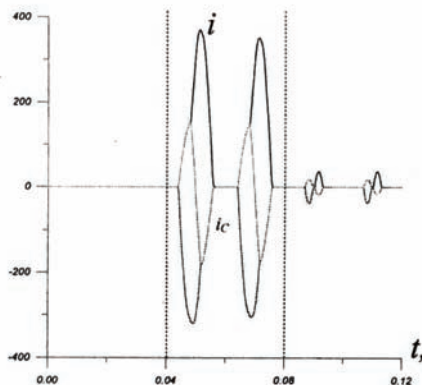


Fig. 8. Time diagrams of currents of ТДТН-110/35/10 in idling conditions.

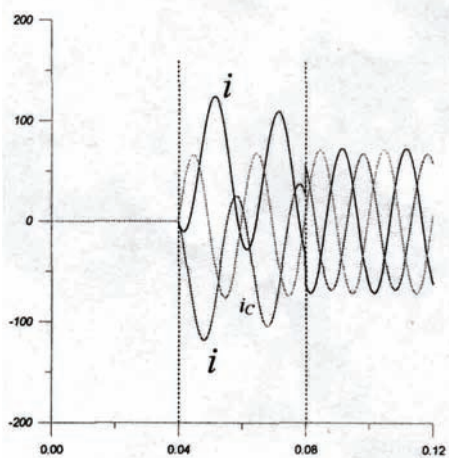


Fig. 9. Time diagrams of currents of ТДТН-110/35/10 in short-circuit conditions.

Below the time diagrams of currents of the turbo-generator ТГБ-200 are produced; they are given for single-phase-to-ground-fault during the nominal regime.

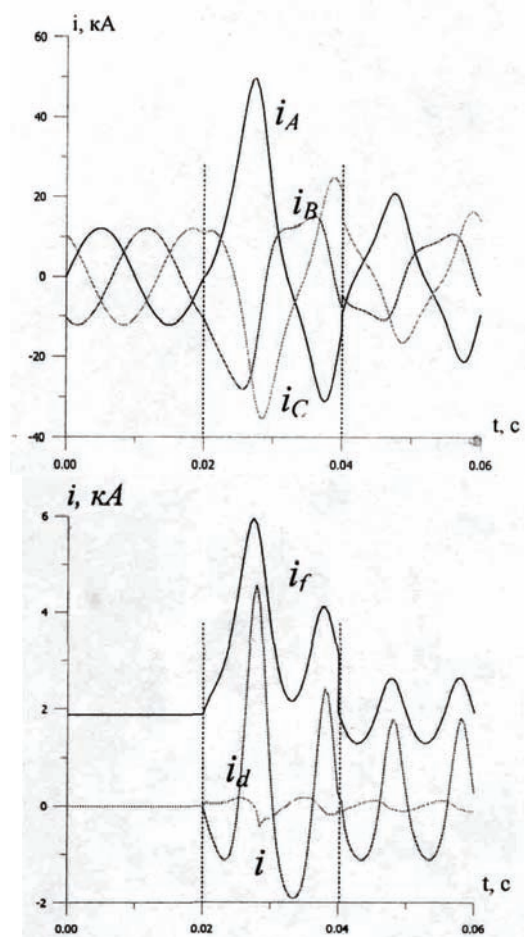


Fig. 10. Time diagrams of currents of ТГБ-200 for single-phase-to-ground-fault during the nominal regime.

Acknowledgment

The authors thank the Assistant Professor T. Ryzhyy for his help in software implementation.

REFERENCES

- [1] V. Perkhach, O. Skrypnyk, V. Horyachko, and T. Ryzhyy, Mathematical model of asynchronous turbo-generator as an element of extra-high-voltage transmission system, *Electrical Power and Electromechanical systems*, 347 (1998), 133–138. В. Перхач, О. Скрипник, В. Горячко, Т. Рижий, Математична модель асинхронізованого турбогенератора як елемента електропересильні надвисокої напруги, *Електроенергетичні та електромеханічні системи*. Вип. 347, с. 133-138, 1998.
- [2] R. Filc, Mathematical foundations of the theory of electromechanical transformers, *Kyiv: Naukova Dumka*, 1986. Р. Фильц, Математические основы теории электро-механических преобразователей, *Наукова думка*, 1986.
- [3] O. Plakhtyna, Mathematical modelling of power & rectifier valve systems, *Lviv: Vyshcha Shkola*, 1986. (In Russian) О. Плахтына, Математическое моделирование электромагнитно-вентильных систем, *Вища школа*, 1986.

Authors: Ass. Prof., Cand. of Techn. Sc. Vsevolod Horyachko, E-mail: MaKaryn2004@yahoo.com and Ass. Prof., Cand. of Phys.-Math. Sc. Mariya Howykowycz, National University Lviv Polytechnic, Institute of Energetics and Control Systems, 12 Bandery Street, 79012, Lviv, Ukraine, E-mail: howykowycz@ieeee.org.

Increasing of effectiveness of electromagnetic process analysis in nonlinear time-varying circuits due to separation of equivalence classes

Abstract. In paper it is appraised state and development prospects of methods of electromagnetic processes analysis in electric energy converters. Possibility of equivalence classes selection of nonlinear parametric processes types is shown. The example of estimation of equivalence class is considered regarding to additional integral characteristics.

Abstract. W artykule przedstawiono szacowany stan i perspektywy rozwoju metod związanych z analizą procesów elektromagnetycznych w konwerterach energii elektrycznej. Pokazano możliwości doboru odpowiadających sobie klas nieliniowych parametrów. Rozważono przykład estymacji klasy zgodności uwzględniając dodatkową charakterystykę całkową. (Zwiększenie efektywności analizy procesów elektromagnetycznych w stanach nieustalonych obwodów nieliniowych za pomocą wyróżniania klas zgodności)

Keywords: nonlinear circuits, power quality, equivalence classes.

Słowa o kluczowe: obwody nieliniowe, jakość energii, klasy zgodności.

Introduction

One of important problems of power electronics development is perfection of existing analysis methods and development of new ones, optimization, synthesis and computer design. Effective application of analysis methods provides considerable advancement not only at creation of semiconductors power devices, electric energy converters (EEC) and their control systems but also assists in development of new energy generators, expansion of possible types and ranges of loadings functioning, achieving the necessary levels of stability and reliability of the systems with EEC (SEEC).

Most converters execute simultaneously serial and parallel energy quantization operations after levels and time and deal with two very different streams – energy and informational flows. The processing of these flows is realized by a power structure and control, diagnostics and protection system accordingly. In EEC and SEEC the next models are widespread enough: they characterized by unsymmetry, imbalance and nonsinusoidality, appearance of subharmonics, impulsive sending (single impulses, "packs" of impulses), signal modulation. Here energy flows diversify both from the point of intensity view and direction change frequencies of their leaking. All of that determines the modern features of processes design and analysis in EEC and SEEC.

Converters are complex dynamic systems. All variables that describe such dynamic systems we will divide into three plurals: entering variables V , internal variables X and outgoing variables Y . Entering variables, that describe the external actions on the system entrances, will be a vector

$V = \|f, U\|'$. The subvector f fits outside operating sources in the power scheme of converter, and the subvector U represents the presence of signals from the control system. Vector X marks the system variables that are internal variables. The set of last ones fully characterizes system properties fully. The vector Y marks outgoing variables that represent the reactions on external actions and also system states that are of interest during calculation and designing of EEC.

For EEC description as dynamic system we will use the vector of parameters $Q = \|Q_1, Q_2\|'$. The subvectors Q_1 and Q_2 contain accordingly the parameters of converter's power scheme and its control system (CS), and also graphs G_1

and G_2 that represent the power scheme and CS topology accordingly. In general case the subvectors Q_1 and Q_2 include not only passive parameters of converter's power scheme, CS and parameters of key elements but also passive parameters of operating sources f and external signals of driving CS sources. Outgoing variables Y are periodic functions with a period that is determined by the work of operating sources, EEC power schemes, loadings and CS. For component vectors X and Y identity $X \equiv Y$ or $X' \equiv Y'$ can be executed, where X' (Y') are subvectors of vector X (Y). However, in general case, dependence between vectors X and Y is represented by nonlinear transformation: $Y = C(X, V)X + D(X, V)X$, where $C(X, V)$ and $D(X, V)$ are the matrix functionals, elements type and parameters of which are determined by the elements of vector Q and EEC power scheme topology (by a graph G_1).

Dynamic system, its entering and outgoing variables are three interconnected objects that are simultaneously determined for every concrete case by the description of the system (by a component structure and properties), and also by the set plurals of entering and outgoing variables. Depending on what objects are known and which must be defined, the different task types are selecting. These task types in a general form are given in Table 1, where the followings symbolic notations are entered: [+] – a variable is known, [?] – a variable must be defined; [?]* – a variable must be defined at the set limitations and/or an objective function (scalar or vector). In the sequel from the pointed plural of tasks let us give our mind on consideration the analysis tasks.

The analysis results are not only an electromagnetic processes calculation (currents $i(t)$ and voltage $u(t)$) but also analysis of instantaneous and integral power characteristics and coefficients, realization of signal spectral analysis. During analysis the forming of the followings models is possible: linear, "quasi-linear", nonlinear, nonstationary, parametric and their random combinations.

There are two basic problems that appears at the analysis of EEC nonlinear parametric circuits: adequate description of the nonlinear system, i.e. the selection of nonlinear elements descriptions, selection of correct equivalent circuit and analysis of nonlinear equations that describe processes in nonlinear electric circuits.

Table 1. Plural of task types

| Task type | Variable type | | | | | | | |
|--------------------------------|---------------|------|-------|-------|-------|-------|------|------|
| | f | U | Q_1 | Q_2 | G_1 | G_2 | X | Y |
| Analysis | [+] | [+] | [+] | [+] | [+] | [+] | [?] | [?] |
| Parametric synthesis | [+] | [+] | [?] | [?] | [+] | [+] | [?]* | [+] |
| Structure synthesis | [+] | [+] | [+] | [+] | [?] | [?] | [?]* | [+] |
| Outgoing signal synthesis | [+] | [?]* | [?] | [?]* | [?] | [?]* | [?]* | [?]* |
| Structure-parametric synthesis | [+] | [?] | [?] | [?] | [?] | [?] | [?]* | [+] |
| Identification | [?] | [?] | [+] | [+] | [+] | [+] | [+] | [+] |
| Parameters optimization | [+] | [+] | [?]* | [?]* | [+] | [+] | [?]* | [+] |
| Behaviors optimization | [+] | [?]* | [?]* | [?]* | [+] | [+] | [?]* | [?]* |
| Structure optimization | [+] | [+] | [+] | [+] | [?]* | [?]* | [?]* | [+] |
| General optimization | [+] | [?]* | [?]* | [?]* | [?]* | [?]* | [?]* | [?]* |

The problem of adequate description, in the turn, contains a few tasks that differ depending on group of methods (analytical, graphic or numeral) the equations analysis will be appraised with.

The problem of nonlinear equations analysis that describe processes in EEC model is determined by the limitation on the use in nonlinear electric circuits such usual and comfortable methods for linear circuits (as superposition principle and symbolical method). Well developed theory of linear differential equations appears useless for an analysis of nonlinear electric circuits.

With the purpose of generalization of electromagnetic and power processes analysis methods of nonlinear parametric circuits that can be typical for the different classes of EEC and SEEC, known classes of power schemes and proper processes types are expediently to detail in more "narrow" classes.

Separation of equivalence classes

One of possible ways of such division is a selection of quasi-linearity classes as follows [1, 2]:

1) *X-quasi-linearity*:

$$\|A_{CP} - A_i\| < \varepsilon_{X1}; \|B_{CP} - B_i\| < \varepsilon_{X2};$$

$$\|C_{CP} - C_i\| < \varepsilon_{X3}; \|D_{CP} - D_i\| < \varepsilon_{X4}; i = 1, \dots, m,$$

where $\varepsilon_{Xj} > 0; j = 1, \dots, 4; A_{CP}, B_{CP}, C_{CP}, D_{CP}$ are matrix coefficients for the linear modeling of the selected scheme with the use of differential equations in the normalized form Cauchy (type (1), (2));

2) *P-quasi-linearity*:

$$(P_{\Sigma} - P_1) / P_1 < \varepsilon_P,$$

where P_{Σ} – the sum of active power of all harmonics, P_1 – active power of first harmonic, $\varepsilon_P > 0$;

3) *Q-quasi-linearity*:

$$(Q_F^2 - Q_1^2) / Q_1^2 < \varepsilon_Q,$$

where Q_F – Fryze reactive power, Q_1 – reactive power of first harmonic, $\varepsilon_Q > 0$.

Along with the selection of quasi-linear classes a

necessity of determination of classes' boundaries appears. For this purpose it is suggested to use family of test (typical) signals that are typical in point to functioning of separate types of converters.

Will consider as an example a periodic signal that represents rectangular impulses. A controlling delay angle α is changing in a range $[0^{\circ}; 90^{\circ}]$ (Fig. 1). Maximal value of pulsation factor $K_{p\infty}$ depending on controlling delay angle α is represented in Fig. 2, the number of harmonics that influence the current part of pulsation factor depending on the parameter α is represented in Fig. 3.

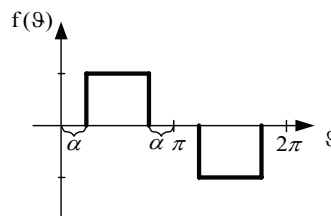


Fig. 1. Signal representation in time

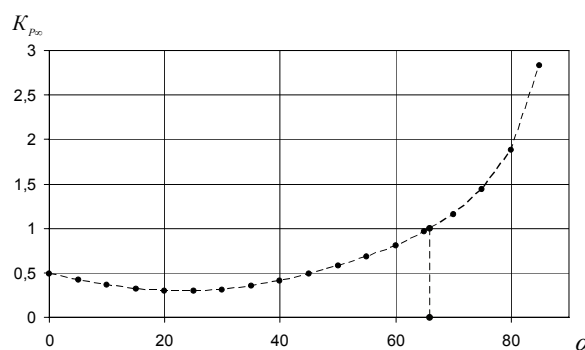


Fig. 2. Maximal value of pulsation factor depending on controlling delay angle

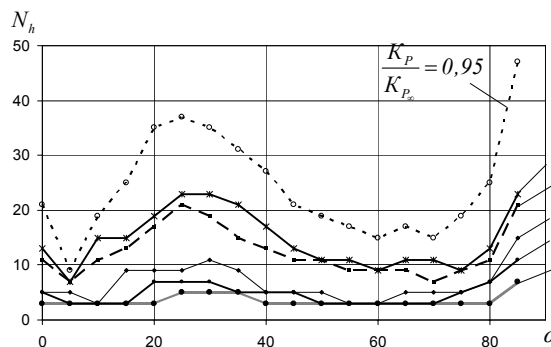


Fig. 3. The number of harmonics that influence the current part of pulsation factor depending on the controlling delay angle

If we have to define the α turndown when maximal value of pulsation factor $K_{p\infty}$ not exceed the value 0.5, from Fig. 2 we can find that angle α have to change in range from 0° to 45° . And if in this case it is allowed to neglect 10% from $K_{p\infty}$, it is necessary to take into account during calculations the first 21 harmonic components of signal.

Consideration of known and additional integral characteristics

Simplicity of striking the balance of electric power $S^2 = P^2 + Q^2$, reflection of the real physical processes in linear circuits and connection between integral and instantaneous descriptions resulted to the transfer of concept of the power orthogonal system S, P, Q to circuits, where the nonsinusoidal signals $u(t), i(t)$ operate. The most

widespread efficiency criteria system of power processes for circuits with nonsinusoidal signals is a plural of indexes of power processes quality that takes beginning from works of Krijger, dated 1923 [3], and describes the change of voltage (current) phase displacement, distortion of its form, unsymmetry between phases and unevenness of electric power consumption. Power proportions are based on powers (power characteristics): active power P , reactive power Q , distortion power T , unsymmetry power H , full power S and also ratios: displacement factor $\cos\varphi_1$, distortion coefficient ν , unbalance factor k_{ns} and power factor λ . The last are determined thus:

$$(1) \quad \cos\varphi_1 = P / \sqrt{P^2 + Q^2};$$

$$(2) \quad \nu = \sqrt{P^2 + Q_1^2} / \sqrt{P^2 + Q_1^2 + T^2};$$

$$(3) \quad k_{ns} = \sqrt{P^2 + Q_1^2 + T^2} / \sqrt{P^2 + Q_1^2 + T^2 + H^2} = \sqrt{P^2 + Q_1^2 + T^2} / S;$$

$$(4) \quad \lambda = P / S = \cos\varphi_1 k_{ns},$$

where $S = UI = U_{m(1)}I_{m(1)} / 2$; $P = UI \cos\varphi_1$;
 $Q_1 = UI \sin\varphi_1$.

Following coefficients can be additional integral characteristics:

$$(5) \quad R_{||} = u(t) / i(t) = U^2 / P;$$

$$(6) \quad R_{\perp} = U^2 / Q_F.$$

Parameter R_{\perp} characterizes «reactivity» of circuit, $R_{||}$ gives the description of consumption levels of active power. Parameters $R_{||}$ and R_{\perp} have a dimension of resistance.

So, correlation $R_{\perp} = R_{||}P / Q_F$ takes place. Thus, the value $R_{\perp} / R_{||} = P / Q_F$ is the index of relative level of signals distortions during consideration of minimum losses criterion of electric power.

Let us consider the next example.

Let have crossing of scheme where voltage and current can be presented as the following sums:

$$u(t) = U_{m(1)} \sin \omega t + U_{m(3)} \sin(3\omega t + \psi_3^u);$$

$$i(t) = I_{m(1)} \sin(\omega t + \psi_1^i) + I_{m(3)} \sin(3\omega t + \psi_3^i).$$

If for this signal next values are set as $U_{m(1)} = 100\sqrt{2}$ V, $I_{m(1)} = 10$ A, then knowing the pulsation factors by the third harmonic for voltage and current, values $U_{m(3)}$ and $I_{m(3)}$ can be determined from the followings relations:

$$U_{m(3)} = U_{m(1)} \sqrt{K_{PU}^2 - 1}; \quad I_{m(3)} = I_{m(1)} \sqrt{K_{PI}^2 - 1},$$

where K_{PU} , K_{PI} are pulsation factors after voltage and current accordingly that are determined as:

$$K_{PU} = \sqrt{\sum_{k=1}^{N_h} U_k^2} / U_1; \quad K_{PI} = \sqrt{\sum_{k=1}^{N_h} I_k^2} / I_1,$$

where U_k , I_k are effective values of k harmonic component of voltage and current accordingly, N_h – the quantity of harmonics which needs to be accounted.

Dependences of R_{\perp} and $R_{||}$ from the angles values ψ_3^u and ψ_1^i at the followings terms: $U_{m(3)} = 50\sqrt{2}$ V; $I_{m(3)} = 2\sqrt{2}$ A; $\psi_3^i = \pi/4$ are presented in Fig. 4 (a, b) and Fig. 5 (a, b) accordingly.

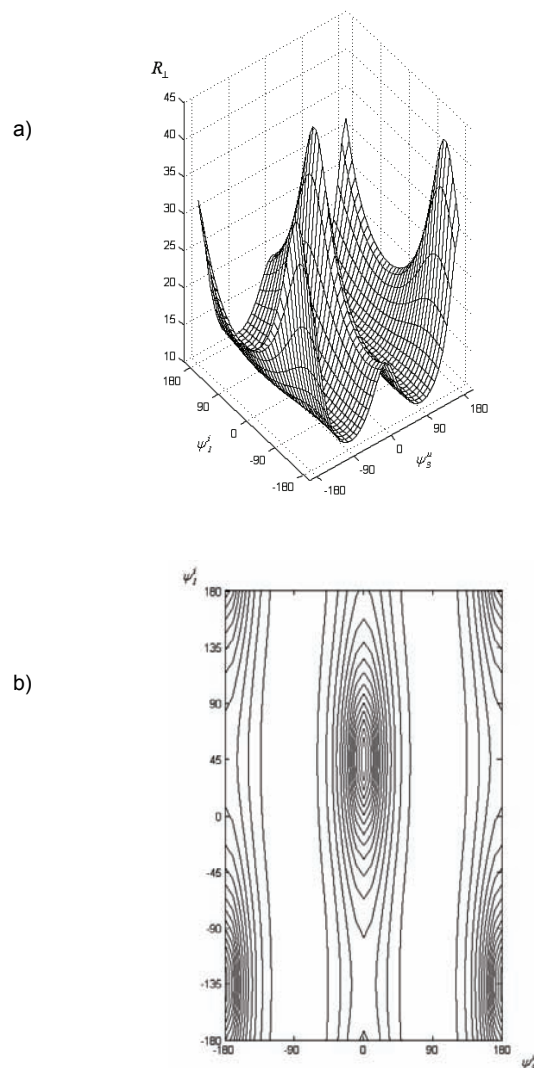


Fig. 4. Dependences of R_{\perp} from the values of angles ψ_3^u and ψ_1^i at the followings terms: $U_{m(3)} = 50\sqrt{2}$ V; $I_{m(3)} = 2\sqrt{2}$ A; $\psi_3^i = \pi/4$

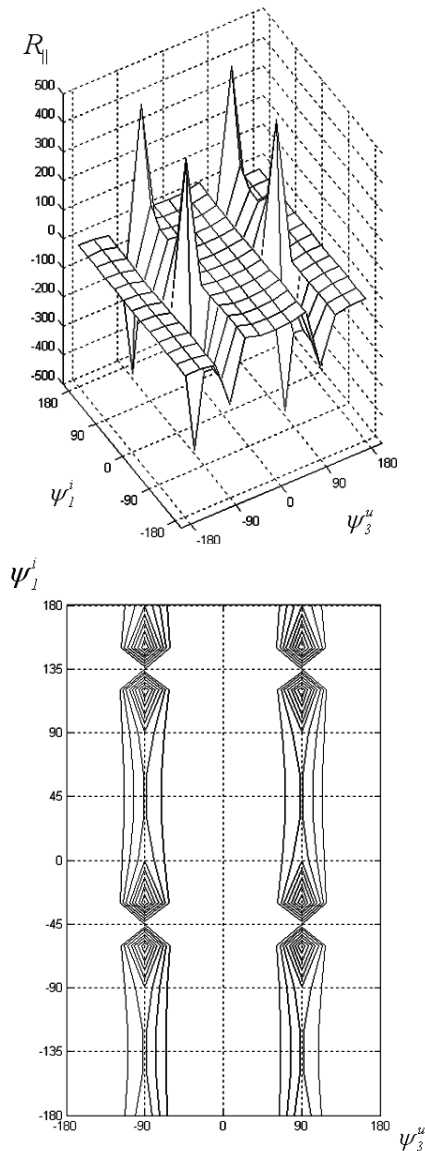


Fig. 5. Dependences of $R_{||}$ from the values of angles ψ_3^u and ψ_1^i at the followings terms: $U_{m(3)} = 50\sqrt{2}$ V; $I_{m(3)} = 2\sqrt{2}$ A; $\psi_3^i = \pi/4$

Conclusions

Constituents of instantaneous power fully enough characterize the energy transmission, conversion and consumption processes. They can be an estimation basis of energy efficiency of exchange processes.

Thus, for schemes functioning of what is characterized by a certain signal, electromagnetic and power processes can be parted in classes with the proper descriptions of X -, P - and Q -quasi-linearity. As a result all electric circuits can be divided in an equivalence criterion as follows: linear circuits (processes are standardized and can be described by a minimum of integral descriptions); nonlinear circuits (for such description of processes it is necessary to find the maximal quantity of integral descriptions); quasi-linear circuits that can be parted in turn to X -, P - and Q -quasi-linear classes on a certain criterion.

REFERENCES

- [1] В.Я. Жуйков, С.П. Денисюк, К.О. Міназова. Особливості формування алгоритмів розрахунку енергетичних характеристик і показників при виділенні класів еквівалентності перетворювачів електричної енергії. //Техн. електродинаміка. Тем. випуск. – 2006.
- [2] Денисюк С.П., Міназова К.О. Особливості формування моделей структури та процесів систем з перетворювачами електроенергії. Праці Інституту електродинаміки НАНУ. Збірник наукових праць. – К. – 2006 – № 1 (13).
- [3] Денисюк С. П. Аналіз процесів енергообміну в системах з пристроями силової електроніки //Техн. електродинаміка. Темат. вип. "Пробл. сучасної електротехніки". Ч. 8. – 2000.

Authors: *prof. Sergey Denysyuk, Institute of Electrodynamics of the Ukrainian Academy of Science, Kyiv, 03057, Ukraine, E-mail: office@pekinform.com.ua; Kateryna Minazova, Department of Electronics, National University of Ukraine "Kyiv Polytechnic Institute", Kyiv, Ukraine, E-mail: k_minazova@ukr.net.*

The analysis of self-oscillatory processes in a nonlinear electrochemical circuit

Abstract. Mathematical model of electrolyzer of metal's deposition has been submitted. On its basis the stability of electromagnetic processes in the circuit with an electrochemical element which has N - figurative characteristic has been investigated. With the help of the method of variables' transformation we have received the analytical solution of the equation of an electromagnetic state of a circuit in the mode of self-oscillations. The interval of parameters at which self-oscillatory mode of the circuit takes place has been determined.

Abstract. Przedstawiono matematyczny model elektrolizy osadzania się metalu. Na tej podstawie przeanalizowano stabilność procesów elektromagnetycznych w obwodach z elementami elektrochemicznymi posiadającymi charakterystykę symboliczną N . Przy pomocy metody transformacji zmiennych uzyskaliśmy analityczne rozwiązanie równania stanu elektromagnetycznego obwodu w trybie własnych oscylacji. Wyznaczono przedział parametrów w których zachodzi zjawisko oscylacji. (Analiza procesów oscylacyjnych w nieliniowym obwodzie elektrochemicznym)

Keywords: electrolyzer, self-oscillation, electrochemical element

Słowa kluczowe: elektrolizer, oscylacje rezonansowe, element elektrochemiczny

Introduction

This work is devoted to the further development of researches in the field of modeling of the electric circuits containing nonlinear electrochemical elements. Such circuits are widely applied at electroplating and refinement of metals and alloys, in the processes of hydrometallurgy, chemotronics, etc. The most typical examples of these circuits are electrolyzers of metal plating. The basic practical tasks in the given branch of technics are improvement of quality and speed of electro-plating, and also reduction of power consumption of technological processes. Usually these problems are solved in two ways. The first way is to develop of the new, more perfect electrolytes, the second – to apply the energy sources generating pulses of various form and duration (pulse electrolysis). Using one of the above-mentioned ways there is a problem of forecasting the parameters of quantitative growth and quality of precipitated coatings. It can be solved by either carrying out experimental researches or with the help of mathematical modeling. The last way is the most acceptable from the point of view of cost of carrying out the researches, and allows considerably to reduce a necessary number of laboratory experiments. There are some works [1-3] devoted to a mathematical modeling of electric circuits with nonlinear electrochemical elements. However they are devoted to modeling of the electrochemical circuits containing nonlinearity, described by the classical Tafel's equation (exponential curve). Besides they do not take into account features of the processes occurring at presence of surface-active substances in electrolyte which are added to its structure with the purpose of improvement of quality of received coatings. In this case modernization of an energy source is not required and electrolysis is carried out on a direct current. But according to the experimental data shown in [4] under certain conditions a break-down of the set deposition mode is observed and there is a periodic change of reaction of system to external influence at influence of direct currents or voltage. Thus, self-oscillations in nonlinear electrochemical circuits, their mathematical description and conditions of occurrence remain scantily studied and important field of electrical engineering from the practical point of view.

Formatting of the text

The typical length of the paper should be limited to no more than 5 pages. The whole paper is written using Type size 9 and Arial font with the indentation set at 5 mm.

Directly after section headings (type size 9 using Arial bold), place the text in justified style. For figure captions, names of the tables and footnotes use Arial font with type size 8. When symbols need to be inserted into the text, use option "insert/symbol" (for example $\Delta\alpha$ or $\mathfrak{G}\in\infty$). Please do not use the equation editor. The equation editor should only be used if a symbol does not exist in the symbol list – for example \hat{H} . Although the whole text is written using Arial font, for symbols please use the Times New Roman italic – for example J and not J (i.e. the same symbols as in the equations).

Electrolyzer equivalent circuit

Fig. 1 shows equivalent scheme of replacement of metal's deposition electrolyzer with a feed from a source of a constant voltage. It reflects the processes of metal deposition (nonlinear element HP_{mk}), formations of a double layer of charges at the surface of the cathode (Ca), heating of the electrolyte (R) and formations of a magnetic field in it (L). The anode is considered to be not polarizable and practically insoluble, and an energy source - an ideal source of voltage. Besides we use the assumption about insignificance of process of hydrogen allocation on the cathode in comparison with the process of metal's deposition.

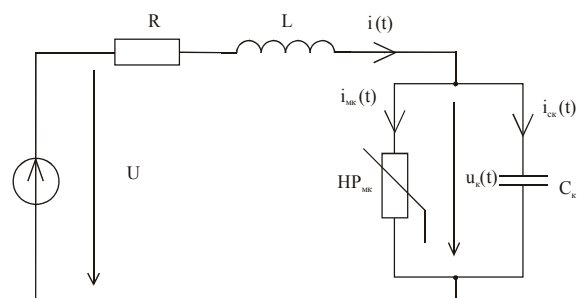


Fig. 1. equivalent scheme of replacement of metal's deposition electrolyzer

Mathematical model of electrolyzer circuit

At presence of surface-active substances in electrolyte volt - ampere characteristic of nonlinear element HP_{mk} has N - figurative form. At its approximation by a cubic polynomial (fig. 2) the system of equations of an electromagnetic state of the circuit (fig. 1) is the following:

$$(1) \quad R \cdot i(t) + L \cdot \frac{di(t)}{dt} + u_k(t) = U,$$

$$(2) \quad i(t) = i_{MK}(t) + i_{CK}(t),$$

$$(3) \quad i_{MK}(t) = S_K \left(z_{01} \cdot u_k(t) + z_{02} \cdot u_k^2(t) + z_{03} \cdot u_k^3(t) \right),$$

$$(4) \quad i_{CK}(t) = S_K \cdot C_K \frac{du_k(t)}{dt}.$$

Independent initial conditions

$$(5) \quad u_k(0) = 0; \quad i(0) = 0.$$

In the equations (1) - (4): $i(t)$ – total electrolyzer current; $i_{MK}(t)$ – partial current of ion discharge of metal on the cathode;

$$(6) \quad i_{MK}(t) = S_K \cdot j_{MK}(t),$$

where $j_{MK}(t)$ – current density of ions discharge of metal on the cathode; S_K – area of the cathode; C_K – capacitance of a cathodic double layer of the charges equal to

$$(7) \quad C_K = C_0 \cdot S_K,$$

where C_0 – specific cathode capacitance; $i_{CK}(t)$ – a capacitive current of the cathode; u_k, u_a – a cathodic overvoltage; R – active resistance of electrolyte

$$(8) \quad R = \frac{d}{\gamma S_K},$$

where γ – specific active conductance of electrolyte; d – distance between electrodes; z_{01}, z_{02}, z_{03} – factors of volt-ampere characteristics border cathode – electrolyte; L – electrolyte inductance.

Self-oscillations

Active resistance R defined by the formula (8) is not constant during electrolyzer work as due to reduction of concentration of metal ions in the electrolyte, spent for a coating, specific conductance of electrolyte γ changes. Let's analyze an opportunity of onset of self-oscillations at change of γ by the example (fig. 1). For this purpose we use a classical method of analytical research of stability according to M. Lyapunov. Such equilibrium position is considered to be steady if at a primary perturbation the deviation from equilibrium position will not exceed any small size.

The Lyapunov's method consists of replacement of the characteristic of nonlinear element of a tangent to it in the point of researched condition. We'll transform system (1) - (4) to the form

$$(9) \quad S_K \cdot C_K \frac{du_k(t)}{dt} = i(t) - \Phi(u_k),$$

$$(10) \quad L \cdot \frac{di(t)}{dt} = U - u_k - R \cdot i(t),$$

where $\Phi(u_k)$ it is described by the expression (3). Let's write Δu_k and Δi for the values of a cathodic overvoltage u_{k0} and current of the circuit i_0 in equilibrium position of perturbation

$$(11) \quad u_k = u_{k0} + \Delta u_k,$$

$$(12) \quad i = i_0 + \Delta i.$$

Let's substitute expressions (11), (12) in the equations (9) and (10). At expansion of $\Phi(u_{k0} + \Delta u_k)$ in-to series for Δu_k we take only first two components

$$(13) \quad \Phi(u_{k0} + \Delta u_k) = \Phi(u_{k0}) + \Delta u_k \Phi'(u_{k0}),$$

we receive

$$(14) \quad \Delta i = S_K \cdot C_K \frac{d\Delta u_k(t)}{dt} + \Delta u_k \Phi'(u_{k0}),$$

$$(15) \quad L \cdot \frac{d\Delta i(t)}{dt} + \Delta u_k + R \Delta i = 0.$$

Taking into account that

$$(16) \quad \Phi'(u_{k0}) = \frac{1}{R_d},$$

where R_d – stands for differential resistance of a nonlinear element in a working point. From the expressions (14) and (15) we receive the equation of variations

$$(17) \quad b_0 \frac{d^2 \Delta u_k(t)}{dt^2} + b_1 \frac{d\Delta u_k(t)}{dt} + b_2 \Delta u_k(t) = 0,$$

where

$$(18) \quad b_0 = 1; \quad b_1 = \frac{R}{L} + \frac{1}{S_K \cdot C_K \cdot R_d}; \quad b_2 = \frac{1 + \frac{R}{R_d}}{L \cdot S_K \cdot C_K}.$$

In accordance with Routh-Hurwitz criterion at $b_0 > 0$ state of equilibrium will be steady, if

$$(19) \quad b_1 > 0; \quad b_2 > 0.$$

From the condition (19) we receive inequalities

$$(20) \quad \frac{L}{R \cdot S_K \cdot C_K} < |R_d|,$$

$$(21) \quad R < |R_d|.$$

At performance of the condition (20) fluctuations stop to increase. Performance of an inequality (21) guarantees that the working point will remain on a site of negative differential resistance. We define a corresponding interval of specific active electrolyte conductances at which the working point gets on the specified site. Borders of this interval are in conformity with extremum of dependence 2 (fig. 3). We'll define these extremums from the equation:

$$(22) \quad \frac{d\Phi(u_k)}{du_k} = S_K \left(z_{01} + 2 z_{02} u_k + 3 z_{03} u_k^2 \right) = 0.$$

Therefore the abscises of extremums are equal to

$$(23) \quad u_{e1,2} = \frac{-z_{02} \pm \sqrt{z_{02}^2 - 3 z_{03} z_{01}}}{3 z_{03}}.$$

The computation is performed for the following parameters of an equivalent circuit fig. 1: $U=0,42$ V; $L=6 \cdot 10^{-6}$ H; $C_K=500 \cdot 10^{-6}$ F/cm²; $S=3 \cdot 10^{-3}$ cm²; $d=10$ cm; $\gamma_0=2,1 \dots 2,27$ S/cm. Factors of approximation: $z_{01}=1,053$ S/cm²; $z_{02}=-6,202$ S/(V·cm²); $z_{03}=10,691$ S/(V²·cm²). According to the formula (22) $u_{e1}=0,126$ V; $u_{e2}=0,261$ V. Corresponding values of specific conductance by (8) $\gamma_{e1}=1,89$ S/cm; $\gamma_{e2}=2,667$ S/cm. If the size of specific conductance is in these limits, the working point will appear on a site of negative differential resistance and remain in its limits in case of performance of an inequality (21).

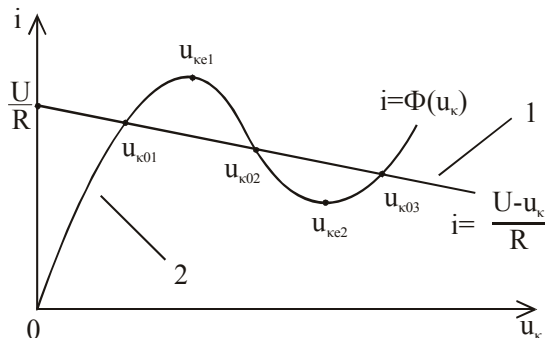


Fig. 2. Mathematical model of electrolyzer circuit - its approximation by a cubic polynomial

For example, at $\gamma_0=2$ S/cm value of the cathodic overvoltage an equilibrium position of balance, we shall define from the equation

$$(24) \quad S_K(z_{01} u_K + z_{02} u_K^2 + z_{03} u_K^3) = \frac{U - u_K}{R}.$$

Thus, $u_{k0}=0,146$ B. Differential resistance in this point is $R_d = -4,497 \cdot 10^{-4}$ Ohm, that is, the inequality (21) is performed. There is a similar way to check up the performance of the given inequality in other points of the specified interval. The Results of the performed calculations (fig. 3) show the reduction of frequency of self-oscillations along with the growth of conductivity. The maximal and minimal values of a cathodic overvoltage and a total current of the circuit remain constant within a considered interval.

The analytical solution

It's possible to reduce the system of equations (1)-(4) to the nonlinear differential equation of the second order in the form

$$(25) \quad \ddot{u}_K(t) + N(u_K(t))\dot{u}_K(t) + M(u_K(t)) = 0,$$

where

$$(26) \quad N(u_K(t)) = n_0 + n_1 u_K(t) + n_2 u_K^2(t),$$

$$(27) \quad n_0 = \frac{R}{L} + \frac{z_{01}}{C_K}; \quad n_2 = \frac{2z_{02}}{C_K}; \quad n_3 = \frac{3z_{03}}{C_K},$$

$$(28) \quad M(u_K(t)) = m_1 u_K(t) + m_2 u_K^2(t) + m_3 u_K^3(t) + \delta,$$

$$(29) \quad m_1 = \frac{R z_{01} S_K + 1}{L C_K S_K}; \quad m_2 = \frac{R z_{02}}{L C_K};$$

$$(30) \quad m_3 = \frac{R z_{03}}{L C_K}; \quad \delta = -\frac{U}{L C_K S_K}.$$

We receive the analytical solution of the equation (25) with the help of a method of variables' transformation [5]. For this purpose we perform the following substitution

$$(31) \quad y(t) = u_K(t) + x_1, \quad x_1 = \frac{z_{02}}{3z_{03}}.$$

As a result we receive the equation

$$(32) \quad \ddot{y}(t) + N^*(y(t))\dot{y}(t) + M^*(y(t)) = \delta^*,$$

where

$$(33) \quad N^*(y(t)) = n_0^* + n_2 y^2(t),$$

$$(34) \quad n_0^* = n_0 - n_1 x_1 + n_1 x_1^2,$$

$$(35) \quad M^*(y(t)) = m_1^* y(t) + m_3 y^3(t),$$

$$(36) \quad m_1^* = m_1 - \frac{z_{02}^2}{3z_{03}}, \quad \delta^* = \frac{z_{02}}{3z_{03}} \left(m_1 - \frac{2z_{02}^2}{9z_{03}} \right) - \delta.$$

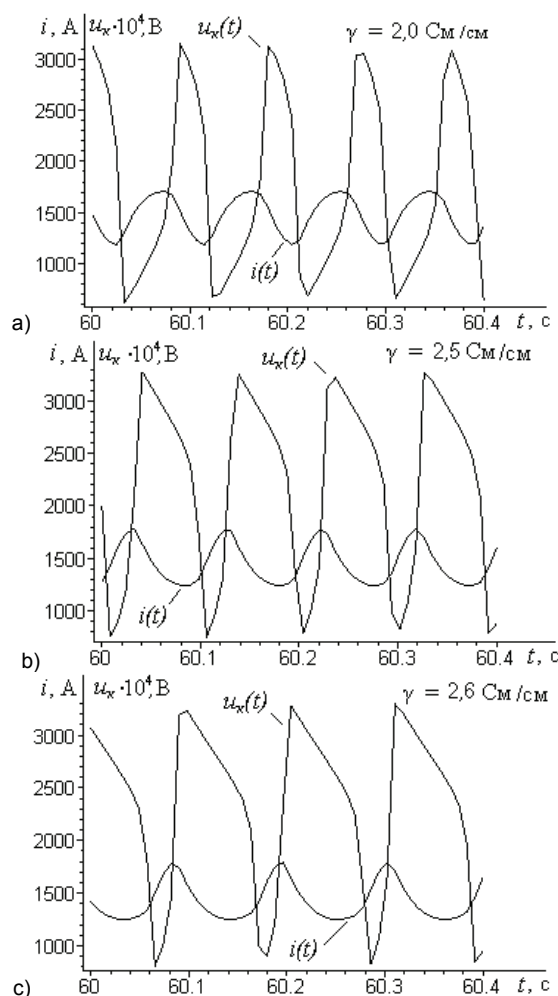


Fig. 3. Results of the performed calculations

Let's transform the equation (32) on the linear non-uniform differential equation with constant factors in the form

$$(37) \quad h''(v) + h(v) = W(v)$$

with the help of relations

$$(38) \quad h(v) = g(y)e^{\psi(t)},$$

$$(39) \quad v = \varphi(t),$$

$$(40) \quad g'(y) = \dot{\varphi}(t).$$

We'll differentiate (38) twice by v and substitute the result into (37). As a result of transformations we receive the equation

$$(41) \quad \ddot{y}(t) + 2\dot{\psi}(t)\dot{y}(t) + \frac{g(y)}{g'(y)}(\ddot{\psi}(t) + \dot{\psi}^2(t) + \dot{\phi}^2(t) - \frac{\ddot{\phi}(t)}{\dot{\phi}(t)}\dot{\psi}(t)) = \frac{\dot{\phi}^2(t)}{g'(y)}W(v)e^{-\psi(t)}.$$

Let's compare the equations (32) and (41). They coincide under the following condition:

$$(42) \quad M^*(y) = \frac{g(y)}{g'(y)}\left(\ddot{\psi}(t) + \dot{\psi}^2(t) + \dot{\phi}^2(t) - \frac{\ddot{\phi}(t)}{\dot{\phi}(t)}\dot{\psi}(t)\right),$$

$$(43) \quad N^*(y(t)) = 2\dot{\psi}(t),$$

$$(44) \quad W(v) = \frac{\delta^*}{\dot{\phi}^2(t)}e^{\psi(t)}.$$

From the formula (42) we define approximately the function $g(y)$, taking into account only the component $\dot{\phi}^2(t)$ which is the most significant one:

$$(45) \quad g(y) = \left[2 \int M^*(y) dy\right]^{\frac{1}{2}}.$$

Linearising the function $\varphi(t)$, we receive

$$(46) \quad g'(y) = \dot{\phi}(t) = \theta.$$

Further we write down the approximate solution of the equation (37) in the form

$$(47) \quad h(v) = \left[G_1^* \cos \theta t + G_2^* \sin \theta t + \frac{\delta^*}{\theta} e^{\psi(t)} \right].$$

Returning to the former variables and having written

$$(48) \quad \lambda(t) = \psi(t) - \psi(0),$$

We receive the approximate solution of the equation (32) in an implicit form

$$(49) \quad \alpha + \beta y^2(t) = e^{-\lambda(t)} \left[G_1^* \cos \theta t + G_2^* \sin \theta t \right] + \frac{\delta^*}{\theta}.$$

Having defined the constants of integration with the help of initial conditions (5) and passing to an obvious form we finally receive the solution of the equation (25)

$$(50) \quad u_{\varepsilon}(t) = \sqrt{\frac{1}{\beta} \left[e^{-\lambda(t)} \left(\left(g(y(0)) - \frac{\delta^*}{\theta} \right) \cos \varphi(t) + \frac{N^*(y(0))}{2} \left(g(y(0)) - \frac{\delta^*}{\theta^2} \right) \sin \varphi(t) \right) + \frac{\delta^*}{\theta} - \alpha \right]} - x_1.$$

In the formula (50) the function $\lambda(t)$ is calculated by the from expressions (43) and (48) with the use of zero approximation in the form of sinusoid. The function $\varphi(t)$ is defined more exactly according to the technique submitted in [5]. Results of calculation by formula (50) are illustrated in fig. 4 (curve 1) simultaneously with numerical calculation (curve 2). Comparison of the results shows that the approximate expression (50) gives a correct presentation about the character of self-oscillations in the circuit (fig. 1).

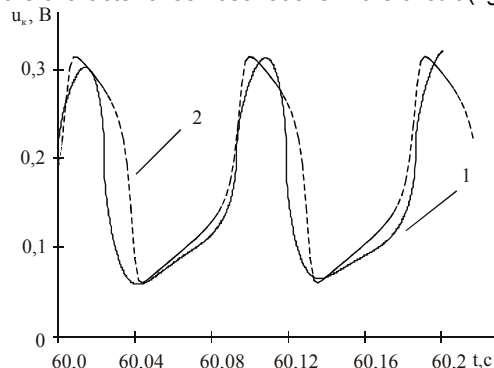


Fig. 4. Results of calculation by formula (50)

Conclusions

Mathematical modeling is a prospective way of research of nonlinear electrochemical circuits in various modes of their work. The self-oscillatory operating mode is an emergency one for these circuits as it is characterized by break-down of the set technological process of metal deposition and significant relaxation oscillations of a current in a electrolyzer circuit. The approach offered in the work allows to reveal the conditions at which self-oscillations are set up in electrochemical circuits, foresee their emergence and establish functional interrelation between parameters of arising self-oscillations and parameters of an electrolyzer circuit.

REFERENCES

- [1] Bondar I.L., Kostin N.A., Research of nonlinear electrochemical circuits with the help of Taylor's transformations, *Electronic modeling*, 1980, nr 3, 55-57
- [2] Kostin N., Sheikina O., Artemchuk V., Mathematical Modeling of Non-linear Electrochemical Circuits, *V International Workshop. Computational Problems of Electrical Engineering*, Jazleevets, Ukraine, 2003, 114-116
- [3] Kostin N., Sheikina O., Artemchuk V., Mathematical Modeling of Non-linear Electrochemical Circuits with Pulse Sources of Voltage, *VI International Workshop. Computational Problems of Electrical Engineering*, Zakopane, Poland, 2003, 182-185
- [4] Nechiporuk V.V., Elgurt I.L., Self-organizing in electrochemical systems, M.: the Science, 1992, 168 p.
- [5] Bondar O.I., Analysis of electrical circuits with nonlinear electrochemical elements by the method of variables transformation, *Thesis for the candidate of technical science degree in specialty 05.09.05 – theoretical electrical engineering*, G.E.Pukhov's Institute of Modeling Problems in Power Engineering of the National Academy of Sciences of Ukraine, Kiev, 2006, 181 p.

Authors: D.Sc., Prof. Nikolay Kostin, Oleg Bondar', Oksana Reutskova, National University of Railway Transport named after acad. V. Lazaryan. 2, acad. V. Lazaryan St. Dnipropetrovsk 49010 Ukraine.

Features of subcircuits matching with components described by discrete parameters during analysis of electric circuits transient processes

Abstract. In the paper features of solutions matching of subcircuits with distributed and lumped parameters which should be integrated explicit and implicit numerical schemes. Usage of multirate method using test example of long line in no-load condition with respective limitations of integration step.

Streszczenie. W artykule przedstawiono właściwości dopasowywania rozwiązań podukładów z rozproszonymi oraz zagnieżdżonymi parametrami, które powinny być scałkowane za pomocą jawnych i uwikłanych schematów numerycznych. (Własności dopasowania podobwodów z elementami opisanymi przez parametry o wartościach dyskretnych w analizie stanów nieustalonych w obwodach elektrycznych)

Keywords: diakoptic, multirate method, subcircuit, transient simulation, long line.

Słowa kluczowe: diakoptyka, metoda rozdzielonego analiza podschematów, analiza czasowa, linia długa.

Introduction

Development of computer systems intended for analysis of complex heterogeneous systems is characterised by maximum universality concerning the class of systems to be modelled. Here contradiction between universality and features of some semantic methods usage appears. Modern software intended for electric systems simulation contain some week means for analogue and digital systems modelling [1, 3].

The goal of presented work is a development of modelling tools with advanced possibilities for simulation of electric circuits which contain components with distributed parameters.

Creation of mathematical model

Diakoptic mathematical model of electric circuit defined by adequacy of separate elements mathematical models and circuit topology can be created by artificial splitting of electric circuit on separate parts with considering of mutual influence of separate parts using some additional values. They can be modeled using, for example, controlled power sources. Circuit interpretation of analyzed circuit can be represented as it was done using fig.1, where multiports N_1, N_2, \dots, N_R are separate parts of splitted circuit (subcircuits). Their state is defined by internal variables $\mathbf{x}_1, \mathbf{x}_2, \dots, \mathbf{x}_R$ and external input \mathbf{v} and output \mathbf{w} variables which are common for neighbor subcircuits. In the fig. 1b external variables are depicted by some dual system of power sources controlled by external variables of neighbor subcircuit. Subcircuit structure on modern level of electrotechnic and electromechanical models development consists of voltage and current sources, nonlinear reactive elements, linear electric resistances (conductances), linearly controlled power sources and long lines.

Diakoptic mathematical model, for example, of electric circuit with lumped parameters can be represented using set of differential and algebraic equations:

$$(1) \quad F_r \left(\frac{d\mathbf{x}_r}{dt}, \mathbf{x}_r, \mathbf{v}, \mathbf{w} \right) = 0, \quad r = 1, \dots, R,$$

$$\mathbf{x}_r(t_0) = \mathbf{x}_{r0}, \quad t \in [t_0, t_f], \quad t_0 < t_f.$$

$$(2) \quad G(\mathbf{v}, \mathbf{w}) = 0,$$

where \mathbf{x}_r is vector of internal variables of r -th subcircuit; $F_r(\bullet)$ is a set of differential and algebraic equations which

describes dynamic processes in r -th subcircuit; $G(\bullet)$ is a set of topological equations that describes relations between subcircuits; R is a number of subcircuit.

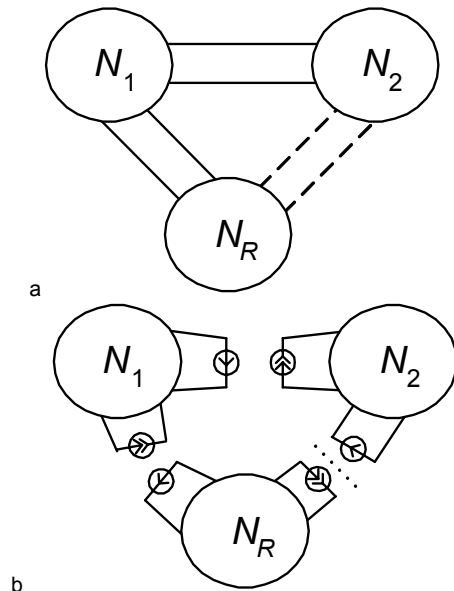


Fig. 1. Circuit interpretation of subcircuits method (a) and using additional power sources (b).

Subcircuit with distributed parameters can be described using system of differential equations with distributed parameters (hyperbolic equations). In matrix form such type equations look like as

$$(3) \quad \mathbf{A} \frac{\partial \mathbf{x}_r}{\partial t} + \mathbf{B} \frac{\partial \mathbf{x}_r}{\partial s} + \mathbf{D} \mathbf{x}_r = 0, \\ \mathbf{x}_r(t_0, s) = \mathbf{x}_r(s), \quad \mathbf{x}_r(t, s_0) = \mathbf{x}_r(t).$$

Transient processes simulation of such heterogeneous systems considering physical processes which define behaviour of mentioned systems is an actual task, because there are no universal method for it solution.

Results of investigations of numerical methods intended for hyperbolic equations solution have shown that it is expedient to use two-step explicit Lax net method [4] which has some features suitable for its usage with multirate

method: high adequacy and stability under transition boundary conditions; possibility to state boundary conditions until results with some discrete character will be obtained.

Numerical scheme of the method used for integration of subcircuit with distributed parameters look as follows:

$$u_t^s = \frac{\Delta t}{2c_0\Delta s} (i_{t-1}^{s-1} - i_{t-1}^{s+1}) + \frac{1}{2} \left(1 - \frac{g_0\Delta t}{c_0} \right) (u_{t-1}^{s-1} + u_{t-1}^{s+1});$$

$$i_t^s = \frac{\Delta t}{2l_0\Delta s} (u_{t-1}^{s-1} - u_{t-1}^{s+1}) + \frac{1}{2} \left(1 - \frac{r_0\Delta t}{l_0} \right) (i_{t-1}^{s-1} + i_{t-1}^{s+1}),$$

$$t \in [t_0, T], s \in \overline{1, k}.$$

It is evident that parameters of fictitious sources as external coordinates depend on boundary conditions of internal variables $u_t^0, i_t^0, u_t^{k+1}, i_t^{k+1}$.

Using of multirate method

It is proposed to use diakoptic handling of multirate method with introducing of additional sources $\mathbf{v} = \mathbf{v}_1 \oplus \mathbf{v}_2 \oplus \dots \oplus \mathbf{v}_R$ [2]. In such a case it is possible to represent heterogeneous system in the form shown in Fig. 2.

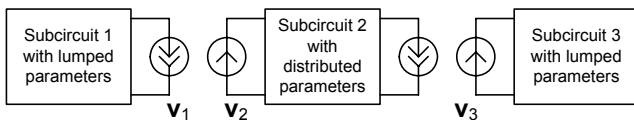


Fig. 2. Connection of subcircuits using additional sources method.

The essence of the method is as follows: each subcircuit and each equation system of mathematical model respectively should be quantized and integrated separately with methods corresponding to their mathematical type. On some time interval, namely, correction step H_n of independent parameters of additional sources \mathbf{v} their values can be fixed and sets of differential equations of each subcircuit should be solved separately. After this external variables of coupling can be defined using coupling equations. After their recalculation solution of differential equations is continued until necessary tolerance of obtained result will be obtained. In the Fig. 3 graphical interpretation of congruence step and integration steps is shown.

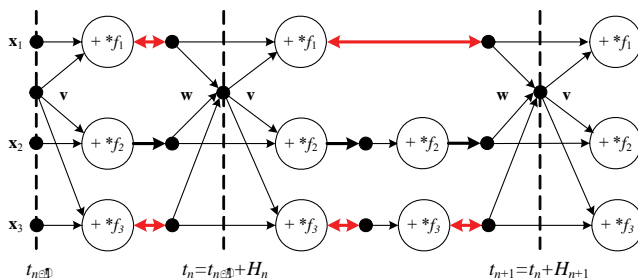


Fig. 3. Graphical interpretation of congruence step.

Advantage of this method lies in possibility to use the numerical method which is the most effective one for this equations. The method is parallel in its internal nature, therefore it allows to create effective system of modelling with possibility of its usage in splitted systems.

Examples

Advantages of proposed approach are noticeable when complex circuits should be calculated (they contain parts of different physical nature which are represented by different mathematical models with lumped parameters and mathematical models with distributed parameters as, for example, for calculation of transients in transmission line loaded by RC-branch). Voltage source is connected to the input nodes of this line which is switched on in initial moment $t_0 = 0$. Therefore, electric circuit is shown in the Fig. 4.

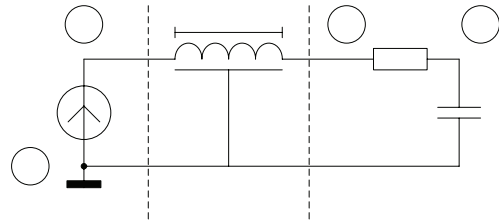


Fig. 4. Схема лінії електропередачі.

To couple long line with other subcircuits it should be represented by one LC-branch (Fig. 5).

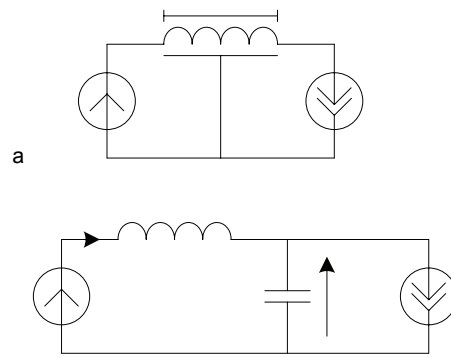


Fig. 5. Representation of subcircuit with long line (a) by LC-branch (b) to couple it with other subcircuits.

We present an example of calculation of long line in the form of equivalent diagram of power transmission line loaded on RC circuit. Time charts of transient processes (capacitor voltages, output voltage and input current) of long line are shown in Fig. 6.

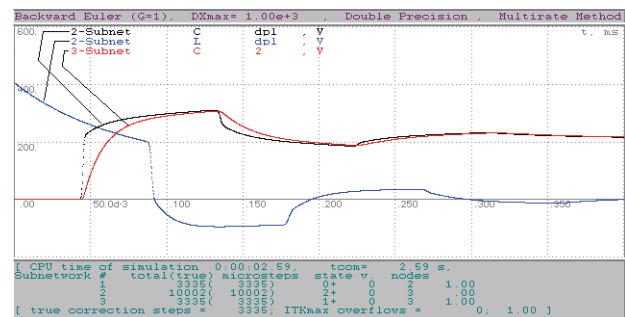


Fig. 6. Power line transient processes.

During numerical experiments reduction of maximum integration step was observed, namely subcircuits correction step that is evident for used integration methods:

implicit Lax method for subcircuit with distributed parameters and explicit Euler method for subcircuit with lumped parameters. Besides it when resistance of RC-branch was reduced limitation of minimal value was noticed (tab. 1-3) that can be explained by discretization of integration step of subcircuits by value equal to time discretization step of difference numerical scheme of long line.

Table 1. Limitations of correction step of subcircuits when C=25 pF

| R [kOhm] | Hmax [μ s] | Hmin [μ s] |
|----------|-----------------|-----------------|
| 1 | 0.12 | 0.12 |
| 1.2 | 1 | 0.12 |
| 1.4 | 1.2 | 0.12 |
| 1.8 | 1.5 | 0.08 |
| 2 | 4 | <0.02 |
| >5 | >10 | <0.02 |

Table 2. Limitations of correction step of subcircuits when C=250 pF

| R [kOhm] | Hmax [μ s] | Hmin [μ s] |
|----------|-----------------|-----------------|
| 0.79 | 0.32 | 0.32 |
| 0.8 | 0.4 | 0.24 |
| 1 | 1.1 | 0.12 |
| 1.4 | 1.2 | <0.02 |
| 1.8 | 1.5 | <0.02 |
| >2 | >10 | <0.02 |

Table 3. Limitations of correction step of subcircuits when C=2500 pF

| R [kOhm] | Hmax [μ s] | Hmin [μ s] |
|----------|-----------------|-----------------|
| 0.6 | 0.4 | 0.32 |
| 0.8 | 1.2 | 0.12 |
| 1 | 5 | <0.02 |
| >2 | >10 | <0.02 |

Parameters of long line were as follows: $l_0 = 0.490$ mH/m, $r_0 = 10.0$ Ohm/m, $c_0 = 1.66$ nF/m, $g_0 = 50.0$ pS/m, $\Delta t = 40.0$ ns, $\Delta s = 50.0$ mm, $k = 1000$.

Conclusion

Presented results have shown that it is possible to analyze transient processes in complex circuits which contain subcircuits with different physical nature. Besides it congruence points of subcircuits depend on the most slow one. Besides it is necessary to pay much attention to used difference schemes because they have essential influence on character of calculation process.

REFERENCES

- [1] Petcu D., Parallelism in solving ordinary differential equations, Mathematical Monographs 64, Tipografia Universitatii din Timisoara, 1998, 232 pages
- [2] Stakhiv P., Analysis of dynamic regimes in electronic circuits with multiports. – Lviv, 1998, 154 pages (in Russian)
- [3] Puhon J., Tuma T., Optimization of Analog Circuits with SPICE 3F4, Proceedings, European Conference on Circuit Theory and Design, Budapest, Hungary, (1997), 177-180
- [4] Numerical Recipes – William H. Press, Saul A. Teukolsky, William T. Vetterling, Brian P. Flannery. – Cambridge University Press, 1992

Authors: D.Sc Serhiy Rendzinyak, Lviv Polytechnic National University, Institute of Electric Power Engineering and Control Systems, S. Bandera str. 12, 79013, Lviv, Ukraine; postgr. Andriy Korud, Lviv Polytechnic National University, Institute of Electric Power Engineering and Control Systems, S. Bandera str. 12, 79013, Lviv, Ukraine, E-mail: spg@polynet.lviv.ua; Ass. Prof., Cand. of Techn. Sc Bohdan Melnyk, Ivan Franko National University of Lviv, Universytetska str. 1, 79000, Lviv, Ukraine.

Model for forecasting good yield of microcircuit chips by results of test control

Abstract. The model is proposed for forecasting good yield of microcircuit chips (IC) and the system of the quality test control of the IC technological processes. It ensures the veritable spread of the control results of the test structure parameters on the IC chips, makes it possible to perform the comprehensive quality evaluation of the individual technological fabrication operations of microcircuits, to perform optimization of the technological process and to forecast good yield of the microcircuit chips.

Abstract. Zaproponowano model pozwalający prognozować wydajność niezawodność procesów wytwórczych mikroukładów (IC) oraz system testów kontroli jakości procesów technologicznych IC. Zapewnia on wiarygodne różnice wyników kontroli parametrów testowanych struktur układów IC. Pozwala wykonać kompleksowe oszacowanie jakości poszczególnych technologicznych operacji produkcji mikroukładów. Pozwala wykonywać optymalizację procesów technologicznych oraz prognozować wydajność produkcji mikroukładów. (Model do przewidywania niezawodności mikroukładów na podstawie wyników testów jakościowych)

Keywords: microelectronics, test structure, good yield percentage of microcircuits, optimization of processes.

Słowa kluczowe: mikroelektronika, struktury testowe, wysoki procent wydajności mikroukładów, procesy optymalizacji.

Introduction

At the time of fabrication of the integrated microcircuits (IC) the silicon wafers are subjected to a large number of the individual operations (up to 300), which together compile the fabrication process. In the process of fabrication only several key operations, usually about 30 – 50 have the direct influence on the operating characteristics of circuits. As the final good yield (number of chips on the wafer, passed control and meeting the quality requirements) depend upon good yield on the separate operations, then it is necessary to have the diagnostics methods for detection of defects on these key operations.

Good yield of chips is determined on the functional control operation at the end of the technological fabrication process of microcircuits and the given parameter reflects the quality of the technological process as a whole. It does not provide the quality deciphering of the individual operations of the technological process. In order to determine quality of the individual operations performance it is required to create the special test structures. Each kind of the test structures should determine the performance quality of the definite operations. Such approach may enable to perform the post-operational reject separation of the microcircuit chips and ensure the good yield forecasting by operations and as a whole by the technological process. For this it is necessary to solve the following tasks:

- Area of the test structures is considerably smaller, than the area of the microcircuit chip. Therefore, good yield of the test structures will be considerably greater, than good yield of the IC chips. It is necessary to construct a model for computation of good yield of the microcircuits by the measured value of the good yield percentage of the test structures;

- To develop the design of the special teststructures for the post-operational reject separation of the microcircuit chips, forecasting good yield by operations and as a whole by the technological process.

Good yield simulation of microcircuits

Good yield simulation is a quite actual problem in fabrication of the integrated microcircuits with the submicron design rules. Having determined the simulation parameters, it is possible to forecast the fabrication cost and efficiency of the new circuits, to determine quality of the individual technological operations and optimize the technological fabrication process of microcircuits, to reveal the most critical operations and perform their perfecting.

Simulation parameters of the IC good yield for the given process or the technological chain, having the considerable variations for the concrete circuit, point to the circuit sensitivity to the parameters of devices. On the basis of the further researches it is possible to foresee the possible alterations in the design of the circuit or process, which will result in the considerable increase of the good yield of the devices. IC production is a constantly developing process. Good yield simulation of the circuits takes into account those processes and mechanisms, which limit the IC good yield. After revealing the factors, limiting the IC good yield, the technological process is perfected or, if necessary, some separate operations are excluded. For instance, the contact lithographical print was replaced with the projection optical print, which resulted in reduction of the defect density; dry etching replaced the liquid etching, in view of this the accuracy increased of reproduction of the element sizes; ion implantation is used instead of diffusion, owing to which there was improvement of the resistance value and transition depth control. Simulation of the IC good yield is not a method of forecasting the future development, it is more likely, an instrument of perfecting the contemporary processes and designs of circuits.

IC good yield in the considerable degree is determined by the defectness of the individual technological operations. The developed model of the post-operational separation of defects (rejects) and good yield simulation of the microcircuits is based on the following assumptions:

- Defect – deviation of the layer structure (margin of the layers separation), resulting in failure of the microcircuit;

- Density of defects D_0 does not depend on the area value, it is the same both on the test structure and on the microcircuit chip;

- Good yield percentage of the microcircuits is equal to the probability of the defect absence on the entire area of a chip;

- Expression, describing interaction of the good yield percentage of the microcircuits with the chips area value and defect density is the Poisson expression. In the given case evaluation of the IC good yield P_i on the i -st operation is performed by the ratio [1]:

$$(1) \quad P_i = e^{-S_{kp} \cdot D_i}$$

where: S_{kp} - IC chip area, D_i - defect density, introduced by the i -th operation.

Area of the scribe paths, which is occupied by the specialized test module, is considerably smaller, than the area of the IC appropriate chip (S_{kp}), i.e.

$$(2) \quad S_{tc} \ll S_{kp}$$

where: S_{tc} - area of a separate test structure.

In this case (1) will assume an expression:

$$(3) \quad P_i = \left(e^{-(S_{tc} \cdot D_i)} \right)^b = x_i^b$$

where: $x_i = e^{-(S_{tc} \cdot D_i)}$ - good yield TS by the i -th parameter,

$b = \frac{S_{kp}}{S_{tc}}$ or $b = \frac{N}{n}$, N - number of elements in IC, n - number of elements in TS.

Knowing the forecasted IC good yield by the separate operations, it is possible to compute the IC good yield as a whole by the technological process:

$$(4) \quad P = \prod_{i=1}^m P_i$$

where: m - number of operations, applied in IC.

Error Δ_i of determining the good yield value of TS (x_i) depends on the number of measurements M and is determined by the ratio:

$$(5) \quad \Delta_i = \frac{t}{\sqrt{M}} \cdot \sigma_i$$

where: $\sigma_i = \sqrt{x_i \cdot (1 - x_i)}$ - a mean quadratic deviation of the good yield value of TS, t - Student ratio, determined by the level of confidence.

Therefore the IC good yield on the i -th operation P_i and by the technological process as a whole P is equal appropriately:

$$(6) \quad P_i = x_i^b \cdot \left(1 \pm \frac{t}{\sqrt{M}} \cdot \sqrt{\frac{1 - x_i}{x_i}} \right)^b$$

$$(7) \quad P = \prod_{i=1}^m P_i = \prod_{i=1}^m x_i^b \cdot \left(1 \pm \frac{t}{\sqrt{M}} \cdot \sqrt{\frac{1 - x_i}{x_i}} \right)^b$$

where: m - number of independent parameters, determining the IC good yield. As it follows from (6), (7) for ensuring the practically applied error ($\leq 10\%$) computation of the IC good yield it is necessary to pexecute the condition:

$$(8) \quad M \gg (bt)^2 \cdot \frac{1 - x_i}{x_i}$$

Thus, if the ratio between the number of elements in the test structures and the number of the appropriate elements in the circuit is equal to $b = 10$, then the number of measurements in compliance with the ratio (8) constitutes:

- a) during analysis of a separate wafer -80 measurements; error of determining the IC good yield will be equal to 12%;
- b) during the lot analysis – not less, than 200 measurements; error of determining the IC good yield will be equal to 5%;
- c) during the package analysis – not less than 500 measurements; error of determining the IC good yield will be equal to 2%.

Juxtaposition of the actual and computed and good yield shows their good congruence. Thus, the proposed simulation procedure esures the efficient forecasting the microcircuit chips good yield and makes it possible to perform optimization of the technological processes of the microcircuit fabrication.

Experimental results and discussion

The designed automated system of the quality test control of the technological processes is based on usage of the test structures, reflecting all main structural IC elements with consideration of the actual sizes of elements and gaps between them, the actual relief of the layers. The peculiarity of the given control system is that selection of the number of the analyzed elements in composition of the test structures was performed with consideration of the number of the appropriate elements on the IC chip. The test modules, designed for the automated control system, contain the specialized test structures (TS), enabling to receive the expanded information about the electric, physical and geometric parameters, reflecting the quality of the technological process.

TM is located on the scribe paths, covering several working chips of the integrated microcircuits, and contains up to 64 contact pads. Such design of TM ensures the possibility of the technical processes control in the system of the IC layout projection transfer to the wafers.

TM consists of the test structures of two kinds:

- parametric TSs (transistors, transistor cells, resistors, etc.);
- statistic test structures (chains of contacts to the various areas, TSs for control of rupture of the prolonged buses, leakages and shorts between the different layers).

The parametric TSs are intended for control of the physical and electric parameters of the single elements, used in ICs. The subsequent statistic processing of the results makes it possible to determine reproducibility of the controlled parameters on the wafer, lot, package. The correlation analysis makes it possible to preset the ranges of the optimum values of parameters, determining the good yield.

The statistic TS are intended for control of defect of the individual technological operations, which is attained by usage in TSs of the large number (n) of the single type elements, connected in series or in parralel depending on the type of the controled element.

The correct selection of design, sizes of the test elements, composition of the test module makes it possible to perform the post-operational separation od rejects in the technological processes of IC creation, making it possible to forecast the good yield of circuits.

Fig. 1 shows the image of the designed test module for analysis of the technological process of the submicron CMOS IC of the static RAM (SRAM). The given IC is fabricated under the 0.8 μ m design rules (bus width of PCS-gate – 0.8 μ m, Al2 – 1.4 μ m, Al1 – 1.2 μ m, the gates in the layer of Al1 and Al2 – 1.0 μ m, contacts 0.8 x 1.0 μ m) and contains two metallization layers, one layer of polisilicon (PCS) gates. The test module contains about 40 specialized

test structures, including the structures, characterizing the properties of the dielectric layers. The test module is located on the scribe paths with the width of 250 μm , surrounding two working IC chips, i.e. occupies the unused area among the IC chips and, what is important, realized in the system for image projection print of the chip layers on the silicon wafers and makes it possible to obtain the expanded information about the electric, physical and geometric parameters of layers and operations of the IC technological process.

For the comprehensive quality evaluation of the dielectric layers CMOS ICs are intended the tests: №1 – for control of parameters of the interlayer insulating dielectric No. 1 with the thickness of 0.7 μm , deposited on the polysilicon layer with the developed relief (in the polysilicon layer with the thickness of 0.7 μm there are open 3500 windows with the size $1.0 * 1.0 \mu\text{m}^2$) and the covered by the continuous layer of aluminium with the thickness of 0.9 μm ; №2 – for control of parameters of the gate dielectric with the common length of the margin silicon-insulating oxide ("beak") 120 μm , covered with the continuous layer of polysilicon (MOS-capacitor with the developed relief); №3, №4 - MOS-capacitors polysilicon – gate oxide - silicon n and p type of conductivity appropriately (size of capacitors $250*600 \mu\text{m}^2$); №5, №6 - test MOS-transistors appropriately p and n channel; №7, №8, №9, №10 - parasitic MOS-transistors p and n channel with the aluminium and polysilicon gates; № 11, № 12 – prolonged paths of polysilicon, the first and second metallization level (appropriately, width 0.8, 1.2 and 1.4 μm) on the complex layout IC relief (for determination of availability of PCS bus ruptures and metallization); № 13, № 14 – tests for determination of availability of shorts between metal of the first and second level of metallization (extended couples of paths with the gap 1.0 μm).

Parameter control of the test structures in composition of TM is performed on the automated system «AIK Test-2» by the program, ensuring measurement, intermediate processing (computation of parameters) and finishing data processing (statistic processing, plotting the histograms). This will make it possible to obtain a great statistic information under the conditions of the mass production about the individual operations

And about the IC technological process as a whole, to perform the post-operational rejection selection, to set the factors, determining the good yield.

The developed mathematical software contains a number of the service programs, making it possible to perform immediately after measurement:

- accumulation and storage of the control results (per shift, day, month);
- formatting the required data array, subject to processing;
- intermediate and complete statistic processing of control results;
- correlation analysis;
- plotting distribution of parameters on the wafer area in the double and triple coordinate systems;
- submission of references by the control results.

Table 1 shows the main results of the quality analysis of the fabrication technological processes of CMOS microcircuits. Coincidence of the actual and forecasted good yield of chips from the wafer confirms efficiency of the proposed control method of the technological process defectness.

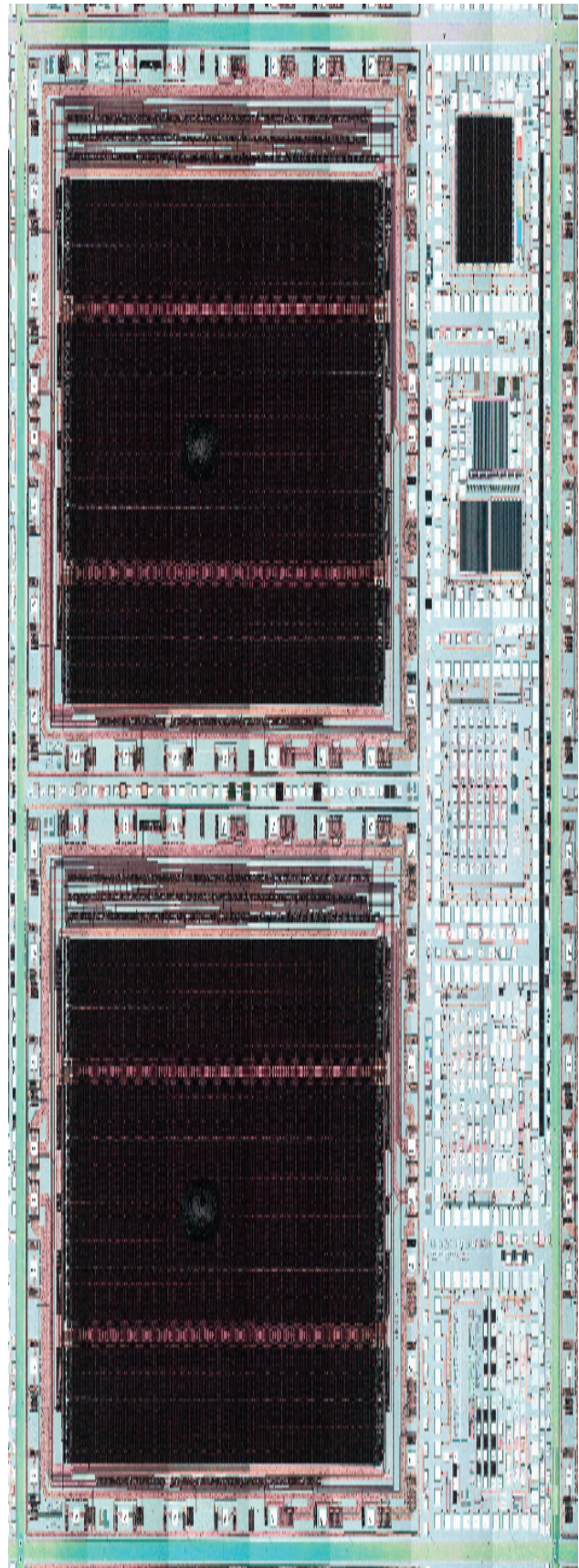


Fig. 1. Photograph of test module CMOS IC

Reject distribution by operations in IC production, making it possible with high probability to reveal "the bottlenecks" of the technological process.

From Table 1 it follows, that the most imperfect is the block of operations on creation of the double level metallization:

- for CMOS microcircuits – block of operations on formation of contacts AI2-AI1 and on performance of photolithographies of the first and second metallization levels (defects, resulting in the bus shorts).

Reduction of reject percentage of these operations will provide a considerable increase in IC good yield.

Test control possesses a great number of reserve potentialities, which makes it an indispensable means for analysis of the VLIC technologies. The continuous enhancement of the VLIC functional complexity, their integration degree becomes impossible without application of the advanced informational test control methods. The further enhancement of the test control should occur primarily on the way of perfection of the mathematic software (creation of the data processing service programs, including the complete statistic and correlation analysis) and automated measuring equipment.

Table 1. Test control results of the technological process of the submicron CMOS IC SRAM

| Reject Kind of IC Chips | $b = \frac{s_{kp}}{s_{TC}}$ | Measured Good Yield TS P _{TC} , % | Computed Good Yield of IC Chips P _{инмс} =(P _{TC}) ^b , % |
|-------------------------|-----------------------------|--|--|
| Bus shorts AI2-AI2 | 5 | 95.5 | 79.4 |
| Bus shorts AI1-AI1 | 5 | 96.1 | 82.0 |
| Non-contact AI2-AI1 | 5 | 98.5 | 92.7 |
| Bus rupture AI2 | 5 | 98.9 | 94.6 |
| Bus rupture AI1 | 5 | 99.3 | 96.5 |
| Bus shorts AI2-AI1 | 5 | 99.5 | 97.5 |

Total good yield 88.3 % 53.7 %
 Actual IC good yield 51.5 %

Thus, the developed quality control test system of the IC technological ensures the veritable spread of the control results of the test structure parameters on IC chips as a whole.

Thus, the designed quality control test system of the IC technological processes ensures the veritable spread of the control results of the test structure parameters on IC chips as a whole, makes it possible to perform the comprehensive quality evaluation of the various layers, applicable to their usage in ICs, to perform optimization of the technological process and forecast the good yield of the microcircuit chips. Introduction of the quality control test system of the IC fabrication technological process, including: location of the test structures on the scribe paths, surrounding several IC working chips; automated collection and processing of the measurement data, procedure of data processing and

forecasting the IC good yield, depending on the IC integration degree, ensures the effective control on the technological process status.

Conclusion

1. The quality control test system of the IC fabrication technological process, including: location of the test structures on the scribe paths, surrounding several IC working chips; automated collection and processing of the measurement data; procedure of data processing and forecasting the IC good yield, depending on the IC integration degree.
2. Test control at the design stage and mass production makes it possible:
 - to veritably identify "the bottlenecks" of the technological process;
 - to establish the reject distribution (defect) by operations of the technological process on the wafer, lot, package;
 - to certify the technological equipment and operations of the technological process;
 - to forecast the good yield by operations and, as a whole, by the technological process;
 - to analyze the ranges of parameters, determining the good yield.
3. Technology analysis of the submicron CMOS IC SRAM made it possible to determine distribution of the good yield percentage of the IC chips by the main blocks of operations:
 - bus shorts AI2-AI2 – 79.4 %
 - bus shorts AI1-AI1 – 82.0 %
 - non-contact AI2-AI1 – 92.7 %
 - bus rupture AI2 – 94.6 %
 - bus rupture AI1 – 96.5 %
 - bus shorts AI2-AI1 – 97.5 %
4. The proposed procedure ensures simulation of the microcircuit good yield and is actual during fabrication of the integrated microcircuits with the submicron design rules. Having determined the simulation parameters, one can forecast the cost and efficiency of the new circuits fabrication, to determine quality of the individual technological operations and to optimize the fabrication technological process of microcircuits, to reveal the most critical operations and to perform their perfection.
5. The test control system is applied in the mass production of Research and Production Corporation «Integral» on all fabricated ICs and the test control is introduced on all ICs under design.

REFERENCES

- [1] Zi S, Technology VLIC, Moscow, «Mir», 1986, 397c.

Authors: Doctor of Technical Sciences, Prof. A. I. Belous; A.V. Emel'yanov; V. S. Syakersky; Candidate of Technical Sciences G.G. Chigir; Research and Production Corporation "Integral", 12, Korzhenevsky St., Minsk-220108, E-mail: office@bms.by

Effective computation of high-frequency plane waves field scattered on electrically resistive strip

Abstract. A thin electrically resistive strip is in a uniform background (in two-dimensional Euclidean space) and subjected to an incident plane harmonic wave. Using the representation theorem for the tangential component of the electric field the related boundary-value problem is formulated as a matrix Wiener-Hopf equation that is solved through Khrapkov method. High frequency asymptotics for the scattered fields in the wave zone of the strip and in the strip tips vicinity are expressed in a closed form that is computationally effective. Application that uses obtained formulae allows computing the scattered field in computationally effective manner.

Streszczenie. Cienkie włączenie opornika znajduje się w jednorodnym ośrodku w dwuwymiarowej przestrzeni Euklidesowej i jest poddane działaniu padającej płaskiej fali harmonicznej. Odpowiednie zagadnienie brzegowe jest sprowadzone do macierzowego równania Wienera-Hopfa, które jest rozwiązane przy użyciu metody Khrapkova. Rozwiązanie dla rozproszonego pola w strefie falowej włączenia oraz w okolicy końców włączenia dla zakresu wysokich częstotliwości przedstawione jest w postaci analitycznej. Aplikacja wykorzystująca uzyskane wzory pozwala obliczyć rozproszone pole w sposób wydajny obliczeniowo. (Efektywne obliczanie rozpraszania płaskich fa o wysokiej częstotliwości przez taśmę przewodzącą.)

Keywords: effective computation technique, thin walled inclusion

Słowa kluczowe: metoda wydajna obliczeniowo, cienkoscienne włączenie

Introduction

When studying wave propagation in inhomogeneous media consisting of thin-walled layers, one comes across the problem of replacement of boundary conditions and equations for thin-walled inhomogeneity by appropriate approximate conditions. The general purpose of the approximate boundary conditions, usually referred to as an effective boundary conditions or imperfect interface conditions, is to simplify the numerical solution of wave scattering problem involving complex structures by, e.g., converting a two media problem into a single media problem. Approximate boundary and interface conditions have been widely used in problems of wave propagation and diffraction in acoustics, electromagnetics, and elastodynamics [1-8].

Using effective boundary conditions for the tangential component of the electric field, the original boundary-value problem for resistive strip is formulated as a matrix Wiener-Hopf equation that is solved through Khrapkov method. High frequency asymptotic for the scattered fields in the wave zone of the strip and in the strip tips vicinity are expressed in a closed form that is computationally effective.

Application that uses obtained formulae is also presented.

Problem formulation

Let us consider a uniform medium in which there is an electrically resistive strip. The inhomogeneity occupies the region $S = \{|x_1| < a, |x_3| < h/2, |x_2| < \infty$, where h is the thickness, (x_1, x_2, x_3) are the Cartesian coordinates and the quantity $\varepsilon = h/a$ is the small parameter. A plane, incident wave of the form

$$(1) \quad u^i(\mathbf{x}) = A_0 \exp[ik(l_1 x_1 + l_3 x_3)]$$

impinges on the inclusion (the time factor of the form $e^{-i\omega t}$ is omitted throughout the analysis). Here

$$\mathbf{l} = (\sin \theta_0, -\cos \theta_0)$$

is the direction of wave propagation, k is the propagation constant with $\text{Im}k > 0$ and typical wavelength kh satisfies the condition $kh \ll 1$.

The total wave $u = u^i + u^s$ is decomposed into the given incident wave u^i and the unknown scattered wave u^s , which is required to satisfy the Sommerfeld radiation condition

$$(2) \quad u^s(\mathbf{x}) = \frac{e^{ik|\mathbf{x}|+i\pi/4}}{\sqrt{8\pi k|\mathbf{x}|}} f(\omega; \mathbf{l}, \nu),$$

$$\mathbf{x} = (x_1, x_3), |\mathbf{x}| \rightarrow \infty,$$

where $f(\omega; \mathbf{l}, \nu)$ is the complex amplitude or far-field pattern of the scattering wave, $\nu = \mathbf{x}/|\mathbf{x}| = (\sin \theta, \cos \theta)$ is the direction of observation, ω is the circular frequency.

The scattering problem of time harmonic waves is described by the wave equations

$$(3) \quad (\Delta + k^2)u(\mathbf{x}) = 0, \mathbf{x} \in R^2 \setminus S,$$

$$(\Delta + k_0^2)u^0(\mathbf{x}) = 0, \mathbf{x} \in S,$$

and the following conditions along the boundary S of the inhomogeneity:

$$(4) \quad u(\mathbf{x}) = u^0(\mathbf{x}), \frac{\partial u(\mathbf{x})}{\partial \mathbf{n}} = \gamma_0 \frac{\partial u^0(\mathbf{x})}{\partial \mathbf{n}},$$

$$x \in \partial S \setminus \left\{ x_3 = -\frac{h}{2} \right\},$$

$$u(\mathbf{x}) = u^0(\mathbf{x}) = 0, x_3 = -h/2,$$

where \mathbf{n} denotes the outer normal direction, $0 \leq |\gamma_0| \leq \infty$.

Our objective is to find the numerical and asymptotic representations of the solution to the problem (1)-(4) for the small but nonvanishing ε and at high values of the dimensionless wave number $x = ka$.

As follows from results obtained previously in [3, 4], the field $u(x)$ satisfies in the domain $R^2 \setminus S$ the wave equation and the following effective boundary conditions on the interval $|x_1| < a$

$$(5) \quad u^+(x_1) = 2Zk^{-1} \frac{\partial u^+(x_1)}{\partial x_3}, u^-(x_1) = 0,$$

$$Z = x \frac{\varepsilon}{2} \gamma_0^{-1}, \quad u^\pm = \lim_{\varepsilon \rightarrow 0} u(x_1, \pm \varepsilon),$$

which describes, asymptotically exactly up to terms of $O(\varepsilon)$, the solution to the problem (3) and (4). Here Z is the normalized impedance of the material relative to the intrinsic impedance of the external medium. The major benefit of approach (5), as compared to the use of an exact solution, would be that no solution $u^0(x)$ in the domain S is needed at all.

From Green's theorem for $x \in R \setminus S$ we obtain that the scattering field can be described in the form (6)

$$u^s(x) = \int_{-a}^a \left[kg(x, y) \Phi_1(y_1) - \Phi_3(y_1) \frac{\partial g(x, y)}{\partial y_3} \right]_{y_3=0} dy_1,$$

$$g(x, y) = -\frac{i}{4} H_0^{(1)}(k|x-y|),$$

$$k\Phi_1(x_1) = \left[\frac{\partial u^+(x)}{\partial x_3} - \frac{\partial u^-(x)}{\partial x_3} \right]_{x_3=0},$$

$$\Phi_3(x_1) = u^+(x_1) - u^-(x_1) = u^+(x_1).$$

Here $H_0^{(1)}$ is the Hankel function of the first kind.

As a middle surface of the scatterer is a plane, let us use the expansion of fundamental solution of the Helmholtz equation (cylindrical wave) $g(x, y)$ via plane waves. This will allow to deal with symbols of corresponding pseudo-differential operators only. As a result the following singular integral equations for $\Phi_\beta(x_1)$, $\beta = 1, 3$ are obtained from Eqs. (1), (3), (5) and (6)

$$(7) \quad \Phi_1(x_1) + \frac{k}{Z} \int_{-a}^a \Phi_1(p) K_3(k|x_1-p|) dp - k \int_{-a}^a \Phi_3(p) K_1(k|x_1-p|) dp = q_1 \exp(ikl_1 x_1),$$

$$\Phi_3(x_1) + k \int_{-a}^a \Phi_1(p) K_3(k|x_1-p|) dp = q_3 \exp(ikl_1 x_1),$$

$$|x_1| < a, \quad K_1(|z|) = \frac{1}{2\pi} \int_{\Gamma} \gamma(\alpha) e^{\pm i\alpha z} d\alpha,$$

$$K_3(|z|) = \frac{1}{2\pi} \int_{\Gamma} \gamma^{-1}(\alpha) e^{\pm i\alpha z} d\alpha,$$

$$q_1 = A_0 \left(2il_3 + \frac{2}{Z} \right), \quad q_3 = 2A_0, \quad \gamma = \sqrt{\alpha^2 - 1}.$$

Herein the contour Γ coincides with the real axis everywhere except for the branching points $\alpha = \pm 1$ and passes these points below in the right-hand half-plane of complex variable α and above in the left-hand one according to the limiting absorption principle and the point $\alpha = 0$ is situated below the contour Γ , as shown in Fig.1a. The square root function $\gamma(\alpha)$ is defined by the condition $\text{Im}\sqrt{\alpha^2 - 1} < 0$ for $|\alpha| < 1$.

Analysis

The principal terms of the asymptotic expansion (as $x = ka \gg 1$) of the solution to the equations (7) we represented in the form

$$(8) \quad \Phi_\beta(x_1) = \Phi_\beta^+(x_1) + \Phi_\beta^-(x_1) - \vartheta_\beta(x_1), \quad |x_1| < a, \quad \beta = 1, 3,$$

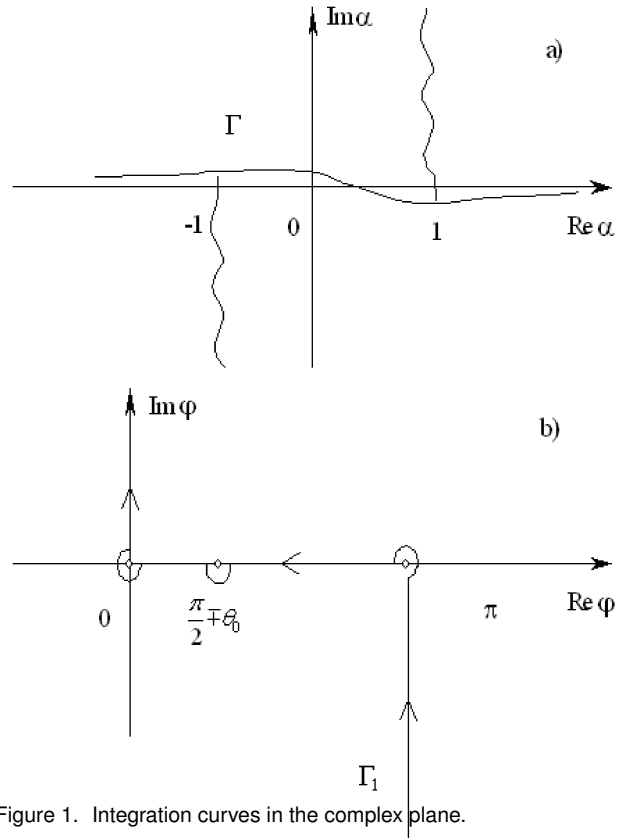


Figure 1. Integration curves in the complex plane.

where the functions $\Phi_\beta^\pm(\eta) = \Phi_\beta(\mp a \pm \eta k^{-1}) \exp(\pm ixl_1)$ satisfy the corresponding convolution-type equations:

$$(9) \quad \Phi_1^\pm(\eta) + \frac{1}{Z} \int_0^\infty \Phi_1^\pm(\zeta) K_3(|\eta - \zeta|) d\zeta - \int_0^\infty \Phi_3^\pm(\zeta) K_1(|\eta - \zeta|) d\zeta = q_1 \exp(\pm i\eta l_1), \quad 0 < \eta < \infty,$$

$$\Phi_3^\pm(\eta) + \int_0^\infty \Phi_1^\pm(\zeta) K_3(|\eta - \zeta|) d\zeta = q_3 \exp(\pm i\eta l_1),$$

$$\vartheta_\beta(\eta) = \Phi_\beta(\eta k^{-1}), \quad \vartheta_\beta(\eta) = W_\beta \exp(i\eta l_1),$$

$$W_1 = -A_0 \frac{2il_3}{1 - 2il_3 Z}, \quad W_3 = -A_0 \frac{4il_3 Z}{1 - 2il_3 Z}.$$

The Fourier transform

$$\phi_\beta^\pm(\alpha) = \int_0^\infty \Phi_\beta^\pm(\eta) \exp(i\alpha\eta) d\eta,$$

$$Y_\beta^-(\alpha) = \int_{-\infty}^0 \Phi_\beta^\pm(\eta) \exp(i\alpha\eta) d\eta$$

can be employed to reduce the integral equations (9) to a matrix Wiener-Hopf equation

$$(10) \quad \mathbf{G}(\alpha) \begin{pmatrix} \phi_1^\pm(\alpha) \\ \phi_3^\pm(\alpha) \end{pmatrix} = \frac{i}{\alpha \pm l_1} \begin{pmatrix} q_1 \\ q_3 \end{pmatrix} + \begin{pmatrix} Y_1^-(\alpha) \\ Y_3^-(\alpha) \end{pmatrix},$$

$$\alpha \in \Gamma, \quad \mathbf{G}(\alpha) = \begin{pmatrix} g(\alpha) & -\gamma \\ \gamma^{-1} & 1 \end{pmatrix}, \quad g(\alpha) = 1 + \frac{1}{Z\gamma(\alpha)}.$$

In order to obtain a unique solution of (10) it is necessary to take into account the following edge conditions [4]

$$(11) \quad u^s(r, \phi) = a_0^\mp(\omega) + a_1^\mp(\omega)r^{1/4} \left(\cos \frac{\phi}{4} + \sin \frac{\phi}{4} \right) + o(r^{1/4}),$$

$$-\pi \leq \phi \leq \pi, \quad r \rightarrow 0, \quad \gamma_0 = o(\varepsilon), \quad \varepsilon \rightarrow 0,$$

$$(12) \quad u^s(r, \phi) = b_0^\mp(\omega) + b_1^\mp(\omega)r^{1/2} \cos \frac{\phi}{2} + o(r^{1/2}),$$

$$-\pi \leq \phi \leq \pi, \quad r \rightarrow 0, \quad \gamma_0 = O(1), \quad \gamma_0^{-1} = o(\varepsilon), \quad \varepsilon \rightarrow 0,$$

where the minus and plus sign indicates the right and left inclusion end, respectively; r is the distance from the inclusion tip and ϕ is the polar angle. The parameters describing the material properties of inclusion and load, are entered in the quantities $a_0^\mp(\omega)$ and $b_1^\mp(\omega)$. The nature of the asymptotic of fields $u^s(r, \phi)$ is determined by relations between parameters γ_0 and ε .

Now, it can be shown easily that for $\varepsilon \rightarrow 0$

$$(13) \quad \phi_1^\pm(\alpha) = O(\alpha^{-1/4}), \quad \phi_3^\pm(\alpha) = O(\alpha^{-5/4}), \quad |\alpha| \rightarrow \infty,$$

$$\gamma_0 = O(\varepsilon),$$

$$(14) \quad \phi_1^\pm(\alpha) = O(\alpha^{-1/2}), \quad \phi_3^\pm(\alpha) = O(\alpha^{-3/2}), \quad |\alpha| \rightarrow \infty,$$

$$\gamma_0 = O(1), \quad \gamma_0 = O(\varepsilon^{-1}),$$

First at all we consider the case $\gamma_0 = 0(\varepsilon)$, $\varepsilon \rightarrow 0$. As is well known [9] the first step in the factorization procedure is to rearrange the kernel (10) into the Khrapkov form:

$$(15) \quad \mathbf{G}(\alpha) = \frac{1}{2}(1 + g(\alpha))\mathbf{I} + \frac{1}{\gamma(\alpha)}\mathbf{J}(\alpha),$$

$$\mathbf{J}(\alpha) = \begin{pmatrix} (2Z)^{-1} & -\gamma^2 \\ 1 & -(2Z)^{-1} \end{pmatrix}, \quad \mathbf{J}^2(\alpha) = -\gamma_1^2(\alpha)\mathbf{I}(\alpha),$$

$$\gamma_1(\alpha) = \sqrt{\alpha^2 - \xi^2}, \quad \xi^2 = 1 + \frac{1}{4Z^2},$$

where \mathbf{I} is the identity matrix. The matrix given by (15) is of a special form which can be factorized through the Khrapkov method. The result is

$$\mathbf{G}(\alpha) = \mathbf{G}_-(\alpha)\mathbf{G}_+(\alpha) = \mathbf{G}_+(\alpha)\mathbf{G}_-(\alpha),$$

$$(16) \quad \mathbf{G}_\pm(\alpha) = 2^{1/4}r_\pm^{1/2}(\alpha) \cos[\gamma_1(\alpha)\theta_\pm(\alpha)]\mathbf{I} +$$

$$+ 2^{1/4}r_\pm^{1/2}(\alpha) \frac{1}{\gamma_1(\alpha)} \sin[\gamma_1(\alpha)\theta_\pm(\alpha)]\mathbf{J}(\alpha),$$

where

$$r_+(\alpha)r_-(\alpha) = \frac{1}{2}(1 + g(\alpha)),$$

$$\theta_+(\alpha) + \theta_-(\alpha) = \frac{1}{\gamma_1(\alpha)} \tan^{-1} \left(\frac{\gamma_1(\alpha)}{\gamma(\alpha) + (2Z)^{-1}} \right).$$

Note that $\gamma_1(\alpha)$ has branch-points in both half-planes, but they are not present in $\mathbf{G}_\pm(\alpha)$ because the latter are in fact functions of the square of $\gamma_1(\alpha)$.

So, $\theta_\pm(\alpha)$ are found from the sum split formula:

$$\theta_\pm(\alpha) = \frac{\pm 1}{2\pi i} \int_\Gamma \frac{\tan^{-1}(\gamma_1(\zeta)/(\gamma(\zeta) + 1/2Z))}{\gamma_1(\zeta)(\zeta - \alpha)} d\zeta,$$

where $\pm\alpha$ lies above Γ and $r_\pm(\alpha)$ are founded from the product split formula:

$$r_\pm(\alpha) = \exp[\pm\chi_\pm(\alpha)],$$

$$\chi_\pm(\alpha) = \frac{1}{2\pi i} \int_\Gamma \frac{\ln \left(1 + \frac{1}{2Z\gamma(\zeta)} \right)}{\zeta \pm \alpha} d\zeta,$$

where α lies above (below) ζ for $\chi_+(\alpha)$ ($\chi_-(\alpha)$). Omitting all details it is found that

$$(17) \quad \chi_\pm(\alpha) = -\frac{1}{\pi} \int_0^\infty \tan^{-1} \left[\frac{1}{2Z\sqrt{1 + \tau^2}} \right] \frac{id\tau}{i\tau \pm \alpha} +$$

$$+ \frac{1}{\pi} \int_0^1 \tan^{-1} \left[\frac{1}{2Z\sqrt{1 - \sigma^2}} \right] \frac{d\sigma}{\sigma \pm \alpha},$$

$$\theta_-(\alpha) = \frac{i}{4\gamma_1(\alpha)} \ln \frac{(\alpha + \sqrt{\alpha^2 - \xi^2})(1 - \alpha)}{\alpha - \xi^2 + \sqrt{\xi^2 - 1}\sqrt{\xi^2 - \alpha^2}},$$

$$\theta_+(\alpha) = \theta_-(\alpha).$$

When we let $|\alpha| \rightarrow \infty$ in the upper half-plane, from (16) and (17) we have

$$(18) \quad \mathbf{G}_+(\alpha) \approx 2^{-3/4} \left[(\alpha^{1/4} + \alpha^{-1/4})\mathbf{I} + \right.$$

$$\left. + \frac{1}{i\alpha}(\alpha^{1/4} - \alpha^{-1/4})\tilde{\mathbf{J}}(\alpha) \right],$$

$$\mathbf{G}_+^{-1}(\alpha) \approx 2^{-5/4} \left[(\alpha^{1/4} + \alpha^{-1/4})\mathbf{I} - \right.$$

$$\left. - \frac{1}{i\alpha}(\alpha^{1/4} - \alpha^{-1/4})\tilde{\mathbf{J}}(\alpha) \right],$$

$$\tilde{\mathbf{J}}(\alpha) = \begin{pmatrix} 0 & -\alpha^2 \\ 1 & 0 \end{pmatrix}.$$

Since the factorization of the kernel matrix is now accomplished, (10) can be rearranged as

$$(19) \quad \mathbf{G}_+(\alpha) \begin{pmatrix} \phi_1^\pm \\ \phi_3^\pm \end{pmatrix} - \frac{i}{\alpha \pm l_1} \mathbf{G}_+^{-1}(\mp l_1) \begin{pmatrix} q_1 \\ q_3 \end{pmatrix} =$$

$$= \mathbf{G}_+^{-1}(\alpha) \begin{pmatrix} Y_1^- \\ Y_3^- \end{pmatrix} + \frac{i}{\alpha \pm l_1} [\mathbf{G}_+^{-1}(\alpha) - \mathbf{G}_+^{-1}(\mp l_1)] \begin{pmatrix} q_1 \\ q_3 \end{pmatrix}.$$

The left hand of (18) is regular in the lower half-plane. Hence, by analytic continuation principle they define an entire matrix-value function $\mathbf{C}(\alpha)$.

By taking into account the order relations (13) and (18) one concludes from Liouville's theorem that the $\mathbf{C}(\alpha)$ is a

constant matrix of the form $\mathbf{C}(\alpha) = \begin{pmatrix} c \\ 0 \end{pmatrix}$.

Thus, the solution of (19) reads

$$\begin{pmatrix} \phi_1^\pm \\ \phi_3^\pm \end{pmatrix}(\alpha) = \mathbf{G}_+^{-1}(\alpha) \begin{pmatrix} I_1^\pm(\alpha) + c \\ I_3^\pm(\alpha) \end{pmatrix},$$

with

$$\begin{bmatrix} I_1^\pm(\alpha) \\ I_3^\pm(\alpha) \end{bmatrix} = \frac{2^{-1/4}i}{(\alpha \pm l_1)r_\pm^{1/2}(\mp l_1)} \times$$

$$\times \begin{bmatrix} q_1 \left(\cosh \phi_0^\pm - \frac{\sinh \phi_0^\pm}{2Z\phi_1} \right) - q_3 l_3^2 \frac{\sinh \phi_0^\pm}{\phi_1} \\ -q_1 \frac{\sinh \phi_0^\pm}{\phi_1} + q_3 \left(\frac{\sinh \phi_0^\pm}{2Z\phi_1} + \cosh \phi_0^\pm \right) \end{bmatrix},$$

$$\phi_0^\pm = \theta_-(\mp l_1)\phi_1, \quad \phi_1 = \left(l_3^2 + \frac{1}{4Z^2} \right)^{1/2}.$$

The unknown constant c can be specified by taking into account the order relations in (13). By using (18), one obtains

$$\begin{pmatrix} \phi_1^\pm \\ \phi_3^\pm \end{pmatrix}(\alpha) \approx 2^{-5/4}(c - i\tilde{I}_3^\pm) \begin{pmatrix} \alpha^{1/4} \\ i\alpha^{-3/4} \end{pmatrix} + O \begin{pmatrix} \alpha^{-1/4} \\ \alpha^{-5/4} \end{pmatrix},$$

$$\tilde{I}_3^\pm = \lim_{\alpha \rightarrow \infty} \alpha I_3^\pm(\alpha).$$

The correct behavior of $\phi_{1,3}^\pm(\alpha)$ is recovered if we choose $c = i\tilde{I}_3^\pm$. So, the explicit expressions for $\phi_{1,3}^\pm(\alpha)$ read

$$(20) \quad \begin{aligned} \phi_1^\pm(\alpha) &= 2^{-1/4} r_+^{-1/2}(\alpha) \times \\ &\times \left\{ [I_1^\pm(\alpha) + i\tilde{I}_3^\pm] \left(\cos \gamma_1 \theta_+(\alpha) - \frac{\sin \gamma_1 \theta_+(\alpha)}{2Z\gamma_1(\alpha)} \right) + \right. \\ &\quad \left. + \frac{\gamma^2(\alpha)}{\gamma_1(\alpha)} I_3^\pm(\alpha) \sin \gamma_1 \theta_+(\alpha) \right\}, \\ \phi_3^\pm(\alpha) &= 2^{-1/4} r_+^{-1/2}(\alpha) \times \\ &\times \left\{ [-I_1^\pm(\alpha) + i\tilde{I}_3^\pm] \frac{1}{\gamma_1(\alpha)} \sin \gamma_1 \theta_+(\alpha) + \right. \\ &\quad \left. + I_3^\pm(\alpha) \left(\cos \gamma_1 \theta_+(\alpha) + \frac{\sin \gamma_1 \theta_+(\alpha)}{2Z\gamma_1(\alpha)} \right) \right\}. \end{aligned}$$

The integral representation of the function $\Phi_\beta^\pm(\eta)$ can be obtained by taking inverse Fourier transform of (20):

$$(21) \quad \begin{aligned} \Phi_\beta^\pm(\eta) &= \frac{1}{2\pi} \int_{\Gamma} e^{-i\eta\alpha} \phi_\beta^\pm(\alpha) d\alpha = \\ &= -\frac{1}{2\pi} \int_{\Gamma_1} e^{i\eta \cos \phi} \phi_\beta^\pm(-\cos \phi) \sin \phi d\phi, \end{aligned}$$

where Γ_1 is the new integration contour shown in Fig. 1b. The critical points of (20) can be classified as the pole ($\phi = \frac{\pi}{2} \mp \theta_0$) and the edge point ($\phi = 0$). When η is large, the main contribution to the integral (21) comes from these points. By taking into account the relations

$$(22) \quad \begin{aligned} r_-^{-1/2}(\alpha) \sin[\gamma_1 \theta_-(\alpha)] &= f_s(\alpha) [\gamma(\alpha) + (2Z)^{-1}]^{-1/2}, \\ f_s(\alpha) &= -ir_+^{1/2}(\alpha)(2\sqrt{\xi})^{-1}(\alpha+1)^{1/4} [f_+^{1/4}(\alpha) - f_-^{1/4}(\alpha)], \\ f_\pm(\alpha) &= \left(\alpha \pm i\sqrt{\xi^2 - \alpha^2} \right) \left(\xi^2 - \alpha \mp \frac{1}{2Z} \sqrt{\xi^2 - \alpha^2} \right) \end{aligned}$$

one concludes from (21) and (22) that

$$(23) \quad \begin{aligned} \Phi_1^\pm &= \nu_1(\pm\eta) + O(\eta^{-3/2}), \\ \Phi_3^\pm &= \nu_3(\pm\eta) + \sqrt{\frac{1}{2\pi\eta}} e^{i(\eta-\pi/4)} g_0^\pm(\eta) + O(\eta^{-3/2}), \\ g_0^\pm(\eta) &= 2^{-3/4} r_+^{1/2}(1)\xi^{-1/2} \left(1 - \frac{i}{2Z} \right)^{1/4} \times \end{aligned}$$

$$\times \left[i\tilde{I}_3^\pm + \frac{1}{1 \pm l_1} \left(\frac{\tilde{I}_3^\pm}{2Z} - \tilde{I}_1^\pm \right) \right] e^{i\frac{\eta}{8Z^2}} F \left(\sqrt{\frac{\eta}{8Z^2}} \right),$$

where

$$F(u) = \frac{e^{i\pi/4}}{\sqrt{\pi}} \int_u^\infty e^{-i\nu^2} d\nu$$

is the Fresnel integral.

On the basis of (8) and (23) we can then write approximately

$$(24) \quad \begin{aligned} \Phi_1(x_1) &\approx W_1 \exp(ikl_1 x_1), \\ \Phi_3(x_1) &\approx W_3 \exp(ikl_1 x_1) + \\ &+ \sum_{\pm} D^\pm \frac{e^{ik(\alpha \pm x_1)}}{(\alpha \pm x_1)^{1/2}} g_0^\pm[k(\alpha \pm x_1)], \\ D^\pm &= \sqrt{\frac{1}{2\pi k}} e^{-i\pi/4} e^{\mp i x l_1}. \end{aligned}$$

When η is small, from (20) and (21) we have

$$(25) \quad \begin{aligned} \Phi_3^\pm(\eta) &\approx 2^{-1/4} \tilde{I}_3^\pm \frac{1}{2\pi} \int_{\Gamma} \exp(-i\alpha\eta) \alpha^{-5/4} d\alpha + \Phi_3^0(\eta), \\ \Phi_3^0(\eta) &\approx -A_* \frac{i}{2\pi} \int_{\Gamma} \exp(-i\alpha\eta) \frac{\alpha^{-1/4}}{\alpha-1} d\alpha. \end{aligned}$$

The function $\Phi_3^0(\eta) = A_* e^{-i\eta}$, $\eta < 0$ corresponds to the incident rays, whose fields are the product of subsequent diffractions at two inclusions ends.

Since

$$\int_{\Gamma} \exp(-i\alpha\eta) \alpha^{-5/4} d\alpha = -\frac{4\pi}{\Gamma(1/4)} e^{i3\pi/8} \eta^{1/4},$$

where Γ is the Gamma function, the evaluation of integral (25) for $\eta \ll 1$ yields

$$(26) \quad \Phi_3^\pm(\eta) \approx -2 \frac{e^{i3\pi/8}}{\Gamma(1/4)} \eta^{1/4} \left(2^{-1/4} \tilde{I}_3^\pm - iA_* \right).$$

The latter shows that the function $\Phi_3^\pm(\eta)$ will be defined near inclusion ends if quantity A_* is determined.

>From (24) we observe that the primary diffracted fields decay as x^{-1} for $Z \neq \infty$ and as $x^{-1/2}$ for $Z = \infty$. On the basis of (26) we can then write approximately

$$(27) \quad \Phi_3^\pm(x_1) = -2 \frac{e^{i3\pi/8}}{\Gamma(1/4)} [k(\alpha \pm x_1)]^{1/4} \left(\frac{\tilde{I}_3^\pm}{\sqrt{2}} - iA_*^\pm \right) e^{\mp i x l_1},$$

$$A_*^\pm = (2a)^{-1/2} D^\mp e^{2ix} g_0^\mp(2x), \quad x_1 \rightarrow \mp a, \quad x \gg 1.$$

Finally, by combining equations (2), (6) and (23) and equations (27) and (11), we find

$$(28) \quad \begin{aligned} f(k; \mathbf{l}, \nu) &= -2 \frac{\sin[x(l_1 - \nu_1)]}{l_1 - \nu_1} (W_1 + i\nu_3 W_3) - \\ &- i\nu_3 \sqrt{\frac{2}{\pi}} \sum_{\pm} e^{\mp i x (l_1 - \nu_1)} \int_0^{\sqrt{2x}} e^{i\nu^2(1 \mp \nu_1)} g_0^\pm(\nu^2) d\nu, \end{aligned}$$

$$(29) \quad a_1^\pm(\omega) = -\frac{e^{i3\pi/8}}{\Gamma(1/4)} \left(\frac{k}{2} \right)^{1/4} \left(\tilde{I}_3^\pm - 2^{1/4} iA_*^\pm \right) e^{\mp i x l_1}.$$

The system integral equations (7) for the case $\gamma_0 = O(1)$, $\gamma_0^{-1} = o(\varepsilon)$ as $\varepsilon \rightarrow 0$ are susceptible to a treatment by iterations. The first order solutions may be expressed as follows

$$(30) \quad \Phi_1(x_1) = \Phi_1^{(0)}(x_1) + Z\Phi_1^{(1)}(x_1) + \dots,$$

$$\Phi_3(x_1) = Z\Phi_3^{(1)}(x_1) + \dots,$$

where functions $\Phi_\beta^{(i)}(x_1)$, $\beta = 1, 3$, $i = 0, 1$ satisfies the following equations

$$(31) \quad k \int_{-a}^a \Phi_1^{(i)}(p) K_3(k|x_1 - p|) dp = a_i, \quad i = 0, 1; \quad |x_1| < a,$$

$$\Phi_3^{(1)}(x_1) - 2il_3 \exp(ikl_1 x_1), \quad a_0 = q_3 \exp(ikl_1 x_1),$$

$$a_1 = -\Phi_3^{(0)}(x_1).$$

Applying the Wiener-Hopf technique to solving equation (31) we obtain

$$(32) \quad f(k; 1, \nu) = -2 \frac{\sin[x(l_1 - \nu_1)]}{l_1 - \nu_1} (W_1 + i\nu_3 W_3),$$

$$(33) \quad b_1^\pm = 2q_3 Z \sqrt{1 \mp i\pi k} (\pi k)^{1/2} e^{-i\pi/4} e^{\mp i x l_1}.$$

Consequently expressions (28) and (32) give the solution to the problem in the wave zone of a scatterer and equations (11) (29) and (33) describe the solution the outer problem near the ends of inhomogeneity. These solutions are valid at high frequencies where the wavelength is short compared with the inclusion width.

Numerical solution of the integral equations

In view of the edge condition we represent the solution of the integral equations (7) in the complete system of the Jacobi polynomials as

$$(34) \quad \Phi_\beta(x_1) = q_\beta (1 - p^2)^{\mu_\beta} \sum_{n=0}^{\infty} a_{n,\beta} P_n^{(\mu_\beta, \mu_\beta)}(p), \quad p = x_1/a,$$

where $P_n^{(\mu_\beta, \mu_\beta)}$ are the Jacobi polynomials and the peculiarity exponents μ_β are defined by the relations (11) and (12): $\mu_1 = -3/4$, $\mu_3 = 1/4$ for $\gamma_0 = O(\varepsilon)$ and $\mu_1 = -3/2$, $\mu_3 = 1/2$ for $\gamma_0 = o(\varepsilon^{-1})$ and $\gamma_0 = O(1)$.

>From the equations (7) and (34) we obtain an infinite system of linear algebraic equations for the unknown coefficients

$$(35) \quad \sum_{n=0}^{\infty} \left[a_{n,1} (A_{nm,1} + \frac{B_{nm,1}}{Zx}) - a_{n,3} q_0^{-1} B_{nm,2} \right] = b_m,$$

$$(36) \quad \sum_{n=0}^{\infty} \left[a_{n,3} A_{nm,3} + a_{n,1} \frac{q_0}{x} B_{nm,1} \right] = b_m,$$

$$m = 0, 1, 2, \dots,$$

$$B_{mn,\beta} = (m+1) \sum_{j=0}^{\infty} i^{m-j} (j+1) B_{nj}^\beta J_{m,j,\beta}, \quad q_0 = \frac{q_1}{q_3},$$

$$\beta = 1, 3, \quad B_{nj}^1 = \int_{-1}^1 (1-p^2)^{\mu_1} P_n^{(\mu_1, \mu_1)}(p) U_j(p) dp,$$

$$B_{nj}^3 = \int_{-1}^1 (1-p^2)^{\mu_3} P_n^{(\mu_3, \mu_3)}(p) U_j(p) dp,$$

$$A_{nm,1} = \int_{-1}^1 (1-p^2)^{\mu_1} P_n^{(\mu_1, \mu_1)}(p) U_m(p) dp,$$

$$A_{nm,3} = \int_{-1}^1 (1-p^2)^{\mu_3} P_n^{(\mu_3, \mu_3)}(p) U_m(p) dp,$$

$$I_{mn,1} = \frac{1}{2} \int_{\Gamma} \frac{1}{\gamma(\alpha)} J_{m+1}(x\alpha) J_{n+1}(x\alpha) \alpha^{-2} d\alpha,$$

$$I_{mn,3} = \frac{1}{2} \int_{\Gamma} \gamma(\alpha) J_{m+1}(x\alpha) J_{n+1}(x\alpha) \alpha^{-2} d\alpha,$$

$$b_m = \frac{\pi}{x l_1} i^m (m+1) J_{m+1}(x l_1),$$

where $U_m(p)$ are the Chebyshev polynomials of the second kind and $J_{m+1}(\alpha)$ are the Bessel cylindrical functions.

The scattering amplitude

$$(37) \quad f(\omega; 1, \nu) = - \int_{-l}^l [\Phi_1(p) + ik\nu_3 \Phi_3(p)] e^{-ik\nu_1 p} dp$$

taking into the relations (34) is directly connected with the coefficients $a_{m,\beta}$.

It is obvious that in numerical calculations the numbers m and n in the equations (34), (35) and (36) are limited and the quantities $B_{nm,\beta}$, ($\beta = 1, 3$ and consequently $a_{m,\beta}$ can be calculated with a sufficient accuracy by appropriate numerical procedures. Indeed, an accuracy of one percent is obtained if $m = n \approx 2x$.

Examples

In the Fig.2 the dimensionless total cross-section $\sigma^0 = \sigma(0)/2a$, where $\sigma(\theta_0) = \frac{1}{A_0 k} \text{Im} f(\omega; 1, 1)$, for incident angles $\theta_0 = 0$ and for $\gamma_0 = 0$ and $\gamma_0 = \infty$ is plotted as a function of x . As is seen in the Fig.2 the approximate solution is in excellent agreement with the exact solution for $x > 1$. Fig. 3 and 5 illustrate the monostatic radar cross section ($\text{RCS} = 20 \log [A_0^{-1} |f(\omega, 1, -1)|]$) as a function of incident angle for $x = 15$, $\gamma_0 = 0$ and $\gamma_0 = 0.02$ respectively. In view of the two RCS curves for resistive strip, the backscattering field is not affected by the impedance of the strip surface in directions closed to the normal incidence.

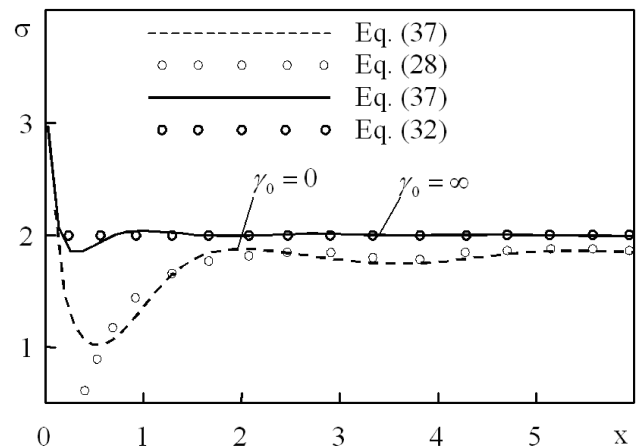


Figure 2. The normalized total cross-section versus dimensionless wave number $x = ka$ for normally incidence ($\theta_0 = 0$) wave.

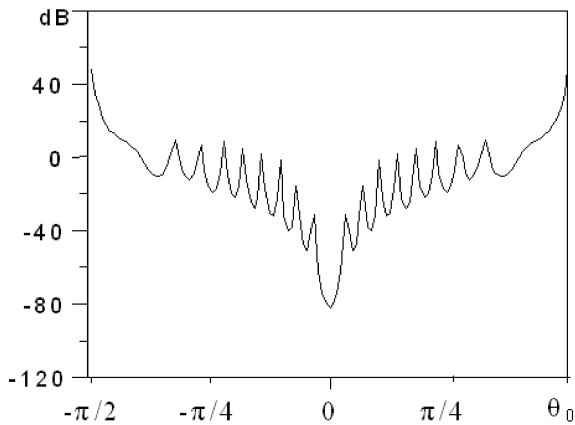


Figure 3. The monostatic radar cross section as a function of incident angle for $x = 15$ and $\gamma_0 = 0$.

Description of the application

In order to implement the algorithm based on analytical solution, Java language and Mathematica package were used. They were chosen so that the application could be available for a wide range of operating systems and computer hardware. Programs developed in Java can be run in any operating system that provides Java Virtual Machine (JVM), which in fact means any modern operating system. Mathematica package, which is leading software for advanced mathematical computations, is also available for a wide variety of systems.

The application performs computations in a number of steps. First, it starts the Mathematica kernel through a standard interface J/Link. Then it sends a request to load definitions of functions used in the algorithm implementation as well as numerical system coefficient tables. Subsequently it sends parameters fed by the user and a request to perform calculations and obtains their results from the kernel through J/Link. Finally, it closes the kernel.

The application allows obtaining a total scattering cross-section for a wave scattered from inclusion located in an elastic material. The following parameters: angle of observation, shear modulus and density of the inclusion as well as of the material are provided by the user.

The application generates charts of scattering cross-section related to dimensionless quantity x and monostatic radar cross section (RCS) as can be seen in Fig. 4.

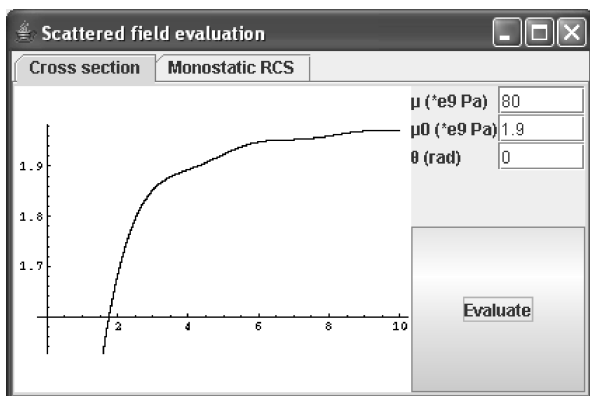


Figure 4. The monostatic radar cross section as a function of incident angle for $x = 15$ and $\gamma_0 = 0.02$

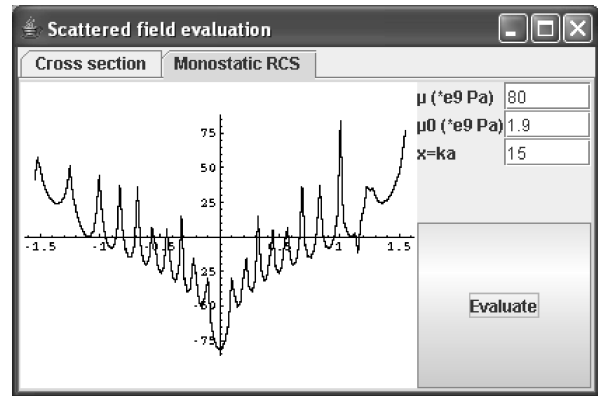


Figure 5. The normalized total cross-section versus dimensionless wave number $x = ka$ for normally incidence wave ($\theta_0 = 0$), $\gamma_0 = 0.02$

Conclusion

In this paper the high frequency asymptotic solution to the scattering problem of horizontally polarized waves on a plane, thin-walled, electrically resistive strip are given. The asymptotic solution to the problem is expressed in a closed form what is computationally effective.

The application that can be used as a tool in nondestructive testing of materials with thin plane inclusions is also presented. The application implements an algorithm based on analytical solution that is computationally effective and yields accurate results in the resonance region of the dimensionless wave numbers.

REFERENCES

- [1] Gökhan Çinar, Alinur Büyükaksoy, Diffraction of plane waves by an acoustically penetrable strip located between two soft/hard half-planes, *Z. Angew. Math. Mech.*, Vol. 83, No.6, 2003, Pages:384-396.
- [2] Alinur Büyükaksoy, Gökhan Çinar, Hamit Serbest, Scattering of plane waves by the junction of transmissive and soft-hard half-planes, *Z. Angew. Math. Mech.*, Vol. 55, 2004, Pages:483-499.
- [3] Ammari H, He. S. Effective impedance boundary conditions for an inhomogeneous thin layer on a curved metallic surface, *IEEE Trans. Antenn. Propag.*, Vol. 46, 1998, Pages:710-715.
- [4] Emets V. F., Kunets Ya. I., Matus V. V., Scattering of SH Waves by an elastic thin-walled rigidly supported inclusions, *Archive of Appl. Mech.*, Vol. 73, 2004, Pages:769-780.
- [5] Johansson G., Niklasson A. J., Approximate dynamic boundary conditions for a thin piezoelectric layer, *J. Solids Struct.*, Vol. 40, 2003, Pages:3477-3492.
- [6] Johansson G., Niklasson A.J., Approximate dynamic boundary conditions for a thin piezoelectric layer, *Intern. J. Solids and Structures*, Vol.40, 2003, Pages:3477-3492.
- [7] Niklasson A.J., Datta S.K., On the modeling of guided waves in plates with thin superconducting layers, *Thompson D.O., Chimenti D.E. (Eds.), Review of progress in quantitative NDE*, Vol. 19A, American Institute of Physics, New York, 2000, Pages:185-192.
- [8] Pan E., Datta S.K., Ultrasonic waves in multilayered superconducting plates, *Journal of Applied Physics*, Vol. 86, No.1, 1999, Pages:543-551.
- [9] Abrahams I. D., On the application of the Wiener-Hopf technique to problems in dynamic elasticity, *Wave Motion*, Vol. 36, 2002, Pages:311-333.

Authors: prof. Volodymyr Emets, mgr inż. Jan Rogowski, Politechnika Łódzka, Instytut Informatyki, ul. Wólczańska 215, 93-005 Łódź, email: (wfemets,jasiorog)@ics.p.lodz.pl

Fast orthogonal neural networks for 2D signal processing

Streszczenie. W pracy przedstawiono metodę konstrukcji szybkich ortogonalnych sieci neuronowych przeznaczonych do przetwarzania danych dwuwymiarowych. Jako podstawę konstrukcji schematu połączeń neuronalnych wykorzystano dwuetapowy algorytm szybkiej transformaty kosinusowej. Omówione zostały dwa warianty przetwarzania możliwe do realizacji w oparciu o zaproponowaną architekturę. Znaczące przyspieszenie procesu uczenia w stosunku do klasycznej liniowej sieci neuronowej zostało zademonstrowane na podstawie przeprowadzonych testów.

Abstract. The paper presents a method of constructing fast orthogonal neural networks suitable for two-dimensional data processing. The neural connection scheme is based on a two-stage fast cosine transform algorithm. Two processing variants applicable to the proposed architecture are discussed. A substantial acceleration of the learning process, as compared to a classical linear neural network, is demonstrated on the basis of the simulation experiments.

Słowa kluczowe: Szybkie ortogonalne sieci neuronowe

Keywords: Fast orthogonal neural networks

Introduction

Neural networks constitute a class of adaptive tools that have been successfully applied for many signal processing tasks such as filtering, signal compression, pattern recognition, parameter estimation and system identification [1]. One of the key elements influencing the effectiveness of neural networks application is their complexity expressed in the number of neural weights subjected to adaptation. This in turn is dependent on the architecture of connections between neurons in adjacent layers. The general approach to the construction of feed-forward networks assumes that every output of a layer is connected to every input of the next layer which yields the number of weights of the order of $O(N^2)$.

The concept of fast neural networks, first introduced in [2, 3], is based on utilizing a fast two-stage algorithm of an orthogonal transform in the process of a feed-forward multi-layer perceptron construction. The flow graph of the algorithm defines the neural connection scheme and its basic operations are converted to neurons. The neural network of this type may be based on any orthogonal transform for which a fast two-stage algorithm exists, e.g.: fast Fourier transform (FFT), fast cosine transform (FCT), fast sine transform (FST) or fast Hartley transform (FHT) [2, 4, 5, 6]. The substantial difference in comparison to a typical feed-forward neural network is that the factorization of the transform matrix obtained as a result of the fast algorithm construction process is reflected in the sparseness of the connections between adjacent layers. The complexity of the network, expressed in the number of weights, is therefore reduced from $O(N^2)$ to $O(N \log N)$.

A method of additional two-fold weights number reduction, exploring the orthogonality of basic operations of the underlying fast transform algorithm was presented in [7] and a special fast algorithm with tangent multipliers also made the four-fold reduction possible. A network constructed according to that approach is referred to as a fast orthogonal neural network (FONN) and the basic operations of the transform take the form of basic operation orthogonal neurons (BOONs) with two outputs orthogonal to each other. Apart from reducing the adaptation time, the introduction of BOONs considerably simplifies the error backpropagation and gradient computation process.

The recursive properties of the architecture of fast neural networks were used to derive alternative methods of adaptation in [8] and the application of FONN in the field of feature extraction and classification was presented in [9].

In this paper we investigate fast orthogonal neural networks designed for two-dimensional data processing. The general neural architecture is based on the rows-columns approach and the benefit resulting from the application of FONN is assessed in terms of the number of epochs and the training time. Two 2D-FCT, type II (2D-FCT2) algorithms have been applied as the basis of the neural network construction. The generality of the presented approach enables, however, to use it with other fast algorithms of orthogonal transforms for which the rows-columns approach is applicable. We also discuss the structure of the first stage of the transform with respect to the possibility of recursive teaching and dynamic adjustment of the final accuracy achieved by the network.

The aim of the work is to provide an adaptive tool for two-dimensional data, in particular image content, analysis. The necessity of performing data decorrelation and reducing the computational complexity is crucial in a great number of image processing tasks, including image enhancement, analysis, recognition and compression, and orthogonal transforms such as FFT or FCT are frequently used for this purpose. The possibility of replacing a standard FFT or FCT block with a fast orthogonal neural network may therefore increase flexibility and adaptation potential of many solutions applied in the image processing field.

Fast orthogonal neural network construction

The general architecture of a fast orthogonal neural network based on two-stage FCT, type II algorithm (FCT2) is presented in Fig. 1 and the description of the basic operations is given in Fig. 2. The symbols u , w denote the weights which are adapted during the network teaching process. The filled triangles correspond therefore to non-trivial basic operation orthogonal neurons (BOONs) as compared to trivial, i.e. non-adaptable operations applied in the first stage of the algorithm [7].

The network in Fig. 1 is capable of learning a class of linear transforms including N -point discrete cosine transform, type II given as [10]:

$$(1) \quad L_N^{II}(k) = \text{DCT}_N^{II}\{x_n\} = \sum_{n=0}^{N-1} x_n C_{4N}^{(2n+1)k},$$

where $n, k = 0, 1, \dots, N-1$; $C_K^r = \cos(2\pi r/K)$.

The inputs x_0, \dots, x_{N-1} must be decimated, i.e. supplied in a bit-reversed order and the outputs are obtained in natural order. The output of the network in Fig. 1 corresponding to $L_N^{II}(N/2)$ must be multiplied by a coefficient:

$$(2) \quad s = \frac{\sqrt{2}}{2}.$$

in order to yield the proper value defined by (1). The presented architecture can also be applied in a more efficient way in which the non-trivial basic operations contain the weight w only, while the weight u has a fixed value equal to one. In this case we do not use the coefficient (2) but every output $L_N^{II}(0), \dots, L_N^{II}(N-1)$ must be multiplied by a corresponding coefficient U_N^0, \dots, U_N^{N-1} defined by the following recursive formula:

$$(3) \quad \begin{aligned} U_N^0 &= 1, U_4^1 = \sqrt{2}/2 \cdot C_{16}^1, U_K^k = U_{K/2}^k C_{4K}^k, \\ U_K^{K/2-k} &= U_{K/2}^k C_{4K}^{K/2-k}, U_N^{N/2} = \sqrt{2}/2, \\ U_K^{K/4} &= \sqrt{2}/2 \cdot C_{4K}^{K/4}, K = 8, 16, \dots, N, \\ U_N^{N/2+k} &= U_N^{N/2-k}, U_N^{N-k} = U_N^k, \\ k &= 1, 2, \dots, K/4 - 1, \end{aligned}$$

This second variant of processing, enabling to reduce the number of weights by half, is based on a two-stage FCT2 algorithm with tangent multipliers (mFCT2) [7].

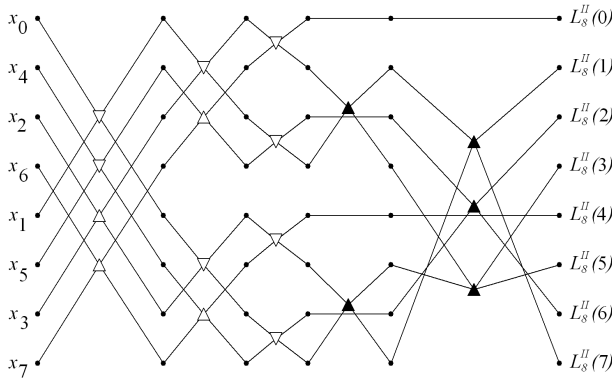


Figure 1. FCT2-based network architecture of size 8 (1D case)

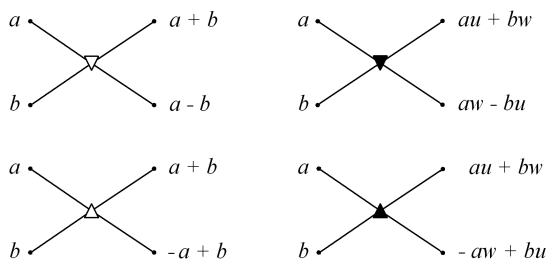


Figure 2. Basic operations of a fast orthogonal neural network

Both variants were shown to learn the one-dimensional FCT2 successfully [7] offering low computational complexity, also in comparison to fast neural networks with non-orthogonal neurons [2]. In the following section we will show

a method of extending the presented architecture in both processing variants to the 2D case.

Two-dimensional FONN architecture

In the two-dimensional case we need a neural network capable of learning the 2D FCT2 transform given as [10]:

$$(4) \quad \begin{aligned} L_{NM}^{II}(p, q) &= \text{DCT}_{NM}^{II}\{x_{n,m}\} = \\ &= \sum_{n=0}^{N-1} \sum_{m=0}^{M-1} x_{n,m} C_{4N}^{(2n+1)p} C_{4M}^{(2m+1)q}, \end{aligned}$$

where $n, p = 0, 1, \dots, N-1$; $m, q = 0, 1, \dots, M-1$.

In the following part we will assume that $N = M$, although the presented approach may be easily extended to data represented by rectangular matrices.

The neural architecture design is based on the fact that the two-dimensional FCT2 transform may be computed by performing the 1D FCT2 on every row of the input data followed by 1D FCT2 computation performed on every column. The first column of the 2D FCT2 output may be therefore computed with the network in Fig. 3.

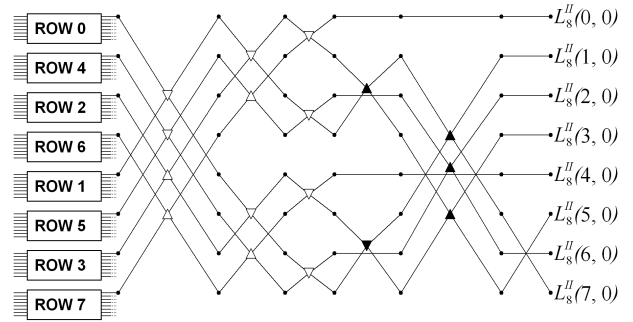


Figure 3. Two-dimensional FONN architecture (first column)

Each of the blocks on the left computes 1D FCT2 of a single row of the input and has the same architecture as the network performing the computation of the first column, constituting the main part of the figure. This network has a slightly different structure than the one presented in Fig. 1. Both structures are actually equivalent - the "more regular" structure in Fig. 3 requires to change the type of some basic operations in the second stage and performing an additional permutation P_N^i , $i = 0, 1, \dots, N-1$ of its outputs. The permutation P_N^i may be defined by the following recursive formulas:

$$(5) \quad \begin{aligned} P_2^0 &= 0, P_2^1 = 1, \\ P_{2K}^k &= P_K^k, P_{2K}^{K+k} = P_K^{K-k} + K, \\ P_{2K}^0 &= 0, P_{2K}^K = K, \\ k &= 1, 2, \dots, K-1, \\ K &= 2, 4, 8, \dots, N/2. \end{aligned}$$

It should be noted, that the row blocks are arranged in a bit-reversed order, similar to single inputs in Fig. 1 and the outputs are in a natural order.

The remaining columns are computed in the same way, which may be reflected by duplicating the column part of the network presented in Fig. 3 for every output of the row blocks. It is also worth noting that the linearity of the row blocks enables to move them into the middle of the column part of the network. As a result of these operations we obtain the final 2D neural network shown in Fig. 4.

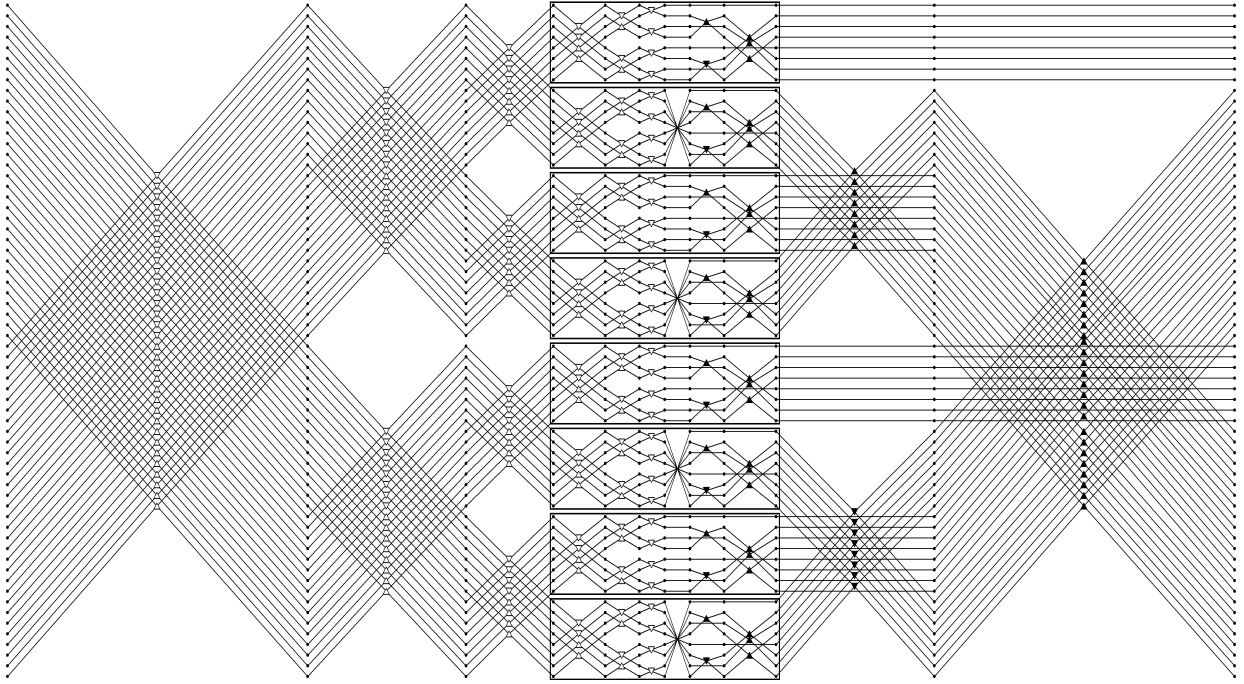


Figure 4. Complete two-dimensional FONN architecture of size 8x8

The row blocks, marked by rectangular frames, are now placed in the central part of the network which enables to divide it again into two stages - non-adaptable and adaptable, similarly to a 1D case (Fig. 1). Moreover, the structure of the first, non-adaptable stage of the 2D network of size $N \times N$ is identical to the first stage of a 1D network of size $N \cdot N$. A closer examination reveals that simply duplicating the column part in Fig. 3 leads to a deviation of the first stage structure from the one-dimensional layout which may be corrected by inverting the outputs order of the trivial part of every second row block, as may be seen in Fig. 4.

The inputs of the network presented in Fig. 4 are decimated both row and column-wise so the required input sequence is obtained by concatenating the rows of the decimated array $[x_{D_i, D_j}]$, where $i, j = 0, 1, \dots, N-1$ and where D_i denotes a vector of bit-inversed indexes from the range $\{0, 1, \dots, N-1\}$.

The output vector of the network is a concatenation of the rows of the following array:

$$\begin{bmatrix} L_{NN}^{II}(P_N^0, P_N^0) & \cdots & L_{NN}^{II}(P_N^0, P_N^{N-1}) \\ L_{NN}^{II}(P_N^1, P_N^0) & \cdots & L_{NN}^{II}(P_N^1, P_N^{N-1}) \\ \vdots & \ddots & \vdots \\ L_{NN}^{II}(P_N^{N-1}, P_N^0) & \cdots & L_{NN}^{II}(P_N^{N-1}, P_N^{N-1}) \end{bmatrix},$$

where P_N^i is the permutation defined by (5).

In the first processing variant, involving the adaptation of both weights u and w per each non-trivial basic operation, the network outputs corresponding to 2D FCT2 elements: $L_{NN}^{II}(0, N/2)$, $L_{NN}^{II}(N/2, 0)$ and $L_{NN}^{II}(N/2, N/2)$ should be multiplied by s , s and s^2 (2) accordingly.

In the second variant the non-trivial basic operations represented by up-pointing triangles have the coefficient u set to one and excluded from adaptation. The remaining non-trivial operations have, conversely, the coefficient w fixed so that only the weight u gets adapted. In this variant each output $L_{NN}^{II}(p, q)$ is obtained by multiplying the corresponding

network output by a coefficient:

$$(6) \quad U_{NN}^{(p,q)} = U_N^p \cdot U_N^q,$$

where U_N^p, U_N^q are defined in (3).

The obtained neural architecture, presented in Fig. 4, is capable of learning the 2D FCT2 transform of size $N \times N$ with arbitrary accuracy which will be verified in the next section. It is worth mentioning that the second stage of the network may be extended to the form similar to the case of 1D network performing the 1D FCT2 of size $N \cdot N$, as we have done for the first stage. This would, however, imply an addition of some extra BOONs to the column part of the second stage which would widen the class of possible linear transforms at the expense of slowing down the learning process. The number of BOONs in the presented architecture for $N \times N$ input is equal to:

$$(7) \quad B = N^2 (\log_2 N - 2) + 2N.$$

It should be noted that it is also possible to use the presented architecture to construct a fast orthogonal neural network performing fast Fourier transform (2D FFT) or fast Hartley transform (2D FHT) by adding some simple input and output blocks [2].

Simulation results and discussion

The network constructed in the previous section has been implemented and its learning capabilities have been compared to a simple linear neural network with an unbiased, densely connected layer [1, 11]. It should be noted that the difference between both kinds of neural networks corresponds to a difference between the fast cosine transform (FCT2) and the direct discrete cosine transform (DCT2). The inputs for the networks comprised square matrices of sizes 8x8, 16x16, 32x32, 64x64, initialized with random values. The experiments involved supervised learning for which the targets have been computed with the direct formula (4).

All the tests were performed on an experimental platform designed for implementation and teaching of both fast orthog-

onal networks and classical dense feedforward neural networks. The conjugate gradient algorithm has been chosen for teaching the networks, mainly due to its good scalability for problems involving a big number of the adapted weights. For the directional minimization we applied an algorithm based on the third order polynomial approximation of the error function described in [1].

Table 1 presents the results of the adaptation process, performed on a computer with Intel Celeron M, 1.40 GHz processor, for the dense linear network (DCT2), the first variant of fast orthogonal network (FCT2) and the second variant based on the algorithm with tangent multipliers (mFCT2). In all the cases the adaptation was stopped after reaching the error value less than 10^{-9} . Each test was repeated at least ten times and the table shows the mean values. The value P denotes the number of input/target matrices of size $N \times N$.

Table 1. The results of the adaptation

| NxN | | 8x8 | 16x16 | 32x32 | 64x64 |
|---------------|-------|-------|-------|---------|-------|
| P | | 32 | 128 | 512 | 512 |
| Mean epochs | DCT2 | 96.2 | 163.7 | >300 | n/a |
| | FCT2 | 53 | 77.8 | 129.5 | 220.3 |
| | mFCT2 | 26.37 | 26.7 | 30.2 | 35.8 |
| Mean time [s] | DCT2 | 0.71 | 90.2 | >1 hour | n/a |
| | FCT2 | 0.081 | 2.85 | 90.47 | 868.7 |
| | mFCT2 | 0.05 | 1.13 | 30.94 | 188.3 |

It may be observed that the dense neural network (DCT2) is highly inefficient for greater sizes of input data. On the other hand, the fast orthogonal network offers a reasonable computation time, especially in the case of the mFCT2 variant which mainly results from the dramatic weights number reduction introduced by the proposed architecture (Table 2). The achieved results mean that we need as little as three minutes for the teaching process based on 512 images of size 64x64, which may be a sufficient resolution for image content analysis and recognition tasks.

Table 2. The number of the adapted weights

| NxN | 8x8 | 16x16 | 32x32 | 64x64 |
|-------|------|-------|---------|----------|
| P | 32 | 128 | 512 | 512 |
| DCT2 | 4096 | 65536 | 1048576 | 16777216 |
| FCT2 | 160 | 1088 | 6272 | 33024 |
| mFCT2 | 80 | 544 | 3136 | 16512 |

Moreover, the two-stage architecture of the network and the special structure of the first stage enable to apply the approach known from [8] to recursively add and adapt consecutive blocks leading to a gradual enhancement of the input data resolution. This may further decrease the computational time and it would be possible to use the achieved accuracy to dynamically decide on the addition of the next blocks and the continuation of the learning process.

Conclusion and future works

The architecture of a fast orthogonal neural network suitable for two-dimensional data processing has been presented. The constructed network is capable of learning the fast cosine transform and may also be applied as a basis for fast orthogonal networks performing other orthogonal transforms such as FFT or FHT. The construction process has been described step by step starting from the one-

dimensional approach and rows-columns method and the resulting structure has been transformed to the form of a two-stage network. Two variants of application of the proposed architecture have been presented.

The results achieved by the proposed network show its definite superiority over a classical linear neural network, basically due to the dramatic reduction of the number of the adapted neural weights. The obtained time complexity is sufficiently low to justify a conclusion that the presented fast orthogonal neural network may appear suitable for direct raw image data analysis. The application possibilities in the field of image recognition and classification will be the subject of future works. Our research will also concentrate on the possibility, sketched in the discussion, to apply a dynamic recursive approach to the two-dimensional fast orthogonal neural network construction process.

LITERATURA

- [1] Osowski S., Neural networks for information processing. (in Polish) OWPW, Warsaw (2000)
- [2] Szczepaniak P.S., Intelligent computations, fast transforms and classifiers. (in Polish) EXIT Academic Publishing House, Warsaw (2004)
- [3] Jacymirski M., Szczepaniak P.S., Neural realization of fast linear filters. In: Proc. of the 4th EURASIP - IEEE Region 8 International Symposium on Video/Image Processing and Multimedia Communications. (2002) pp. 153-157
- [4] Bracewell R.N., The Hartley Transform, Oxford University Press, New York (1986)
- [5] Ahmed N., Natarajan T., Rao K., Discrete Cosine Transform IEEE Trans. Computers, 23, no. 1, (1974) pp. 90-93
- [6] Wang Z., Fast algorithms for the discrete W transform and for the discrete Fourier transform. IEEE Trans. on Acoustics, Speech, and Signal Processing 32 (1984) pp. 803-816
- [7] Stasiak B., Yatsymirskyy M., Fast orthogonal neural networks. Lecture Notes in Artificial Intelligence No. 4029. Artificial Intelligence and Soft Computing ICAISC 2006, Springer Verlag 2006, ISSN 0302-9743, ISBN 3-540-35748-3, pp. 142-149
- [8] Stasiak B., Yatsymirskyy M., Recursive Learning of Fast Orthogonal Neural Networks. In: Proc. Of International Conference on Signals and Electronic Systems ICSES06, pp. 653-656
- [9] Stasiak B., Yatsymirskyy M., On Feature Extraction Capabilities of Fast Orthogonal Neural Networks. Lecture Notes in Computer Science, No. 4432, ISBN 3-540-71590-8, Springer Verlag 2007, pp. 27-36
- [10] Rao K.R., Yip P., Discrete cosine transform. Academic Press, San Diego (1990)
- [11] Rutkowski L., Methods and techniques of artificial intelligence. (in Polish) Polish Scientific Publishers PWN (2005)

Autorzy: mgr inż. Bartłomiej Stasiak
email: basta@ics.p.lodz.pl
prof. dr hab. Mykhaylo Yatsymirskyy
email: jacym@ics.p.lodz.pl
Politechnika Łódzka
Instytut Informatyki
ul. Wólczńska 215,
93-005 Łódź, Poland

A Visibility Matrix determination using space subdivision methods for Diffuse Optical Tomography

Abstract. Analysis of the Visibility Matrix determination algorithm will be presented in this paper. Algorithm is compared with reference to two space subdivision schemes. The space that encloses considered objects is partitioned into regular or binary grid. The Visibility Matrix defines whether nodes of given object see each other. It results from process of detection whether along straight line between selected two nodes there is an empty space or another object is situated. Further sections describe in details space subdivision schemes, summary of the Visibility Matrix algorithm and the results for given objects (two spheres).

Streszczenie. W artykule zostanie przedstawiony algorytm tworzenia macierzy widoczności. Algorytm korzysta z dwóch metod podziału przestrzeni w zależności od których porównywana jest jego wydajność. Przestrzeń obejmująca rozpatrywany obiekt jest dzielona przy użyciu siatki regularnej lub binarnej. Macierz widoczności określa czy węzły danego obiektu widzą się i jest jedną z metod podnoszenia wydajności obliczeń w dyfuzyjnej tomografii optycznej. **Tworzenie macierzy widoczności dla dyfuzyjnej tomografii optycznej z użyciem technik podziału przestrzeni.**

Keywords: Diffuse Optical Tomography, Visibility Matrix, regular and binary space partitioning.

Słowa kluczowe: Dyfuzyjna Tomografia Optyczna, macierz widoczności, regularny i binarny podział przestrzeni.

Introduction

In recent years a great progress has been made with optical tomography applied to medicine [1] [2]. However algorithms used in optical tomography are marked by high computational complexity. There is a number of ways to reduce computational cost and one of them is using a Visibility Matrix [3]. A Visibility matrix determines whether along straight line between any pairs of objects nodes there is no concealing them elements. As an objects we understand two spheres (one includes another). These spheres are treated as extremely simplified model of infant's head. In particular there are modeled two layers filled with cerebrospinal fluid.

Space partitioning

There are two popular space partition schemes: constant size voxel partitioning [4] and binary space partitioning [6]. The first scheme has an advantage of fast traversing the grid. Moving to another voxels placed along the ray is relatively cheap. In the second case the space subdivision is adjusted to the shape of the objects. This adaptive partitioning makes possible efficient data storage in computer memory and takes advantage of limiting the overall amount of voxels.

The regular grid partitioning is marked by constant resolution in the whole space (even in empty not occupied by objects edges places). The binary subdivision scheme increases grid density in places taken up by objects edges and decreases in the hollow space. The Visibility Matrix algorithm was described in details in [3]

The regular grid space partitioning

Using regular grid we obtain constant size voxel partitioning. The space is evenly divided in three axes (directions) regardless of the shape of objects (Fig. 1). The traversal algorithm takes advantage of this homogeneous division and allows for very fast moving across voxels along the ray. If we have information about the size of all voxels in the space we can easily calculate the parameters for the ray remaining in given voxel. It is crucial to the regular grid traversal algorithm [4].

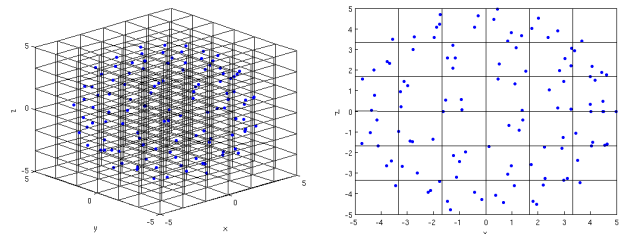


Figure 1. Regular grid including two spheres as a cloud of nodes.

The binary grid space subdivision

The main reason to use the binary subdivision is an automatic adaptation amount and size of voxels to the shape of the objects. The biggest voxels include empty space in contrast to the smallest ones which are concentrated on the objects surfaces. The space is recursively divided into smaller and smaller parts till we satisfy grid density condition (Fig. 2). The recursive division ensures effective storage in tree structure and fast memory searching thus efficient access to currently needed information about the grid. On account of fact that the space is divided automatically we don't know size of any voxel except for that in which we currently remain. This drawback implies necessity of use time-consuming voxel traversal algorithm [5].

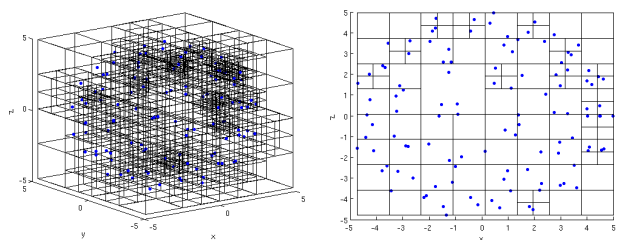


Figure 2. Binary grid including two spheres as cloud of nodes.

The Visibility Matrix algorithm comparison with regular and binary space partition scheme

Regardless of the space partition scheme the Visibility Matrix algorithm consists of following steps: space partitioning then attaching boundary elements to enveloping them voxels, moving across the grid along the ray from nodes of the external layer to another nodes of the same layer checking intersections if voxels are not empty, as above but now we consider external and internal layer, as above but with only internal layer, successive filling out the Visibility Matrix (during previous three steps).

As a result we obtain sparse matrix depicted in Fig. 3.

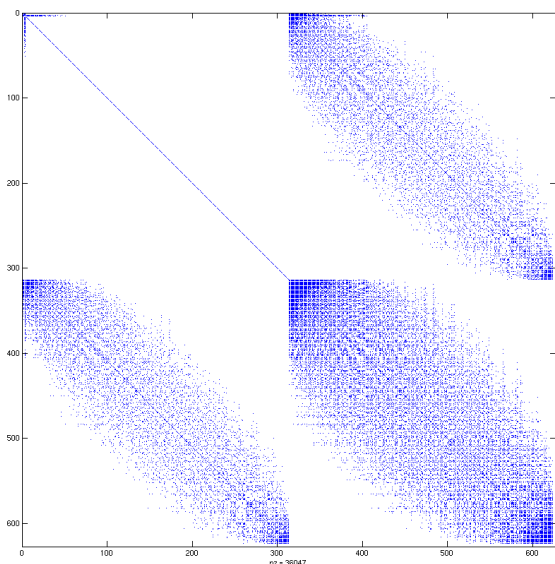


Figure 3. The Visibility Matrix of two spheres.

Presented algorithm reduces computational complexity from $O(n^3)$ to $O(n^2)$. However improvement of efficiency will be reached only if we properly choose resolution of the grid. Too high amount of voxels reflects waste of time during traversing the grid. In turn too low amount of voxels causes increase of collision detection tests.

The most important thing during building the Visibility Matrix is to strike a good traversing speed/grid complexity balance. The time of creation of the Visibility Matrix strongly depends on approved grid resolution as well as the partition scheme. Results for objects composed of 246, 626 and 3278 nodes are shown in the Table 1. The second row with "Brutal force" field includes results for the Visibility Matrix algorithm without space partitioning. We simply check ray intersections with all triangles of the scene for this case.

Table 1. Results

| Nodes number | | 246 | 626 | 3278 |
|------------------|--------------|-------|-------|----------|
| Partition scheme | brutal-force | 12,1s | 3m12s | 4h36m47s |
| | regular | 2,9s | 26,9s | 33m11,1s |
| | binary | 1,8s | 9,9s | 4m51,9s |

According to obtained results the use of binary grid will be more effective solution than constant size voxel partitioning, especially for objects combined of higher amount of nodes than those discussed in this paper.

The curves depicted in Fig. 4 are derived from interpolation of the obtained results. Additionally to enable algo-

gorithm comparison with respect to two kinds of space partitioning schemes, we've changed only functions responsible for space subdivision. The other parts of code remained the same all the time.

Conclusion

Regardless of the fact that the object's nodes can be either placed regularly or assembled in some region of the space, the Visibility Matrix algorithm should be based on binary space partitioning. This choice is justified by the lack of necessity of dividing empty, not "filled" by objects space. Thus we save resources during attaching boundary elements to the voxels procedure. Additionally the cost of traversing the binary grid is compensated by low amount of voxels in relation to dense regular grid. Our research group aims to utilize the Visibility Matrix algorithm with the binary space partitioning in Diffuse Optical Tomography in the future.

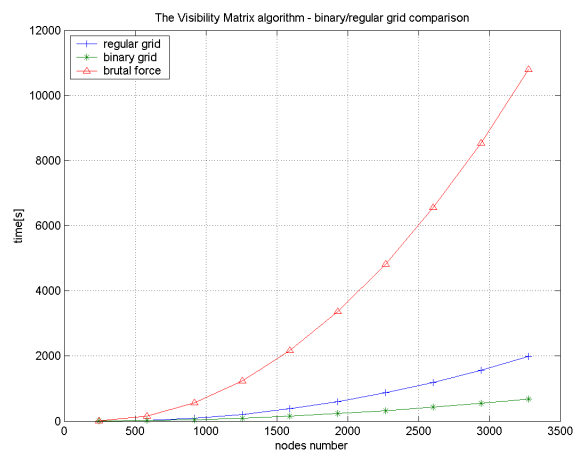


Figure 4. Time of creating the Visibility Matrix depending on the object's complexity.

REFERENCES

- [1] Arridge S.R. Optical tomography in medical imaging, *Inverse Problems*, 15(2), 1999, R41-R93.
- [2] Arridge S.R., Sikora J., Sokołowski J., Sensitivity analysis for light propagation in diffusive media with non-scattering regions using 3D-BEM, *International Workshop on Shape optimization in life sciences and environment*, Toulouse, March 2004.
- [3] Grzywacz T., Gruca J., Sikora J. Efficient Algorithm of Visibility Matrix Determination for Diffusive Optical Tomography, *AMTEE05 Proc.*, Vol. II, Sep 2005, Pages: 15 - 110.
- [4] Woo A., Amanatides J. A Fast Voxel Traversal Algorithm for Ray Tracing, *Eurographics 87*, Aug 1987, Pages: 3 - 10.
- [5] Glassner A.S. Space Subdivision for Fast Ray Tracing, *IEEE Computer Graphics and Applications*, 4(10), May 1987, Pages: 15 - 22.
- [6] BSP Trees, <http://www.gamedev.net/reference/articles/article657.asp>

Autor: Mgr inż. Tomasz Grzywacz
 Politechnika Warszawska
 Wydział Elektryczny
 Instytut Elektrotechniki Teoretycznej i Systemów
 Informacyjno-Pomiarowych
 ul. Koszykowa 75
 00-662 Warszawa
 email: tgrzywacz@iem.pw.edu.pl

Experimental validation of diagnostic symptoms for technical state estimation of several units of rotary electric-power machines

Abstract. Were validated some of diagnostic symptoms for technical state estimation of several units of rotary electric-power machines on basis of the probabilistic analysis results of physical vibration processes and of speed rotation nonuniformity for these machines. Using the statistical diagnostic model IBC was experimentally validated qualitative and quantitative estimations of diagnostic symptoms, received as a result of spectrum-correlation and histogram analysis of some diagnostic signals.

Streszczenie. Praca przedstawia metody walidacji cech diagnostycznych użytecznych w diagnostyce (ocenie stanu technicznego) części maszyn elektrycznych używanych w energetyce. Diagnostyka dokonywana jest na podstawie analizy statystycznej fizycznych procesów wibracji i niejednorodnych zmian prędkości maszyny. Model diagnostyczny IBC opracowany na podstawie cech diagnostycznych został sprawdzony eksperymentalnie, a wyniki jakościowe i ilościowe diagnostyki porównane dla wybranej grupy sygnałów diagnostycznych. (Eksperymentalna walidacja cech diagnostycznych użytecznych w oceniastanu technicznego części maszyn elektrycznych)

Keywords: electric power machine, diagnostic system, statistical signal analyzer.

Słowa kluczowe: maszyna elektryczna, system diagnostyczny, analiza statystyczna sygnałów.

Introduction

Stochastic periodicity (rhythmicity, cyclicity) resides in informational signals which accompany electric power machines functioning. This periodicity is caused by the rotor rotation which is a component of the electric power machine. Mathematical models of linear periodical random processes (LPRP) are one of possible classes of random process which take into consideration this periodicity [1]. For the purpose of treatment and analysis of previously mentioned information signals, which can be represented in the form of angular observations, statistical methods have some distinguishing features. For example, when it is necessary to introduce the definition of a distribution function, characteristic function and of moments, which are consistent with the periodicity that appears when considering them on the circle. These distinguishing features and methods of angular observation analysis are examined and validated in [2].

Mathematical models are based on the LPRP theory; they describe vibration processes and nonuniformity of rotational moment changes which appear on the rotary electric-power machines shafts. Results of indicated models analysis concerning wind-electric (WES) and diesel-electric sets (DES) are examined in detail in [1]. Probabilistic analysis of constructed models gives a possibility to validate in theory the series of diagnostic symptoms which will allow to determinate the technical state of several units of rotary electric-power machines.

Informational signal parameters which can be used to determine the technical state of electric-power set were proved on basis of the analysis of mathematical models of physical processes which accompany the functioning of their units. In its turn this caused the development and selection of appropriate statistical methods, which allow obtaining estimations of observable signals parameters. Obtained signals have become the theoretical grounds for the further development of algorithms and software that realises the monitoring algorithm, technical state analysis and diagnostics of electrotechnical facilities.

The validation of diagnostic symptoms received on the basis of LPRP theory was realized in the present article by means of experimental data treatment software. A question of algorithms and of software development was examined. This software realises these algorithms and is destined for the functioning in the structure of the corresponding information-measuring systems which allow determining the

technical state of electrotechnical facilities with defined precision and probability. This program is built on the system of K. Pirson curves for the purpose of histograms smoothing [3].

The proposed software was built in the form of application package in the DELPHI environment. It can be used to determine the characteristics of time series which represent diagnostic signals. The ergodic hypothesis is valid for these time series, as well as moments up to the 4th inclusively are finite.

Results of mathematical models analysis

The detailed analysis of mathematical models was performed in the works [1,4,5]. Let's make a brief mention of main results received upon this analysis.

Models which describe rotary electric-power machines functioning should take into consideration the periodicity of shaft rotation probabilistic characteristic. At the same time they should give the possibility to determinate statistical estimations of different physical processes which appear in the operating rotary electric-power machine and which are caused by the shaft rotation. Linear periodical random process is one of these models. It can be defined in the form of stochastic integral:

$$(1) \quad \xi(t) = \int_{-\infty}^{\infty} \varphi(\tau, t) d\eta(\tau), \quad t \in (-\infty, \infty),$$

where for any fixed t nonrandom numerical function (kernel) $\varphi(\tau, t) \in L_2(-\infty, \infty)$, $\{\eta(t), \tau \in (-\infty, \infty)\}$ – is nonuniform (uniform) random process with independent increments, which is usually called generating process. Model (1) belongs to the constructive ones, it's because any element which belongs to it has completely determined physical interpretation.

As a consequence of many experiments it was established that the mathematical expectation $M[\xi(t)] = M[\eta(1)] \sum_{j=1}^n a_j$ and dispersion $R(0)$ of observable

vibrations are ineffective diagnostic symptoms. Third and fourth moments contain more information about the character of probability density distribution function; they can be used in the capacity of diagnostic symptoms for the purpose of technical state estimation of units of rotary electric-power machines. However, it is much more easy to

use in practice the coefficient of skewness k and the coefficient of excess γ rather than third and fourth moments. They are expressed through formulas:

$$(2) \quad k = \mu_3 / \mu_2^{3/2},$$

$$(3) \quad \gamma = \beta_2 - 3,$$

where

$$(4) \quad \beta_2 = \mu_4 / \mu_2^2,$$

μ_2, μ_3 and μ_4 are central moments; they can be expressed through next formula:

$$(5) \quad \mu_k = \frac{1}{n} \sum_{j=1}^n (\xi_j - v_1)^k, k = 2, 3, \dots,$$

where $v_1 = \frac{1}{n} \sum_{j=1}^n \xi_j$ – is a linear estimate of ordinary moments.

Values of the first four ordinary and central moments and also the view of probability density distribution function can be used in the capacity of diagnostic symptoms for REM diagnosing by means of the LPRP model.

The nonuniformity of angular velocity of shaft rotation can be used as diagnostic symptom for REM diagnosing.

The rotation angle of the REM shaft φ_t time function is expressed as:

$$(6) \quad \varphi_t = \varphi_0 + \omega_0 t + \varphi_{\delta}(t),$$

where φ_0 – is an initial phase, which is determined by means of special sensor (for WES – zero mark (ZM), and for DES – top dead point mark (TDP)), consequently it can be considered as equal to zero, ω_0 – average value of angular speed, it is expressed from the relationship $\omega_0 = \frac{\pi n}{30}$, n – revolutions of shaft per minute,

$\varphi_{\delta}(t)$ – unevenness of the shaft rotation angle.

The function $\varphi_{\delta}(t)$ is nothing else but the shaft rotation angle fluctuation relative to its rotation angle which varies uniformly. Consequently, the value $\varphi_{\delta}(t)$ will be liable to study in particular, since it contains the information on of the shaft rotation angle unevenness. The last can be related to the defect development in various units of the REM. Stochastic periodicity is inherent to $\varphi_{\delta}(t)$, therefore it's necessary to apply the mathematical apparatus of LPRP theory for its studies.

When solving the problem of WES diagnosing it's possible to use the value of moment on its shaft. The dynamics of WES functioning can be described by the equation:

$$(7) \quad J \frac{d\omega_p}{dt} = M_p [V(t), \omega_p, \varphi_{\delta}(t)] - M_{nm}(\omega_p, M_{\bar{a}}) - K_M [M_{\bar{a}}(\omega_{\bar{a}}) + M_{n\bar{a}}(\omega_{\bar{a}}, M_{\bar{a}})],$$

where J – is the summed moment of inertia of the WES rotating units, reduced to the motors shaft; $\omega_p, \omega_{\bar{a}}$ – angular velocities of the WES rotor and generator; M_p – moment on the output shaft of the WES rotor; φ_n – rotation angle of the WES blades; $M_{nm}, M_{n\bar{a}}$ – moments of loss of the energy in the transmission and in the generator; K_M – gear ratio of the multiplying gear; $M_{\bar{a}}$ – load torque of the generator; $V(t)$ – instantaneous value of the wind speed.

As far as the change of wind speed that affects the wind wheel of the WES has stochastic properties, the most of parameters, which enter into the equation (7), vary stochastically. In other words, values of torques $M_p, M_{nm}, M_{n\bar{a}}, M_{\bar{a}}$ can be considered as stochastic functions $M_p(t), M_{nm}(t), M_{n\bar{a}}(t), M_{\bar{a}}(t)$, which have some fluctuations relative to average values $\overline{M}_p, \overline{M}_{nm}, \overline{M}_{n\bar{a}}, \overline{M}_{\bar{a}}$. Thus, the LPRP theory can be used for analysis of these functions characteristics.

During DES diagnosing parameters $\varphi_{\delta}(t), \varphi'_{\delta}(t)$ and $\varphi''_{\delta}(t)$, which characterize the nonuniformity of diesel crankshaft rotation, can be used in the capacity of diagnostic symptoms. Some of cylinders, which have failed, can be determined after the study of these signals.

The method of DES diagnosing is build in compliance with equation (6). But the nature of nonuniformity of angular velocity of DES shaft rotation, in comparison with WES, is caused by other factor, namely it's caused by the non-identity of cylinders functioning in the diesel piston-cylinder unit. This non-identity occurs in the case of one or few of the cylinders fail; so the crankshaft rotates not with acceleration but with deceleration on the corresponding to a certain cylinder zone of the rotation angle.

The angular speed of shaft rotation can be expressed from the equation (6) as:

$$(8) \quad \omega_t = \varphi'_t = \omega_0 + \varphi'_{\delta}(t),$$

and the acceleration:

$$(9) \quad \omega'_t = \varphi''_t = \varphi''_{\delta}(t).$$

It is significant that the deviation of shaft rotation angle in its turn can be expressed as:

$$(10) \quad \varphi_{\delta}(t) = \varphi^{\delta}_{\delta}(t) + \xi(t),$$

where $\varphi^{\delta}_{\delta}(t)$ – deterministic component, it's caused directly by the DES functioning; $\xi(t)$ – random component, which is described by the LPRP model.

Software selection

The developed application package performs to determinate estimations of ordinary and central moments, up to the 4th inclusive, coefficients of skewness and excess, measurement interval, to build histograms on basis of the specified diagnostic symptoms and to smooth them according to the system of Pirson curves. Also, it allows receiving smoothed power spectrum estimations and amplitude cross-spectrums with dispersion estimation of received spectrums estimations.

The series of time-ordered sequential readings, which is called time series, is obtained in the issue of experimental observations of ergodic random processes realizations.

The ergodic condition performs to replace ensemble averaging of the realizations presented as time series with time averaging upon the determination of statistic estimations for these realizations.

Description of the studied object and experimental conditions

Experimental validation of the developed diagnostic signals, mathematical models and of the developed software was realized in compliance with data received in experiments on the next objects:

– powerwind generator of type USW 56-100 which was tested on the test bench of the daughter enterprise «BO Південмаш»;

– diesel-generator set of type 10Д100 which was tested on the test bench of the «ВО завод ім. Малишева».

Accelerometers of type ABC-017 were used for the purpose of vibration measurement in the units of powerwind generator. Using this IMS sample vibration signals were measured at several points of the powerwind generator and then processed. As a result of realized analysis estimations of spectral characteristics and of vibration signals probability distribution, were received which can be used in the capacity of diagnostic symptoms of the technical state of powerwind generator.

Attaching points of accelerometers are shown on the fig.1, namely:

- transmission module (points 3, 4, 5);
- box of main shaft unit (points 1, 2);
- generator (point 6).

Two regimes of functioning were envisaged during tests: start-up and rotating in motor mode. Measurement, registration and determination of statistical characteristics were made for this last regime of functioning.

It should be also noted that the start-up regime is enough short in time (a few seconds), it is transient (non-stationary) process, which is not typical for the functioning of powerwind generator. Hence, vibrations testing for the start-up regime of the IBC sample were not realized.

In the motor mode of functioning the high-speed shaft rotated with the average angular speed 1449 rpm, and the shaft of the wind wheel hub (slow-speed shaft) rotated with the average angular speed 72 rpm.

Sampling time for transforming analog signals into digital form was equal to 65 μ s (sampling frequency 15625 Hz). The amount of registered information is equal to 16000 counts.

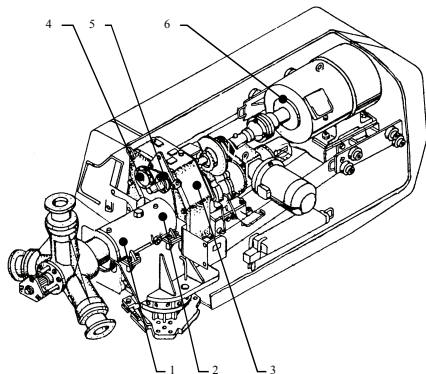


Fig.1. Structure of powerwind generator

The experiment was made on the diesel-generator 10Д100 for the purpose of description of power distribution between diesel-generator cylinders. Sensor ПДФ-3, which realizes the angular speed transformation into the pulse repetition frequency, was installed at the free end of the crankshaft to provide measurement and further processing of the pulse sequence. Output signals of the sensor are generated in the form of two series of pulses for two separated channels. The number of pulses per one turn of the shaft in each series is 600. The period start time is detected by means of the fixed top dead point sensor (TDP).

The time of impulse passing varies randomly, corresponding to the nonuniformity of shaft rotation.

When considering the problem of diesel-generator shaft rotation nonuniformity the series of time intervals between pulses provoke interest [6].

Thus, one observes (for one cycle of diesel functioning) the series of values of time intervals between evenly

spaced rotation angles of the rotating shaft. As a result of experimental investigations we obtained the shaft rotation time versus shaft rotation angle quantized curve with corresponding number of samples.

After two turns of the shaft the series of acceleration counts was registered for one cycle (two turns) of crankshaft rotation with certain duration. Several of these cycles are then written in the PCs memory; their total amount is determined in compliance with [6].

Analysis of results received after experimental data processing

First of all, consider results of experimental data processing received for the wind-electric set USW 56-100.

The results of analysis for the bearing unit are shown as an example.

Accelerometer was installed on the bearing unit cover from the side of high-velocity shaft in the radial direction relative to the shaft (figure 1, point 6). Results of measurement and processing are presented below.

Fig.2,a,b,c present accordingly diagrams of normalized correlation function and of spectral power density, histogram with smoothing curve.

It is possible to establish one frequency component stable enough. The diagram of spectral density of the analyzed vibration signal (fig.2,b) shows distinctly enough the main frequency component of this signal in the region of 335 Hz. Besides, it is possible to establish very little spectral components at frequencies in the region from 50 Hz up to 600 Hz.

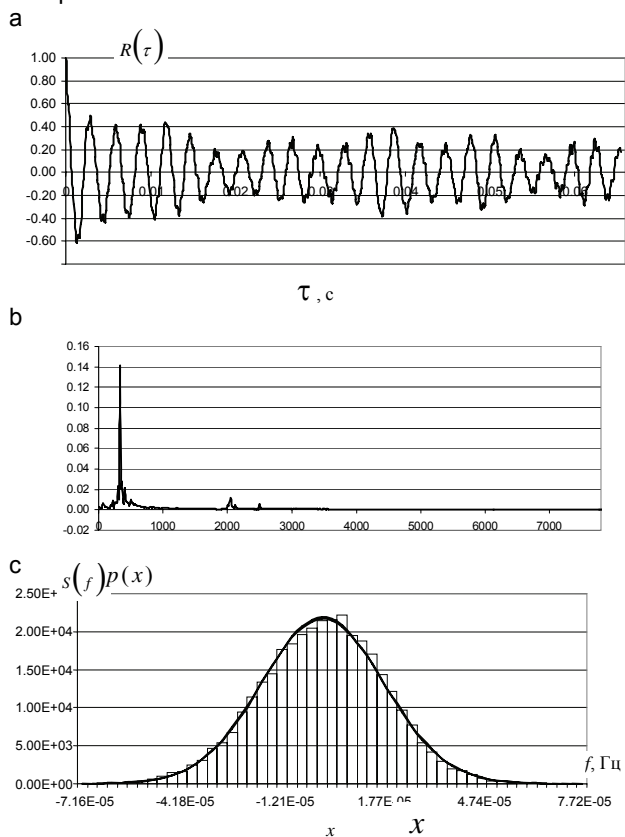


Fig.2. Statistical characteristics of the wind-electric set vibrations

Processed results of registered signal in point 6 which were received with application of the histogram analysis program, are shown on the fig.2,c. The histogram presented on this figure can be smoothed with 7th or 13th type of curves, which enter into the system of Pirson curves. In other words analyzed vibrations in this point do not contradict the Gaussian distribution law.

Estimations of vibration signals parameters and characteristics received by means of laboratory IBC sample are basic quantitative estimations of diagnostic symptoms, which correspond to conditionally faultless units of the wind-electric set. For the purpose of practical use of the developed IMS sample (realization of vibration diagnostic analysis in the situation of wind power station) special method of diagnostics was created. This method provides realization of experiments in the diagnostic space choice and formation in these spaces teaching sets which correspond to the normal state or to some faults in units of the diagnosed wind-electric set.

Let us consider the results of signal measurement and processing experiments which characterize the nonuniformity of crankshaft angular speed and which were received for the diesel-electric set 10Д100.

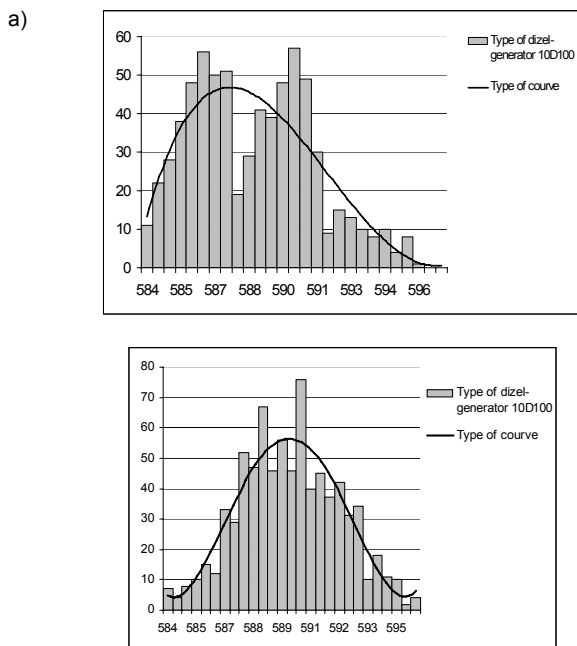


Fig. 3. Histogram containing the processed data received in the experiment on the diesel-generator 10Д100 with 2nd cylinder turned off (a) and results of experimental data processing for the case of properly operating diesel-generator (b).

Fig.3 shows the results of registered information signals processing which was realized with application of histogram analysis program. Fig.3,a shows histogram and smoothing curve which correspond to a failure state of the diesel-generator PCU (failure of the 2nd cylinder) and fig.3,b shows histogram and its smoothing curve which correspond to a properly operation of the diesel-generator PCU.

Table 1. Parameters of the distribution law

| Parameters | The 2 nd cylinder is turned off fig. 3. a) | Properly operation of ЦПГ fig. 3. b) |
|-----------------------------------|---|--------------------------------------|
| Kappa Pirson | -1,19E-07 | -2,25E-09 |
| Asymmetry | 3,85E-08 | 4,03E-09 |
| Excess | -3 | -3 |
| Parameters of Pirson distribution | | |
| L1 | -9 | -9 |
| L2 | 6 | 6 |
| B1 | 1,48E-15 | 1,62E-17 |
| B2 | 3,36E-15 | 1,94E-15 |
| Type of Pirson curve | 1, 2 | 1, 2 |

As can be seen from the presented histograms on fig.3, failure of one cylinder in the diesel PCU leads to a change in the histogram view. It becomes bimodal (fig.3,a)

comparing to the histogram that corresponds to properly operation state of the diesel PCU (fig.3,b). By the way the type of smoothing curve for both of histograms remains the same, the second type.

As a result of realized processing were also noticed changes of some statistical parameters which characterize distribution of received Pirson curves and which correspond to different technical states of the diesel PCU. Estimations of these parameters are presented in the table 1.

Table 1 shows observed changes in the statistical estimations of Kappa Pirson parameter, coefficients of asymmetry and of excess and also changes of related with them parameters β_1 and β_2 [5, 8] for different technical states of the diesel PCU.

Thus, these parameters can be used in the capacity of diagnostic symptoms for the purpose of diesel PCU diagnosing.

Conclusions

1. According to results of the statistical processing of experimental data received for the diesel-generator 10Д100 several parameters were analyzed which can be used further in the capacity of diagnostic symptoms for the purpose of diesel-generator PCU diagnosing.

2. Vibration signals in several units of the wind-electric set were experimentally studied. According to results of statistical processing of these signals their statistical estimations and characteristics were received, which can be used in the capacity of diagnostic symptoms for the purpose of wind-electric set technical state estimation.

REFERENCES

- [1] *Вольтерс А.О., Мислович М.В., Соболевська Л.Г.* Модели лінійних і лінійних періодичних випадкових процесів та їх використання в інформаційно-вимірjuвальних системах діагностики роторних енергетичних машин.
- [2] *Мардья К.* Статистический анализ угловых наблюдений. – М.: Наука, 1978. – 240 с.
- [3] *Мислович М.В., Сисак Р.М.* Інформаційно - вимірjuвальні системи статистичної діагностики електроенергетичного обладнання на основі використання системи кривих Пірсона. // Техн. електродинаміка. Тематичний випуск. Проблеми сучасної електротехніки. Ч.1. 2002. - С.109-112.
- [4] *Зварич В.Н., Мислович В.М., Сисак Р.М., Федоза А.А., Шульга В.Г.* Інформаційно-измерительная система диагностики ветроэлектрических агрегатов с использованием первичных датчиков, основанных на поверхностных акустических волнах // Техн. електродинаміка. Тематичний випуск. Моделювання електричних, енергетичних та технологічних систем. Частина 1. – 1999. – С. 42–47.
- [5] *Марченко Б.Г., Мислович М.В.* Вибродіагностика подшипниковых узлов электрических машиню – Киев: Наукова думка, 1992, 195 с
- [6] *Марченко Б.Г., Мислович М.В.* Теория диагностики энергоагрегатов по девиации вращающихся узлов и её практическое применение для дизель – электрических генераторов. // Техн. електродинаміка. Ч.1- 1998, №5 – С.36-40; Ч.2 – 1998, №6 – С. 39 – 42; Ч.3 – 1999, №1 – С. 59 – 63; Ч.4 – 1999, №4 – С. 40 – 45.
- [7] *Васько В.П., Васько П.Ф.* Динамика нагрузочных режимов работы ветроэлектрической установки, обусловленная порывами скорости ветра //Вісник ДонДАБА. Будівельні конструкції, будівлі та споруди. Вплив вітру на будинки і споруди. - 2001. - №4(29). - С.140-144.
- [8] *Марченко В.Б.* Ортогональные функции дискретного аргумента и их приложение в геофизике. – Киев: Наукова думка, 1992, 210 с.

Authors: A.A. Wolters, L.G. Sobolevskaaya, Kyiv national university of construction and architecture, Povitroflotsky avenue 31, 03037, Kyiv, Ukraine; e-mail: sobolesya@yandex.ru; M. V. Mislovich, Institute of electrodynamics of Ukrainian NAS, Peremoga avenue 56, 03680, Kyiv, Ukraine.

Epileptic seizure detection using single-class SVM

Abstract. The paper presents the application of single-class Support Vector Machine (SVM) for the detection of the epileptic seizure using the EEG waveform. On the basis of the registered EEG signals the diagnostic features are generated first. These features are applied as the input signals to the single-class SVM, serving as the classification tool. Single class SVM is learned using only the baseline segments of EEG. Any discrepancy to the learned prototypes is treated as novelty and after some preprocessing may be associated with the seizure. The results of numerical experiments regarding seizure detection of 32 patients are given and discussed in the paper.

Streszczenie. Praca przedstawia zastosowanie jednoklasowych sieci SVM w wykrywaniu momentu ataku padaczkowego na podstawie zarejestrowanych sygnałów EEG. Ważnym elementem rozwiązania jest generacja odpowiednich cech diagnostycznych różnicujących stan normalny (typowy) od epileptycznego. W pracy bazujemy na cechach energetycznych i średniej długości sygnału. Stanowią one sygnały wejściowe dla jednoklasowej maszyny SVM, pracującej w trybie klasyfikatora wykrywającego zmiany sygnałów w stosunku do prototypu wytrenowanego do rozpoznania stanów normalnych. Praca przedstawia wyniki eksperymentów numerycznych dotyczących detekcji napadu padaczkowego na przykładzie 32 pacjentów oddziału neurologicznego szpitala klinicznego na ul. Banacha w Warszawie. (Wykrywanie napadu padaczkowego przy pomocy jednoklasowych sieci SVM)

Keywords: EEG, epilepsy detection, single-class SVM.

Słowa kluczowe: EEG, wykrywanie padaczki, jednoklasowa sieć SVM.

Introduction

The electroencephalogram (EEG) is a very useful signal for the analysis of the epileptic seizure activity of the brain [2]. Epilepsy is a group of brain disorders characterized by the recurrent paroxysmal electrical discharges of the cerebral cortex, that result in irregular disturbances of the brain functions. They are associated with the significant changes of the EEG signal. The spatio-temporal dynamical changes in EEG, beginning several minutes before and ending several minutes after the seizure, evolve in a characteristic pattern, culminating in a seizure. The EEG registration for this period is different from the typical interictal state, and further will be called the baseline.

Many different techniques have been used in the past for seizure detection [1,2,3,4,5,6]. Starting from 1970-ties a lot of methods have been developed. Among them we may mention: the coherence of the inter-channel difference, time and frequency domain characterization of EEG and application of k-nearest neighbour classifier or self-organizing map, autoregressive modelling, chaotic measures application, etc.

In this paper we will investigate the phenomena of the EEG internal dynamics, culminating in a seizure, using the single-class SVM. On the basis of the energetic measures we generate diagnostic features characterizing the EEG waveform. These features are supplied as the input signals to the single-class SVM, serving as the classifier. The SVM is trained on the baseline segments of the EEG responding with ones when the actual data is compatible with the learned pattern, and with minus ones when the actual pattern differs significantly from the learned one. In this way the single-class SVM is specialized in discovering the novelties appearing in EEG. We will show that applying some measures of probability of detecting the novelty we can recognize the beginning of the epilepsy attacks.

The results of numerical experiments regarding the seizure detection of 32 patients are given and discussed in the paper. They confirm good quality of the proposed solution.

The problem description

The EEG waveform carries a lot of information of the actual state of the brain. The seizure is a disturbance characterized by the changes in the neuronal activities which cause the abnormal discharges in a large cell population of the brain, giving rise to the clinical symptoms. They are reflected by the changes in EEG, registered by the electrodes on the scalp. Fig. 1 presents the EEG fragments

corresponding to the baseline (the typical waveform in the interictal state) and the disturbance of the EEG caused by the epileptic seizure.

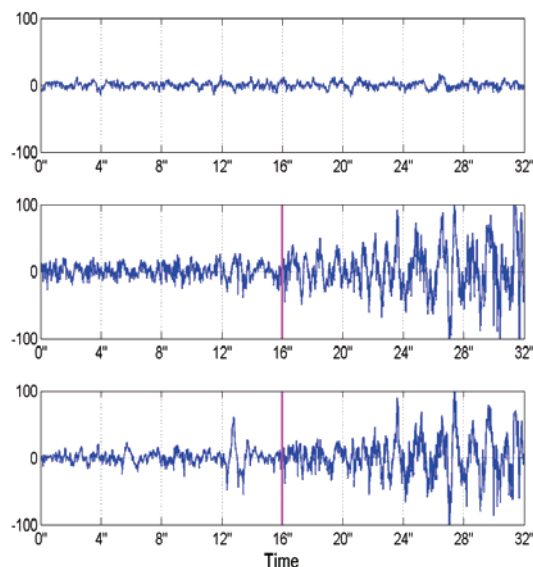


Fig.1. The typical baseline (upper subplot) and seizure onset epochs of EEG data measured by two electrodes (two lower subplots)

The baseline (the upper subplot) is characterized by the small values of the chaotically changing signals. Approaching the onset of the seizure the EEG waveform changes its character (more regularity) and its magnitude. Two lower subplots present the EEG of two channels in the vicinity of the seizure. The vertical line in these subplots points to the time instance of the beginning of the seizure onset, indicated by expert neurologist. The differences of EEG waveforms corresponding to both states are easily visible.

Our task is to develop the method that will be able to detect automatically these changes, associating them with the seizure. We will make use of the novelty detection principle, provided by the single-class SVM network developed by Scholkopf [10]. In this application we train the SVM network on one type of data, belonging to the baseline. The network is adapted to recognize the typical data belonging to one class only. In the process of learning the parameters of the SVM are adjusted in such a way, that

the data in feature space is separated from the origin by the maximum margin hyperplane. At testing phase the actual data is compared with the learned prototype. If it is outside the margin region established in the learning phase, it is regarded as the “novelty”. On the basis of the number of detected novelties we estimate the probability of the seizure occurrence. If this probability is above some threshold, adjusted individually for each patient, it is treated as the seizure onset.

Single-class SVM

In Scholkopf formulation of the learning problem of the single-class SVM the data belonging to the baseline of EEG is used in training the classifier. The data is first mapped to the feature space using the kernel function and then maximally separated from the origin using a hyperplane. The primary problem of learning is defined in the way [10]

$$(1a) \quad \min \left(\frac{1}{2} \|w\|^2 + \frac{1}{\nu p} \sum_{i=1}^p \xi_i - \rho \right)$$

subject to

$$(1b) \quad \langle w, \Phi(x_i) \rangle \geq \rho - \xi_i$$

with $\xi_i \geq 0$ for $i = 1, 2, \dots, p$, where p is the number of learning samples. Here Φ means the map from the input space to feature space, w and ρ are hyperplane parameters, ν is the parameter denoting the asymptotic fraction of outliers allowed, and ξ is the slack variable. The solution of this primary problem is obtained in an identical way as in SVM approach [10] by introducing the Lagrange multipliers α_i and transforming the task to the dual problem, that is finally solved using quadratic programming algorithms. As a result the decision function can be expressed in the form of the kernel expansion [10]

$$(2) \quad y = f(x) = \text{sgn} \left(\sum_i \alpha_i K(x_i, x) - \rho \right)$$

with $K(x_i, x)$ the kernel function, defined on the basis of Φ , as $K(x_i, x) = \Phi^T(x_i) \Phi(x)$. To apply this approach we have to define the type of the kernel function, kernel parameters, separating point in the feature space and the outlier fraction. The kernel function should encode the prior information about the problem [4,10]. Here we will apply the Gaussian kernel $K(x, x_i) = \exp(-\gamma \|x - x_i\|^2)$, the most universal kernel function used in support vector machine research of only one hyperparameter γ . The outlier fraction should incorporate the prior knowledge regarding the frequency of novelty occurrences. We have applied here the genetic algorithm, used for determining (at the same time) the optimal values of ν and γ . The Scholkopf formulation [10] of the separation problem of the multidimensional data samples from the origin of the coordinate system (defined in the feature space) has been implemented using the Matlab platform [7].

Feature generation

The efficient application of the single-class classifier for the novelty recognition needs some preprocessing of the crude EEG data to form the diagnostic features. It is well known that extraction of “good” features directly influences the performance of the classifier in terms of the accuracy, learning time, necessary examples of learning data and also computational complexity. The features should be sensitive to the changes of EEG, observed in the process of

formation of the seizure. After the careful study of the literature [2,3,4] we have tried three features f_1 , f_2 and f_3 associated directly with the signal length and energy, corresponding to the actual time point n . They include

- mean curve length $f_1(n)$

$$(3) \quad f_1(n) = \log \left(\frac{1}{N} \sum_{m=n-N+1}^n x(m) - x(m-1) \right)$$

- mean energy $f_2(n)$

$$(4) \quad f_2(n) = \log \left(\frac{1}{N} \sum_{m=n-N+1}^n x(m)^2 \right)$$

- mean Teager energy $f_3(n)$

$$(5) \quad f_3(n) = \log \left(\frac{1}{N} \sum_{m=n-N+3}^n x(m-1)^2 - x(m)x(m-2) \right)$$

where $x(m)$ is the physiological time series and N is the applied window length. We have used 1s window (at the applied sampling frequency of 250Hz it corresponds to $N=250$). Fig. 2 presents the typical changes of these three features along time for the baseline segment and the onset of seizure for the EEG signal of one chosen electrode.

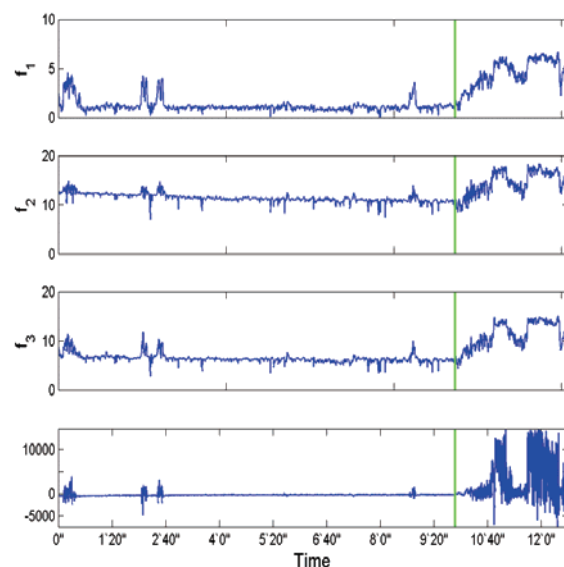


Fig. 2 The typical changes of the generated features f_1 , f_2 and f_3 for EEG containing the baseline segment and the segment corresponding to the onset of the seizure; the lower subplot is the EEG waveform corresponding partly to the baseline and partly to the seizure onset period

There is visible abrupt change of the character of the features corresponding to the seizure period. This change will be treated by the single-class SVM as the novelty and eventually (after some preprocessing) associated with the seizure onset.

To take into account the most important kernel of information of many channels of EEG, registered at the same time, we have applied the Principal Component Analysis (PCA) for the crude EEG data and map the multidimensional data vector into the first principal component. Let us assume that at the time instant t we have registered M channels forming the original vector $\mathbf{x} = [x_1, x_2, \dots, x_M]^T$. The PCA transformation is described by the linear relation [9]

$$(6) \quad y = Wx$$

where W is the transformation matrix, defined by the eigenvectors of the most important eigen values of the correlation matrix R_{xx} . The first component y_1 of the vector y is taken into account for further analysis. It contains the most important part of the information carried by the EEG signals of many channels. Fig. 3 presents the shape of 4 EEG signals and the resultant principal component curve corresponding to them

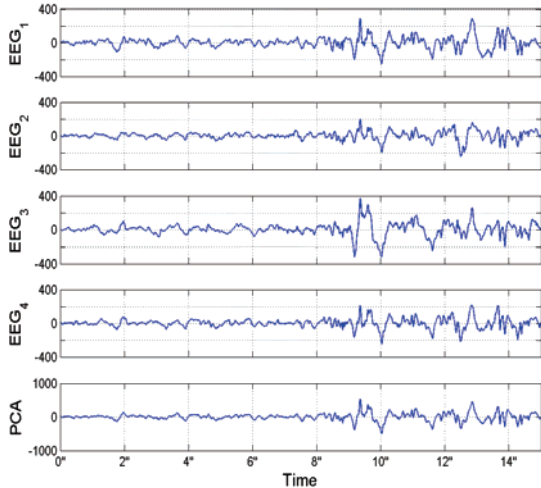


Fig. 3 The example of PCA transformation of EEG of 4 channels; four upper subplots illustrate the EEG signals of four channels, the lower subplot represents the first principal component of the PCA transformation of these four original signals

The system of seizure detection

The proposed system of seizure detection is working on-line. The few minutes period of EEG registration is used for the SVM learning and the next succeeding data points of the same time span are used for testing. The system is retrained after testing using the previous testing data as the learning one. The windows of one second (250 points) are used for the generation of the features used in learning and testing the data. The general scheme of the on-line seizure detection system is presented in Fig. 4.

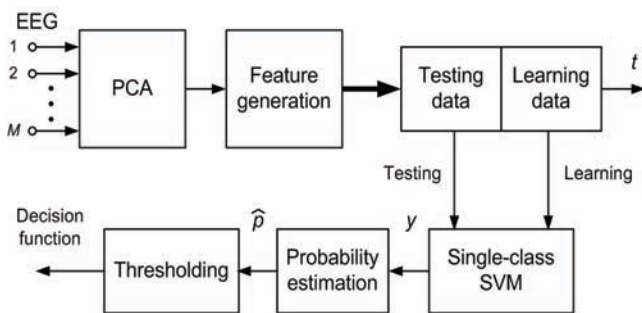


Fig. 4 The on-line seizure detection system using single-class SVM

The M-channel EEG registration is transformed first through the PCA to one resultant waveform, on the basis of which the diagnostic features are generated on-line using the window of 1s. These features form the time series delivered as the learning and testing data for the SVM. The single-class SVM is first trained on the stream of data of the length of three minutes and then tested on the succeeding stream following the learning one. Only the testing results are taken into account at the estimation of the performance of the system.

A simple sequential hypothesis test has been applied to control the rate of the false alarms. We estimate the probability that EEG exhibits novel behaviour for the considered frame of data. For the sequence of N observations of the output signals y of the SVM ($y=1$ for baseline and $y=-1$ for outlier) the following hold

$$(7) \quad N^+ + N^- = N$$

$$(8) \quad N^+ - N^- = \sum_{i=1}^N y_i$$

where N^+ and N^- are the number of positive (baseline) and negative (outlier) occurrences of the SVM output. If we assume that the outputs are identically independently distributed the maximum likelihood estimate of the probability that a novelty occurred, can be defined by

$$(9) \quad p = \frac{N^-}{N} = 0.5 \left(1 - \frac{1}{N} \sum_{i=1}^N y_i \right)$$

This operation is performed by the block "Probability estimation". The decision function declaring the k th frame as the baseline or seizure onset is taken by using the threshold operation

$$(10) \quad decision(k) = sgn(p_k - p)$$

where p is the user specified threshold. The positive sign indicates the seizure onset and the negative one – the baseline.

The results of numerical experiments

The results of numerical experiments concerning 32 patients of neurophysiology hospital will be presented in the paper. The optimal values of the learning parameter ν and the width parameter γ of the Gaussian kernel function

$K(x, x_i) = e^{-\gamma \|x - x_i\|}$ have been adjusted by using the genetic algorithm on the basis of part of the data. The optimization process has been aimed on minimizing the number of false alarms for the cases of known destinations, determined by the neurologist. The obtained values: $\nu=0.013$ and $\gamma=0.72$ have been used in all experiments.

The value of the ν parameter indicates that approximately 1.3% or less of the entire data may be estimated to be novel. The frame length used for feature generation was equal 1 second, and the time sequence used for learning and testing was 3 minutes.

The retraining of the SVM has been performed every 3 minutes, by using the testing data as the learning ones for the next cycle. Fig. 5 presents the results of novelty detection for 4 chosen patients on the basis of EEG depicted at the bottom of each figure (the EEG registration of one channel). The upper subplots present the estimated probability of the seizure onset. The baseline period is characterized by the small values of probability. Approaching the seizure this probability rises sharply. The first vertical (dashed) line indicates the time instance of the onset of the seizure determined by the neurologist on the basis of EEG inspection. The second (solid) vertical line indicates the seizure determined on the basis of the clinical symptoms (the precise time). Usually the clinical symptoms are slightly delayed with respect to the point indicated by the experienced neurologist after inspection of the EEG. At proper determination of the threshold value p we can observe the strict relation between the detected novelty and the seizure onset. They coincide very well.

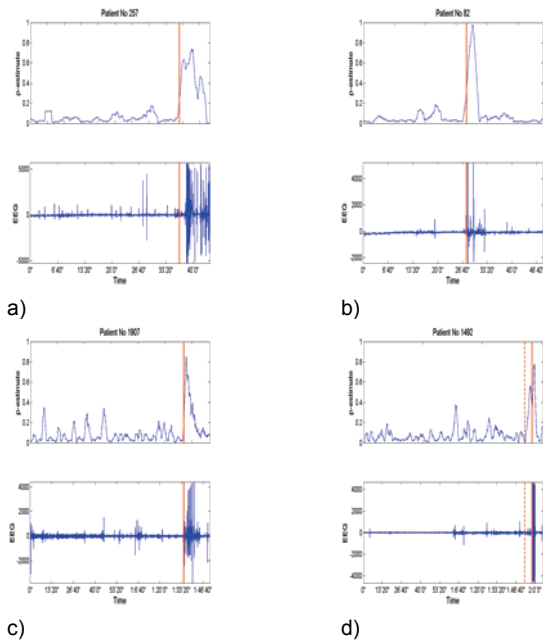


Fig. 5 The results of probability estimation of the seizure occurrence for 4 patients; lower curves – the EEG signal of one channel, the upper curves – the probability estimation values versus time

Fig. 6 illustrates some problems of interpretation of the results of probability estimation that may be encountered at the analysis of different cases in the hospital practice.

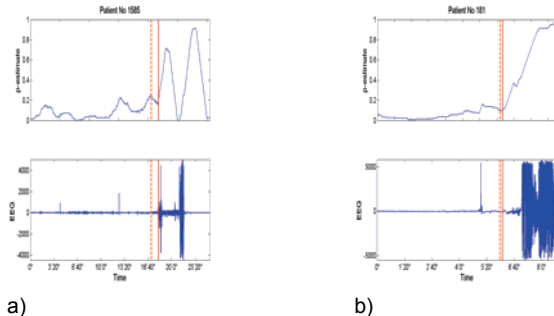


Fig. 6 The illustration of some problems of the seizure onset detection on the basis of EEG analysis for two patients: lower subplots – the registered EEG waveform, upper subplots – the p-estimate values

In the cases of Fig. 6a we can observe the abrupt decrease of EEG signals in the seizure period, lasting limited time. It is reflected in two maximum points in p-estimate, which may stand some interpretation problems of the results. In Fig. 6b we see the significant delay of the p-estimate increasing point with respect to the clinical symptoms. It means that the detection is a bit delayed.

For 32 patients under investigation we have made some statistical examination of the system. The recognition of the seizure was regarded as proper when the peak of the p-estimate was observed in the time period beginning 3 minutes before the onset point indicated by the neurologist on the basis of EEG and ending 7 minutes after beginning of the clinical symptoms of epilepsy. Only two patients have not passed this test. It means that the mean error of seizure recognition was equal 6.25%.

Conclusions

The paper has presented the study of the detection of the seizure onset on the basis of the inspection of the EEG waveform. We have applied the single-class Support Vector Machine, which performs the role of novelty detection. The SVM is trained on the EEG data corresponding to the baseline (typical EEG signal). The seizure onset results in the abrupt change of the character of EEG signal and this change is discovered by the SVM classifier, pointing in this way to the seizure. To increase the efficiency of the detection system we have made some preprocessing of the crude EEG data. First the PCA transformation maps the multi-electrode EEG waveforms into one resultant signal. This signal is used for generation of the diagnostic features for SVM classifier. On the basis of the novelties discovered by SVM we determine the probability of the seizure occurrence. The statistical experiments performed for 32 patients of neurological hospital have confirmed quite good performance of the system for recognition of seizure. The measured error of seizure detection was equal 6.25%. The more intensive checking of the system is still needed, and we will continue this research in the future.

Acknowledgments:

The research presented in the paper has been supported by the Brain Science Institute, RIKEN, Japan.

REFERENCES

- [1] Babloyantz A., Destexhe A., Low dimensional chaos in an instance of epilepsy, Proc. Natl. Acad. Sci. USA, 83(1986), 3513-3517
- [2] Esteller R., Detection of seizure onset in epileptic patients from intracranial EEG signals, in ECE, internal report of Georgia Institute of Technology, 2000
- [3] Esteller R., Echauz J., Tcheng T., Litt B., Pless B., Line length: an efficient feature for seizure onset detection, 23rd Int. Conf. of IEEE Eng. in Medicine and Biology Society, 2001
- [4] Gardner A., A novelty detection approach to seizure analysis from intracranial EEG, Ph.D, Atlanta, USA, 2004
- [5] Gevins A., Remond A., Handbook of EEG and clinical neurophysiology, Elsevier, Amsterdam, 1987
- [6] Iasemidis L. D., Principe J. C., Sackellares J. C., Measurement and quantification of spatio-temporal dynamics of human epileptic seizures, in "Nonlinear Signal Processing in Medicine", ed. M. Akay, IEEE Press, 1999, pp. 1-27
- [7] Matlab Statistics toolbox, MathWorks, Natick, 2002, USA
- [8] Nikias C., Petropulu A., Higher order spectral analysis, Prentice Hall, N. J., 1993
- [9] Osowski S., Neural networks for information processing (in Polish), Oficyna Wydawnicza PW, 2006
- [10] Schölkopf B., Smola A., [Learning with kernels](#), MIT Press, Cambridge, MA, 2002

Authors: mgr Bartosz Świdorski, Warsaw University of Technology, Institute of the Theory of Electrical Engineering, Measurement and Information Systems, Email: swidersb@iem.pw.edu.pl; prof. dr hab. inż. Stanisław Osowski, Warsaw University of Technology, Institute of the Theory of Electrical Engineering, Measurement and Information Systems, Military University of Technology, Institute of Electronic Systems, Email: sto@iem.pw.edu.pl; prof. dr hab. inż. Andrzej Cichocki, Brain Science Institute, Tokyo, Japan and Warsaw University of Technology, Institute of the Theory of Electrical Engineering, Measurement and Information Systems, Email: cia@bsp.brain.riken.go.jp

Modeling and simulation of the interaction of the nonlinear load and traction power system

Abstract. The paper presents the results of modeling & simulation of the influence of the rectifier network (6-pulses) on the supply sources in the traction systems. The simulation results in the form of higher harmonics of voltage and currents have been compared with the measurements made in the real substation. The results of comparison confirm good agreement of the developed model with the real measurements.

Streszczenie. W referacie przedstawiono wyniki modelowania i symulacji pracy układu: stacja transformatorowa 110/15kV, linia zasilająca 15kV, transformator Yd11, prostownik 6-pulsowy, odbiornik o charakterze indukcyjnym. Modele obwodowe poszczególnych elementów układu opracowano przy wykorzystaniu pakietu symulacyjnego Microcap 8. Wyniki analizy numerycznej porównano z wynikami pomiarów parametrów jakości energii elektrycznej na szynach 15kV podstacji trakcyjnej. (Modelowanie i symulacja interakcji nieliniowego obciążenia i systemu zasilania trakcji)

Keywords: higher harmonics of voltages and currents, 6-pulse converter.

Słowa kluczowe: wyższe harmoniczne napięcia i prądu, prostownik 6-pulsowy.

Introduction

Development of the numerical methods and computer engineering has great accelerated the process of analysis of the phenomena in electrical circuits and systems. The paper will present the application of computer approach to study of the cooperation of the nonlinear load with the power system. The aim of this study is the determination of the parameters, characterizing the quality of electrical energy as well as electromagnetic compatibility of the system.

The research is directed to the qualitative and quantitative description of the phenomena in the power system, working for the nonlinear load. The electrical energy delivered to the customers may be characterized using few parameters, changing in time. They describe the quality of energy and its utility in practice. In this paper we will investigate the nonlinear load, represented by the traction substations, on the Polish Power System. All experiments have been performed on the level of 15 kV. Such measurements represent the reliable evaluation of the quality of traction system. The results of measurements will be compared with the results of simulation of the system containing 6-pulse rectifiers, modeled by using MicroCap-8 program.

System description

Figure 1 presents general structure of the simulated system.

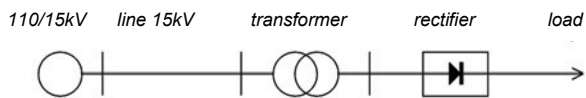


Fig. 1. The general structure of the simulated system

The recommended short-circuit power in the electroenergetic system:

- Voltage 110 kV $S_{zw} 110 \text{ kV} = 400 \div 600 \text{ MVA}$
- Voltage 15 kV $S_{zw} 15 \text{ kV} = 150 \div 200 \text{ MVA}$

In our experiments we have assumed the transformer 110/15kV of the short circuit power equal $S_{zw} = 150 \text{ MVA}$. The parameters of the model have been determined using following formulas

$$(1) \quad X_s = \frac{1.1 \cdot U_p^2}{S_{zw}} = \frac{1.1 \cdot (15 \cdot 10^3)^2}{150 \cdot 10^6} = 1.65 \Omega$$

$$(2) \quad R_s = 0.1 X_s = 0.165 \Omega, \quad L_s = \frac{X_s}{\omega} = 5.25 \text{ mH}$$

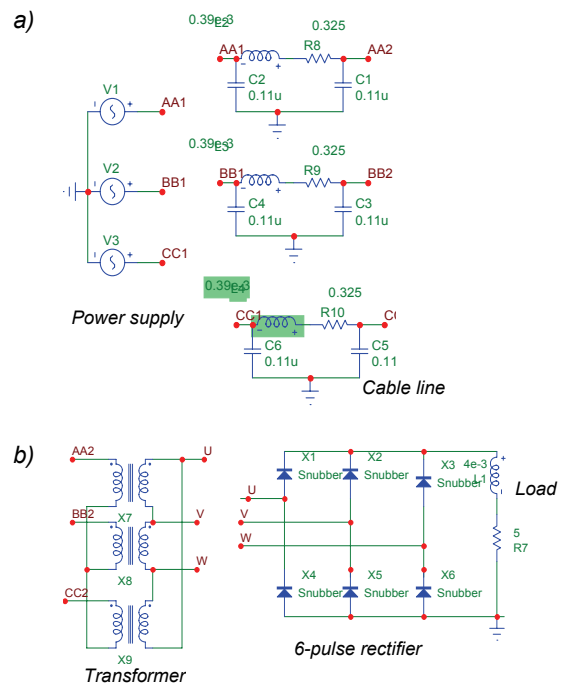


Fig. 2. The detailed circuit structure of the supply of the traction using 6-pulse rectifier (3kV)

The model (Fig. 2.) presented below is composed of the following elements: the main supplying point (GPZ) of 15kV and short-circuit power of 150 MVA, 1 km cable line of 120 mm² cross-section, transformer Y/d 11 and the load.

Applying these parameters for the network of Fig. 2 we got the simple model of 3-phase voltage source of the assumed short-circuit power and voltage.

The supplying 15 kV line can be modeled by the 2-port of π structure and parameters depending on the elementary resistance, conductance and capacitance as well as the length of it.

For example, the 1-wire cable of the cross section $S=120 \text{ mm}^2$ is characterized by the following parameter values:

- $R_0 = 0,325 \Omega/\text{km}$,
- $L_0 = 0,39e^{-3} \text{ H}/\text{km}$
- $C_0 = 0,23e^{-6} \text{ F}/\text{km}$

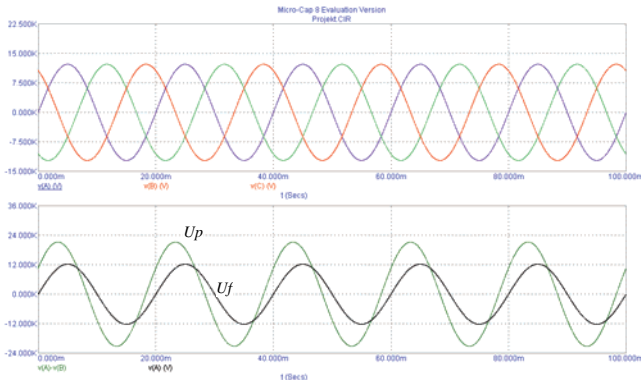


Fig. 3. Transient values of the voltage in the simulated system

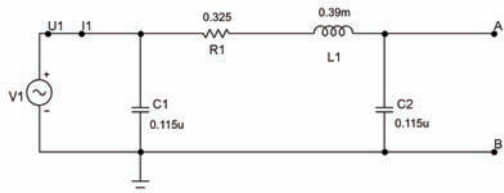


Fig. 4. Model of the 1km cable line

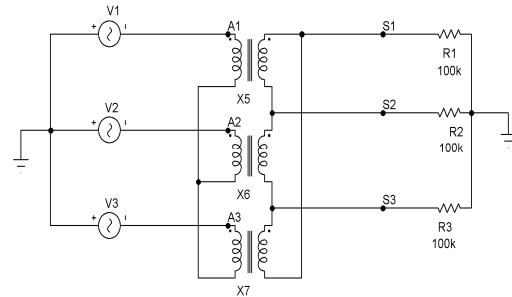


Fig. 5. Model of the transformer Y/d11 for 6-pulse supply

One of the most important element of the system is transformer. It transforms the input voltage into the output voltage of the required level. At the same time the input and output currents are also accordingly transformed.

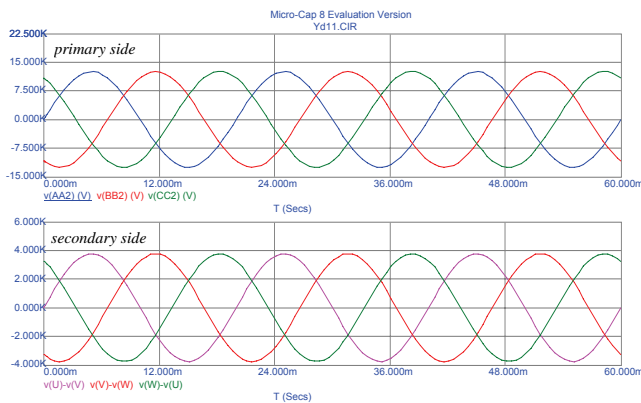


Fig. 6. The transient voltage of the primary and secondary side of the transformer Y/d11 for 6-pulse supply

In sequence these currents determine the distortion of the voltages on both sides of the transformer. For 6-pulse Y/d11 transformer the model was presented as three identical (ideal) 1-phase transformers (Fig. 5).

Assuming the voltage ratio of the transformer equal 0.3 and magnitude of supply voltage 12600V we have got the transient voltages of the primary and secondary side in the form presented in Fig. 6.

The load of the simulated system is formed by the traction engines, converting the electrical energy into mechanical. We have applied the RL model of such engine, of the parameters adjusted adequately.

The numerical results

To get the parameters concerning the deformation of the voltage and current in the system we have to know the transient values of the corresponding variables. Fig. 7. illustrates these transients used in further analysis.

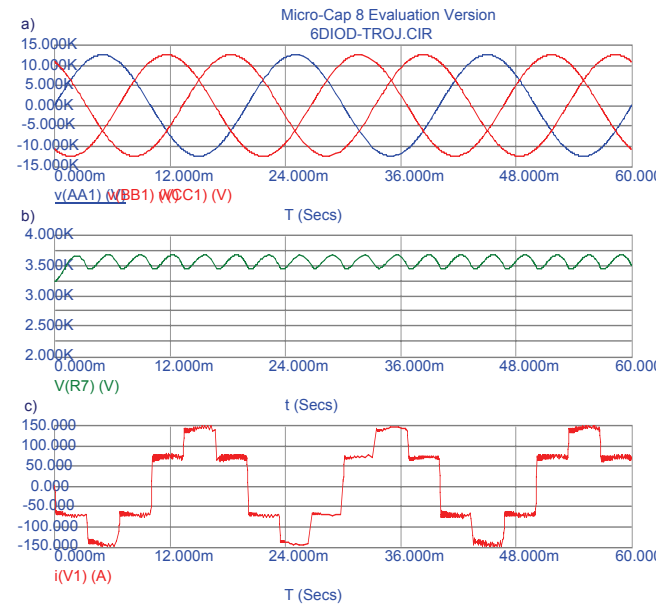


Fig. 7. Transient of: a) supplying voltage, b) the rectified voltage, c) the current of one phase of 3-phase system

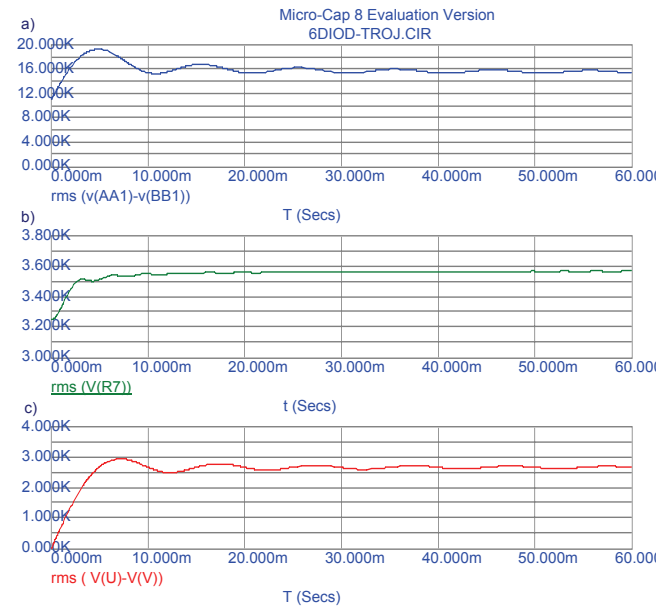


Fig. 8. RMS values of a) line supplying voltage, b) the rectified voltage, c) the voltage of secondary side of transformer Y/d11

The next step is the Fourier analysis (FFT) of the transient responses of the analyzed period from 40ms to 60ms. The results of such analysis are presented below.

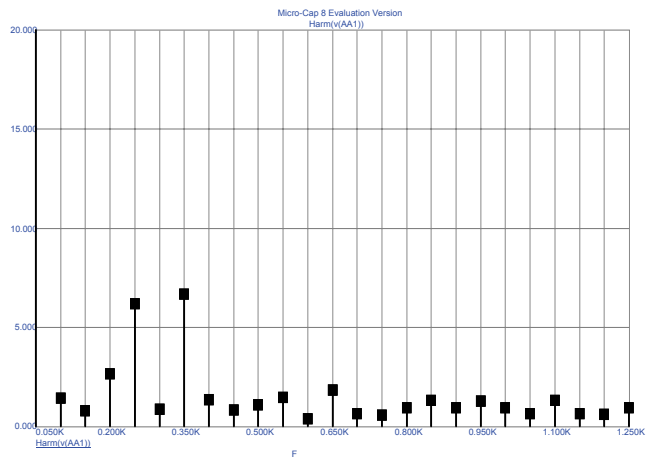


Fig. 9. Spectrum of the supplying voltage

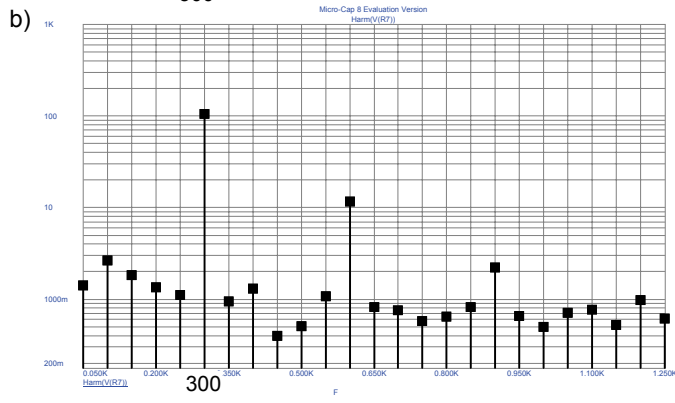
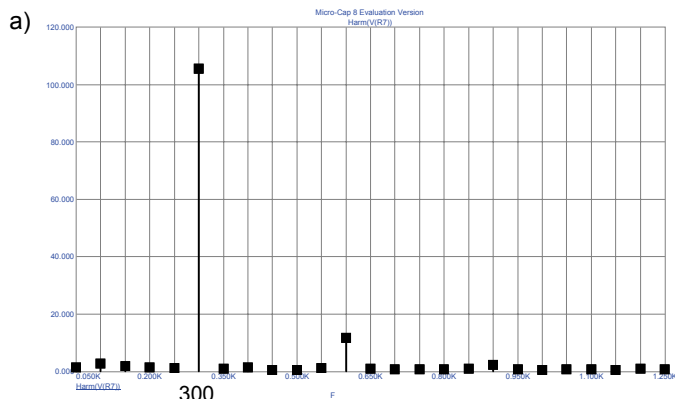


Fig. 11. Spectrum of the rectified voltage: a) linear scale, b) logarithmic scale

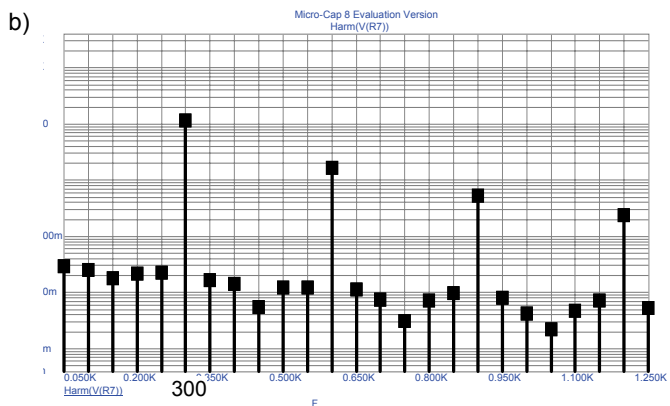
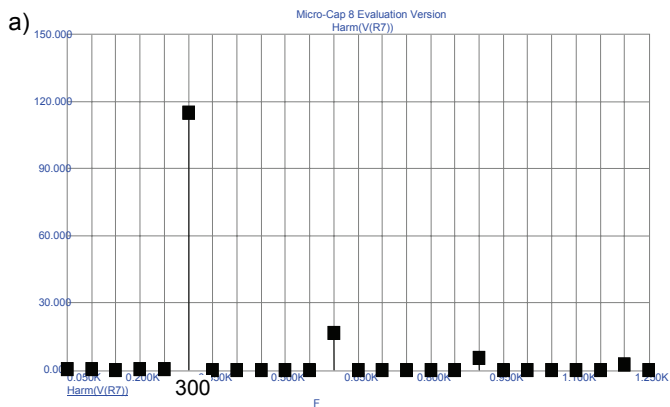


Fig. 10. Spectrum of the rectified current: a) linear scale, b) logarithmic scale

Fig. 10 and 11 present spectrums of the rectified current and the rectified voltage respectively.

Figures 12 and 13 illustrate the results concerning higher harmonics of voltage, measured on the traction substation.

The presented results have been obtained based on the registration which has been carried out by using measuring instruments MEMOBOX according to EN 50160 standard.

The supply voltage contains the 5th and 7th harmonics, generated by the 6-pulse rectified network (Fig. 9 and 12).

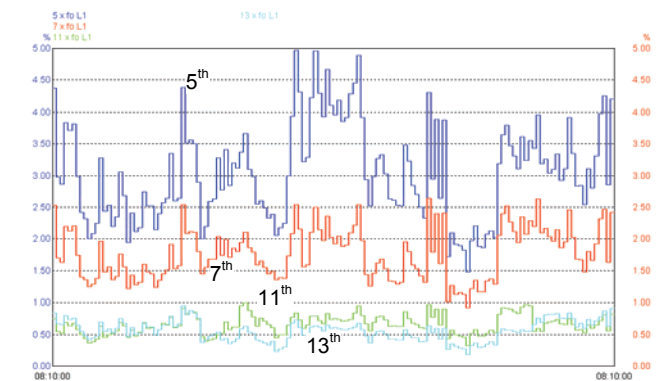


Fig. 12. The higher harmonics of measured voltage (harmonics no 5,7,11,13)

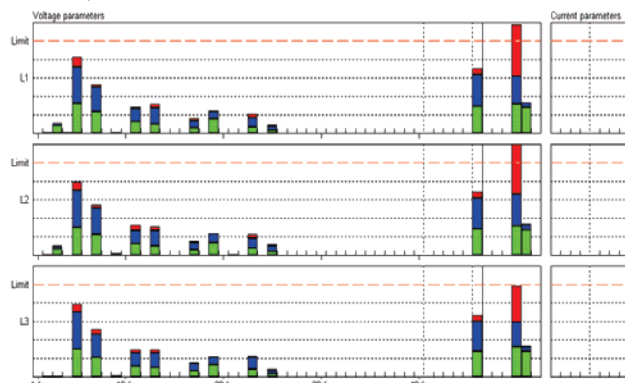


Fig. 13. Spectrum of the supplying voltage in the 3 – phase system

The contribution of the 11th and 13th harmonics is 3 times lower than the above mentioned ones (Fig. 12 and Fig. 13). On the other hand we observe the significant contribution of 6th harmonics in the current and voltage of the load (Fig. 10 and Fig. 11).

Conclusions

The developed computer programs for modeling of the transformer Yd11 and the rectifier allow to obtain the reliable values of the currents and voltages of the analysed system in real exploitation conditions.

The simulated models describe well the most important phenomena occurring in the traction system and its influence on the quality on energy of the power supplying system.

The comparison of the shapes of the currents in the 3 phase real system and in our model has confirmed the accuracy of the proposed approach.

The results of simulation and measurements allow to assess the level of generated higher harmonics by nonlinear loads and influence of these harmonics on electroenergetic system

Taking into consideration that the measurement has been carried out in the typical supply system of traction substation the obtained results are representative for majority of traction sub-stations.

The modeling and simulation of the 6-pulse rectifier systems used in electrical tractions is a handy and recommended tool for the analysis of the power system cooperating with the nonlinear load.

REFERENCES

[1] W. Brociek, R. Wilanowicz, „Estymacja wyższych harmonicznych i migotania napięcia w stacji transformatorowej zasilającej odbiornik nieliniowy z 12-pulsowym przekształtnikiem”, *Przeгляд Elektrotechniczny*, 2'2005, pp. 29-32.

[2] W. Brociek, R. Wilanowicz, K. Siwek, „Electric power quality parameters in transformer station supplying nonlinear load”, *Przeгляд Elektrotechniczny*, 11/2003, pp. 861-864.

[3] W. Brociek, R. Wilanowicz, „Analiza odkształcenia napięcia w układzie z 12-pulsowym przekształtnikiem”, *IC-SPETO 2004*, Gliwice-Niedzica 26-29.05.2004, pp. 175-178.

[4] W. Brociek, R. Wilanowicz, „Ocena korelacji między wybranymi parametrami jakości energii elektrycznej w układach nieliniowych”, *XXVIII IC-SPETO 2005*, Gliwice-Ustroń 2005, pp. 325-328.

[5] A. Szelaż, „Zagadnienia analizy i projektowania systemu trakcji elektrycznej prądu stałego z zastosowaniem technik modelowania i symulacji”, *ZN Elektryka PW, Oficyna Wydawnicza PW, Zeszyt 123/2002*.

[6] W. Brociek, R. Wilanowicz, K. Siwek, „Determination of electric power quality parameters in transformer station supplying nonlinear load: experimental and numerical study”, *V International Workshop "Computational Problems of Electrical Engineering" (CPEE 2003)*, Jazłowiec, Ukraina, 26-29.08.2003, str. 141-144.

[7] K. Mikołajuk, S. Kwiczak, „Optimalization methods for current harmonics estimation”, *VI International Workshop "Computational Problems of Electrical Engineering" (CPEE 2004)*, Zakopane 1-4.09.2004, pp. 213-216.

Authors: Dr inż. Wiesław Brociek, *Instytut Elektrotechniki Teoretycznej i Systemów Informacyjno-Pomiarowych, Politechnika Warszawska, ul. Koszykowa 75, 00-661 Warszawa, E-mail: wbrociek@iem.pw.edu.pl*, dr inż. Robert Wilanowicz, *Zakład Elektrotechniki i Energetyki, Politechnika Radomska, ul. Malczewskiego 26, 26-600 Radom, E-mail: robwilan@poczta.onet.pl*

Thin toroidal superconducting magnetic energy storage (SMES) with tilted coils: magnetic fields, forces and support system requirements

Abstract. A concept of toroidal SMES with tilted coils is considered. A mathematical model of thin toroidal SMES with current sheet composed of infinite number of current filaments is used. The two components of linear density forces are analyzed: the component in plane of each coil and the component that directed perpendicularly to plane of coils. Volumes of support system material requirements have been estimated on the base of integral forces. It is shown considerable reduction in support material requirements compare to traditional toroidal configurations without tilted coils.

Streszczenie. W pracy omówiono koncepcję kondycjonera mocy z cewką nadprzewodzącą (SMES) o pochylonych cewkach. Zastosowano model matematyczny cienkiego, toroidalnego SMES z układem prądowym w postaci nieskończonej liczby cienkich włókien. Przeanalizowano dwie składowe liniowej gęstości sił: komponent położony w płaszczyźnie każdej z cewek i komponent prostopadły do płaszczyzny cewek. Na podstawie analizy sił oszacowano wymagania na ilość materiału podpierającego cewki. Wykazano, że konstrukcja z przechylonymi cewkami wymaga znacznie mniej podpór, niż konstrukcje tradycyjne. (Cienki toroidalny kondycjoner mocy z cewką nadprzewodzącą: pole magnetyczne, siły i wymagania dla systemu mocującego)

Keywords: superconducting magnetic energy storage, magnetic field, electrodynamic forces, support system, tilted coils.

Słowa kluczowe: kondycjoner mocy z cewką nadprzewodzącą, pole magnetyczne, siły elektrodynamiczne, mocowanie, pochylone cewki.

Introduction

Considerable electromagnetic forces which act on windings are one of the basic problems which appear on a way of increase in the accumulated energy of SMES. Therefore actual research is to study such geometry of SMES at which it is possible to reduce electromagnetic forces. A simple way of reducing forces is to tilt the flat coils from the vertical [1-3]. This introduces a poloidal component to the already present toroidal component of the magnetic field. An example of the application of this concept on a large scale is a study that was performed to assess the impact of tilting the coils of the International Thermonuclear Experimental Reactor [4]. Earlier in [5] it has been shown, that the toroidal solenoid with tilted coils is one of appropriate magnetic systems for SMES. The simple mathematical model in the form of thin toroidal current sheet then a ratio of small radius of torus to large one (the inverse aspect ratio) is small has been presented in [6]. The magnetic fields of circular torus have been analyzed.

In this paper the analytical model is used for study of integral forces, which act to coils. Volumes of support system material requirements are estimated on the base of integral forces.

Mathematical model

It is supposed that current flows on toroidal surface. Current sheet is composed of an infinite number of current filaments. The configuration of each filament is the same as the configuration of the curvilinear axis of a coil. So, the mathematical model of current distribution is the same as in [6] and it is applied also for determine integral forces and support system material requirements.

In this paper a magnetic system with flat tilted coils is considered. The geometry of current system is shown on Fig. 1.

In the general case the configuration of a current line is determined by the following equations:

$$(1) \quad \begin{aligned} \sin(\varphi - \varphi_0) &= -\tan \beta \frac{z}{\rho} \\ \rho &= \rho(\chi), \quad z = z(\chi) \end{aligned}$$

where ρ , φ , z are cylindrical coordinates. The first expression is the equation of a flat surface that is turned around the radial axis on angle β ; the next ones are parametric equations that determine a surface of rotation about the z -axis.

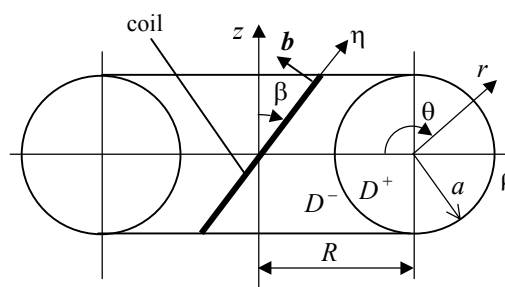


Fig.1. Circular-section torus composed of tilted coils

The equations for a circular-section torus (Fig. 1) may be written as

$$(2) \quad \rho(\theta) = R(1 - \varepsilon \cos \theta), \quad z(\theta) = R\varepsilon \sin \theta$$

where $\chi = \theta$ and $\varepsilon = a/R$ is the relative size of the torus (the inverse aspect ratio). The shape of the tilted coils depends on both ε and angle β .

For thin torus at $\varepsilon \ll 1$ it may be used a mathematical model of cylinder composed of tilted coils (Fig. 2a). The shape of each coil is ellipse with semi axes a and $a/\cos \beta$ as it shown on Fig. 2b.

The equations that determined shape of the coil are the following:

$$(3) \quad \xi = a \cos \theta, \quad \zeta = a \sin \theta, \quad l = -a \tan \beta \sin \theta$$

where ξ and ζ are coordinates in cross-section of cylinder, l is longitudinal coordinate.

The unit tangent vector to current line has components in cylindrical coordinate system:

$$(4) \quad t = t_\theta \cdot e_\theta + t_l \cdot e_l,$$

where

$$t_\theta = \frac{1}{\sqrt{1 + \cos^2 \theta \cdot \tan^2 \beta}}, t_l = -\frac{\cos \theta \cdot \tan \beta}{\sqrt{1 + \cos^2 \theta \cdot \tan^2 \beta}},$$

e_θ and e_l are unit vectors of the coordinate system.

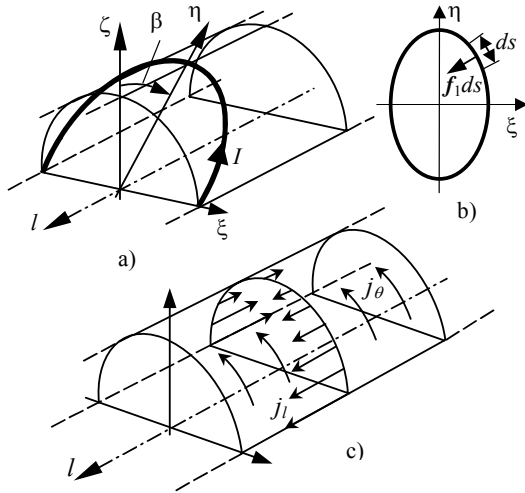


Fig.2. Circular-section torus at $\varepsilon \ll 1$ composed of tilted coils; a) cylindrical model, b) current contour configurations, c) orientation of two current density components

As the vector \mathbf{j} (surface density current) is parallel to Vector \mathbf{t} , it has the same components:

$$(5) \quad \mathbf{j} = j_\theta \cdot \mathbf{e}_\theta + j_l \cdot \mathbf{e}_l.$$

From continuity condition of \mathbf{j} following that poloidal component is given by

$$(6) \quad j_\theta = I_0 = \frac{IN}{2\pi R},$$

where N is total number of coils in the torus and I is the current per coil (NI is the total ampere turns in the current sheet).

The toroidal component of current density is determined by equation:

$$(7) \quad j_l = j_\theta \frac{t_l}{t_\theta} = -\frac{IN}{2\pi R} \cos \theta \tan \beta$$

Fig. 2c illustrates orientation of two current density components.

In contrast to non-tilted coils ($\beta=0$), the magnetic field of tilted coil torus has both toroidal B_t and poloidal B_p components. The component B_t is created by currents j_θ and is confined within the torus. For model of thin torus the component B_t take on a constant value:

$$(8) \quad B_t = \frac{\mu_0 IN}{2\pi R}.$$

The component B_p is created by currents j_l and, in contrast to B_t , is non-zero both inside and outside of the torus. The poloidal field B_p is uniform inside torus. This field component is the same that magnetic field that is created

by magnetic moment distributed along longitudinal axis with linear density:

$$(9) \quad \lambda = \frac{INa^2}{2R} \tan \beta e_\zeta.$$

Since the main problem in this paper is to analyse of forces we give the magnetic field only at current surface of torus. The equations for magnetic fields inside B^+ and outside B^- at current surface are the following:

$$(10) \quad \mathbf{B}^+ = \frac{\mu_0 IN}{2\pi R} \left(\frac{1}{2} \tan \beta \sin \theta e_r + \frac{1}{2} \tan \beta \cos \theta e_\theta + e_l \right)$$

$$\mathbf{B}^- = \frac{\mu_0 IN}{2\pi R} \left(\frac{1}{2} \tan \beta \sin \theta e_r - \frac{1}{2} \tan \beta \cos \theta e_\theta \right)$$

Each incremental length ds of the coil (Fig. 2b) experiences an electromagnetic force $d\mathbf{F}_1 = \mathbf{f}_1 ds$, which is perpendicular to the current line. The linear density force \mathbf{f}_1 , is given by

$$(11) \quad \mathbf{f}_1 = \frac{I}{2} \mathbf{t} \times (\mathbf{B}^+ + \mathbf{B}^-).$$

The vector \mathbf{f}_1 for a toroidal system with tilted coils has two components

$$(12) \quad \mathbf{f}_1 = f_{1n} \mathbf{n} + f_{1b} \mathbf{b},$$

where f_{1n} is the component directed along the normal \mathbf{n} to the current contour and f_{1b} is the component oriented along binormal \mathbf{b} perpendicularly to flat of the coil.

Taking into account that unit vector \mathbf{b} is equal

$$(13) \quad \mathbf{b} = \sin \beta e_\zeta - \cos \beta e_l$$

and $\mathbf{n} = \mathbf{b} \times \mathbf{t}$, the components of linear density force are given by

$$(14) \quad f_{1n} = -\frac{\mu_0 I^2}{4\pi R} \frac{\sin \beta \tan \beta (1 + \tan^2 \beta \sin^2 \theta \cos^2 \theta) + \cos \beta}{1 + \tan^2 \beta \cos^2 \theta}$$

$$f_{1b} = -\frac{\mu_0 I^2}{4\pi R} \frac{\sin \beta \tan^2 \beta \sin \theta \cos^2 \theta}{\sqrt{1 + \tan^2 \beta \cos^2 \theta}}$$

Equations (14) are differed from corresponding ones obtained in [6], where some mistakes took place.

Components of linear density force as a function of angle θ are shown in Fig. 3 and Fig. 4 for some values of β . As it following from (14) in toroidal systems in the case $\beta=0$ only the normal force density component f_n is present. If the coils are tilted, however, both components have to be taken into account.

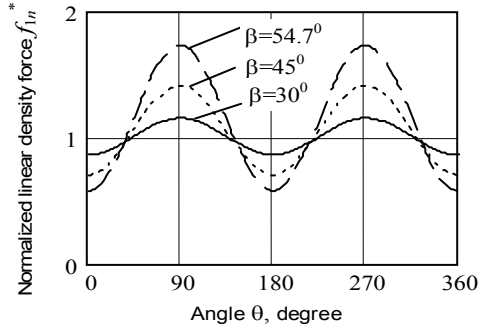


Fig. 3. Distribution of normal linear density force $f_{in}^* = f_{in}(4\pi R / \mu_0 I^2)$ along perimeter of coil at different tilting angle β

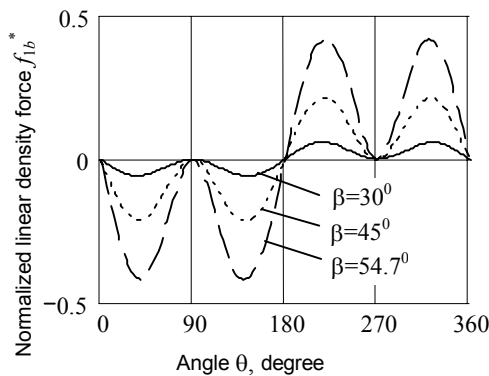


Fig. 4. Distribution of binormal component of density force f_{lb}^* along perimeter of coil at different tilting angle β .

Integral parameters: energy, forces, support system requirements

Energy

Since in anyone point toroidal and poloidal components of magnetic field are perpendicularly each to other the total energy stored in the magnetic field W is the sum of the energy stored in the toroidal W_t and poloidal W_p components. At $\varepsilon \ll 1$ these components are easily determined from model for straight cylinder with surface density current. The total energy is found by the equation

$$(15) \quad W = W_\varphi + W_p = \frac{\mu_0 I^2 N^2 R}{4} k_w(\varepsilon, \beta),$$

where non-dimensional parameter is determined as following:

$$k_w(\varepsilon, \beta) = \varepsilon^2 \left(1 + \frac{1}{2} \tan^2 \beta \right).$$

Radial forces

As it is well known, if $\beta=0$, the total electromagnetic force that acts on each coil is directed along the radial ρ -axis and is non-zero. This radial force is directed to the z -axis [7].

For systems with tilted coils, an additional oppositely directed force appears associated with the azimuth (toroidal) current j_t . If $\varepsilon \ll 1$, this force takes the form of an

interaction of the magnetic moment distributed along a circle of radius R with its own magnetic field [8] and it compensates radial force caused of poloidal current. In this case, the total radial force F_R that acts on all coils is

$$(16) \quad F_R = \frac{1}{4} \mu_0 I^2 N^2 k_{FR}(\varepsilon, \beta)$$

where non-dimensional parameter is

$$k_{FR}(\varepsilon, \beta) = -\varepsilon^2 \left(1 - \frac{1}{2} \tan^2 \beta \right)$$

At $\beta = \beta_e = \tan^{-1}(\sqrt{2}) \approx 54.7^\circ$ the force $F_R = 0$ and the coils are in an equilibrium position. If $\beta < \beta_e$, the force $F_R < 0$ directed inward to the z -axis; when $\beta > \beta_e$, the radial force is directed outward along the radial axis.

Toroidal energy storage customarily have a central backing cylinder as a component of of the support system. Forces arising in backing cylinder balance the radial forces and, for example at $\beta=0$, the cylinder is in compression. The backing cylinder may be constructed of support rings with different thicknesses such that stresses σ_c in the rings are constant.

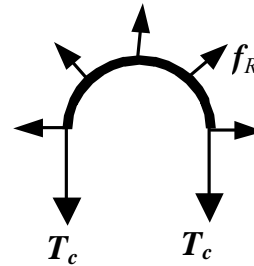


Fig. 5. Forces at half of support ring

All N coils presses down each element with length dl of the support ring with force $dF_R = f_R dl$ (Fig. 5). In this case, the mechanical stress in the ring is $\sigma_c = \frac{T_c}{S_c} = \frac{F_R}{2\pi\pi_c}$, where S_c is the area of a ring cross section. The volume V_c of the support ring will be

$$(17) \quad V_c = 2\pi R S_c = \frac{F_R R}{\sigma_c}$$

Applying (15) and (16) give the following equation to determine the volume of support system that balance the radial forces:

$$(18) \quad V_c = \frac{W}{\sigma_c} |Q_c|.$$

Here non-dimensional factor Q_c is given by

$$(19) \quad Q_c = \frac{k_{FR}(\varepsilon, \beta)}{k_w(\varepsilon, \beta)} = -\frac{1 - \frac{1}{2} \tan^2 \beta}{1 + \frac{1}{2} \tan^2 \beta}$$

Factor Q_c is shown as a function of angle β in Fig. 6. The negative values correspond to compression mechanical

stresses of support ring and the positive values correspond to tension stresses. As it follows from Fig. 5 tilting of coils reduce volume of support ring.

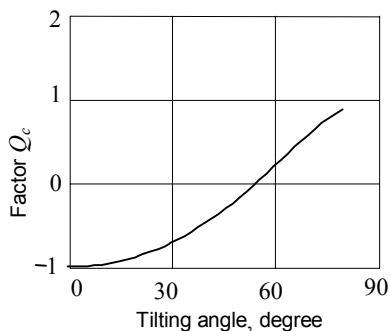


Fig. 6. Dimensionless factor to determine the volume of support ring compensating the radial forces in thin torus

Forces in plane of coil

The distributed normal component force f_{1n} also causes tension in the coils. For example, Fig. 7 shows the tension forces $T_{1\eta}$ at $\eta=0$. The tension in a thin torus at $\beta=0$ is constant. However, for torus with tilting coils the tension varies along the coil and clamping belts are usually applied to compensate the tension forces. The volume of this part of the support system may be approximated using the average tension force along coil perimeter.

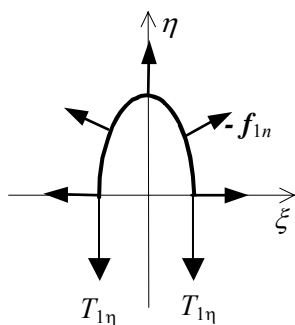


Fig. 7. Forces at top half of tilted coil

For estimation we will assume that tension force along perimeter of coil is equal to value at $\eta=0$. Tension forces $T_{1\eta}$ at the $\eta=0$ in the coil equilibrate force $F_{1\eta}$ that acts in direction of η -axis on half of coil, that is $T_{1\eta} = \frac{F_{1\eta}}{2}$. The force $F_{1\eta}$ is given by

$$(20) \quad F_{1\eta} = - \int_0^{s/2} f_{1n} e_\eta ds$$

Applying (14), this force is the following:

$$(21) \quad F_{1\eta} = \frac{1}{4} \mu_0 I^2 N k_{F\eta}(\epsilon, \beta),$$

where

$$k_{F\eta}(\epsilon, \beta) = \frac{2}{\pi} \epsilon \cos \beta \left(1 + \frac{2}{3} \tan^2 \beta \right).$$

The mechanical stresses σ_t in clamping belts is estimated as $\sigma_t = \frac{T_{1\eta}}{S_\eta}$, where S_η is the area of clamping belts cross section. The volume V_η of corresponding part of support system for all N coils will be

$$(22) \quad V_\eta = \frac{T_{1\eta} N}{\sigma_t} s.$$

Here length of elliptical coil is

$$(23) \quad s = R \cdot 4\epsilon \frac{E(\sin \beta)}{\cos \beta},$$

where $E(\sin \beta)$ is full elliptic integral of module $k = \sin \beta$.

Applying equations given above the volume of material V_η is found by the equation

$$(24) \quad V_\eta = \frac{W}{\sigma_t} |Q_\eta|,$$

where non-dimensional factor Q_η is

$$(25) \quad Q_\eta = \frac{4E(\sin \beta)}{\pi} \cdot \frac{1 + \frac{2}{3} \tan^2 \beta}{1 + \frac{1}{2} \tan^2 \beta}$$

The factor Q_η connected with volume V_η weakly decreases with increasing tilting angle β as shown in Fig. 8.

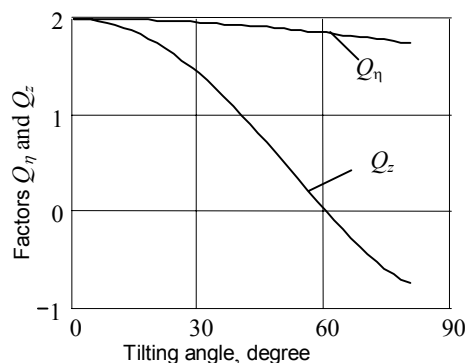


Fig. 8. Dimensionless factors to determine the volume of support system compensating the forces in plane of coil and vertical forces

Vertical forces

Another method to react the tension forces may yield more favourable results. The support system can be designed so that the forces in the toroidal shell enclosing all the coils compensate the tension forces in the coils. Estimation of volume V_z of this part of support system may be based on determination of total z-directed force that acts on the top half of torus. Tension forces at the $z=0$ in the shell equilibrate this vertical force.

If the coils are tilted both components f_{1n} and f_{1b} have to be taken into account for calculation vertical force F_z that acts to top half of torus.

The vertical force is determined as following

$$(26) \quad F_z = N \int_0^{s/2} f_1 e_z ds$$

Evident equation for vertical force may be obtained using (4), (12) and (14). Combining then with (15) the volume of corresponding part of support system V_t is found by the analogous equation:

$$(27) \quad V_z = \frac{W}{\sigma_t} |Q_z|,$$

where

$$(28) \quad Q_z = \frac{4E(\sin\beta)}{\pi} \cdot \frac{1 - \frac{1}{3}\tan^2\beta}{1 + \frac{1}{2}\tan^2\beta}$$

The factor Q_z significantly decreases with increasing tilting angle β . One can see from Fig. 8 the volume V_z of support system material is considerable lesser compare to volume V_η . Therefore using shell enclosing all the coils may be more preferable configuration.

Conclusion

Toroidal magnetic systems with tilted coils could require significantly smaller quantities of support system materials compared to traditional configurations without tilted coils, despite the more complicated geometry in the former. So, tilted coil systems, with the twin advantages of lower

support costs and lower stray fields, could provide attractive alternatives to conventional coil systems in the development of large-scale SMES devices. The future investigations of toroidal systems with tilted coils may be directed to configuration with larger relative size of torus cross-section and to analysis torus with non-circular cross-section.

REFERENCES

- [1] Georgievskiy A.V., Martynov S.A., Rudakov V.A., et al. A Magnetic System of a Plasma Trap with Stellarator Configuration of a Magnetic Field. Autors Certificate SU N 1562957, *Bulleten Izobretenij*, (1990), No 17, 264 (in Russian).
- [2] Georgievskiy A.V., Martynov S.A., Rudakov V.A., et al. Magnetic Configuration Circular Stellarator System. *Voprosy Atomnoj Nauki i Tekniki (BAHT) Ser: Termoyadernyj Sintez*. Moscow: TsNIIAtominform. (1989), issue 4, 28-35 (in Russian).
- [3] Bykov V.E., Volkov E.D., Georgievskiy A.V., et al. Optimization Studies of Compact Torsatrons. *Proc. 12th Int. Conf. Plasma Physics and Contr. Nucl. Fusion Research*, 1988, Nice, (1989), Vienna, rept. IAEA-CN-50/C-1-5, 403-410.
- [4] "ITER Outline Design", January (1994).
- [5] Vasetsky Yu., Georgiyevskiy A., Ostrow S., Rotachov Yu. Toroidal magnetic systems with tilted coils for superconducting magnetic energy storage (SMES). *Technical Electrodynamics.. Problem of Present-day Electrotechnics*. (2004), No 2, 3-6.
- [6] Vasetsky Yu., Rotachev Yu. Magnetic Fields and Forces in Thin Toroidal Magnetic Energy Storage. *Przeglad Electrotechniczny*. 81 (2005), No 2, 51-53.
- [7] Thome R.J., Tarrh J.M. MHD and Fusion Magnets. Field and Force Design Concepts. USA: A Wiley-Interscience publication, (1982).
- [8] Vasetsky Yu. Multipole Representation of Electric and Magnetic Fields in Systems with Curved Conductors. *Electrichestvo*, (1999), No 11, 49-53 (in Russian).

Authors: Dr.Sc. Yuriy Vasetsky, Institute of Electrodynamics, 56, Peremogy Avenue, 03680, Kiev-57, Ukraine, E-mail: vasets@svitonline.com; PhD Iryna Mazurenko, Institute of Electrodynamics, Yuriy Aristov, Institute of Electrodynamics.

Application of equivalent circuits in power theory for systems with nonsinusoidal waveforms – critical remarks

Abstract. The goal of this paper consists in analysis of a newly emerged power theory based on equivalent circuits. The theory assumes approximation of all electrical systems with T -periodical waveforms by series or parallel connections of a linear resistor, an inductor and a capacitor. The disadvantages of the theory have been presented. Theoretical considerations have been illustrated by an example.

Streszczenie. Celem artykułu była analiza nowej teorii mocy opartej zbudowanej w oparciu o obwody równoważne. Teoria ta zakłada aproksymację dowolnych układów elektrycznych z przebiegami T -okresowymi przy użyciu szeregowego lub równoległego połączenia liniowego rezystora, cewki i kondensatora. W artykule pokazano wady takiego podejścia. Rozważania teoretyczne zilustrowano przykładem. (Zastosowanie obwodów równoważnych w teorii mocy układów z przebiegami niesinusoidalnymi – uwagi krytyczne).

Keywords: approximation methods, system modeling, harmonic analysis.

Słowa kluczowe: metody aproksymacji, modelowanie układów, analiza harmoniczna.

Introduction

The concept of power theory for electrical circuits has not been precisely defined. Usually, it is assumed that the theory should ensure realization of two tasks [1, 2]. The first one, of cognitive nature, consists in describing, analyzing and interpreting circuit energetic properties as well as defining power concepts. The second one, of application nature, results from the necessity of circuit modification required to achieve some goals [3, 4, 5, 6], e.g.:

- improving the power factor of energy sources,
- reducing voltage and current distortions in circuits,
- defining as well as identifying some factors of energy transmission losses used among others for energy cost calculations.

So far the second task, at least as refers to improving the power factor and reducing waveform distortions, has been achieved to a great extent. Methods of design of active compensators and their control algorithms, usually based on instantaneous reactive power theory (introduced originally by H. Akagi, A. Nabae and Y. Kanazava [7]) and its generalizations [8], are well developed and widely applied.

As for the first, cognitive, task the solution seems to be still far away. Despite many papers published during last 100 years there are no generally accepted power definitions and power interpretations [1, 2, 3, 4, 5, 6, 8, 9]. The complete conformity of views on power theory ends with single phase circuits with sinusoidal waveforms. Interpretation differences start already with multi-phase systems [5, 6, 10]. It looks as if the following conditions should be fulfilled while creating a new power theory:

1. Powers ought to be defined correctly for a given class of signals, e.g. periodic, almost periodic or aperiodic, and cover single phase as well as multi-phase systems.
2. Powers are supposed to have physical interpretation and enable estimation of:

- electromagnetic field energy stored in reactive circuit elements,
- oscillations of energy flow between sources and loads.

3. There should be possibility of defining powers in time as well as in frequency domain (classical Fourier series is a very special representation of time waveforms).

The argument used in the past that evaluation of new power definitions should be based on simplicity of devices which enable their measurements does not seem to be rational nowadays. For sure the possibility of easy device construction for specific power measurement cannot be

used as the only argument for introducing new power concepts as it happened.

It seems that among many power theories for systems with nonsinusoidal waveforms there is no even one that satisfies all conditions mentioned above. Never-ending modifications of these theories are contributing a lot to generation of new concepts which undergo endless criticism. It is not possible to describe, compare and evaluate all these theories within the scope of this paper.

This paper is an extension of critical analysis of a power theory [9, 11, 12] which was given in [13]. The analysis is followed by a proposition of a way how to correct the theory which is presented in a successive paper [14]. The idea that can be called approximation concept [14] differs to a great extent from the concepts introduced by I. Budeanu [15], S. Fryze [16], H. Akagi [7] and their generalizations [8].

Idea of Approximation Approach

The idea consists in assignment of a series or parallel equivalent branch consisting of a resistor, an inductor and a capacitor (RLC) to a one-port (Fig. 1) with given input voltage $u(t)$ and current $i(t)$ [9, 12]. The idea has been introduced only for circuits with T -periodical current and voltage waveforms which belong to Hilbert signal space L_T^2 with norm $\|\cdot\|_{L_T^2}$ and scalar product $(\cdot, \cdot)_{L_T^2}$ defined as follows:

$$(1) \quad \|f\|_{L_T^2} = \sqrt{\frac{1}{T} \int_0^T f^2(t) dt}, \quad f \in L_T^2,$$

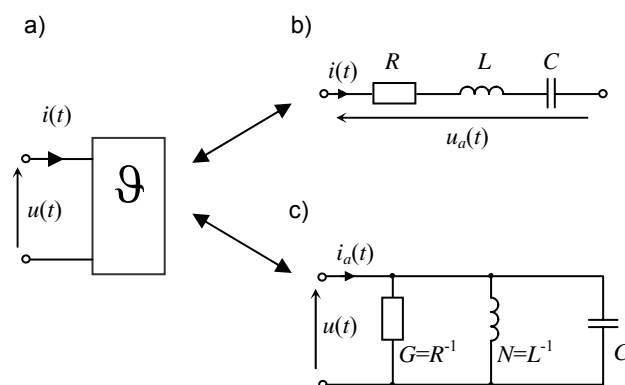


Fig. 1. One-port (a) and its series (b) and parallel (c) model

$$(2) \quad (f, g)_{L_T^2} = \frac{1}{T} \int_0^T f(t)g(t)dt, \quad f, g \in L_T^2.$$

Subsequent considerations are limited only to parallel representation structure (Fig. 1c) because for the series one they are analogical.

Taking into account the first Kirchhoff's law for the parallel structure:

$$(3) \quad i(t) = Gu(t) + Cu'(t) + N\bar{u}(t),$$

where:

$$(4) \quad u'(t) = \frac{du}{dt}, \quad \bar{u}(t) = \int_0^t u(t)dt,$$

and some known for T -periodical waveforms identities:

$$(5) \quad (u, u')_{L_T^2} = 0, \quad (u, \bar{u})_{L_T^2} = 0, \quad (u', \bar{u})_{L_T^2} = -\|u\|_{L_T^2}^2$$

it can be proved that [9, 12]:

$$(6) \quad (u, i)_{L_T^2} = G\|u\|_{L_T^2}^2,$$

$$(7) \quad (\bar{u}, i)_{L_T^2} = N\|\bar{u}\|_{L_T^2}^2 - C\|u\|_{L_T^2}^2,$$

$$(8) \quad (u', i)_{L_T^2} = C\|u'\|_{L_T^2}^2 - N\|u\|_{L_T^2}^2.$$

Solving system of equations (6) to (8) gives parameter G , N and C values [9, 12]:

$$(9) \quad G = \frac{(u, i)_{L_T^2}}{\|u\|_{L_T^2}^2},$$

$$(10) \quad N = \frac{(u', i)_{L_T^2} \|u\|_{L_T^2}^2 + (\bar{u}, i)_{L_T^2} \|u'\|_{L_T^2}^2}{\|u'\|_{L_T^2}^2 \|\bar{u}\|_{L_T^2}^2 - \|u\|_{L_T^2}^4},$$

$$(11) \quad C = \frac{(u', i)_{L_T^2} \|\bar{u}\|_{L_T^2}^2 + (\bar{u}, i)_{L_T^2} \|u\|_{L_T^2}^2}{\|u'\|_{L_T^2}^2 \|\bar{u}\|_{L_T^2}^2 - \|u\|_{L_T^2}^4}.$$

For the parallel equivalent circuit (Fig. 1c) with parameters described by (9) to (11) determining active power dissipated in the one-port as well as energy stored in the circuit reactance elements is very straightforward and defined in a unique way which does not bring about any controversy. Orthogonal decomposition of currents (voltages) is also possible for this circuit and moreover it is a special case of the decomposition proposed in [17].

However, the theory, even so attractive as the one described above, should comply with some conditions that we can call applicability conditions:

- I. Structure parameters (Fig. 1c) should not be a result of some intuitive mathematical transformations but rather a consequence of solving some mathematical problems with given physical interpretation.
- II. Formulae (9) to (11) expressing equivalent structure parameter values should be valid for monoharmonic waveforms (a special case of T -periodical signals).

III. Equivalent structure (Fig. 1c) is applicable only if the difference between input currents of systems shown in Fig. 1a and 1c is equal to zero or at least it is sufficiently small for any T -periodical current and voltage waveforms.

IV. If the given one-port (Fig. 1a) is passive then the equivalent structure parameters G , N and C have to be always non-negative.

The following chapter of the paper is devoted to verification of these conditions.

Verification of Applicability Conditions

Verification of the Condition I

The problem of equivalent structure determination for one-ports and multi-poles can be always brought to solving optimization tasks [18, 19, 20, 21, 22]. For the one-port and its parallel equivalent structure shown in Fig. 1a and 1c this task can be formulated as follows: determine parameters G , N and C which ensure that the difference between the equivalent circuit current $i_d(t)$ and the original one-port current $i(t)$ is sufficiently small in the sense of RMS norm assuming that the voltage $u(t)$ and the current $i(t)$ are given and the one-port and the equivalent circuit are supplied with the same voltage $u(t)$. Thus, the following problem of functional $J(G, N, C)$ minimization has to be solved:

$$(12) \quad \min_{G, N, C} J(G, N, C) = \min_{G, N, C} \|i(t) - Gu(t) - Cu'(t) - N\bar{u}(t)\|_{L_T^2}^2 \\ = \min_{G, N, C} \left[(i, i)_{L_T^2} + G^2 (u, u)_{L_T^2} + C^2 (u', u')_{L_T^2} + N^2 (\bar{u}, \bar{u})_{L_T^2} - 2G(u, i)_{L_T^2} - 2C(u', i)_{L_T^2} - 2N(\bar{u}, i)_{L_T^2} + 2GC(u, u')_{L_T^2} + 2GN(u, \bar{u})_{L_T^2} + 2CN(u', \bar{u})_{L_T^2} \right].$$

The necessary conditions of the minimization task (12) result in the system of equations:

$$(13) \quad \begin{bmatrix} (u, u)_{L_T^2} & (u, u')_{L_T^2} & (u, \bar{u})_{L_T^2} \\ (u, u')_{L_T^2} & (u', u')_{L_T^2} & (u', \bar{u})_{L_T^2} \\ (u, \bar{u})_{L_T^2} & (u', \bar{u})_{L_T^2} & (\bar{u}, \bar{u})_{L_T^2} \end{bmatrix} \begin{bmatrix} G \\ C \\ N \end{bmatrix} = \begin{bmatrix} (u, i)_{L_T^2} \\ (u', i)_{L_T^2} \\ (\bar{u}, i)_{L_T^2} \end{bmatrix},$$

which after substitution identities (5) reduces itself to the system of equations (6) to (8) and consequently has the same solution expressed by formulae (9) to (11). This solution determines equivalent one-port parameters G , N and C which are chosen in the way that ensures minimization of the difference in the sense of a norm between given and equivalent one-port output currents for the same input voltage $u(t)$.

Verification of the Condition II

It can be proved that sufficient conditions of functional (12) minimum are fulfilled if the denominator in formulae (10) and (11) is strictly positive. On the other hand taking into account Schwarz inequality and identity (5) the denominator can be rewritten as:

$$(14) \quad \|u'\|_{L_T^2}^2 \|\bar{u}\|_{L_T^2}^2 - \|u\|_{L_T^2}^4 = \\ \left(\|u'\|_{L_T^2} \|\bar{u}\|_{L_T^2} - \|u\|_{L_T^2}^2 \right) \left(\|u'\|_{L_T^2} \|\bar{u}\|_{L_T^2} + \|u\|_{L_T^2}^2 \right) = \\ \left(\|u'\|_{L_T^2} \|\bar{u}\|_{L_T^2} + (u', \bar{u})_{L_T^2} \right) \left(\|u'\|_{L_T^2} \|\bar{u}\|_{L_T^2} + \|u\|_{L_T^2}^2 \right) \geq 0.$$

So the dominator is equal to 0 only if signals $u'(t)$ and $\bar{u}(t)$ are anti-parallel:

$$(15) \quad u'(t) = \alpha \bar{u}(t), \quad \alpha = -1.$$

The last condition is equivalent to:

$$(16) \quad u''(t) + u(t) = 0.$$

The monoharmonic function is the only solution to differential equation (16).

Thus, solution to optimization problem (12) does not exist for sinusoidal waveforms. Consequently, equation (10) and (11) as well as the power theory described in [9, 11, 12] and based on (10) and (11) is not valid for systems with sinusoidal waveforms.

Verification of the Condition III

The equivalence between the one-port shown in Fig. 1a and the parallel connection of G , N and C elements shown in Fig. 1c takes place only if the extreme, defined by formulae (9) to (11), of functional (12) is arbitrary small. Substituting formulae (9), (10) and (11) to goal function in formula (12) and taking into account identities (5) results in:

$$(17) \quad \begin{aligned} J_0 = J(G_{opt}, N_{opt}, C_{opt}) = & \\ = & \|i\|_{L_T^2}^2 - \frac{(u, i)_{L_T^2}}{\|u\|_{L_T^2}} + \\ & + \frac{\left((u', i)_{L_T^2} \|\bar{u}\|_{L_T^2}^2 + (\bar{u}, i)_{L_T^2} \|u\|_{L_T^2}^2 \right)^2}{\left(\|u'\|_{L_T^2}^2 \|\bar{u}\|_{L_T^2}^2 - \|u\|_{L_T^2}^4 \right)^2} \|u'\|_{L_T^2}^2 + \\ & + \frac{\left((u', i)_{L_T^2} \|u\|_{L_T^2}^2 + (\bar{u}, i)_{L_T^2} \|u'\|_{L_T^2}^2 \right)^2}{\left(\|u'\|_{L_T^2}^2 \|\bar{u}\|_{L_T^2}^2 - \|u\|_{L_T^2}^4 \right)^2} \|\bar{u}\|_{L_T^2}^2 - \\ & - 2 \frac{(u', i)_{L_T^2} \|\bar{u}\|_{L_T^2}^2 + (\bar{u}, i)_{L_T^2} \|u\|_{L_T^2}^2}{\|u'\|_{L_T^2}^2 \|\bar{u}\|_{L_T^2}^2 - \|u\|_{L_T^2}^4} (u', i)_{L_T^2} - \\ & - 2 \frac{(u', i)_{L_T^2} \|u\|_{L_T^2}^2 + (\bar{u}, i)_{L_T^2} \|u'\|_{L_T^2}^2}{\|u'\|_{L_T^2}^2 \|\bar{u}\|_{L_T^2}^2 - \|u\|_{L_T^2}^4} (\bar{u}, i)_{L_T^2}. \end{aligned}$$

Analysis of functional (17), expressing the extreme of the goal function, leads to a conclusion that in general J_0 is not equal to zero for arbitrary waveforms $u(t)$ and $i(t)$ belonging to L_T^2 [13]. The subset of T -periodical currents and voltages for which the value of functional (17) is close to zero is unknown. For sure it does not contain sinusoidal waveforms. Thus, one-port approximation by the parallel branch G , N and C is possible only for some pairs of voltage and current signals and in addition it is hard to define the set of these pairs in advance. Construction of a power theory applicable only to some voltage-current pairs ($u(t)$; $i(t)$) is not rational as it is obvious that such theory should be valid for all T -periodical currents and voltages.

Verification of the Condition IV

In the case of passive one-ports the scalar product $(u, i)_{L_T^2}$, interpreted as active power delivered to its terminals, is always positive. It guarantees that the optimum conductance G expressed by (9) is also positive but it does not mean that the parameters N and C are positive as well. In fact, analysis of formulae (10) and (11) leads to a conclusion that depending on the value of scalar products $(u', i)_{L_T^2}$ and $(\bar{u}, i)_{L_T^2}$ the parameters N and C can take also negative values. The following example illustrates this case.

Example

A one-port (Fig. 1a) is described by the input voltage $u(t)$ and current $i(t)$ being periodic signals with fundamental pulsation ω_0 and amplitudes $|U_m|$ and $|I_m|$, respectively:

$$(18) \quad u(t) = \sum_{h=1}^n \frac{4|U_m|}{(2h-1)\pi} \sin[(2h-1)\omega_0 t],$$

$$(19) \quad i(t) = \sum_{h=1}^n \frac{8|I_m|}{[(2h-1)\pi]^2} \sin\left[(2h-1)\left(\omega_0 t + \frac{\alpha\pi}{180^\circ}\right) + (h-1)\pi\right].$$

Let us consider what are the changes of functional (12) minimum and the optimum parameter values if the waveform $u(t)$ is fixed and the waveform $i(t)$ is shifted by angle α , $\alpha \in (0^\circ; 360^\circ)$.

The parallel structure (Fig. 1c) parameter values calculated on the base of formulae (9) to (11) depend on input current phase shift α . It has been shown in Fig. 2 and Fig. 3 for $\omega_0 = 314$ rad/s, amplitudes $|U_m| = 1$ V and $|I_m| = 1$ A.

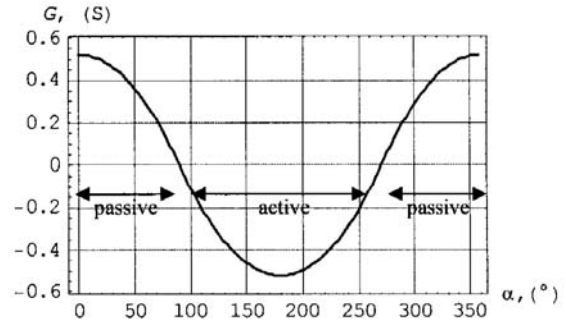


Fig. 2. Optimum conductance G of the parallel structure as a function of input current phase shift α

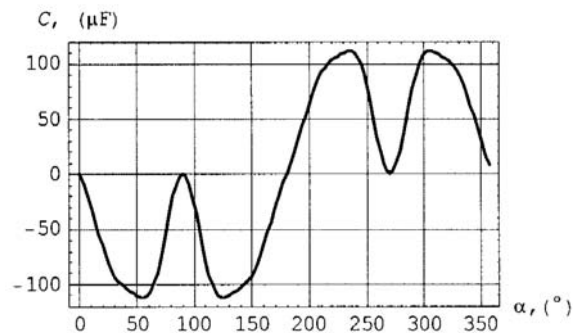


Fig. 3. Optimum capacitance C of the parallel structure as a function of input current phase shift α

It is evident that optimum parameters can take negative values. They are positive only if $\alpha \in (270^\circ; 360^\circ)$, otherwise at least one of them is negative. Moreover, functional J_0 (12) in the extreme point defined by the G , N and C calculated according to (9), (10) and (11) does not take the value 0 with exception to two points for which the phase shift α is equal to 90° or 270° . It can be also seen when analyzing the dependence of relative approximation error δ_i° on the phase shift α . The relative approximation error enables evaluating approximation results despite the signal level – see Fig. 4. It has been defined as a ratio of differential current RMS value and given current RMS value:

$$(20) \quad \delta_i^\circ = \frac{\|\Delta i(t)\|_{L_T^2}}{\|i(t)\|_{L_T^2}} 100\% = \frac{\|i(t) - i_\alpha(t)\|_{L_T^2}}{\|i(t)\|_{L_T^2}} 100\%.$$

It has been checked that even in the case of the input data generated using LLS (linear, lumped and stationary) systems functional (12) does not necessary take the value 0.

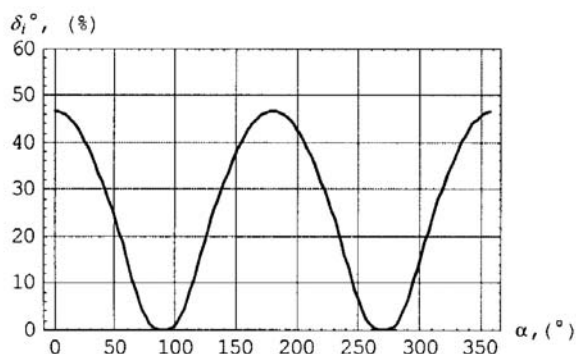


Fig. 4. Relative error δ_i° as a function of input current phase shift α

Conclusions

At first sight the idea of parallel or series simple RLC system assignment to one-ports with given input voltages and currents seems to be very attractive, especially if powers or energies should be defined successively. The paper shows that:

- this idea always leads to solving some optimization problem,
- the problem does not have solution for sinusoidal waveforms,
- the one-port approximation by the RLC system can be of very low quality, which is confirmed by large value of the relative approximation error,
- the RLC parameters could take negative values even for passive one-ports.

The disadvantages listed above are not observed only in some points of periodic voltage and current signal spaces. Power theory, similarly to any other theory, have to be valid not only for some periodic signals but for all of them. So any attempt to build a new power theory or describe energetic properties of circuits on the base of the idea described in [9, 11, 12] is useless. A proposition how to fix this theory in order to obtain correct energetic description of electrical systems has been shown in [14].

REFERENCES

- [1] Czarnecki L. S., Powers and Compensation in Circuits with Periodic Voltages and Currents. Part 2. Outline of the history of power development, *Electr. Power Quality and Utiliz.*, 2 (1997), 37-46
- [2] Ghassemi F., New Concept in AC Power Theory, *IEE Proc. Gen. Transm. and Distrib.*, 147 (2000), 417-424

- [3] Czarnecki L. S., What Is Wrong with the Budeanu's Concept of Reactive and Distortion Powers and Why It Should Be Abandoned, *IEEE Trans. Instr. Meas.*, 36 (1987), 834-837
- [4] Willems J. L., Reflections on Apparent Power and Power Factor in Nonsinusoidal and Polyphase Situations, *IEEE Trans. Power Delivery*, 19 (2004), 835-840
- [5] Czarnecki L. S., Energy Flow and Power Phenomena in Electrical Circuits. Illusions and Reality, *Electr. Eng.*, 82 (2000), 119-126
- [6] Emanuel A. E., Powers in Nonsinusoidal Situations. A Review of Definitions and Physical Meaning, *IEEE Trans. Power Delivery*, 5 (1990), 1377-1389
- [7] Akagi H., Kanazawa Y., Nabe A., Generalized Theory of the Instantaneous Reactive Power in Three-phase Circuits, *Proc. JIEE-IPEC*, (1983), 1375-1380
- [8] Willems J. L., A New Interpretation of Akagi-Nabe Power Components for Nonsinusoidal Three-phase Situations, *IEEE Trans. Instr. Meas.*, 41 (1992), 523-527
- [9] Kijonka J., Circuit Parameter Definitions by Means of Scalar Product of Time-varying Quantities, *Proc. of SPIE Series Microwave and Optical Technology*, 5445 (2004), 266-269
- [10] Emanuel A. E., Summary of IEEE Standard 1459: Definitions for the Measurement of Electric Power Quantities under Sinusoidal, Nonsinusoidal, Balanced and Unbalanced Conditions, *IEEE Trans. Ind. Appl.*, 40 (2004), 869-876
- [11] Kijonka J., Circuit Parameter Determination by Means of Measured Voltage, *Proc. of SPIE Series Microwave and Optical Technology*, 5445 (2004), 270-273
- [12] Orsag P., Kijonka J., Zajaczek S., Benova M., A New Approach to Electrical Circuit Analysis under Nonsinusoidal Conditions, *Proc. of XXVIII Int. Conf. Fundamentals of Electrotechnics and Circuit Theory IC-SPEO*, (2005), 221-224
- [13] Walczak J., Grabowski D., Disadvantages of Equivalent Circuit Application in Power Theory, *Proc. of XXIX Int. Conf. Fundamentals of Electrotechnics and Circuit Theory IC-SPEO*, vol. 2 (2006), 525-528
- [14] Walczak J., Grabowski D., Application of Equivalent Circuits in Power Theory for Systems with Nonsinusoidal Waveforms – New Optimization Concept, *Proc. of International Workshop "Computational Problems of Electrical Engineering"*, (2007), to be published
- [15] Budeanu C. I., Puissance Reactives et Fictives, Inst. Romain de l'Energie, Bucharest, Romania, 1927
- [16] Fryze S., Wirk-, Blind- und Scheinleistung in Elektrischen Stromkreisen mit nicht Sinusformigen Verlauf vom Strom und Spannung, *Elektrotechnische Zeitschr.*, 25 (1932), 569-599
- [17] Czarnecki L. S., Scattered and Reactive Current, Voltage and Power in Circuits with Nonsinusoidal Waveforms and Their Compensation, *IEEE Trans. Instr. Meas.*, 40 (1991), 399-404
- [18] Barba P., Savini A., An Optimization Approach to the Analysis and Synthesis of Circuits and Fields, *Proc. of 3-rd IEEE Conf. Computation in Electromagnetic.*, (1996), 370-375
- [19] Grabowski D., Synthesis of Linear and Nonlinear Electrical Systems by Means of Optimization Methods, Ph.D. dissertation, Faculty of Electrical Eng., Silesian Univ. of Technology, Gliwice, 2000.
- [20] Walczak J., Grabowski D., Optimization Approach to Synthesis of Electrical Circuits, Monograph, 89 (2005), The Publishing House of the Silesian University of Technology, Gliwice
- [21] Walczak J., Grabowski D., A Step Method of Synthesis of Hybrid Filters, *Proc. of IEEE Symp. Power Electronics, Electrical Drives, Advanced Machines, Power Quality SPEEDAM*, (1996), B4-18-21
- [22] Grabowski D., Walczak J., An Optimization Method of Nonlinear System Synthesis, *Proc. of IASTED Conf. Signal and Image Processing and Applications*, (1996), 52-55

Authors: prof. dr hab. inż. Janusz Walczak, Politechnika Śląska, Instytut Elektrotechniki Przemysłowej i Informatyki, ul. Akademicka 10, 44-100 Gliwice, E-mail: janusz.walczak@polsl.pl; dr inż. Dariusz Grabowski, Politechnika Śląska, Instytut Elektrotechniki Przemysłowej i Informatyki, ul. Akademicka 10, 44-100 Gliwice, E-mail: dariusz.grabowski@polsl.pl.

Application of equivalent circuits in power theory for systems with nonsinusoidal waveforms – new optimization concept

Abstract. This work is a continuation of a previous paper containing critical analysis of a newly emerged power theory. The theory assumes approximation of all electrical systems with T -periodical waveforms by series or parallel connections of a linear resistor, an inductor and a capacitor. The paper shows a proposition of its modification which fixes most of the problems. Theoretical considerations have been illustrated by examples.

Streszczenie. Artykuł stanowi kontynuację poprzedniej publikacji i zawiera propozycję modyfikacji sposobu wyznaczania obwodów równoważnych dla układów elektrycznych z przebiegami T -okresowymi. Rozważania teoretyczne zilustrowano przykładami. (Zastosowanie obwodów równoważnych w teorii mocy układów z przebiegami niesinusoidalnymi – nowa koncepcja optymalizacyjna).

Keywords: approximation methods, system modeling, harmonic analysis.

Słowa kluczowe: metody aproksymacji, modelowanie układów, analiza harmoniczna.

Introduction

It is evident [1] that the power theory as it was developed in [2, 3, 4] is practically useless. Generally, the nature of electrical phenomena is too complicated to be described well by a very simple linear system consisting of three basic elements. Nevertheless, it is possible to modify and generalize the method in order to eliminate the drawbacks described in [1].

Idea of synthesis method of equivalent circuits

The modified synthesis algorithm has been shown in Fig. 1 and described below.

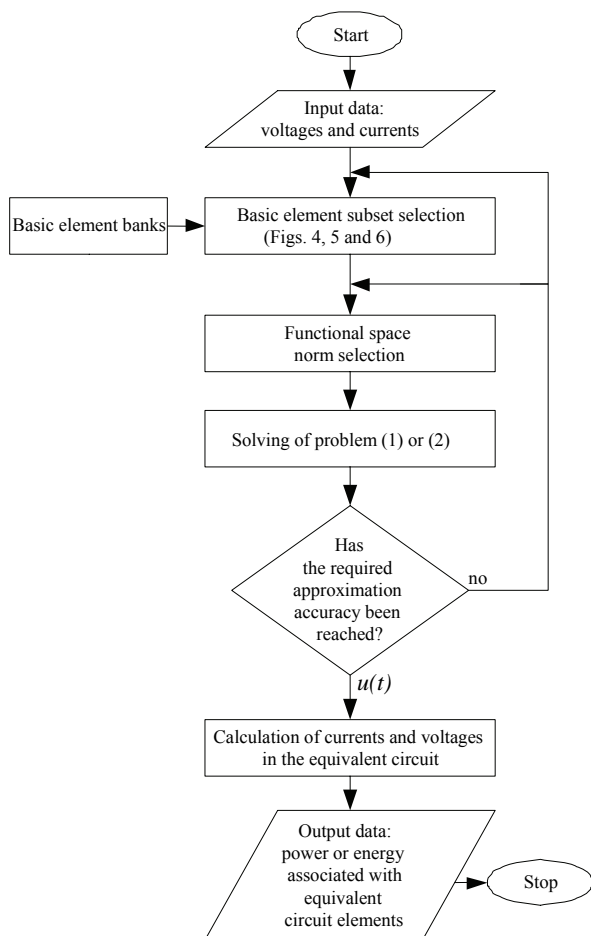


Fig. 1. Algorithm of the generalized approximation method

For a given current-voltage description of a one-port ($u(t), i(t)$) or a multi-port ($\mathbf{u}(t), \mathbf{i}(t)$), $\mathbf{u}(t)=[u_1(t), u_2(t), \dots, u_n(t)]$, $\mathbf{i}(t)=[i_1(t), i_2(t), \dots, i_n(t)]$, the proposed method consists in solving one of the following optimization tasks:

$$(1) \quad \min_X \|i(t) - i_a(t, X)\|_X,$$

or

$$(2) \quad \min_{X^n} \|\mathbf{i}(t) - \mathbf{i}_a(t, X^n)\|_{X^n},$$

with respect to equivalent circuit parameters X or X^n , respectively. The optimization takes place in a signal space to which original circuit voltage-current signals belong and is carried out using scalar (1) or vector norm (2). Depending on a class of signals (e.g. periodic, almost periodic, with finite energy etc.) norms (1) and (2) take different forms and have different physical meaning. Currents $i_a(t)$ and $\mathbf{i}_a(t)$ are responses of an approximation one-port or multi-port to the voltage excitation $u(t)$ or $\mathbf{u}(t)$. Approximation of a system with voltage excitations and current responses is also possible but it does not add anything new to the described concept.

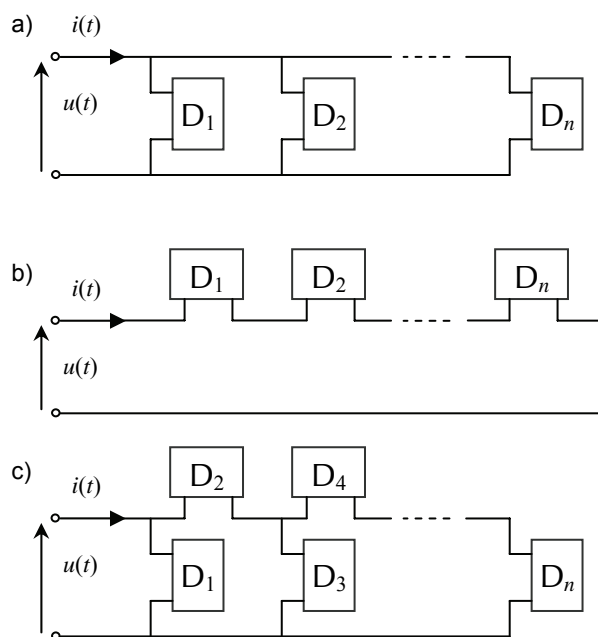


Fig. 2. Basic synthesis structures of one-ports: a) parallel, b) series, c) ladder

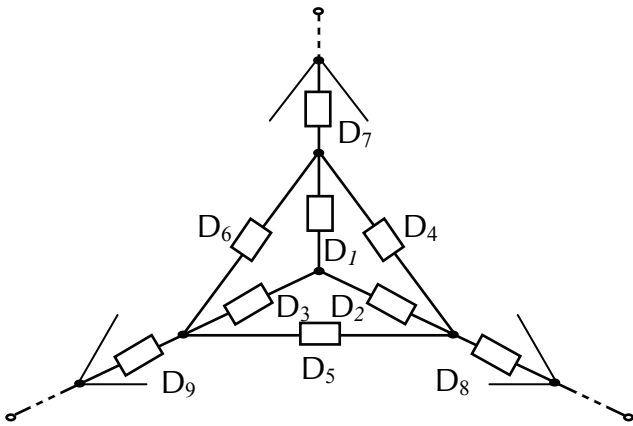


Fig. 3. Exemplary structure of a three terminal system

Approximation one-ports or multi-ports are designed choosing an adequate fixed or varying structure, Figs. 2 and 3. Exemplary banks of basic elements that form the structures are shown in Fig. 4. Some evolution schemes of structures designed with the help of formulae (1) and (2) are presented in Figs. 5 and 6. The optimization tasks are solved by means of gradient or non-gradient methods [5, 6, 7] including neural networks [8] and genetic algorithms [9, 10].

Depending on available information about original system basic element banks (Fig. 4) can include:

- only passive and positive elements R, L, C, M ,
- passive and active elements,
- time-varying elements,
- nonlinear elements,

and also some combination of above classes.

Solution to problems (1) and (2) gives a set of equivalent circuit parameters X or X^n . The value of the corresponding norm (1) or (2) is an indicator of the approximation quality. If it exceeds an acceptable approximation error ε then before repetition of the synthesis procedure:

- the structure of an equivalent circuit can be changed, e.g. parallel replaced by ladder etc. (Fig. 2),
- the varying structure (Figs. 5 and 6) can be used instead of fixed one (Figs. 2 and 3),
- the signal space norm applied as a goal function during optimization process can be changed, e.g. Sobolev norm as an alternative to RMS norm [6, 7],
- a mixture of above suggestions can be used.

The proposed method always allows designing an equivalent circuit (a representing circuit) of a one-port or a multi-port using a given set of structures [5]. Optimization problems (1) and (2) are in fact circuit synthesis problems and so they usually do not have a unique solution. However, it does not bring any restriction to the proposed concept.

The last step consists in analysis of the equivalent circuit obtained by solving of the optimization task. Application of well-known analysis methods results in currents of all circuit branches and voltages across all elements of the circuit. It allows calculation of power and energy associated with circuit elements. Total instantaneous as well as active power and total energy stored in reactive elements L, C and M can be determined with the help of power and energy conservation theorems. Subsequently these quantities, which are time functions except for the active power, can be used as a base for defining some indices playing an important role in power theory. However, it is the other issue and is not covered in this paper.

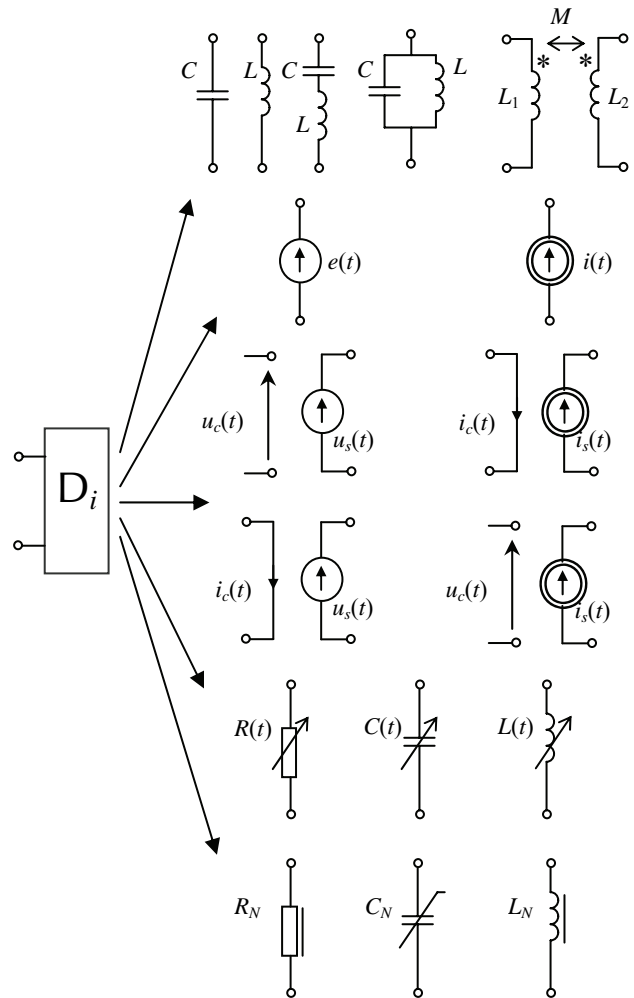


Fig. 4. Exemplary banks of basic elements

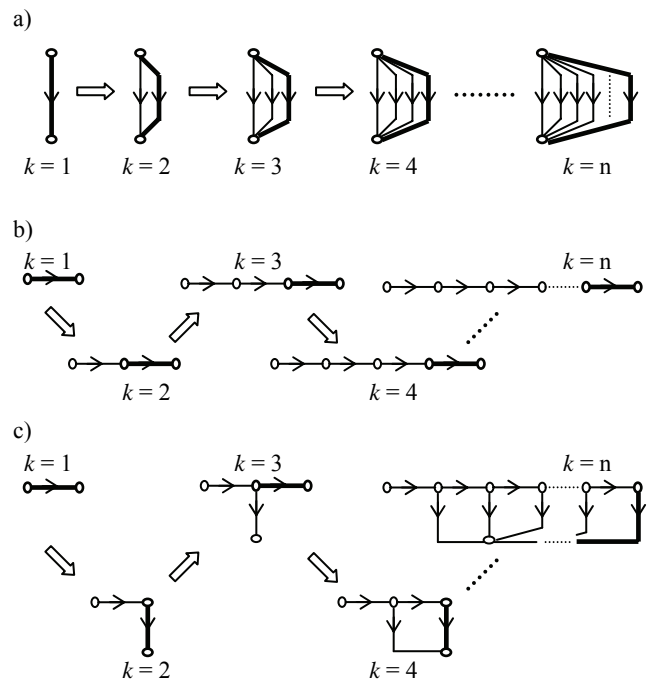


Fig. 5. Evolution of one-port graphs for the successive steps of procedure (1): a) parallel structure, b) series structure c) ladder structure

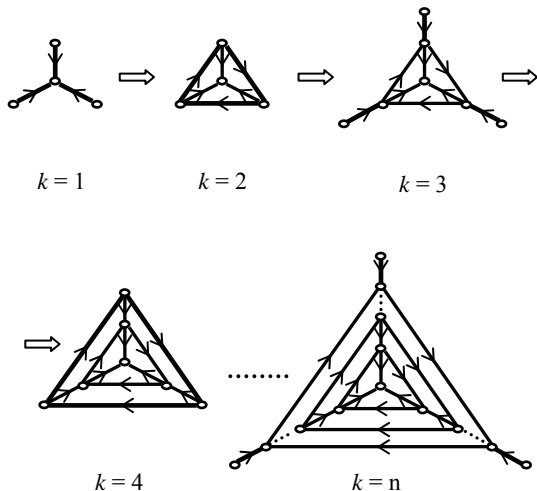


Fig. 6. Exemplary evolution of a three-terminal system graph for the successive steps of procedure (2)

Example 1

Let us consider a one-port with the input voltage $u(t)$ and current $i(t)$ being periodic signals with fundamental pulsation ω_o and amplitudes $|U_m|$ and $|I_m|$, respectively, Fig. 7:

$$(3) \quad u(t) = \sum_{h=1}^n \frac{4|U_m|}{(2h-1)\pi} \sin[(2h-1)\omega_o t],$$

$$(4) \quad i(t) = |I_m| \cos(3\omega_o t).$$

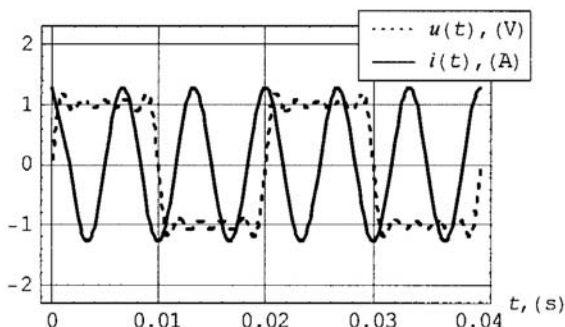


Fig. 7. Given voltage $u(t)$ and current $i(t)$ time waveforms

The one-port filters the input rectangular voltage signal $u(t)$ and as a result gives only the third harmonic output current signal $i(t)$. For $\omega_o = 314$ rad/s, $n = 5$ and amplitudes $|U_m| = 1$ V and $|I_m| = 1.25$ A, the parallel structure (Fig. 2a) obtained on the base of formula (1) using the bank of passive reactive elements (Fig. 4) and genetic algorithms [9, 10] is shown in Fig. 8.

Functional (1) in the extreme point defined by the L_{opt} and C_{opt} takes the value $J_o = 0.0034$ A².

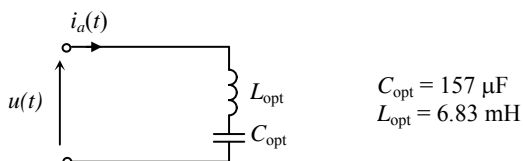


Fig. 8. The designed one-port and its parameters obtained for the proposed optimization approach

The relative approximation error δ_i° [1] is equal to 6.5%. The quality of approximation can be evaluated on the base of Fig. 9 which presents approximation current $i_a(t)$ obtained for the structure (Fig. 8) and given current $i(t)$.

Results, obtained using approach presented in [2, 3, 4], are shown in Fig. 10. In that case the functional (1) reaches only the value $J_o = 0.63$ A² what is equivalent to the relative approximation error $\delta_i^{\circ} = 88\%$.

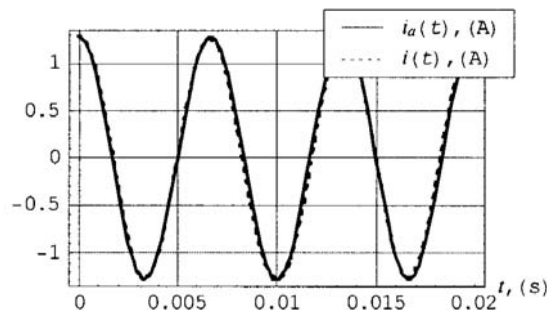


Fig. 9. Comparison of given current $i(t)$ and approximation current $i_a(t)$ obtained for the proposed optimization approach

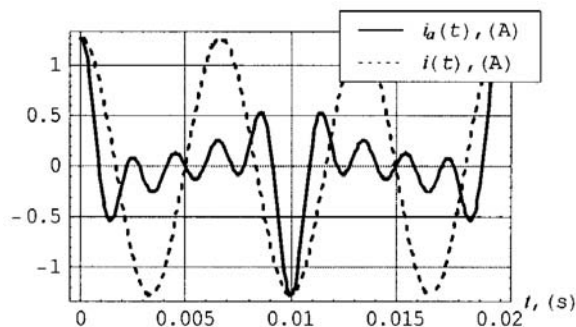


Fig. 10. Comparison of given current $i(t)$ and approximation current $i_a(t)$ obtained for the method described in [2, 3, 4]

Analysis of the designed circuit (Fig. 8) allows calculating energy stored in reactive elements:

$$(5) \quad w_C(t) = \frac{1}{2C_{opt}} \left(\int_{-\infty}^t i_a(t) dt \right)^2 \cong \frac{|I_m|^2}{18\omega_o^2 C_{opt}} \sin^2(3\omega_o t),$$

$$(6) \quad w_L(t) = \frac{1}{2} L_{opt} i_a^2(t) \cong \frac{1}{2} L_{opt} |I_m|^2 \cos^2(3\omega_o t).$$

The energies are functions of current-voltage state of the original circuit ($u(t)$, $i(t)$) and the equivalent circuit parameter values $X = \{L_{opt}, C_{opt}\}$. The example does not include calculation of instantaneous power as well as active power for the one-port (Fig. 8) because their determination is self-evident and does not require synthesis of any equivalent circuit.

Example 2

If a one-port is supplied with the input voltage $u(t)$ given by (3) but we increase the number of harmonics in the current $i(t)$ (Fig. 11):

$$(7) \quad i(t) = \sqrt{2}|I_3|\cos(3\omega_0 t) + \sqrt{2}|I_7|\cos(7\omega_0 t),$$

then the structure shown in Fig. 8 does not allow to reach sufficiently low approximation error. The evolution of the structure according to the scheme in Fig. 5a results in a system shown in Fig. 12.

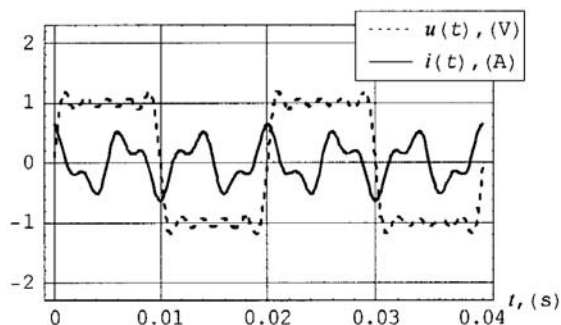


Fig. 11. Given voltage $u(t)$ and current $i(t)$ time waveforms

The parallel structure parameters obtained on the base of formula (1) using the bank of passive reactive elements (Fig. 4) and genetic algorithms [9, 10] for $|I_3| = 0.3$ A and $|I_7| = 0.15$ A are shown in Fig. 12.

Functional (1) in the extreme point defined by the L_1 , C_1 , L_2 and C_2 takes the value $J_o = 0.0005$ A².

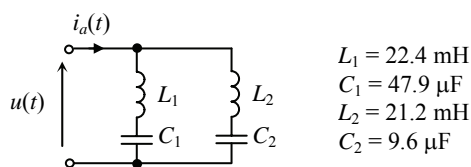


Fig. 12. The designed one-port and its parameters obtained for the proposed optimization approach

The relative approximation error δ_i° [1] is equal to 6.3%. The quality of approximation can be evaluated on the base of Fig. 13 which presents approximation current $i_a(t)$ obtained for the parallel structure (Fig. 12) and given current $i(t)$.

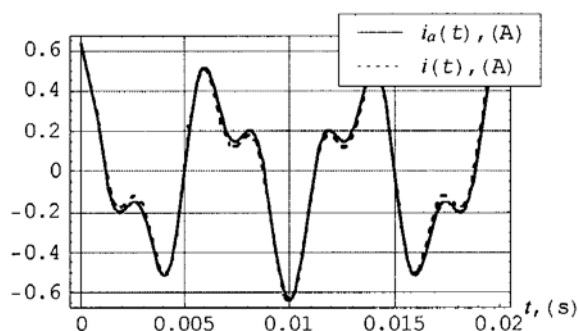


Fig. 13. Comparison of given current $i(t)$ and approximation current $i_a(t)$ obtained for the proposed optimization approach

Results, obtained using approach presented in [2, 3, 4], are shown in Fig. 14. In that case the functional (1) reaches only the value $J_o = 0.065$ A² what is equivalent to the relative approximation error $\delta_i^\circ = 76\%$.

Analysis of the designed circuit (Fig. 12) allows calculating energy stored in reactive elements in a similar way as in Example 1.

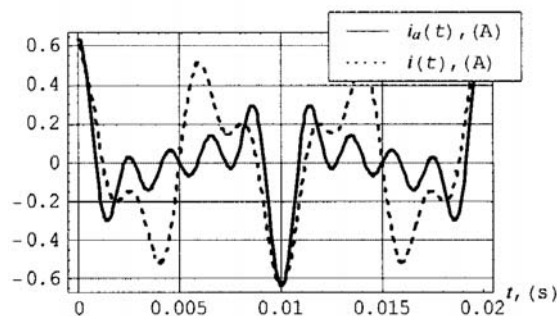


Fig. 14. Comparison of given current $i(t)$ and approximation current $i_a(t)$ obtained for the method described in [2, 3, 4]

Conclusions

The generalization of the theory described in [2, 3, 4] has been proposed in the paper. In fact it is a new concept which should not bring about arguments. The concept consists in association of an equivalent system to a given system with known transmission description. The equivalent system structure is chosen from a bank of available structures and base elements by means of solving some optimization tasks. Analysis of currents and voltages in the equivalent system allows determining powers and/or energies associated with circuit elements. Construction of new power definitions on the base of calculated quantities is the other problem which remains unsolved up to now.

REFERENCES

- [1] Walczak J., Grabowski D., Application of Equivalent Circuits in Power Theory for Systems with Nonsinusoidal Waveforms – Critical Remarks, *Proc. of Int. Workshop Computational Probl. of Electr. Eng.*, (2007), to be published
- [2] Kijonka J., Circuit Parameter Definitions by Means of Scalar Product of Time-varying Quantities, *Proc. of SPIE Series Microwave and Optical Techn.*, 5445 (2004), 266-269
- [3] Kijonka J., Circuit Parameter Determination by Means of Measured Voltage, *Proc. of SPIE Series Microwave and Optical Techn.*, 5445 (2004), 270-273
- [4] Orsag P., Kijonka J., Zajaczek S., Benova M., A New Approach to Electrical Circuit Analysis under Nonsinusoidal Conditions, *Proc. of XXVIII Int. Conf. Fund. of Electrotechn. and Circuit Theory IC-SPETO*, (2005), 221-224
- [5] Walczak J., Grabowski D., Optimization Approach to Synthesis of Electrical Circuits, Monograph, 89 (2005), The Publishing House of the Silesian University of Technology, Gliwice
- [6] Walczak J., Grabowski D., A Step Method of Synthesis of Hybrid Filters, *Proc. of IEEE Symp. Power Electronics, Electrical Drives, Advanced Machines, Power Quality SPEEDAM*, (1996), B4-18-21
- [7] Grabowski D., Walczak J., An Optimization Method of Nonlinear System Synthesis, *Proc. of IASTED Conf. Signal and Image Processing and Applications*, (1996), 52-55
- [8] Grabowski D., Walczak J., Swiszczyk P., The Neural Solution to Reactive Compensation Problem in Systems with Nonsinusoidal Waveforms, *Proc. of ICSC/IFAC Symp. Neural Computation*, (1998), 499-505
- [9] Walczak J., Grabowski D., Application of Genetic Algorithms to Design of Passive Filters, *Proc. of IEEE Conf. Power Electronics and Motion Control PEMC*, (1998), 7-89-92
- [10] Goldberg D. E., Genetic Algorithms in Search, Optimization and Machine Learning, Addison-Wesley, 1989

Authors: prof. dr hab. inż. Janusz Walczak, Politechnika Śląska, Instytut Elektrotechniki Przemysłowej i Informatyki, ul. Akademicka 10, 44-100 Gliwice, E-mail: janusz.walczak@polsl.pl; dr inż. Dariusz Grabowski, Politechnika Śląska, Instytut Elektrotechniki Przemysłowej i Informatyki, ul. Akademicka 10, 44-100 Gliwice, E-mail: dariusz.grabowski@polsl.pl

Models of nonlinear one-ports supplied with periodic and discontinuous waveforms

Abstract. Analysis of harmonics propagation in electrical systems requires information about nonlinear one-ports which are the main source of harmonics. A method of determination of parameters of the model of one-port has been described in this article for periodical and discontinuous excitations. This method has been developed assuming that mathematical description of a nonlinear one-port is known.

Streszczenie. Analiza propagacji harmoniczných w układach elektrycznych wymaga znajomości modeli dwójników nieliniowych stanowiących podstawowe źródła tych harmoniczných. W artykule opisano metodę wyznaczania parametrów wymienionego modelu dwójnika nieliniowego dla wymuszeń okresowych i nieciągłych. Metoda ta zakłada znajomość opisu matematycznego charakterystyki dwójnika nieliniowego. (Modele nieliniowych dwójników dla wymuszeń okresowych i nieciągłych)

Keywords: nonlinear systems, harmonics propagation, harmonic analysis.

Słowa kluczowe: układy nieliniowe, propagacja harmoniczných, analiza harmoniczna.

Introduction

Analysis of phenomena occurring in electrical systems with nonsinusoidal waveforms requires information about nonlinear one-ports [3] which are the main source of harmonics. Nonlinear elements included either in load or switching part of the system are the main reason of distortions. In contemporary electrical energy conversion and utilization systems distorted waveforms are present in control circuits for power elements or at the output terminals of these elements. Methods used for distorted waveforms generation include among others impulse modulation techniques [9]. The very important and complex point consists in their analysis which can be done either in time or frequency domain. The complexity of the problem in the case of time analysis increase along with the complexity of switching circuit [1],[2]. The proposed method allows determination of nonlinear frequency models of systems supplied with periodic and discontinuous time waveforms assuming that solution contains periodic component having representation in the form of Fourier series. Example of waveforms under consideration have been shown in Fig. 1.

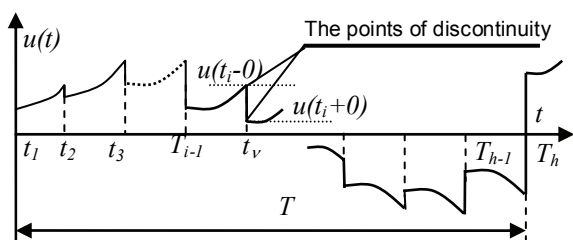


Fig. 1 Exemplary periodic and discontinuous polynomial waveform of voltage

Frequency representations for these waveforms can be determined by many methods, e.g. the double Fourier series, the Fourier theory with jumps FTJ, the harmonic balance method, the describing function method [1],[2],[9]. These methods together with methods introduced earlier [7],[8] enable to obtain accurate solutions in a closed form.

Formalisation of the problem

The waveforms shown in Fig. 1 can be analytically described in time and frequency domains. A case of periodic and piecewise continuous function with period T (Fig. 1) has been considered in this article. The period T has been divided into $h-1$ time intervals in which function

$u(t)$ has h discontinuous points. This function can be expressed by the following formula [5],[6]:

$$(1) \quad u(t) = \sum_{i=1}^{h-1} \gamma_i t^{l_i},$$

where: γ_i, l_i - integer values, t_{h_i} - the discontinuous point.

The function (1) can be treated as homogenous function for the constant coefficient α in every time interval. This case considerably simplifies carried out considerations. The function (1) have the following property in every interval, except bounds [4]:

$$(2) \quad u^{(p)}(t) = \frac{1}{l_i(l_i-1) \cdot \dots \cdot (l_i-p+1)} \sum_{i=1}^{h-1} \gamma_i t^{l_i-p},$$

where: $p \leq l_i$ and $u^{(p)}(t)$ denotes p -th order derivative of $u(t)$, and:

$$(3) \quad u(t) e^{\beta t} \Big|_0^T = - \sum_{i=1}^h \delta_i^{(p)} e^{\beta t_i},$$

where: $\delta_i^{(p)} = f^{(p)}(t_i+0) - f^{(p)}(t_i-0)$ is the jump of the function (1) in point t_i , β - integer value.

The property (3) has been obtained from the following formula by collecting terms with the same index i :

$$(4) \quad u^{(p)}(t) e^{\beta t} \Big|_0^T = \sum_{i=1}^h \left[u^{(p)}(t_i-0) e^{\beta t_i} - u^{(p)}(t_{i-1}+0) e^{\beta t_{i-1}} \right],$$

where: $u^{(p)}(t_i-0)$ - a $u^{(p)}$ - the left hand limit at point t_i ,
 $u^{(p)}(t_{i-1}+0)$ - a $u^{(p)}$ - the right hand limit at point t_{i-1} .

Coefficients of the Fourier series can be written as follows:

$$(5) \quad C_h = \frac{2}{T} \int_0^T u(t) \cos\left(h \frac{2\pi}{T} t\right) dt,$$

$$(6) \quad D_h = \frac{2}{T} \int_0^T u(t) \sin\left(h \frac{2\pi}{T} t\right) dt$$

Using the properties (2) and (3) the coefficients C_h, D_h of the Fourier series can be expressed by the following formulae:

$$(7) \quad C_h = \frac{2}{T} \sum_{p=0}^l \sum_{i=1}^h \frac{(-1)^{p+1}}{\left(h \frac{2\pi}{T}\right)^{2p+1}} \cdot \left[\frac{\delta_i^{(2p+1)}}{h \frac{2\pi}{T}} \cos\left(h \frac{2\pi}{T} t_i\right) + \delta_i^{(2p)} \sin\left(h \frac{2\pi}{T} t_i\right) \right]$$

$$(8) \quad D_h = \frac{2}{T} \sum_{p=0}^l \sum_{i=1}^h \frac{(-1)^{p+1}}{\left(h \frac{2\pi}{T}\right)^{2p+1}} \cdot \left[\delta_i^{(2p)} \cos\left(h \frac{2\pi}{T} t_i\right) + \frac{\delta_i^{(2p+1)}}{h \frac{2\pi}{T}} \sin\left(h \frac{2\pi}{T} t_i\right) \right]$$

In relation to (7) and (8) the waveform of the voltage $u(t)$ can be determined by:

$$(9) \quad u(t) = \sum_{h=1}^l C_h \cos\left(h \frac{2\pi}{T} t\right) + D_h \sin\left(h \frac{2\pi}{T} t\right)$$

Models of the nonlinear one-phase loads for the nonsinusoidal waveforms have been shown in Fig. 2.

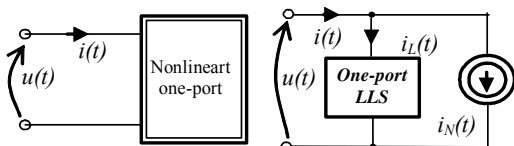


Fig. 2. Models of the nonlinear one-phase loads for the nonsinusoidal waveforms

Assuming that nonlinear load is described by the polynomial inertialess operator:

$$(10) \quad i_N(t) = \sum_{k=1}^n a_k u^k(t), \quad a_k \in R.$$

The expression of the current (Fig. 2) can be written as:

$$(11) \quad i(t) = i_L(t) + i_N(t) = \int_0^T y(t-\tau) u(\tau) d\tau + \sum_{h \in N} A_h(C_h, D_h) \cos\left(h \frac{2\pi}{T} t\right) + B_h(C_h, D_h) \sin\left(h \frac{2\pi}{T} t\right)$$

where: $y(\cdot)$ - the impulse response function of the one-port, $u(t)$ - the voltage (8) across system terminals (Fig. 2), $A_h(C_h, D_h), B_h(C_h, D_h)$ - harmonics of current of the current source (Fig. 2).

The coefficients $A_h(C_h, D_h), B_h(C_h, D_h)$ can be expressed in form:

$$(12) \quad A_h(C_h, D_h) = \frac{2}{T} \int_0^T \left(\sum_{k=1}^n a_k \left(\sum_{h=1}^l C_h \cos\left(h \frac{2\pi}{T} t\right) + D_h \sin\left(h \frac{2\pi}{T} t\right) \right) \cos\left(h \frac{2\pi}{T} t\right) \right) dt$$

$$(13) \quad B_h(C_h, D_h) = \frac{2}{T} \int_0^T \left(\sum_{k=1}^n a_k \left(\sum_{h=1}^l C_h \cos\left(h \frac{2\pi}{T} t\right) + D_h \sin\left(h \frac{2\pi}{T} t\right) \right) \sin\left(h \frac{2\pi}{T} t\right) \right) dt$$

Impedance Z_1 :

$$(14) \quad Z_1 = (\{C_h\}, \{D_h\}) = \frac{C_1 - jD_1}{A_1(\{C_h\}, \{D_h\}) - jB_1(\{C_h\}, \{D_h\})} R(\{C_h\}, \{D_h\}) - jX(\{C_h\}, \{D_h\})$$

represents the LLS one-port in the model shown in Fig. 2. The diagram has been presented in Fig. 3 for single harmonic and assumed for nonlinear one-port characteristic.

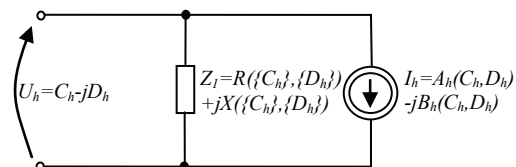


Fig. 3 Schematic diagram of the systems from fig. 2 for a single harmonic

Further calculations have been made for specific parameter values of the voltage $u(t)$ (1) and polynomial element described by formula (9).

Example

On the basis of carried out considerations, the calculation example has been done using symbolic operation of the *MatLab*™ software. This example concerns a simple system containing a relaxation oscillator with a voltage limiter. The system has been presented in fig. 4.

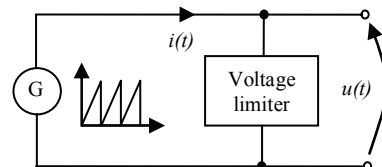


Fig. 4 Schematic diagram of the considered system

In accordance with the formula (1), the waveform of the voltage of relaxation oscillator can be describe by the following polynomial function:

$$(15) \quad u(t) = t^2, \text{ for } 0 \leq t \leq T.$$

This waveform is shown in Fig. 5.

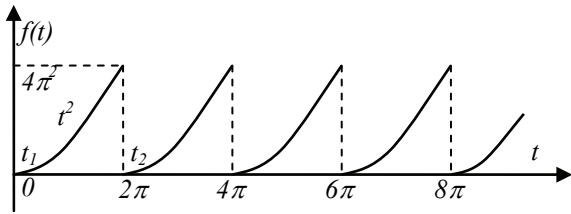


Fig. 5 The waveform of the voltage of relaxation oscillator

The function (15) has two points of discontinuity (Fig. 1). The required parameters for calculations of Fourier coefficients C_h (7) and D_h (8) have been shown in Table 1.

Table 1. The parameters for calculations of Fourier coefficients C_h (7) and D_h (8)

| Discontinuity point | Value at the discontinuity point | Value of the first derivative at discontinuity point | Value of the second derivative at discontinuity point |
|---------------------|----------------------------------|--|---|
| $t_1=0$ | $\delta_1=0$ | $\delta'_1=0$ | $\delta''_1=2$ |
| $t_2=2\pi$ | $\delta_2=-4\pi^2$ | $\delta'_2=-4\pi$ | $\delta''_2=-2$ |

The constant component and the Fourier coefficients (7) (8) for the parameters from Table 1 are equal:

$$(16) \quad U_o = \frac{8\pi^2}{3},$$

$$(17) \quad C_h = \frac{4}{h^2},$$

$$(18) \quad D_h = -\frac{4\pi}{h}.$$

The characteristic of the nonlinear one-port has been described by the following formula:

$$(19) \quad i = 0.00006u + 0.000015u^3,$$

and shown in Fig. 6.

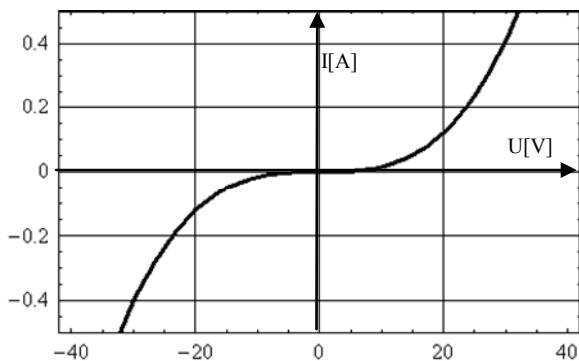


Fig. 6 The characteristic of the nonlinear one-port

The exemplary results of calculations of Fourier coefficients (12), (13) for the known coefficients of polynomial functions (19) show the following expressions:

$$(20) \quad A_1 = 0.00001125 D_2 C_4 D_5 + 0.00001125 C_1 C_5^2 - 0.00001125 D_1 D_3 C_5 + 0.00001125 D_2 C_2 D_5 + 0.00003 C_1 + 0.5625e-5 C_1^3 + 0.5625e-5 C_1 D_1^2 + 0.00001125 D_1 C_3 D_5 + 0.00001125 C_1 D_1 D_3 + 0.0000225 U_0 D_3 D_4 + 0.00001125 C_1 C_3^3 + 0.0000225 U_0 C_1 C_2$$

$$-0.00001125 D_2 D_1 C_4 + 0.0000225 U_0 D_2 D_3 + 0.00001125 C_2 D_4 D_5 + 0.00001125 C_1 D_3 D_5 + 0.00001125 C_2 D_3 D_4 + 0.00001125 C_3 D_3 D_5 + 0.00001125 D_2 C_3 D_4 + 0.5625e-5 C_1^2 C_3 - 0.5625e-5 D_2 C_5 + 0.00001125 C_1 D_2^2 D_4 + 0.0000225 U_0 C_3 C_4 + 0.0000225 U_0 D_1 D_2 + 0.0000225 U_0 D_4 D_5 + 0.0000225 U_0 C_2 C_3 + 0.5625e-5 C_3^2 C_5 + 0.00001125 C_1 D_2^2 + 0.00001125 C_2 C_3 C_4 - 0.5625e-5 D_3^2 C_5 + 0.00001125 D_2 C_2 D_3 + 0.00001125 C_1 D_4^2 + 0.00001125 C_1 D_3^2 + 0.00001125 C_1 C_2 C_4 - 0.562500e-5 D_1^2 C_3 - 0.5625e-5 D_2^2 C_3 + 0.5625e-5 C_2 C_3 + 0.00001125 C_1 C_4^2 + 0.5625e-5 C_2^2 C_5 - 0.00001125 D_2 D_4 C_5 + 0.00001125 C_2 C_4 C_5 + 0.0000225 U_0 C_4 C_5 + 0.0000112500 C_1 C_3 C_5 - 0.00001125 D_2 D_3 C_4 + 0.00001125 C_1 C_2^2 + 0.00001125 C_1 D_5^2 + 0.00001125 D_1 C_2 D_4 + 0.0000225 U_0^2 C_1$$

$$B_1 = 0.0000225 U_0 C_4 D_5 - 0.5625e-5 D_1^2 D_3 - 0.00001125 C_1 D_1 C_3 + 0.00001125 D_2 C_3 C_4 + 0.0000225 U_0 C_3 D_4 - 0.0000225 U_0 D_3 C_4 + 0.5625e-5 C_1^2 D_1 + 0.00001125 D_2 C_4 C_5 + 0.5625e-5 D_1^3 + 0.00003 D_1 + 0.00001125 C_1 C_2 D_4 - 0.00001125 C_1 D_3 C_5 + 0.00001125 D_1 D_3^2 + 0.00001125 C_3 D_3 C_5 + 0.00001125 D_1 D_4^2 - 0.00001125 C_2 C_4 D_5 + 0.00001125 D_1 C_2^2 - 0.0000225 D_2 U_0 C_3 - 0.00001125 D_2 C_2 C_5 + 0.0000225 U_0 C_1 D_2 - 0.00001125 C_1 D_2 C_4 - 0.5625e-5 C_3^2 D_5 + 0.00001125 D_1 C_3^2 + 0.00001125 D_2 C_2 C_3 + 0.00001125 D_2 D_4 D_5 - 0.00001125 D_2 D_1 D_4 + 0.0000225 U_0^2 D_1 + 0.0000225 U_0 C_2^2 D_3 + 0.00001125 C_2 D_3^2 C_4 - 0.5625e-5 C_2 D_3 + 0.5625e-5 D_3 D_5 - 0.0000225 C_0 D_4 C_5 - 0.5625e-5 D_2^2 D_5 + 0.00001125 C_2 D_4 C_5 + 0.00001125 D_1 D_2^2 + 0.5625e-5 C_1^2 D_3 + 0.00001125 D_1 C_4^2 + 0.00001125 D_1 D_5^2 + 0.00001125 C_1 C_3 D_5 - 0.00001125 D_1 C_2 C_4 - 0.00001125 C_2 C_3 D_4 - 0.00001125 D_1 D_3 D_5 - 0.0000225 C_0 D_1 C_2 + 0.00001125 D_2 D_3 D_4 + 0.00001125 D_1 C_5^2 + 0.5625e-5 D_2^2 D_3 + 0.5625e-5 C_2^2 D_5 - 0.00001125 D_1 C_3 C_5$$

The frequency representation of the system shown in fig. 3 can be written in the closed form by the following generalized expressions:

$$(22) \quad Z_1 = \frac{C_1 - jD_1}{A_1 - jB_1},$$

$$(23) \quad i_h(t) = |I_{mh}| \sin(2\pi h t + \varphi_h),$$

where:

$$(24) \quad |I_{mh}| = \sqrt{A_h^2 + B_h^2},$$

$$(25) \quad \varphi_h = \text{ArcTan} \frac{B_h}{A_h}.$$

The exemplary dependences of:

- the first and third harmonic modules $|I_{m1}|$ and $|I_{m3}|$ of the current source (Fig. 2),
 - the phases φ_1 and φ_3 of the first and third harmonic of the source current,
- on coefficients C_1 and D_1 have been presented in Fig. 7, 8, 9 and 10 in form of 3D diagrams.

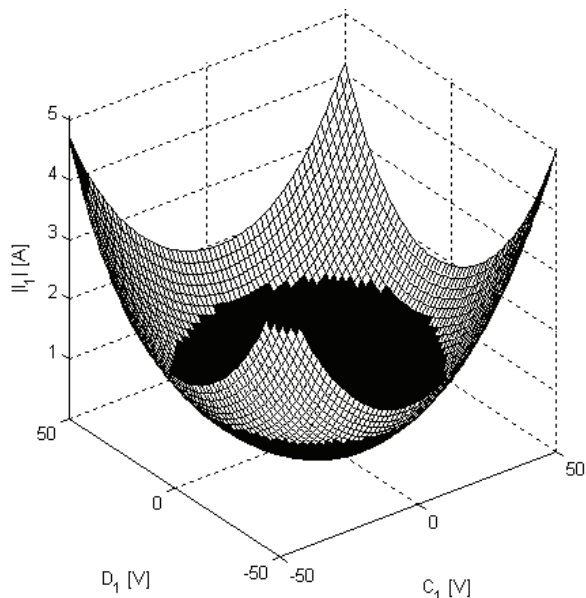


Fig. 7 The dependence of the first harmonic module $|I_{m1}|$ of the current source on coefficients C_1 and D_1

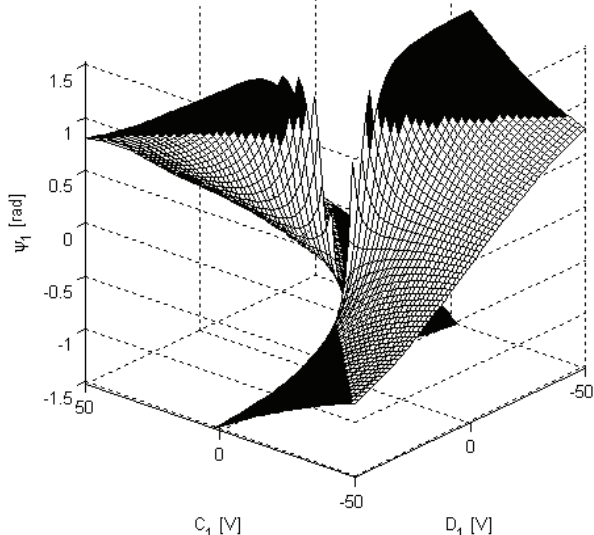


Fig. 8 The dependence of the phase ϕ_1 of the first harmonic of the current source on coefficients C_1 and D_1

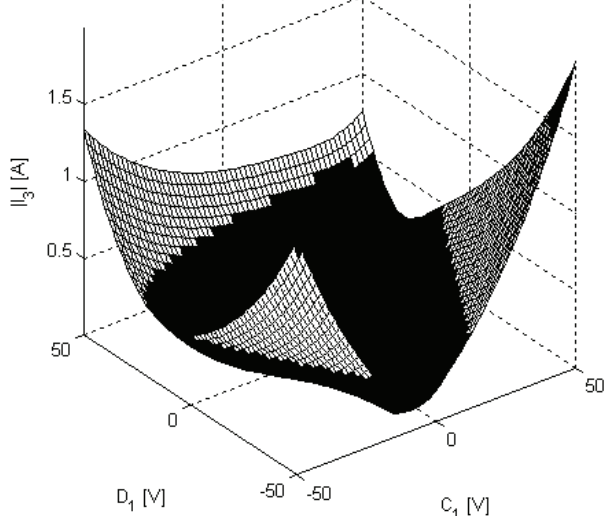


Fig. 9 The dependence of the third harmonic module $|I_{m3}|$ of the current source on coefficients C_1 and D_1

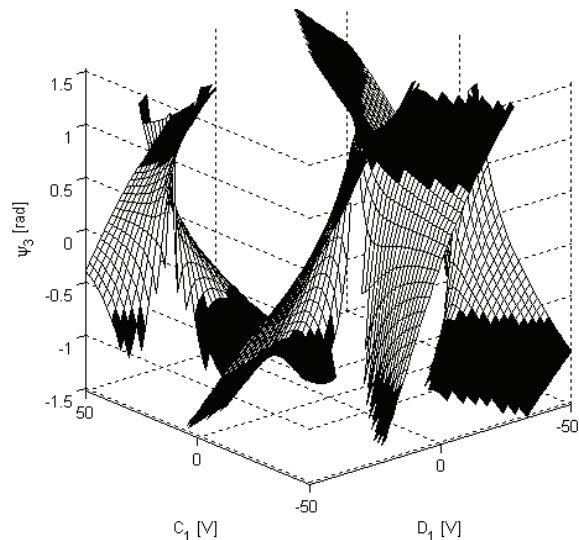


Fig. 10 The dependence of the phase ϕ_3 of the third harmonic of the current source on coefficients C_1 and D_1

Summary

The presented method in the paper enables relatively simple the determination of: the Fourier coefficients of the periodic and discontinuous function $u(t)$. This method replace the integrating operation by the algebraic additions of the jumps of the functions $u(t)$ and its derivative at the points of discontinuity. This approach enables to obtain the frequency parameters of the one-port in closed form for periodic and discontinuous excitations. Closed-form expressions allow to obtain effective control algorithm for various electrical energy conversion systems.

REFERENCES

- [1] Brambilla A, D'Amore D.: A Filter-Based Technique for the Harmonic Balance Method. *IEEE Trans. On CAS- I: Fundamental Theory and Appl*, Vol. 43, No. 2 February 1996, pp. 92-97.
- [2] Chung H.S.H., Ioinovici A.: Frequency Domain Simulation of Power Electronics Circuits by Using Describing Functions in a Modified Nodal Approach. *Proceeding on the 37 Midwest Symposium on Circuits and System*. 3-5 Autost 1994, Lafayette, USA, vol. 2, pp. 1269-1272.
- [3] Heydt G., Neil-Carillo O., Zhou R.: The Modelling of Nonlinear Loads in Electrical Engineering. *IEEE Trans. On Power Delivery*, no 5, Vol. 16, May 1996, pp. 523-530.
- [4] Kreyszig E.: *Advanced Engineering Mathematics*. (8th ed.) New York, John Wiley & Sons, Inc. 1999.
- [5] Slonim M.A.: Harmonic Analysis of periodic Discontinuous Functions (New Method). Part I-Exponential Functions. *Proceedings of the IEEE*, Vol. 67, No. 6 June 1979, pp. 952-953.
- [6] Slonim M.A.: Harmonic Analysis of periodic Discontinuous Functions (New Method). Part II-Exponential Functions. *Proceedings of the IEEE*, Vol. 67, No. 6 June 1979, pp. 953-954.
- [7] Walczak J., Świszcz P.: Frequency Representations of One-Port Networks. *COMPEL The Int. J. for Comp. and Math. in Electrical and Electronic Engineering*, Vol. 24, No. 4, 2005, pp. 1142-1151.
- [8] Walczak J., Świszcz P.: Models of Nonlinear and Inertiales Loads in Frequency Domain. *XXV IC SPETO*. 22-25 May, Ustroń, 2002, pp. 257-260.
- [9] Tooth D.J., Finney S.J., Williams B.W.: Fourier Theory of Jumps Applied to Converter Harmonic Analysis. *IEEE Trans. on Aerospace and Electronic Systems*, Vol. 37, No. 1, January 2001, pp. 109-122.

Author: dr inż. Piotr Świszcz, Politechnika Śląska, Instytut Elektrotechniki Przemysłowej i Informatyki, ul. Akademicka 10, 44-100 Poznań, E-mail: piotr.swiszcz@polsl.pl.

Sensitivity analysis of linear regression solution based on modified York's equation

Abstract. This paper presents a new approach to York's equation. The problem relies on sensitivity analysing of linear relation measurement data depending on its uncertainty. The calculated calibration straight line slope is presented using modified York's equation. The modification relies on considering solution sensitivity versus measurement data uncertainty.

Streszczenie. Praca poświęcona jest analizie wrażliwości relacji liniowej uwzględniającej na niepewności oszacowania danych pomiarowych. Artykuł przedstawia modyfikację problemu zaprezentowanego przez York'a i dotyczy równania nachylenia prostej kalibracyjnej z analizą wrażliwości rozwiązania. (Analiza wrażliwości relacji liniowej uwzględniająca niepewności oszacowania danych pomiarowych)

Keywords: sensitivity analysis of linear regression, modified York's equation

Słowa kluczowe: analiza wrażliwości rozwiązania regresji liniowej, zmodyfikowane równanie York'a

Introduction

In the industry and scientific world the information how the linear approximation relation is changing for the measurement data, is often needed. Measurement data characterizes the uncertainty of its estimation. A basic linear relation can be obtained by using regression analysis. However the information characterizing relation between the calibrating straight line and the uncertainty measurement data is still needed.

The linear regression analysis is used in a lot of problems, for example in model of the asynchronous machine [9].

The first articles in the above mentioned domain, has taken place in sixtieth years of previous age (York [1], Williamson [2]) and nowadays this domain is still active and the scientists discover fresh view on this problem [3, 4].

This paper considers the new quadratic equation aspect for estimating the best slope b [3]. The new approach relies on modifying York's equation. Additionally the solution of the sensitivity analysis problem is considered.

The purpose of this paper is to describe an easy programmable least-squares method which is applied to fit experimental data to straight-line models with any number of variables which are subject to error.

Table 1. Applied notation in the article.

| Symbol | Meaning |
|------------------|--|
| a, b | Intercept and slope of the best line $y=a+bx$ |
| X_i, Y_i | observed data points |
| x_i, y_i | least-squares adjusted points expectation values of X_i, Y_i |
| $w(X_i), w(Y_i)$ | weights of X_i, Y_i |
| W_i | weight factor W_i for each point |
| \bar{X} | $\frac{\sum_i W_i X_i}{\sum_i W_i}$ |
| \bar{Y} | $\frac{\sum_i W_i Y_i}{\sum_i W_i}$ |
| s_x^2 | variance of X_i |
| s_y^2 | variance of Y_i |

Slope and intercept estimation

In this paper we apply the same notation as in the original paper [3].

Finding the best fit line describing the experimental data relies on minimization of the following equation:

$$(1) \quad S = \sum_{i=1}^n W_i (Y_i - a - bX_i)^2$$

Solution of equation (1) for a and b using minimization of the function S is complex because the obtained normal equations are non-linear. Hence the weight vector W_i is in the non-linear relation with the slope and the measurement data variances.

Used in a lot of articles weight vector, introduced by York and Deming, is given by (2).

$$(2) \quad W_i = \frac{1}{b^2 s_x^2 + s_y^2}$$

The other forms of the weight vector are presented in references [4], [7] which are non-linear as well. The minimization of the objective function S leads to the following equations.

(3a)

$$\frac{dS}{db} = -2 \sum_i W_i X_i (Y_i - bX_i - a) + \sum_i \frac{dW_i}{db} (Y_i - bX_i - a)^2 = 0$$

$$(3b) \quad \frac{dS}{da} = -2 \sum_i W_i (Y_i - bX_i - a) = 0$$

Using the notations from table 1 we obtain:

$$(4) \quad \bar{Y} = a + b\bar{X}$$

Signifying $U_i = -\frac{1}{2} \frac{dW_i}{db}$ after many transformations we obtain the following second degree equation (5)

$$(5) \quad B_1 \cdot b^2 + B_2 \cdot b + B_3 = 0$$

where:

$$(6) \quad B_1 = \sum_i U_i X_i^2 + \bar{X}_i^2 \sum_i U_i - 2\bar{X}_i \sum_i U_i X_i$$

$$(7) B_2 = -\sum_i W_i X_i^2 + \bar{X} \sum_i W_i X_i - 2 \sum_i U_i X_i Y_i + 2 \bar{Y} \sum_i U_i Y_i - 2 X_i Y_i \sum_i U_i$$

$$(8) B_3 = \sum_i W_i X_i Y_i - \bar{Y} \sum_i W_i X_i - \sum_i U_i Y_i + Y_i^2 \sum_i U_i - 2 Y \sum_i U_i Y_i$$

The equation (5) will be applied for the further analysis presented in the paper.

Analysis of solution

York presented cubic, quadratic and linear equations for the best slope b . All three equations yields are identical to the best b calculated using (5). He developed the iterative method called "least squares cubic" consisting of estimating initial values for the calibration line slope and then solved cubic equation, given by:

$$(9) f(b) = b^3 - 3ab^2 + 3\beta b - \gamma = 0$$

In the references [3] York has re-examined the method and tried to clarify some points. The problem relies on the equation (9) which is really cubic because of the implicit dependence on the slope. Williamson [2] showed that equation in York's method is redundant and can be written as a linear equation.

Mentioned above regression methods characterize various computing complexity and different forms of W_i coefficient. Nowadays the research showed that the best algorithm used to linear regression coefficients calculation does not exist in general case. The statistical properties of data set and uncertainty measurement data decide which form of algorithm is the best. The important property of equation (5) is universality applying different forms W_i .

Variance computing optimisation

From the measurement point of view the variance optimisation of slope and intercept point is important, because sometimes we can obtain uncertainty reduction of mentioned parameters by applying variance modification of measurement points.

The estimation error in the slope b is given by

$$(10) (\sigma_b)^2 = \sum_i \left[\left(\frac{db}{dX_i} \right)^2 \cdot s_X^2 + \left(\frac{db}{dY_i} \right)^2 \cdot s_Y^2 \right]$$

with

$$(11) \frac{db}{dX_i} = \frac{dF/dX_i}{dF/db}$$

where

$$(12) F = B_1 \cdot b^2 + B_2 \cdot b + B_3$$

The derivative $\frac{dF}{db}$ is only the scaling coefficient and it hasn't any influence on the relationship between the variances s_X^2 , s_Y^2 and σ_b^2 .

After transformation we obtain partial derivatives of the parameters B_1, B_2, B_3 regarding to X_i, Y_i in the form

$$(13a) \frac{dB_1}{dX_i} = 2U_i X_i - 2 \bar{X} U_i - 2W_i \sum_i U_i X_i / \sum_i W_i + 2 \bar{X} W \sum_i U_i X_i / \sum_i W_i$$

$$(13b) \frac{dB_2}{dX_i} = 2U_i (\bar{Y} - Y_i) + 2W_i (\sum_i U_i Y_i - \bar{Y} \sum_i U_i) / \sum_i W_i - 2W_i (X_i - \bar{X})$$

$$(13c) \frac{dB_3}{dY_i} = W_i (Y_i - \bar{Y})$$

Similarly we obtain:

$$(14a) \frac{dB_1}{dY_i} = 0$$

$$(14b)$$

$$(14c) \frac{dB_2}{dY_i} = 2U_i X_i - 2 \bar{X} W_i \sum_i U_i / \sum_i W_i + 2W_i \sum_i U_i X_i / \sum_i W_i$$

$$\frac{dB_3}{dY_i} = W_i X_i - 2\bar{Y} U_i + 2Y_i U_i - 2W_i \sum_i U_i Y_i / \sum_i W_i + 2W_i Y_i \sum_i U_i / \sum_i W_i - W_i \sum_i W_i X_i / \sum_i W_i$$

In this defined optimization task, the goal function is described by relationship (10). The constraint is function F (12) with gradients described by the equations (13a, 13b, 13c, 14a, 14b, 14c). The start point of solution is the value of b parameter obtained iteratively for measurement data set. The partial derivatives presented in this paper make the optimization problem more accurate in the numerical implementation.

The results of numerical experiments

As a guide for scientists debugging their own programs York has given example commonly seen in the literature – "Pearson's data with York's weights". The original data traces back to a paper of Karl Pearson in 1901, the weights (reciprocal variance) are from York's 1966 paper. The basic York data is given in table 2.

Table 2 Pearson data and York's weights

| X_i | $W(X_i)$ | Y_i | $W(Y_i)$ |
|-------|----------|-------|----------|
| 0,0 | 1000 | 5,9 | 1 |
| 0,9 | 1000 | 5,4 | 1,8 |
| 1,8 | 500 | 4,4 | 4 |
| 2,6 | 800 | 4,6 | 8 |
| 3,3 | 200 | 3,5 | 20 |
| 4,4 | 80 | 3,7 | 70 |
| 5,2 | 60 | 2,8 | 70 |
| 6,1 | 20 | 2,8 | 70 |
| 6,5 | 1,8 | 2,4 | 100 |
| 7,4 | 1 | 1,5 | 500 |

The results for the slope and intercept point have been compared with those obtained by other algorithms and the exact generalized least squares.

Table 3 Results obtained in data in Table 2 using different procedures

| Method | a | b |
|---------------|-----------|-------------|
| In this paper | 5.4799063 | - 0.4805331 |
| Williamson | 5.4799150 | - 0.4805329 |
| York | 5.4799151 | - 0.4805330 |

We performed the numerical experiments relying on the error optimization given by equation (10). We applied sequential quadratic programming (SQP) method. In this method, the function solves a quadratic programming (QP) subproblem at each iteration. An estimate of the Hessian of the Lagrangian is updated at each iteration using the BFGS (Broyden-Fletcher-Goldfarb-Shanno) formula.

The optimization relies on searching for the minimum of variance of b using the equation (10). In the optimization we change the uncertainties of vector X and Y in ± 30 range values. Moreover, very important thing is to save slope

nearly constant. We have considered three bounds at the optimization process.

$$(15) \quad 0.7 \cdot s_x^2 < s_x^2 < 1.3 \cdot s_x^2$$

$$(16) \quad 0.7 \cdot s_y^2 < s_y^2 < 1.3 \cdot s_y^2$$

$$(17) \quad |b - b'| < \varepsilon, \varepsilon = 0.01$$

On the basis of these bounds we performed the optimization process and results are presented in table 4.

Table 4 Results of optimization.

| s_x^2 | s_y^2 | $(\sigma_b)^2$ | b |
|---------|---------|----------------|------------|
| 0.00077 | 0.97249 | 0.0046408978 | -0.4701431 |
| 0.0013 | 0.49234 | | |
| 0.0014 | 0.175 | | |
| 0.00162 | 0.0875 | | |
| 0.0035 | 0.035 | | |
| 0.00875 | 0.035 | | |
| 0.02167 | 0.01857 | | |
| 0.035 | 0.01 | | |
| 0.42581 | 0.007 | | |
| 0.7 | 0.0014 | | |

The convergence of this optimization process is presented in the figure 1.

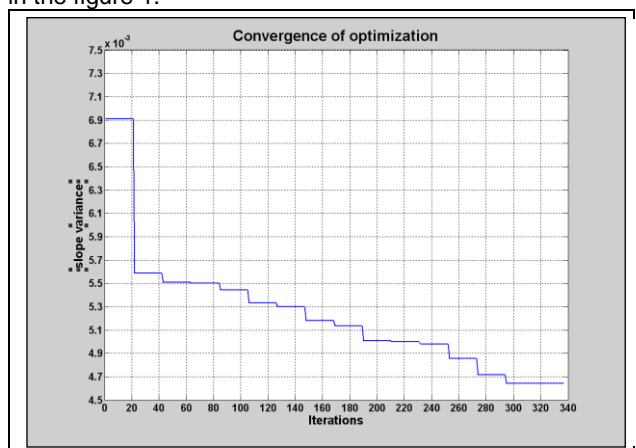


Fig.1. The convergence of the optimization process.

Comparing the value of slope variance obtained using real uncertainty of X and Y vector and the slope variance obtained using uncertainty as result of the optimization, we see that the slope variance has decreased about 32%. The percentage of the obtained uncertainties as result of optimization was presented in table 4.

Table 4 Percentage change of uncertainty measurement data set.

| Number of points from Table 2 | Δs_x^2 [%] | Δs_y^2 [%] |
|-------------------------------|--------------------|--------------------|
| 1 | 0.022 | 2.75 |
| 2 | 0.03 | 6.32 |
| 3 | 0.06 | 7.5 |
| 4 | 0.037 | 3.75 |
| 5 | 0.15 | 1.5 |
| 6 | 0.37 | 1.5 |
| 7 | 0.5 | 0.42 |
| 8 | 1.5 | 0.42 |
| 9 | 12.9 | 0.3 |
| 10 | 30 | 0.06 |

Based on results of the percentage change of the uncertainty measurement data set, we may say that the highest change of uncertainty concerns 9th and 10th point.

So we may conclude that these two points are responsible for the decrease of the estimation error of the slope, providing the same value of the slope (17).

Conclusion

The standard least-squares procedure is not applicable for curve fit when both x and y contain measurement uncertainty, because the underlying assumptions are violated and the method produces biased estimates of the fit parameters. The information considered in this article will enable a practitioner to fit the line and calculate approximate confidence intervals for the associated parameters.

Selection of the regression straight line is important especially in the measurement devices calibration. For example is used for the identification of the asynchronous motor parameters [9]. Nowadays it is believed that optimization of uncertainty selection is the cheapest way for the correction of parameters of the metrological devices.

Calculations of uncertainties of the regression straight line parameters presented in this paper let us check how they correspond to the change of uncertainties to straight line slope and intercept. This optimization procedure presented in the paper is simple to implement in the Matlab environment. Comparison with the previously reported general least squares procedures allows to believe that the presented method is competitive and may find application in engineering, especially measurements and instrumentation techniques.

REFERENCES

- [1] York D., Least-squares fitting of a straight line, *Canadian Journal of Physics*, 44 (1967), 1079-1085
- [2] Williamson J.H., Least-squares fitting of a straight line, *Canadian Journal of Physics*, 46 (1968), 1845-1847
- [3] York D., Evensen N.M., Martinez M.L., Delgado J., Unified equations for slope, intercept, and standard errors of the best straight line, *American Journal of Physics*, 72 (2004), No. 3, 367-375
- [4] Moreno C., A least-squares-based method for determining the ratio between two measured quantities, *Measurement Sci. Technol.*, 7 (1996), 137-141
- [5] Balsamo A., On the best fit of line to uncertain observation pairs, *Journal of Chemical Educator*, 42 (2005), 376-382
- [6] Milton M.J.T., Harris P.M., Smith I.M., Brown A.S., Goody B.A., Implementation of a generalized least-squares method for determining calibration curves from data with general uncertainty structures, *Metrologia* 43 (2006), S291-S298
- [7] Riu J., Rius F.X., Univariate regression models with errors in both axes, *Journal of chemometrics*, 9 (1995), 343-362
- [8] Reed B.C., Linear least-squares fits with errors in both coordinates. II: Comments on parameter variances, *Am. Journal Phys.* 60 (1995) No. 1, 59-62
- [9] C. Bergmann, B. Feuvrie, An approach of parameter identification for asynchronous machine, *Industrial Electronics, Control, and Instrumentation*, 1996., Proceedings of the 1996 IEEE IECON 22nd International Conference.

Authors: dr inż. Leszek Moszczyński, Warsaw University of Technology, Institute of the Material Technologies, ul. Narbuta 85, 02-524 Warszawa, E-mail: l.moszczyński@wip.pw.edu.pl; mgr inż. Jarosław Kurek, Warsaw University of Technology, Institute of the Theory of Electrical Engineering, Measurement and Information Systems, Email: kurekj@iem.pw.edu.pl

Steady state calculation of nonlinear circuits by the secants method

Abstract The effective variant of a secants method of solution of systems of the nonlinear algebraic equations is used for the steady state calculation of the nonlinear dynamic systems. Efficiency of the developed algorithms is confirmed by the numerical experiments.

Streszczenie. W pracy przedstawiono wariant metody siecznych umożliwiającą efektywne rozwiązywanie nieliniowych równań algebraicznych otrzymanych w wyniku analizy stanów ustalonych w obwodach nieliniowych. Zalety przedstawionej metody zilustrowano na wybranych przykładach numerycznych. (*Analiza stanów nieustalonych w obwodach nieliniowych przy pomocy metody siecznych*)

Keywords: nonlinear circuits mathematical model, steady state calculation.

Słowa kluczowe: układy nieliniowe, model matematyczny, stan ustalony.

We shall consider the search of a periodic mode in the electronic circuit which mathematical model is:

$$(1) \quad \dot{x} = f(x, t),$$

where $x \in \mathbf{R}^n$, $f: \mathbf{R}^{n+1} \rightarrow \mathbf{R}^n$,

$$f(x, t+T) = f(x, t), \forall t, T > 0.$$

The vector function $f(x, t)$ is assumed continuous on t and continuously differentiated on x . A trajectory of the system (1), with the initial conditions $x(t_0) = x_0$, is denoted as $x(t) = \varphi(t, t_0, x_0)$.

Search of a periodic mode of the system (1) can be found by solving the following equation

$$(2) \quad y - p(y) = 0 \quad y \in \mathbf{R}^n, \quad p: \mathbf{R}^n \rightarrow \mathbf{R}^n,$$

where $y = x_0$ – an initial conditions vector;

$p(y) = \varphi(t_0 + T, t_0, y)$ – represent a point y along a trajectory of system (1) over the period T .

In the most widespread algorithms of the accelerated search of periodic modes of system (1) for the decision of the equation (2) various modifications of Newton method, gradient methods, methods of extrapolation [3] are used. Considerably less attention is paid to the methods of secants. Even when the derivative $p'(y)$ is not obtained analytically, the advantage is given to the discrete Newton methods.

It will be shown, that at least one modification of a secants method is quite appropriate to be used for the search of periodic modes of system (1).

The description of algorithm

Solving the equation (2) by means of a method of secants, we will take into consideration affine model [2,3] in a vicinity of each point of the iterative process y_k , $k = 2, 3, \dots$ (y_0, y_1 - are set) instead of (2):

$$(3) \quad l_k(y) = y_k - p(y_k) + A_k(y - y_k),$$

where $A_k \in \mathbf{R}^{n \times n}$ - some square matrix.

Since the model (3) must satisfy a condition

$$(4) \quad l_k(y_{k-1}) = y_{k-1} - p(y_{k-1}),$$

we obtain:

$$(5) \quad p(y_k) - p(y_{k-1}) = B_k(y_k - y_{k-1}),$$

where $B_k = I - A_k$.

The equation (5) is called the relation of secants for the equation (2).

It is obvious, that the matrix B_k from the equation (5) is not defined unambiguously (except in case $n=1$). Therefore, usually, in case of construction a model (3) together with a point y_k a set of auxiliary points $y_{k,i}$, $i = 1, 2, \dots, n$ which are chosen on the certain algorithm are considered, and it is required, that model (3) should satisfy the relation of secants (5) for all these points, that is:

$$(6) \quad p(y_k) - p(y_{k,i}) = B_k(y_k - y_{k,i}), \quad i = 1, 2, \dots, n.$$

Points $y_{k,i}$ are chosen so that vectors $h_{k,i} = y_k - y_{k,i}$ are linearly independent and the system (6) unambiguously determine the matrix B_k . Then, comparing (3) to zero, one obtains the iteration process of the secants method:

$$(7) \quad y_{k+1} = y_k - [I - B_k]^{-1}(y_k - p(y_k)).$$

Depending on the way of auxiliary points $y_{k,i}$ choice, different modifications of the secants method are obtained [3]. They are simple enough to be implemented in a computer program and some of them under certain conditions still have essential features of a method of Newton. However, these methods are not yet extensively used in the dynamic systems analysis. Significant memory sizes and considerable computing expenses ($n+1$ calculations of p representations during one iteration). More difficulties are concerned with the fact that vectors $h_{k,i} = y_k - y_{k,i}$ become close to the linearly dependent ones that makes finding of a matrix B_k an incorrectly imposed problem.

The most successful approach to generalize a secants method on a multivariate case has been offered by C.Broyden [5]. It consists in the recalculation of the matrix B_{k-1} of the previous iteration into the matrix B_k which satisfies the relation of secants (5).

Consider that $Q \subset \varphi^{n \times n}$ denotes the set of matrices B which satisfy the relation (5), that is $B \in Q$

$$(8) \quad s_{k-1} = B h_{k-1},$$

where $s_{k-1} = p(y_k) - p(y_{k-1})$, $h_{k-1} = y_k - y_{k-1}$ – the set vectors. Since during the calculation of the matrix B_k and the matrices B_{k-1} , no new information about affine model exists (3), it is natural to keep the maximum of that already existing. Therefore the matrix B_k in the Broyden algorithm is chosen so that distance between B_k and B_{k-1} in some metrics is minimal. In other words the solution of the problem

$$(9) \quad \min_{B \in Q} \|B - B_{k-1}\|.$$

is searched for.

If in (9), the matrix norm $\|\cdot\|$ is l_2 -norm, as shown in [2], the solution of the problem (9) exists and looks like:

$$(10) \quad B_k = B_{k-1} + \frac{(s_{k-1} - B_{k-1} h_{k-1}) h_{k-1}^T}{h_{k-1}^T \cdot h_{k-1}}.$$

The following statement is the simplified variant of Broyden, Dennis, More [2] theorem for the equation (2).

Consider the representation of $p(y)$ has a motionless point y_* . If in some open vicinity D of the point y_* the derivative $p'(y)$ is continuous (in the Lipschitz sense) and the matrix $[I - p'(y_*)]$ is non-exceptional there exist constants $\varepsilon > 0$, $\delta > 0$ such, that if $\|y_0 - y_*\|_2 < \varepsilon$ and $\|B_0 - p'(y_*)\|_2 < \delta$, the sequence $\{y_k\}$ which is generated by iteration process (7), (10), is correctly defined and converges to y_* overlinearly (here $\|\cdot\|_2$ denotes the l_2 -norm).

So, the algorithm of Broyden method for the solution of the equation (2) can be expressed as:

Set conditions: x_0 B_0 , the criterion of the iteration process termination (7).

- 1) accept $k=0$;
- 2) find y_{k+1} and $h_k = y_{k+1} - y_k$;
- 3) find $p(y_{k+1})$ та $s_k = p(y_{k+1}) - p(y_k)$;
- 4) If the criterion of the iteration process termination (7) is fulfilled – stop the calculation;
- 5) find $B_{k+1} = B_k + \frac{(s_k - B_k h_k) h_k^T}{h_k^T \cdot h_k}$;
- 6) accept $k=k+1$ and go to step no. 2.

A choice of the matrix B_0 in this algorithm is uncertain. If the calculation of the derivative $p'(y)$ is possible, it is obviously necessary to accept $B_0 = p'(y_0)$. If the derivative $p'(y)$ can not be determined at this stage of the calculation of $p'(y_0)$ it is possible to use the final differences or to approximate $p'(y_0)$ by means of one of the secants method modifications (6).

Numerical experiments

We shall examine the examples of the periodic modes search of given electronic circuits. In Figs. 1 and 2 the circuits of the rectifier and the resonant amplifier, respectively, are represented. Inputs are sine signals.

Competing methods for the solution of the equation (2) are methods of Newton and the secants method in the notation of C.Broyden. The numerical integration of the equations (1) in order to find the representation of p for both circuits was carried out by the second order PDN method with the variable step. A representation derivative over the period $p'(y)$ in the method of Newton was searched simultaneously with calculation of $p(y_k)$ as for the solution of the equations in variations for system (1) along a trajectory $x(t) = \varphi(t, t_0, y_k)$:

$$(11) \quad \dot{\Phi}_k = J_k(t) \cdot \Phi_k, \quad \Phi_k(t_0) = I,$$

where $\Phi_k \in \mathbf{R}^{n \times n}$ $J_k(t) = \left. \frac{\partial f}{\partial x} \right|_{x = \varphi(t, t_0, y_k)}$.

The system in variations (11) was integrated over the interval $[t_0, t_0 + T]$ by the same method, as the basic system (1), and assuming $p'(y_k) = \Phi_k(t_0 + T)$.

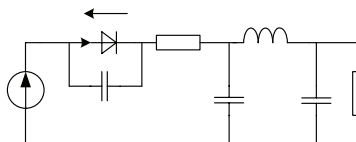


Fig.1. Nonlinear circuit with periodic input. $E(t) = 10 \sin(120\pi t)$, $I_D = 10^{-6} (\exp(40U_D) - 1)$

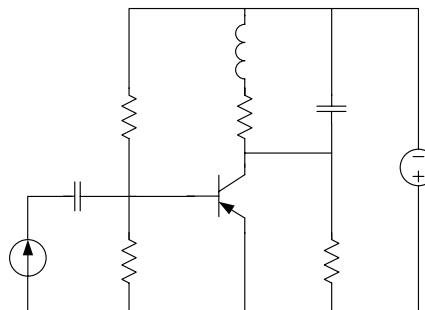


Fig.2. The network of the resonant amplifier. $U_{in} = 0.1 \sin(3200\pi t)$ V

For the rectifier circuit the periodic mode was searched starting from zero initial conditions, and for the circuit of the amplifier - from the initial conditions which correspond to the static mode of the circuit. The first iteration in the algorithm which worked according to the secants method, was carried out according to the method of Newton, that is, accepting $B_0 = p'(y_0)$.

Table 1. Calculation of a periodic mode in the circuit in fig.1

| Iteration | Error on iteration | |
|-----------|------------------------|------------------------|
| | Newton method | Secans method |
| 1 | $0,620 \cdot 10^{-2}$ | $0,620 \cdot 10^{-2}$ |
| 2 | $0,312 \cdot 10^{-3}$ | $0,153 \cdot 10^{-2}$ |
| 3 | $0,103 \cdot 10^{-5}$ | $0,958 \cdot 10^{-4}$ |
| 4 | $0,172 \cdot 10^{-9}$ | $0,161 \cdot 10^{-6}$ |
| 5 | $0,269 \cdot 10^{-13}$ | $0,651 \cdot 10^{-8}$ |
| 6 | | $0,961 \cdot 10^{-11}$ |

Results of the numerical calculations are listed in the table 1 and table 2. The error of the iteration process of the solution of the equation (2) on k -th iteration here is defined as follows:

$$\delta_k = \frac{\|p(y_k) - y_k\|}{\|y_k\|}, \quad k = 1, 2, \dots$$

Table 2 Calculation of a periodic mode in the circuit in fig.2

| Iteration | Error on iteration | |
|-----------|------------------------|------------------------|
| | Newton method | Secans method |
| 1 | $0,828 \cdot 10^{-2}$ | $0,828 \cdot 10^{-2}$ |
| 2 | $0,105 \cdot 10^{-4}$ | $0,374 \cdot 10^{-3}$ |
| 3 | $0,443 \cdot 10^{-9}$ | $0,218 \cdot 10^{-5}$ |
| 4 | $0,547 \cdot 10^{-13}$ | $0,679 \cdot 10^{-7}$ |
| 5 | | $0,124 \cdot 10^{-9}$ |
| 6 | | $0,317 \cdot 10^{-11}$ |

Results of calculations testify that in order to reach the necessary accuracy of the secants method only 1 or 2 iterations more than in the method of Newton are needed. Considering, that in the secants method only one calculation per iteration is required (except for the first iteration, and for the method of Newton, implicit formulas of the numerical integration are used (the computational expenses are 1,5-2,0 times larger), the mentioned above methods are approximately identical in the sense of

efficiency. So, the results of calculations testify, that even in case of using the implicit formulas of the integration, the algorithms which are based on the method of secants, can compete successfully enough in the programs of the analysis of stationary modes of dynamic systems with the method of Newton. If the obvious formulas are used for the numerical integration of (1) and (11) then for one Newton iteration the same numerical expenses are necessary in both cases. In the latter case the advantages of the secants method (in particular, when n is large) is obvious.

REFERENCES

- [1] Дэнис Дж., Шнабель Р. Численные методы безусловной оптимизации и решения нелинейных уравнений / Пер. с англ. М.: Мир, 1988.
- [2] Ортега Дж., Рейнболдт В. Итерационные методы решения нелинейных систем уравнений со многими неизвестными / Пер. с англ. М.: Мир, 1975.
- [3] Скельбоз С. Временной стационарный анализ нелинейных электрических систем, *ТМЭЭР*. 70 (1982), No. 10, 89-111.
- [4] Broyden C.G. A class of methods for solving nonlinear simultaneous equations *Math. Comp.* 19 (1965), 577-593

Authors: Yaroslav Shmygelsky, Ivan Franko National University of L'viv, Department of Electronics, Tarnavsky str. 107, 79017 Lviv, E-mail: shmygelsky@electronics.wups.lviv.ua

Simulation of physical processes in eddy-current transformer during its interaction with the tested ferromagnetic specimen

Abstract. The work contains the results of theoretical research of interaction between a laying-in U-type core eddy-current transformer and tested ferromagnetic material. There has been developed a mathematical simplified model and received equations for engineering calculation of introduced real (active) resistance and reactance (reactive resistance) which can be used for development eddy-current defectoscopes.

Streszczenie. Praca zawiera rezultaty teoretycznych badań nad interakcją pomiędzy rdzeniem transformatora o stałej wartości prądu uzwojenia wtórnego a badanym materiałem ferromagnetycznym. W wyniku prac stworzono uproszczony model matematyczny i otrzymano równania inżynierskie dla dodatkowej rezystancji i reakcji. Wzory można wykorzystać do projektowania urządzeń do defektoskopii wiroprądowej. (Symulacja procesów fizycznych w transformatorze o stałej wartości prądu uzwojenia wtórnego w czasie jego interakcji z badanym obiektem ferromagnetycznym)

Keywords: eddy-current transformer, eddy-current ndt, mathematical model.

Słowa kluczowe: transformator o stałej wartości prądu uzwojenia wtórnego, defektoskopia prądów wirowych, model matematyczny.

Introduction

It is difficult to determine in practice the pattern of interaction of ECT with conducting medium by carrying out defectoscopy of ferromagnetic parts and units. It is conditioned by complex mathematical apparatus used to explain such interaction [1]. It is especially difficult to describe interaction of eddy-current transformer (ECT) with U-type rod and with the tested ferromagnetic specimen that contains a crack-type defect [2]. Such construction of ECT in comparison with a usual rod-type one has greater sensitivity to feature anisotropy of the tested specimen, for example, the one caused by weld defect of "fusion" type [3]. The objective of the research is creation of a new simplified mathematical model that can describe interrelation between ECT with U-type rod and the tested ferromagnetic specimen and enables to obtain expressions for simplified calculation (engineering calculation) of active and reactive resistance introduced into ECT.

In previous research [4] there has been considered the mathematical model that took into account only active constituent of resistance introduced into ECT, but this is not enough for precise determining the value of ECT output signal.

Let us consider interrelation between ECT and the tested ferromagnetic specimen as interrelation between electromagnetic field created by ECT and a ferromagnetic metal plate.

ECD with U-type rod along with the tested specimen in the form of an electrical transformer

U-type lying-in parametrical ECT consists of a coil with a ferrite U-type rod on which there has been coiled high-frequency winding with quantity of turns w . Magnetic flux Φ from ECT induces eddy-currents in the tested specimen, intensity of which is determined by electromagnetic features of the tested specimen material. Dependence of current strength in ECT winding is:

$$(1) \quad \dot{I} = \frac{\dot{U}}{Z_0 + Z_{\dot{a}i}} = \frac{\dot{U}}{Z},$$

where U – voltage of the current feeding ECT; Z_0 – resistance of ECT winding in air; $Z_{\dot{a}i}$ – additional resistance, introduced to ECT by the specimen; Z – full resistance of ECT winding.

Impedance of ECT winding consists of active resistance R and inductive resistance X_L :

$$(2) \quad Z = \sqrt{R^2 + X_L^2} = \sqrt{R^2 + (2\pi fL)^2},$$

where f – current frequency; L – inductance of ECT winding, which equaling:

$$(3) \quad L = L_0 + L_{\dot{a}i} = \frac{W \cdot \dot{O}}{I},$$

where L_0 – inductance of ECT winding in air; $L_{\dot{a}i}$ – additional inductance introduced by ECT specimen.

With substantial values of magnetic permeability of ECT core and the tested specimen, we may ignore dispersion flux and assume that the entire magnetic flux is closed through the specimen:

$$(4) \quad \dot{O} = \frac{I \cdot W}{R_i},$$

where R_M – magnetic resistance of the circuit ECT-specimen, $R_M = R_{cm} + R_3$ (R_{cm} – magnetic resistance of the core and ferromagnetic steel the part is made of; R_3 – magnetic resistance of the air gap).

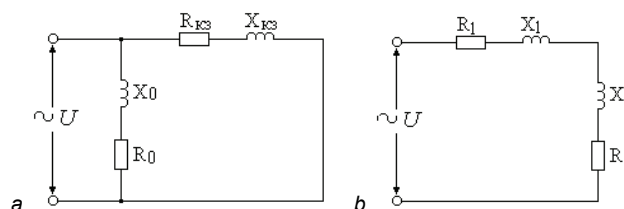


Fig. 1. Equivalent circuit ECT in case when it is positioned on the metal of the tested specimen (a), and when ECT is positioned in the air (b).

ECT along with the metal of the tested specimen can be imagined as an electrical transformer whose primary winding is the winding for ECT with quantity of turns w_1 . Secondary winding of the transformer has one turn ($w_2=1$) with complex impedance Z . This winding is a squirrel-cage

one. The turn ratio in this case equals the number of ECT turns: $k_{12}=w_1$. Equivalent circuit for this transformer is shown on fig.1a. If ECT is not laid on the tested metal specimen, i.e. is positioned in the air, then there will be no secondary turn in equivalent circuit, and equivalent circuit will look like the one shown on fig.1b. In this case one can assume that the transformer works on idling.

Mathematical model of physical processes which occur in the tested ferromagnetic layer

The flux induced in the tested layer is determined by correlation:

$$(5) \quad U_1 = 4,44 f w_1 \hat{O}_m,$$

where U_1 - effective voltage of the winding; f - working frequency; \hat{O}_m - amplitude value of the working magnetic flux; w_1 - number of winding turns.

Amplitude value of the working magnetic flux:

$$(6) \quad \hat{O}_m = \frac{U_1}{4,44 f w_1}.$$

We shall view the tested layer as secondary winding of electrical transformer with number of turns $w_2=1$. Voltage U_2 in the tested layer:

$$(7) \quad U_2 = \frac{U_1}{w_1}.$$

To obtain parameters introduced into ECT by the tested layer of the specimen we shall go to the model of the tested layer in the form of a plate of ferromagnetic specimen, which is positioned under the poles of U-type ECT core (fig. 2).

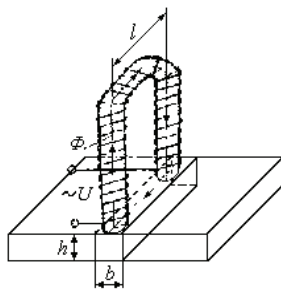


Fig. 2. Assumed look of the tested ferromagnetic specimen in the form of a plate positioned under the poles of U-type core.

Complex power which is absorbed by the tested layer is determined through Umov–Poynting vector. Vectors of electromagnetic field created in the tested layer is determined through assumption that this layer is a plate of ferromagnetic material positioned in the alternating magnetic field. Electric field intensity and magnetic inductance equations are taken from [6]:

$$(8) \quad \dot{E}_m = -j B_{\delta \tilde{n} \delta} \frac{\omega b}{2} \cdot \frac{\tilde{sh} p y}{\tilde{sh} p \frac{b}{2}},$$

$$(9) \quad \dot{B}_m = B_{\delta \tilde{n} \delta} \frac{p b}{2} \cdot \frac{\tilde{ch} p y}{\tilde{sh} p \frac{b}{2}},$$

where B_{mcp} – average value of magnetic inductance in the tested layer ($B_{\delta \tilde{n} \delta} = \frac{\hat{O}_\delta}{b \cdot h}$); $\tilde{p} = \sqrt{j \omega \mu_a \gamma} = k + jk$; $k = \sqrt{\frac{\omega \mu_a \lambda}{2}}$; ω – cyclic frequency ($\omega = 2\pi f$); μ_a – absolute magnetic permeability ($\mu_a = \mu \mu_0$); γ – specific electric conductivity of the tested layer; b – width of the tested layer; h – thickness of the tested layer.

Umov-Poynting vector is determined through equation:

$$(10) \quad \dot{\Pi} = \frac{1}{2} (\dot{E}_m \dot{B}_m)_{y=\pm \frac{b}{2}}.$$

If we put the coordinate value $y = \frac{b}{2}$ into equations (4) and (5) we shall get the following:

$$(11) \quad (\dot{E}_m \dot{B}_m)_{y=\pm \frac{b}{2}} = -j B_{\delta \tilde{n} \delta}^2 \frac{\omega b}{2} \cdot \frac{p b}{2} \tilde{cth} p \frac{b}{2}.$$

Hyperbolic cotangent of complex argument as is known from the [7] is recorded the following way:

$$(12) \quad \tilde{cth} p \frac{b}{2} = \tilde{cth} \left(k \frac{b}{2} + jk \frac{b}{2} \right) = \frac{\tilde{sh} kb - j \sin kb}{\tilde{ch} kb - \cos kb}.$$

Using equation (12) and equation $\tilde{p} = k + jk$ and transforming the equation (11) we get the following:

$$(13) \quad (\dot{E}_m \dot{B}_m)_{y=\frac{b}{2}} = \frac{B_{\delta \tilde{n} \delta}^2 \omega b^2 k}{4 \mu_a} \left[\frac{\tilde{sh} kb - \sin kb}{\tilde{ch} kb - \cos kb} - j \frac{\tilde{sh} kb + \sin kb}{\tilde{ch} kb - \cos kb} \right]$$

Complex power which is absorbed by the tested layer:

$$(14) \quad S = 2l \cdot h \left(\frac{\dot{E}_m \cdot \dot{B}_m}{2} \right)_{y=\frac{b}{2}} = \frac{B_{\delta \tilde{n} \delta}^2 \omega b k \cdot V}{4 \mu_a} \times \frac{\tilde{sh} kb - \sin kb - j(\tilde{sh} kb + \sin kb)}{\tilde{ch} kb - \cos kb}$$

where $l \cdot h$ – surface area whereon Umov-Poynting vector was being determined; V - the volume of the tested layer ($V = b \cdot h \cdot l$).

Complex power is determined by U_2 and resistance of the tested layer through the following equation:

$$(15) \quad \underline{S} = \frac{U_2^2}{\underline{Z}},$$

where \underline{Z} – conjugate complex resistance of the tested layer.

From the equation (15) we get the following:

$$(16) \quad \underline{Z}^* = \frac{U_2^2}{S}$$

If we put equation (14) into equation (16), we get the following:

$$(17) \quad \underline{Z}^* = \frac{2\mu_a U_2^2 (\operatorname{ch} kb - \cos kb) [\operatorname{sh} kb - \sin kb + j(\operatorname{sh} kb + \sin kb)]}{B_{\delta}^2 \tilde{n} \delta \omega b k \cdot V (\operatorname{sh}^2 kb + \sin^2 kb)}$$

Singling out real and a imaginary parts from equation (17), we shall get expressions for determining active and reactive resistances of the tested layer:

$$(18) \quad R = \frac{2\mu_a U_2^2 (\operatorname{ch} kb - \cos kb) \cdot (\operatorname{sh} kb - \sin kb)}{B_{\delta}^2 \tilde{n} \delta \omega \cdot b \cdot k \cdot V (\operatorname{sh}^2 kb + \sin^2 kb)}$$

$$(19) \quad X = \frac{2\mu_a U_2^2 (\operatorname{ch} kb - \cos kb) \cdot (\operatorname{sh} kb + \sin kb)}{B_{\delta}^2 \tilde{n} \delta \omega \cdot b \cdot k \cdot V (\operatorname{sh}^2 kb + \sin^2 kb)}$$

Putting the equations $B_{\delta} \tilde{n} \delta = \frac{U_1}{4,44 f w_1 b h}$ and $U_2 = \frac{U_1}{w_1}$

into equations (18) and (19) we shall come to expressions for introduced constituents of active R and reactive X resistances for ECT when interacting with the tested ferromagnetic specimen:

$$(20) \quad R = \frac{19,72 f \mu_a h (\operatorname{ch} kb - \cos kb) \cdot (\operatorname{sh} kb - \sin kb)}{\pi k l (\operatorname{sh}^2 kb + \sin^2 kb)}$$

$$(21) \quad X = \frac{19,72 f \mu_a h (\operatorname{ch} kb - \cos kb) \cdot (\operatorname{sh} kb + \sin kb)}{\pi k l (\operatorname{sh}^2 kb + \sin^2 kb)}$$

Standardized value of active R and reactive X resistances of the tested layer:

$$(22) \quad R' = R n^2 = \frac{19,72 f \mu_a h \cdot w_1^2 (\operatorname{ch} kb - \cos kb) \cdot (\operatorname{sh} kb - \sin kb)}{\pi k l (\operatorname{sh}^2 kb + \sin^2 kb)}$$

$$(23) \quad X' = X n^2 = \frac{19,72 f \mu_a h \cdot w_1^2 (\operatorname{ch} kb - \cos kb) \cdot (\operatorname{sh} kb + \sin kb)}{\pi k l (\operatorname{sh}^2 kb + \sin^2 kb)}$$

where n – turn ratio ($n = \frac{w_1}{w_2} = w_1$).

Conclusions

Equations (22) and (23) may be used for engineering calculation of active and reactive resistance introduced into ECT when it's interacting with the tested ferromagnetic specimen. This mathematical model (equations for engineering calculation) can be used for development eddy-current defectoscopes.

REFERENCES

- [1] Соболев В.С., Шкарлет Ю.М. Накладные и экранные датчики. Новосибирск: Наука, 1967.
- [2] Гамалий В., Трушаков Д. Моделирование вихорострумового перетворювача з П-подібним магнітопроводом, розташованого над ферромагнітним зразком із тріщиною // Теор. електротехніка. 2005. Вип. 58. С. 176-182.
- [3] Серебренников С.В., Трушаков Д.В. Дослідження вихорострумових перетворювачів з П-подібним та стержневим осерддям // Фізичні методи та засоби контролю середовищ, матеріалів та виробів. 2005. Вип. 10. С. 126-130.
- [4] Smirnov V.G., Trushakov D.V. Basic equations of physical processes arising in eddy-current transformer with u-type rod if intersected with a ferromagnetic material // Proceedings of the XIII International Symposium on Theoretical Electrical Engineering. 2005. P. 299-303.
- [5] Бессонов Л. А. Теоретические основы электротехники. М.: Высш. школа, 1996. 623 с.
- [6] Купальян С.Д. Теоретические основы электротехники. Ч.3. М.: Энергия, 1970. 247 с.
- [7] Двайт Г.Б. Таблицы интегралов и другие математические формулы. М.: Наука, 1977. 224 с.

Authors: Senior Teach. Vitaliy V. Martinov, Cand. Sc., Ass. Prof. Dmitro V. Trushakov, Kirovograd National Technical University, 8 University Avenue, 25006, Kirovograd, Ukraine, E-mail: miek@kdtu.kr.ua.

High-pass elliptic filter using the wide-band biquadratic structure VES OPA-RC „b” - 02

Abstract. In this paper it was presented the wide-band biquadratic elliptic structure named as VES OPA-RC „b”-02. In cascade of these structures it is realized the high-pass elliptic filter. Characteristic feature of describing structure is big band-width, which by suitable choice of elements can achieve the value that is close to wide-band (f_T) of using operational amplifiers (OPA). In this connection the structure can have application in analog high frequency filtration.

Streszczenie. W artykule przedstawiono szerokopasmową bikwadratową strukturę eliptyczną, dla której przyjęto oznaczenie VES OPA-RC „b”-02. W kaskadzie takich struktur realizuje się górnoprzepustowy filtr eliptyczny. Cechą charakterystyczną opisaną strukturą jest duża szerokość pasma, która poprzez odpowiedni dobór elementów może osiągnąć wartość bliską szerokości pasma (f_T) zastosowanych wzmacniaczy operacyjnych (OPA). W związku z tym struktura może mieć zastosowanie w wysokoczęstotliwościowej filtracji analogowej. (Górnoprzepustowy filtr eliptyczny z użyciem szerokopasmowej struktury bikwadratowej VES OPA-RC „b” - 02)

Keywords: OPA amplifier, unity gain bandwidth, biquadratic structure, high-pass elliptic filter.

Słowa kluczowe: wzmacniacz OPA, pole wzmocnienia, struktura bikwadratowa, górnoprzepustowy filtr eliptyczny.

Introduction

Described structure belongs to group of type “b” elliptic structures, which have application in construction of high-pass elliptic filter. The active element of the structure is a operational amplifier (OPA). Limited bandwidth (f_T) of OPA amplifiers causes, that the amplitude characteristics deforms itself, however bandwidth of the structure and thus whole filter gives in limitation. The advantage of presented structure is bandwidth SBW is big and can approach to bandwidth f_T of using amplifiers by suitable choice of elements values. It is difficult result to achieve in others worked out structures (for example the structure named as VES OPA-RC „b”-01 – based directly on the GIC converter [2], [5]).

The type „b” structure

The type „b” structure realizes following operator transmittance:

$$(1) \quad K(s) = N \frac{s^2 + \omega_z^2}{s^2 + 2\sigma s + \omega_p^2}, \text{ at } \omega_p > \omega_z.$$

On the amplitude characteristic (fig. 1) it possible to distinguish 3 following bands: pass-band ($0, f_p$), transition band (f_p, f_z) and stop-band (f_z, ∞). For $f \approx f_p$ there is maximum K_{max} , which approximately equals:

$$(2) \quad K_{max} \approx NQ, \text{ gdzie } Q = \frac{\omega_p}{2\sigma}.$$

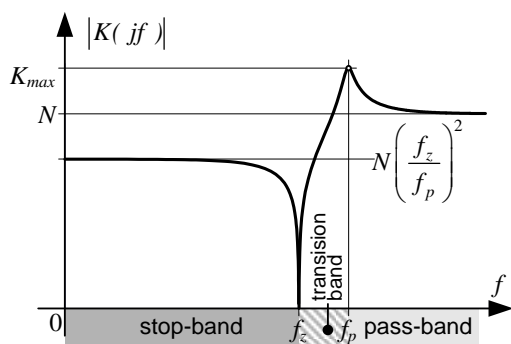


Fig. 1. Amplitude characteristics of the type „b” structure

High-pass elliptic filter

The elliptic filter from among all known ones is distinguished by the biggest selectivity [1], [3], at the cost of appearing oscillations on the characteristic in pass-band and stop-band. The starting point of the filter synthesis is determination of the filter transmittance $K(s)$ [1] fulfilling the assumed filtration parameters, such as:

- K_r – transmission level of filter in the pass-band,
- r – filter order,
- f_{gr} – cut-off frequency,
- ε – ripple coefficient of pass-band,
- k – elliptic integral coefficient.

The amplitude characteristic $|K(jf)|$ of even order r high-pass elliptic filter was showed on fig. 2.

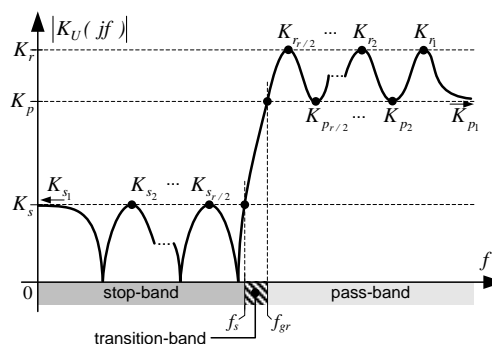


Fig. 2. The amplitude characteristics of even order r high-pass elliptic filter

Even order r high-pass elliptic filter realizes in the cascade of $r/2$ biquadratic structures and $r/2$ proportional structures [4], [7]. The block diagram illustrating the construction of high-pass elliptic filter in cascade of biquadratic and proportional structures showed on fig. 3.

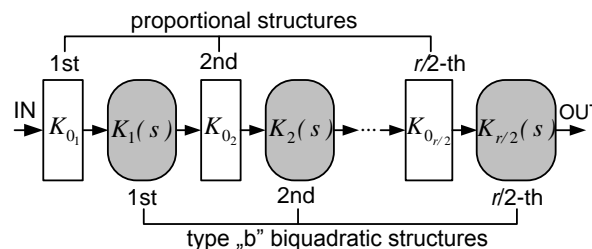


Fig. 3. The construction of high-pass elliptic filter in cascade of biquadratic and proportional structures

Transmittance of the cascade is described by the formula:

$$(3) \quad K_U(s) = \frac{U_{OUT}}{U_{IN}} = \prod_{i=1}^{r/2} K_{0i} \prod_{i=1}^{r/2} K_i(s)$$

where: $K_i(s)$ – transmittance of i -th biquadratic type „b” structure:

$$(4) \quad K_i(s) = N_i \frac{s^2 + \omega_{z_i}^2}{s^2 + 2\sigma_i s + \omega_{p_i}^2}, \text{ at } \omega_{p_i} > \omega_{z_i},$$

$N_i, \omega_{z_i}, \sigma_i, \omega_{p_i}$ - parameters of i -th biquadratic structure; K_{0i} – transmission level of i -th proportional structure (most often passive one):

$$(5) \quad K_{0i} = \frac{K_r}{\sqrt{1+\varepsilon^2}} \frac{1}{N_i}, \text{ and } K_{0i} = \frac{1}{N_i} \text{ for } i = 2, 3, \dots, r/2.$$

Frequency macromodel of OPA

In order to analyse how the biquadratic structure behaves after using real amplifiers OPA (fig. 4a), it is absolutely necessary to assume proper frequency macromodel of amplifier [6], [10]. It takes into consideration limited bandwidth at typical 1-pole characteristic, with bend for frequency f_0 (fig. 4b).

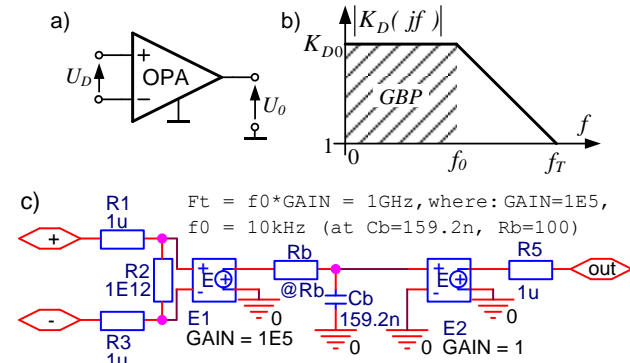


Fig. 4. Frequency model of OPA: a) symbol; b) amplitude characteristics; c) SPICE™ simulation macromodel

Transmittance of OPA is determined by formula:

$$(6) \quad K_D(jf) = \frac{U_O}{U_D} = \frac{K_{D0}}{1 + j \frac{f}{f_0}}, \text{ and } GBP = K_{D0} f_0 = f_T,$$

where: K_{D0} – DC gain; f_T – unity gain bandwidth; GBP – gain bandwidth product.

The macromodel was implemented in SPICE™ [8] simulator in circuit with controlled sources (fig. 4c).

Bandwidth analysis of the VES OPA–RC „b” - 02 structure

Scheme of the structure was presented on fig. 5. Operator transmittance, for ideal amplifiers, is determined by formula:

$$(7) \quad K_U(s) = \frac{U_{OUT}(s)}{U_{IN}(s)} = N \frac{s^2 + \omega_z^2}{s^2 + 2\sigma s + \omega_p^2} = \left(1 + \frac{R_2}{R_7}\right) \frac{s^2 + \frac{R_2 R_7}{C_4 C_6 R_1 R_3 R_5 (R_2 + R_7)}}{s^2 + \frac{R_2 R_9}{C_4 R_3 R_5 R_7} s + \frac{R_2 (R_1 + R_7 + R_9)}{C_4 C_6 R_1 R_3 R_5 R_7}}$$

and:

$$(8) \quad N = 1 + \frac{R_2}{R_7}$$

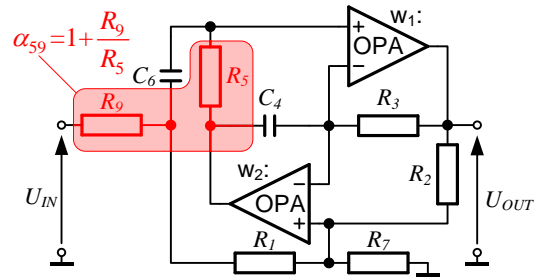


Fig. 5. The VES OPA–RC „b” - 02 structure

Characteristics of VES OPA–RC „b” - 02 structure is mainly shaping by amplifier w_1 with bandwidth f_{T1} . It introduces bend with 20 dB/dec roll-off, for frequency f_{b1} (proportional to f_{T1}), thus determining the structure bandwidth. Amplifier w_2 with bandwidth f_{T2} answers for amplitude excess effect, which is the bigger, when f_{T2} is the lower than f_{T1} . Influence of amplifiers on the characteristic was illustrated on fig. 6.

Bend frequency f_{b1} is enough complicated dependence on elements values R_2, R_5, R_7, R_9 :

$$(9) \quad f_{b1} \approx f_{b10} \sqrt{1 - \frac{(f_p / f_z)_{\min}^2}{(f_p / f_z)^2}}, \quad (f_p / f_z) \geq (f_p / f_z)_{\min}$$

where:

$$(10) \quad f_{b10} = f_{T1} \frac{R_5}{R_5 + R_9} \frac{1}{N}, \quad (f_p / f_z)_{\min} = \sqrt{\left(1 + \frac{R_9}{R_7}\right) N},$$

N – described by formula (8).

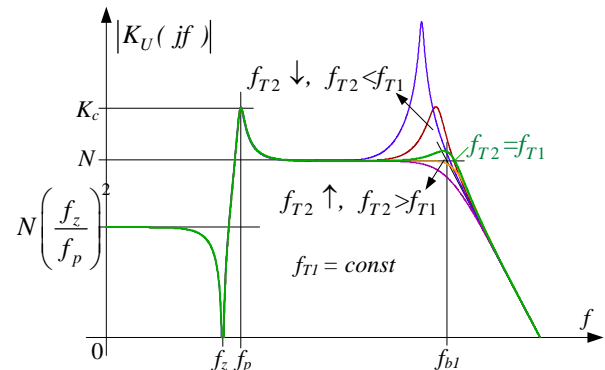


Fig. 6. The characteristics of VES OPA–RC „b” - 02 structure in dependence on f_{T2} , at $f_{T1} = \text{const}$

On fig. 7 it was illustrated, how elements values R_2, R_5, R_7, R_9 influence on frequency f_{b1} , at variable value of (f_p/f_z) . From the diagram it can draw following conclusions:

- values (f_p/f_z) lower than $(f_p/f_z)_{\min}$ are not realized,
- for low values (f_p/f_z) , near $(f_p/f_z)_{\min}$, it obtains low frequency f_{b1} , ($f_{b1} < f_{b10}$),
- frequency f_{b1} is the biggest, near f_{b10} , at $(f_p/f_z) > 2$.

Frequency f_{b1} limits the structure bandwidth SBW . In case, when amplitude excess is negligible (at $f_{T2} > f_{T1}$), it assumes that $SBW = f_{b1}$. However it is not much practical case, because it concerns the use of amplifier w_2

unnecessarily faster from w_1 . More practical situation takes place, when amplifiers have identical bandwidth $f_{T1} = f_{T2} = f_T$. Consenting to 20-percentage amplitude excess it obtains widened band SBW' , which approximately amounts:

$$(11) \quad SBW' = f'_{b1} \cong 1.83 f_{b1},$$

where: f'_{b1} – limit frequency according to criterion of roll-off amounted $\sqrt{2}$.

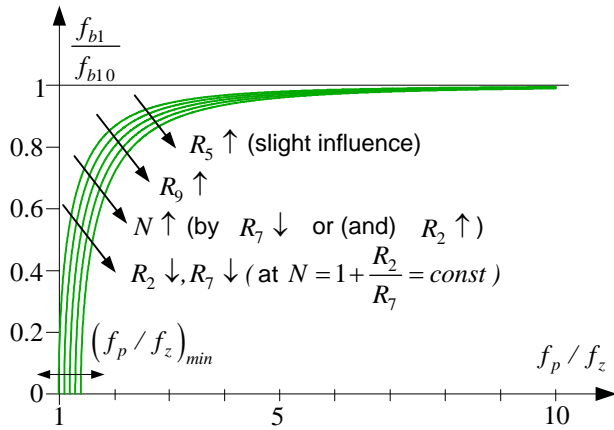


Fig. 7. The influence values R_2, R_5, R_7, R_9 on characteristics of dependence $\frac{f_{b1}}{f_{b10}} = f\left(\frac{f_p}{f_z}\right)$ for $\left(\frac{f_p}{f_z}\right)_{min} = var$

How the bandwidth structure is shaping was showed on fig. 8.

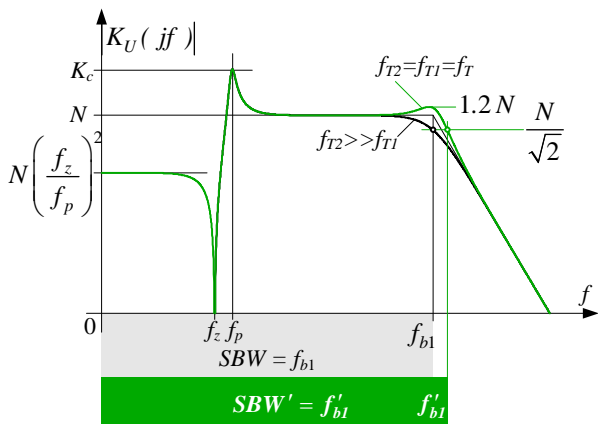


Fig. 8.

Fig. 9. The shaping of VES OPA-RC "b" - 02 structure bandwidth

Bandwidth SBW' may achieve magnificent value, especially for $(f_p/f_z) > 2$, when $SBW' \cong 1.83f_{b10}$. The best result obtains by choosing elements values R_2, R_5, R_7, R_9 to maximization f_{b10} , that is with preservation N i α_{59} as near unity as is possible. It gives SBW' may approach to f_T , and even exceed f_T . For confirmation of this, it was tested bandwidth of the structure realized transmittance with parameters: $Q = 4$, $f_p = 1$ kHz, $f_z = 10$ kHz, by using amplifiers with bandwidth $f_T = 1$ GHz. Values elements chosen at $N = 1.2$, $\alpha_{59} = 1.1$ and obtained the structure bandwidth $SBW' \cong 1.3$ GHz, so exceeded f_T (fig. 10).

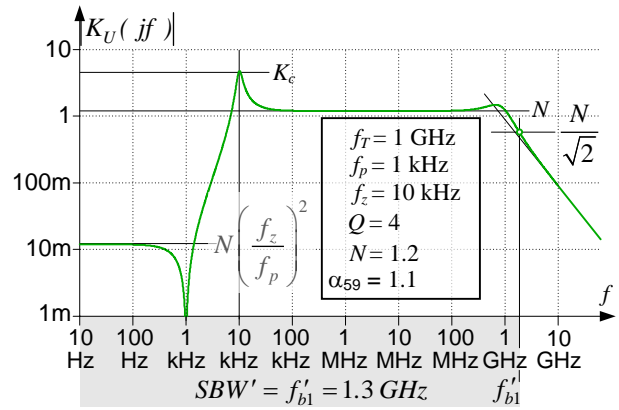


Fig. 10. Characteristics of VES OPA-RC "b" - 02 structure ($Q = 4$, $f_p = 1$ kHz, $f_z = 10$ kHz) at $f_T = 1$ GHz, $N = 1.2$, $\alpha_{59} = 1.1$

High-pass elliptic filter using the biquadratic structure VES OPA-RC „b” - 02

With using the structure VES OPA-RC „b” - 02 it is possible to get the filter with bandwidth FSW approaching to bandwidth f_T of amplifiers, if elements values of the structure become selected at $N = 1.2$, $\alpha_{59} = 1.1$ (then bandwidth of structures equals $SBW' \cong 1.3 f_T$). This big bandwidth of filter is difficult to achieve after using others worked out structures, such as e.g. the structure VES OPA-RC „b” - 01. How the bandwidth of filter shapes itself after using both of these mentioned structures was tested in programme SPICE™. The scheme of filter composed of VES OPA-RC „b” - 01 structures was showed on fig. 11, next filter composed of VES OPA-RC „b” - 02 structures on fig. 12.

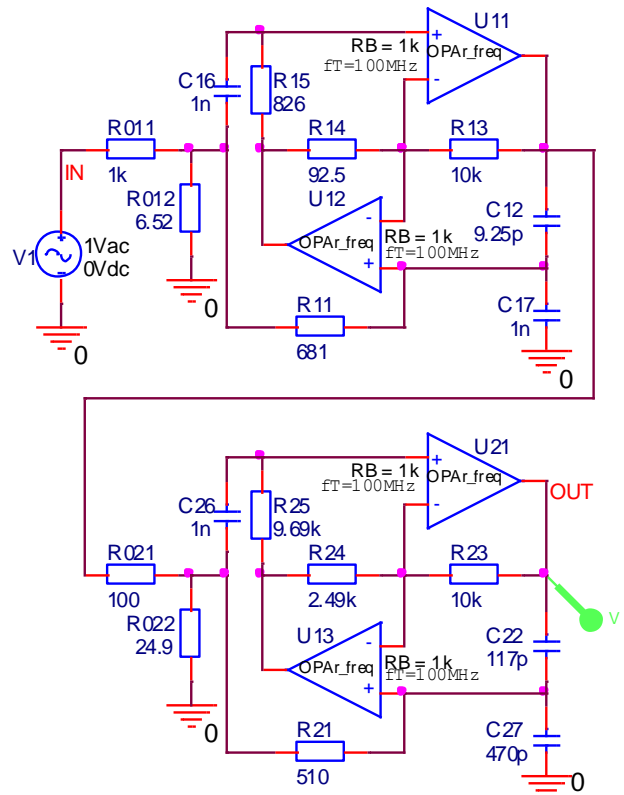


Fig. 11. Scheme of the high-pass filter composed of two VES OPA-RC "b" - 01 structures

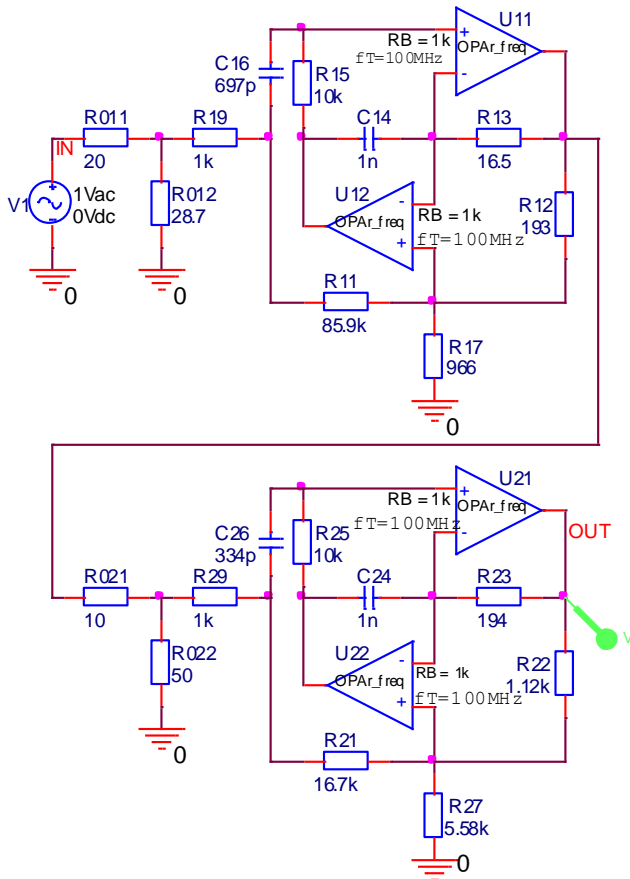


Fig. 12. Scheme of the high-pass filter composed of two VES OPA-RC "b" - 02 structures

Parameters of tested filters are following: order $r = 4$ (two structures in the cascade), $\varepsilon = 1$, $k = 0.5$, $f_{gr} = 100$ kHz. Bandwidth of amplifiers equals $f_T = 100$ MHz. Amplitude characteristics both of filters is showed on comparative diagram (fig. 13).

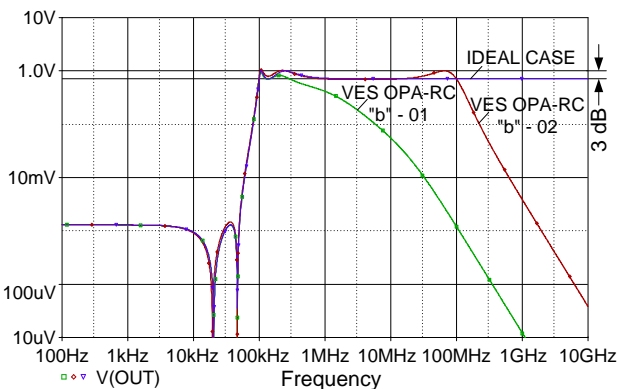


Fig. 13. Amplitude characteristics of high-pass filter realized on VES OPA-RC "b" - 01 and VES OPA-RC "b" - 02 structures

Assuming the criterion of 3 dB fall to determine bandwidth of the filter, it follows that bandwidth of filter composed from VES OPA-RC "b" - 02 structures is approximately equals $f_T = 100$ MHz. Bandwidth of filter composed from VES OPA-RC "b" - 01 structures is much smaller – equals about 300 kHz although it was used amplifiers with the same bandwidth f_T .

Summary

Finite bandwidth of amplifiers causes the amplitude characteristics of type "b" structures is deformed, and bandwidth of these structures gives unfavourably in narrowing. It leads consistently to narrow whole bandwidth of filter, which is composed of structures cascade.

Bandwidth of presented structure VES OPA-RC „b” -02 can be modelled to some degree by suitable choice of elements values. Choosing these elements at $N = 1.2$, $\alpha_{59} = 1.1$ the bandwidth that exceeds f_T is achieved: $SBW' \cong 1.3 f_T$. Bandwidth of filter composed of structures with in this way chosen elements achieves value approached to f_T . It is difficult to get with others type "b" structures, such as for example the VES OPA-RC „b” -01 structure based directly on the GIC converter. Bandwidth of this structure depends only on parameters of realizing biquadratic transmittance and cannot be in any way pulled up by choosing elements values. Moreover it is considerably smaller than bandwidth of filter composed of VES OPA-RC „b” - 02 structures.

Structure VES OPA-RC „b” - 02 can find application in the high-frequencies filtration [9]. Frequency range is laid by bandwidth of using amplifiers, which currently achieves values approaching to 2-3 GHz (table 1).

Table 1. Bandwidth f_T of modern produced OPA

| manufacturer | device | f_T |
|-------------------------|---------|----------|
| Analog Devices | AD8000 | 1.58 GHz |
| Analog Devices | AD8003 | 1.65 GHz |
| National Semiconductors | LMH6702 | 1.7 GHz |
| Texas Instruments | THS4508 | 2 GHz |
| Texas Instruments | THS4302 | 2.4 GHz |
| Texas Instruments | THS4304 | 3 GHz |

REFERENCES

- [1] Adrikowski T., Pasko M.: *Practical realization of even order elliptic filters using biquadratic structures*. SCI Letters "Elektryka" 182, p. 101-122 (2002), (in Polish).
- [2] Adrikowski T., Pasko M.: *Bandwidth analysis of elliptic biquadratic structures OPA-RC*. IC-SPETO'2007, Gliwice-Ustroń 2007, p. 199-200.
- [3] Adrikowski T., Pasko M.: *Voltage biquadratic elliptic structures using amplifiers OPA, OTA and OTRA*. "Elektronika" 12'2006, p. 44-49 (2006), (in Polish)
- [4] Adrikowski T., Pasko M.: *Low-pass and high-pass even order elliptic filters in current mode using transconductance amplifiers OTA and BOTa*. "Elektronika" 10'2006, p. 45-49 (2006), (in Polish).
- [5] Fliege N.: *A New Class of Second Order RC-Active Filters with Two Operational Amplifiers*. Nachrichtentech. Z., vol. 26, Germany 1973, p. 279-282.
- [6] Gray P. R. and Meyer R. G.: *Analysis and Design of Analog Integrated Circuits*. John Wiley & Sons, New York, 3 edition, 1993.
- [7] M. Pasko and T. Adrikowski: *Even order elliptic filter design using OTA-C or OTA-RC biquadratic structures*. Acta Techn. CSAV 49, p. 223-234 (2004).
- [8] Porębski J., Korohoda P.: *SPICE. Nonlinear analysis program of electronic circuits*. WNT, Warszawa 1996, (in Polish).
- [9] Tajalli A., Atarodi S. M.: *A compact biquadratic gm-C filter structure for low-voltage, high-frequency applications*. IEEE ISCAS(1), p. 501-504 (2003).
- [10] Topór-Kamiński L.: *Electronic amplifiers in active circuits*. Publishing house of Silesian University of Technology, Gliwice 2000, (in Polish).

Authors: prof. dr hab. inż. Marian Pasko, E-mail marian.pasko@polsl.pl,
dr inż. Tomasz Adrikowski, E-mail: tomasz.adrikowski@polsl.pl,
Politechnika Śląska, Instytut Elektrotechniki Przemysłowej i Informatyki, ul. Akademicka 10, 44-100 Gliwice

Mathematical description of eddy-currents in a non-homogenous area with using electric scalar potential

Abstract. The article presents an efficient implementation of mathematical description of eddy-currents excited in human body by external, time-varying magnetic fields. The description was formulated on the basis of the electric scalar potential with simplifying assumptions allowed for bioelectromagnetic problems. The new formulation of interface condition on the boundaries of different tissues is presented. This allows substantial reduction of computational burden for finite element model. The numerical tests confirmed the correctness of the method, as well as its high computational efficiency.

Streszczenie. W artykule przedstawiono wydajny opis matematyczny prądów wirowych przy wolnozmiennych wymuszeniach elektromagnetycznych pochodzących od płynącego w cewce prądu elektrycznego. Polem zastosowań prezentowanego rozwiązania są problemy bioelektromagnetyczne, z czego wynikają zastosowane założenia upraszczające. Opis został sformułowany w oparciu o skalarny potencjał elektryczny. Zaprezentowano autorskie rozwiązanie zagadnienia na granicach niejednorodności, podczas obliczeń metodą elementów skończonych. Testy numeryczne potwierdziły poprawność metody, oraz jej wysoką wydajność obliczeniową. (**Matematyczny opis prądów wirowych w obszarze niejednorodnym z wykorzystaniem skalarnego potencjału elektrycznego**)

Keywords: eddy currents, electric scalar potential, FEM

Słowa kluczowe: prądy wirowe, skalarny potencjał elektryczny, MES

Introduction

Modeling of eddy-currents in living organisms is connected with many difficulties [6]. The largest challenge for researchers is taking into consideration the complicated internal structure of organisms, as well as complicated electrical parameters of tissues [4, 5].

In order to simulate the field distribution, the authors applied the finite element method (FEM), which is successfully used in solving problems referring to complicated geometry. The necessity of realistic shapes mapping of the examined human organs causes the fact that digitizing of the area has to be exceptionally dense [3]. Therefore, the rash choice of a simulation method can result in too long time of calculations.

The authors offer a solution, which aims at a considerable acceleration of the modeling of the eddy-currents phenomenon in non-homogenous, low conducting areas. Application of the electric scalar potential is optimal for the reason of the number of the unknowns, and thus, the burdening of the memory of a computer solving the linear system of equations.

Mathematical model

The researched area is presented schematically in Fig. 1. Sub-area Ω_4 is the source of the low-frequency magnetic field. This area is galvanically separated by a dielectric area Ω_3 from conducting sub-areas Ω_1 and Ω_2 , which symbolize non-homogenous conducting environments. Eddy-currents are induced in them.

As far as bioelectromagnetic issues are concerned, omitting the phenomena of: skin effect, electric current displacement as well as the impact of magnetic field coming from the current flowing in a low-conducting researched area, has a positive influence on the rate of calculations, and at the same time it does not change the accuracy of the simulation results. The mentioned assumptions allow for considerable simplifications while building the numerical model. Further considerations will be based on the following equations:

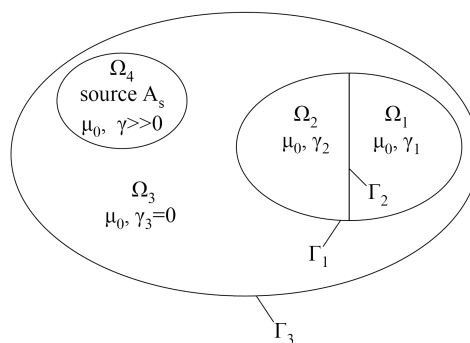


Figure 1. Notation used in this paper: considered domain $\Omega_1 \cup \Omega_2$; Ω_3 – insulator; Ω_4 – source

$$(1) \quad \nabla \times \vec{E} = -\frac{\partial \vec{B}}{\partial t},$$

$$(2) \quad \nabla \cdot \vec{B} = 0,$$

$$(3) \quad \vec{B} = \mu \vec{H}.$$

Usage of potentials which are continuous over the domains with different material parameters usually simplifies the computer simulations of eddy-currents distribution [1]. The present paper makes use of electric scalar potential (φ) and magnetic vector potential (\vec{A}) [2].

The definition of magnetic vector potential \vec{A} : $\vec{B} = \nabla \times \vec{A}$ can be substituted to the equation (1), giving

$$(4) \quad \nabla \times \vec{E} = -\frac{\partial}{\partial t} \nabla \times \vec{A}.$$

The definition of \vec{A} is not unique. Curl of the gradient of any scalar function is zero: $\nabla \times (\nabla \varphi) \equiv 0$, thus we can

rewrite (4) as

$$(5) \quad \nabla \times (\vec{E} + \frac{\partial \vec{A}}{\partial t}) = -\nabla \times (\nabla \varphi),$$

what leads to the description of the total electric field as

$$(6) \quad \vec{E} = -\nabla \varphi - \frac{\partial \vec{A}}{\partial t}.$$

Equation (6) describes distribution of the electric field intensity within the researched area. It consists of two parts. The $\frac{\partial \vec{A}}{\partial t}$ is due to external sources and can be calculated on the basis of the Biot-Savart law. Value of $\nabla \varphi$ will be calculated with finite elements method.

After multiplying equation (6) by conductivity γ and after taking into consideration the equation $\vec{J} = \gamma \vec{E}$, we obtain the equation for the current density within the conducting area:

$$(7) \quad \vec{J} = -\gamma \nabla \varphi - \gamma \frac{\partial \vec{A}}{\partial t}.$$

Taking divergence operation of both sides of the equation (7) the following equation is obtained:

$$(8) \quad \nabla \cdot \vec{J} = -\nabla \cdot (\gamma \nabla \varphi) - \nabla \cdot (\gamma \frac{\partial \vec{A}}{\partial t}).$$

The vector field \vec{J} is a divergence free field, what can be written as $\nabla \cdot \vec{J} = 0$. When moving one of the parts to the right side, the final form of the partial differential formula equation, describing distribution of φ yields:

$$(9) \quad \nabla \cdot (\gamma \nabla \varphi) = -\nabla \cdot (\gamma \frac{\partial \vec{A}}{\partial t}).$$

Solving equation (9) is the main aim of this article.

Boundary conditions

Specifying the boundary conditions on the surface of the researched conducting area Γ_1 , is possible after noticing that the electric current does not flow through the surfaces Γ_1 , which is in accordance with the equation:

$$(10) \quad \vec{J} \cdot \vec{n} = 0,$$

where \vec{n} vector is perpendicular to the external surface of the conducting area.

If (10) is linked with (7), the condition for normal derivative on the external boundary of the conducting area will be obtained:

$$(11) \quad \gamma \frac{\partial \varphi}{\partial n} = -\gamma \frac{\partial A_n}{\partial t}$$

Equation (11) describes a non-zero Neumann condition, which can be taken into consideration when forming right side vector in a matrix description of an element, while applying the finite elements method. However, giving such a boundary condition on the whole boundary surface brings about the fact that the numerical stability of the analyzed problem requires fulfilling the condition:

$$(12) \quad \oint_S \gamma \frac{\partial \varphi}{\partial n} ds = \oint_S -\frac{\partial A_n}{\partial t} ds = 0$$

Satisfying (12) can be treated as test for convergence of the presented method. If the condition is not satisfied because of numerical errors, the problem is formulated incorrectly and the solution can not be obtained.

Exciting field

In a magnetically homogenous area, distribution of the magnetic field can be described using Biot-Savart law:

$$(13) \quad \vec{B} = \frac{\mu_0}{4\pi} \int_V \frac{\vec{J}_s \times \vec{r}}{|\vec{r}|^2} dv.$$

After making appropriate transformations of (13), the distribution of vector magnetic potential \vec{A} will be described as

$$(14) \quad \vec{A} = \frac{\mu_0}{4\pi} \int_V \frac{\vec{J}_s}{|\vec{r}|} dv.$$

Magnetic permeability of tissues of living organisms is signified as μ_0 and thus the above formula can be used for semi-analytical calculation of the external field term.

Solution 1: Natural FEM

While applying the finite element method, differential equation must be transposed to a discrete area of the finite element. For this purpose, it is necessary to determine the dependences which make it possible to create matrix and the right sides vector for each of the elements.

Equation (9) that is to be solved, is a classical elliptical equation, and therefore, the form of the expression for elements of the matrix is well known and amounts to:

$$(15) \quad M_{i,j} = \int_{V_e} \gamma \nabla N_i \cdot \nabla N_j dV,$$

where N_i is shape function of tetrahedron finite element.

Transposing the right side of the equation (9) to the right side vector of the finite element is possible through the following dependence:

$$(16) \quad b_i = \int_{V_e} \gamma \nabla N_i \cdot \frac{\partial \vec{A}}{\partial t} dV$$

Implementation of the equation (16) requires determining value of the field \vec{A} in all integration points. It is a possible yet time-consuming procedure. Therefore, often the average linear interpolation over a single element [1] is used, and then the equation (16) takes the following form:

$$(17) \quad b_i = 1/4 \sum_{j=1}^4 \int_{V_e} \gamma \nabla N_i \cdot \frac{\partial \vec{A}_j}{\partial t} dV$$

Solution 2: Based on condition for the current continuity

Alternate way to solve presented problem is take advantage of equality normal component of current density vector. For non-homogenous areas, within which the field distribution is described with the equation (9), the problem of the non-homogeneity materials boundary occurs.

Equation (9) can be transformed into the form:

$$(18) \quad \nabla \cdot (\sigma \nabla \varphi) = -(\nabla \sigma) \cdot \frac{\partial \vec{A}_s}{\partial t} - \sigma (\nabla \cdot \frac{\partial \vec{A}_s}{\partial t}).$$

With assumption about zero divergence of \vec{A}_s one can see that only gradient of conductivity is real source function. So the right term of this equation can be interpreted as pseudo-source of the field on the boundary of sub-areas of different conductivities. Because of digitizing of the area, the conductivity gradient is not clearly defined on the surface.

The modification of a partial differential equation describing the analyzed problem as well as formulating the boundary

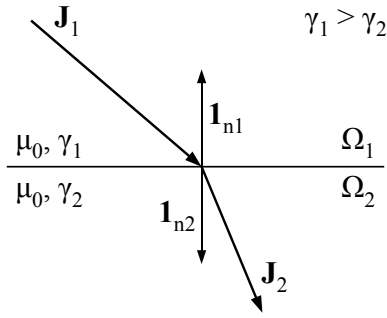


Figure 2. Illustration of the normal constituent continuance condition of current density vector during crossing through the boundary between areas of different conductivity

condition were conducted on the basis of Figure 2. The authors suggest procedure of avoiding the numerically difficult expression $\nabla\gamma$ within non-homogenous areas through simplifying the equation (9) to the following form:

$$(19) \quad \nabla \cdot (\gamma \nabla \varphi) = 0,$$

with simultaneous introduction of additional interface conditions on all faces of finite elements situated on the non-homogeneity boundary. This interface condition assures the continuity of the normal component of the current density vector on those boundaries.

We shall start with the continuity condition for normal components of current density: $\vec{J}_{n1} = -\vec{J}_{n2}$. These components are expressed by the following equations:

$$(20) \quad \vec{J}_{n1} = -\gamma_1 \frac{\partial \varphi_1}{\partial n} \cdot \vec{1}_{n1} - \gamma_1 \frac{\partial \vec{A}_{n1}}{\partial t}$$

$$(21) \quad \vec{J}_{n2} = -\gamma_2 \frac{\partial \varphi_2}{\partial n} \cdot \vec{1}_{n2} - \gamma_2 \frac{\partial \vec{A}_{n2}}{\partial t}$$

Taking into consideration that $\vec{J}_{n1} = -\vec{J}_{n2}$, and subtracting (20) and (21) site by site, we obtain:

$$(22) \quad \gamma_2 \frac{\partial \varphi_2}{\partial n} \Big|_{\Omega_2} - \gamma_1 \frac{\partial \varphi_1}{\partial n} \Big|_{\Omega_1} = \gamma_2 \frac{\partial \vec{A}_{n2}}{\partial t} - \gamma_1 \frac{\partial \vec{A}_{n1}}{\partial t}$$

The potentials should be continuous: $\varphi_1 = \varphi_2 = \varphi$ and $A_{n1} = A_{n2} = A_n$, and thus (22), may be replaced by the following system of equations

$$(23) \quad \begin{cases} \gamma_1 \frac{\partial \varphi}{\partial n} = -\frac{\gamma_2 - \gamma_1}{2} \frac{\partial A_n}{\partial t} \\ \gamma_2 \frac{\partial \varphi}{\partial n} = -\frac{\gamma_1 - \gamma_2}{2} \frac{\partial A_n}{\partial t} \end{cases}$$

These conditions must be applied on both side of the interface.

It can easily be shown that in case of homogenous domains, the system of equations (23) reduces to natural Neumann condition for continuity of the potential. However, on the external surface of the conducting area (Γ_1), equation (22) reduces to the form:

$$(24) \quad \frac{\partial \varphi}{\partial n} \Big|_{\Omega_1} = -\frac{\partial A_n}{\partial t},$$

what is identical with (11), describing boundary condition on the external border of the conducting area.

Test problems

The presented numerical model was implemented as a computer program in C++ language, making use of libraries assisting in solving of the Diffpack differential equations.

While solving test problems, a special field \vec{A}_s was used, which corresponded with homogenous magnetic induction $\vec{B}_s = [0, 0, 1]T$. In order to receive the specified vector of magnetic induction, the vector field \vec{A} will be used.

$$(25) \quad \vec{A}_s(x, y, z) = [0.5y, -0.5x, 0].$$

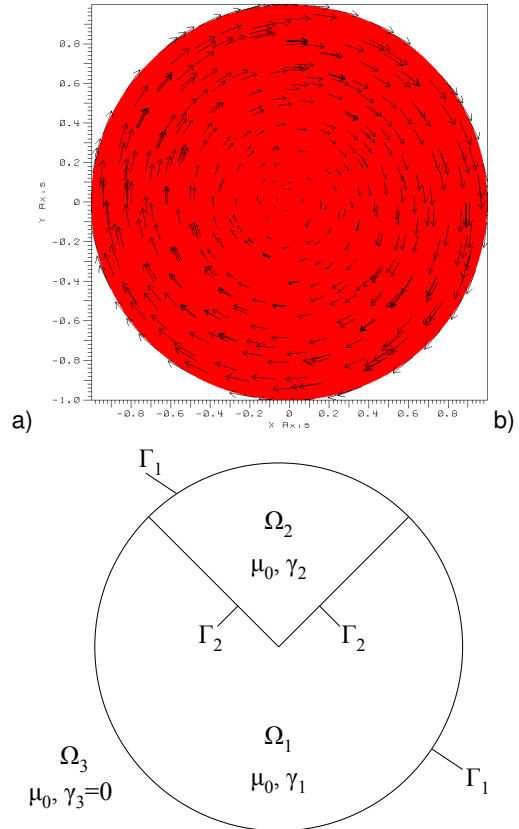


Figure 3. a) Potential distribution \vec{A}_s bringing homogeneous field \vec{B}_s which corresponds with equation (25); b) Scheme of the model consisted of two sub-domains with different electrical conductivity. Plane section transverse to symmetry axis of cylinder.

Test problems checking correctness of the presented modifications were conducted on simple geometrical solids consisting of two sub-areas (look at figure 3b)). The area signified as Ω_2 constitutes a cylinder sector. The test example was selected so that intuitive checking of the correctness of the eddy currents distribution would be possible. It is also important that the surface Γ_2 is perpendicular to the field \vec{A}_s , because then the case which is more difficult concerning the effect of non-homogeneity area on the calculation boundary.

The distribution of φ potential within the researched non-homogenous area was presented on the Figure 4a). Places, where the value of the φ potential differs significantly from the rest, are situated on the borders of sub-areas, on which the boundary condition described by equation system (23) should be fulfilled.

On the surfaces Γ_2 , artificial pseudo-sources of the current were introduced. It is clearly noticeable on the Figure 4b) showing the gradient φ distribution. It is an one of the equa-

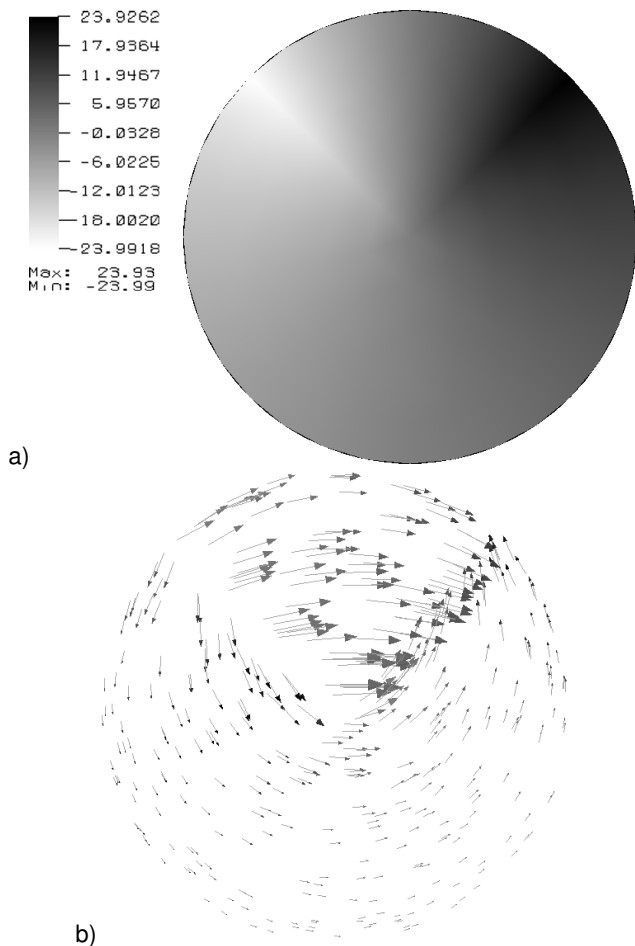


Figure 4. Results of simulation in non-homogeneous domain: a) potential φ value, b) distribution of the gradient value $\nabla\varphi$.
 tion (6) terms, and after putting it together with values \vec{A}_n presented on the Figure 3a), distribution of the electric field intensity \vec{E} will be received.

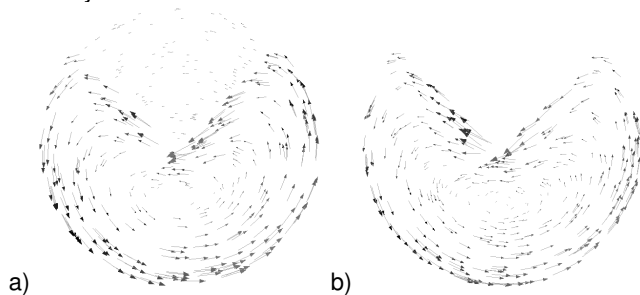


Figure 5. Vector of eddy-current distribution density \vec{J} . Figure a) non-homogeneous domain consisting of two electrical conductors with conductivity $\gamma_1/\gamma_2 = 20$, and figure b) homogeneous domain with cut-out.

Figure 5 presents the final vector \vec{J} distribution, a) in a non-homogeneous area, b) in a homogeneous area created by rejecting the area Ω_2 from the model. The value of the conductivity dependence in the non-homogeneous model amounts to $\gamma_1/\gamma_2 = 20$.

After the first look at the results it can be noticed that both solutions are of similar nature. According to intuitive predictions, in both models, the center of circulation of eddy-currents changed its location in reference to homogeneous cylinder, when the currents distribution will be precisely axis-symmetrical.

Quantitative comparison of the results for a homogeneous and non-homogeneous area also proceeds successfully. In

case of the homogeneous area 5b), the maximal value of the current density vector is bigger and amounts to $2.0 \times 10^3 \frac{A}{m^2}$, than in relation to the non-homogeneous area (presented on the figure 5 a)), where it amounts to $1.7 \times 10^3 \frac{A}{m^2}$. It is in accordance with intuition, because the current does not have the possibility to flow in the sector, and therefore, it is more condensed in the area Ω_1 .

Summary

The results received in each of two presented solutions are compatible with each other. However, the methods differ from each other as far as algorithms implementation and problems connected with this are concerned.

The natural solution FEM is saddled with more difficult and more time-consuming stage of forming the linear equations system. However, it is of importance that the process of its solving converges and is already stable.

The reverse situations can be observed in case of the second of presented solutions. Equation system is received faster, but its conditioning is much worse. The problem results from the considerable sensitivity for the accuracy of the arrangement of boundary conditions. Correct formulating of the problem requires that the complete balance of Neumann condition to the zero.

The effectiveness of the description made with scalar potential is of interest in bioelectromagnetic problems which require a considerable numerical machine power. The presented usage of potential pair φ and \vec{A} builds hope, but only further research will show the true usefulness in modeling the real bioelectromagnetic issues.

REFERENCES

- [1] W. Wang and S. R. Eisenberg: *A Three-Dimensional Finite Element Method for Computing Magnetically Induced Currents in Tissues*, IEEE Transactions on Magnetics, vol. 30, no. 6, pp. 5015-5023, November 1994
- [2] Maria A. Stuchly and Trevor W. Dawson: *Human Organ and Tissue Induced Currents by 60 Hz Electric And Magnetic Fields*, Proceedings - 19th International Conference - IEEE/EMBS, vol. 6, pp. 2464-2467, 30 Oct.-2 Nov. 1997
- [3] Erion Gjonaj, Michael Bartsch, Markus Clemens, Sooren Schupp, and Thomas Weiland: *High-Resolution Human Anatomy Models for Advanced Electromagnetic Field Computations*, IEEE Transactions on Magnetics, vol. 38, no. 2, March 2002
- [4] Trevor W. Dawson and Maria A. Stuchly: *High-Resolution Organ Dosimetry for Human Exposure to Low-Frequency Electric Fields*, IEEE Transactions on Power Delivery, vol. 13, no. 2, April 1998
- [5] Maria A. Stuchly and Trevor W. Dawson: *Interaction of Low-Frequency Electric and Magnetic Fields with the Human Body*, Proceedings of the IEEE, vol. 88, no. 5, May 2000
- [6] N. Siauve, R. Scorretti, N. Burais, L. Nicolas, A. Nicolas: *Electromagnetic fields and human body: a new challenge for the electromagnetic field computation*, COMPEL, Vol. 22 No. 3, 2003
- [7] Kurt Preis, Oszkar Biro, Igor Ticar: *Gauged Current Vector Potential and Reentrant Corners in the FEM Analysis of 3D Eddy Currents*, IEEE Transactions on Magnetics, vol. 36, no. 4, pp. 840-843, July 2000

Authors: mgr inż. Przemysław Płonecki, dr inż. Bartosz Sawicki, dr inż. Jacek Starzyński, prof. dr hab. inż. Stanisław Wincenciak, Politechnika Warszawska, Wydział Elektryczny, Instytut Elektrotechniki Teoretycznej i Systemów Informacyjno-Pomiarowych, ul. Koszykowa 75, 00-662 Warszawa, email: (ploneckp, sawickib, jstar, win)@iem.pw.edu.pl

Open Source Boundary Element Method Library for Diffusion Optical Tomography

Abstract. This article presents the project of the new open source Boundary Element Method library. It discusses main goals of the project and its characteristics consistent with the 'good open source project'. It covers license conditions, chosen technology, design of the project as well as development process.

Streszczenie. W artykule została zaprezentowana nowa biblioteka implementująca Metodę Elementów Brzegowych o otwartym kodzie źródłowym. Scharakteryzowano główne cele i założenia projektu. Opisano proces projektowania, rozwoju i zastosowanej technologii. (Biblioteka MEB dla dyfuzyjnej tomografii optycznej realizowana na licencji GNU)

Keywords: Boundary Element Method, Open Source BEM library, Diffusion Optical Tomography

Słowa kluczowe: Metoda Elementów Brzegowych, otwarte oprogramowanie, Dyfuzyjna Tomografia Optyczna

Introduction

For a few decades rapid development of Boundary Element Method (BEM) can be observed [1, 2, 3]. During that time range of BEM's application has increased [4, 5]. Among other it is applied in electrotechnics, mechanics, aviation energetics, acoustics or medicine. However it is not easy to find ready to use BEM implementations. It is even worse when we try to find the free open source software especially specialised one, applicable to, for example, Diffusion Optical Tomography. The result of broad searches of BEM software is presented in table 1. The reason why this state is maintained, may be complexity of integration during BEM calculations (especially singular integrals). Despite of difficulties this problem was overcome [6]. It appears that industrial and sci-

| Library (software) | Environment | Distribution conditions | Purpose |
|--------------------------------------|--------------------------|---------------------------|-------------------------------------|
| ABEM [7] | Fortran | commercial, open source | acoustics |
| LibBem [8] | C++ | semi commercial | Laplace eq. |
| BEMLIB [9] | Fortran | GPL | Laplace, Helmholtz, Stokes flow |
| BIEPACK [10] | Fortran | free open source | Laplace eq. |
| BEA [11] | Fortran | distributed with the book | acoustics |
| BEASY [12] | Windows or Unix binaries | commercial | construction engineering, acoustics |
| Integrated Engineering Software [13] | Windows binaries | commercial | fields, wave, thermal analysis |

Table 1. BEM library review

entific groups would like to have a well designed platform for BEM calculations. It should be universal but at the same time its modularity should easily enable application in very specific tasks. If needed, writing own plugins/modules, extending its functionality of solving other Boundary Integral Equations (BIE), usage of other for example integration algorithms or set of linear equations solvers, must be simple. Moreover ability of using only selected, single modules in external projects is

expected.

The needs and expectations mentioned above caused that the platform for BEM calculations is being realised. Particular elements of the project are introduced in the following sections.

BEM and Diffusion Optical Tomography

At first stage the description of the projects' algorithm and its example application has to be introduced. Here Boundary Element Method in Diffusion Optical Tomography (DOT) will be used. DOT was chosen, despite of many excellent papers in which implementation of Finite Element Method (FEM) is presented [14, 15]. However only the BEM offered a very simple and effective from patient to patient creation of the good quality surface meshes of the heads' layers, including the cerebrospinal fluid (CSF) layer [16]. Generation of the good quality surface meshes is much easier and more effective in BEM than in FEM [17], especially in three dimensions. Description will be limited only to general concepts important to the model and its implementation.

Diffusion equation (1) is the approximation used in DOT [5] and it will be used as an example to present BEM library internal build and operation.

$$(1) \quad \nabla^2 \Phi(\mathbf{r}) - k^2 \Phi(\mathbf{r}) = b$$

where the potential function Φ represents the photon density, k is the wave number and b represents internal sources.

As BEM uses Boundary Integral Equations (BIE) we have the integral form of equation 1:

$$(2) \quad C(\mathbf{r})\Phi(\mathbf{r}) + D \int_{\Gamma} \frac{\partial G(R)}{\partial n} \Phi(\mathbf{r}') d\Gamma(\mathbf{r}') = D \int_{\Gamma} G(R) \frac{\partial \Phi(\mathbf{r}')}{\partial n} d\Gamma(\mathbf{r}') + \iint_{\Omega} G(R) b d\Omega(\mathbf{r}')$$

where $C(\mathbf{r})$ for the smooth surfaces takes the value $\frac{1}{2}$, D is the diffusion parameter (to see details consult [17]) and $R = |\mathbf{r} - \mathbf{r}'|$ is the distance between the fixed interior or here boundary point \mathbf{r} and any point \mathbf{r}' on the boundary Γ of the region Ω .

To simplify further equations, we assume $b = 0$. Now, discretization of the boundary Γ into J elements has to be

done and it leads to the following equation:

$$(3) \quad C(\mathbf{r})\Phi(\mathbf{r}) + D \sum_{j=1}^J \int_{\Gamma_j} \frac{\partial G(R_j)}{\partial n} \Phi(\mathbf{r}_j) d\Gamma = D \sum_{j=1}^J \int_{\Gamma_j} G(R_j) \frac{\partial \Phi(\mathbf{r}'_j)}{\partial n} d\Gamma$$

Special attention must be drawn to the integrals in the equation 3. If \mathbf{r} belongs to the same boundary element as \mathbf{r}'_j then singularity occurs and singular integration have to be used otherwise non-singular one.

Finally, we will obtain the set of J (for the constant boundary element) linear boundary equations by choosing point \mathbf{r} from the different boundary element for each equation, which will result in the matrix form equation 4. Generally, the number of equations is represented by the number of nodes, which is also applicable for boundary elements of the higher order.

$$(4) \quad \mathbf{A}\Phi = \mathbf{B} \frac{\partial \Phi}{\partial \mathbf{n}}$$

After applying Neumann, Dirichlet and/or Robin boundary conditions we will obtain:

$$(5) \quad \mathbf{a} \begin{bmatrix} \Phi_{\mathbf{x}} \\ \frac{\partial \Phi_{\mathbf{x}}}{\partial \mathbf{n}} \end{bmatrix} = \mathbf{b}$$

where $\Phi_{\mathbf{x}}$ and/or $\frac{\partial \Phi_{\mathbf{x}}}{\partial \mathbf{n}}$, in the equation 5, represent only unknown boundary values as known ones (boundary conditions) are integrated into \mathbf{a} and \mathbf{b} BEM matrices.

Now system of linear equations 5 can be solved with the appropriate solver for example iterative GMRES algorithm or LU decomposition [18]. Afterwards we will know all the Φ and $\frac{\partial \Phi}{\partial \mathbf{n}}$ values on the boundary.

Finally value of the function Φ in any point \mathbf{r} from the inside of the considered region can be calculated using only simple operations as shown in the equation 6 (the equation 6 is valid in case of discretization with constant boundary elements):

$$(6) \quad \Phi(\mathbf{r}) = \sum_{j=1}^J \left(\frac{\partial \Phi_j}{\partial n} \int_{\Gamma_j} G_j d\Gamma - \Phi_j \int_{\Gamma_j} \frac{\partial G_j}{\partial n} d\Gamma \right)$$

where $\Phi_j = \Phi(R_j)$ and $G_j = G(R_j)$. $C(\mathbf{r})$ was skipped as for any internal point it takes the value of 1 [19].

Modelling

When the theoretical and mathematical description of the algorithm is done, we are ready to create its activity diagrams. They will help to divide the project into components.

The general BEM algorithm description from the previous section has to be 'translated' to the programming language. Finally a lot of source code will be generated where obviously assimilability is not its essence. Human better assimilates clear drawings or diagrams, where its elements are appropriately grouped. However mess in drawings can make them worthless. Therefore to avoid such situation it is better to use formal notation of drawn components. This would prevent inaccuracy and misunderstanding. Therefore such a 'language' of making diagrams has been created. Now the standard is Unified Modelling Language (UML), which will be used for making diagrams in the whole project's process [20].

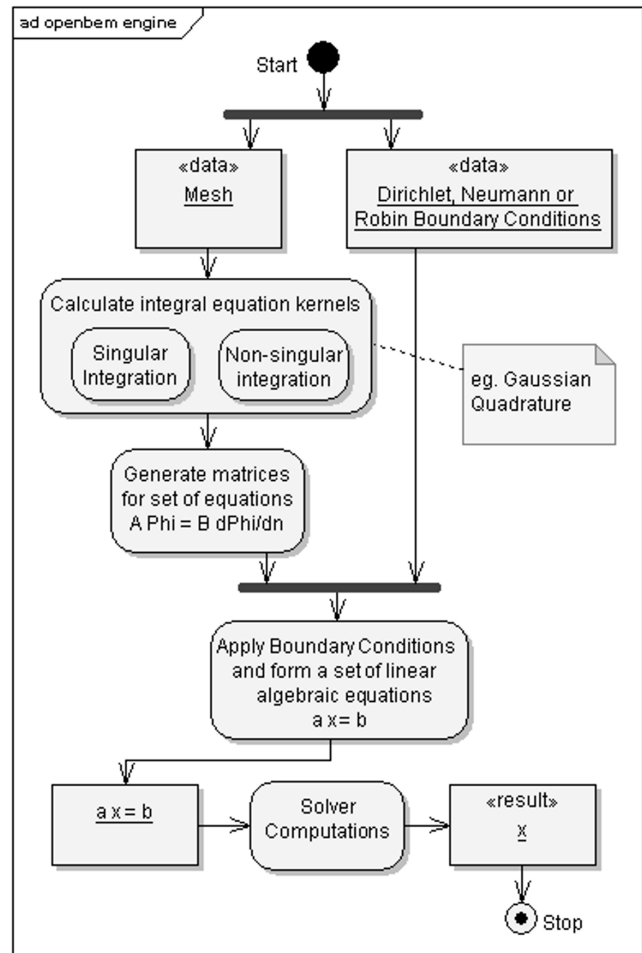


Figure 1. BEM engine activity diagram

The one-by-one BEM algorithm's elements are presented in the figure 1.

There are two input data types for BEM library computations: the generated mesh and boundary conditions. There is also the third one: parameters for internal sources defined on the right hand side of the equation 1. The problem solved using the library will be encapsulated into the programme which will comply from chosen library components. Mesh generation is out of the scope of this library, therefore external programmes have to be used. One of them is NETGEN. Together with mesh, boundary conditions have to be supplied.

When all input data are available, calculations can be started. At first all integral equation kernels from equation 3 has to be calculated:

$$\int_{\Gamma_j} \frac{\partial G(|\mathbf{r}-\mathbf{r}'_j|)}{\partial n} \Phi(\mathbf{r}_j) d\Gamma \text{ and } \int_{\Gamma_j} G(|\mathbf{r}-\mathbf{r}'_j|) \frac{\partial \Phi(\mathbf{r}'_j)}{\partial n} d\Gamma.$$

The number of singular and non-singular kernels which has to be evaluated is the product of numbers of *nodes*, *boundary elements* and *number of points in the boundary element*. In most cases integration is made numerically [6]. The singular integration occurs when kernel is calculated for two points belonging to the same element. The Green's function G is the fundamental solution specific for the given BIE.

After all kernels are calculated we can generate the set of linear equations shown in the equation 4. However it has too many unknowns. Fortunately Boundary Conditions (BC) comes with help. They may be of Dirichlet (Φ_j), Neumann ($\frac{\partial \Phi_j}{\partial n}$) and/or Robin ($\frac{\partial \Phi_j}{\partial n} = -\frac{1}{2D} \Phi_j$) type, but there must be enough of them.

When BCs are applied we can generate a set of linear

equations from the equation 5. Now very time consuming calculations come as, for the homogeneous regions, matrix \mathbf{A} is asymmetric and fully populated. Any of the adapted to the library solvers can be used, as they all have common interface. They are grouped in the 'Solvers' component.

After solving the equation 5 we have all boundary values known. Therefore now we can set about calculating function Φ as well as $\frac{\partial \Phi}{\partial n}$ values in the points from the inside of the region according to the equation 6. Unquestionable advantage of BEM is that calculations can be made only in needed internal points – not in all of them defined by the volume mesh as it is in case of the FEM.

Library Structure

As the BEM algorithm is already described by the activity diagram in the figure 1, the structure of the library can be introduced. The main activities without feedback, isolated in the mentioned diagram, help in creating proper components of the library. The library's assumption of the component build and independence of particular elements led to the component diagram presented in figure 2.

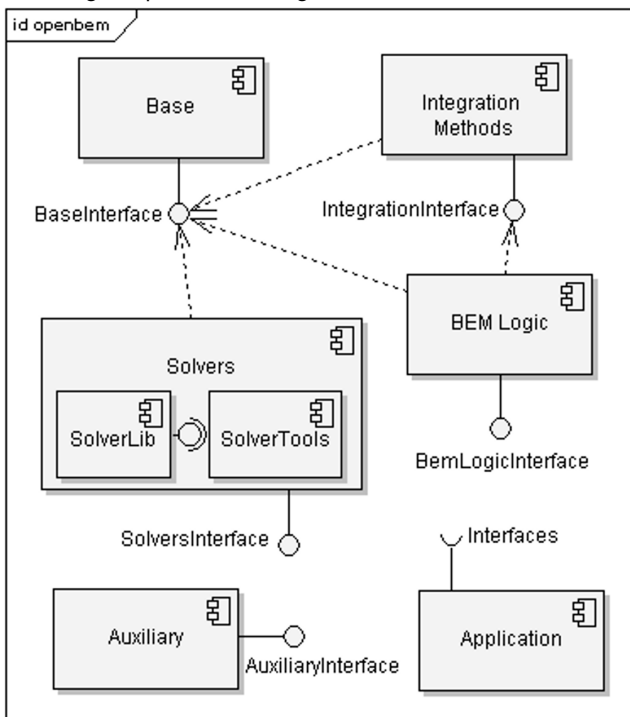


Figure 2. BEM library component diagram

In such a project structures for storing and exchanging data between components, user and external programmes, are required. They are combined into the 'Base' component, which is used by all other components. This component is in charge of importing and exporting data from/to MathWorks' Matlab matrices format. It will cover both complex and real number representation.

According to the activity diagram (figure 1) the next required component should cover integration algorithms. It exports the common interface which can be implemented by internal library or self-implemented algorithms and by wrappers to external libraries.

The next component is the 'BEM Logic'. It is combined from subcomponents which are in charge of generating \mathbf{A} , \mathbf{B} matrices from equation 4 and \mathbf{a} , \mathbf{b} from equation 5 for enabled BIEs and among others application of BCs.

'Solvers' is another component. At this stage it is combined of wrappers to the external libraries (for example

CSpaskit2 wrapper [21] to Spaskit library) as solver computation is complex. However if the demand for own solver implementations occur, they can be developed realising the 'SolverInterface' and then easily included to the library.

There are also needed some auxiliary procedures and classes combined into 'Auxiliary' component. Among others they are used for logging and statistics. The 'Application' component represents the specific user's programme, which solves the specified problem. It uses selected classes and procedures implementing other components' interfaces.

Each component exports and imports interface. It is also build up of two subcomponents as shown for the 'Solver'. One is library, and the other one represents programme, which allows running component's calculations externally. Input and export data are in Matlab format.

Open Source Project Technology

There were two main factors which affected choosing technology. The library is an open source project primarily to be run in Linux/Unix environment. The second one is the chosen programming language. The following section will briefly justify and characterise chosen technology.

Licensing — License aim is to give users rights for software running, analysing, copying, modifying and distributing with improvements. The chosen license is a widely used in open source environment: Gnu Public License (GPL) [22]. Among others it allows redistributing modified binary software only if the source code is open. Particular license conditions in GPL are grouped in 4 liberties (0–3). There is also a possibility that, in a future, some parts of code will be distributed with Berkeley Software Distribution (BSD) compliant license.

Programming Language — There are two programming languages which can be considered for this kind of project. They are C and C++. Other programming languages like Java, C# have many advantages. They have open source implementation (mono for C#). They are easy to use, objective and have good documentation (especially Java). They are portable because they use virtual machines, available on most operating systems, to run programmes compiled to bytecode. But they have one main disadvantage. They are slow for numerical computations. As it is easier to design and implement software using objective programming the project is being implemented in C++. Gnu C++ compiler is used [22] as it is very popular and available on almost all platforms.

Source Code Version Control — Source Code Version Control system allows keeping the source code in control and follow the changes. It is also the only possible way of work with the code by many people. Concurrent Versions System (CVS) and Subversion (commonly referred to as SVN) were considered as the project's choice. Both are popular but as SVN is the successor of CVS and lacks many of predecessor's disadvantages, it will be used by the project. Also, there is to be the web interface for SVN, which sometimes eases work with the code.

Source Code Manager — One of the main demands of the users of the software is ability to use one. The open source community mainly uses GNU [22] 'autotools' [23] to make distributions from the C/C++ source code and afterwards configure software properly on the clients machine, build and finally install in the clients operating system. Autotools is the common referrer for naming GNU automake, autoconf and libtool altogether. They are being used in this project despite of their disadvantages (complicated configuration, unclear source code or differences of usage between platforms, which has to be manually patched). Another con-

sidered possibility was usage of CMake, which is used by inter alia K Desktop Environment (KDE) project, but it is not a standard yet and may not become one.

Documentation — Documentation is essential for majority of people as it makes usage of software easier. It should follow users needs, and it seems that there should be three major types of documentation: installation instructions, tutorial and code documentation. These types help users on different stages of library usage.

It seems that tutorial or in Unix/Linux environment HOWTO is very important from the user's points of view. It makes possible a very fast start of using the software. There are to be tutorials covering major functionality of software. They practically illustrate simple and advanced features through examples. They cannot be wordy but have to show only library's essence. Tutorials will be aided by Unix style manuals especially for enclosed programmes.

As users are becoming skilled in using software or they would like to improve software they will need source code documentation. Unlike Java, C++ does not have a native built-in documentation tool like 'javadoc' or xml-based style interpreter as 'monodoc' for C#. However, as C/C++ is widely used, some documentation syntaxes and generators came into being. This library is using Doxygen, which is also used by MySQL database developers. It is not perfect but substantially better than other available open source generators. The good source code documentation can be generated only if the source code itself is properly documented. Javadoc is to be used as the code documentation syntax.

Portal — The 'good open source project' must exist in the internet as it is the most popular and accessible place for distributing software and documentation, submitting bug reports and improvements, exchanging ideas. The project portal should have at least the downloads, documentation and news sections. Mailing lists and forum are advisable. Library sources, binary software packages in DEB and RPM file format for Linux distributions will be available as well as ports for FreeBSD Unix and Gentoo Linux. The portal will be managed by a group of people. Therefore Content Management System (CMS) like Drupal or Joomla will be used. Documentation will be maintained with MoinMoin wiki. The next step will be mailing list. It will be managed by GNU Mailman [22]. If necessary forum will be created. The considered possibilities, also open source, are phpBB (inter alia used by gentoo) or less probably, java based jforum. Along with the growth of the project and its community bug tracking system will be introduced. So far perl-based bugzilla is considered.

Conclusions

There are not any open source, universal BEM projects available for community. There are only few implementations, mostly in Fortran and only applicable for restricted problems. In this situation properly designed, developed and maintained open source project may popularise BEM and its application. As the library and enclosed programmes' are compatible with the Linux/Unix products style, its usage is intuitive and does not require special technological knowledge. Modular and

component architecture will enable using only selected parts in own programmes and implementations. If the project will be good enough, it will gather people creating the community, which will improve and expand it.

REFERENCES

- [1] A.A. Becker. *The Boundary Element Method in Engineering. A complete course*. McGraw-Hill Book Company, 1992.
- [2] G. Beer. *Programming the Boundary Element Method. An Introduction for Engineers*. John Wiley & Sons, 2001.
- [3] G. Chen and J. Zhou. *Boundary Element Methods*. Academic Press, 1992.
- [4] K. Amaratunga. A wavelet-based approach for compressing kernel data in large-scale simulations of 3D integral problems. *Computing in Science and Engineering*, pages 34–45, July/August 2000.
- [5] J. Sikora, A. D. Zacharopoulos, A. Douiri, M. Schweiger, L. Horesh, S. R. Arridge, and J. Ripoll. Diffuse Photon Propagation in Multilayered Geometries. *Physics in Medicine and Biology*, 51(3):497–516, 2006.
- [6] M. H. Aliabadi and W.S. Hall. The regularizing transformation integration method for boundary element kernels. Comparison with series expansion and weighted Gaussian integration methods. *Engineering Analysis with Boundary Elements*, 6(2):66–70, 1989.
- [7] Abem. <http://www.boundary-element-method.com/>.
- [8] Libbem. <http://www.mis.mpg.de/scicomp/software/>.
- [9] Bemlib. <http://dehesa.freeshell.org/BEMLIB/>.
- [10] Biepack. <http://math.uiowa.edu/~atkinson/bie.html>.
- [11] T. W. Wu. *Boundary Element Acoustics: Fundamentals and Computer Codes*. WitPress, 2000.
- [12] Beasy. <http://www.beasy.com/>.
- [13] Ies. <http://www.integratedsoft.com/bem.asp>.
- [14] S. R. Arridge, M. Schweiger, M. Hiraoka, and D. T. Delpy. A finite element approach for modeling photon transport in tissue. *Medical Physics*, 20(2):299–309, 1993.
- [15] S. R. Arridge, H. Dehghani, M. Schweiger, and E. Okada. The finite element model for the propagation of light in scattering media: A direct method for domains with nonscattering regions. *Medical Physics*, 27(1):252–264, 2000.
- [16] J.D. Riley, H. Dehghani, M. Schweiger, S. R. Arridge, J. Ripoll, and M. Nieto-Vesperinas. 3D optical tomography in the presence of void regions. *OPTICS EXPRESS*, 7(13), 2000.
- [17] S. R. Arridge. Optical tomography in medical imaging. *Inverse Problems*, 15(2):R41–R93, 1999.
- [18] Y. Saad and M. H. Schultz. GMRES: A generalized minimal residual algorithm for solving nonsymmetric linear systems. *SIAM J. Sci. Statist. Comput.*, 7(3):856–869, April 1986.
- [19] M. H. Aliabadi. *The Boundary Element Method; Volume 2; Applications in Solids and Structures*. John Wiley & Sons, LTD, 2002.
- [20] Scott W. Ambler. *The Object Primer Agile Model-Driven Development with UML 2.0*. Cambridge University Press, 2004.
- [21] Csparskit2. <http://www.iem.pw.edu.pl/~wielebap/csparskit2/>.
- [22] Gnu. <http://www.gnu.org/>.
- [23] Gary V. Vaughan, Ben Elliston, Tom Tromej, and Ian Lance Taylor. *GNU Autoconf, Automake, and Libtool*. Sams, 2000.

Authors: Paweł Wieleba, Jan Sikora, Warsaw University of Technology, Institute of Theory of Electrical Engineering, Measurement and Information Systems, ul. Koszykowa 75, 00-662 Warszawa, Poland, e-mail: p.wieleba@iem.pw.edu.pl

Requirements Specification Language

Abstract. Requirements are currently undervalued in the software modelling world. Most of the model transformation approaches ignore requirements as not being precise enough to offer the possibility to construct certain uniform transformation and reuse mechanisms. In this paper we introduce a proposition of a unified language to specify requirements. This language allows for unambiguous transformation from requirements to design. The language offers refined use cases model for capturing functional requirements through scenarios. Sentences describing not only use case scenario sentences, but requirements in general, are structured according to Subject-Predicate constructs, where Subjects and Predicates are defined in a coherently linked vocabulary, which forms a precise domain vocabulary model. The language is currently being validated in practice by several software organisations, and has already been evaluated in student projects.

Streszczenie. Wymagania systemów informatycznych są obecnie niedocenione w świecie modeli oprogramowania. Większość metod transformowania modeli nie uwzględnia wymagań, traktując je jako zbyt mało precyzyjne, by opierać na nich mechanizmy przekształceń i ponownego użycia. Artykuł przedstawia ujednolicony język specyfikacji wymagań. Język ten pozwala na jednoznaczne przekształcenie z wymagań na projekt implementacyjny. Język zawiera udoskonalony model przypadków użycia, pozwalający na wyrażenie wymagań funkcjonalnych poprzez scenariusze. Zdania opisujące scenariusze przypadków użycia oraz bardziej ogólne formy wymagań są skonstruowane wg. wzorca Subject-Predicate (podmiot - grupa orzeczenia). Konstrukcje Subject-Predicate są spójne ze słownikiem dziedziny. Omawiane rozwiązanie jest obecnie w trakcie weryfikacji w realnych projektach i zostało już zweryfikowane w projektach studenckich. (Język specyfikacji wymagań)

Keywords: requirement specifications, use cases, scenarios, domain vocabulary, grammars

Słowa kluczowe: specyfikacje wymagań, przypadki użycia, scenariusze, słownik dziedziny, gramatyki

Introduction

Requirements specification seems to be such element of the software development lifecycle that has the lowest support in model-driven development. The tendency is such that requirements have to be transformed manually into more precise notations in order to be included into an automatic handling path. This is due to the fact that requirement representations lack a precise definition. In practice, requirements are usually written as paragraphs of natural language text. Such requirements specifications usually do not have precise links to the domain vocabulary. The vocabulary is often used inconsistently throughout the whole specification. This lack of common vocabulary also prevents from achieving any significant level of requirements reuse (see eg. [4] for a discussion on use case reuse). Typical scenarios (eg.: press button + show window + enter data + validate data + store data + show acknowledgement) get repeated over and over in many applications. Possibility of reuse of such standard scenarios that have unambiguously mapped design and code to it, could have tremendous value to software development organisations.

Unfortunately, multitude of approaches in various methodologies and ambiguity of natural language requirements lead to serious problems in translating them into design models and assuring traceability (including traceability between different projects). Thus, the current paper presents an approach to unify various tendencies in requirements modelling into a single coherent language.

Precise requirements models

Here we have to note limitations of having requirements represented in just the natural language. First limitation is caused by the fact that requirements as such are managed as wholes. This means that traces or mappings to or from requirements are done on the basis of “whole” requirements, not considering the requirement details (expressed through

appropriate representations). Second limitation is based on inability to analyse the contents of requirements for comparison. Since the contents are paragraphs of text, the only way to compare requirements is through natural language processing which has serious limitations. This makes it practically impossible to compare different requirements specifications in order to achieve certain reuse of their contents (reuse of functionality descriptions, reuse of term descriptions and so on).

What can we do with “whole” requirements? These requirements units can be traced one onto another and can be assigned certain attributes. We can also trace certain requirements into design. Such functionality is offered by major Requirements Management tool vendors (RequisitePro, DOORS, etc.). Finally, some level of reuse can be achieved by attaching certain “manifestation” information to the requirement artifacts (as in Reusable Asset Specification [12]). It can be noted that maintaining traces or manifestation information is quite laborious and has to be done manually. Moreover we can assure that requirements are met in design only on a coarse grained level (whole requirements).

What we really would like to do with requirements is to use their contents for certain tasks in a software development lifecycle. We would like to perform some automatic operations on the contents of several requirements.

In order to reach repeatability between requirements specifications we need a common syntax for individual elements of such specifications. This syntax is part of a language which we will call the Requirements Specification Language (RSL).

Complementary representations of use case scenarios

In RSL, the basic units for capturing functional requirements are use cases. Use cases are treated as “requirements as such” and can have different representations expressing possible use case scenarios. In RSL there are three

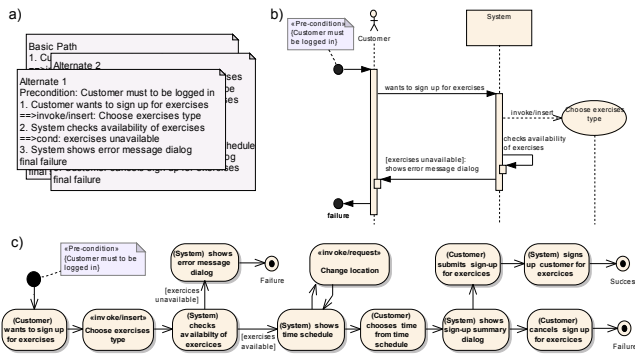


Figure 1. Example of concrete syntax for use case scenario representations in RSL: a) constrained language representation b) interaction representation c) activity representation

complementary use case scenario representations: constrained language representation, activity representation, interaction representation.

Each of these representations is capable of expressing exactly the same scenarios but it put emphasis on some aspects of interactions while suppressing some others, thus making it usable for diverse groups of people having different roles in the software project.

The constrained language representation is a purely textual representation, where scenarios are written as sequences of numbered sentences in the SVO grammar (this grammar is described in details in section "Grammars"), interlaced with condition and control sentences. These are special sentences used in scenarios to control the flow of scenario execution. A single scenario represents a single story without alternative paths. This representation is most readable for "ordinary people" like users or stakeholders who are usually reluctant to any technical notation.

Some people, usually analysts, prefer precise structure for use case scenarios in a graphical form. Activity scenario representation utilises UML activity diagrams to present use case scenarios. In this way, it allows for showing all possible scenario paths of a single use case in one picture. This precisely reflects the flow of control in a use case as a single unit of functional requirement.

Interaction representation presents a single scenario as a sequence of messages send between the system, the actors and other use cases in the form of UML sequence diagram. This representation clearly reflects temporal interaction of the actors with the system as well as actions performed by the system in response to the actors' interaction. It seems to be most suitable for designers as it prepares them for transformation into design level interaction diagrams.

Figure 1 shows examples of concrete syntax for these three representations. Figure 1a presents one of scenarios of a use case in constrained language. In Figure 1b, the interaction representation of the same scenario is shown. We can see that all sentences from the constrained language scenario have their equivalents in the interaction scenario in the form of messages between lifelines. The activity scenario representation in Figure 1c shows all scenarios of the use case in one diagram. Scenario sentences are presented as activity nodes or edges (in case of condition sentences).

Domain Vocabulary

Most requirements specifications have a section somewhere close to the end entitled "Vocabulary" or "Glossary". Requirements specifiers usually put there some list of terms with their definitions. Usually, this list is far from being complete and soon after being introduced becomes obsolete and

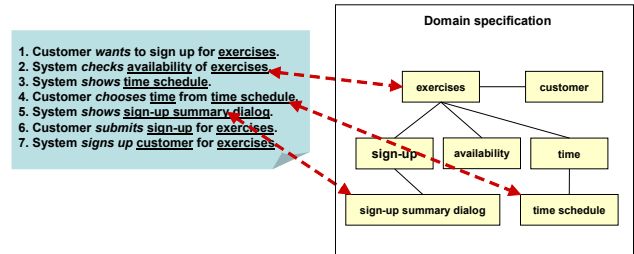


Figure 2. Separated Domain Vocabulary

inconsistent with the rest of the document. Unfortunately, this practice is one of key reasons why requirements specifications are usually incoherent and imprecise. This is caused by lack of uniformly used domain vocabulary. Most often, the vocabulary is in fact buried throughout the whole specification. All the definitions of domain notions are scattered everywhere leading in many places to contradictions (eg. different definitions of the same term). On the other hand, having a separate description of the environment is the key to creating internally coherent specifications [17, 5].

Most often, glossaries for requirements specifications concentrate mostly on the "noun" aspects of the domain. "Verbs" and "adjectives" are left undefined and their definitions are scattered usually within the functional (verbs) and non-functional (adjectives) requirements (see [14, 6] for approaches that include also verbs). It thus can be argued that the vocabulary should contain definitions of whole phrases. Phrase-based languages have been recognised to have an advantage over word-based languages since they allow us to capture dependencies between long spanning elements in requirements (see [13]).

In this paper we propose a notation for formulating requirements with the use of phrases contained in a central vocabulary. The RSL is structured to use this vocabulary extensively. Sentences in the language are structured in a specific grammar, so that their subjects and predicates point to specific phrases in the vocabulary (see Fig. 2).

Using a central domain vocabulary gives us also an additional possibility of introducing high levels of reuse to requirements. Having a uniform terminology used, allows us to compare requirements and retrieve certain parts of them for reuse. If an external terminology with a thesaurus (generally: some semantic net) is used, phrases in the vocabulary can be compared even if lexically different (see [3, 6, 1] for some approaches to this).

While creating requirements specifications for computer-based systems it is essential to recognise entities that exist in business environment of future software system [7]. Those entities can represent data handled by the system and system's elements. Capturing more or less complete list of notions for domain vocabulary is a key to understand the way environment of new system works and therefore to create a good basis for requirement specification [14]. In the following paragraph we present a taxonomy of domain vocabulary components.

While identifying domain vocabulary entities, they can be grouped in certain packages (for logical separation for instance). Vocabulary elements can be also assigned a type, to distinguish data to be handled by the system from actors interacting with its components (system elements and user interface elements). Every part of the composite system that is referred to in the requirements specification can be system element (this includes user interface elements), actor or notion. All these vocabulary elements can be referred

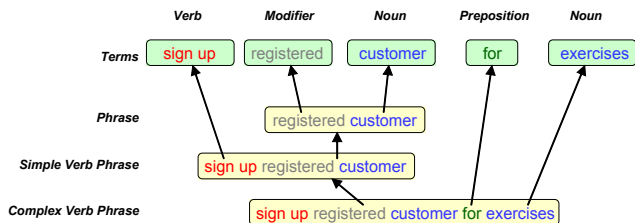


Figure 3. Building phrases

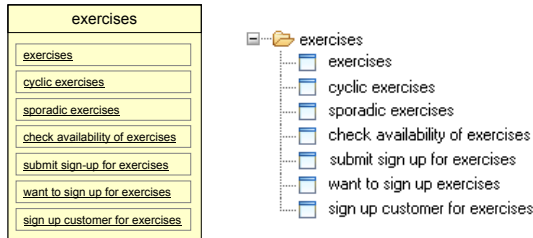


Figure 4. Notion example

to in functional and non-functional requirements. Even actors, which participate in scenarios and use cases (functional requirements), may also be referred to in non-functional requirements.

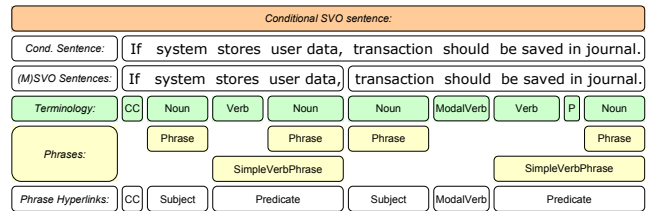
It is worth to note that new notions can be introduced at any stage of writing requirements specification, according to analysts' needs [18]. For example new systems entities can be discovered during describing or defining already existing notions.

All noun-based expressions are defined as phrases. Only such expressions can describe domain entities, their behaviour and their characteristics. The base "phrase" contains a noun and optionally determiner and modifier (latter two can be different parts of speech in different languages). "Verb phrases", in addition, contain verbs ("simple verb phrase") or verbs and other nouns ("complex verb phrase"). Verb phrases may be enriched by prepositions. All these phrases are shown in Figure 3. Main vocabulary entry (a notion) groups phrases relevant for given notion (see Figure 4)

All phrases are sequences of hyperlinks (see the following paragraphs) pointing at terms, which are stored (with their forms, inflections, cases) in an external, global structure – Terminology. The Terminology contains relations between Terms. These relations define the semantics of Terms. Such structure in fact is an ontology and can be based on existing dictionaries/ontologies (e.g. WordNet [8]).

The idea of using hyperlinks is the basis for element representation's content, that consists of other elements without copying their names, but by pointing to their definitions. Hyperlink may point at exactly one element. This allows for building a requirements specification where behavioural and quality requirements are based on the domain vocabulary, and domain vocabulary is based on external terminology. Such approach is beneficial only with strong software support. Hyperlinks, when applied in requirements specifications are basic facilitators of coherence [10].

The precision of requirements specifications is assured by using hyperlinks that link requirements text with definitions of phrases. These hyperlinks can be embedded in free text requirement representations, structured language representations, like SVO sentences (Subject, Predicate hyperlinks - see the following section).



CC – Conditional Conjunction
P - Preposition

Figure 5. Example of Conditional Sentence

Grammars

During creation of a requirements specification for a software system, several aspects have to be described and different types of structured sentences could be used for this. If sentences are structured, they are easy to understand for the users, moreover, they can be automatically processed (edited, compared, even translated in a "word-by-word" fashion, to give some hints about the meaning).

It can be argued that most of software requirements could be covered by 3 types of sentences – SVO sentences, modal SVO sentences and conditional sentences. All of these sentences can be built from phrases used as atomic "lexemes". Detailed description of sentence structures with examples is presented in the following subsections.

SVO Sentence is a statement in a simple SVO(O)¹ grammar [9]. SVO sentence can be defined using two phrases: a subject phrase and a predicate phrase. Subject can include any notion from a domain vocabulary, possibly grouped with its determiner and modifier (together forming a subject phrase). Predicate is a more complex phrase, which in addition to strictly noun-related elements (like determiner or modifier) contains a verb. Such verb phrase forms the VO (simple verb phrase) or VOO (complex verb phrase – a verb phrase referring also to another notion) part of the sentence.

SVO sentences should be used to describe system's behavioural features or interaction between a user or a system, as they contain activity description and actor or component responsible for triggering and/or performing it.

Modal SVO sentence is a SVO sentence extended with a modal verb. This type of sentence adds to information carried by a SVO sentence modality aspect allowing to express priority of the described activity, an attribute or circumstance that denotes mode or manner of the described activity or an obligation (a possibility) of the subject to perform an action (described by a Predicate).

Conditional sentence is an ordered set of two structured sentences defined above. First of the sentences, forming a conditional sentence describes state, possibility or in general, a condition in which the activity expressed in the second sentence can occur. Type of the condition is additionally determined by conditional conjunction linking these two sentences. Terms like "if", "when", "upon", "during" etc. can be used as conjunctions for conditional sentence. In Figure 5, example of a conditional sentence (containing modal and regular SVO sentence) is provided.

Upon examination of sentence concept we are able to note that from the syntactic point of view, it forms a regular grammar (in the context of formal languages and compilers). In this grammar terms used in sentences are terminal symbols. We can thus use a simple analyzer based on a finite state machine to parse SVO and ModalSVO sentences. In Figure 6 such finite state machine is presented.

¹(Subject – Verb – Object – (Object))

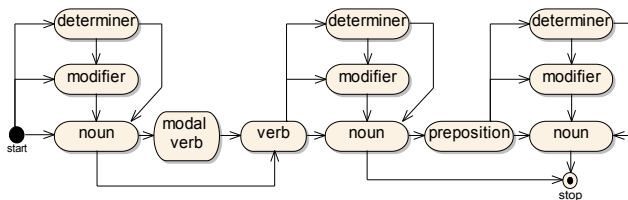


Figure 6. Simple SVO sentence grammar state machine

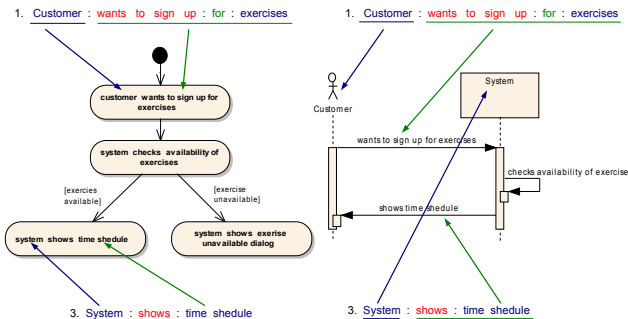


Figure 7. Use of SVO sentences' predicate and subject for different representation of use case.

Conclusions – Towards precise requirements

Presented approach was validated in a case study conducted by students during Software Engineering courses at the Carlos III University of Madrid and at the Warsaw University of Technology. The case study included creation of several student projects (consisting of requirements specifications) using structured grammars and vocabulary separated from behaviour description. Also, as part of the ReDSeeDS project, the user comprehension of the language is being currently validated (complete results are expected by the end of July '07).

As mentioned case study provided, concepts of using in requirements descriptions precisely defined domain vocabulary along with structured grammars allow for creating more coherent, and therefore simply better, requirements specifications. While working within such “discover notions – write structured sentences in use case scenarios” framework, analysts are encouraged to be acquainted with software system's environment and are stimulated to write precise, clearly formulated requirements statements.

Presented ideas allow for better management of “software cases” (in a form of Requirements Model – precisely expressed problem statement – connected with architecture, design and code artefacts [16]). Such “software cases” (SCs) based on well formulated and structured requirements could be easily compared [2]. If a repository of comparable SCs existed, analyst could search for similar SCs, while developing new ones, which in turn would trigger better reuse possibilities, as requirements would be traced to architecture, detailed design and code. Other options for SCs management (like versioning) would be also possible.

Concepts described in this paper fit well into today's analyst workspace, as for example notions can be presented on diagrams, which follow OO principles. Also SVO sentences are very useful for describing use cases scenarios [17]. Moreover, they can be used for many representations of use case scenarios information (see Fig. 7).

Another factor enhancing the process of analyzing software requirements is a proposition of a 2-level ontology: one level is formed locally for every SC, the other one is global within the SC repository or software organisation. This allows for using the same terms for many SCs, but redefining

them according to the needs of a certain client/domain.

This work is partially funded by the EU: Requirements-driven Software Development System (ReDSeeDS) (contract no. IST-2006-33596 under 6FP). The project is coordinated by Infovide-Matrix, Poland with technical lead of Warsaw University of Technology and with University of Koblenz-Landau, Vienna University of Technology, Fraunhofer IESE, University of Latvia, HITEC e.V. c/o University of Hamburg, Heriot-Watt University, PRO DV, Cybersoft and Algoritmu Sistemas.

REFERENCES

- [1] Althoff K-D., Birk A., Hartkopf S., Miller W., Nick M., Surmann D., Tautz C. Systematic population, utilization, and maintenance of a repository for comprehensive reuse. *Lecture Notes in Computer Science*, 1756:25–50, 2000.
- [2] Ambroziewicz A. Software model library with visual query language. In *International Workshop on Model Reuse Strategies - MoRSe*, pages 33–36, 2006.
- [3] Bailin S.C. Software reuse as ontology negotiation. *Lecture Notes in Computer Science*, 3107:242–253, June 2004.
- [4] Biddle R., Noble J., Tempero E. Supporting reusable use cases. *Lecture Notes in Computer Science*, 2319:210–226, 2002.
- [5] Castro J., Kolp M., Mylopoulos J. A requirements-driven development methodology. *Lecture Notes in Computer Science*, 2068, 2001.
- [6] Chan C.W. Knowledge and software modeling using uml. *Software and Systems Modeling*, 3(4):294–302, 2004.
- [7] Evermann J., Wand Y. Toward formalizing domain modeling semantics in language syntax. *IEEE Transactions on Software Engineering*, 31(1):21–37, January 2005.
- [8] Fellbaum C., editor. *WordNet: An Electronic Lexical Database*. MIT Press, 1998.
- [9] Graham I.M. Task scripts, use cases and scenarios in object-oriented analysis. *Object-Oriented Systems*, 3(3):123–142, 1996.
- [10] Kaindl H. Using hypertext for semiformal representation in requirements engineering practice. *The New Review of Hypermedia and Multimedia*, 2:149–173, 1996.
- [11] Kalnins A., Barzdins J., Celms E. Model transformation language MOLA. In *Lecture Notes in Computer Science, Springer, v. 3599, 2005. Proceedings of MDAFA 2004*, 2004.
- [12] Object Management Group. *Reusable Asset Specification: Final Adopted Specification, ptc/04-06-06*, 2004.
- [13] Riccardi G., Bangalore S. Automatic acquisition of phrase grammars for stochastic language modeling. In *Proceedings of ACL Workshop on Very Large Corpora, Montreal*, 1998.
- [14] Some S. S. Beyond scenarios: Generating state models from use cases. In *Scenarios and state machines: models, algorithms and tools - ICSE 2002 Workshop*, Orlando, Florida, 2002.
- [15] Śmiałek M. From user stories to code in one day? *Lecture Notes in Computer Science*, 3556:38–47, 2005.
- [16] Śmiałek M. Mechanisms for requirements based model reuse. In *International Workshop on Model Reuse Strategies - MoRSe*, pages 17–20, 2006.
- [17] Śmiałek M., Bojarski J., Nowakowski W., Straszak T. Scenario construction tool based on extended UML metamodel. *Lecture Notes in Computer Science*, 3713:414–429, 2005.
- [18] Watahiki K., Saeki M. Scenario patterns based on case grammar approach. In *5th IEEE International Symposium on Requirements Engineering*, pages 300–301, 2001.

Authors: dr inż. Michał Śmiałek, mgr inż. Albert Ambroziewicz, mgr inż. Jacek Bojarski, mgr inż. Wiktor Nowakowski, mgr inż. Tomasz Straszak, Politechnika Warszawska, Wydział Elektryczny, Instytut Elektrotechniki Teoretycznej i Systemów Informacyjno-Pomiarowych, ul. Koszykowa 75, 00-662 Warszawa, Poland, email: {smialek, ambrozia, bojarsj1, nowakoww, straszat}@iem.pw.edu.pl

Segmentation and characterization of grandular ducts in microscopic colon image

Abstract. The paper presents the methods of the microscope colon image processing for segmentation and computation of numerical features of grandular ducts. In the first part we describe the grandular ducts segmentation algorithms applying the morphological functions. The second part contains the description of the techniques of the grandular ducts features computation algorithm. The paper describes shortly the main morphological functions, the numerical characterization of the grandular ducts and the segmentation algorithms. The work contains also medical introduction, problem explanation and description of the main goals. The results of the numerical experiments will be also presented and discussed.

Streszczenie. Praca poświęcona jest opracowaniu metod przetwarzania obrazu wycinka jelita grubego dla potrzeb wspomagania diagnozy lekarskiej w chorobach Leśniowskiego-Crohna. Praca prezentuje proces wyodrębniania i określania cech numerycznych opisujących cewy gruczołowe. W pierwszej części opisano algorytm ekstrakcji cew gruczołowych z zastosowaniem funkcji morfologicznych. Część druga zawiera opis technik określania cech numerycznych skojarzonych z cewami oraz opis algorytmu służącego do mierzenia odległości między dwoma najbliższymi cewami. W pracy znalazło się również krótkie wprowadzenie medyczne, wyjaśniające wagę medyczna problemu i opis głównych celów badawczych jak również dyskusję wyników uzyskanych dla kilkudziesięciu pacjentów. (*Charakterystyka i segmentacja cew gruczołowych w obrazie mikroskopowym jelita*)

Keywords: digital image processing, morphological operations, medical diagnosis of Leśniowski-Crohn disease.

Słowa kluczowe: cyfrowe przetwarzanie obrazów, operacje morfologiczne, choroba Leśniowskiego-Crohna.

Introduction

Inflammatory Bowel Diseases belongs to the group of chronic, incurable diseases of gastrointestinal tract. They are characterized by the spontaneous remissions and relapses of their etiology not explained up to now. To this type of Inflammatory Bowel Diseases we may include on one hand the Colitis Ulcerosa and Lesniowski-Crohn disease, and on the other one the microscope colitis (collagenous colitis) and also some non-specific inflammations [4,8]. When grandular ducts are attacked by the human defense system the important problem is to diagnose the beginning of the illness. The microscopic image shows how the human defence cells attack the grandular ducts and the destruction followed by them. The important consequence of the attack is the appearance of the liquid in the stoma of tissue, extension of the area between the neighbouring granular ducts as well as beginning of the division process of the granular ducts.

The paper will be concerned with the segmentation of the microscopic image, recognition of the grandular ducts and characterization of them by the numerical diagnostic features. The most important stages of this task include: cleaning of the image by filtration, application of morphological operations, extraction of the individual granular ducts, generation of numerical features for each extracted duct and as a final stage computation of the distances and spaces between the separate granular ducts.

As a result of such complex process we can determine precisely what is the intensity of the inflammation, the most important factor in medical diagnosis. The main goal of this work is to estimate the numerical features of the grandular ducts at different stages of the development of the illness. Thanks to this one can associate the actual measurement results of the ducts with the values of the proper numerical features. In this way the results of the work are of great help for medical staff in the process of undertaking the diagnosis of the patients.

The problem description

The input data in our experiment is a microscopic digitized colon image [8]. It is the image of the biopsy of the tissue of the magnification equal 10. The image is saved as the bitmap file for further processing. The typical image of

this kind is depicted in Fig. 1. The large, oval, dark objects of the image are of our interest. They represent the grandular ducts and should be segmented. All other small objects (tissue cells) don't belong to the grandular ducts and should be removed from the image.



Fig.1. The typical microscopic image of the colon

The first step of processing is the extraction of the granular ducts through segmentation process and elimination of the other small size elements. We achieve it using the morphological operations. After segmentation each granular duct represents the individual image which must be preprocessed in order to be characterized by the numerical features. These features are of geometrical nature. For the medical diagnosis the most important is the measurement of the distances between the nearest granular ducts. These distances are the evidence of the development of the illness. As the result of the first preprocessing steps we get the objects containing single granular ducts described by the numerical features. In the second stage of algorithm we determine the distances

between the closest neighboring ducts.

The paper is concerned with the following details of the processing of the tissue image:

- extraction of the individual grandular ducts from the microscopic colon image through the segmentation steps,
- generation of the geometrical features of the individual ducts in a way to get the best characterization of the process of development of the inflammation,
- computation of the distances between the nearest neighboring grandular ducts,
- creation of the data basis containing the results of measurements of the ducts associated with different stages of inflammation process of the Lesniowski-Crohn disease.

After computation of all needed distances and creation of the geometrical features one can estimate if any of the numerical features are associated with the disease. This is done in an automatic way. The results given by the automatic system will be used by the medical doctor to assess the intensity of inflammation and the advancement of the illness in the human organism.

Segmentation algorithm

The introductory step of the colon image processing is the extraction of the grandular ducts from the image. We have done it by applying the filtering and segmentation processes. The applied algorithm consists of the following stages [1,6,7].

- Reading the input bitmap image. It is normally saved in the matrix form $I(x,y,3)$, in which x and y are the coordinates in horizontal and vertical axes, while the third coordinate means the intensity levels of three color components (the red, green and blue).
- Contrast adjustment:
 - ✓ The background is transformed to white color.
 - ✓ The other objects are transformed to dark colors.
- Transformation of the image to the binary one.
- Removing the smallest elements:
 - ✓ Implementation of the morphological operation of opening. We have used the structural element in the form of a disk of the size equal 3.
 - ✓ Morphological operation of closing by the structural element in the form of a disk of a size equal 7.
 - ✓ Morphological operation of filling the holes. The largest objects which represent the grandular ducts are empty and after this operation we get the filled elements.
 - ✓ Morphological operation of dilation with structural elements of size equal 20, followed by morphological closing.
 - ✓ Morphological operation of reconstruction. Fig. 2 depicts the markers and Fig. 3 - the mask of an exemplary image of Fig. 1 containing the grandular ducts.
- Morphological closing by structural element of the size equal 5 and filling the holes, followed by the repetition of opening, closing, filling the holes and once again closing. In this way all small objects (smaller than 5000 pixels) are eliminated from the image and the grandular ducts filled by the black color pixels (no holes inside).

As a result of such preprocessing we obtain the image with the filled segmented grandular ducts and all small objects removed. Fig. 4 presents the preprocessed image corresponding to the original image depicted in Fig. 1.

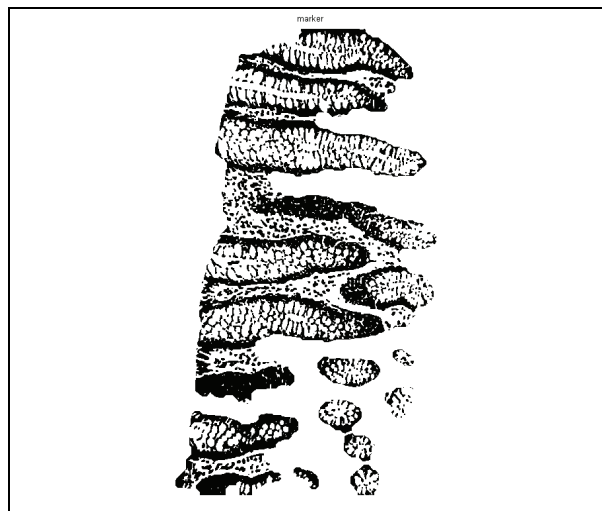


Fig.2 The marker used in the morphological operation of reconstruction

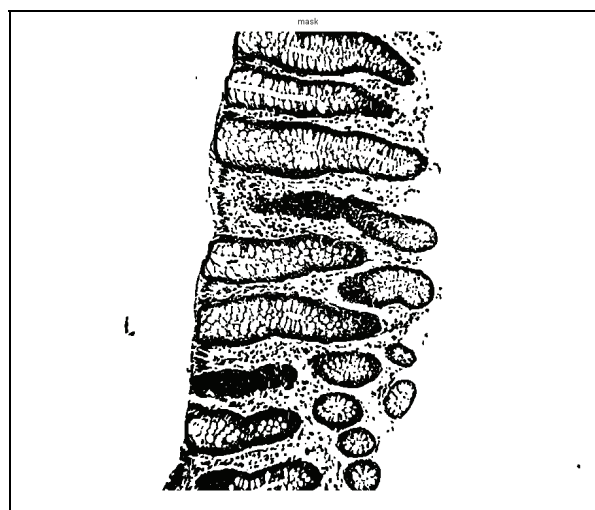


Fig. 3 The mask used in the morphological operation of reconstruction



Fig.4 The final form of the processed image. The black objects represent the grandular ducts.

Sometimes small errors of segmentation may happen and two neighboring ducts are still not disconnected. This is the result of large differentiation of colors between the parts of the images of various ducts. In some images the color of duct changes significantly from dark (in one part) to very

light (in another part of it). It is very difficult to find an universal setting of all adjustable parameters of the algorithm resulting in absolute accuracy of segmentation. In the case of segmentation problems we have to cut manually the area between bad segmented grandular ducts in order to extract all grandular ducts from the image. The proper graphical tools for doing it are provided by the program written in Matlab [5].

After getting the segmented image the next stage is to compute the numerical features associated with the grandular ducts, and determine the distances between the segmented ducts.

The computation of the numerical features

The grandular ducts are characterized by the following numerical features [4,9]:

- Area (A) is the real area covered by the grandular ducts (given in pixels).
- Radius (R) is the quantity defined in two mutually perpendicular directions. We recognize the long radius and the short one. The long radius is the distance (in pixels) between two most distant pixels belonging to the same duct. The short radius is determined by finding the longest perpendicular line to the long radius. It is also given in pixels. The graphical interpretation of the long and short radiuses of the grandular duct is depicted in Fig. 5.



Fig. 5 The interpretation of the long and short radiuses of the grandular duct

- Factor of circularity is defined as the ratio of the short and long radius of the duct

$$(1) \quad F_C = \frac{L_s}{L_l}$$

where L_s and L_l denote the short and long radius, respectively.

- Real perimeter (P) is the number of pixels placed on the periphery of the duct (in pixels).
- Convex perimeter (P_c) is the perimeter of the polygon circumscribed on a duct.
- Convex area (A_c) is the area of the polygon circumscribed on a duct.

These features are very important from the medical point of view to differentiate between different stages of disease. Table I presents the exemplary values of the above parameters determined for five chosen grandular ducts extracted from the image of Fig. 1. The number of the first column means the numbering of ducts, depicted in Fig. 6. As it is seen the grandular ducts differ by the size measured by areas and perimeters, and the shape, characterized by the convexity parameters. The values of these parameters may be treated as the diagnostic features differentiating various ducts existing in the image of colon tissue.

After the grandular ducts are extracted from the image and the numerical features computed we may start to determine the distances between the neighboring ducts. These distances are very important for diagnosing the

inflammation stage and determining the type of this inflammation.

Table I. The values of the numerical features of the grandular ducts (GD)

| GD | L_s | L_l | A | F_c | P | P_c | A_c |
|----|-------|-------|-------|--------|------|-------|-------|
| 1 | 186 | 357 | 49563 | 0.5233 | 811 | 622 | 50255 |
| 2 | 264 | 418 | 65710 | 0.6317 | 1009 | 919 | 66804 |
| 3 | 199 | 419 | 59490 | 0.4749 | 924 | 778 | 61164 |
| 4 | 192 | 278 | 38654 | 0.6915 | 675 | 478 | 38792 |
| 5 | 425 | 195 | 64222 | 0.4592 | 905 | 670 | 64516 |

The computation of the distances between the grandular ducts

For the medical diagnosis the most important are the distances between the closest neighboring ducts calculated on the basis of the parallel (or almost parallel) long radiuses. To compute the distances between the neighboring grandular ducts we have developed the following algorithm.

- The first step is to find the long radius of each grandular duct. It is the most important information characterizing the orientation of it in the image.
- After getting the long radius we find the series of lines perpendicular to it with the distance of 5 pixels.
- If the perpendicular line intersects the long radius of the other neighboring grandular duct the distance between the boundary pixels of both ducts are saved
- Then the mean distance and standard deviation of these distances between the closest neighboring ducts are computed. Standard deviation characterizes the diversity of all distances taken into account at the estimation process. Small value of standard deviation denotes high parallelism of two neighboring ducts.
- The obtained results in the form of the distinctive numeric notations of the ducts forming the closest neighbors, the mean distances between them and corresponding standard deviations are saved in the database.

Fig. 6 illustrates the applied method of the computation of distances between the neighboring ducts. The components forming the mean distances between the grandular ducts are visible as the lines between the long radiuses. For the purpose of diagnosis only the smallest distance between the succeeding duct and its closest neighbor is taken into account. The other distances are not collected in the data base.

Table II presents the numerical values of the distances and standard deviations between the closest neighboring ducts of Fig. 6 for the original image of the colon tissue illustrated in Fig. 1. For each grandular duct the mean value of this distance and standard deviation are given.

Note that the neighbors of the grandular ducts may vary. For example the closest neighbor for duct No 1 is the duct No 2 and vice versa. However it is not the general rule. For example the closest neighbor of duct No 8 is duct No 12, but for duct No 12 the closest neighbor is duct No 5. Note that neighbors are selected on the basis of the average distances for all lines connecting two ducts. This is the reason, why the ducts No 3 and 5 are not the closest neighbors, although on a short section they are very close.

Small values of standard deviations are associated with the pairs close to each other and highly parallel on the whole distance taking part in calculations (ducts No 1 and 2 or 10 and 11). On the other side high value of standard deviation means lack the parallelism between the boundaries of the grandular ducts (ducts No 9 and 15).

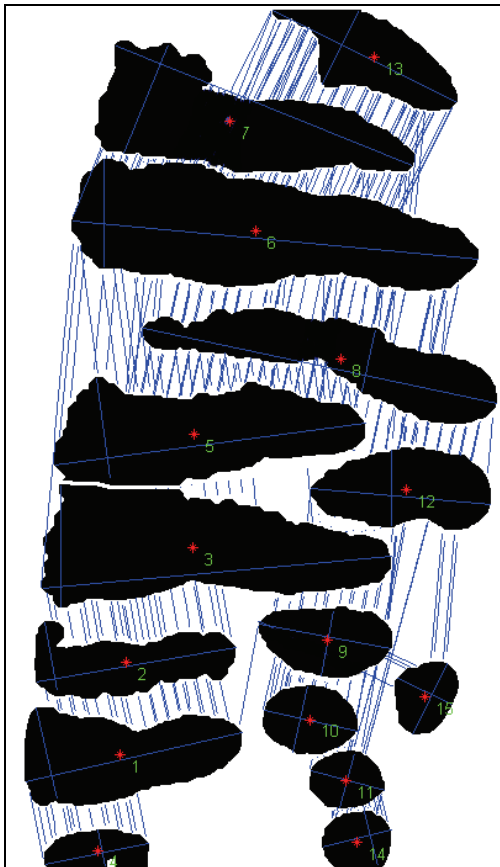


Fig.6 The illustration of the computation of distances between the neighbouring grandular ducts

Table II. The distances between the grandular ducts

| GD | Neighbour | Distance | Std |
|----|-----------|----------|-----|
| 1 | 2 | 10 | 3 |
| 2 | 1 | 10 | 3 |
| 3 | 9 | 5 | 4 |
| 4 | 1 | 12 | 10 |
| 5 | 12 | 5 | 2 |
| 6 | 7 | 23 | 22 |
| 7 | 6 | 23 | 22 |
| 8 | 12 | 23 | 11 |
| 9 | 3 | 5 | 4 |
| 10 | 11 | 8 | 2 |
| 11 | 10 | 8 | 2 |
| 12 | 5 | 5 | 2 |
| 13 | 7 | 37 | 20 |
| 14 | 11 | 9 | 7 |
| 15 | 9 | 23 | 51 |

The numerical experiments of grandular ducts segmentation have been performed for the data base of 193 microscopic colon images acquired in the Institute of Pathomorphology, Warsaw Military Hospital. All of them were of the magnification equal 10. The number of 193 images used in the numerical experiments corresponds to the same number of patients. The results saved in the

database are of great value for diagnosing the Crohn-Lesniowski disease. The developed automatic system of processing the image of the colon tissue enables significant acceleration of recognition of the development of the disease and let to undertake the proper treatment of the patients.

Conclusions

The paper has presented the automatic method of the grandular ducts segmentation and generation of the numerical features characterizing the grandular ducts on the basis of colon tissue image. The results described in the work are only the first step in the research directed to find the correlation between the particular type of the disease and the numerical features associated with the ducts. The next step is to build fully automatic system able to find this correlation. At this stage the system will only support the medical diagnosis in a semi-automatic way.

It is difficult now to estimate the numerical accuracy of the results. The only way of confirmation of the correctness of the results is the visual inspection of the image by the human expert and comparison of the obtained relative values of the parameters. The great help at this stage is the standard deviation of the distances, since its value is in direct connection with parallelism of the boundaries of the neighboring ducts and this is easy for visual inspection.

REFERENCES

- [1] P. Soille, *Morphological Image Analysis*, Principles and applications, Springer, 2003
- [2] Z. Wróbel, R. Koprowski, *Praktyka przetwarzania obrazów w programie Matlab*, Akademicka Oficyna Wydawnicza EXIT, Warszawa 2004
- [3] R. Tadeusiewicz, P. Korohoda *Komputerowa analiza i przetwarzanie obrazów*, Wydawnictwo Fundacji Postępu Telekomunikacji, Kraków 1997
- [4] K. W. Zieliński, *Wstęp do morfometrii i patologii ilościowej*, Wydawnictwo Naukowe PWN, Warszawa-Łódź 2002
- [5] Matlab user manual – *Image processing toolbox*, MathWorks, Natick, 1999
- [6] R. C. Gonzalez, R. E. Woods, *Digital Image Processing*. 1992, Reading, Massachusetts: Addison-Wesley.
- [7] H. J. Heijmans, *Morphological Image Operators. Advances in Electronics and Electron Physics*. 1994, Boston: Academic Press.
- [8] I. T. Young, *Quantitative Microscopy*. IEEE Engineering in Medicine and Biology, 1996.
- [9] Z. Kulpa, *Area and perimeter measurement of blobs in discrete binary pictures*. Computer Vision, Graphics and Image Processing, 1977.

Authors: mgr inż. Michał Kruk, Warsaw University of Technology, Institute of the Theory of Electrical Engineering, Measurement and Information Systems, Email: kruk@iem.pw.edu.pl; prof. dr hab. inż. Stanisław Osowski, Warsaw University of Technology, Institute of the Theory of Electrical Engineering, Measurement and Information Systems, Military University of Technology, Institute of Electronic Systems, Email: sto@iem.pw.edu.pl. med. dr Robert Koktyś, department of Pathology, Military Institute of the Health Services, rkoktyś@poczta.onet.pl.

Rotor bar fault diagnosis of induction motor based on single-class SVM

Abstract. The paper presents a new automatic method of the cage diagnosis of the asynchronous electrical engine by applying the 1-class Support Vector Machine (SVM). The diagnosis is made on the basis of phase current of the engine. The important point in this solution is the generation of the diagnostic features, on the basis of which the recognition of the state of the object will be done. In this approach we normalize the time series of the phase current which makes the method universal and applicable without retraining for wide range of engines. The recognition of fault is done by the 1-class SVM network on the basis of the harmonic components corresponding to twice slip of the motor. The results of testing the system on a series of 24 engines have proved high accuracy of the performance.

Streszczenie. Praca poświęcona jest opracowaniu nieinwazyjnej metody diagnostyki prętów klatki wirnika maszyny indukcyjnej, pracującej w trybie online. Diagnostyka prętów klatki wirnika polega na wykryciu uszkodzonych prętów za pomocą klasyfikatora neuronowego jakim jest jednoklasowa sieć SVM. Ze względu na różne moce silników indukcyjnych, szereg czasowy prądu jest normalizowany, a następnie poddany szybkiej transformacji Fouriera. Na podstawie informacji o częstotliwości poślizgu silnika indukcyjnego generowane są cechy diagnostyczne wprowadzane następnie na klasyfikator neuronowy, który określa stan prętów wirnika. (Diagnostyka uszkodzeń prętów klatki wirnika silnika indukcyjnego za pomocą jednoklasowej sieci SVM)

Keywords: induction motor diagnosis, broken bars, broken bars detection, single class SVM

Słowa kluczowe: diagnostyka wirnika, diagnostyka silnika klatkowego, jednoklasowa sieć SVM, cechy diagnostyczne

Introduction

The well-known engineering problem in the industry is the maintenance of the induction motor in a non-invasive way. Actually applied approach is an invasive one based on visual inspection of disassembled engine. To reduce the maintenance cost and prevent unscheduled shutdowns of the motor there is a need of the non-invasive and on-line diagnostic system.

The paper presents the new automatic method of the cage diagnosis of the asynchronous electrical engine by applying the 1-class Support Vector Machine (SVM).

The principal reason of the cage damage is usually the first broken bar in the cage. In relatively short period of time it causes the avalanche damage of the following bars in the cage. The obvious fact is that the motor can still work for some (rather short) period of time but after that the next bars are damaged and finally a machine stops.

There are few principal faults in induction motors such as rotor bars fault, stator windings fault and damage of bearings. This paper describes the non-invasive and on-line rotor bars diagnostic method relying on detection at least one broken bar in the rotor cage.

It's very important to catch the moment when only one or at least few bars are broken (the beginning of the avalanche process) because the repairing cost of induction motor in this stage is relatively low, comparing to the faults at dozen bars broken. The most difficult thing is to catch the moment of the first bar broken. In the first stage of the cage damage, there aren't any symptoms of faults that could be discovered visually. Hence, it's important to create a non-invasive and on-line method, which would be able to recognize the state of the induction motor cage in its first phase of damage.

On the basis of observation of the phase current of the machine with broken bars we have found the peaks in frequency characteristics of the current, appearing on both sides of the fundamental frequency of 50Hz. These peaks are strictly correlated with the slip of the motor. The relative magnitude of the peaks with respect to the neighbouring values can lead to the generation of the diagnostic features, used by SVM classifier to recognize the fault.

In the proposed solution we will use the classifier in the form of 1-class SVM network, trained on the data information drawn from the phase current, registered only at the normal state of the cage. This is quite important since in

practice it is difficult to create sufficiently large data base concerning the damage of the bars. The 1-class classifier is trained to recognize the normal state of the motor with some a priori assumed tolerance, formed automatically in the learning process. In the retrieval phase, after supplying the actual data corresponding to the fault of the bars the 1-class classifier will indicate the disagreement with the learned data and this disagreement will be associated with the fault of the cage.

The most important problem for the efficient performance of the neural classifier is generating suitable features on the basis of which the fault could be detected for the induction motors of different power, speed and actual loading.

The diagnostic method presented in this paper is based on current and rotor speed measurements. First of all the current time series should be normalized and then transformed to the frequency domain using FFT.

A lot of information can be obtained from the current frequency characteristics. The most important from our point of view are the frequencies associated with the slip frequency of the rotor. On the basis of them we generate the set of diagnostic features used by 1-class SVM in the recognition process.

The numerical experiments have been performed on the data set created for various cage asynchronous engines of different parameters and at various loading, including the engines with healthy and faulty cages. The results of these experiments will be presented and discussed in the paper.

Current time series registration and normalization

The diagnosis of the bars of the cage induction motor, will apply time series registration regarding the phase current. The registration is done by using the on-line acquisition card (USB-3110) at the sampling frequency $f_s = 20\text{KHz}$. For every engine 10s registration of the phase current has been made. The acquired time series of current should be normalized to make the recognition independent on the power of the engine and its actual loading. The normalization applied in the paper can be described in the following form [5].

$$(1) \quad x_n(t) = \frac{x(t) - x_{mean}}{x_{std}}$$

In this expression $x(t)$ means the real measured values of current and $x_n(t)$ - the normalized values. The x_{mean} is the mean value of current and x_{std} - the standard deviation.

Feature generation

The most important part of each classifier system is the set of diagnostic features, well characterizing the process under recognition [1, 2]. To generate the proper set of them we have to understand the process and try to find the measures well characterizing different states of it, called classes.

First of all need to know some basic information concerning of the engine. The most important one include:

- N_s - the synchronous speed (constant value),
- N_r - the rotor speed (value changing with time),
- f_1 - supply frequency (in our country it is 50Hz).

The induction motor slip is described by the relation:

$$(2) \quad s = \frac{N_s - N_r}{N_s}$$

The bar diagnostic features are associated with the twice slip frequency placed on both sides of fundamental supply frequency f_1 .

$$(3) \quad f_{sb} = f_1(1 \pm 2s)$$

Above equation defines $\pm 2sf_1$ sideband frequencies around the supply frequency f_1 [10,11,12]. They appear as a result of the broken rotor bars.

To find these frequencies there is a need of rotor slip measurement. It is done with some tolerance and this may introduce some errors in determination of twice slip frequency components.

To prevent such problems we are searching the maximum points of frequency characteristics in the range of $\pm 1\%f_1$ around calculated f_{sb} . It means that we are looking for the frequencies satisfying the conditions:

$$(4) \quad \begin{aligned} f_{sb_low} &= \max_f \{x_n(f_1(1-2s) \pm 1\%f_1)\} \\ f_{sb_high} &= \max_f \{x_n(f_1(1+2s) \pm 1\%f_1)\} \end{aligned}$$

Based on the equation (4) we can generate two harmonic components determined at f_{sb_low} (left sideband f_1 .) and at f_{sb_high} (the right sideband).

The relationship between the cage induction motor state and the slip frequency components is quite simple. If the magnitude of the peak for twice slip frequency components is unambiguously exposed it means that the bar/bars are broken. So we conclude that the cage is damaged. In the other hand rotor cage is healthy.

We have have elaborated the features which characterize how much the magnitude of the peek for mentioned components is exposed with regard to the baseline. These feature are defined by the following equations.

$$(5) \quad \begin{aligned} x_{low} &= x(f_{sb_low}) - \frac{x(f_{sb_low}-1\%f_1) + x(f_{sb_low}+1\%f_1)}{2} \\ x_{high} &= x(f_{sb_high}) - \frac{x(f_{sb_high}-1\%f_1) + x(f_{sb_high}+1\%f_1)}{2} \end{aligned}$$

They form the 2-element vector x applied to 1-class SVM.

Fig. 1 and 2 illustrate the harmonic components in the range of $f_1(1 \pm 2s)$ for two engines: the healthy one (Fig. 1) and the engine with one broken bar (Fig. 2a) and three broken bars (Fig. 2b).

The characteristics shown in Fig 1 have been taken for the electrical machine SG132S-4 of the following parameters: he nominal voltage: $U_N = 3 \times 400$ V, frequency: $f = 50$ Hz, nominal power: $P_N = 3.5$ kW, nominal current: $I_N = 7.4$ A, $\cos \varphi_N = 0,89$, speed: $n_N = 1440$ rev/min, slip=0.04. In the case of Fig. 2 (broken bars) the parameters Sg132M-6B-S electrical machine were the following: the nominal voltage: $U_N = 3 \times 400$ V, frequency: $f = 50$ Hz, nominal power: $P_N = 5.5$ kW, nominal current: $I_N = 12.1$ A, $\cos \varphi_N = 0,83$, speed: $n_N = 895$ rev/min, slip=0.105.

In the first case healthy cage the frequency characteristic in the whole range is practically monotonous (no visible peaks below 50dB). At broken bars (Fig. 2) the peaks, placed symmetrically around fundamental frequency, are well visible and their magnitudes are significantly higher than the baseline around them.

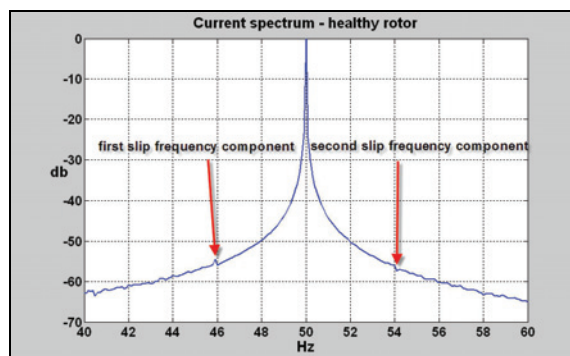


Fig.1. An example of current spectrum of the healthy induction motor.

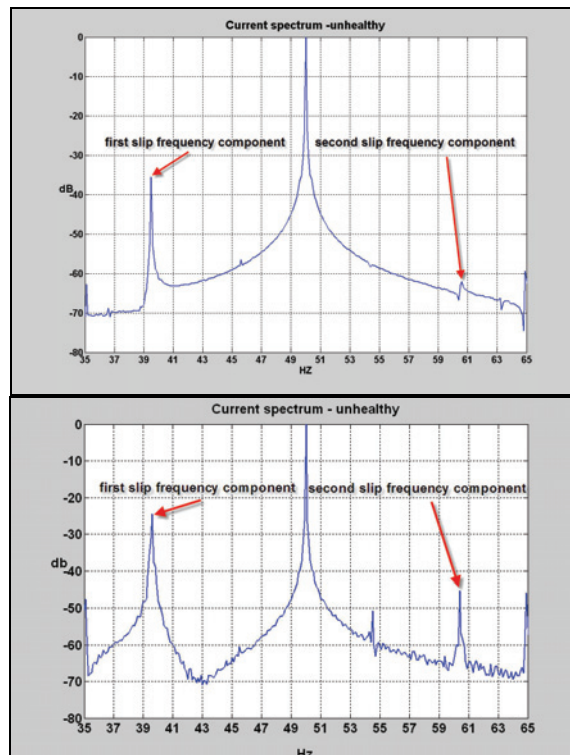


Fig.2. An example of current spectrum for the unhealthy induction motor with a) one bar broken, b) three broken bars.

One-class SVM Classifier

To make the diagnosis of the cage bars of the machine as accurate as possible we have applied the approach of the novelty detection using 1-class SVM [6]. The data belonging to the normal state of the cage forms the baseline used in training of the classifier. In 1-class formulation the data is first mapped to the feature space using the kernel function and then maximally separated from the origin using a hyperplane. The primary problem of learning is defined in the way [6]

$$(6a) \min \left(\frac{1}{2} \|\mathbf{w}\|^2 + \frac{1}{\nu p} \sum_{i=1}^p \xi_i - \rho \right)$$

subject to

$$(6b) \quad \langle \mathbf{w}, \Phi(\mathbf{x}_i) \rangle \geq \rho - \xi_i$$

with $\xi_i \geq 0$ for $i = 1, 2, \dots, p$, where p is the number of learning samples. Here Φ is the map from the input space to feature space, \mathbf{w} and ρ are hyperplane parameters, ν is the parameter denoting the asymptotic fraction of outliers allowed, and ξ is the slack variable. The solution of this primary problem is obtained in an identical way as in SVM approach [4,6,8] by introducing the Lagrange multipliers α_i and transforming the task to the dual problem, that is finally solved using quadratic programming algorithms [6]. As a result of solving this problem the decision function can be expressed in the form of the kernel expansion [6]

$$(7) \quad y = f(\mathbf{x}) = \text{sgn} \left(\sum_i \alpha_i K(\mathbf{x}_i, \mathbf{x}) - \rho \right)$$

with $K(\mathbf{x}_i, \mathbf{x})$ the kernel function, defined on the basis of Φ , $K(x_i, x) = \phi^T(x_i)\phi(x)$. To apply this approach we have to define the type of kernel function, kernel parameters, separating point in the feature space and the outlier fraction. The kernel function should encode the prior information about the problem [7]. Here we will apply the Gaussian kernel $K(\mathbf{x}, \mathbf{x}_i) = \exp(-\gamma \|\mathbf{x} - \mathbf{x}_i\|^2)$, the most universal kernel function used in support vector machine research of only one hyperparameter γ . The outlier fraction should incorporate the prior knowledge regarding the frequency of novelty occurrences. We have applied here $\nu=0.01$, indicating that approximately 1% or less of the entire data may be estimated to be novel. The Scholkopf formulation [6] of the separation problem of the multidimensional data samples from the origin of the coordinate system, defined in the feature space has been implemented using the Matlab platform [9].

The results of numerical experiments

The numerical experiments checking the performance of the system have been performed for 24 engines of different series and parameters (power, current and number of bars). Some of them were quite new and some used for many years in companies (Warsaw metro, Tramwaje Warszawskie).

Table I presents the comparison of the basic data of these machines, including power and nominal slip. The engines have been working at the nominal or close to nominal conditions.

The data of the broken bar engines has been acquired from specially prepared induction motor (Sg132M-6B-S) equipped in the additional head ring with screw connection

to each bar of the squirrel cage. This construction change has enabled us to simulate different stages of the damage, as well as the number of broken bars in the induction motor. The modified engine had 33 bars in the squirrel cage. The simulation of the damage of any bar was possible by simple unscrewing it.

Table I. Details of induction motors parameters used in experiments

| | Type | P _N [kW] | slip |
|----|---------------|---------------------|-------|
| 1 | Sg 132S-6 | 2.5 | 0.03 |
| 2 | Sg 132S-4 | 3.5 | 0.04 |
| 3 | SUDf 112M-4B | 3 | 0.06 |
| 4 | SUDf 112M-4B | 4.4 | 0.06 |
| 5 | SZJe 34 b | 4 | 0.04 |
| 6 | Sf 132 | 5.5 | 0.03 |
| 7 | SZcd 44p | 1.7 | 0.05 |
| 8 | SEMg 80-2b | 0.75 | 0.05 |
| 9 | SFe 90-L4 | 1.1 | 0.02 |
| 10 | Sg132M-6B-S | 5.5 | 0.105 |
| 11 | Ventilator 1 | 75 | 0.05 |
| 12 | Ventilator 2 | 55 | 0.02 |
| 13 | Ventilator 3 | 55 | 0.02 |
| 14 | Lift 1 | 2 | 0.04 |
| 15 | Lift 2 | 2 | 0.04 |
| 16 | Lift 3 | 2 | 0.04 |
| 17 | Lift 4 | 2 | 0.04 |
| 18 | Ventilator 4 | 10 | 0.03 |
| 19 | Ventilator 5 | 10 | 0.03 |
| 20 | Ventilator 6 | 10 | 0.03 |
| 21 | Ventilator 7 | 10 | 0.03 |
| 22 | Ventilator 8 | 10 | 0.03 |
| 23 | Ventilator 9 | 10 | 0.03 |
| 24 | Ventilator 10 | 10 | 0.03 |

To get the sufficiently large set of learning samples we have made the experiments of the machines at different load states, registering the phase current waveforms. The operation of machine has been registered for faulty bars at one, two, three, four, five and six bars broken. In the simulations we have taken into account different positions of the broken bars in the rotor.

For the engines presented in table I we have performed the registration of phase current at their normal operation. The data set obtained in this way contained the samples used for the learning neural classifier and for the testing it. Learning data set consisted of 72 healthy induction motor samples and the testing set consisted of 385 samples corresponding to different cage induction motor state (healthy and broken bars).

Only the data corresponding to the normal operation of the engine has been applied in learning. The 1-class SVM classifier of radial Gaussian function was trained on the set of learning data. The hypersparameter used in learning were as following: $\nu=0.01$, the constant γ of the Gaussian function $\gamma=0.1$.

Table II presents the statistical results of these experiments depicting the relative errors for learning and testing data.

Table II Statistical result of experiments

| | Learning data | Testing data (healthy cases) | Testing data (broken bars) |
|----------------|---------------|------------------------------|----------------------------|
| Relative error | 2% | 4% | 0% |

The results confirm good quality of solution. The recognition of the faulty state of the machine was perfect (no errors). The recognition of the normal state of the bars was not ideal, but the error was negligible (below 4%) and acceptable in practical applications. The nonideality of

recognition follows from different states of the bars in old machines. Some of them were probably on the border between healthy and broken bars.

Conclusion

The paper has presented the diagnostic system of the cage induction motor applying the 1-class Support Vector Machine. On the basis of many performed experiments we may conclude that application of the SVM based classifier combined with the proper feature selection, relying on twice slip frequency harmonics, provides the recognition of the motor fault with good, acceptable in practice accuracy.

The important advantage of this approach is its universality. Thanks to the current time series normalization it is applicable without retraining to wide range of power of engines. It performs well, irrespective of the actual speed and loading. The other point worth of mention is the fact that SVM classifier is trained on the data corresponding to the healthy engines only, which are widely accessible for data acquisition. The system may be retrained any time after gathering new set of measurements. Application of SVM network as the classifier enables to establish soft margin between the healthy and broken bar states.

REFERENCES

- [1] B. Schölkopf, A. Smola, Learning with Kernels, Cambridge, MA, MIT Press, 2002
- [2] C. Hubert, Electric machines: theory, operating applications, and controls, Prentice Hall, 2002
- [3] D. A. Poularikas, The handbook of formulas and tables for signal processing, CRC Press, Boca Raton, 1999
- [4] I. Guyon, A. Elisseeff, An introduction to variable and feature selection. Journal of Machine Learning Research. 3, 2003, 1158 – 1182,
- [5] L. Platt, L. Fast training of SVM using sequential optimization, (in Schölkopf, B., Burges, B., & Smola, A., Eds. Advances in kernel methods – support vector learning. Cambridge: MIT Press), 1998. pp. 185-208
- [6] Matlab user manual, MathWorks, Natick, 1999
- [7] M.Fenger, M.Susnik, P. Laderoute, W. T. Thomson, Development of a tool to detect faults in induction motors via current signature analysis, University of Abertay, Iris Rotating Machine Conference, June 2003, Sanata Monica, Canada
- [8] R. Unnborsson, Model selection in one-class v-SVMs using RBF kernels, 2003, available at <http://www.hi.is/~runson/svm/paper.pdf>
- [9] R. O. Duda, P. E. Hart, P. Stork, Pattern Classification and Scene Analysis, New York: Wiley, 2003
- [10] V. Vapnik, Statistical Learning Theory, N.Y.: Wiley, 1998.
- [11] W.T.Thomson, R.J.Gilmore, Motor current signature analysis to detect faults in induction motor drives-fundamentals, data interpretation, and industrial case histories, Proceedings of the thirty-second turbomachinery symposium 2003

Authors: mgr inż. Jarosław Kurek, Warsaw University of Technology, Institute of the Theory of Electrical Engineering, Measurement and Information Systems, Email: kurekj@iem.pw.edu.pl, dr inż. Adam Biernat Warsaw University of Technology, Institute of the Electrical Machines, Email: A.Biernat@ime.pw.edu.pl, dr inż. Jan Szczyplik Warsaw University of Technology, Institute of the Electrical Machines, Email: J.Szczyplik@ime.pw.edu.pl.

Pixel level data fusion based on local correlation in remote sensing systems

Abstract. In present paper there was done analysis of possibility to use local correlation at pixel level data fusion in order to increase effectiveness of multilevel information fusion method.

Streszczenie. W pracy przeanalizowano możliwość zastosowania korelacji lokalnej na poziomie łączenia pikseli w celu zwiększenia efektywności wielopoziomowej metody integracji informacji. (Zastosowanie integracji informacji na poziomie pikseli na podstawie lokalnej korelacji w systemach teledetekcji)

Keywords: remote sensing, data fusion, pixel level fusion, image processing.

Słowa kluczowe: teledetekcja, integracja danych, łączenie pikseli, przetwarzanie obrazów

Introduction

The problem of development effective methods of image processing, based on data obtained with remote sensing, is now the most relevant. Despite of the existing of numerous multichannel data fusion applications, most of them contain next levels of data processing: pixel, feature and decision fusions [1]. Pixel level data fusion can provide the best results, as it is using data directly from all sensors, but is characterized with high computational complicacy. At the same time the quality of fusion at this level significantly depends on applied methods of further processing.

The quality estimation criteria of object detection

The estimation of detection results is done by comparison of real object's (river's) map with a method's [2] results by calculation of target missing and false alarm probabilities. In the case, when real image's pixel isn't present in obtained image, we're speaking about target missing probability; in vise-versa case, when obtained image's pixel isn't present in real image, we're speaking about false alarm probability. In the reviewed multilevel fusion method in a basic it was necessary Neumann-Pirson criterion in which the main attention was paid for decreasing the value of target missing probability, at the same time keeping false alarm probability on the suitable level. The mentioned probabilities were calculated as follows:

$$(1) \quad P_{tm} = \bigcup P_{river_det} / \bigcup P_{river_real},$$

$$P_{fa} = \bigcup P_{non-river} / \bigcup P_{non-river_real},$$

where P_{tm} , P_{fa} – target missing and false alarm probabilities correspondingly; $\bigcup P_{river_det}$ – a quantity of pixels belonging to desired object (river) in a detected image; $\bigcup P_{river_real}$ – a quantity of pixels belonging to desired object in a real image; $\bigcup P_{non-river_det}$ – a quantity of pixels not belonging to desired object in a detected image; $\bigcup P_{non-river_real}$ – a quantity of pixels not belonging to desired object in a real image.

The usage of local correlation on a pixel level fusion

A pixel level fusion is one of the component levels in the proposed multilevel information fusion method [2] making significant influence on the detection result. In order to increase effectiveness of data processing on pixel level data fusion and the effectiveness of multilevel data fusion method in general, there was done a pixel fusion analysis of

groups of images of separate channels, based on usage of their local cross-correlation. As input images for processing have been used images of spectral bands 1-5 of Landsat 7 ETM+ after Level 1 processing application which includes correction of geometric distortions, data calibration and resampling [3].

Pixel fusion is performed in the next way:

$$(2) \quad I(x, y) = \bigcup_i a_i(x, y) \cdot I_i(x, y),$$

where $I_i(x, y)$ – the intensity of pixel of channel i , depending on spatial coordinates; $a_i(x, y)$ – weight coefficient for pixel's intensity of corresponding channel; $I(x, y)$ – fusion result.

The estimation of weight coefficients is being performed by calculation of local cross-correlation of separate channels' image pairs, creating a matrix of cross-correlation coefficients with a dimensions corresponding to dimensions of a separate image:

$$(3) \quad R(x', y') = \int_{-\infty}^{\infty} \int_{-\infty}^{\infty} I_1(x, y) I_2(x + x', y + y') dx dy,$$

where I_1 , I_2 – the images of 1st and 2nd channels.

Since local cross-correlation of images will be calculated based their local features by moving a "window" of constant size over each of the images, the limits of integral can be replaced in a following way:

$$-\infty; \infty \rightarrow -w_x/2; w_x/2,$$

$$-\infty; \infty \rightarrow -w_y/2; w_y/2,$$

where w_x , w_y – "window" dimensions; $-w_x/2, w_x/2$ and $-w_y/2, w_y/2$ – values describing edge positions of "window's" centre, within image, across and on a vertical accordingly.

Correlation coefficient gets a following form:

$$(4) \quad R(x', y') = \int_{-w_x}^{w_x} \int_{-w_y}^{w_y} I_1(x, y) I_2(x + x', y + y') dx dy$$

The movement of "window" within image looks like as follows:

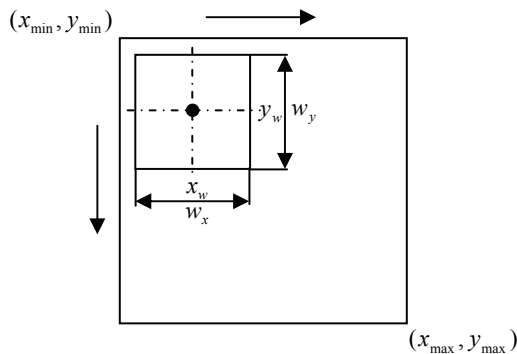


Fig.1. The movement of correlation "window" within image

The coordinates of "window's" centre are being represented by x_w and y_w values. In view of it, the dependence of correlation coefficient is being changed in the following way:

$$R(x', y') \Rightarrow R(x', y', x_w, y_w),$$

$$R(x', y', x_w, y_w) = \int_{-w_x}^{w_x} \int_{-w_y}^{w_y} I_1(x_w, y_w) I_2(x_w + x', y_w + y') dx dy$$

At the same time,

$$x_w \in [x_{min}, x_{max}],$$

$$y_w \in [y_{min}, y_{max}].$$

As a result, weight coefficient for fusion of a pair of channels, depending on spatial coordinates of a separate pixel, will be estimated based on a maximum of cross-correlation coefficient of pair of images within a "window", with a central point, corresponding to a spatial coordinates of appropriate integrated pixels of a separate channels:

$$(5) \quad A(x_w, y_w) = \max_{x', y'} R(x', y', x_w, y_w).$$

It is necessary to note, that within a specific pair of images being integrated, each pair of corresponding pixels of integrated images will have its own weight coefficient depending on spatial coordinates. As a result, the set of weight coefficients for fusion a pair of separate images will appear as a 2-dimensional array with dimensions equal to dimensions of a separate image.

At this stage there is a problem of cross-correlation coefficient computational complicacy, which is defined by required number of mathematical operations for its estimation:

$$(6) \quad n^2 \cdot m^4,$$

were n^2 – the number of pixels in the image; m^2 – the number of pixels in the "window".

In order to decrease the computational complicacy, directly affecting the time, required for estimation of cross-correlation, we're performing calculation of integral within a "window", accepting displacement concerning its center (x', y') equal zero and assuming that maximum of cross-correlation coefficient is being found in the centre of the "window":

$$(7) \quad \max_{x', y'} R(x', y', x_w, y_w) \Big|_{\substack{x'=0 \\ y'=0}} \rightarrow R(x_w, y_w) = A(x_w, y_w),$$

At the same time, the number of operations, required for calculation of a correlation, is melt the following:

$$(8) \quad n^2 \cdot m^2.$$

While making a fusion of groups of images, consisting of three and more channels, in order to estimate weight coefficient for the image of a separate channel, one channel is being assumed as a basic for calculation of cross-correlation. At the same time, the weight coefficient for the basic channel is equal to its autocorrelation coefficient.

Let's note that before the beginning of fusion, each of the images is a subject to a procedure of normalization in order to provide commensurable level of energy in each channel.

After fusion procedure is finished, each of obtained images is being processed on a stage of clusterisation (selection of desired object's pixels):

$$D_i = \text{Cluster}(P_i),$$

where P_i – the quantity of pixels in channel i ; D_i – the quantity of decisions made based on P_i .

During the analysis of the pixel level fusion there were obtained following results:

Table 1. The results of pixel level fusion using manually selected weight coefficients.

| Pixel level fusion | Target missing probability | False alarm probability |
|--------------------|----------------------------|-------------------------|
| P ₁₂₃ | 0.2826 | 0.0028 |
| P ₁₂₄ | 0.5792 | 0.0007 |
| P ₁₃₅ | 0.4557 | 0.0005 |
| P ₁₂₃₄ | 0.5890 | 0.0007 |
| P ₂₃₄₅ | 0.4236 | 0.0009 |
| P ₁₂₃₄₅ | 0.4836 | 0.0007 |

Table 2. The results of pixel level fusion using weight coefficients calculated based on local cross-correlation

| Pixel level fusion | Target missing probability | False alarm probability |
|--------------------|----------------------------|-------------------------|
| P ₁₂₃ | 0.2359 | 0.0036 |
| P ₁₂₄ | 0.3678 | 0.0011 |
| P ₁₃₅ | 0.3287 | 0.0022 |
| P ₁₂₃₄ | 0.3699 | 0.0013 |
| P ₂₃₄₅ | 0.4117 | 0.0012 |
| P ₁₂₃₄₅ | 0.4006 | 0.0011 |

Conclusion

Obtained results show, that usage of local correlation on pixel level data fusion is providing the best values of target missing probability in all groups of channels, comparing with manually selected coefficients. At the same time, probability of false alarm has left on commensurable level, satisfying formulated Neumann-Pirson criterion.

REFERENCES

[1] Hall D. (ed) and Llinas J. (ed.), *Handbook of Multisensor Data Fusion*, CRC Press LLC, 2001.
 [2] Prudyus I.N., Lazko L.V., Semenov S.O., Holotyak T.S. *Information Fusion In Passive Wideband Satellite Remote Sensing Systems Based on Multilevel Method*, Visnyk of National University «Lvivs'ka politechnika», №557 «Radio engineering and telecommunications », 2006, pp. 114-119
 [3] <http://landsat.gsfc.nasa.gov>

Authors: Prudyus I.N., Lazko L.V., Semenov S.O., National University "Lvivs'ka Politehnika", Institute of Telecommunications, Radioelectronics and Electrical Engineering, 2, Pofesors'ka str., 79013, Lviv, Ukraine, E-mail: iprudus@polynet.lviv.ua; lazko_new@yahoo.com; ideafix@ua.fm

Generalized robust parameters distribution model

Abstract. The quality and adequacy of mathematical models on base of Gram-Charlier and Edeworth rows was shown.

Streszczenie. W pracy opisano jakość i dokładność modeli matematycznych opartych o szeregi Grama-Charliera i Edewortha. (Uogólniony odporny model rozkładu parametrów)

Keywords: Gram-Charlier rows, skewness, kurtosis

Słowa kluczowe: szeregi Grama-Chaliera, asymetria, kurtoza.

Introduction

In spite of great number of theoretical and practical investigation, that were made as in Ukraine as in the other countries of the world in the area of analysis and synthesis of electronic devices components parameters, present methods, approaches and software are deficient of state-of-the-art in the high reliable technique.

In connection with the influence of complex products on the technological processes of production many of their control, correcting, stabilizing and other organization/technical factors as well as their output parameters are characterized by a broad range of distributions. The presence of moments of high orders causes deflections of the form of distribution from the normal law in the manner of asymmetries and kurtosis, wherein the manifestation of these deflections can be different either in size, or in sign [1]. This can be explained by the fact that such models do not reflect any relation between their own forms and moments of high orders, especially moments characterizing the degree skewness and kurtosis of real distributions. More flexible models are Gram-Charlier and Edgeworth decompositions [1]. They are characterized by a comparatively simple structure, their members have comprehensible mathematical and physical sense and that is why they continue to be of interest to specialists. However Gram-Charlier and Edgeworth rows as distribution models of product parameters have not yet been adequately studied. The aim of this research is to study the characteristics of Gram-Charlier and Edgeworth rows as mathematical distribution models of the output parameters of products having deviations from the normal law in the form of skewness and kurtosis.

Problem Formulation

The main problem is that most of the works in the known literature deals only with robust estimation for location and no attention has been paid for the robust estimation of skewness and kurtosis. The most famous and well learned by the authors techniques for distributions estimation are Gram-Charlier and Edgeworth series. Their properties are well-known as flexible and universal models of parameters distributions.

On increasing these factors the approximation errors increase. Comparison of the range of A and E obtained also proves the irregularity of these series, thereby depriving us of sufficient grounds needed to take the final decision on the expedient structure of the mathematical models. Statistical research of such models at the big consignment of measurement devices permit to make some conclusions. Histograms of experimentally received distributions and their approximation by Gauss function and Gram-Charlier series are shown in Fig 1.

The model estimation by χ^2 criteria was made. As analytical models Gauss function and Gram-Charlier series of third order were taken Results have shown that the modeling of devices parameters distributions by mean of Gram-Charlier series gave better results than application of

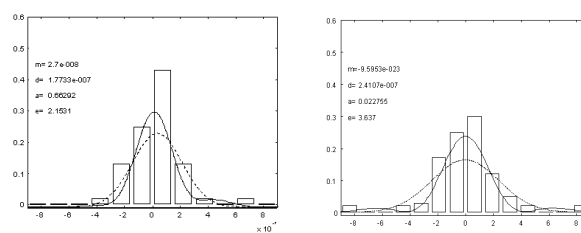


Figure 1. Results of modeling of parameters distribution by Gauss function (---) and by Gram-Charlier rows(—).

Conclusions

Gram-Charlier and Edgeworth series may be used as mathematical models of quasnormal distributions, which are characterized by skewness and kurtosis. Results have shown that modeling with help of Gram-Charlier series gave better results than usage of normal law. For minimal approximation error ensuring skewness need not to exceed $\pm(0,5\div 1)$ for Gram-Charlier series of third order and $\pm(0,25\div 0,75)$ for Gram-Charlier series of fourth order, and kurtosis should be not more than $+(2,5\div 4)$ and $+(2,25\div 2,5)$ respectively [3].

Concerning irregularity of Gram-Charlier series, every case needs individual approach. Addition of the next member of row in most cases improves approximation, but causes the appearance of negative values of distribution density function.

REFERENCES

- [1] Hald. A. The early history of the cumulants and the Gram-Charlier series. // Preprint from the department of theoretical statistic, 1998.
- [2] L. Nedostup, Y. Bobalo, O. Lazko, I. Trelis. Quasi-normal data robust models. // Proceedings of International Conference CADSM 2005. – Lviv-Slavsko. – 2005. –P.374.
- [3] Yuriy Bobalo, Leonid Nedostup, Oxana Lazko, Volodymyr Glemba. Mathematical models of reliability of components parametrical synthesis. // Proceedings of International Conference TCSET2006 (Modern Problems of Radio Engineering, Telecommunications and Computer Science). – Lviv-Slavsko. – 2006. – P. 593-597.

Authors: Prof. Yuriy Bobalo, Prof. Leonid Nedostup, and Dr. Oxana Lazko, National University "Lviv'ska politehnika", Institute of Telecommunications, Radioelectronics and Electrical Engineering, 2, Pofesors'ka str., 79013, Lviv, Ukraine,

Simplified theoretical analysis of measuring systems for eddy current testing of low conductivity materials

Abstract. This paper deals with simplified theoretical analysis of two measuring systems for eddy current testing of low conductivity materials. Simple mathematical models of the compensating and self-comparing probes have been presented. The expressions obtained can be used in procedures of reconstruction of the interior structure of an object under investigation.

Streszczenie. Praca poświęcona jest uproszczonej analizie teoretycznej dwóch układów pomiarowych do wibroprądowego badania materiałów o małej kondukcyjności. Przedstawiono proste modele matematyczne sond pomiarowych o kompensacyjnej i samoporównawczej zasadzie działania. Otrzymane zależności mogą być wykorzystane w procedurach odtwarzania struktury wnętrza badanego obiektu. (Uproszczona analiza teoretyczna układów pomiarowych do wibroprądowego badania materiałów o małej kondukcyjności)

Keywords: nondestructive testing, eddy current method, mathematical models.

Słowa kluczowe: badania nieniszczące, metoda wibroprądowa, modele matematyczne.

Introduction

Eddy current methods are widely used to detect defects in metallic engineering structures. The practice of the eddy current testing consists of exciting an alternating current at a given frequency through a coil located near to the electrically conducting object being tested, and thus to induce eddy currents in the object. As a result of the presence of defects, inhomogeneities, anisotropies, etc. changes take place in the components of the associated magnetic field, which can be detected by magnetic field sensors. Eddy currents can also be induced magnetically in materials of low conductivity, e.g. in the human body, and there has been considerable interest in the applications of this phenomenon for electrical conductivity imaging of human tissues. Such a technique of imaging is known as magnetic induction tomography [1]. The technique is particularly attractive for the detection of pathological processes in the brain as the magnetic field penetrates easily through the skull. The magnetic induction tomography (MIT) has the advantages of reduced biological hazard and less expensive hardware in comparison with the most popular medical imaging techniques: X-ray computed tomography and ultrasonic echoradiography. It is very important from the medical point of view that MIT provides different information. The X-ray displays the variation in the electronic density and the ultrasonic displays the variation in the mechanical property of the tissues, whereas MIT maps the variation of the complex electrical conductivity.

In case of living organisms there are some restrictions on electromagnetic fields, which can be utilized for inspection. From the safety point of view, an excitation frequency as well as an applied magnetic field intensity level have to be limited [2, 3, 4]. It is known that the energy absorption of low frequency fields ($f < 100$ kHz) is negligible. It is caused by a low electrical conductivity of the tissue ($\sigma < 1$ S/m). Assuming upper limits of the frequency and conductivity as indicated above, the electromagnetic field penetration depth is greater than 1 m. Therefore, it is possible to apply transducers having excitation and detection elements on the opposite sides of the tested object. This paper deals with theoretical analysis of two measuring systems for eddy current testing of low conductivity materials, developed and constructed at the Szczecin University of Technology, Poland. Simplified analytical models of the probes have been considered. The expressions obtained can be used in procedures of reconstruction of the interior structure of an object under investigation.

Measuring systems

Two measuring systems have been considered in the paper. The compensating transducer is shown in Fig. 1a.

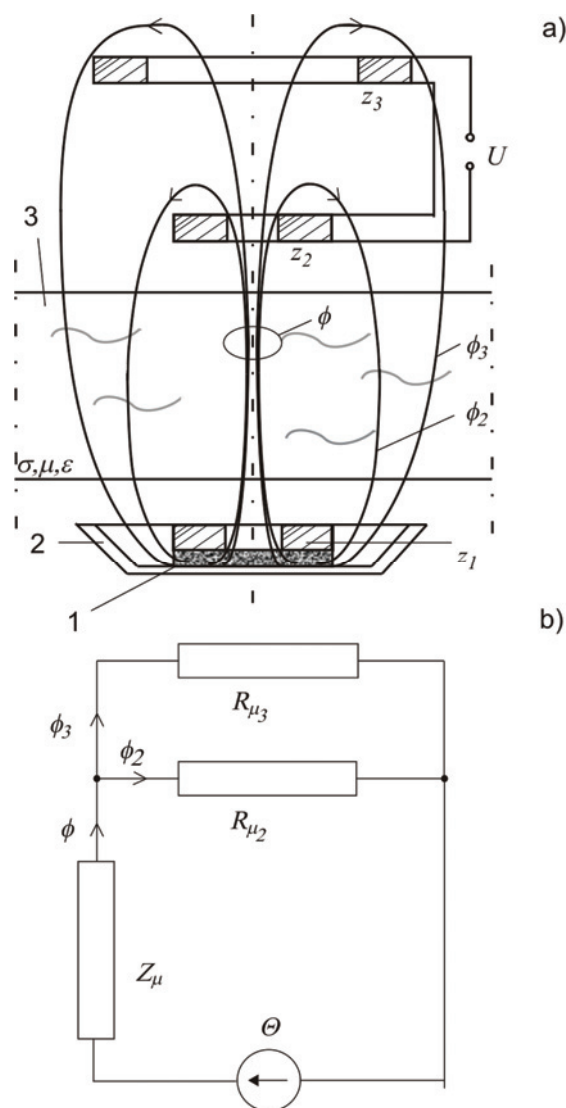


Fig.1. The compensating measuring system: a) schematic view of the arrangement transducer-sample, b) equivalent magnetic circuit

The transducer comprises an excitation coil with z_1 turns and two signal coils connected differentially with z_2 and z_3 turns, respectively. The coils are positioned coaxially. A ferrite core (1) and an aluminium screen (2) forward a magnetic flux generated by the excitation coil in the direction of the signal coils and an object under test (3). The signal coils are spaced by an appropriate distance in such a way that the output voltage U has the required level in case of the uniformly conductive object. Figure 1b shows a simplified equivalent magnetic circuit of the arrangement transducer-sample. With reference to Fig. 1b, the magnetic fluxes can be written as:

$$(1) \quad \phi = \frac{\Theta(R_{\mu_2} + R_{\mu_3})}{R_{\mu_2} \cdot R_{\mu_3} + (R_{\mu_2} + R_{\mu_3})Z_{\mu}},$$

$$(2) \quad \phi_3 = \frac{\Theta \cdot R_{\mu_2}}{R_{\mu_2} \cdot R_{\mu_3} + (R_{\mu_2} + R_{\mu_3})Z_{\mu}}.$$

The output voltage from the transducer is given by:

$$(3) \quad U = -j \cdot \omega(z_2 \cdot \phi - z_3 \cdot \phi_3).$$

Putting $R_{\mu_3} = k_1 \cdot R_{\mu_2}$ and $Z_{\mu} \cong j X_{\mu}$, which is true if the electric conductivity of the material tested "dominates" over its magnetic permeability ($R_{\mu} \ll X_{\mu}$), and combining (1), (2) and (3), we get:

$$(4) \quad U = -j \cdot \omega \cdot \Theta \cdot \frac{z_2 - z_3 \cdot \frac{l}{l_0}}{R_{\mu_2} \cdot \frac{k_1}{1+k_1} + j X_{\mu}}.$$

Now we assume that the uniformly conductive object contains an inclusion of different electrical parameters. The influence of the inclusion on the reactance X_{μ} depends mainly on the volume and position of the inclusion. The reactance can be expressed as:

$$(5) \quad X_{\mu} = X_{\mu_0} \left[1 \pm p \left(1 - \frac{\sqrt{h^2 + l^2}}{l_0} \right)^2 \right],$$

where: $p = \sqrt[3]{\frac{V_z}{V}}$, X_{μ_0} – value of the reactance without the inclusion, and other quantities are explained in Fig. 2.

The inclusion redirects magnetically induced currents. The signs „+” and „-” in (5) correspond to the situation when the inclusion weakens and amplifies the signal, respectively.

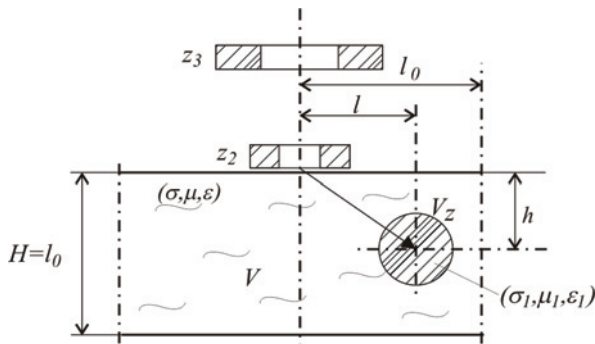


Fig.2. Illustration of quantities in the expression (5): V – volume of the object in the measuring range l_0 , V_z – volume of the inclusion

Putting (5) in (4) and after manipulations, the normalized output voltage has the form:

$$(6) \quad \frac{|U|}{A} = \frac{l - n \cdot \frac{l}{l_0}}{\sqrt{\left(\frac{k_1 \cdot k_2}{1+k_1} \right)^2 + \left[1 \pm p \left(1 - \frac{\sqrt{h^2 + l^2}}{l_0} \right)^2 \right]^2}},$$

where: $k_2 = \frac{R_{\mu_2}}{X_{\mu_0}}$; $n = \frac{z_3}{z_2}$; $A = \frac{\omega \cdot z_2 \cdot \Theta}{X_{\mu_0}}$ [mV].

The relation (6) is presented graphically in Fig. 3 as a function of relative position of the inclusion (l/l_0) for different values of the parameter p .

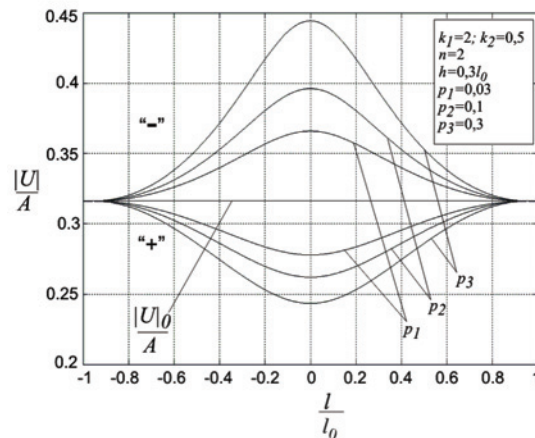


Fig.3. Normalized module of the output voltage for different values of the parameter p , $|U|_0/A$ – level of the output voltage without the inclusion in the measuring range

Figure 4 shows the normalized output voltage as a function of relative position of the inclusion for different "depths" h of the inclusion.

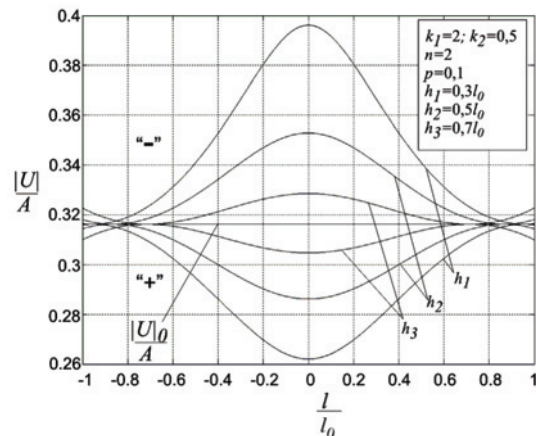
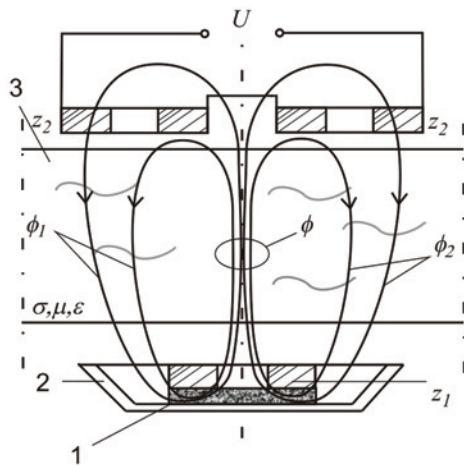


Fig.4. Normalized module of the output voltage for different values of h

The next measuring system is the self-comparing transducer shown in Fig. 5. A voltage appears at the output terminals only if local material parameters of the sample differ at the locations of the first and second signal coils connected differentially, both with z_2 turns. The probe can sense only changes in the sample while cancelling out noise and other unwanted signals that affect both the coils.



a) Combining (7), (8) and (9) we get:

$$(10) \quad U = -j \cdot \omega \cdot z_2 \cdot \Theta \cdot \frac{Z_{\mu_2}' - Z_{\mu_1}'}{Z_{\mu_1}' \cdot Z_{\mu_2}' + (Z_{\mu_1}' + Z_{\mu_2}')Z_{\mu}}$$

Assuming $R_{\mu_1}' + R_{\mu_1} = R_{\mu_2}' + R_{\mu_2} = R_{\mu}$, we obtain:

$$(11) \quad U = \omega \cdot z_2 \cdot \Theta \frac{X_{\mu_2} - X_{\mu_1}}{3R_{\mu}^2 - (X_{\mu}X_{\mu_1} + X_{\mu}X_{\mu_2} + X_{\mu_1}X_{\mu_2}) + j \cdot 2R_{\mu}(X_{\mu_1} + X_{\mu_2} + X_{\mu})}$$

When the inclusion is situated "in the centre" of the measuring system or in a large distance from it, the output voltage is equal to zero. In such a case, the real and imaginary parts of (11) must be equal to zero. Then, from (11), we have:

$$(12) \quad 3R_{\mu}^2 - (X_{\mu}X_{\mu_1} + X_{\mu}X_{\mu_2} + X_{\mu_1}X_{\mu_2}) = 0$$

Now, we assume (see Fig. 6):

$$X_{\mu_1} = k_1 \cdot X_{\mu}, \quad X_{\mu_2} = k_2 \cdot X_{\mu}$$

$$(13) \quad k_1 = 1 - \frac{p}{x_1}, \quad k_2 = 1 - \frac{p}{x_2}$$

where:

$$x_1 = \frac{l_1}{l_0} = \frac{l_0 + l}{l_0} = 1 + x, \quad x_2 = \frac{l_2}{l_0} = \frac{l_0 - l}{l_0} = 1 - x,$$

$2l_0$ – distance between the signal coils, x_1 and x_2 – relative distances between the signal coils and the inclusion, x – relative displacement of the inclusion, p – relative volume and position of the inclusion dependent coefficient.

When the inclusion is in the middle of the measuring system, then $x = 0$, and combining (12) and (13) we obtain the following result:

$$(14) \quad R_{\mu} = X_{\mu} \sqrt{\frac{(3-p)(1-p)}{3}}$$

Now, by using (11), (13) and (14), we get the expression for the module of the output voltage:

$$(15) \quad |U| = \frac{\omega \cdot z_2 \cdot \Theta}{X_{\mu}} \cdot \frac{2\sqrt{3} \cdot p \cdot x}{\sqrt{3[p^2(4-p)^2 + 12(3-p)(1-p)]x^4 + \dots - 24(3-2p)(3-p)(1-p)x^2 + 4(3-2p)^2(3-p)(1-p)}}$$

All the quantities used in the above equations are illustrated in Fig. 6.

b)

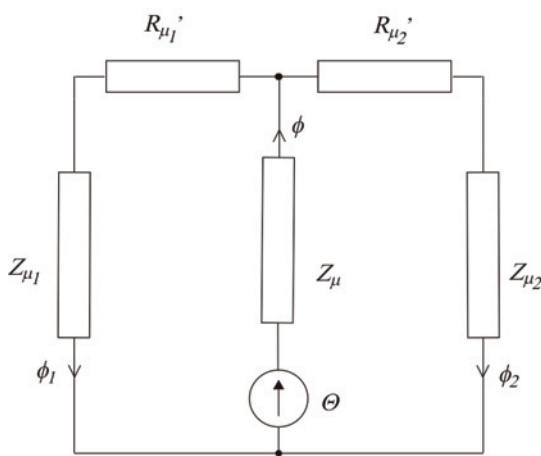


Fig. 5. The self-comparing measuring system: a) schematic view of the arrangement transducer-sample, b) equivalent magnetic circuit

Figure 5b shows a simplified equivalent magnetic circuit of the arrangement transducer-sample. With reference to Fig. 5b, the total magnetic flux generated by the exciter can be written as:

$$(7) \quad \phi = \Theta \cdot \frac{Z_{\mu_1}' + Z_{\mu_2}'}{Z_{\mu_1}' \cdot Z_{\mu_2}' + (Z_{\mu_1}' + Z_{\mu_2}')Z_{\mu}}$$

where: $\Theta = I \cdot z_1$,

$$Z_{\mu_1}' = R_{\mu_1}' + R_{\mu_1} + jX_{\mu_1},$$

$$Z_{\mu_2}' = R_{\mu_2}' + R_{\mu_2} + jX_{\mu_2}, \quad Z_{\mu} = R_{\mu} + jX_{\mu}$$

The magnetic fluxes ϕ_1 and ϕ_2 are given by:

$$(8) \quad \phi_1 = \frac{\Theta - \phi \cdot Z_{\mu}}{Z_{\mu_1}'}; \quad \phi_2 = \frac{\Theta - \phi \cdot Z_{\mu}}{Z_{\mu_2}'}$$

The output voltage of the self-comparing transducer has the following form:

$$(9) \quad U = -j \cdot \omega \cdot z_2 (\phi_1 - \phi_2)$$

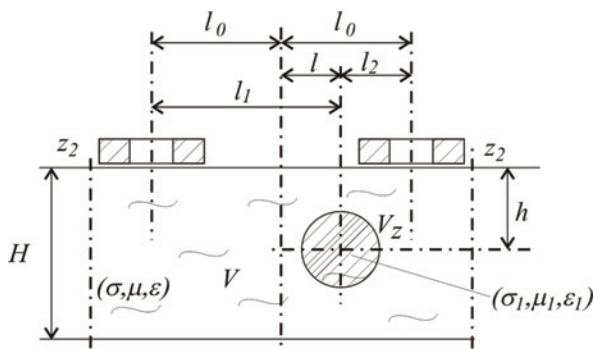


Fig. 6. Parameters of the self-comparing measuring system: z_2 – number of turns of the signal coils, V – volume of the object in the measuring range, V_z – volume of the inclusion

We assume, that influence of the inclusion on eddy currents excited in the sample depends on volume and position of the inclusion. Now, the parameter p has the form:

$$(16) \quad p = \sqrt{\frac{H-h}{H}} \cdot \sqrt[3]{\frac{V_z}{V}}$$

Based on carried out experimental researches, and to make up for some far-reaching simplifications needed to adopt when developing the equivalent circuit, corrective coefficient has been introduced in (15). Finally, the normalized output voltage has the form:

$$(17) \quad \frac{|U|}{A} = \frac{2\sqrt{3} \cdot p^3 \cdot x}{\sqrt{3[p^2(4-p)^2 + 12(3-p)(1-p)]x^4 + -24(3-2p)(3-p)(1-p)x^2 + 4(3-2p)^2(3-p)(1-p)}}$$

where: $A = \frac{\omega \cdot z_2 \cdot \Theta}{X_\mu}$ [mV].

The above relation is presented graphically for different volumes and positions of the inclusion in Figs. 7 and 8, respectively.

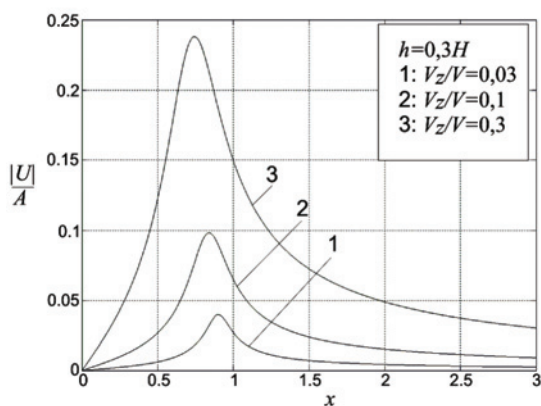


Fig. 7. Normalized module of the output voltage for different volumes of the inclusion according to (17)

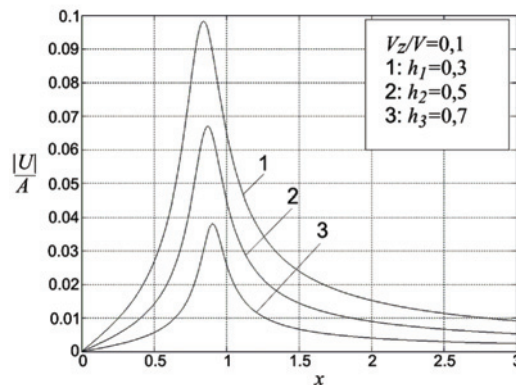


Fig. 8. Normalized module of the output voltage for different positions of the inclusion according to (17)

Conclusions

In this paper simple mathematical models of the compensating and self-comparing probes for eddy current testing of low conductivity objects have been presented. It is well known that for most practical problems in eddy current non-destructive evaluation techniques the geometry is too complicated for closed-form analytical solutions, therefore, numerical solutions are required. However, the semi-analytical models proposed in this paper give eddy current output signals for a wide variety of inclusion sizes and positions and can be used as a training mechanism for the development of automated inclusion characterization schemes, for example using neural networks. In the next stage of the project comparison of theoretical and experimental results will be given.

Acknowledgement

This work was supported by the Ministry of Education and Science, Poland, under the grant 3 T10A 033 30 (2006-2009).

REFERENCES

- [1] Scharfetter H., Lackner H, Rosell J., Magnetic induction tomography: hardware for multi-frequency measurements, *Physiol. Meas.*, 22 (2001), 131-146
- [2] Mnich S., Jordan A., Efekty biologiczne promieniowania elektromagnetycznego o częstotliwości sieciowej, radiowej i mikrofalowej, Instytut Naukowo Badawczy ZTUREK, Warszawa, marzec 2001, 66-81
- [3] Presman A.S., Electromagnetic fields and Life, Plenum Press, New York – London, 1970
- [4] Polk C., Postow E., CRC Handbook of biological effects of electromagnetic fields, CRC Press, Boca Raton, Florida, 1986
- [5] Sikora R., Gratkowski S., Komorowski M., Chady T., High sensitivity eddy current probe for inspection of low conductivity materials, *Review of Progress In Quantitative Nondestructive Evaluation*, American Institute of Physics, vol. 23 A (2004), 382-389

Authors: Ph.D., D.Sc., Eng. Stanisław Gratkowski, prof, PS, E-mail: sg@ps.pl; Ph.D., Eng. Mieczysław Komorowski; Tomasz Pietruszewicz, tp@ps.pl; Szczecin University of Technology, Department of Electrical and Computer Engineering, ul. Sikorskiego 37, 70-313 Szczecin, Poland

Realization problem for positive 2D hybrid systems with one delay in state and input vectors

Abstract. The realization problem for 2D positive hybrid systems with one delay in state and input vectors is formulated and a method for finding positive realizations of a given proper transfer matrix is proposed. Sufficient conditions for the existence of a positive realization of a given proper transfer matrix are established. A procedure for computation of a positive realization is proposed and illustrated by a numerical example.

Streszczenie. Sformułowana została metoda wyznaczania realizacji dodatnich dla dwuwymiarowych dodatnich układów hybrydowych z jednym opóźnieniem w wektorze stanu i wymuszeniu na podstawie danej transmitancji. Podane zostały warunki wystarczające istnienia realizacji dodatniej dla danej transmitancji właściwej. Na koniec została podana procedura wyznaczania realizacji dodatniej, którą zilustrowano przykładem numerycznym. (Problem realizacji dla dodatnich dwuwymiarowych układów hybrydowych z jednym opóźnieniem w wektorze stanu i wektorze sterowania)

Keywords: hybrid, 2D system, delay, positive realization, existence.

Słowa kluczowe: Dwuwymiarowe układy hybrydowe, opóźnienia, realizacja dodatnia, istnienie.

Introduction

In positive systems inputs, state variables and outputs take only non-negative values. Examples of positive systems are industrial processes involving chemical reactors, heat exchangers and distillation columns, storage systems, compartmental systems, water and atmospheric pollution models. A variety of models having positive linear systems behaviour can be found in engineering, management science, economics, social sciences, biology and medicine, etc.

The main purpose of this paper is to present a method for computation of positive realizations of a given transfer matrix. Sufficient conditions for the existence of a positive realization of a given proper transfer matrix will be established and a procedure for computation of positive realizations will be proposed.

To the best knowledge of the authors the realization problem for positive 2D hybrid systems with delays in state and input vectors has not been considered yet.

Preliminaries and problem formulation

Let $R^{n \times m}$ be the set of $n \times m$ matrices with entries from the field of real number R and Z_+ be the set of nonnegative integers. The $n \times n$ identity matrix will be denoted by I_n .

Consider a hybrid system with one delay in state and input vectors described by the equations

$$(1a) \quad \begin{aligned} \dot{x}_1(t, i) &= A_{11}^0 x_1(t, i) + A_{12}^0 x_2(t, i) + A_{11}^1 x_1(t-d, i) \\ &+ A_{12}^1 x_2(t, i-1) + B_1^0 u(t, i) + B_1^1 u(t-d, i-1) \end{aligned}$$

$$(1b) \quad \begin{aligned} x_2(t, i+1) &= A_{21}^0 x_1(t, i) + A_{22}^0 x_2(t, i) + A_{21}^1 x_1(t-d, i) \\ &+ A_{22}^1 x_2(t, i-1) + B_2^0 u(t, i) + B_2^1 u(t-d, i-1) \end{aligned}$$

$$(1c) \quad \begin{aligned} y(t, i) &= C_1 x_1(t, i) + C_2 x_2(t, i) + Du(t, i), \\ t &\in R_+ = [0, +\infty), \quad i \in Z_+ \end{aligned}$$

where $\dot{x}_1(t, i) = \frac{\partial x_1(t, i)}{\partial t}$, $x_1(t, i) \in R^{n_1}$, $x_2(t, i) \in R^{n_2}$,

$u(t, i) \in R^m$, $y(t, i) \in R^p$ and A, B, C, D are real matrices with appropriate dimensions.

Boundary conditions for (1a) and (1b) have the form

$$(2) \quad \begin{aligned} x_1(-kd, i) &\in R_+^{n_1} \quad \text{and} \quad x_2(t, -k) \in R_+^{n_2}, \quad k=0,1, \\ t &\in [0, \infty), \quad i \in Z_+ \end{aligned}$$

Let $R_+^{n \times m}$ be the set of $n \times m$ real matrices with nonnegative entries and $R_+^n = R_+^{n \times 1}$.

Definition 1. The hybrid system with delays (1) is called (internally) positive if $x_1(t, i) \in R_+^{n_1}$, $x_2(t, i) \in R_+^{n_2}$, and $y(t, i) \in R_+^p$, $t \in R_+$, $i \in Z_+$ for arbitrary boundary conditions $x_1(-kd, i) \in R_+^{n_1}$, $x_2(t, -k) \in R_+^{n_2}$, $k=0,1$ and inputs $u(t, -k) \in R_+^m$, $t \in [-d, 0)$, $k=0,1$.

Let M_n be the set of $n \times n$ Metzler matrices (real matrices with nonnegative off-diagonal entries).

Theorem 1. The hybrid system with one delay (1) is internally positive if and only if

$$(3) \quad \begin{aligned} A_{11}^0 &\in M_{n_1}, \quad A_{11}^1 \in R_+^{n_1 \times n_1}, \quad A_{12}^k \in R_+^{n_1 \times n_2}, \\ A_{21}^k &\in R_+^{n_2 \times n_1}, \quad A_{22}^k \in R_+^{n_2 \times n_2}, \quad B_1^k \in R_+^{n_1 \times m}, \\ B_2^k &\in R_+^{n_2 \times m}, \quad C_1 \in R_+^{p \times n_1}, \quad C_2 \in R_+^{p \times n_2}, \quad D \in R_+^{p \times m} \end{aligned}$$

for $k=0,1$.

The transfer matrix $T(s, z)$ of the system (1) is given by

$$(5a) \quad T(s, z) = [C_1 \quad C_2] \left[\begin{array}{cc} I_{n_1} s & 0 \\ 0 & I_{n_2} z \end{array} - A \right]^{-1} B + D$$

where

$$(5b) \quad A = \begin{bmatrix} A_{11} & A_{12} \\ A_{21} & A_{22} \end{bmatrix}, \quad B = \begin{bmatrix} B_1 \\ B_2 \end{bmatrix}$$

and

$$(5c) \quad \begin{aligned} A_{11} &= A_{11}^0 + A_{11}^1 e^{-sd} = A_{11}^0 + A_{11}^1 w_s, \\ A_{12} &= A_{12}^0 + A_{12}^1 z^{-1} = A_{12}^0 + A_{12}^1 w_z, \\ A_{21} &= A_{21}^0 + A_{21}^1 e^{-sd} = A_{21}^0 + A_{21}^1 w_s, \\ A_{22} &= A_{22}^0 + A_{22}^1 z^{-1} = A_{22}^0 + A_{22}^1 w_z, \\ B_1 &= B_1^0 + B_1^1 z^{-1} e^{-sd} = B_1^0 + B_1^1 w_{sz}, \\ B_2 &= B_2^0 + B_2^1 e^{-sd} z^{-1} = B_2^0 + B_2^1 w_{sz} \end{aligned}$$

In this case

$$(5d) \quad w_s = e^{-sd}, \quad w_z = z^{-1}, \quad w_{sz} = e^{-sd} z^{-1}$$

Definition 2. The matrices (3) are called the positive realization of the transfer matrix $T(s, z)$ if they satisfy the equality (5a). A realization is called minimal if the matrices A_{11} and A_{22} have minimal dimensions among all positive realizations of $T(s, z)$.

The realization problem can be stated as follows.

Given a proper rational matrix $T(s, z) \in R^{p \times m}(s, z)$, find its positive realization (3), where $R^{p \times m}(s, z)$ is the set of $m \times n$ rational matrices in s and z .

Problem solution.

The proposed method for solving of the realization problem for positive 2D hybrid systems is based on the following two lemmas.

Lemma 1. The transfer matrix (5) can be written in the form

$$(6a) \quad T(s, z) = C(s)[I_{n_2} z - A(s)]^{-1} B(s) + D(s)$$

or

$$(6b) \quad T(s, z) = C(z)[I_{n_1} s - A(z)]^{-1} B(z) + D(z)$$

where

$$A(s) = A_{22} + A_{21}[I_{n_1} s - A_{11}]^{-1} A_{12},$$

$$B(s) = A_{21}[I_{n_1} s - A_{11}]^{-1} B_1 + B_2,$$

$$(6c) \quad C(s) = C_2 + C_1[I_{n_1} s - A_{11}]^{-1} A_{12},$$

$$D(s) = C_1[I_{n_1} s - A_{11}]^{-1} B_1 + D$$

and

$$A(z) = A_{11} + A_{12}[I_{n_2} z - A_{22}]^{-1} A_{21},$$

$$B(z) = A_{12}[I_{n_2} z - A_{22}]^{-1} B_2 + B_1,$$

$$(6d) \quad C(z) = C_1 + C_2[I_{n_2} z - A_{22}]^{-1} A_{21},$$

$$D(z) = C_2[I_{n_2} z - A_{22}]^{-1} B_2 + D$$

Proof. Using the Laplace transform (L) to t and the Z-transform (Z) to i for the equations (1) with zero boundary conditions (2) we obtain

$$(7a) \quad sX_1 = A_{11}^0 X_1 + A_{12}^0 X_2 + A_{11}^1 e^{-sd} X_1 + A_{12}^1 z^{-1} X_2 + B_1^0 U + B_1^1 e^{-sd} z^{-1} U$$

$$(7b) \quad zX_2 = A_{21}^0 X_1 + A_{22}^0 X_2 + A_{21}^1 e^{-sd} X_1 + A_{22}^1 z^{-1} X_2 + B_2^0 U + B_2^1 e^{-sd} z^{-1} U$$

$$(7c) \quad Y = C_1 X_1 + C_2 X_2 + DU$$

where

$$X_k = X_k(s, z) = Z\{L[x_k(t, i)]\}, \quad k = 1, 2;$$

$$U = U(s, z) = Z\{L[u(t, i)]\}, \quad Y = Y(s, z) = Z\{L[y(t, i)]\}.$$

From (7b) we have

$$(8) \quad X_2 = [I_{n_2} z - A_{22}^0 - A_{22}^1 z^{-1}]^{-1} ([A_{21}^0 + A_{21}^1 e^{-sd}] X_1 + B_2^0 U + B_2^1 e^{-sd} z^{-1} U)$$

Substitution of (8) into (7a) yields

$$(9) \quad X_1 = [I_{n_1} s - A_{11}^0 - A_{11}^1 e^{-sd} - (A_{12}^0 + A_{12}^1 z^{-1}) \times [I_{n_2} z - A_{22}^0 - A_{22}^1 z^{-1}]^{-1} (A_{21}^0 + A_{21}^1 e^{-sd})]^{-1} \times \{(A_{12}^0 + A_{12}^1 z^{-1}) [I_{n_2} z - A_{22}^0 - A_{22}^1 z^{-1}]^{-1} \times (B_2^0 + B_2^1 e^{-sd} z^{-1}) + (B_1^0 + B_1^1 e^{-sd} z^{-1})\} U$$

and after substituting (9) into (8) we obtain

$$(10) \quad X_2 = [I_{n_2} z - A_{22}^0 - A_{22}^1 z^{-1}]^{-1} (A_{21}^0 + A_{21}^1 e^{-sd}) \times \{[I_{n_1} s - A_{11}^0 - A_{11}^1 e^{-sd} - (A_{12}^0 + A_{12}^1 z^{-1}) \times [I_{n_2} z - A_{22}^0 - A_{22}^1 z^{-1}]^{-1} (A_{21}^0 + A_{21}^1 e^{-sd})]^{-1} \times ((A_{12}^0 + A_{12}^1 z^{-1}) [I_{n_2} z - A_{22}^0 - A_{22}^1 z^{-1}]^{-1} \times (B_2^0 + B_2^1 e^{-sd} z^{-1}) + (B_1^0 + B_1^1 e^{-sd} z^{-1}))\} U + [I_{n_2} z - A_{22}^0 - A_{22}^1 z^{-1}]^{-1} (B_2^0 + B_2^1 e^{-sd} z^{-1}) U$$

Finally substituting of (9) and (10) into (7c) yields (6b).

The proof of (6a) is similar (by interchanging the role of s and z). \square

Lemma 2. Let $A(s)$, $B(s)$, $C(s)$, $D(s)$ and $A(z)$, $B(z)$, $C(z)$, $D(z)$ be defined by (6c) and (6d). Then

$$(11a) \quad \lim_{s \rightarrow \infty} \begin{bmatrix} A(s) & B(s) \\ C(s) & D(s) \end{bmatrix} = \begin{bmatrix} A_{22} & B_2 \\ C_2 & D \end{bmatrix}$$

$$(11b) \quad \lim_{z \rightarrow \infty} \begin{bmatrix} A(z) & B(z) \\ C(z) & D(z) \end{bmatrix} = \begin{bmatrix} A_{11} & B_1 \\ C_1 & D \end{bmatrix}$$

and

$$(12a) \quad \lim_{s \rightarrow \infty} s \begin{bmatrix} A(s) - A_{22} & B(s) - B_2 \\ C(s) - C_2 & D(s) - D \end{bmatrix} = \begin{bmatrix} A_{21} \\ C_1 \end{bmatrix} \begin{bmatrix} A_{12} & B_1 \end{bmatrix}$$

$$(12b) \quad \lim_{z \rightarrow \infty} z \begin{bmatrix} A(z) - A_{11} & B(z) - B_1 \\ C(z) - C_1 & D(z) - D \end{bmatrix} = \begin{bmatrix} A_{12} \\ C_2 \end{bmatrix} \begin{bmatrix} A_{21} & B_2 \end{bmatrix}$$

Proof. From (6c) we have

$$(13) \quad \begin{bmatrix} A(s) & B(s) \\ C(s) & D(s) \end{bmatrix} = \begin{bmatrix} A_{21} \\ C_1 \end{bmatrix} [I_{n_1} s - A_{11}]^{-1} \begin{bmatrix} A_{12} & B_1 \end{bmatrix} + \begin{bmatrix} A_{22} & B_2 \\ C_2 & D \end{bmatrix}$$

Taking into account that $\lim_{s \rightarrow \infty} [I_{n_1} s - A_{11}]^{-1} = 0$, from (13) we obtain (11a). The proof of (11b) is similar.

From (13) we have

$$\lim_{s \rightarrow \infty} s \begin{bmatrix} A(s) - A_{22} & B(s) - B_2 \\ C(s) - C_2 & D(s) - D \end{bmatrix} = \lim_{s \rightarrow \infty} s \begin{bmatrix} A_{21} \\ C_1 \end{bmatrix} [I_{n_1} s - A_{11}]^{-1} \begin{bmatrix} A_{12} & B_1 \end{bmatrix} = \begin{bmatrix} A_{21} \\ C_1 \end{bmatrix} \begin{bmatrix} A_{12} & B_1 \end{bmatrix}$$

since $\lim_{s \rightarrow \infty} s [I_{n_1} s - A_{11}]^{-1} = I_{n_1}$. The proof for (12b) is similar. \square

It is well-known [5] that any 2D transfer matrix can be always written in the form

$$(14a) \quad T(s, z) = \frac{N_{q_1}(z)}{d_{q_1}(z)} + \frac{N_{q_1-1}(z)s^{q_1-1} + \dots + N_1(z)s + N_0(z)}{s^{q_1} - d_{q_1-1}(z)s^{q_1-1} - \dots - d_1(z)s - d_0(z)}$$

or

$$(14b) \quad T(s, z) = \frac{N_{q_2}(s)}{d_{q_2}(s)} + \frac{N_{q_2-1}(s)z^{q_2-1} + \dots + N_1(s)z + N_0(s)}{z^{q_2} - d_{q_2-1}(s)z^{q_2-1} - \dots - d_1(s)z - d_0(s)}$$

where

$$N_{q_1}(z) = N_{q_1, q_2} z^{q_2} + N_{q_1, q_2-1}(w_{sz}) z^{q_2-1} + \dots + N_{q_1, 1}(w_{sz}) z + N_{q_1, 0}(w_{sz}) \in R^{p \times m}[z],$$

$$N_{q_2}(s) = N_{q_2, q_1} s^{q_1} + N_{q_2, q_1-1}(w_{sz}) s^{q_1-1} + \dots + N_{q_2, 1}(w_{sz}) s + N_{q_2, 0}(w_{sz}) \in R^{p \times m}[s],$$

$$d_{q_1}(z) = d_{q_1, q_2} z^{q_2} + d_{q_1, q_2-1}(w_s) z^{q_2-1} + \dots + d_{q_1, 1}(w_s) z + d_{q_1, 0}(w_s) \in R[z],$$

$$d_{q_2}(s) = d_{q_2, q_1} s^{q_1} + d_{q_2, q_1-1}(w_z) s^{q_1-1} + \dots + d_{q_2, 1}(w_z) s + d_{q_2, 0}(w_z) \in R[s],$$

$$N_k(z) = N_{k, n_k}(w_{sz}) z^{n_k} + N_{k, n_k-1}(w_{sz}) z^{n_k-1} + \dots + N_{k, 1}(w_{sz}) z + N_{k, 0}(w_{sz}) \in R^{p \times m}(z)$$

$$d_k(z) = d_{k, n_k}(w_s) z^{n_k} + d_{k, n_k-1}(w_s) z^{n_k-1} + \dots + d_{k, 1}(w_s) z + d_{k, 0}(w_s) \in R(z)$$

$$N_l(s) = N_{l, n_l}(w_{sz}) s^{n_l} + N_{l, n_l-1}(w_{sz}) s^{n_l-1} + \dots + N_{l, 1}(w_{sz}) s + N_{l, 0}(w_{sz}) \in R^{p \times m}(s)$$

$$d_l(s) = d_{l, n_l}(w_z) s^{n_l} + d_{l, n_l-1}(w_z) s^{n_l-1} + \dots + d_{l, 1}(w_z) s + d_{l, 0}(w_z) \in R(s)$$

for $k = 0, 1, \dots, q_1 - 1$, $l = 0, 1, \dots, q_2 - 1$ and $R^{p \times m}[z]$

($R^{p \times m}[s]$) is the set of $p \times m$ polynomial matrices in z (s), w is notation of delay (corresponding to (5c) and (5d)), coefficients N_{q_1, q_2} , N_{q_2, q_1} , d_{q_1, q_2} , d_{q_2, q_1} are independent of delay w .

Using one of the well-known methods [5] we can find a realization $A(z)$, $B(z)$, $C(z)$, $D(z)$ of (14a) and a realization $A(s)$, $B(s)$, $C(s)$, $D(s)$ of (14b). For example it is easy to verify that the matrices

$$A(z) = \begin{bmatrix} 0 & 0 & \dots & 0 & d_0(z)I_p \\ I_p & 0 & \dots & 0 & d_1(z)I_p \\ 0 & I_p & \dots & 0 & d_2(z)I_p \\ \vdots & \vdots & \vdots & \vdots & \vdots \\ 0 & 0 & \dots & I_p & d_{q_1-1}(z)I_p \end{bmatrix},$$

$$(15a) \quad B(z) = \begin{bmatrix} N_0(z) \\ N_1(z) \\ N_2(z) \\ \vdots \\ N_{q_1-1}(z) \end{bmatrix}, \quad C(z) = [0 \quad 0 \quad \dots \quad 0 \quad I_p],$$

$$D(z) = \frac{N_{q_1}(z)}{d_{q_1}(z)}$$

are a realization of (14a) and the matrices

$$A(s) = \begin{bmatrix} 0 & 0 & \dots & 0 & d_0(s)I_p \\ I_p & 0 & \dots & 0 & d_1(s)I_p \\ 0 & I_p & \dots & 0 & d_2(s)I_p \\ \vdots & \vdots & \vdots & \vdots & \vdots \\ 0 & 0 & \dots & I_p & d_{q_2-1}(s)I_p \end{bmatrix},$$

$$(15b) \quad B(s) = \begin{bmatrix} N_0(s) \\ N_1(s) \\ N_2(s) \\ \vdots \\ N_{q_2-1}(s) \end{bmatrix}, \quad C(s) = [0 \quad 0 \quad \dots \quad 0 \quad I_p],$$

$$D(s) = \frac{N_{q_2}(s)}{d_{q_2}(s)}$$

are a realization of (14b).

Let us define

$$T_\infty = \lim_{s, z \rightarrow \infty} T(s, z) = \lim_{s \rightarrow \infty} \frac{N_{q_2}(s)}{d_{q_2}(s)} = \lim_{z \rightarrow \infty} \frac{N_{q_1}(z)}{d_{q_1}(z)}$$

$$d_{k\infty} = \lim_{z \rightarrow \infty} d_k(z), \quad \bar{d}_{k\infty} = \lim_{z \rightarrow \infty} z[d_k(z) - d_{k\infty}],$$

$$(16) \quad N_{k\infty} = \lim_{z \rightarrow \infty} N_k(z), \quad k = 0, 1, \dots, q_1 - 1$$

$$d_{l\infty} = \lim_{s \rightarrow \infty} d_l(s), \quad \bar{d}_{l\infty} = \lim_{s \rightarrow \infty} s[d_l(s) - d_{l\infty}],$$

$$N_{l\infty} = \lim_{s \rightarrow \infty} N_l(s), \quad l = 0, 1, \dots, q_2 - 1$$

Theorem 2. There exist a positive realization of $T(s, z)$ given by (14) if

1. $T_\infty \in R_+^{p \times m}$
2. $d_{k\infty} \in R_+$ for $k = 0, 1, \dots, q_1 - 2$ and $d_{q_1-1, \infty}$ is arbitrary
3. $N_{k\infty} \in R_+^{p \times m}$ for $k = 0, 1, \dots, q_1 - 1$
4. $d_{l\infty} \in R_+$, $N_{l\infty} \in R_+^{p \times m}$ for $l = 0, 1, \dots, q_2 - 1$
5. $\bar{d}_{k\infty} \in R_+$ for $k = 0, 1, \dots, q_1 - 1$ and $\bar{d}_{l\infty} \in R_+$ for $l = 0, 1, \dots, q_2 - 1$

Proof. If $T_\infty \in R_+^{p \times m}$ then $D \in R_+^{p \times m}$ since $T_\infty = \lim_{s, z \rightarrow \infty} T(s, z)$. From (11b) and the form of $A(z)$ it

follows that if the condition 2 is met then A_{11}^0 is a Metzler matrix, i.e. $A_{11}^0 \in M_{n_1}$ and $A_{11}^1 \in R_+^{n_1 \times n_1}$. If the condition 3

is satisfied then by (11b) $B_1^0, B_1^1 \in R_+^{n_1 \times m}$. Similarly if the condition 4 holds then by (11a) we have $A_{22}^0, A_{22}^1 \in R_+^{n_2 \times n_2}$ and $B_2^0, B_2^1 \in R_+^{n_2 \times m}$. From (12) it follows that $A_{12}^0, A_{12}^1 \in R_+^{n_1 \times n_2}$ and $A_{21}^0, A_{21}^1 \in R_+^{n_2 \times n_1}$ if the condition 5 is satisfied. \square

If the assumptions of Theorem 2 are satisfied then a positive realization (3) of (14) can be found by the use of the following procedure.

Procedure 1.

Step 1. Write $T(s, z)$ in the forms (14).

Step 2. Knowing $d_k(z)$, $N_k(z)$ for $k=0,1,\dots,q_1$ and $d_l(s)$, $N_l(s)$ for $l=0,1,\dots,q_2$ and using one of the well-known methods find realizations $A(z)$, $B(z)$, $C(z)$, $D(z)$ and $A(s)$, $B(s)$, $C(s)$, $D(s)$, for example the realizations (15).

Step 3. Using (11) find matrices $A_{11} = A_{11}^0 + A_{11}^1 w_s$,

$$A_{22} = A_{22}^0 + A_{22}^1 w_z, \quad B_1 = B_1^0 + B_1^1 w_{sz},$$

$$B_2 = B_2^0 + B_2^1 w_{sz}, \quad C_1, C_2 \text{ and } D.$$

Step 4. Using (12a) (or (12b)) find matrices

$$A_{12} = A_{12}^0 + A_{12}^1 w_z \text{ and } A_{21} = A_{21}^0 + A_{21}^1 w_s.$$

Example

Find a positive realization (3) of the transfer function

$$(17) \quad T(s, z) = \frac{(s-c(w))(z^2 + n_1(w)z + n_0(w))}{(s-c(w))(z^2 - d_1(w)z - d_0(w))}$$

where the coefficient of numerator and denominator in general case according to (5c) can have the form:

$$c(w) = c^0 + c^1 e^{-sd} + c^2 z^{-1} + c^3 e^{-sd} z^{-1},$$

$$d(w) = d^0 + d^1 e^{-sd} + d^2 z^{-1} + d^3 e^{-sd} z^{-1},$$

$$n(w) = n^0 + n^1 e^{-sd} + n^2 z^{-1} + n^3 e^{-sd} z^{-1}$$

In this case $m = p = 1$, $q_1 = 1$ and $q_2 = 2$.

Using Procedure 1 we obtain the following.

Step 1. The transfer function in the form (14a) is

$$(18a) \quad T(s, z) = \frac{z^2 + n_1(w)z + n_0(w)}{z^2 - d_1(w)z - d_0(w)} + \frac{0}{s-c(w)} \\ = \frac{N_1(z)}{d_1(z)} + \frac{N_0(z)}{s-d_0(z)}$$

where coefficients of decomposed transfer function have the form

$$(18b) \quad d_1(z) = z^2 - d_1(w_s)z - d_0(w_s), \quad d_0(z) = c(w_s),$$

$$N_1(z) = z^2 + n_1(w_{sz})z + n_0(w_{sz}), \quad N_0(z) = 0$$

and in the form (14b) is

$$(19a) \quad T(s, z) = \frac{s-c(w)}{s-c(w)} + \frac{(d_1(w) + n_1(w))z + (d_0(w) + n_0(w))}{z^2 - d_1(w)z - d_0(w)} \\ = \frac{N_2(s)}{d_2(s)} + \frac{N_1(s)z + N_0(s)}{z^2 - d_1(s)z - d_0(s)}$$

where coefficients of decomposed transfer function have the form

$$(19b) \quad d_2(s) = s - c(w_z), \quad d_1(s) = d_1(w_z), \\ d_0(s) = d_0(w_z), \\ N_2(s) = s - c(w_{sz}), \quad N_1(s) = d_1(w_z) + n_1(w_{sz}) \\ N_0(s) = d_0(w_z) + n_0(w_{sz})$$

Step 2. Using (15) we obtain

$$A(z) = [d_0(z)] = [c(w_s)],$$

$$(20a) \quad B(z) = [N_0(z)] = [0],$$

$$C(z) = [1], \quad D(z) = \frac{N_1(z)}{d_1(z)} = \frac{z^2 + n_1(w_{sz})z + n_1(w_{sz})}{z^2 - d_1(w_s)z - d_0(w_s)}$$

and

$$A(s) = \begin{bmatrix} 0 & d_0(s) \\ 1 & d_1(s) \end{bmatrix} = \begin{bmatrix} 0 & d_0(w_z) \\ 1 & d_1(w_z) \end{bmatrix},$$

$$(20b) \quad B(s) = \begin{bmatrix} N_0(s) \\ N_1(s) \end{bmatrix} = \begin{bmatrix} d_0(w_z) + n_0(w_{sz}) \\ d_1(w_z) + n_1(w_{sz}) \end{bmatrix},$$

$$C(s) = [0 \quad 1], \quad D(s) = \frac{N_2(s)}{d_2(s)} = \frac{s - c(w_{sz})}{s - c(w_z)}$$

Step 3. From (11) and (20) we have

$$(21a) \quad A_{11} = \lim_{z \rightarrow \infty} A(z) = [c(w_s)], \quad B_1 = \lim_{z \rightarrow \infty} B(z) = [0],$$

$$C_1 = \lim_{z \rightarrow \infty} C(z) = [1], \quad D = \lim_{z \rightarrow \infty} D(z) = [1]$$

and

$$A_{22} = \lim_{s \rightarrow \infty} A(s) = \begin{bmatrix} 0 & d_0(w_z) \\ 1 & d_1(w_z) \end{bmatrix},$$

$$(21b) \quad B_2 = \lim_{s \rightarrow \infty} B(s) = \begin{bmatrix} d_0(w_z) + n_0(w_{sz}) \\ d_1(w_z) + n_1(w_{sz}) \end{bmatrix},$$

$$C_2 = \lim_{s \rightarrow \infty} C(s) = [0 \quad 1], \quad D = \lim_{s \rightarrow \infty} D(s) = [1]$$

Step 4. Using (12) and (21) we obtain

$$(22a) \quad \lim_{z \rightarrow \infty} z \begin{bmatrix} A(z) - A_{11} & B(z) - B_1 \\ C(z) - C_1 & D(z) - D \end{bmatrix} \\ = \lim_{z \rightarrow \infty} \begin{bmatrix} 0 & 0 \\ 0 & \frac{(n_1(w_{sz}) + d_1(w_s))z^2 + (n_0(w_{sz}) + d_0(w_s))z}{z^2 - d_1(w_s)z - d_0(w_s)} \end{bmatrix} \\ = \begin{bmatrix} 0 & 0 \\ 0 & n_1(w_{sz}) + d_1(w_s) \end{bmatrix} = \begin{bmatrix} A_{12} \\ C_2 \end{bmatrix} \begin{bmatrix} A_{21} & B_2 \end{bmatrix}$$

and

$$(22b) \quad \lim_{s \rightarrow \infty} s \begin{bmatrix} A(s) - A_{22} & B(s) - B_2 \\ C(s) - C_2 & D(s) - D \end{bmatrix} \\ = \begin{bmatrix} 0 & 0 & 0 \\ 0 & 0 & 0 \\ 0 & 0 & -c(w_{sz}) - c(w_z) \end{bmatrix} = \begin{bmatrix} A_{21} \\ C_1 \end{bmatrix} \begin{bmatrix} A_{12} & B_1 \end{bmatrix}$$

From (22) we have

$$\begin{aligned}
& \begin{bmatrix} 0 & 0 \\ 0 & n_1(w_{sz}) + d_1(w_s) \end{bmatrix} \\
& = \begin{bmatrix} A_{12} \\ \dots \\ 0 & 1 \end{bmatrix} \begin{bmatrix} A_{21} & : & n_0(w_{sz}) \\ & & n_1(w_{sz}) \end{bmatrix} \Rightarrow A_{12} = \begin{bmatrix} 0 & 0 \end{bmatrix} \\
(23) \quad & \begin{bmatrix} 0 & 0 & 0 \\ 0 & 0 & 0 \\ 0 & 0 & -c(w_{sz}) - c(w_z) \end{bmatrix} \\
& = \begin{bmatrix} A_{21} \\ \dots \\ 1 \end{bmatrix} \begin{bmatrix} A_{12} & : & 0 \end{bmatrix} \Rightarrow A_{21} = \begin{bmatrix} 0 \\ 0 \end{bmatrix}
\end{aligned}$$

The desired realization is given by:

$$\begin{aligned}
A_{11} &= [c(w_s)], \quad A_{12} = \begin{bmatrix} 0 & 0 \end{bmatrix}, \\
A_{21} &= \begin{bmatrix} 0 \\ 0 \end{bmatrix}, \quad A_{22} = \begin{bmatrix} 0 & d_0(w_z) \\ 1 & d_1(w_z) \end{bmatrix}, \\
(24) \quad B_1 &= \begin{bmatrix} 0 \end{bmatrix}, \quad B_2 = \begin{bmatrix} n_0(w_{sz}) \\ n_1(w_{sz}) \end{bmatrix}, \\
C_1 &= [1], \quad C_2 = \begin{bmatrix} 0 & 1 \end{bmatrix}, \quad D = [1]
\end{aligned}$$

Taking into account (5c) realization is given by matrices:

$$\begin{aligned}
A_{11}^0 &= [c^0], \quad A_{11}^1 = [c^1], \quad A_{12}^0 = \begin{bmatrix} 0 & 0 \end{bmatrix}, \quad A_{12}^1 = \begin{bmatrix} 0 & 0 \end{bmatrix}, \\
A_{21}^0 &= \begin{bmatrix} 0 \\ 0 \end{bmatrix}, \quad A_{21}^1 = \begin{bmatrix} 0 \\ 0 \end{bmatrix}, \quad A_{22}^0 = \begin{bmatrix} 0 & d_0^0 \\ 1 & d_1^0 \end{bmatrix}, \quad A_{22}^1 = \begin{bmatrix} 0 & d_0^1 \\ 0 & d_1^1 \end{bmatrix}, \\
(25) \quad B_1^0 &= \begin{bmatrix} 0 \end{bmatrix}, \quad B_1^1 = \begin{bmatrix} 0 \end{bmatrix}, \quad B_2^0 = \begin{bmatrix} n_0^0 \\ n_1^0 \end{bmatrix}, \quad B_2^1 = \begin{bmatrix} n_0^1 \\ n_1^1 \end{bmatrix}, \\
C_1 &= [1], \quad C_2 = \begin{bmatrix} 0 & 1 \end{bmatrix}, \quad D = [1]
\end{aligned}$$

Concluding remarks

A method for computation of positive realizations of a given proper transfer matrix of 2D hybrid systems with one delay in state and input vectors has been proposed. Sufficient conditions for the existence of a positive realization of a given proper transfer matrix have been established. A procedure for computation of positive realizations has been proposed. The procedure has been illustrated by an example. Proposed method is easy extendable for positive hybrid systems with multi delays. An open problem is formulation of the necessary and sufficient conditions for the existence of solution of the positive realization problem for 2D hybrid systems in the general case. An extension of those considerations for 2D hybrid systems described by models with structures similar to the 2D general model [14] or the 2D second Fornasini-Marchesini model [18] are also open problems.

Acknowledgment

The work was supported by the State Committee for Scientific Research of Poland under grant No. 3 T11A 00627.

REFERENCES

- [1] L. Benvenuti and L. Farina, *A tutorial on the positive realization problem*, IEEE Trans. Autom. Control, vol. 49, No 5, 2004, pp. 651-664.
- [2] L. Farina and S. Rinaldi, *Positive Linear Systems; Theory and Applications*, J. Wiley, New York, 2000
- [3] M. Busłowicz and T. Kaczorek, *Reachability and minimum energy control of positive linear discrete-time systems with one delay*, 12th Mediterranean Conference on Control and Automation, June 6-9, 2004, Kasadasi, Izmir, Turkey
- [4] T. Kaczorek, *Some recent developments in positive systems*, Proc. 7th Conference of Dynamical Systems Theory and Applications, pp. 25-35, Łódź 2003.
- [5] T. Kaczorek, *Positive 1D and 2D systems*, Springer Verlag, London 2001.
- [6] T. Kaczorek, *A realization problem for positive continues-time linear systems with reduced numbers of delay*, Int. J. Appl. Math. Comp. Sci. 2006, Vol. 16, No. 3, pp. 325-331.
- [7] T. Kaczorek, *Realization problem for positive multivariable discrete-time linear systems with delays in the state vector and inputs*, Int. J. Appl. Math. Comp. Sci. 2006, Vol. 16, No. 2, pp. 101-106.
- [8] T. Kaczorek, *Realization problem for positive discrete-time systems with delay*, System Science, Vol. 30, No. 4, 2004, pp. 17-13.
- [9] T. Kaczorek, *Positive minimal realizations for singular discrete-time systems with delays in state and delays in control*, Bull. Pol. Acad. Sci. Techn., Vol 53, No 3, 2005, pp.
- [10] T. Kaczorek and M. Busłowicz, *Minimal realization problem for positive multivariable linear systems with delay*, Int. J. Appl. Math. Compt. Sci., Vol. 14, No. 2, 2004, pp. 181-187.
- [11] T. Kaczorek and M. Busłowicz, *Reachability and minimum energy control of positive discrete-time linear systems with multiple delays in state and control*, Pomiar Automatyka Kontrola, 2006, (in press).
- [12] T. Kaczorek, *Positive 2D hybrid linear systems*, Bull. Pol. Acad. Sci. Techn. Sci. Vol. 55, No. 3, 2007.
- [13] J. Klamka, *Controllability of dynamical systems*, Kluwer Academic Publ., Dordrecht, 1991.
- [14] J. Kurek, *The general state-space model for a two-dimensional linear digital system*, IEEE Trans. Autom. Contr. AC-30, June 1985, pp. 600-602.
- [15] V. M. Marchenko, O. N. Poddubnaya, *Relative controllability of stationary hybrid systems*, 10th IEEE Int. Conf. on Methods and Models in Automation and Robotics, 30 Aug. -2 Sept. 2004, Międzyzdroje, Poland pp. 267-272.
- [16] V. M. Marchenko, O. N. Poddubnaya, Z. Zaczekiewicz, *On the observability of linear differential-algebraic systems with delays*, IEEE Trans. Autom. Contr. Vol. 51, No. 8, 2006, pp. 1387-1392.
- [17] R. B. Roesser, *A discrete state-space model for linear image processing*, IEEE Trans. on Automatic Control, AC-20, 1 (1975), pp. 1-10.
- [18] M. E. Valcher, *On the initial stability and asymptotic behavior of 2D positive systems*, IEEE Trans. on Circuits and Systems, I, Vol. 44 (1997), No, 7, pp. 602-613.

Authors: prof. dr hab. inż. Tadeusz Kaczorek, Białystok Technical University, Faculty of Electrical Engineering, 15-351 Białystok, Wiejska 45D, Poland, E-mail: kaczorek@isep.pw.edu.pl; mgr inż. Łukasz Sajewski, Białystok Technical University, Faculty of Electrical Engineering, 15-351 Białystok, Wiejska 45D, Poland, E-mail: lsajewski@doktoranci.pb.edu.pl.

Differential eddy current transducer with high spatial resolution

Abstract. In this paper FEM simulations of two differently sized eddy current differential transducers are presented. A 3D-finite element software package was used to analyse various configurations of the excitation coils and select optimal design. Numerical analysis was verified by measurements of INCONEL thin plates. A set of experiments were carried out in order to prove usability of the transducer.

Streszczenie. Przedstawiono koncepcję różnicowego przetwornika wiropiędowego wykorzystywanego w badaniach nieniszczących. W celu analizy różnych konfiguracji wzbudzenia przetwornika oraz wyboru optymalnej konstrukcji przeprowadzono trójwymiarowe symulacje metodą elementów skończonych. Obliczenia numeryczne zostały zweryfikowane za pomocą pomiarów cienkich płyt z materiału INCONEL600. (Różnicowy przetwornik wiropiędowy o dużej rozdzielczości przestrzennej)

Keywords: nondestructive testing, eddy current, differential transducer.

Słowa kluczowe: badania nieniszczące, prądy wirowe, przetworniki różnicowe.

Introduction

Detection and identification of shallow defects located on the opposite surface of element under examination is a great merit of eddy current inspection. The main goal is to design a transducer generating high amplitude output signal in presence of a flaw and signal close to zero in case of homogenous material. Excellent sensitivity of the previously developed transducer [1] was confirmed by the experiments. Unfortunately, it was an absolute transducer and because of high background voltage, it was necessary to use a high resolution AD converter. Therefore a new differential configuration of the transducers is proposed.

Transducers and measuring system

A view of the transducer is shown in Fig.1(a). It consists of a cylindrical ferrite core with five symmetrically placed columns. A pickup coil is wound on the central column and four excitation coils are placed on remaining columns in pairs on two perpendicular axes. One pair of the excitation coils produce in the pickup coil flux flowing in opposite direction in comparison to the flux caused by another pair. The resulting flux in the pickup coil is close to zero in equilibrium state. Output signal U_{out} depends on difference of fluxes ϕ_x and ϕ_y . Simplified electrical scheme of the transducer is presented in Fig. 1(b). In this paper properties of two different size differential eddy current transducers UniBig and UniSmall are presented. Their dimensions are shown in Fig.2 and Table 1. UniBig is approximately 1.3 times bigger than UniSmall. The probe is sensitive to orientation of the flaws, as it is shown in Fig.3. A flaw parallel to one pair of exciting columns (for example columns A and B) causes growth of the output signal's amplitude in comparison to the signal's amplitude from unflawed area. If the flaw is parallel to the second pair of columns (C and D), the output signal is decreasing. This property is very useful in case of 3D flaws imaging.

Table 1. Comparison of dimensions

| Parameter [mm] | UniBig | UniSmall |
|----------------|--------|----------|
| D_1 | 12 | 8.5 |
| D_2 | 2 | 1.5 |
| L_1 | 5 | 3.5 |
| H_1 | 10 | 7 |
| H_2 | 6 | 4.5 |

Results of numerical analysis 3D FEM

Results of 3D FEM analysis of the proposed transducer are presented in Fig.4. In Fig.5 one can see distribution of eddy currents in homogenous plate. Induced current density with presence of the flaw is shown in Fig.6. The relative depth of the outer flaw equals 60%, length 3.5 mm, width 0.2 mm. As we expected the mean current density is higher

in case of sensor UniBig, thus UniBig has better sensitivity to shallow flaws placed on the opposite side of the measured specimen. But in case of UniSmall the area of eddy current concentration is smaller, and therefore sensor has better resolution. Those properties are confirmed by results of experiments presented in next section.

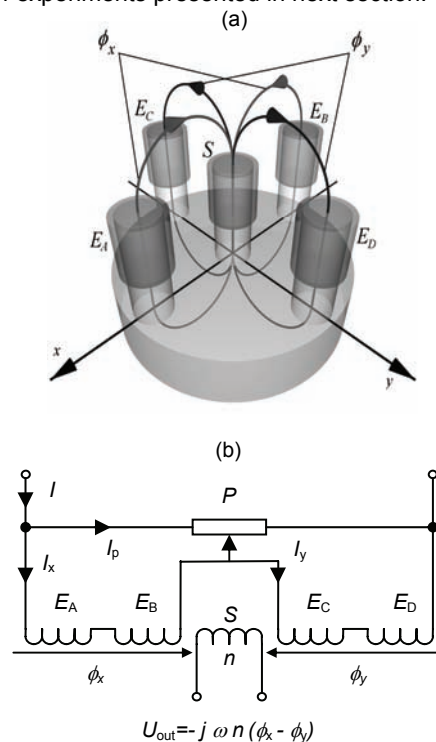


Fig.1. View and simplified electrical scheme of the transducer; $E_A...E_D$ – excitation coils, (S) – pickup coil, (ϕ_x , ϕ_y) – magnetic fluxes, P – potentiometer that controls magnetic fluxes ϕ_x and ϕ_y , n – number of turns in the pickup coil S

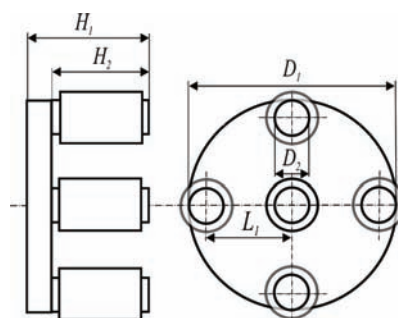


Fig.2. Dimensions of the transducers

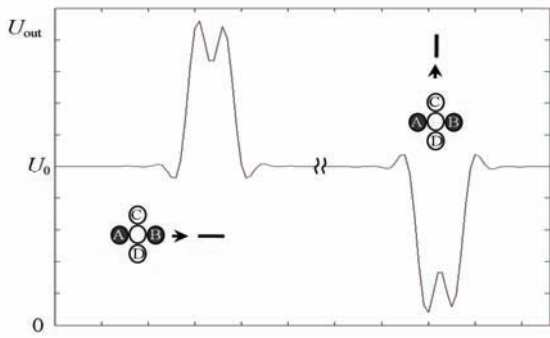


Fig.3. Amplitude of output voltage caused by the flaws having different orientation

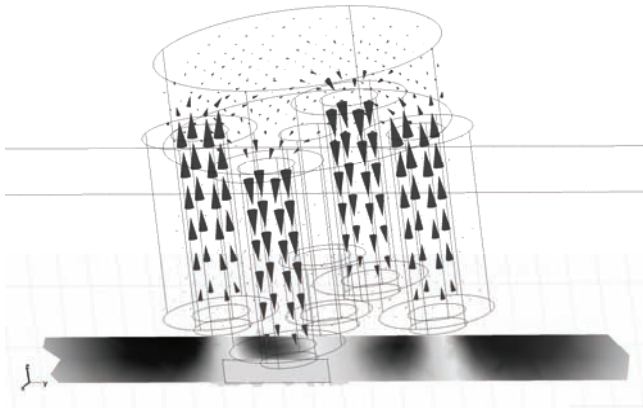


Fig.4. Results of 3D FEM analysis of the proposed EC transducer (magnetic flux distribution – arrow plot, induced current density in cross section of tested specimen – slice plot)

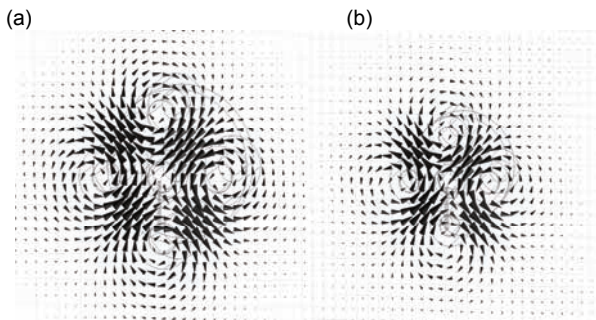


Fig.5. 3D distribution of eddy currents in flawless area of examined specimen: a) UniBig, b) UniSmall

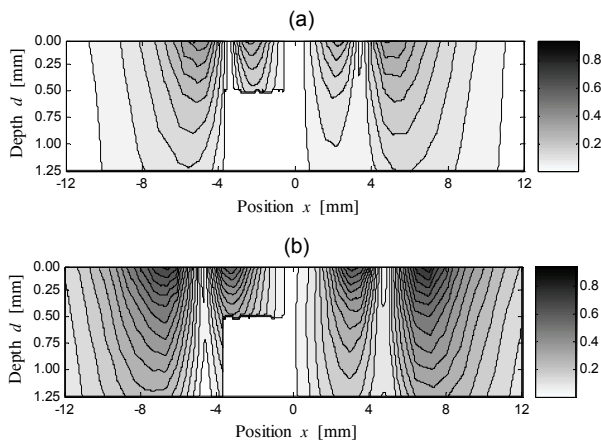


Fig.6. Induced relative current density in cross-section of conducting plate (component perpendicular to a flaw plane); a) UniSmall with presence of a flaw, b) UniBig with presence of a flaw

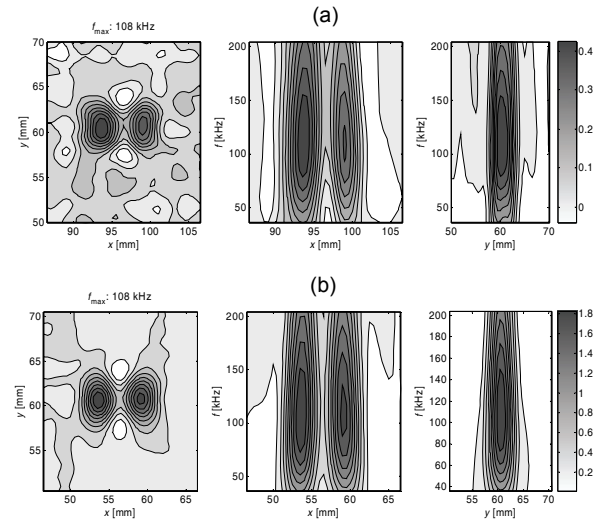


Fig.7. Signals caused by 3 mm length flaws (UniBig), a) depth 10%, b) depth 20%

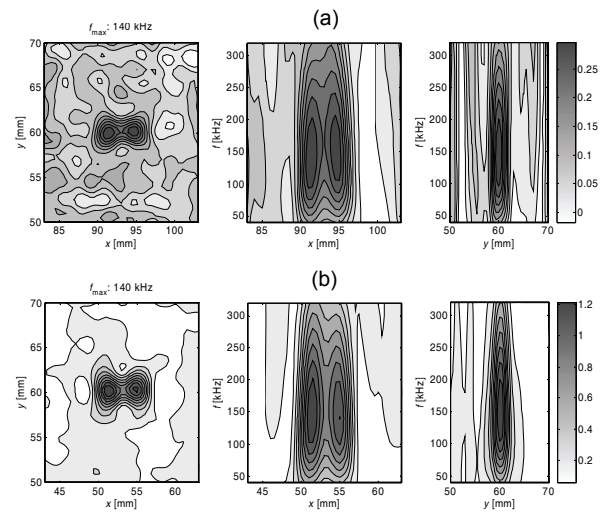


Fig.8. Signals caused by 3 mm length flaws (UniSmall), a) depth 10%, b) depth 20%

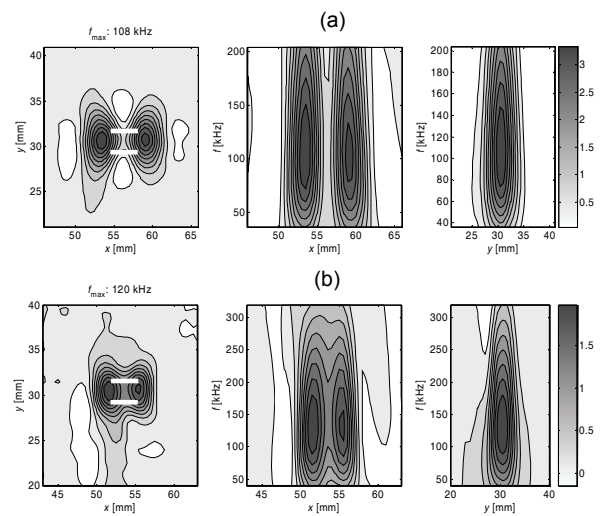


Fig.9. Signals caused by set of two self parallel 3 mm 20% flaws distance 2mm. a) UniBig, b) UniSmall

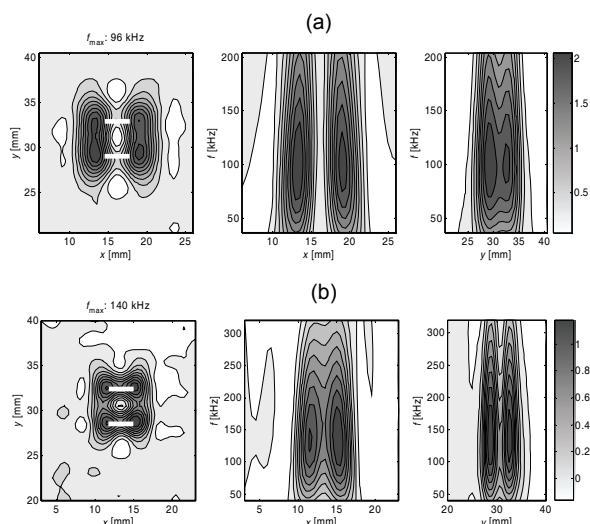


Fig.10. Signals caused by set of two self parallel 3 mm 20% flaws distance 4mm. a) UniBig, b) UniSmall

Table 2. SNR [dB] of the transducers (for outer flaws)

| | length [mm] | relative depth [%] | | | | |
|----------|-------------|--------------------|-------|-------|-------|-------|
| | | 10 | 20 | 40 | 60 | 80 |
| UniBig | 2 | 15.37 | 28.22 | 38.90 | 47.74 | 53.31 |
| | 3 | 17.55 | 30.76 | 42.35 | 50.80 | 56.27 |
| | 5 | 21.79 | 33.32 | 44.57 | 51.33 | 57.43 |
| | 7 | 18.50 | 35.22 | 48.62 | 54.19 | 57.54 |
| UniSmall | 2 | 11.00 | 22.24 | 33.70 | 44.06 | 50.62 |
| | 3 | 12.38 | 24.50 | 36.30 | 46.07 | 52.77 |
| | 5 | 15.22 | 29.35 | 40.88 | 47.77 | 54.36 |
| | 7 | 8.03 | 29.17 | 44.09 | 50.71 | 55.03 |

Results of experiments

All experiments were carried out using measurement system based on Multi-Frequency Excitation and Spectrogram Method (MFES) which was proposed in [2]. Basic idea of this method is to use a complex signal containing selected harmonic components as an exciting signal and a spectrogram for precise crack characterization. Plates made of INCONEL600 (thickness 1.23 mm) with EDM notches were used to evaluate sensitivity and resolution of the transducer. The probe was moved along the flaw in steps of 0.5 mm. The liftoff was measured to be 0.3 mm. The excitation signal consists of 15 sinusoidal components having frequency from 36 kHz to 204 kHz for UniBig sensor and frequency from 40 kHz to 320 kHz for UniSmall. Table 2 consists of signal to noise ratio of both sensors. The advantage of UniBig probe (mainly in case of

flaws with smaller depths) is noticeable. The results prove the high sensitivity of the transducer (signal noise ratio close to 20 dB). Optimal frequencies (f_{opt}) of the signals caused by the same flaws are approximately 50 kHz lower for UniBig than in case of UniSmall.

Figures 7 and 8 show measurements obtained in case of hidden flaws having relative depth 10% and 20%, length of 3 mm. In Figures 9 and 10 measurements of complex flaws (two parallel 3 mm 20% outer flaws, distance 2 and 4 mm) are presented. UniSmall distinguishes two close to each other flaws better than UniBig.

In the event of all kinds of flaws the following condition is fulfilled:

$$(1) \quad L_1 \cdot f_{optFL} = const.$$

where: L_1 – distance between axes of columns of the transducers (Fig.2), f_{optFL} – optimal frequency for given flaw.

This confirms the higher resolution but lower sensitivity of measurements made by smaller probe.

Conclusions

The principal conclusion drawn from this paper is that the proposed sensors have very good properties for evaluation of shallow outer flaws. A considerable concentration of eddy currents has a positive influence on sensitivity and spatial resolution of the transducers. By choosing dimensions of probes a compromise between better SNR or better resolution should be done. Fusion of signals received from probes having considerably different size would be very effective solution for flaws evaluation.

Acknowledgments: This work was supported in part by the State Committee for Scientific Research, Poland, under the Grant no: 3T10A 017 30 (2006-2009).

REFERENCES

- [1] Chady T., Enokizono M., Todaka T., Tsuchida Y., Sikora R., A Family of Matrix Type Sensors for Detection of Slight Flaws in Conducting Plates, *IEEE Transactions on Magnetics*, Vol. MAG-35, No. 5, 1999, s. 3655-3657
- [2] Chady T., Sikora R., Gratkowski S., Komorowski M., Borkowski B., Lopato P., Computerized System for Complex Electromagnetic Nondestructive Evaluation, *XIII International Symposium on Theoretical Electrical Engineering ISTE'05*, Lviv 2005.

Authors: prof. dr inż. Ryszard Sikora, e-mail: rs@ps.pl, dr hab. inż prof.PS. Tomasz Chady, e-mail: tchady@ps.pl, mgr inż Przemysław Łopato, e-mail: plopato@ps.pl, dr inż. Mieczysław Komorowski, Szczecin University of Technology, Department of Electrical and Computer Engineering, ul. Sikorskiego 37, 70-313 Szczecin, Poland

Optimization of starting characteristics of asynchronous motor with phase rotor

Abstract. A method and algorithm for optimizing the resistance of starting characteristics of asynchronous motor with phase rotor has been proposed. The method enables obtaining dependencies of mode coordinates on resistance value, taking on board saturation of the magnetic path.

Streszczenie. W pracy zaproponowano algorytm optymalizacji rezystancji charakterystyki rozruchowej pierścieniowego silnika asynchronicznego. Metoda umożliwia wyznaczenie zależności pomiędzy współrzędnymi modalnymi a wartością rezystancji z uwzględnieniem nasycenia obwodu magnetycznego. (**Optymalizacja charakterystyki rozruchowej pierścieniowego silnika asynchronicznego**)

Keywords: algorithm, mathematical model, asynchronous motor.

Słowa kluczowe: algorytm, model matematyczny, silnik asynchroniczny.

Introduction

For electric drives with enhanced starting torque, asynchronous motors (AM) with phase rotor are used. It is known [1] that the form of the AM mechanical characteristic depends on the value of the active resistance of the starting rheostat. Motor mechanical characteristic can be calculated/designed using equivalent circuits by simplified equations [1]. However, they offer fairly low precision and have to be experimentally tested. In addition, they aim at solving problems of analysis. The modern level of computational mathematics, electrical mechanics and IT technologies allows developing a mathematical model which would make it possible not only to design high-adequacy mechanical characteristics of AM with phase rotor, using mathematical simulation, but also to form them by varying resistance of the starting rheostat. This issue is important due to the fact that the too low starting resistance or wrong choice of its stages leads to the underuse of AM power or its excess. A very important problem is calculation of additional resistance in the rotor circuit, which would allow obtaining a mechanical characteristic of a specified form. Apparently, valid results can be obtained only by using a high-adequacy mathematical model of asynchronous motor.

The authors in [2] propose the technique for parametric synthesis of AM mechanical characteristic, which is based on so-called circuit simulation and which allows taking into account saturation of the magnetic path. Circuit model enables reducing the problem of analyzing processes in AM to the analysis of non-linear DC electric circuit with controlled linear and non-linear current sources. It is mentioned that the approach is characterized by a complex mathematical description, saturation being approximately taken into account.

Main principles

The article proposes a method which enables studying the effect of the additional resistance in the rotor circuit on the starting characteristics, using an AM model taking on board the phenomenon of magnetic path saturation on the way of both the main magnetic path and the leakage flux. The model makes it possible to form the necessary characteristics with high adequacy by methods of mathematical simulation. The essence of the method is presented below.

In the steady-state operating mode, processes in the windings of AM stator and rotor are periodical, thereat, due to the mutual movement of the rotor with reference to the stator, the periods of time dependencies of the circuit state variables in the physical coordinates are not equal. They

are characterized by periodical variation of coordinates, which is why for designing electromagnetic processes in symmetric steady-state modes, the system of orthogonal coordinates x, y rotating synchronously with the field is the most rational [3].

At a constant sliding s , the equation for electromagnetic equilibrium of the stator circuits transformed onto the axes x, y has the following form:

$$(1a) \quad \Omega \vec{\psi}_s + R_s \vec{i}_s = \vec{u}_s,$$

where $\vec{\psi}_s = (\psi_{rx}, \psi_{ry})^T$, $\vec{i}_s = (i_{sx}, i_{sy})^T$, $\vec{u} = (u_x, u_y)^T$ – vectors of flux linkage, stator circuit currents and applied voltage respectively; (the superscript symbol “T” means transposition); $R_s = \text{diag}(R_{sx}, R_{sy})$ – diagonal matrix of active resistances of the transformed stator circuits;

$\Omega = \begin{bmatrix} & -\omega_0 \\ \omega_0 & \end{bmatrix}$ – matrix in which ω_0 – cyclic frequency of supply voltage.

Similar equations for the rotor circuits on condition of equivalent the three-phase rotor winding by two orthogonal circuits on axes x, y have the form presented below:

$$(1b) \quad s\Omega_r \vec{\Psi}_r + R_r \vec{i}_r = 0,$$

where $\vec{\Psi}_r = (\psi_{rx}, \psi_{ry})^T$, $\vec{i}_r = (i_{rx}, i_{ry})^T$ – vectors of flux linkage and rotor circuit currents;

$R_r = \text{diag}(R_{rx} + R_\delta, R_{ry} + R_\delta)$ – diagonal matrix each element of which consists of the sum of the active resistance in the appropriate circuit and additional resistance R_δ of the starting rheostat.

Vector equations (1) describe the steady-state AM operating mode for any value of sliding s and resistance R_δ of the rheostat in the rotor circuit. Specifying the values of sliding, rheostat resistance and supply voltage, on the basis of the equations (1) and characteristics of magnetizing parts of the AM magnetic path [4], currents as well as electromagnetic torque can be calculated by the formula.

$$(2) \quad M = \frac{3p}{2} (\psi_{sx} i_{sy} - \psi_{sy} i_{sx}),$$

where p – number of pairs of the motor poles.

For the reason of saturation-caused non-linear dependence of flux linkage of every circuit on currents in all circuits, these equations are non-linear, which is why they can be solved by one of the numerical iteration methods such as Newton's one. However, it is known to be locally convergent. Therefore, there is a problem of searching for initial approximation which would be located in the vicinity of convergence of the method. In addition, solution of the equation (1) at the constant sliding gives only one point. Change of electromagnetic torque vs. rheostat resistance in the rotor circuit at a specified sliding s can be studied in the following way. First, coordinates values are calculated for $s=1.0$, $R_\delta=0.0$ and a specified supply voltage. In order to avoid difficulties associated with solving the non-linear system of equations (1) for electric equilibrium, the method of differentiating by the parameter is applied [5]. To this end, the variables in the equation (1) are substituted with $s=1.0$, $R_\delta=0.0$ respectively and parameter ε ($0 \leq \varepsilon \leq 1.0$) is introduced by multiplying supply voltage vector \vec{u} by ε , i.e. $\vec{u} = \varepsilon \vec{u}_0$, where \vec{u}_0 – a specified voltage. Differentiating the obtained system of equations by ε results in

$$(3) \quad \left(\begin{array}{c|c} \Omega & \\ \hline & \Omega \end{array} \times \begin{array}{c|c} \frac{\partial \bar{\Psi}_s / \partial \vec{i}}{\partial \bar{\Psi}_r / \partial \vec{i}} & \\ \hline & \end{array} + \begin{array}{c|c} R_s & \\ \hline & R_r \end{array} \right) \times \frac{d\vec{i}}{d\varepsilon} = \begin{array}{c|c} \vec{u} & \\ \hline & 0 \end{array}.$$

Differentials $\partial \bar{\Psi}_s / \partial \vec{i}$ and $\partial \bar{\Psi}_r / \partial \vec{i}$ form the full matrix of differential inductances, determined as described in [4].

As a result of integrating the system (3) by ε within the range from $\varepsilon=0.0$ to $\varepsilon=1.0$, values of currents and electromagnetic torque for $s=1.0$, $R_\delta=0.0$ and the specified AM supply voltage are obtained. To study the influence of the rheostat resistance R_δ on electromagnetic torque at $s=1.0$, it is necessary to differentiate the system (1) by R_δ , which results in

$$(4) \quad \left(\begin{array}{c|c} \Omega & \\ \hline & \Omega \end{array} \times \begin{array}{c|c} \frac{\partial \bar{\Psi}_s / \partial \vec{i}}{\partial \bar{\Psi}_r / \partial \vec{i}} & \\ \hline & \end{array} + \begin{array}{c|c} R_s & \\ \hline & R_r \end{array} \right) \times \frac{d\vec{i}}{dR_\delta} = \begin{array}{c|c} 0 & \\ \hline & \vec{i}_r \end{array}.$$

Finally, for any value of rheostat resistance R_δ the whole static starting characteristic can be calculated for the range of sliding from $s=1.0$ to $s=0.0$. For this, the system (1) is to be differentiated by s . As a result, the following is obtained:

$$(5) \quad \left(\begin{array}{c|c} \Omega & \\ \hline & \Omega \end{array} \times \begin{array}{c|c} \frac{\partial \bar{\Psi}_s / \partial \vec{i}}{\partial \bar{\Psi}_r / \partial \vec{i}} & \\ \hline & \end{array} + \begin{array}{c|c} R_s & \\ \hline & R_r \end{array} \right) \times \frac{d\vec{i}}{ds} = \begin{array}{c|c} 0 & \\ \hline & -s\Omega \end{array} \times \begin{array}{c|c} \bar{\Psi}_s & \\ \hline & \bar{\Psi}_r \end{array}.$$

Integrating the system (5) by s , having taken coordinates values at $s=1.0$ and a specified value of R_δ as initial conditions, all the values of the static characteristic are obtained.

Conclusions

The method proposed enables selecting resistance of the starting rheostat and its stages, which would ensure the optimal mechanical characteristic of AM with phase rotor form the point of view of starting duration and the respective value of electromagnetic torque, taking on board the magnetic path saturation.

REFERENCES

- [1] Design of electric machines/Edited by I.P.Kopylov.– Moscow: Energia Publishing House, 1980.– 496 pp.
- [2] Kanov L.N. Parametric synthesis of mechanical characteristics of asynchronous motor based on the method of circuit simulation//Electrical Engineering and Electromechanics Journal. – 2006. – No2. – pp. 26-29.
- [3] Kopylov I.P., Filts R.V., Yavorkyi Y.Y.: Equations of asynchronous motor in various systems of coordinates, Proceedings of the higher educational institutions of the USSR, Electromechanics Journal, vol.3, pp. 22-33, 1986.
- [4] Filts R.V.: Mathematical fundamentals of theory of electrical mechanical converters, Naukova Dumka Publishing House, Kyiv, 1979, – 208 pp.
- [5] Yakovlyev M.N. On solution of systems of non-linear equations by differentiating by parameter//JVM and MF, vol.4. – 1964. – No1. – pp. 146-149.

Authors: *Vasyl Malyar, Doctor of Engineering, Professor with the Department of Theoretical and General Electric Engineering, Lviv Polytechnic National University; Andriy Malyar, PhD, Associate Professor with the Department of Electric Drive, Lviv Polytechnic National University, 12 Bandera Str., 79013 Lviv, Ukraine, e-mail: svmalyar@polynet.lviv.ua.*

Performance tuning of the ray tracing process running in a multi-processor environment

Abstract. Ray tracing is a way of creating photo-realistic images with a very accurate reflection and shadow mapping. Despite high computational complexity of ray tracing, its work principle allows partitioning and dividing the job for parallel processing in quite simple way. Theoretically every pixel may be computed separately by a different processor. Virtually each processor is assigned to computing a rectangular fragment of the output image. However, performance may be degraded if the fragments are not assigned in a proper order. This paper describes an algorithm for scheduling task assignment that tries to avoid improper task ordering.

Streszczenie. Metoda śledzenia promieni pozwala generować obrazy z bardzo dokładnie odwzorowanymi cieniami i odbiciami światła. Pomimo dużej złożoności obliczeniowej, metoda pozwala na bardzo łatwy podział zadania na mniejsze fragmenty dla potrzeb przetwarzania równoległego. Teoretycznie barwa każdego piksela mogłaby być wyznaczana przez inny procesor. W praktyce obraz dzieli się na niewielkie prostokątne fragmenty, z których każdy przypisywany jest do innego procesora. Na wydajność takiego procesu znaczny wpływ może mieć kolejność przydzielania fragmentów do obróbki. Niniejszy artykuł opisuje algorytm kolejkowania zadań w środowisku równoległym pozwalający zapobiegać przypadkowemu spadkowi wydajności. (**Poprawa wydajności metody śledzenia promieni w środowisku wielo-procesorowym**)

Keywords: ray tracing, parallel processing, performance

Słowa kluczowe: metoda śledzenia promieni, przetwarzanie równoległe, wydajność

Introduction

Ray tracing is a method for creating photorealistic images. All properties of objects visible in an image such as shape, colour, reflectivity etc. are mathematically described. This description is used as an input data for algorithms that calculate colour of each pixel. If the image is to be accurate it takes a lot of time to generate it.

However, because pixels' colours does not depend on each other, ray tracing is great candidate for parallel processing. On the other hand it poses a big problem too, that is not very common among tasks run in parallel environments. It's non-deterministic dependency between size of input and output data and the computational complexity. Even very simple ray tracing programme would calculate thousands of void pixels in few seconds. But try to put few objects acting as mirrors and even the best optimised programmes would stuck calculating infinite reflections, even if only for one pixel.

Parallelism problem in ray tracing

When calculations get done on a single processor it does not really matter which part of an image would contain only void and which would be full of smoke and mirrors. It has to be calculated as whole. Should computation be partitioned and distributed among several nodes it starts to make difference which node receives which parts and when. The most pessimistic case is when the most complex part is assigned as the last one and a single processor is working as hard as it can while all the others have finished their jobs and stay idle.

It is clear now that a proper scheduling algorithm is needed. It can't be one of algorithms used in operating systems to schedule task switching. Those algorithms are designed to work under continuous, neverending load, while ray tracing an image is a finite job. Although the goal is quite similar: equal distribution of processing capabilities between tasks. The best distribution of a finite job is such that all processors finish their work at the same moment. Yet, in both cases the decisions are based on completely different data. OS schedulers can collect information about each process

and assume that they would be valid at least for few hundred switches. Ray tracing tasks are unique no information gathered for previous parts is useful for predicting the complexity of upcoming ones. The situation isn't that bad as it may seem. Some estimations are quite feasible.

Although each pixel may be computed by different processor it is rather uncommon to do so. More often pixels are grouped together to avoid communication overhead which might consume all gains from parallel processing. Processor receives a task of computing single line or a rectangular region.

Before going parallel a thumbnail a preview can be generated where each pixel corresponds to a region to be assigned. For example if the target image is to be 1024x768 pixels and is divided into squares of 64x64 pixels then the thumbnail will be 16x12 pixels. Complexity of calculations can be recorded as an image with bright (time consuming) and dark (simple) pixels each corresponding to appropriate pixel of the thumbnail. Such capability is available in POV-Ray ray tracer used in experiments.

The biggest issue, however, is not the complexity itself but the deviation between different tasks. If the task switching in the operating systems happens after some fixed period of time, then on a multiprocessor doing ray tracing it occurs when a node finishes its task and asks for the next one. Tasks with different complexities make switching happen in completely random order and pose the risk of leaving a single node with a very complex task at the very end when all others have finished. This may significantly delay accomplishment of the job especially when a multiprocessor consists of nodes with different computational capacity for example in clusters assembled from commodity hardware.

Introduced method

As complexity is known, decision has to be made on how to distribute the work. It is a subset choice problem but with more than two output sets to fill. Let N be a number of processors and T a set of tasks (pieces of image).

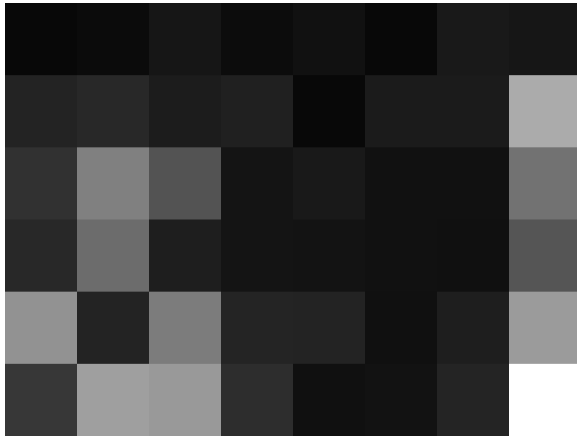


Figure 1. CPU utilisation histogram for a thumbnail preview of `glasschess.pov` scene generated with POV-Ray.

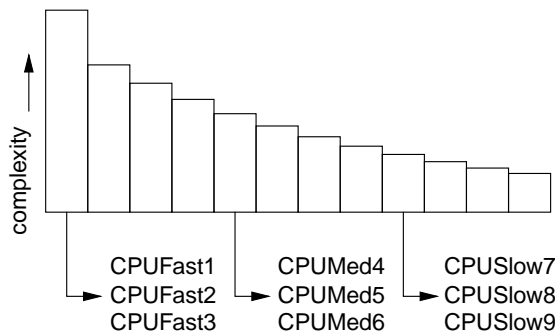


Figure 2. A sorted queue of tasks and exit points for different processing units.

$$(1) \quad T = t_1, t_2, \dots, t_m$$

Sets A_i have to be found such that

$$(2) \quad A_1, A_2, \dots, A_N \subset T$$

and

$$(3) \quad a_i = \sum_{t \in A_i} c(t), a_1 = a_2 = \dots = a_N$$

where $c(t)$ is a measure of complexity of a single task.

There is no easy and deterministic way of finding solution to this problem as the total number of combinations is $N^{\|T\|}$ for N nodes and $\|T\|$ tasks. Given the example above and a multiprocessor comprising 8 processing units it makes approximately $2.4 \cdot 10^{173}$ combinations. Everything becomes even more complex if the processing units are of unequal computing capacity. Then

$$(4) \quad C_1 a_1 = C_2 a_2 = \dots = C_N a_N$$

dependency has to be satisfied where C_i is computing capacity of a node. The solution has to be estimated again.

The following algorithm is proposed to solve problems described above.

1. Central node generates CPU utilisation histogram (1) for a thumbnail where each pixel's brightness corresponds to complexity of one piece of final image. Figure (6)

shows the image used for tests. Glass chess pieces are far more complex to compute than the sky or checkerboard hence corresponding regions on the histogram are brighter.

2. A queue of tasks (pieces) is created and sorted in descending order according to estimated complexity of tasks. Parallel processing is started.
3. Tasks from the queue are assigned to nodes. Either from the beginning of the queue or a place appropriate for a node according to its computational capacity as drawn in figure (2). The most complex tasks, which are marked with brighter grey on the histogram get accomplished first. The figure (3) is a screenshot in the middle of computation.
4. The queue is sorted after each piece is removed. Steps 3. and 4. are repeated until the queue is not empty.

The biggest advantage of this algorithm is its simplicity. The only requirement that must be met is the possibility of estimating of complexity before starting parallel processing. As soon as all nodes start their work the main node need to do only few simple operations which makes the algorithm quite scalable.

The algorithm of parallel processing is a lot simpler than the one proposed in [1] and has its limitations, however, it is a lot easier to implement whether in an existing sequential programme or when writing software from scratch. It is also more general and may be applied to any problem with no correlation between data and complexity.

1. It prevents hardest task from being assigned near the end of computation.
2. Deviation of adjacent jobs' complexity is minimised hence "task switching" is more predictable.
3. Nodes with different computational capacity get tasks which at the moment are more suitable for them. Slower nodes may receive tasks placed few positions after the head of the queue.

Before the algorithm can be applied several decisions have to be taken.

First, the size of a single piece of output image has to be specified. On one hand the less task to distribute between



Figure 3. Partially rendered image with most complex parts accomplished.

nodes the easier it should be to choose the right subsets according to (3). On the other hand, however, it makes a lot harder to achieve satisfying results with approximate algorithm described above. This is because moving one bigger piece from one subset (node) to another may influence the final effect to much larger degree than when a small piece is moved.

Next, proper estimation of pieces' complexity is required. It seemed that one, two or four rays per (e.g. 64x64) piece is very rough so an experiment has been made with different methods and accuracy levels of anti-aliasing with up to tens of thousands rays per pixel. Of course such accuracy required unacceptably long time (as far as estimation is concerned) to accomplish the estimation. Those tests have proved that no more than ten rays per piece are required to determine the order in which pieces should be sent to nodes.

Results

The cluster used in experiments comprised two groups of machines. There were two Celeron 300MHz nodes and nine Celeron 2.4MHz. The slower ones were given jobs from different places of the queue. The final image was always 480 pixels wide and 360 pixels high.

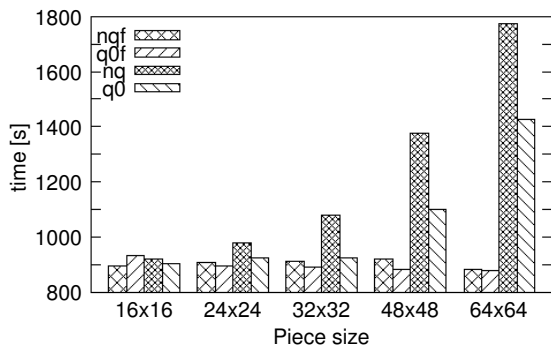


Figure 4. Times for different job partitioning, with and without slow nodes, exit point always in front. ngf – fast nodes, no sorting; qdf – fast nodes, sorted queue; nq – mixed nodes, no sorting; q0 – mixed nodes, sorted queue, exit offset 0

Figure (4) gives comparison between sorted and unsorted queue for cluster with and without slow nodes. However, there is no apparent difference for the case of homogeneous cluster, connecting slow machines can make computations take nearly twice as long as before if the queue is not sorted.

Figure (5) presents time versus exit point position dependency for different sizes of tasks. The results for 64x64 pieces at 10th position had too big deviation to be considered meaningful. There is no surprise as far as the size of a task is concerned. The bigger pieces the stronger dependency on the queue exit position. That is because there are more ways of choosing near-optimal A_i sets for smaller pieces than for bigger ones. It seems quite intuitive that it is easier to divide fine grained structures into equal pieces. It is worth notice that properly chosen exit point gives evident improvement for 64x64 pieces. However, the author knows no method other than experimental, to determine the best value for a given job. Since each job has got a different distribution of complexity,

the settings has to be changed with every new job.

Summary

The experiments conducted show that the method described in this paper may be one of the easiest to schedule irregular problems, like ray tracing, for parallel execution. The software doesn't need to implement complex interprocess communication, in fact only few changes need to be made to sequential programme to make it run in parallel. The estimation of complexity should be accurate enough to distinguish "hard" tasks from "simple" ones so it may be quite quick.

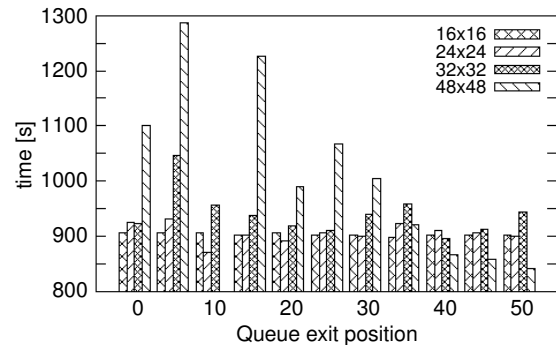


Figure 5. Times for different job partitioning and queue exit points



Figure 6. Sample scene, `glasschess.pov` by Ingo Janssen, used for tests

REFERENCES

- [1] Erik Reinhard *Hybrid Scheduling for Parallel Ray Tracing*, Faculty of Technical Mathematics and Informatics, Delft University of Technology, 1996.

Author: Łukasz Stelmach, Warsaw University of Technology, Institute of Theory of Electrical Engineering, Measurement and Information Systems, ul. Koszykowa 75, 00-662 Warszawa, Poland, e-mail: lukasz.stelmach@iem.pw.edu.pl

Ambiguity groups in linear dynamic analog circuit

Abstract. The method for finding ambiguity groups in linear dynamic analog circuits is presented in the paper. This method is derived using sensitivity of the circuit response in time and frequency domain. The sensitivity analysis of the circuit in time domain as well as in frequency domain is performed with usage of the state-space description of the circuit.

Streszczenie. W referacie zaprezentowano metodę umożliwiającą wyznaczanie grup niejednoznaczności w układach analogowych, bazującą na funkcjach wrażliwości układu w dziedzinie czasu i częstotliwości. Funkcje wrażliwości układu w obu dziedzinach wyznacza się wykorzystując opis układu za pomocą zmiennych stanu. (**Grupy niejednoznaczności w liniowych dynamicznych układach analogowych**)

Keywords: ambiguity groups, sensitivity analysis, fault diagnosis.

Słowa kluczowe: grupy niejednoznaczności, analiza wrażliwości, wykrywanie uszkodzeń.

Introduction

An ambiguity group is such a set of elements of the circuit that the influence of the change of the parameter of one of them on the response of the circuit can be compensated by the changes of the parameters of the rest of the elements of the ambiguity set. The knowledge about ambiguity groups is essential in case of building algorithms for fault diagnosis, this is why determining them is an important problem. In general ambiguity groups in analog circuits are determined performing analysis of the testability matrix [2], however it is also possible to determine them on the basis of the knowledge about sensitivities of the circuit response in time and frequency domain. These two last approaches are presented in the paper.

Ambiguity groups determination

In case of dynamic circuits an ambiguity group consists of the same set of elements for any instant of time. If $y(\mathbf{x}, t)$ is the response of the circuit, $\mathbf{x} = \{x_1, \dots, x_n\}$ is the vector of the parameters of the elements of the ambiguity set $X = \{X_1, \dots, X_n\}$ and $d\mathbf{x} = \{dx_1, \dots, dx_n\}$ is the vector of deviations of the parameters \mathbf{x} the following formula should be satisfied for any ambiguity group and for any instant of time

$$(1) \quad 0 = \frac{\partial y(\mathbf{x}, t)}{\partial x_1} dx_1 + \frac{\partial y(\mathbf{x}, t)}{\partial x_2} dx_2 + \dots + \frac{\partial y(\mathbf{x}, t)}{\partial x_n} dx_n.$$

Let's assign

$$(2) \quad f_{txk}(\mathbf{x}, t) = \frac{\partial y(\mathbf{x}, t)}{\partial x_k}, \quad k=1 \dots n,$$

$f_{txk}(\mathbf{x}, t)$ - sensitivity of the response $y(\mathbf{x}, t)$ to change of the parameter x_k in continuous time domain.

Let's apply the Laplace transform to the equation (1)

$$(3) \quad 0 = \frac{\partial}{\partial x_1} (L(y(\mathbf{x}, t))) dx_1 + \dots + \frac{\partial}{\partial x_n} (L(y(\mathbf{x}, t))) dx_n$$

and substitute

$$(4) \quad L(y(\mathbf{x}, t)) = Y(\mathbf{x}, s) = T_s(\mathbf{x}, s) E(s).$$

Where $T_s(\mathbf{x}, s)$ is a transfer function and $E(s)$ is an input signal in s domain. The input signal $E(s)$ does not depend on \mathbf{x} thus equation (3) can be rewritten in following form

$$(5) \quad 0 = \frac{\partial T_s(\mathbf{x}, s)}{\partial x_1} dx_1 + \dots + \frac{\partial T_s(\mathbf{x}, s)}{\partial x_n} dx_n.$$

Let's substitute $s=j\omega$ and assign

$$(6) \quad T_{sxk} = \frac{\partial T_s(\mathbf{x}, j\omega)}{\partial x_k}, \quad k=1 \dots n,$$

T_{sxk} - sensitivity transfer function between the sensitivity of the response $Y(\mathbf{x}, s)$ to changes of the parameter x_k and input signal $E(s)$.

The equations (1)-(6) are written in continuous time domain and in s domain however we can discretize time in equation (1) and rewrite above equations in discrete time domain and in z domain. Thus for $m=1..l$ and for given sampling time t_s following formulas are obtained

$$(7) \quad 0 = \frac{\partial y(\mathbf{x}, m)}{\partial x_1} dx_1 + \frac{\partial y(\mathbf{x}, m)}{\partial x_2} dx_2 + \dots + \frac{\partial y(\mathbf{x}, m)}{\partial x_n} dx_n.$$

$$(8) \quad f_{dxk}(\mathbf{x}, m) = \frac{\partial y(\mathbf{x}, m)}{\partial x_k}, \quad k=1 \dots n,$$

$f_{dxk}(\mathbf{x}, m)$ - sensitivity of the response $y(\mathbf{x}, m)$ to change of the parameter x_k in discrete time domain.

After applying Z transform to equation (7)

$$(9) \quad 0 = \frac{\partial}{\partial x_1} (Z(y(\mathbf{x}, m))) dx_1 + \dots + \frac{\partial}{\partial x_n} (Z(y(\mathbf{x}, m))) dx_n$$

and substituting

$$(10) \quad Z(y(\mathbf{x}, m)) = Y(\mathbf{x}, z) = T_z(\mathbf{x}, z) E(z).$$

the formula similar to (5) is derived

$$(11) \quad 0 = \frac{\partial T_z(\mathbf{x}, z)}{\partial x_1} dx_1 + \dots + \frac{\partial T_z(\mathbf{x}, z)}{\partial x_n} dx_n.$$

Let's use bilinear transformation $z=e^{j\omega t_s}$ and assign

$$(12) \quad T_{zsk} = \frac{\partial T(\mathbf{x}, e^{j\omega t_s})}{\partial x_k}, \quad k=1 \dots n,$$

T_{zsk} – sensitivity transfer function between the sensitivity of the response $Y(x,z)$ to changes of the parameter x_k and input signal $E(z)$ derived on the basis of Z transform.

On the basis of (1)-(2) and (7)-(8) it can be concluded that the set of n elements X^n is an ambiguity group for given measured signal if sensitivities in time domain f_{tsk} or f_{dsk} , $k=1...n$, are linear dependent functions.

On the basis of (5)-(6) and (11)-(12) it can be concluded that the set of n elements X^n is an ambiguity group for given measured signal if sensitivity transfer functions T_{tsk} or T_{zsk} , $k=1...n$, are linear dependent functions.

To check linear dependence of sensitivity functions the $\{p \times n\}$ matrix K^n have to be built. Where n – number of elements under consideration, p – number of values of sensitivity function for given instants of time or for given frequencies. p has to be greater then n , $p > n$. If rank r of matrix K^n is equal to n , $r=n$, the sensitivity functions are linear independent and the set of elements under consideration is not an ambiguity group. If rank r of matrix K^n is smaller then n , $r < n$, the sensitivity functions are linear dependent and the set of elements under consideration is an ambiguity group.

Sensitivity in time and frequency domain

Let's assume that the circuit under consideration is described by state space model with state variables $v = \{v_1, \dots, v_p, i_1, \dots, i_j\}$ and one input signal $e(t)$ only

$$(13.1) \quad \frac{\partial v(x,t)}{\partial t} = A_t(x) v(x,t) + B_t(x) e(t)$$

$$(13.2) \quad y(x,t) = C_t(x) v(x,t) + D_t(x) e(t)$$

Let's differentiate these equation with respect to variable x_k and assign

$$(14) \quad \dot{v}_{x_k}(t) = \frac{\partial v(x,t)}{\partial x_k},$$

$$(15) \quad \dot{y}_{x_k}(t) = \frac{\partial y(x,t)}{\partial x_k},$$

$$(16) \quad \frac{\partial \dot{v}_{x_k}(t)}{\partial t} = \frac{\partial}{\partial t} \left(\frac{\partial v(x,t)}{\partial x_k} \right) = \frac{\partial}{\partial x_k} \left(\frac{\partial v(x,t)}{\partial t} \right).$$

It leads to the relations

$$(17) \quad \begin{aligned} \frac{\partial \dot{v}_{x_k}(t)}{\partial t} &= A_t \dot{v}_{x_k}(t) + \left[\frac{\partial A_t}{\partial x_k} \quad \frac{\partial B_t}{\partial x_k} \right] \begin{bmatrix} v(t) \\ e(t) \end{bmatrix} \\ \dot{y}_{x_k}(t) &= C_t \dot{v}_{x_k}(t) + \left[\frac{\partial C_t}{\partial x_k} \quad \frac{\partial D_t}{\partial x_k} \right] \begin{bmatrix} v(t) \\ e(t) \end{bmatrix} \end{aligned}$$

which still have a form of state-space equations. Dependence on x of some quantities is omitted intentionally in above and underneath chosen equations to make them shorter. The equation (17) where $v(t)$ is the solution of the equation (13.1) enables us to find out sensitivities in continuous time domain of any output signal $y(t)$. After applying Laplace transform to the equation (17) sensitivity transfer functions between sensitivities of output signals $Y(x,s)$ to variable x_k and input signal $E(s)$ are obtained

$$(18) \quad T_{sxx}(s) = T_{s1xx}(s) T_s(s) + T_{s2xx}(s),$$

where $T_s(s)$ - transfer function between state variables $V(s)$ and input signal $E(s)$ derived on the basis of state equation.

$$(19) \quad T_s(s) = (s I - A)^{-1} B_t,$$

and T_{s1xx} , T_{s2xx} - transfer function given by formulas

$$(20) \quad T_{s1xx}(s) = C_t (s I - A_t)^{-1} \frac{\partial A_t}{\partial x_k} + \frac{\partial C_t}{\partial x_k},$$

$$(21) \quad T_{s2xx}(s) = C_t (s I - A_t)^{-1} \frac{\partial B_t}{\partial x_k} + \frac{\partial D_t}{\partial x_k}.$$

In general, dynamic analysis of the circuits is performed using their discrete time description. There are a few commonly used numerical method applied in this field. One of them is Backward Euler Method which could be used to describe circuit using discrete time state space model.

Let's assume that the considered circuit is described by discrete state space model with only one input signal $e(m)$

$$(22.1) \quad v(x, m+1) = A_d(x) v(x, m) + B_d(x) e(m),$$

$$(22.2) \quad y(x, m) = C_d(x) v(x, m) + D_d(x) e(m).$$

Let's differentiate these equation with respect to variable x_k . It leads to the relations

$$(23) \quad \dot{v}_{x_k}(m+1) = A_d \dot{v}_{x_k}(m) + \left[\frac{\partial A_d}{\partial x_k} \quad \frac{\partial B_d}{\partial x_k} \right] \begin{bmatrix} v(m) \\ e(m) \end{bmatrix}$$

$$\dot{y}_{x_k}(m) = C_d \dot{v}_{x_k}(m) + \left[\frac{\partial C_d}{\partial x_k} \quad \frac{\partial D_d}{\partial x_k} \right] \begin{bmatrix} v(m) \\ e(m) \end{bmatrix},$$

$$(24) \quad \dot{v}_{x_k}(m) = \frac{\partial v(x, m)}{\partial x_k},$$

$$(25) \quad \dot{v}_{x_k}(m+1) = \frac{\partial v(x, m+1)}{\partial x_k},$$

$$(26) \quad \dot{y}_{x_k}(m) = \frac{\partial y(x, m)}{\partial x_k}.$$

The equation (23) where $v(m)$ is the solution of the equation (22.1) enables us to find out sensitivities in discrete time domain of any output signal $y(m)$. After applying Z transform to the equation (23) sensitivity transfer functions between sensitivities of output signals $Y(x,z)$ to variable x_k and input signal $E(z)$ are obtained. They have similar form to (18)-(21) but instead of s variable z variable has to be substituted.

$$(27) \quad T_{zxx}(z) = T_{z1xx}(z) T_z(z) + T_{z2xx}(z),$$

$$(28) \quad T_z(z) = (z I - A_d)^{-1} B_d,$$

$$(29) \quad T_{z1xx}(z) = C_d (z I - A_d)^{-1} \frac{\partial A_d}{\partial x_k} + \frac{\partial C_d}{\partial x_k},$$

$$(30) \quad T_{z2xx}(z) = C_d (z I - A_d)^{-1} \frac{\partial B_d}{\partial x_k} + \frac{\partial D_d}{\partial x_k}.$$

Example 1

Let's consider circuit depicted in figure 1. The voltages $v_1(t)$ and $v_2(t)$ are state variables. The circuit is driven by DC voltage source $v_{in}(t)=1$. The measured signal is output voltage $v_{out}(t)$. The problem is to find out all ambiguity groups taking into consideration set of elements $S=\{C_1, C_2, R_1, R_2, R_3\}$.

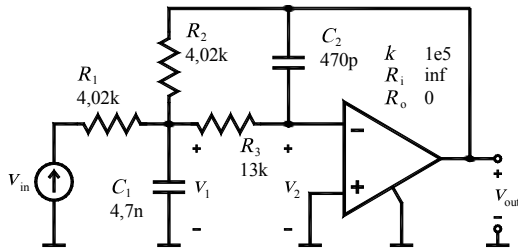


Fig.1. Multiple feedback low-pass filter.

With the assumption that the operational amplifier is replaced by its simplified model, which is voltage-controlled voltage source with gain k , circuit can be described by state space model

$$(31) \quad \frac{\partial \mathbf{v}(t)}{\partial t} = \begin{bmatrix} -1.222e5 & -5.293e9 \\ 1.637 & -1.637 \end{bmatrix} \mathbf{v}(t) + \begin{bmatrix} 5.293e4 \\ 0 \end{bmatrix} v_{in}(t)$$

$$y(t) = \begin{bmatrix} 0 & -1e5 \end{bmatrix} \mathbf{v}(t) + \begin{bmatrix} 0 \end{bmatrix} v_{in}(t)$$

To calculate for example sensitivity function with respect to capacitance C_1 the following state space model on the basis of (17) has to be built

$$(32) \quad \frac{\partial \dot{\mathbf{v}}_{x_k}(t)}{\partial t} = \begin{bmatrix} -1.222e5 & -5.293e9 \\ 1.636 & -1.636 \end{bmatrix} \dot{\mathbf{v}}_{x_k}(t) + \begin{bmatrix} 2.600e13 & 1.126e18 & -1.126e13 \\ 0 & 0 & 0 \end{bmatrix} \begin{bmatrix} \mathbf{v}(t) \\ v_{in}(t) \end{bmatrix}$$

$$\dot{y}_{x_k}(t) = \begin{bmatrix} 0 & -1e5 \end{bmatrix} \dot{\mathbf{v}}_{x_k}(t) + \begin{bmatrix} 0 & 0 & 0 \end{bmatrix} \begin{bmatrix} \mathbf{v}(t) \\ v_{in}(t) \end{bmatrix}$$

The sensitivity of the output voltage with respect to the capacitance C_1 obtained on the basis of above equations as well as sensitivities of the output voltage to the rest of the considered parameters are shown in figure 2.

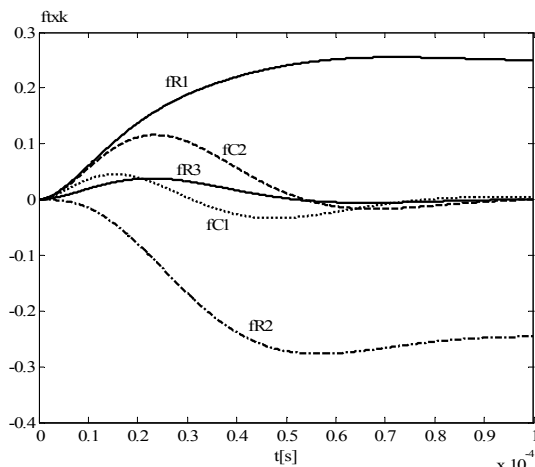


Fig.2. The sensitivities of output voltage to $C_1[1/nF]$, $C_2[1/0,1nF]$, $R_1[1/k\Omega]$, $R_2[1/k\Omega]$, $R_3[1/k\Omega]$ in time domain.

Let's built matrix K^n $n=2...5$, for each combination of obtained time domain sensitivities. The number of such defined matrices is 26. After calculating the rank of each matrix K^n it is found out that only set of five elements, any set of four elements and also one set of three elements $X_1^3=\{C_1, C_2, R_3\}$ are the ambiguity groups. The rest of the three element sets as well as each of two element sets are not the ambiguity groups.

Let's derive sensitivity transfer function with respect to capacitance C_1 using (18)-(21). The transfer functions have following forms

$$(33) \quad T_{s1C1}(s) = \frac{1.443e-7 \cdot s - 4.256e18}{s^2 + 1.222e5 \cdot s + 8.662e9} \cdot \frac{-5.339e-6 \cdot s - 1.843e023}{s^2 + 1.222e5 \cdot s + 8.662e9}^T$$

$$(34) \quad T_s(s) = \frac{5.293e4 \cdot s + 8.662e4}{s^2 + 1.222e5 \cdot s + 8.662e9} \cdot \frac{8.662e4}{s^2 + 1.222e5 \cdot s + 8.662e9}$$

$$(35) \quad T_{s2C1}(s) = \frac{-1.455e-11 \cdot s + 1.843e18}{s^2 + 1.222e5 \cdot s + 8.662e9}$$

The sensitivity transfer functions to all parameters for the range of frequency $f=(0.1...1MHz)$ are shown in figure 3 on the complex plane.

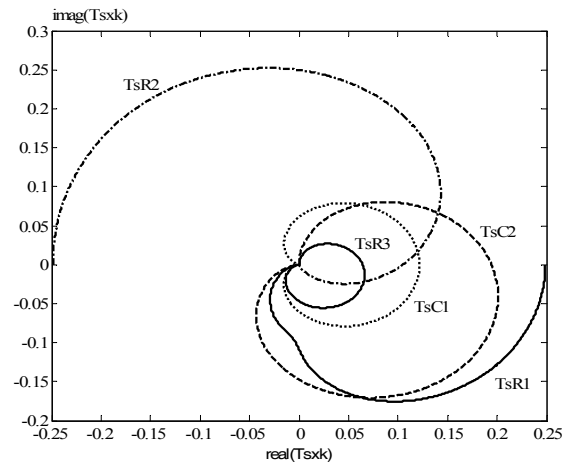


Fig.3. The sensitivity transfer function in frequency domain to $C_1[1/nF]$, $C_2[1/0,1nF]$, $R_1[1/k\Omega]$, $R_2[1/k\Omega]$, $R_3[1/k\Omega]$ on complex plane.

The matrix K^n $n=2...5$, was built for all combination of sensitivity transfer function and for given set of frequencies and the same results were obtained as in case of the sensitivities in time domain.

Let's built discrete model of given circuit using Backward Euler Method with sampling time $t_s=100ns$. Discrete models of the resistor, capacitor and voltage-controlled voltage source are given by

$$(36) \quad v(m+1) = R i(m+1)$$

$$(37) \quad i(m+1) = \frac{C}{t_s} v(m+1) + \frac{C}{t_s} v(m)$$

$$(38) \quad v_o(m+1) = k v_i(m+1)$$

where: k -gain of the voltage-controlled voltage source, t_s -sampling time.

It leads to discrete state space circuit description of the circuit

$$(39) \quad \begin{aligned} \mathbf{v}(m+1) &= \begin{bmatrix} 9.878e-1 & -5.228e2 \\ 1.617e-7 & 9.999e-1 \end{bmatrix} \mathbf{v}(m) \\ &+ \begin{bmatrix} 5.2283e-3 \\ 8.5569e-10 \end{bmatrix} v_{in}(m) \\ y(m) &= [0 \quad -1e5] \mathbf{v}(m) + [0] v_{in}(m) \end{aligned}$$

Sensitivity functions in time and frequency domain with respect to capacitance C_1 are determined using

$$(40) \quad \begin{aligned} \dot{\mathbf{v}}_{x_k}(m+1) &= \begin{bmatrix} 9.878e-1 & -5.228e2 \\ 1.617e-7 & 9.999e-1 \end{bmatrix} \dot{\mathbf{v}}_{x_k}(m) \\ &+ \begin{bmatrix} 2.5556e6 & 1.0989e11 & -1.0989e6 \\ 4.1826e-1 & 1.7985e4 & -1.7985e-1 \end{bmatrix} \begin{bmatrix} \mathbf{v}(m) \\ v_{in}(m) \end{bmatrix} \\ \dot{y}_{x_k}(m) &= [0 \quad -1e5] \dot{\mathbf{v}}_{x_k}(m) + [0 \quad 0 \quad 0] \begin{bmatrix} \mathbf{v}(m) \\ v_{in}(m) \end{bmatrix} \end{aligned}$$

$$(41) \quad \mathbf{T}_{z1C1}(z) = \begin{bmatrix} -4.183e4 \cdot z - 9.992e-10 \\ z^2 - 1.988 \cdot z + 0.9878 \\ -1.798e9 \cdot z - 3.742e-4 \\ z^2 - 1.988 \cdot z + 0.9878 \end{bmatrix}^T,$$

$$(42) \quad \mathbf{T}_z(z) = \begin{bmatrix} 5.228e-3 \cdot z + 5.228e-3 \\ z^2 - 1.988 \cdot z + 0.9878 \\ 8.557e-10 \cdot z \\ z^2 - 1.988 \cdot z + 0.9878 \end{bmatrix},$$

$$(43) \quad T_{z2C1}(z) = \frac{1.798e4 \cdot z}{z^2 - 1.988 \cdot z + 0.9878}.$$

The sensitivity characteristic and results of ambiguity groups finding obtained on the basis of discrete models of the circuit are of course equivalent to that obtained on the basis of continuous time and frequency models.

Example 2

Two stages Sallen Key low-pass filter depicted in figure 4 is considered as a second example. The circuit is driven by DC voltage source $v_{in}(t)=1$. The voltages $v_1(t)$, $v_2(t)$, $v_3(t)$, $v_4(t)$ across capacitors are state variables. The measured signal is output voltage $v_{out}(t)$. The problem is to find out all ambiguity groups taking into consideration set of elements $S=\{C_1, C_2, R_1, R_2, R_3, R_4, C_3, C_4, R_5, R_6, R_7, R_8\}$. Performing procedure described in section 'Ambiguity groups determination' the following results are obtained for given measured signal. The two sets of two elements $X_1^2=\{R_3, R_4\}$ and $X_2^2=\{R_7, R_8\}$ are ambiguity groups. These are correct results because elements R_3, R_4 and R_7, R_8 constitute feedbacks of noninverting amplifiers. On the basis of the gain formula of non-inverting amplifier $AMP1$

$$(43) \quad k_{AMP1} = 1 + \frac{R_3}{R_4}$$

it could be concluded that the change of R_3 could be compensated by the change of R_4 . Similarly in case of amplifier $AMP2$ gain and resistors R_7, R_8 .

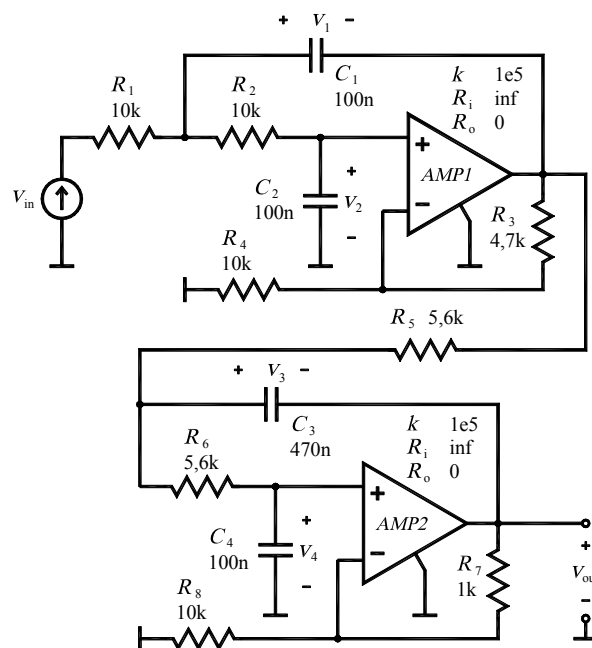


Fig.4. Two stages Sallen Key low-pass filter.

Each set of three elements which contains any of above mentioned to elements ambiguity sets is also ambiguity group. There are eight additional ambiguity groups consisting of three elements which do not contain sets X_1^2 and X_2^2 as subsets. These are $X_1^3=\{C_1, C_2, R_1\}$, $X_2^3=\{C_1, C_2, R_2\}$, $X_3^3=\{C_1, R_1, R_2\}$, $X_4^3=\{C_2, R_1, R_2\}$, $X_5^3=\{C_3, C_4, R_5\}$, $X_6^3=\{C_3, C_4, R_6\}$, $X_7^3=\{C_3, R_5, R_6\}$, $X_8^3=\{C_4, R_5, R_6\}$. Similarly as above each set of four elements which contains ambiguity set of three elements as a subset is ambiguity group. There are no additional four elements ambiguity sets which do not include three element ones as well as there are no additional five elements ambiguity sets which do not contain four elements ambiguity subsets. All the sets of sixth and more elements constitute ambiguity groups. It means that in this case the ambiguity groups distribution is determined by two and three elements ambiguity sets.

Conclusions

The presented method is useful for ambiguity group determination. It is easy to use for example with usage of MATLAB software. The results are reliable. They were compared with results obtained on the basis of testability matrix analysis and they were the same.

REFERENCES

- [1] Tadeusiewicz M., Kuczyński A., Soft-Fault Diagnosis of Dynamic Circuits, *Przegląd Elektrotechniczny*, 2003, nr 10, ISTET'03, 125-128
- [2] Fedi G., Giomi R., Luchetta A., Manetti S., Piccirilli M.C., Symbolic Algorithm for Ambiguity Group Determination in Analog Fault Diagnosis, *Proceedings ECCTD'97*, 1997, 1286-1291
- [3] Kaczorek T., *Teoria układów regulacji automatycznej*, WNT, 1977

Author: mgr inż. Piotr Sidyk, Politechnika Łódzka, Instytut Elektrotechniki Teoretycznej, Metrologii i Materiałoznawstwa, ul. Stefanowskiego 18/22, 90-924 Łódź, e-mail: psidyk@p.lodz.pl

Active source localization in 3D BEM multilayer model

Abstract. Boundary Element Method for simulation of spatially heterogeneous objects of electroencephalography is presented in this paper. The four layer spherical model (representing skin, skull, CSF layer and brain) of the real head approximated with isoparametric six nodes triangles was consist. Forward and invers problem for active source localization was presented in this paper.

Streszczenie. W artykule przedstawiono zastosowanie metody elementów brzegowych do modelowania przestrzennych obiektów niejednorodnych. Stosowano w badaniach uproszczony cztero warstwowy model sferyczny, aproksymowany izoparametrycznymi elementami drugiego rzędu, będący przybliżeniem ludzkiej głowy. Model ten zawierał następujące tkanki: skóra, kości czaszki, płyny rdzeniowo mózgowie oraz mózg. W artykule przedstawiono rozwiązania zadania prostego z użyciem transformaty falkowej oraz zadania odwrotnego dla sygnału zaszumianego. (**Lokalizacja aktywnych źródeł w przestrzennych modelach wielowarstwowych**)

Keywords: boundary element method, active source localization, wavelet transformation, inverse problem.

Słowa kluczowe: metoda elementów brzegowych, lokalizacja źródeł aktywności, transformata falkowa, zadanie odwrotne.

Introduction

Boundary Element Method (BEM) [1], [7] in active source localization process requires construction of matrices, in which information about shape and material coefficients of the object are stored. Boundary of the object could be approximated by triangle elements of zero-order or by isoperimetric elements of the second-order. The final system of equations for the whole object is obtained by adding the set of boundary integral equations of governing equation for each region in conjunction with compatibility and equilibrium conditions between their interfaces. Different equations and boundary conditions are used to the numerical analysis. Poisson equation with Neumann boundary conditions and internal active source (current dipole) was used in localization process.

Simplified head model of diameter 0.25 m with an internal active source (as a group of active neurons in stimulated region of the brain) was used in presented work. Potential distribution V on the boundary of the object under consideration can be determined by BEM. Multilayered object is consist of four homogeneous regions, coupled by interfaces. Those regions and their conductivities correspond with anatomical description of a human head:

- cerebral cortex, 0.33 S/m,
- cerebrospinal fluid (CSF), 1.0 S/m,
- skull, 0.0042 S/m to 0.042 S/m,
- skin, 0.33 S/m.

Multilayer model with active source

Boundary element method (BEM) was used to build the multilayer numerical model. In BEM, integral equation was used to describe of active source localization. Poisson equation with Neumann and Dirichlet boundary conditions was used to describe this problem. The active source localization describes integral equation. The integral equivalent of differential equation is introduced as follows

$$(1) \quad \frac{1}{2} \mathbf{V}(\mathbf{r}) + \int_{\Gamma} \frac{\partial}{\partial n} G(\mathbf{r}, \mathbf{r}') \mathbf{V}(\mathbf{r}') d\Gamma = \int_{\Gamma} \frac{\partial \mathbf{V}(\mathbf{r}')}{\partial n} G(\mathbf{r}, \mathbf{r}') d\Gamma + \int_{\Omega} \mathbf{b} G(\mathbf{r}, \mathbf{r}_0) d\Omega$$

where: G – Green function, \mathbf{V} – potential on the surfaces, \mathbf{b} – internal source function.

In boundary equation Green function was used which for 3D space was described as:

$$(2) \quad G(\mathbf{r}, \mathbf{r}') = \frac{1}{4\pi r}$$

$$\text{where: } r = \sqrt{(x-x')^2 + (y-y')^2 + (z-z')^2}.$$

Radius from the (1) and (2) equation were showed on the fig.~1.

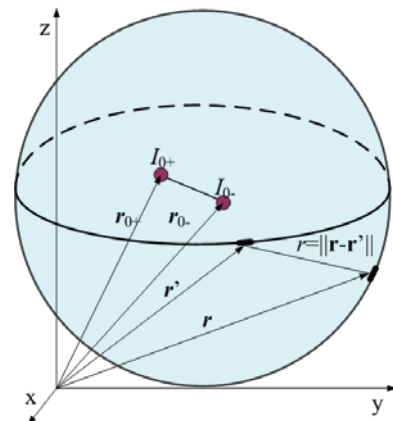


Fig.1. Homogenous model

Source function which was described by last integral in (1) equation was presented as:

$$(3) \quad \mathbf{b} = \sum \frac{1}{\sigma} I_{\pm} G(\mathbf{r}, \mathbf{r}_0) = \frac{1}{4\pi\sigma} \sum \frac{I_{\pm}}{\sqrt{(x_{0\pm} - x)^2 + (y_{0\pm} - y)^2 + (z_{0\pm} - z)^2}}$$

where: $x_{0\pm}$, $y_{0\pm}$, $z_{0\pm}$, – coordinates of current source, x , y , z – coordinates of boundary element, I_{\pm} – amplitude of source.

$$(4) \quad \mathbf{A} \mathbf{V} = \mathbf{B} \frac{\partial \mathbf{V}}{\partial n} + \mathbf{b}$$

The linear system of integral equations which describes spherical model was transformed to matrix form (4). Matrix form for four layer spherical model was presented in (5). After rearranging and multiplying the right side final system of equations was shown on fig.2

$$(5) \quad \mathbf{A} \mathbf{x} = \mathbf{b}$$

where \mathbf{A} is a fully populated matrix with unsymmetrical block structure.

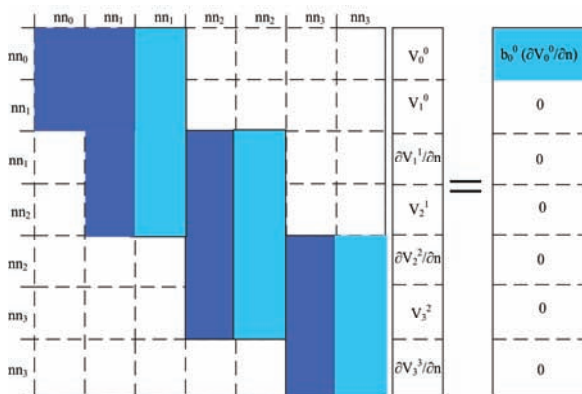


Fig.2. Rearranging process of the final system of equations

We get the system of algebraic equation ready to solve forward problem. To solve this problem GMRES method was applied.

Numerical Simulation results

We applied two kinds of numerical calculations. Zero order and isoperimetric second order triangular boundary element. The inverse problem, for the four layer spherical model, was solved iteratively using variable metric method with BFGS scheme.

The inverse problem was solved many times and noise effect on the current source localization accuracy was investigated. In numerical experiments was used data with white noise. Noise was generated in order to simulate a measuring disturbance.

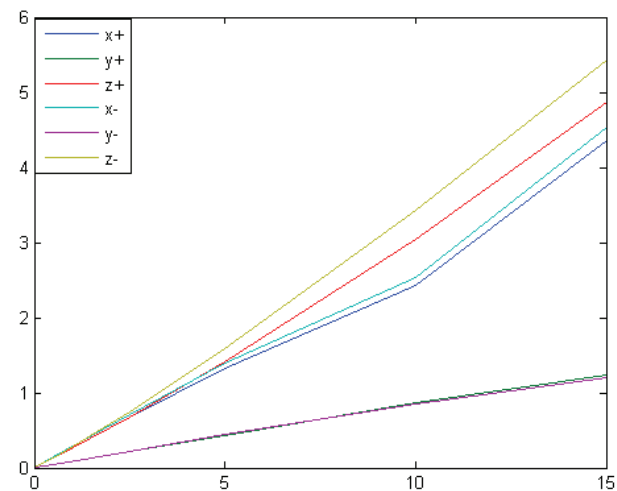


Fig.3. Noise effect on the current source localization accuracy

We used noise from 0% to 15%. When the noise was equal 15% the active source localization was good because maximal absolute error was less then five and half millimetres. When the noise was equal 5%, the absolute error was less then one and half millimetres. Results of experiments were presented on the fig. 3.

Fast wavelet transform

Inverse problem was solved iteratively, so the CPU time for each iteration is crucial. In the multilayer BEM we obtained block nonsymmetric matrix and solution time increased dramatically with matrix size. Fast discrete wavelet transform (DWT) and fast wavelet transform based on binary partition techniques (BFWT), introduced in [5] was

applied to make matrix sparse. In the first case matrix size must equal to 2^n , where n was integer number and $n > 0$, so we added additional columns and rows to fulfill this condition [2]. The BFWT technique can be applied to matrices with arbitrary sizes.

Table 1. Comparison of wavelet transformation

| Rank of matrix | Transform | Iterative method | Time [s] |
|----------------|-----------|------------------|----------|
| 8078 | - | GMRES | 352.90 |
| | BFWT | GMRES | 389.21 |
| | BFWT | BICGSTAB | 354.10 |
| | DWT | GMRES | - |
| | DWT | BICGSTAB | 416.00 |
| 10766 | - | GMRES | - |
| | BFWT | GMRES | 20.2 |
| | - | BICGSTAB | 30.5 |
| | BFWT | BICGSTAB | 70.4 |

Table 1 presents the times of solving forward problem. Solutions with GMRES and BICGSTAB solvers was compared. DWT and BFWT wasn't useful for matrix with size of 8078×8078 . When matrix size was 10766×10766 application of BFWT technique reduced solving time about 30%

Conclusion

Despite of the loss of information in wavelet transformation, the solution accuracy is precise enough. The localization error was about 2%. Inverse problem was solved much faster after fast wavelet transformation based on binary partition techniques was used. The source localization based on experimental data will be considered in the future, but more realistic head model must be worked out.

REFERENCES

- [1] Beer G., Programming the Boundary Element Method. An Introduction for Engineers, *John Wiley & Sons*, (2001)
- [2] Filipowicz S.F., EEG localization of the internal generators with the aid of 3D Boundary Element Method, *Przegląd Elektrotechniczny*, 02 (2005)
- [3] Filipowicz S.F., Diagnostyka niejednorodnych obiektów przestrzennych metodami tomografii i elektroencefalografii, *Zeszyty Naukowe Elektryka Z.132, Oficyna Wydawnicza Politechniki Warszawskiej*, Warszawa (2005)
- [4] Filipowicz S.F., Nita K., Sikora J., Uproszczony wielowarstwowy model w badaniach elektroencefalograficznych, *ZKwE'06*, Poznań, April 10-12, (2006)
- [5] Gill P.E., Murray P.E., Wright M.H., Practical Optimization, *Academic Press*, (2006)
- [6] Li Y., Yan Y., Song G., Fast wavelet transform based on binary partition techniques, *Journal of Xidian University (Natural science)*, 33(1):107-110, (2006)
- [7] Press W.H., Teukolesky S.A., Vetterling V.T., Flannery B.P., Numerical Recipes in C++. The Art of Scientific Computing 2nd ed., *Cambridge University Press*, (2002)
- [8] Wrobel L.C., The Boundary Element Method, *John Wiley & Sons*, (2002)

Authors: mgr inż. Konrad Nita, *Electrotechnical Institute, ul. Pożaryskiego 28, 04-703 Warszawa, E-mail: k.nita@iel.waw.pl; dr hab. inż. Stefan F. Filipowicz, *Institute of Theory of Electrical Engineering, Measurement and Information Systems, Warsaw University of Technology, Koszykowa 75, 00-662 Warszawa Poland, E-mail: 2xf@nov.iem.pw.edu.pl**

Numerical research of the electromagnetic fields in powerful transformers and reactors

Abstract. The results of numerical research of the electromagnetic fields and parameters of powerful transformers and reactors are discussed. The calculations were made in ANSYS software environment with the purpose of the equipment reliability increase, the energy losses decrease, the dimensional and weight parameters reduction. The magnetic system (MS) of transformers and reactors is examined in three tasks.

Streszczenie. W artykule omówiono wyniki symulacji pola magnetycznego w transformatorach wielkiej mocy i reaktorach. Symulacje wykonano przy pomocy systemu ANSYS a ich celem było zwiększenie niezawodności, zmniejszenie strat oraz redukcja wymiarów i wagi urządzeń. Przedyskutowano przykłady trzech różnych urządzeń. (Numeryczna analiza pola elektromagnetycznego w transformatorach wielkiej mocy i reaktorach)

Keywords: transformer, reactor, coil, winding, loss, magnetic system

Słowa kluczowe: transformator, reaktor, cewka, uzwojenie, straty, obwód magnetyczny.

Introduction

In [1] the results of the ANSYS application for strengthening computations of parts of construction are presented, computation-experimental estimation of seismicity and chatter stability at designing of transformers and electric reactors. In the given work the questions of the ANSYS application for electromagnetic researches of these devices are considered.

Variety of functions, geometries, properties of parts of construction of transformer devices what am going on in them electromagnetic processes, determines the necessity of consideration of different models with the proper raising of computation tasks.

On the fig. 1.1, 1.2 the models of the ANSYS three-bar transformer with lateral yoke and shunting reactor are shown. Models contain the simplified constructions of tanks, magnetic system (MS), yoke beams, magnetic screens on beams and on a tank. On the bars of transformer two windings of low and higher tension are located, on the bars of reactor – working winding. Longitudinal symmetry of devices is used.

Description of basic tasks of design, accepted assumptions, computation models and results of computations, is below presented. Coming from the terms of work transient behaviors of work of devices, three-phase system of feed, are considered, nonlinear dependences of descriptions of magnetization of the electrical engineering and construction steels. For separate tasks the harmonic and static analysis was used.

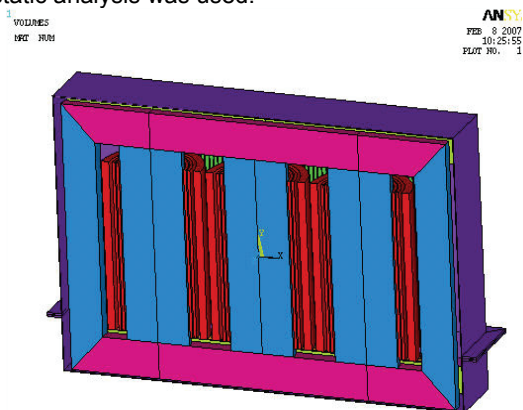


Fig. 1.1 Model of power transformer

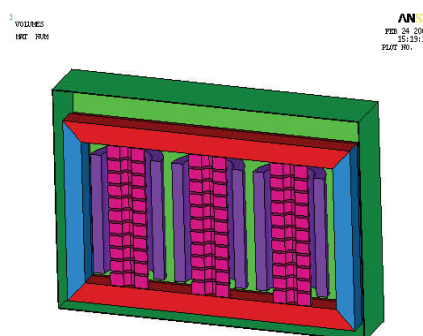


Fig. 1.2 Model of shunting reactor

Computation of the magnetic systems

The magnetic systems of transformers are considered in two tasks. First task deals with the design of streams in the regime of idling. By the field source the set voltage on a feeding winding is adopted. Three-dimensional geometry of bars, yoke maximally approach to the real. The zones of interleaving plates between bars and yoke in detail are not presented. In the plane of the interleaving leaves MS the known nonlinear description of magnetization of electrical engineering steel is set, across interleaving MS – permeability is adopted to be constant.

The same model can be used for the analysis of the regime of inclusion of transformers on idling, tester regime of short circuit at the serve of tension on an external winding at short-circuited internal one. The indicated regimes are characterized by possible considerable saturation of bar of the MS transformer at aggravating remaining magnetization.

For an example on fig.2.1 the computation distributing of values of magnetic induction is shown in the section of the MS transformer in the moment of time of maximal amplitude of voltage in the extreme winding of phase A.

Second task for MS is the design of its basic setting – forming of the magnetic field of transformer and reactor. In this case a model is similar to the first case. The densities of magnetizing forces in windings are set. Distributing of magnetic induction in the section of the MS reactor for a three-phase working current (moment of maximal amplitude in an extreme phase A) is shown on fig.2.2. To the within the framework given model the questions related to shorting on the areas of the MS (mainly on yoke) streams of dispersion of winding of transformers can be considered, the basic magnetic field of shunting reactors.

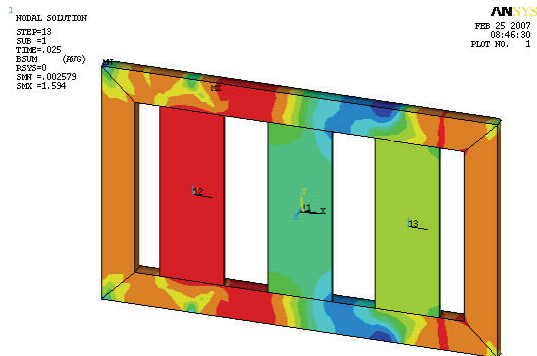


Fig. 2.1 Distributing of induction in MS transformer

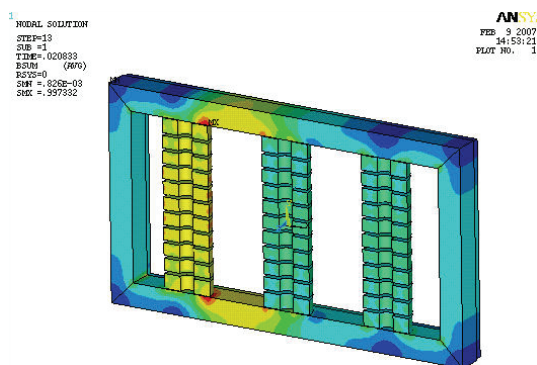


Fig. 2.2 Distributing of induction in MS three-phase shunting reactor

The hysteresis, planar magnetization reversal, streams between plates at presence of air-gaps in joints, eddy currents and local losses are not considered in this work.

Computation of the magnetic field of winding

The characteristic property of sizes of radial channels between coils on the height of winding is the feature of windings of transformers and reactors. The task of the real location of several hundred coils with channels is not possible. From other side, at the tasks of computation of the magnetic field exactly in windings for subsequent computation of additional losses from eddy currents, circulatory currents, electrodynamic forces it is necessary maximally exactly to take into account the unevenness of distributing of magnetizing forces on the height of winding.

For this purpose is developed the following. By the additional programs of coils on the height of windings form group on the zones of even closeness of currents, satisfying to the definite set of criteria. The given information is definitely passed in ANSYS. By the special macros in windings the regular mesh of finite elements, taking into account position of coils, is built, and also the closeness of magnetizing forces within the limits of zones is determined.

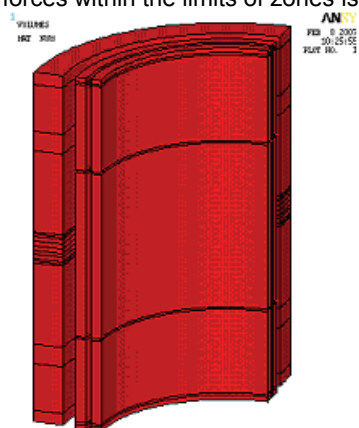


Fig. 3.1 Model of transformer windings with magnetization zones

The model of two windings of transformer with laying out on zones is shown on fig.3.1. On fig.3.2 breaking up of model in ANSYS is presented. Also by the external program in procedure of task on computation the absolute coordinates of center of every coil of winding are passed. It allows to define the values of axial (B_o) and radial (B_r) constituents of magnetic induction in coils on internal (1), middle (2) and outward (3) formative in different its azimuthal sections.

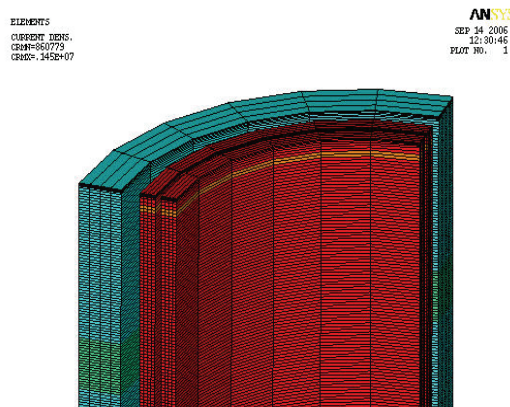


Fig. 3.2 Mesh on the model of windings of transformer

On the fig. 3.3 and 3.4 distributing of constituents of induction of the magnetic field is resulted in the outward winding of the high-voltage (HV) transformer and in the winding of reactor in the section on his small axis – toward a tank. For a reactor notably there is influencing of discrete insertions from electrical engineering steel.

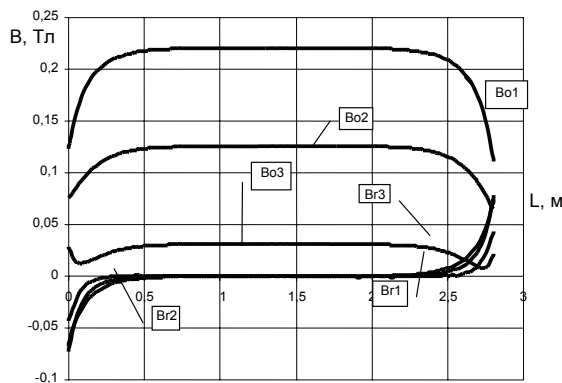


Fig. 3.3 Distributing of constituents of induction on the height of high-voltage (HV) winding of transformer

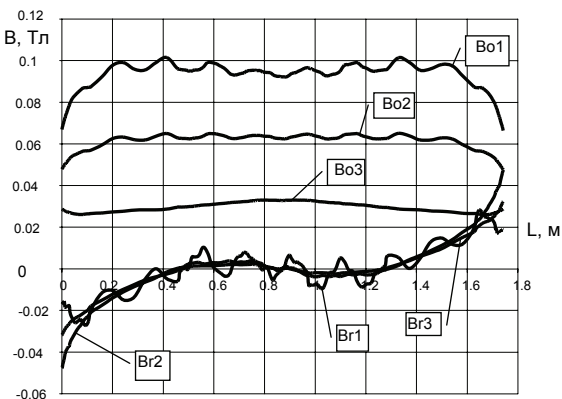


Fig. 3.4 Distributing of constituents of induction on the height of winding of reactor

At research of electromagnetic processes in regions enough remote over puttees the simplified model of distributing in them of magnetizing forces is taken – up to even on all section by virtue of narrow-mindedness of calculable resources.

To the tasks of research of the magnetic field in winding the task of determination of them joins inductance. For the explored reactor on the standard macro ANSYS the value of inductance is definite near to measured. At the values of currents more of nominal inductance of reactor taking into account possible satiation of areas of the magnetic system can be definite.

Computation of the magnetic field and losses in ferromagnetic details

The ferromagnetic elements of construction have two characteristic features: nonlinear, hysteresis of description of magnetization and presence of eddy currents due to electric conductivity, relying on frequency of magnetization reversal and temperature. By virtue of it there are definite problems at the design of such phenomenon as a surface effect [2].

The simplified solving of the given task is considered on the models of tanks of transformer and reactor. For computation of the magnetic field and losses the analysis of the transitional processes ANSYS was used. The body of tank from the side of winding is broken up on layers of which is doubled on the depth of wall of tank. Electric conductivity and dependence of induction from tension of the magnetic field on the basic curve of magnetization for definite construction steel of tank is set. On results the analysis of transitional processes on the surface of tank the values of tangent tension on the first temporal accordion are determined.

On the fig. 4.1 distributing of tangent tension of the magnetic field on the tank of transformer taking into account placed on his surface shunts as the packages of electrical engineering steel, set flatways to the surface of tank and with air-gaps between packages, is shown. In the zone of shunts the considerable effect of the magnetic screening is noticeable. On the fig. 4.2 distributing of tangent tension on the surface of tank of reactor is shown.

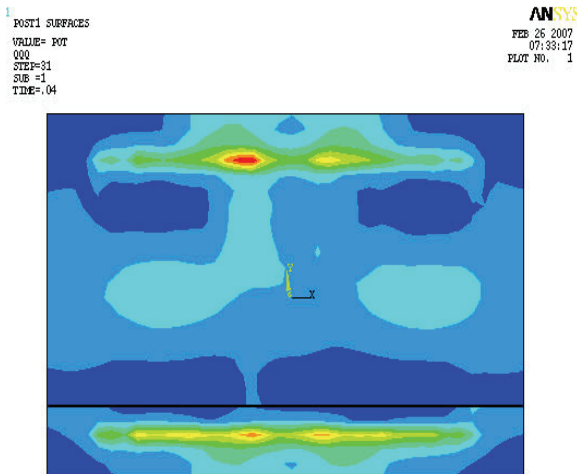


Fig. 4.1 Distributing of tangent tension on the surface of tank of transformer at presence of shunts

Further the surface losses with the use of dependence of surface impedance on tangent tension of the magnetic field by the so-called equivalent magnetic recommendation settle accounts [3]. The calculated distributing of surface losses for the explored constructions of transformer and reactor are shown on fig.4.3 and 4.4. For a transformer the

small zones of selection of losses out of limits of magnetic screen are expressed. For a reactor the magnetic screening is also used usually. For illustration a variant without shunts is shown. The basic regions of losses are concentrated in the zone of middle of winding due to predominance of axial making tension of the magnetic field. On the edges of winding of zone of enlarged losses move between winding, that corresponds part of tangent making along longitudinal side of tank due to the radial fields of winding. The computation total losses in a tank in a sufficient measure correspond to experimental estimations.

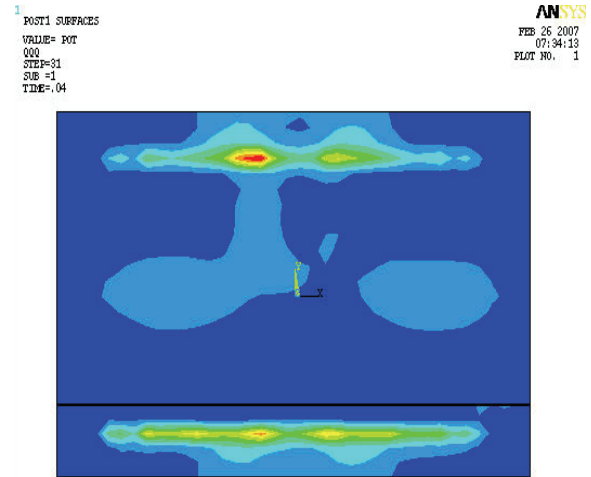


Fig. 4.2 Distributing of tangent tension on the surface of tank of reactor

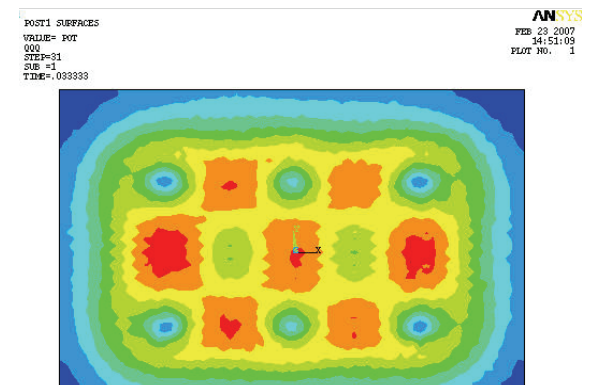


Fig. 4.3 Distributing of surface losses on the wall of tank of transformer

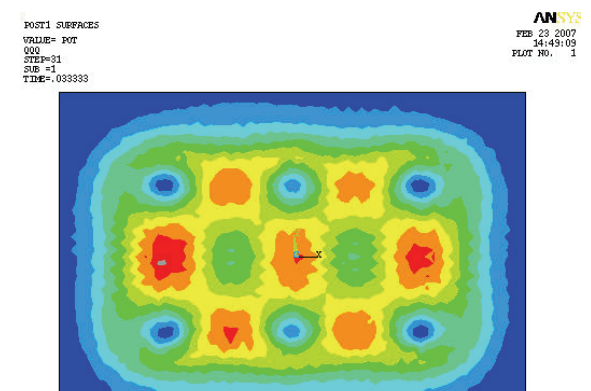


Fig. 4.4 Distributing of surface losses on the wall of tank of reactor

Design of eddy currents and losses in details from nonmagnetic steel

The ANSYS procedures provide the direct design of eddy currents and losses in nonmagnetic details. However elements of construction of active part from nonmagnetic steel, in particular, yoke beams have an elaborate three-dimensional design (fig. 5.1), that entails the increase of dimension of task.

With the purpose of minimization of expenditures of calculable resources without a considerable error in determination of basic value alternative approach to determination of eddy currents and losses in the difficult elements of details from nonmagnetic steel is considered. It consists of a next step-by-step design [4].

On the first stage the value of induction of the magnetic field of normal to the surface detail from nonmagnetic steel is determined. Thus it is possible to use the three-dimensional model of devices, in which into the place of nonmagnetic element a conditional body repeating the overall sizes of construction is put, but material of which does not change the electromagnetic field. The static analysis ANSYS is possible in this case. By the special procedures the value of the magnetic field is read from the nodes of model and passed in a text file for the use on the next stage. In the case of the three-phase system of feed the magnetic fields separately for projections on real and imaginary time axes are determined.

Thus, the task of computation of eddy currents and losses in the elaborate three-dimensional design of beam is taken to the two-dimensional task for the flat plate of the complicated configuration at the set induction of the magnetic field. For its solving the procedure of the ANSYS decision of the Laplace task with the zero terms Dirichlet on the border of computation region with the set distributing of source of excitation is used.

On the fig. 5.2 distributing of real part of induction of the magnetic field on the involute of shelves and wall of yoke beam of transformer is shown. On fig.5.3 distributing of vectors of eddy currents is presented, and on a fig. 5.4 – distributing of total losses for the real and imaginary constituents of induction. On the proper procedure ANSYS estimation of heating of beam at the set terms of heat exchange with a cooling transformer butter is produced.

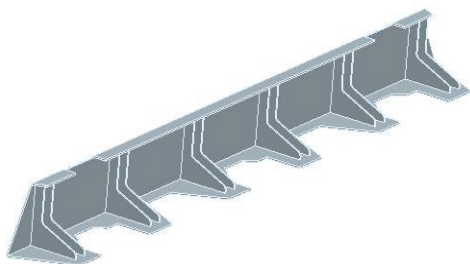


Fig. 5.1 Three-dimensional construction of yoke beam

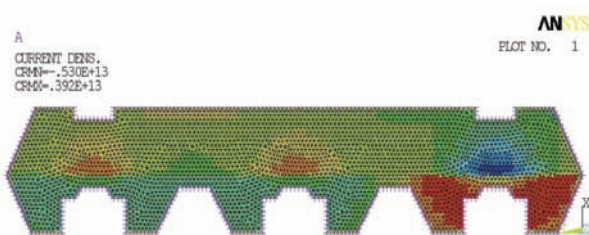


Fig.5.2 Distributing of real constituent of induction

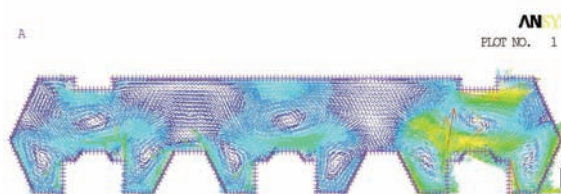


Fig. 5.3 Field of vectors of eddy currents for the real constituent of induction

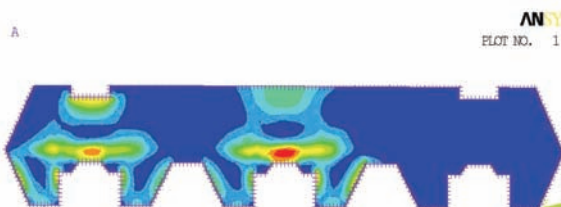


Fig. 5.4 Distributing of losses on the surface of beam

Conclusion

The carried out researches confirm efficiency of application of the program complex ANSYS for the special computations of transformers and electric reactors with the purpose of further rise of competitiveness, reliability of equipment in the conditions of simultaneous rise of the specific loading and decline of losses of energy, reductions of overall and gravimetric indexes. However is present row of difficulties at raising and solving of such type of tasks. To them it is possible to refer to absence of possibility design of anisotropic of cold-rolled electrical engineering steel taking into account the proper curves of magnetization reversal (more one). Possibility of consideration of loop of hysteresis is absent also. In the program complex of ANSYS there are no procedures of design of surface effect in ferromagnetic constructions steel.

REFERENCES

- [1] Бики М.А., Жук В.В., Иванков В.Ф., Сульдин Н.В., Циер Г.И. Применение ANSYS в проектировании трансформаторов и электрических реакторов // Сборник трудов Третьей конференции пользователей программного обеспечения CAD-FEM GmbH (Москва, 23-24 апреля 2003г.) / Под ред. А.С. Шадского. – М.: Полигон-пресс, 2003. - С. 469-477.
- [2] Нейман Л.Р. Поверхностный эффект в ферромагнитных телах. – Л.-М.: «ГЕИ», 1949. - 190 с.
- [3] Кравченко А.Н., Нижник Л.П. Электродинамические расчеты в электротехнике. – Киев. «Техника», 1977. – 184 с.
- [4] Басова А.В., Иванков В.Ф., Кокошин С.С., Химюк И.В. Численное моделирование вихревых токов, нагревов в конструктивных элементах из немагнитной стали трансформаторов и электрических реакторов // XIII Международная научно-техническая конференция "Теоретическая электротехника" ISTET '05. (Львов, 4-7 июля, 2005г.). Тез. докл. - Львов, 2005. - С. 52-54.

Authors: Anastasia Basova senior inż., "Zaporizhtransformator", Ukraine, Zaporizhia, Dnepropetrovskoe shosse, 3; Victor Ivankov, Chief of laboratory, "Zaporizhtransformator", Ukraine, Zaporizhia, Dnepropetrovskoe shosse, 3, E-mail: Victor.Ivankov@ztr.ua; Stanislav Kokoshyn, senior scientist, Institute of electrodynamics of NAN of Ukraine, Ukraine, Kiev, Peremoga street, 56; Ivan Khimjuk, senior scientist, Institute of electrodynamics of NAN of Ukraine, Ukraine, Kiev, Peremoga street, 56, E-mail: khimjuk@ied.org.ua

The magnetic microsensors response

Abstract. This paperwork presents the structure, the operating conditions and the main features of some microsensors realised in the bipolar and the MOS integrated circuits technology. By using numerical simulation, the values of the sensor response for the two analysed devices are compared and it is also emphasized the way in which choosing the geometry and the material features allows getting high-performance sensors.

Streszczenie. W artykule zaprezentowano strukturę, warunki pracy i główne właściwości mikroczujnika magnetycznego zrealizowanego jako obwód scalony w technologii bipolarnej i MOS. Przy użyciu symulacji numerycznej porównano odpowiedzi dwóch analizowanych urządzeń oraz wskazano że przez odpowiedni dobór geometrii i materiału można możliwości otrzymać czujnik o bardzo dobrych parametrach. (Analiza odpowiedzi mikroczujnika magnetycznego).

Keywords: magnetic sensors, double-drain magnetotransistor, signal-to-noise ratio, Hall effect, double-collector magnetotransistor.

Słowa kluczowe: czujniki magnetyczne, magnetotranzystor, stosunek sygnału do szumu, efekt Halla.

Introduction

Figure 1 shows the cross section of a double collector npn vertical magnetotransistor operating on the current deflection principle [1]. This structure is compatible with the bipolar integrated circuit technology.

The most of the n type low-doped epitaxial layer serves as the collector region and is depleted of the charge carriers upon reverse biasing of the collector-base junction.

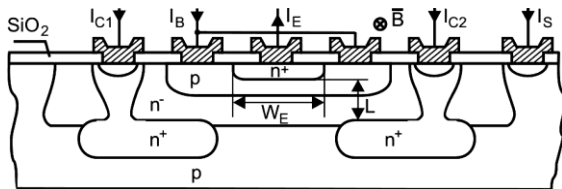


Fig. 1. The structure of a double-collector magnetotransistor

The two collector contacts are realised by splitting the buried layer (n^+). L is the collector-emitter distance, and W_E is the width of the emitter.

In the absence of the magnetic field the electron flow injected into the emitter, which crosses the base is symmetrical and the two collector currents are equal: $I_{C1}=I_{C2}$.

In the presence of a magnetic field having the induction B parallel with the device surface, the distribution of the emitter electron current becomes asymmetrical and causes an imbalance of the collector currents: $\Delta I_C = I_{C1} - I_{C2}$.

The studied magnetotransistors work in the Hall current mode of operation and the deviation ΔI_C is given by the transverse Hall current. Its expression is determined by equalizing the epitaxial layer of the collector region with a short Hall plate and applying the properties of the dual Hall devices. Based upon the Hall current expression in the devices which are in the Hall current mode of operation it can be written [2]:

$$(1) \quad \Delta I_C = \frac{I_H}{2} = \frac{1}{2} \mu_{Hn} \cdot \frac{L}{W_E} \cdot G \cdot I_C \cdot B$$

where $I_C = I_{C1}(0) + I_{C2}(0)$.

The sensor response and the sensitivity

The sensor response is expressed by:

$$(2) \quad h(B) = \frac{\Delta I_C}{(I_{C1} + I_{C2})_{B=0}} = \frac{1}{2} \mu_{Hn} \frac{L}{W_E} \cdot G \cdot B_{\perp}$$

and it is linear for induction values which satisfy the condition: $\mu_H^2 \cdot B_{\perp}^2 \ll 1$.

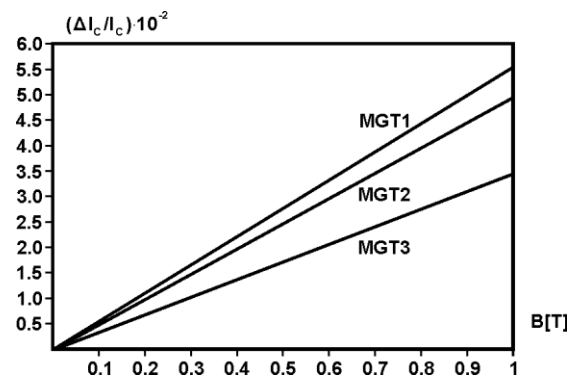


Fig.2. The $h(B)$ dependence of B for three devices of different geometry: MGT1: $W_E/L=0.5$, $(L/W_E)G = 0.72$; MGT2: $W_E/L=1.0$, $(L/W_E)G = 0.68$; MGT3: $W_E/L=2.0$, $(L/W_E)G = 0.46$

In figure 2 it can be seen the geometry influence on $h(B)$ values for three magnetotransistor structures, realised on silicon ($\mu_{Hn} = 0.15 \text{ m}^2 \text{V}^{-1} \text{s}^{-1}$) and having different ratios W_E/L ($W_E = 50 \text{ }\mu\text{m}$).

It is noticed that the response $h(B)$ is maximum for $W_E/L = 0.5$ structure. Decreasing the emitter-collector distance, $h(B)$ decreases with 37.5% for $W_E = 2L$, comparative with the maximum value.

The sensor response decreases with 10.7%, comparative with $W_E/L = 0.5$ structure if the distance between emitter and collector doubles.

For the same geometry $W_E/L = 0.5$, the response is depending on material features.

In figure 3 there are shown $h(B)$ values of three sensors MGT1, MGT2, MGT3 realised on: Si ($\mu_{Hn} = 0.15 \text{ m}^2 \text{V}^{-1} \text{s}^{-1}$), InP ($\mu_{Hn} = 0.46 \text{ m}^2 \text{V}^{-1} \text{s}^{-1}$), GaAs ($\mu_{Hn} = 0.8 \text{ m}^2 \text{V}^{-1} \text{s}^{-1}$).

The magnetic sensitivity related to the devices current is defined as follows:

$$(3) \quad S_I = \frac{1}{I_C} \left| \frac{\Delta I_C}{B_{\perp}} \right| = \frac{1}{2} \mu_{Hn} \frac{L}{W_E} G$$

For a given induction ($B = 0.4 \text{ T}$) and at given collector current $I_C = 1 \text{ mA}$, the sensitivity depends of the device geometry and the material properties. In table 1 are presented the obtained values for five magnetotransistors structures.

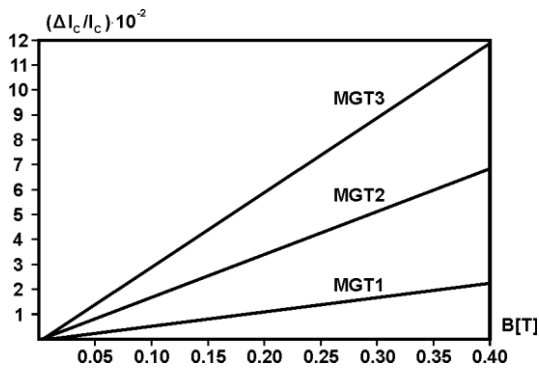


Fig.2. The $h(B)$ dependence of B for three devices of different materials

Table1. The numerical values of the sensitivity

| Device | W_E/L | $\mu_{Hn} [m^2V^{-1}s^{-1}]$ | $S_I [T^{-1}]$ |
|--------|---------|------------------------------|----------------|
| MGT1 | 2 | 0,15 Si | 0,035 |
| MGT2 | 1 | 0,15 Si | 0,05 |
| MGT3 | 0,5 | 0,15 Si | 0,055 |
| MGT4 | 0,5 | 0,46 InP | 0,168 |
| MGT5 | 0,5 | 0,85 GaAs | 0,292 |

Signal-to-noise ratio

The noise affecting the collector current of a magnetotransistor is shot noise and $1/f$ noise. Signal-to-noise ratio is defined by:

$$(4) \quad SNR(f) = \frac{\Delta I_C}{[S_{NI}(f) \cdot \Delta f]^{1/2}}$$

where Δf denotes a narrow frequency band around the frequency f , and $S_{NI}(f)$ denotes the noise current spectral density in the collector current.

In case of shot noise, the noise current spectral density at frequencies over 100 Hz is given by [3]:

$$(5) \quad S_{NI} = 2qI$$

where I is the device current.

By substituting (1) and (5) into (4) it results:

$$(6) \quad SNR(f) = \frac{1}{2\sqrt{2}} \mu_{Hn} \left(\frac{L}{W_E} G \right) \frac{I_C}{(q \cdot I \cdot \Delta f)^{1/2}} B_{\perp} \geq \frac{1}{2\sqrt{2}} \mu_{Hn} \left(\frac{L}{W_E} G \right) \frac{I_C^{1/2}}{(q \Delta f)^{1/2}} B_{\perp}$$

To emphasise the dependence of $SNR(f)$ on device geometry there were simulated (figure 4) three magnetotransistor structure realised on silicon ($\mu_{Hn} = 0.15 m^2V^{-1}s^{-1}$), and having different ratios W_E/L ($W_E = 40 \mu m$, $\Delta f = 1$, $I_C = 1 mA$.)

The device were biased in the linear region at the collector current $I_C = 1 mA$, the magnetic field has a low level ($\mu_{Hn}^2 B^2 \ll 1$). It is noticed that the $SNR(f)$ is maximum for $W_E/L = 0.5$ and for smaller values of this ratio.

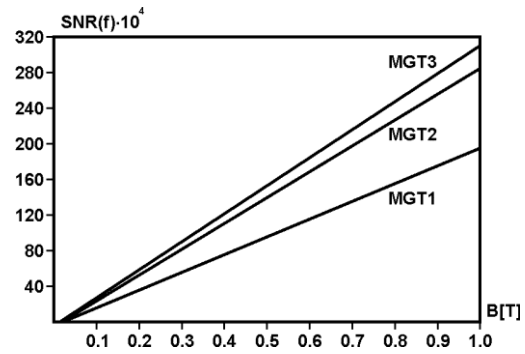


Fig.4. $SNR(f)$ dependence on B for three devices of different geometry: MGT1: $W_E/L = 2$; MGT2: $W_E/L = 1$; MGT3: $W_E/L = 0.5$;

For the same B magnetic induction, increasing the emitter width, $SNR(f)$ decreases with 37.2% for $W_E = 2L$ comparative with the maximum value. In case of $1/e$ noise, the noise current spectral density at the device output is given by [3]:

$$(7) \quad S_{NI}(f) = I^2 \alpha N^{-1} f^{-\beta}$$

where I is the device current, $N = n\delta L W_E$ is the total number of charge carriers in the device, α is a parameter called the Hooge parameter and $\beta \approx 1 \pm 0.1$ (typically). For semiconductors, it is reported that α values range from 10^{-9} to 10^{-7} .

Substituting (1) and (7) into (10) it is obtained:

$$(8) \quad SNR(f) \cong \frac{(ndLW_E)^{1/2}}{2\alpha^{1/2}} \cdot \mu_{Hn} \left(\frac{f}{\Delta f} \right)^{1/2} \cdot \left(\frac{L}{W_E} G \right) \cdot B_{\perp}$$

To illustrate the $SNR(f)$ dependence on device geometry three split-collector magnetotransistor structures realised on Si were simulated (figure5).

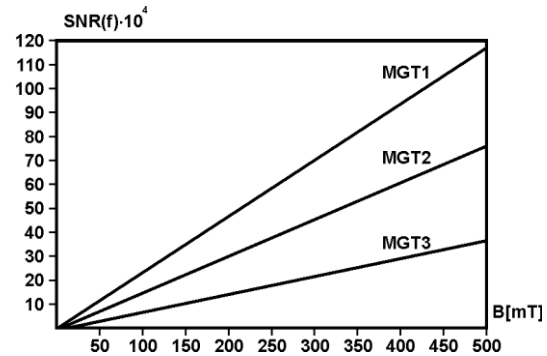


Fig.5. $SNR(f)$ dependence on B for three devices of different geometry: MGT1: $W_E/L = 0.5$; MGT2: $W_E/L = 1$; MGT3: $W_E/L = 2$;

It is considered that: $f = 4 Hz$, $\Delta f = 1 Hz$, $n = 4.5 \cdot 10^{21} m^{-3}$, $d = 4 \cdot 10^{-6} m$, $\alpha = 10^{-7}$, $q = 1.9 \cdot 10^{-6} C$, the devices being biased in the linear region and the magnetic field having a low level.

For the same magnetic induction B , $SNR(f)$ is maximum in case of $L = 2 W_E$.

The increasing of the emitter collector distance causes the decreasing of $SNR(f)$ with 35.2% for a square structure with 69.1% for $W_E = 2L$.

The double-drain magnetotransistor

The double – drain MOS device (Fig.6) is obtained from a MOSFET structure where its conventional drain region is replaced by two adjacent drain regions.

Consequently, the total channel current shared between these two drain regions [5].

The result of the bias is the linear region is the obtained of a continuous channel of approximately constant thickness, which can be assimilated with a Hall plate.

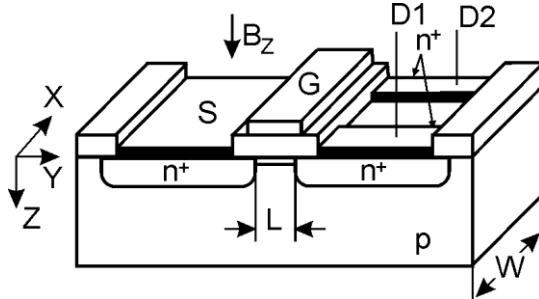


Fig. 6. Double-drain magnetic sensitive MOSFET structure.

The deflection of current lines appears under the action of a magnetic field B_z , perpendicular to the device surface.

The carrier deflection causes a discrepancy between two drain currents:

$$(9) \quad \Delta I_D = |I_{D1}(\vec{B}) - I_{D1}(0)| = |I_{D2}(\vec{B}) - I_{D2}(0)|$$

Since the output signal of the double-drain MOS magnetotransistors consists of the current variation between its terminals, this device operates in the Hall current mode. Using the features of dual Hall devices, and the Hall current expression it results [2]:

$$(10) \quad \Delta I_D = \frac{I_H}{2} = \frac{1}{2} \mu_{H_{ch}} \cdot \frac{L}{W} \cdot G \cdot I_D \cdot B_{\perp}$$

where $\mu_{H_{ch}}$ denote the carriers Hall mobility, G is the geometrical correction factor and I_D is the drain current. The supply-current-related sensitivity of the devices is defined by:

$$(11) \quad S_I = \frac{1}{I_D} \cdot \left| \frac{\Delta I_D}{B_{\perp}} \right| = \frac{1}{2} \mu_{H_{ch}} \cdot \frac{L}{W} G$$

For a given induction ($B = 0.4$ T) and at given drain current $I_D = 1$ mA, the sensitivity depends of the device geometry and the material properties.

In table 2 are presented the obtained values for five magnetotransistors structures.

Table 2. The numerical values of the supply-current sensitivity

| Device | W/L | $\mu_{H_{ch}} [m^2V^{-1}s^{-1}]$ | $S_I [T^{-1}]$ |
|--------|-------|----------------------------------|----------------|
| MGT1 | 2 | 0,07 Si | 0,018 |
| MGT2 | 1 | 0,07 Si | 0,025 |
| MGT3 | 0,5 | 0,07 Si | 0,028 |
| MGT4 | 0,5 | 0,23 InP | 0,084 |
| MGT5 | 0,5 | 0,42 GaAs | 0,146 |

The sensor response

The sensor response is expressed by:

$$(12) \quad h(B) = \frac{\Delta I_D}{(I_{D1} + I_{D2})_{B=0}} = \frac{1}{2} \mu_{H_{ch}} \cdot \frac{L}{W} \cdot G \cdot B_{\perp}$$

and it is linear for induction values which satisfy the condition: $\mu_H^2 \cdot B_{\perp}^2 \ll 1$.

In figure 7 it can be seen the geometry influence on $h(B)$ values for three magnetotransistor structures, realised on silicon ($\mu_{H_{ch}} = 0.07 m^2V^{-1}s^{-1}$) and having different ratios W/L ($W = 50 \mu m$).

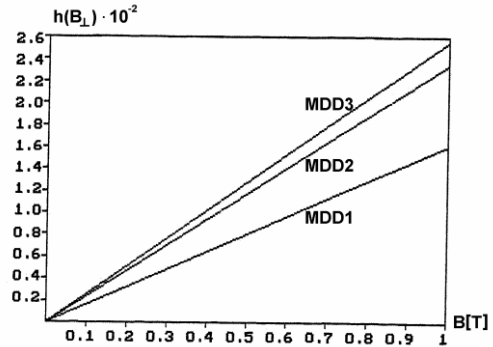


Fig. 7. The $h(B)$ dependence on B for three devices of different geometry: MDD1: $W/L = 0.5$, $(L/W)G = 0.72$; MDD2: $W/L = 1$, $(L/W)G = 0.68$, MDD3: $W/L = 2$, $(L/W)G = 0.46$,

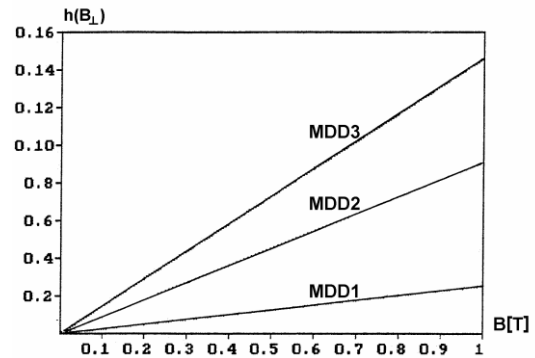


Fig.8. The $h(B)$ dependence on B for three devices on different materials: MDD1, MDD2, MDD3 realised on: Si ($\mu_{H_{ch}} = 0.07 m^2V^{-1}s^{-1}$), InP ($\mu_{H_{ch}} = 0.23 m^2V^{-1}s^{-1}$), GaAs ($\mu_{H_{ch}} = 0.4 m^2V^{-1}s^{-1}$)

It is noticed that the response $h(B)$ is maximum for $W/L=0.5$ structure.

For the same geometry $W/L=0.5$, the response is depending on material features. Decreasing the channel length, $h(B)$ decreases with 37.5% for $W = 2L$, comparative with the maximum value.

The sensor response decreases with 10.7%, comparative with $W/L=0.5$ structure if the channel length doubles. In figure 8 there are shown $h(B)$ values of three sensors

Signal – to – noise ratio

The noise affecting the drain current of a MOSFET magnetotransistors is shot noise and $1/e$ noise. Signal-to-noise is defined by :

$$(13) \quad SNR(f) = \Delta I_D \cdot [S_{NI}(f) \cdot \Delta f]^{-1/2}$$

where Δf denotes a narrow frequency band around the frequency f , and $S_{NI}(f)$ is the noise current spectral density. In case of $1/f$ noise, the noise current spectral density at the device output is given by equation (7).

By analogy with (8) it is deduced:

$$(14) \quad SNR(f) \cong \frac{(ndLW)^{1/2} \mu_{H_{ct}}}{2\alpha^{1/2}} \cdot \left(\frac{f}{\Delta f}\right)^{1/2} \left(\frac{L}{W} G\right) \cdot B_{\perp}$$

In figure 9 is presented the dependence of SNR on B for three magnetotransistors with the same geometry $W/L = 0.5$, $L = 200 \mu\text{m}$ realised from different materials.

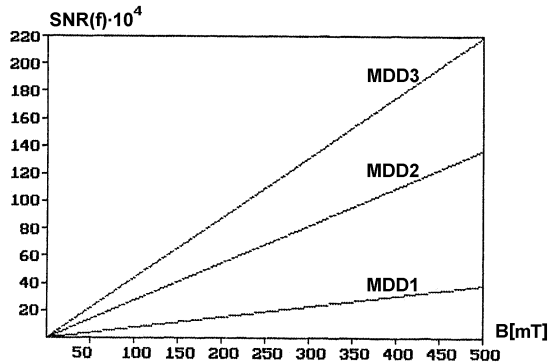


Fig. 9. $SNR(f)$ dependence on B of different materials: MDD1, MDD2, MDD3 realised on: Si ($\mu_{Hn} = 0.07 \text{ m}^2\text{V}^{-1}\text{s}^{-1}$), GaSb ($\mu_{Hn} = 0.25 \text{ m}^2\text{V}^{-1}\text{s}^{-1}$), GaAs ($\mu_{Hn} = 0.42 \text{ m}^2\text{V}^{-1}\text{s}^{-1}$)Si

A high value of carrier mobility cause the increasing of SNR. So for $B = 0.5 \text{ T}$, SNR(f) increase with 65% for GaAs comparative GaSb.

Conclusions

The analysis of the main characteristics of the double-collector magnetotransistor and the double drain magnetotransistor shows that the $W/L = 0.5$ structure is theoretically favourable to high performance regarding the sensor sensitivity. Also substituting the silicon technology by using other materials such as GaAs or InSb with high

carriers mobility values assure higher characteristics of the sensors. The uses of magnetotransistors as magnetic sensors allows the achieving of some current-voltage conversion circuits, more efficient than conventional circuits with Hall plates.

In figure 10 is shown the electrical diagram of a speed of rotation transducers based on a double-collector vertical magnetotransistors.

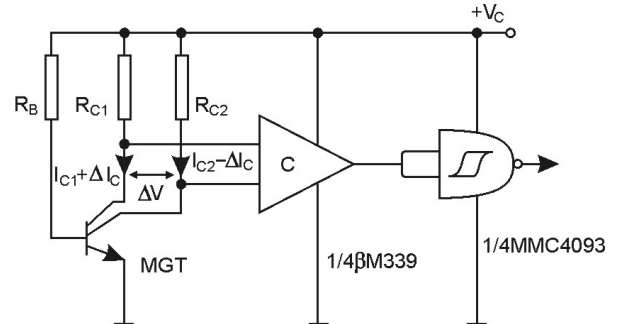


Fig. 10. The electric diagram of transducer

REFERENCES

- [1] Bodea, M., *Tructoare integrate*, Microelectronica, vol. 15, Editura Academiei R.S. România, București, 1987, pp. 73-86
- [2] Căruntu G., *Măsurări galvanomagnetice în dispozitive semiconductoare*, SECOMAR'99, Academia Navală "Mircea Cel Bătrân", Constanța, vol. II, 1999, pp. 69-74
- [3] Gray, R.P., Meyer, G.R., *Circuite integrate analogice. Analize și proiectare*. Editura Tehnică, București, 1993.
- [4] Nathan, A., Huiser, A. M. J., Baltes, H. P., *Two Dimensional Numerical Modeling of Magnetic Field Sensors in CMOS Technology*, *IEEE Trans. Electron Device* ED-32 1212-19, 1985.

Authors: : prof. dr hab. inž. George Căruntu, Maritime University of Constantza, 104, Mircea Cel Bătrân Street, Constantza, Romania, E-mail: rad_o16@yahoo.com

prof. dr hab. inž. Cornel Panait, Maritime University of Constantza, 104, Mircea Cel Bătrân Street, Constantza, Romania, E-mail: rad_o16@yahoo.com

The magnetic sensitive MOS structures

Abstract. In this paperwork based on the adequate models it is analysed the operating conditions, and are established the noise main characteristic for MOS Hall plates. By using the numerical simulation the values of the signal-to-noise ratio and the noise-equivalent magnetic induction for different structure devices are compared and it is also emphasized the way in which choosing the geometry and the material features allows getting high-performance sensors.

Streszczenie. W artykule analizowano warunki pracy czujnika Halla MOS, w tym charakterystykę szumową w oparciu o odpowiedni model. Stosując symulację numeryczną określono stosunek sygnału do szumu i odpowiadającą mu indukcję dla trzech różnych urządzeń. Wskazano metodę poprawy parametrów czujnika drogą optymalizacji geometrii i doboru materiału. (**MOS struktura czuła na pole magnetyczne**).

Keywords: signal-to-noise ratio, offset-equivalent magnetic induction, noise – equivalent magnetic induction

Słowa kluczowe: stosunek sygnału do szumu, czujnik Halla, symulacja komputerowa.

Introduction

The possibility of modelling the channel depth by means of the external supply voltage and low value of area carrier density suggests the possibility of using the MOSFET channel as the active region of a Hall plate.

At the same time, it is outlined the advantage of integrating on the same chip of a magnetic sensor and the signal processing circuit.

Unfortunately a MOS Hall effect device also has a few serious drawbacks: the carrier mobility in the channel amounts to only half its value in the bulk; the increasing of the $1/f$ noise, and the instability of device surface.

The analysis made in this paper outlines the way in which choosing the geometry and material properties influence on the device performances.

The general characterization of the MOS-Hall plates

In a MOSFET structure (figure 1), an extremely thin Hall plate can be realised if the channel constitutes the active region of plate, and the source (S), and drain (D) are the biasing contacts. [1]

For the sensing contacts of the Hall voltage SH_1 and SH_2 are manufactured, two strongly doped regions n^+ type. The channel length is L , and the width is W .

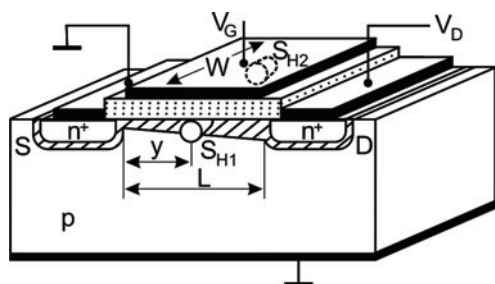


Fig. 1. MOS-Hall plate

The bias in the linear region ensures a continuous channel having a thickness almost constant δ , which could be assimilated with a Hall plate.

Considering the Hall voltage mode of operation, the MOS-Hall plate is equivalent in the linear region with a conventional Hall plate differing by the fact that the charge carriers are due to the surface field effect.

The surface charge density in the channel is approximately constant and it has the following expression [2]:

$$(1) \quad Q_{Ch} = C_{ox}(V_G - V_P)$$

where C_{ox} is the gate oxide capacitance per unit area, V_G the gate to source voltage, and V_P the threshold voltage.

The very low value of the surface charge density in the channel of a MOSFET ensures a high magnetic sensitivity of the MOS-Hall plate. There is also the possibility to modify the channel depth by the drain-source potential difference. In the case of a conventional Hall plate, the generated voltage is [3]:

$$(2) \quad V_H = G(r_H / qn\delta)I \cdot B_{\perp}$$

where G is the geometrical correction factor, r_H the Hall factor and δ the thickness of the plate.

By replacing in (2) the product $qn\delta$ by the surface charge density in the channel Q_{Ch} , and the current I by I_D it results:

$$(3) \quad V_H = G(r_H / Q_{Ch})I_D \cdot B_{\perp}$$

Using the drain current expression:

$$(4) \quad \begin{aligned} I_D &= (W/L)\mu_{Ch} \cdot C_{ox}(V_G - V_P)V_D = \\ &= (W/L)\mu_{Ch}Q_{Ch}V_D \end{aligned}$$

from (3) it results:

$$(5) \quad V_H = \mu_{H_{Ch}}(W/L)GV_D \cdot B_{\perp}$$

where $\mu_{H_{Ch}} = \mu_{Ch} r_H$ represents the Hall mobility of the charge carriers in the channel.

The absolute sensitivity for a Hall device used as a magnetic sensor is:

$$(6) \quad S_A = \left| \frac{V_H}{B_{\perp}} \right|$$

and the supply-voltage-related sensitivity is defined by:

$$(7) \quad S_V = \frac{S_A}{V_D} = \mu_{H_{Ch}}(W/L)G$$

The sensor response is given by:

$$(8) \quad h(B_{\perp}) = \frac{V_H}{V_D} = \mu_{H_{Ch}} \left(\frac{W}{L} G \right) B_{\perp}$$

and it is linear for magnetic induction values that satisfy the condition: $\mu_{H_{Ch}}^2 \cdot B_{\perp}^2 \ll 1$.

In figure 2 it can be seen the geometry influence on $h(B)$ values for three magnetotransistor structures, realised on silicon ($\mu_{Hn} = 0.07 \text{ m}^2\text{V}^{-1}\text{s}^{-1}$) and having different ratios L/W ($L = 100 \text{ }\mu\text{m}$). It is noticed that the response $h(B)$ is maximum for $L/W = 0.5$ structure.

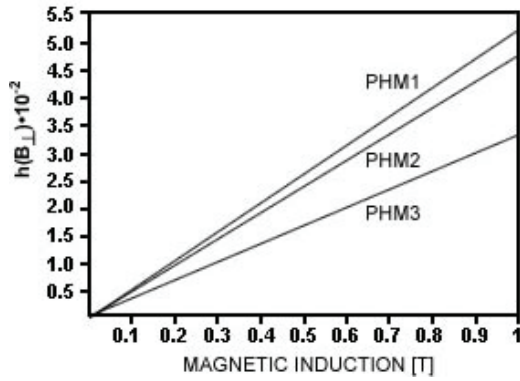


Fig. 2 The $h(B)$ dependence on B for three devices of different geometry: PHM1 $L/W = 0.5$, $(W/L)G = 0.73$; PHM2 $L/W = 1$, $(W/L)G = 0.67$, PHM3 $L/W = 2$, $(W/L)G = 0.46$

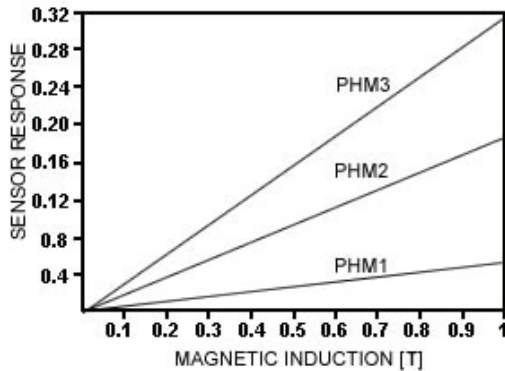


Fig. 3. The $h(B)$ depending on B for three devices on different materials: PHM1 – Si ($\mu_{Hn} = 0.07 \text{ m}^2\text{V}^{-1}\text{s}^{-1}$), GaSb ($\mu_{Hn} = 0.25 \text{ m}^2\text{V}^{-1}\text{s}^{-1}$), GaAs ($\mu_{Hn} = 0.42 \text{ m}^2\text{V}^{-1}\text{s}^{-1}$)

For the same geometry $L/W = 0.5$ the response is depending on material features. In figure 3 there are shown $h(B)$ values of three sensors.

The offset equivalent magnetic induction

The main causes of the offset in the case of Hall plates realised in the MOS integrated circuits technology are due to the misalignment of contacts, to integral non-uniformity, the existence of mechanical stress, and to the fluctuations in the oxide layer charge, or to the variation in the oxide semiconductor interface.

The asymmetries produced by the above causes can be represented by using for the Hall plate the simple Wheatstone bridge circuit model.

In the case of the misalignment of the sensing contacts, for a tolerance ΔL the asymmetrical output voltage or the offset voltage is expressed by [4]:

$$(9) \quad V_{off} = \frac{\Delta L}{W} \cdot \frac{1}{\mu_{Ch} Q_{Ch}} \cdot I_D$$

The value of the magnetic induction corresponding to a Hall voltage equal with V_{off} represents offset equivalent magnetic induction.

In the case of the geometrical offset of the sensing contacts, the expression of the offset equivalent magnetic induction is got by replacing (10) into (7):

$$(10) \quad B_{off} = \frac{V_{off}}{S_A} = \frac{1}{\mu_{H_{Ch}}} \cdot \left(\frac{W}{L}G\right)^{-1} \frac{\Delta L}{L}$$

It is noticed that at given technological misalignment, B_{off} decreases if $\mu_{H_{Ch}}$ is of a high value. In the case of the

MOS-Hall plates this is an inconvenience because the carrier mobility in the channel is half of its value in the volume of the equivalent conventional device.

Assuming that the condition of a low magnetic field is fulfilled, minimal values for B_{off} are obtained if $L/W \leq 0.5$ when the product $(W/L)G$ takes the maximal value 0.74 [3]:

$$(11) \quad (B_{off})_{min} \cong \frac{1}{0,74 \cdot \mu_{H_{Ch}}} \cdot \frac{\Delta L}{L}$$

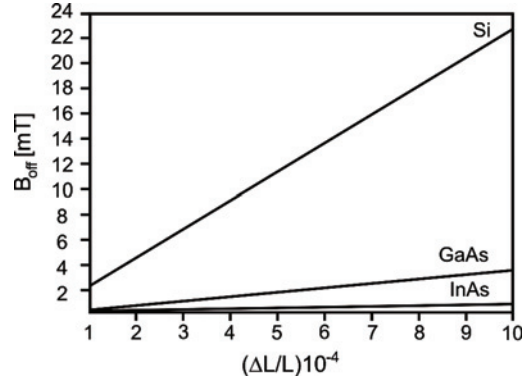


Fig. 4. The B_{off} depending on the geometrical offset $\Delta L/L$ for three devices of different materials

In the figure 4 are represented the values B_{off} for three structures with an optimal geometry of the channel ($L=2W$) realised from different materials. For values of the geometric offset within the range $[10^{-4}, 10^{-3}]$, in the Si device, $(B_{off})_{min}$ varies between 2.2 mT and 22 mT and in GaAs device $(B_{off})_{min}$ covers the range [0.39, 3.9] mT, the increase of the offset equivalent induction slope being of 5.67 times smaller in GaAs.

Signal-to-noise ratio for MOS-Hall plates

At the output of a Hall device the noise voltage is due to the generation-recombination noise, thermal noise, and $1/f$ noise.

In case of a MOS-Hall Plates, at high frequencies, thermal noise dominates. The voltage spectral density of thermal noise is given by [5]:

$$(13) \quad S_{NV} = 4kTR_{out}$$

where $k = 1.38054 \cdot 10^{-23} \text{ JK}^{-1}$ is the Boltzmann constant, and R_{out} is the output resistance of device.

The output resistance of a rectangular MOS-Hall plate with very small sense contacts is given by [6]:

$$(14) \quad R_{out} \cong 2 \frac{\rho_b}{\pi \delta} \ln\left(\frac{W}{s}\right)$$

on condition that: $s \ll W \ll L$.

The coefficient ρ_b denotes the effective material resistivity, and s is the small sense contacts diameter.

If the biased voltage of device is constant, ρ_b practical not depends of magnetic field. By substituting (14) into (13) it results spectral density:

$$(15) \quad S_{NV} = \frac{8kT}{\pi q \mu_{Ch} \delta} \ln\left(\frac{W}{s}\right)$$

For a narrow bandwidth Δf around a frequency f , the signal-to-noise ratio, can be expressed as:

$$(16) \quad SNR(f) = V_H [S_{NV}(f) \cdot \Delta f]^{-1/2}$$

where Δf denotes a narrow frequency band around the frequency f , ($f > 100$ kHz [7]) and $S_{NV}(f)$ is the noise spectral density at the device output.

By substituting (2) and (15) into (16) it results:

$$(17) \quad SNR(f) = \left(\frac{\pi}{8hT} \cdot \frac{\mu_{Ch}}{qn\delta\Delta f \ln(W/s)} \right)^{1/2} r_H G I_D B_{\perp}$$

Since the signal-to-noise ratio increases with the drain current I_D , the maximal $SNR(f)$ is limited only by maximal acceptable device dissipated power P_{max} .

From (2) and (5), we also obtain the Hall voltage as a function of the power $P = V_D I_D$ dissipated in the device. Multiplying (2) and (5) member-by-member it results:

$$(18) \quad V_r = G \left(\frac{W}{L} \right)^{1/2} r_H \left(\frac{\mu_{Ch}}{\theta_{Ch}} \right)^{1/2} P^{1/2} \cdot B_{\perp}$$

where $P = V_D I_D$ is the power dissipated in the device. From (17) and (18) it results:

$$(19) \quad SNR(f) = 1.11 G \left(\frac{W}{L} \right)^{1/2} \left[\frac{\mu_{H_{Ch}}^2 \cdot P}{kT\Delta f \ln(W/s)} \right]^{1/2} B_{\perp} =$$

$$= 9.7 \cdot 10^9 \mu_{H_{Ch}} \left(G \frac{W}{L} \right)^{1/2} \left[\frac{P}{\Delta f \cdot \ln(W/s)} \right]^{1/2} B_{\perp}$$

where $T=300$ K and $k = 1.38054 \cdot 10^{-23} JK^{-1}$.

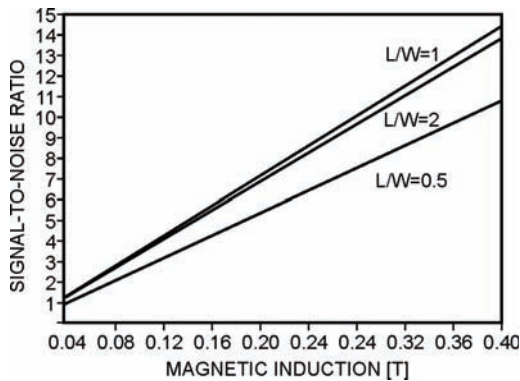


Fig.5. The $SNR(f)$ depending on B_{\perp} for three devices of different geometry : PHM1: $L/W = 0.5$, PHM2: $L/W = 1$, PHM3: $L/W = 2$

The $SNR(f)$ dependence on magnetic induction for a given power dissipation ($P = 200$ mW) and different L/W ratio values are shown in figure 5.

The frequency bandwidth is reduced, $\Delta f = 1$ Hz, and the condition of low induction magnetic field is fulfilled. ($\mu_{H_{Ch}}^2 B^2 \ll 1$). It is noticed the $SNR(f)$ values in maximum for the square device ($L/W = 1$).

These values decrease with 25% when the length is half reduced (PHM1), also with 4.5% if the channel length doubles (PHM3).

The NEMI for MOS –Hall plates

The mean square noise – equivalent magnetic induction, $NEMI$, in a frequency range (f_1, f_2), is obtained by substituting in the absolute sensitivity expression (6), the Hall voltage by the mean square noise voltage:

$$(20) \quad \langle B_N^2 \rangle = S_A^{-2} \cdot \int_{f_1}^{f_2} S_{NV}(f) df$$

At high frequencies, thermal noise dominates. For a narrow bandwidth Δf around a frequency f by substituting (7) and (15) into (20) it results:

$$(21) \quad \langle B_N^2 \rangle = \frac{8kT}{\pi} \cdot \frac{\rho_b \ln(W/s)}{\delta \mu_{H_{Ch}}^2} \cdot \Delta f \left(G \frac{W}{L} \right)^{-2} \cdot V_D^{-2}$$

To emphasize the geometry influence on $NEMI$ there simulated (Fig. 6) three MOS-Hall structures realised on silicon ($\mu_{H_{Ch}} = 0.07$ m²V⁻¹s⁻¹, $\Delta f = 1$ Hz, $\mu_{H_{Ch}}^2 B^2 \ll 1$) and having different ratios L/W .

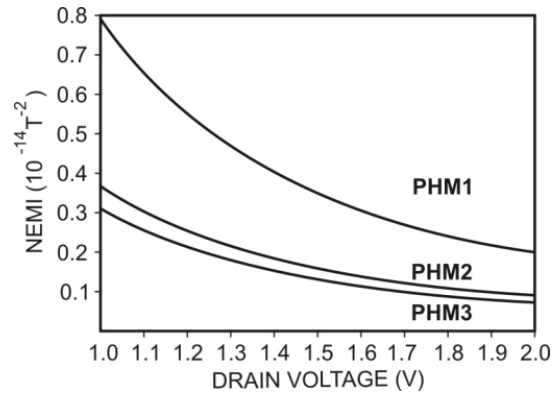


Fig. 6. The $NEMI$ depending on drain voltage, V_D for devices of different geometry: PHM1 $L/W = 2$, PHM2 $L/W = 1$, PHM3 $L/W = 0.5$

The increasing of the channel length causes the decreasing of device performances. If the length increases twice, the noise-equivalent magnetic induction increases with 18% and if the same distance increases four times (PHM1), $NEMI$ increases with 148%.

Conclusions

The analysis of the main noise characteristics of the MOS-Hall plates shows that in case of thermal noise, the square structure ($W=L$) is theoretically favourable to obtain magnetic sensors of performance. The B_{DL} analysis shows that the $l/w = 0.5$ structure is theoretically favorable to obtain magnetic sensors of performance. Also substituting the silicon technology by using other materials such as *GaAs* or *InSb* with high carriers mobility allows the made of higher characteristics devices.

REFERENCES

- [1] Sze S.M., *Semiconductors Sensors*, John Wiley & Sons Inc., New York, 1994.
- [2] Stere R., Bodea M., *Tranzistoare cu efect de câmp*, Editura Tehnică, București, 1972, pp. 117
- [3] Middelhoek S., Audet S.A. *Physics of Silicon Sensors*, Academic Press, London, 1989, pp. 5.20-5.24
- [4] Căruntu G., *Microsenzori magnetici. Aplicații* Editura Societatea Autonomă de Informatică, București, 1998
- [5] R.P. Gray, G. R. Meyer, *Circuite integrate analogice. Analize și proiectare*, Editura Tehnică, București, 1993, pp. 579, 583
- [6] Căruntu G., Consideration about Thermal Noise for Magnetic Sensors, *Proceedings of the 9th International Conference on Applied and Theoretical Electricity*, vol. I, Craiova, June 4-6, 1998, pp. 21-26
- [7] Baltes H., Popović R.S., Integrated Semiconductor Magnetic Field Sensors, *Proc IEEE* **74** 1107-32, 1986

Authors: prof. dr hab. inž. George Căruntu, Maritime University of Constantza, 104, Mircea Cel Bătrân Street, Constantza, Romania, E-mail: rad_o16@yahoo.com
 prof. dr hab. inž. Cornel Panait, Maritime University of Constantza, 104, Mircea Cel Bătrân Street, Constantza, Romania, E-mail: rad_o16@yahoo.com

The selection of genetic algorithm parameters for soft fault diagnosis

Abstract. Some methods for soft fault diagnosis developed in last years use evolutionary computing. Genetic algorithms are the most popular evolutionary method. The genetic algorithms are very sensitive to parameter settings, hence the selection of these parameters seems to be a very important problem. This paper deals with the issue of an optimal determination of genetic algorithm parameters for soft fault diagnosis. The possibilities of the selection for all algorithm parameters, their advantages and disadvantages are presented. The proposed methods of parameter selection are illustrated by some experimental examples.

Streszczenie. W ostatnich latach zostało opracowanych wiele metod diagnostycznych dla uszkodzeń parametrycznych, które wykorzystują ewolucyjne metody obliczeniowe. Najbardziej popularną metodą ewolucyjną są algorytmy genetyczne. Z powodu dużej wrażliwości algorytmów genetycznych na parametry procesu obliczeniowego dobór tych parametrów jest bardzo ważnym zagadnieniem. W przedstawionej pracy analizowany jest problem optymalnego doboru parametrów algorytmu genetycznego zastosowanego do diagnostyki parametrycznej. Przedstawione zostały różne możliwości wyboru parametrów, zalety i wady różnych wariantów. Zaproponowane sposoby doboru parametrów ilustrują zamieszczone wyniki obliczeń. (**Dobór parametrów algorytmu genetycznego w diagnostyce uszkodzeń parametrycznych**).

Keywords: soft fault diagnosis, genetic algorithms (GA).

Słowa kluczowe: diagnostyka uszkodzeń parametrycznych, algorytmy genetyczne (GA).

Introduction

A fault diagnosis of electronic circuits is an important problem of the analysis, design and testing of that circuits. In the contrary to digital systems analog systems are harder to be analyzed. All the methods for analog fault diagnosis can be divided into few groups: with simulation before test (SBT) and simulation after test (SAT), for catastrophic and for soft faults, for single and for multiple faults, with detection only, with localization and with fault identification. Only few methods for multiple soft fault diagnosis were until now proposed and this subject is still open. The paper considers the methods developed in the last years by the authors. They all belong to SAT methods and can be applied in linear and nonlinear DC and AC circuits. They base on the circuit description, some measurements carried out on the test points and obtaining of the differences between the current and nominal values of parameters using genetic algorithm. The number of measurements can be enough to solve the problem of identification element parameters uniquely but in other cases it can enable to find the set of possible solutions. Many elements cause positive or negative result of soft fault diagnosis. One of them is determination of a set of test nodes. Another are parameters of genetic algorithm that are used in calculation of current values of faulty parameters. This problem is developed below.

The assumptions of the described method are:

a) scheme and nominal values of circuit under test parameters or the function g (1) for node voltage vector e calculation are known,

$$(1) \quad e = g(x, u)$$

where x – vector of element parameters, u – vector of excitations.

b) values of all faulty parameters belong to a fixed range (in described examples $\pm 30\%$ of a nominal value)

c) number of faulty parameters is not bigger than in advance was fixed in advance

d) it is possible to measure voltages e_i of accessible nodes in the faulty circuit.

Results presented in the earlier papers were obtained with the heuristic choice of the parameters of the calculation

process, based on a few experiments and some hints founded in the articles [1,2,3,4]. In the paper, results of the experiments enabling us to define the method of optimal choice of some GA parameters responsible for calculation time, accuracy of the solution and possibility of finding multiple solution, were presented and discussed in details. Performed experiments were related to:

- way of coding values of unknown parameters (binary coding, Gray code and floating point representation were investigated),
- method of rating quality of the solution belonging to all the individuals (it means applied fitness function) - the possibility of dynamic change of the fitness function during the numerical process was also considered,
- strength of the population (number of the individuals) defined in terms of the length of chromosome which depends on the method of coding,
- method of the creation of primary population,
- method of the creation of the mating pool (type of the applied selection),
- optimal choice of the probabilities of the genetic operators used by genetic algorithms.

Methods of coding

The method of coding the unknown values, seems to be the most important problem, which has to be solved in the beginning of the process of fault identification. It has condusory influence not only on convergence, fastness or accuracy but also on capability of finding the solution at all. Direct coding of faulty parameters of electrical circuits does not ensure positive effects because these parameters have different ranges that result in possible selection of the individuals (from the initial population) having very small value of the fitness function. Taking advantage of the fact, that area of search is limited to the space of parametric faults, value of i -th parameter fault Δ_i (difference between real value $x_{i,cur}$ and nominal value $x_{i,nom}$) may be coded. To unify search for values it is convenient to code relative faults δ_i (real fault in relation to nominal value of the parameter) [5,6]:

$$(2) \quad \delta_i = \frac{\Delta_i}{x_{i,nom}} = \frac{x_{i,cur} - x_{i,nom}}{x_{i,nom}}$$

For the parametric faults, typical intervals for acceptable values of δ_i are: $\pm 20\%$, $\pm 30\%$ or $\pm 50\%$.

Theory of genetic algorithms convergence [1] demands that we should apply two rules of coding method selection. According to the first one, the selection has to ensure that lower order schemes with small ranges correspond with desirable properties of the solution. The second one is the rule of minimum alphabet selection.

Typical method of coding, used in the classical genetic algorithm, is binary coding assigning to every allele of any gene value 0 or 1. The length of chromosome l_{ch} is defined in his case by the number of unknown parameters n and their assumed accuracy ε . If the value of searched parameter belongs to the interval $[x_{i,min}, x_{i,max}]$ then its coded form as a binary gene having l_g positions is linear mapping of the given above interval into interval of integers $[0, 2^{l_g} - 1]$. It results in obtaining the coding accuracy ε_i of the parameter x_i defines as follows:

$$(3) \quad \varepsilon_i = \frac{x_{i,max} - x_{i,min}}{2^{l_g} - 1}$$

(The length of chromosome is $l_{ch} = n l_g$.)

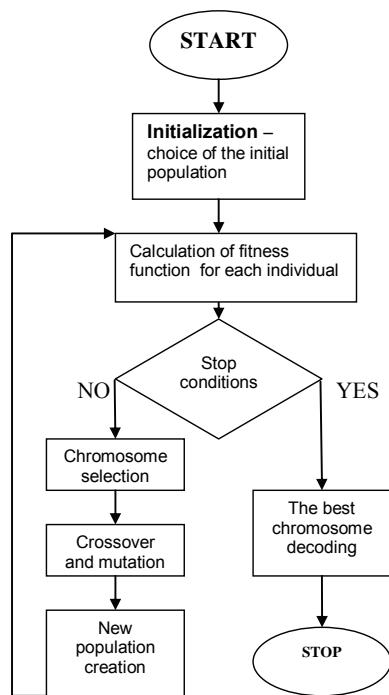


Fig.1. Block diagram of the Genetic Algorithm

If we are looking for the parametric fault belonging to the interval $[-30\%, 30\%]$ using nine-positions gene, the coding accuracy is 0.12% (with one bit of sign). Four unknown parameters result in the length of chromosome equal to 36. The effect related to so-called Hamming edges, seems to be a serious problem of binary coding causing most often problems with finding the solution. For some forms of fitness function, his effect may result in some additional local maximum. To omit the mentioned problem, Gray code (reflected binary code) where two successive values differ in only one digit, is used. Unfortunately, application of the Gray code is not free from negative effects. The third possibility is application of real coding, where genes are real numbers and alleles have in general values from 0 to 9. This method causes considerable extension of the

alphabet, that result in poor convergence of the process of finding the solution. Logarithmic coding (where two digits define sign of the exponential function and exponent and the other part of gene is coded value of the exponent) has no practical sense under the assumption that relative fault defined by formula (1) is coded.

Fitness functions

Genetic algorithms are based on the directional search of solutions space. Direction of the searching process depends on the successive rating of the randomly chosen points (individuals) of the space, creating the set of potential solutions called population. According to the block diagram presented in Fig.1, genetic algorithm is based on the rating of each individual of every population. It is done by calculating the value of the fitness function f . This function determines the goal we wish to achieve. If its nonnegative value is greater, the rated individual is closer to the solution. In the case of fault identification, we are looking for the set of faulty parameters or eventually for the set of relative faults (1), to which some circuits parameters corresponds, compliant with the measured one. For the discussed method, the potentials of the available nodes are the measured values of the faulty circuit. These values are used for fitness function calculation. The following two fitness functions have been applied during the diagnostic calculations:

$$(4) \quad F1 = \sum_{i=1}^p f_i$$

where

$$f_i = 100 \quad \text{if} \quad \left| \frac{e_{i,cal} - e_{i,meas}}{e_{i,meas}} \right| \leq 0.01,$$

$$f_i = 100 - \left| \frac{e_{i,cal} - e_{i,meas}}{e_{i,meas}} \right| 100 \quad \text{if} \quad 0.01 \leq \left| \frac{e_{i,cal} - e_{i,meas}}{e_{i,meas}} \right| 100 \leq 100,$$

$$f_i = 0 \quad \text{if} \quad \left| \frac{e_{i,cal} - e_{i,meas}}{e_{i,meas}} \right| 100 \geq 100$$

p – number of the available nodes of the circuit under test, $e_{i,cal}$ – value of the voltage of i -th node calculated from the formula (1) and from the values of the search for parameters corresponding to the rated individual, $e_{i,meas}$ – measured value of i -th node voltage,

$$(5) \quad F2 = \frac{a}{b + \sum_{i=1}^p (e_{i,cal} - e_{i,meas})^2}$$

where a and b are constant values determined for the every calculation process.

Applied fitness functions presented above have been submitted to dynamic change during the calculation process. $F1$ function () should be scaled, especially in the case of small populations. This operation prevent premature convergence at the beginning phase of procedure, when the average value of the fitness function of the population is close to the maximum. It causes that for the proportional selection the similar number of “best” and “average” individuals is moved to the next population. For the $F1$ function, the linear scaling was applied. Fitness function $F1$ was replaced by the value (6)

$$(6) \quad F'1 = aF1 + b$$

where a and b were determined so that average value of fitness function after scaling should be equal to average value of fitness function before scaling and maximum of the fitness function after scaling should be a multiplicity of the mean value of fitness function. Values of the manifold increase factor belong to the interval [1.2-2.0] at the final stage of calculating process. The other well-known scaling methods like sigma truncation or power law scaling were not applied here.

In the case of fitness function $F2$, the scaling procedure was replaced by the dynamic change of a and b preventing the premature convergence by decreasing the relation between maximum and mean value of fitness function at the beginning of calculation process and decreasing this relation at the final stage.

Population size

Population size belongs to the most important parameters of the GA. When the number of individuals is small, the ability to search solution space decreases, what leads very often to early convergence, i.e. to "break off" in the solution point being usually just a local optimum. Large size of the population is advantageous because of better accuracy of solution space penetration. However, too large number of individuals extends calculation time and computer resources requirements, slows down convergence. To set proper population size we need a compromise between to important parameters: population variety and selection pressure. In the case of fault identification, the value of fitness function is known. It follows from the condition that circuit state we are looking for is equal to the state defined by the faulty circuit measurements. Hence, too early convergence (i.e. local instead global optimum achievement) is identified which makes the correction of population size possible. It is obvious, that number of individuals should be set basing on chromosome length. During calculation processes made for fault identification, the best results were obtained when the size of populations was five to ten times greater than chromosome length. Variable population size was not applied.

Creation of initial population

Initialization, i.e. creation of initial population, is a random choice of the settled earlier number of individuals defined by series, usually binary, having fixed length. During almost all numerical experiments, the limit value for the fitness function was used. It causes, that initial population consists only with individuals having fitness function exceeding the settled value. Although this limit extends population creation time significantly, it improves convergence and decrease total time of calculation process in result. Introducing fitness function limit we decrease the relation between maximum and mean value of fitness function in the initial population

Selection

Selection process is generally based on the choice of individuals, driven by the values of the fitness function. Individual solutions (i.e. members of the population - chromosomes) are selected through a fitness-based process and created parent population (called mating pool) being a base for new generation. Mating pool has the same size as a population under selection. One of the most popular and well-studied method is roulette wheel selection (proportional selection). It is based on N -times random choice of single individual from the current population to

mating pool. (N is the number of individuals). For every N drawing, probability p_i of i -th individual transition towards mating pool of the next generation is proportional to the value of its fitness function:

$$(7) \quad p_i = \frac{F_i}{\sum_{k=1}^N F_k}$$

One of the most important disadvantages of the method is possibility of elimination individuals having even the largest value of fitness function. It is a result of random choice. Too early elimination of the individuals having low-valued fitness functions seems to be next disadvantage of the proportional selection. To eliminate the first negative feature, elitist strategy was used. This procedure consists in unconditional choice of the individual (or individuals) having the greatest value of fitness function. Tournament selection is the next popular method of choosing mating pool members. The groups of individuals having previously defined different sizes are created and the best member (or members) is (are) selected. The choice may be deterministic (deterministic tournament selection) or random (stochastic tournament selection). Creation of the groups and selection of the best individual is continuing to the moment when the mating pool achieves the size of current generation previously defined. Ranking selection is the third method of the selection. Here, the number of individuals copies is defined by the rank of the individual. All the individuals are sorted by increasing values of their fitness and rank is the position of the individual on the rank list. (Treshold selection is a special case of rank selection.)

Proportional selection and tournament selection were applied for the fault identification calculations. However the tournament selection is regarded as the best one, authors did not confirm this observation during the numerical tests.

Crossover and mutation

Crossover and mutation are two basic genetic operators used in the GA programming. Crossover operator plays certainly main role when genetic algorithms are applied. Crossover allows genetic material from two parents to be passed into the offspring. One-point crossover works by selecting a common crossover point inside randomly chosen parents and swapping the corresponding parts of chromosomes. Two-points crossover differs from the previous one only by the fact, that the swapping parts are placed between two selected points. Crossover probability pc depends on the experiment terms. Up and coming results were obtained for pc values belonging to the interval [0.2; 0.5], the most often used value was $pc=0.4$. The simplest form of mutation negates a randomly chosen single bit of chromosomes. The mutation probability pm is often smaller than crossover probability. Typically, the mutation probability is $pm=1/l$, where l is the length of chromosome. In our example the mutation probability is in the range 0.03 to 0.05.

Results

In order to test the various art of genetic algorithm we analyze the circuit in the Fig.2, which is the two stage filter. The source connected to the node 1 is the sinusoidal current source. Complex number method is applied. We assume that only nodes 1 and 7 are accessible in the circuit. Four equations are formulated, two for real parts of node equations for node 1 and 7 and two for imaginary parts of these equations.

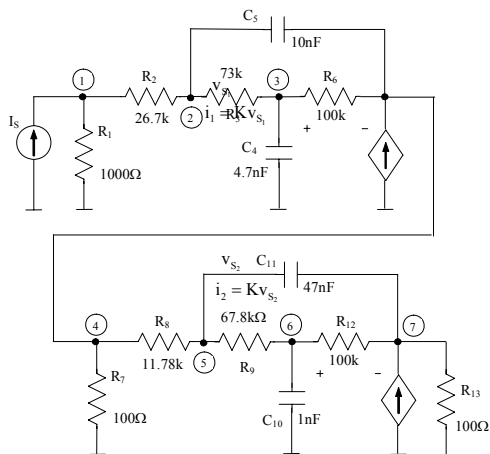


Fig.2. Two stage filter analyzed as an example

Four elements are considered as faulty: R_2 , C_4 , R_8 , C_{10} . Computations of fault parameters are executed with three way of coding: with binary representation of relative value of fault, with applying of Gray code and coding with floating point numbers. In all the cases 10 tests with the same parameters are executed. In the Table 1 the best results for each set of parameters are presented. The crossover probability is in all cases equal to 0.4 and the mutation probability 0.05. Both values are experimentally defined. The size of population is equal 100 and initial populations are created with a limit value of fitness function for each individual equal 5% of its maximal value. The scaling of fitness function is not used. The results of computations using proportional selection (roulette wheel selection) and tournament selection are similar, hence only the best and worst results for proportional selection are presented in the Table 1. Numerical experiments enable us to formulate the following conclusions:

- floating point representation is the most useful coding method,
- application of the function $F1$ (4) ensures much better results,
- rules of the crossover and mutation probabilities selection presented in the paper are effective.

Conclusions

The different types of the most important parameters of genetic algorithm for soft fault diagnosis are described. The possibilities of the parameters selection, their advantages and disadvantages are presented. Based on the results of many experiments, which illustrative example is presented in Table 1, some useful advices and remarks concern with

GA parameters selection may be formulated. The obtained results refer mainly to the method proposed recently by the authors, but the most important demands made to applied calculation algorithms in general are similar. Hence, methods of GA parameters selection are also similar. Further improvement of the algorithm effectiveness needs further modification of the calculation methods. Dynamic change of population size, method of individual's rating, crossover and mutation types seem to be particular interesting and promising research directions.

Table 1. Results of the diagnostic test

| Coding method | Length of | | Number of final population | | | |
|----------------------|-----------|------------|----------------------------|-------|------|-------|
| | | | F1 | | F2 | |
| | gene | chromosome | best | worst | best | worst |
| Binary coding | 9 | 36 | 5340 | 15032 | 8322 | - |
| Gray code | 9 | 36 | 4250 | 13876 | 7380 | 15876 |
| Floating point repr. | 5 | 20 | 3252 | 10812 | 4281 | 12551 |

Acknowledgments:

This work was supported by the Ministry of Education and Science under Grant 3 T11B 055 29.

REFERENCES

- [1] Goldberg David E., Genetic Algorithms in Search, Optimization and Machine Learning, Addison-Wesley Publishing Company, 1989.
- [2] Michalewicz Z., Genetic Algorithms + Data Structures = Evolution Programs, Springer-Verlag Berlin Heidelberg, 1996.
- [3] Arabas J., Wykłady z Algorytmów Ewolucyjnych, Wydawnictwa Naukowo-Techniczne, Warszawa, 2001.
- [4] Rutkowska D., Piliński M., Rutkowski L., Sieci Neuronowe, Algorytmy genetyczne i Systemy Rozmyte, Wydawnictwo Naukowe PWN, Warszawa, 1997.
- [5] Korzybski M., Application of genetic algorithms to fault location and parameter identification, *Proceedings of the International Conference SPETO*, 2002, pp. 443-446, Gliwice, Polska.
- [6] Korzybski M., A method for fault diagnosis of linear and nonlinear electric circuits, *Proceedings of the International Conference SPETO*, 2003, pp. 315-318, Gliwice, Polska.

Authors: mgr inż. Marek Korzybski, Politechnika Łódzka, Instytut Elektrotechniki Teoretycznej, Metrologii i Materiałoznawstwa, ul. Stefanowskiego 18/22, E-mail: markorz@p.lodz.pl, dr inż. Marek Ossowski, Politechnika Łódzka, Instytut Elektrotechniki Teoretycznej, Metrologii i Materiałoznawstwa, ul. Stefanowskiego 18/22, E-mail: marek.ossowski@p.lodz.pl

Evaluation of bidomain model parameters for simulation of a nerve bundle

Abstract. The results presented in the paper are a part of research aimed on the development of realistic and physiologically justified model of a nerve. The electrical activation of neural tissue can be simulated with bidomain model. Bidomain is a multiscale model in which the macroscopic PDE model of tissue is combined with microscopic model of the cell membrane. In the presented paper we study in details the influence of the most important model parameters on simulation results.

Streszczenie. Model dwuobszaru (ang. bidomain) może być wykorzystany do symulacji elektrycznej aktywacji tkanek nerwowych. W przedstawionym artykule przeanalizowano wpływ poszczególnych współczynników tego modelu na wyniki symulacji. Przedstawione wyniki są częścią projektu, którego głównym celem jest stworzenie realistycznego i uzasadnionego fizjologicznie numerycznego modelu nerwu. Wspomniane współczynniki są dodatkowo analizowane pod kątem ich wpływu na pobudzenie pochodzące od zewnętrznej stymulacji elektrycznej. (Ocena parametrów dwuobszarowego modelu nerwu)

Keywords: numerical model, bioelectromagnetism, finite element method

Słowa kluczowe: model numeryczny, bioelektromagnetyzm, metoda elementów skończonych

Introduction

The results presented in this paper are a part of authors' research aimed on creating of a realistic and physiologically justified computational model of neural tissue. The primary goal is to create efficient model of neural tissue to simulate the vagus nerve stimulation therapy. This model will help to work out more efficient medical equipment, better localization of electrodes or develop specific stimulation time patterns. It will also provide a background for the future research on the magnetic stimulator of a nerve bundle. We hope that the evaluated model will also be helpful in developing other electromagnetic therapies.

The properties of neural tissue and especially the nerve bundles are one of the key issues in functional electric stimulation. The stimulating electrodes are usually located in the vicinity of a nerve, on the surface of the head or as it in case of deep brain stimulation, inside the brain. The electric properties of the tissue are the same for electric and magnetic stimulation. Thus, the evaluated model for electrical stimulation can later be used to simulate the magnetic stimulation.

Several authors already studied the response of an isolated single axon to stimulation applied through an extracellular electrode [1,2,3]. A nerve however, contains many axons. The stimulation of a nerve depends not only on properties of axon (such as intracellular and extracellular conductivities or its diameter) but also on the properties of the nerve, such as how tightly the axons are packed. Additionally the current distribution from the stimulating electrodes depends on the complicated geometry of the nerve. We must also consider the influence of electrical properties of the contact of electrodes with the tissue (or the skin as it was studied by the authors in [9]). To consider the response of the whole tissue which is built of thousands of cells, a macroscopic approach which allows for the microscopic properties of the cells must be developed. Such an approach, called bidomain, was proposed by Tung in 70s. It was first used for modeling of the active cardiac tissue [4]. The neural tissue behaves in a similar way [5] as cardiac muscle thus the bidomain was also used to model it by some authors [6,7,8].

Physiological considerations

In bidomain model the neural tissue is simulated with two: intra- and extracellular regions, separated by the cellular membrane. The scheme of tissue is presented in the left part of Fig. 1. The neural cells surrounded by glial

cells and fluid (both treated as passive elements) and are connected with some physiological junctions. The voltage barrier on thin cellular membrane separates two potentials: the one called intracellular Φ_i which is defined within the neural cell bodies and the other one, defined outside of the neural cells, called extracellular Φ_e . Between the domains, on the neurons' cellular membrane we define a membrane potential $V_m = \Phi_i - \Phi_e$. The activation phenomenon is observed as a depolarization of the cellular membrane thus it is described with the membrane potential. The membrane potential is then of the strongest interest in the evaluation of the neural functional stimulation.

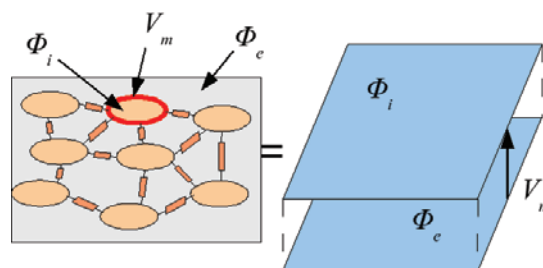


Fig. 1. Continuous representation of discrete tissue in averaged bidomain model.

In the resting state the membrane potential is approximately -85 mV and the sum of currents passing the membrane is 0. During the activation of the neural cell physiological currents are passing through the membrane. The current I_{ion} pass through the ionic channels in the membrane and the current $C_m dV_m/dt$ is caused by capacitive properties of the membrane. The total current is thus expressed as:

$$(1) \quad I_m = C_m \frac{dV_m}{dt} + I_{ion}.$$

The above equation defines surface current passing the membrane in a specific point. We use a special parameter to transform this current in to the volume current source for the bidomain model.

The membrane potential of a cell in a specific point is usually described by a system of ordinary differential equations (ODE). Among the most commonly used ODEs are classical Hodgkin-Huxley, Sherman-Rinzel-Keizer and FitzHugh [1,2,3,5]. The excitation of the cell (action

potential) has three major phases: depolarization, hyperpolarization and repolarization. In the starting phase of depolarization the ionic channels try to compensate the membrane depolarization thus they decrease V_m . When a specific threshold value is exceeded, the ionic channels starts to behave inversely and they increase the depolarization. This phase is called activation. During the repolarization phase (refractory) the membrane can not be activated due to physiological constraints. The excitation of membrane propagates along the neuronal axons. In the continuous, spatial model the propagation can be described by the system of reaction-diffusion equations consisting of a non-linear parabolic equation coupled with an elliptic equation. This system is referred to as bidomain model.

In the bidomain model we assume that the current flowing out of the intracellular space must be equal to the current flowing into the extracellular space with the opposite sign (due the direction of the normal to the membrane):

$$(2) \quad \nabla \cdot \vec{J}_e = -\nabla \cdot \vec{J}_i = \chi I_m.$$

In (2) we can see third part which describes the current passing the membrane χI_m with a unit [A/m^3]. I_m which was defined in (1) couples the macroscopic model of the tissue with the microscopic model of the membrane. We can introduce the volume current source component using χ [$1/m$] which expresses the sum of all membrane surfaces of all axons per unit volume. Different values of this parameter allow simulating various tissues of the nervous system.

Model of the nerve

The model, presented in Fig 2, is build of two domains: the nerve fiber (Ω_N) and surrounding tissue (Ω_T). The nerve is surrounded with the boundary $\partial\Omega_N$ and the tissue is closed with the boundary $\partial\Omega_T$ and two boundaries where the electrical stimulus is applied: $\partial\Omega_{E1}$ and $\partial\Omega_{E2}$.

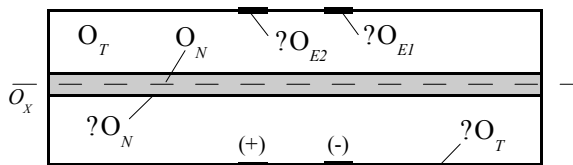


Fig. 2. Domains and boundaries of the cylindrical model.

The bidomain model is a good approximation for the propagation of activation of neurons. We need, however, some modifications to use it for modeling of the external stimulation. We assume that the nerve activation does not influence the distribution of the external potential. This obviously is not true but the influence of the nerve activation is negligible compared to the stimulus. The potential between the stimulating electrodes is of range 12 V, while the activation on the cellular membrane is of the range 140 mV. This simplification was already used by some authors [5].

The assumption on the passive properties of the model with respect to external potential allow us to describe the extracellular potential with Laplace equation

$$(3) \quad \nabla \cdot \gamma_e \nabla \Phi_e = 0$$

with Dirichlet boundary conditions on the electrodes $\partial\Omega_{E1}$ and $\partial\Omega_{E2}$ and natural Neuman condition for the external boundary $\partial\Omega_T$ of the model.

In the area of the nerve we model the active behavior of the cellular membrane. For the purpose of active behavior we will use a transient model in form of parabolic equation derived from (1) and (2):

$$(4) \quad \nabla \cdot \gamma_i \nabla \Phi_i = -\chi \left(C_m \frac{dV_m}{dt} + I_{ion} \right).$$

The left side of (4) defines the current flowing from the intracellular domain and the right hand side expresses the current passing the membrane. We will solve our model for two potentials Φ_i and Φ_e , so we must replace the membrane potential using $V_m = \Phi_i - \Phi_e$. Because the intracellular domain in the bidomain model is isolated with the extracellular domain from the other tissue, we can use the natural Neumann boundary condition for Φ_i on the boundary of the nerve Ω_N .

The second modification of the system used in this paper is the linearization of really nonlinear ionic currents component I_{ion} :

$$(5) \quad I_{ion}^* = \frac{V_m}{R_m}.$$

This assumption seriously simplifies the model and allows concentration on the bidomain model parameters. If we linearize the membrane model, the other parameters are better observable and easier to predict. The linear ionic channel model allows us to neglect the ODE solution, increasing the speed of calculations.

With the above assumptions the total system of equations with boundary and initial conditions can be expressed as:

$$(6) \quad \nabla \cdot \gamma_e \nabla \Phi_e = 0,$$

$$(7) \quad \nabla \cdot \gamma_i \nabla \Phi_i = -\chi \left(C_m \frac{d(\Phi_i - \Phi_e)}{dt} + \frac{\Phi_i - \Phi_e}{R_m} \right),$$

$$(8) \quad \frac{\partial \Phi_e}{\partial n} = 0 \text{ on } \Omega_T,$$

$$(9) \quad \Phi_e = \begin{cases} -u(t)/2 & \text{on } \partial\Omega_{E1} \\ +u(t)/2 & \text{on } \partial\Omega_{E2} \end{cases},$$

$$(10) \quad \frac{\partial \Phi_i}{\partial n} = 0 \text{ on } \Omega_N,$$

$$(11) \quad \Phi_i(t_0) = 0 \text{ where } t_0 < t < T.$$

Numerical implementation

The presented model is solved using the finite element method for the spatial derivatives and a backward Euler scheme for time derivative in (7).

(6) and (7) are solved iteratively. In the first step we solve (6) with boundary conditions adjusted to current value of stimulation signal. In the second step we solve (7) using the results of Φ_e from the previous step. We can express the time derivative with the Euler scheme and (7) becomes:

$$(12) \quad \nabla \cdot \gamma_i \nabla \Phi_i + \left(\frac{\chi C_m}{\Delta t} + \frac{\chi}{R_m} \right) \Phi_i = \frac{\chi C_m}{\Delta t} (\Phi_e + \Phi_i^{(t-1)} - \Phi_e^{(t-1)}) + \frac{\chi}{R_m} \Phi_e,$$

where $\Phi_i^{(t-1)}$ and $\Phi_e^{(t-1)}$ are the values taken from the previous time step.

The spatial derivative is discretized with standard finite element method. We solve (12) with bi-conjugate gradients method with Jacobi preconditioner.

Model parameters

The goal of this paper is to discuss influence of some parameters of the mathematical model to the results of simulation. The importance of this discussion follows from the fact, that many of the parameters can not be measured and by measurements of the others a really large variability is observed [10].

The intra- and extracellular conductivities γ_i and γ_e will be skipped here. We use physiological values taken from experiments. We will have a closer look at the rest of parameters and study their influence on the results:

- Membrane capacitance C_m is most often assumed to be in the range of 1 to 2 $\mu\text{F}/\text{cm}^2$.
- Membrane passive resistance R_m which describes the response of the membrane on the potential amplitude is usually in the range 1 – 50 $\text{k}\Omega\text{-cm}^2$.
- Surface to volume ratio χ which has a wide range for different tissues and depends on the tightness of axons packing. The surface to volume ratio χ is usually in the range of $6 \cdot 10^5$ to $12 \cdot 10^5$ 1/m.

Table 1. Parameters used in the bidomain model

| Parameter | Value range |
|--|---------------------------------------|
| Nerve intracellular conductivity (γ_i) | 0.18 S/m |
| Nerve extracellular conductivity (γ_e) | 0.33 S/m |
| Tissue extracellular conductivity (γ_e) | 0.33 S/m |
| Surface to volume ratio (χ) | $0.1 \cdot 10^5$ - $9 \cdot 10^5$ /m |
| Membrane capacitance (C_m) | 0.01-2 $\mu\text{F}/\text{cm}^2$ |
| Membrane Resistance (R_m) | 0.1-1000 $\text{k}\Omega\text{-cm}^2$ |
| Time step (Δt) | 1-100 μs |
| Pulse stimulation duration (T_s) | 0.5 ms |
| Stimulation amplitude (u) | 12 V |

The studied ranges of all parameters are summarized in Table 1. They are in general a bit broader than ranges reported in literature, but this allows us to test better the bidomain model response.

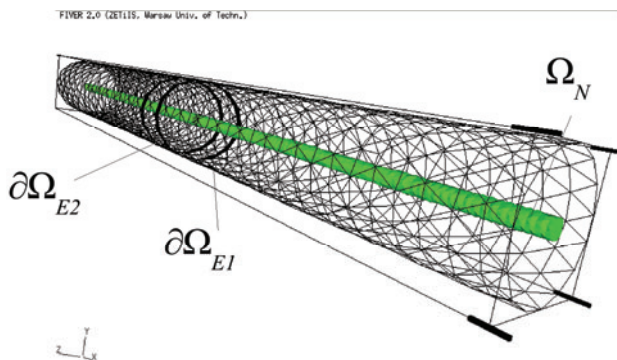


Fig. 3. Three dimensional cylindrical test model.

Test model

The tests were performed on a 3D cylindrical model (Fig. 3). The cylinder had 10 mm in length and external radius of 1 mm. It was discretized with tetrahedral elements

and mesh contained 13985 nodes and 78014 elements. The nerve is simulated with inner cylinder, 0.2 mm thick. The diameter of the nerve is the average of the anatomic human nerve diameters ranging from 0.01 to 3 mm.

Simulation results

In Fig. 4 we can see the isolines of the membrane potential and extracellular potential 250 μs after the stimulation was started. The extracellular potential results come from the solution of (6) and the membrane voltage from (7). The stimulus were two impulses of the bell shaped function with length 500 μs , one at $t_1=0$ s and the second at $t_2=500$ μs . The time step of the simulation was 10 μs .

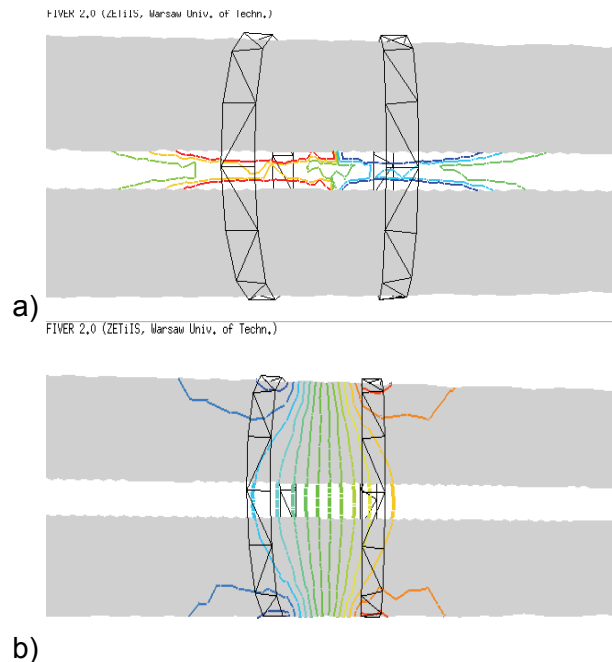


Fig. 4. Distribution in the vicinity of the stimulating electrodes of a) the membrane potential and b) the extracellular potential for $t = 250$ μs from the stimulation start.

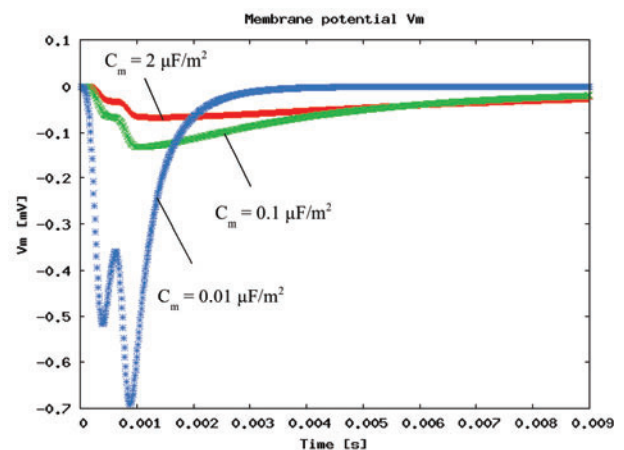


Fig. 5. Time course of the membrane potential in the point P for three membrane capacitances.

Influence of parameters

The influence of the membrane capacitance C_m is presented in Fig. 5. One can notice that the magnitude of the membrane potential increases with decrease of the capacitance. This can be interpreted that the increase of capacitance allows the intracellular potential to follow faster the extracellular potential. We can also notice that the membrane potential will have a great impact on the activation of the membrane.

Second studied parameter was the membrane resistance, presented in Fig. 6. This parameter changed the speed of refractory phase. The lower resistance was the faster membrane potential returned to the resting state. We can also notice that the resistance has much smaller impact on the amplitude of the membrane voltage than the capacitance.

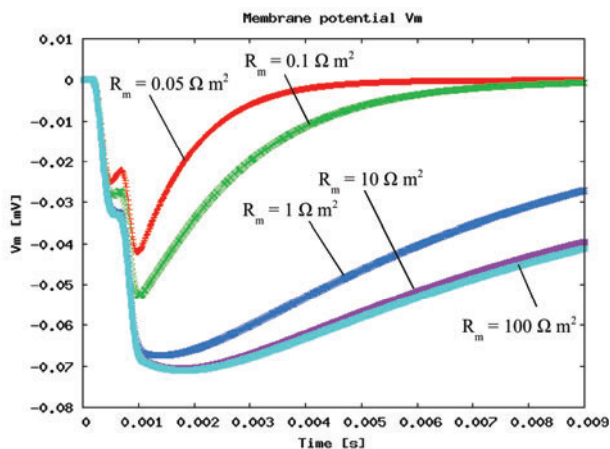


Fig. 6. Time course of the membrane potential in the point P for five membrane resistances.

The third studied parameter was the surface to volume ratio (see Fig. 7). We can notice that this parameter, similarly to the capacitance has a great influence on the membrane potential amplitude. If we increase this parameter we can observe the smaller amplitude of the membrane voltage.

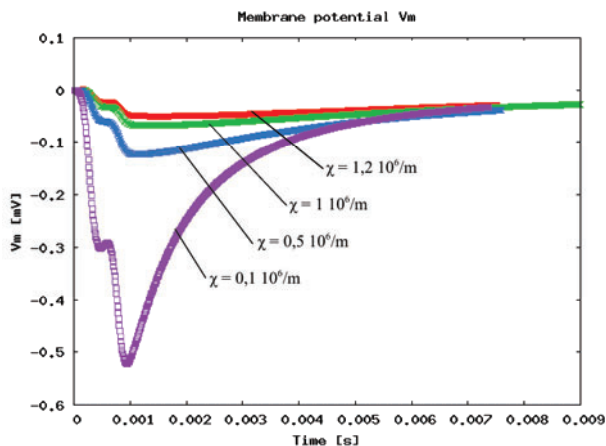


Fig. 7. Time course of the membrane potential in the point P for three surface to volume ratio results.

Conclusions

We can conclude that the presented parameters play a key role in the realistic and physiological simulation of the

neural tissue. Even small changes of the parameters have serious impact on the results. Also, the physiological interpretation of the parameters is very difficult. We would like to conclude that the parameters commonly used in the literature vary very often and are specially adjusted to obtain the results which can be compared to real experimental measurements like for example the speed of action potential propagation.

In our opinion the presented results can help to understand the passive bidomain model and its response to the external stimulus for various model parameters.

This research was supported by the Polish Ministry of Science and Higher Education under Grant No. N510 030 31/1379.

REFERENCES

- [1] Roth B.J., Wikswo J.P., The Magnetic Field of a Single Axon, *Biophysical Journal*, Vol. 48, 1985, 93-109
- [2] Rubinstein J.T., Axon Termination Conditions for Electrical Stimulation, *IEEE Transactions on Biomedical Engineering*, vol. 40, No. 7, 1993, 654-663
- [3] Zierhofer C.M., Analysis of a Linear Model for Electrical Stimulation of Axons – Critical Remarks on the “Activating Function Concept”, *IEEE Transactions on Biomedical Engineering*, Vol. 48, No. 2, 2001, 173-184
- [4] Tung L., A bi-domain model for describing ischemic myocardial D-C potentials, PhD thesis, MIT, Cambridge, MA, 1978
- [5] Malmivuo J., Plonsey R., *Bioelectromagnetism - Principles and Applications of Bioelectric and Biomagnetic Fields*, Oxford University Press, New York, 1995.
- [6] Schnabel V., Struijk J.J., Evaluation of the Cable Model for Electrical Stimulation of Unmyelinated Nerve Fibers, *IEEE Transactions on Biomedical Engineering*, vol. 48, No. 9, 2009, 1027-1033
- [7] Altman, K.W. Plonsey, R., Point source nerve bundle stimulation: effects of fiber diameter and depth on simulated excitation, *IEEE Transactions on Biomedical Engineering*, Vol. 37, No. 7, 1990, 688-698
- [8] Basser P.J., Roth B.J., New Currents in Electrical Stimulation of Excitable Tissues, *Annual Review of Biomedical Engineering*, Vol. 2, August 2000, 377-397
- [9] Szmurło R., Sawicki B., Starzyński J., Wincenciak S., A Comparison of Two Models of Electrodes for ECT Simulations, *IEEE Transactions on Magnetics*, vol. 42, no. 4, 2006, pp. 1395-1398,
- [10] Sunaga T. et al, Measurement of the electrical properties of human skin and the variation among subjects with certain skin conditions, *Physic in Medicine and Biology*, vol. 47, N11-N15, 2002

Authors: dr inż. Robert Szmurło, dr inż. Jacek Starzyński, prof. dr hab. inż. Stanisław Wincenciak, Politechnika Warszawska, Wydział Elektryczny, Instytut Elektrotechniki Teoretycznej i Systemów Informacyjno-Pomiarowych, ul. Koszykowa 75, 00-662 Warszawa, email: (szmurlor, jstar, win)@iem.pw.edu.pl

Evaluation of 2D Model of Vagus Nerve Stimulation with Harmonic Magnetic Field

Abstract. The aim for the research presented hereby is to determine whether it is feasible to evaluate the effect of Vagus Nerve Stimulation with harmonic magnetic field and conduct the initial optimization of the design and position of the excitation coil basing on the 2D model. The approach to implement efficient method for the task was made with use of complex vector magnetic potential \vec{A} in two dimensional domain. As the practice shows, the calculation burden limited to the 2D model gives a considerable benefit of short time analysis which is substantial in inverse problems.

Streszczenie. Celem badań opisanych w niniejszej pracy jest ustalenie, czy możliwe jest oszacowanie efektu stymulacji nerwu błędnego zewnętrznym polem magnetycznym oraz wykonanie wstępnej optymalizacji kształtu i położenia cewki wzbudzającej przy użyciu modelu 2D. Do realizacji celu zaimplementowano wydajną metodę analizy rozkładu pola elektromagnetycznego przy użyciu wektorowego zespolonego potencjału magnetycznego \vec{A} . Z przeprowadzonych badań wynika, że ograniczenie analizy do przestrzeni 2D pozwala na uzyskanie krótkich czasów rozwiązania co jest istotne przy wykonywaniu obliczeń wielu wariantów dla zadań odwrotnych. **(Ocena dwuwymiarowego modelu stymulacji nerwu błędnego harmonicznym polem magnetycznym)**

Keywords: Vagus Nerve Stimulation, Complex Vector Magnetic Potential, 2D Model

Słowa kluczowe: stymulacja nerwu błędnego, wektorowy zespolony potencjał magnetyczny, model dwuwymiarowy

Introduction

Vagus Nerve Stimulation (VNS) is a nonpharmacological method used in epilepsy treatment where the nerve is being stimulated by impulses introduced from an external electric field. The stimulator which is responsible for impulse application has to be implanted to the patient during a surgical procedure. Because the device comprises of two elements: the electrodes and the pulse generator connected together by wire, the surgical procedure is very invasive (see figure 1). Moreover the patient needs to undergo additional surgery every three up to eight years to change the battery. The alternative way to achieve a similar result is by stimulating the nerve by magnetic field indirectly. In such approach the excitation coil generating a time-varying magnetic field is placed near the patient's neck as depicted in figure 2 resulting in eddy currents induction in the nerve. That way of treatment eliminates the need of surgery and allows to utilize the same device for many patients.

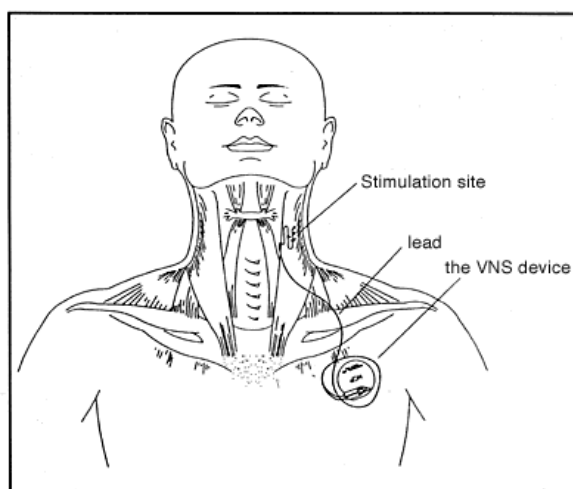


Figure 1. The way of implanting a VNS stimulator into human body. Figure taken from the website of The Royal Children's Hospital in Melbourne.

That idea though has been negated lately by some researchers who has come to the two main counterpoints. First of all, generating an electromagnetic field that is strong enough to cause stimulation effect is not sensibly feasible with currently available technology. But even having a sufficient field source will not solve the stimulation's selectivity. That second problem concerns other parts of human body in particular the other parts of nervous system that are being exposed to electromagnetic field and are subject to side effect stimulation. On the other hand as the Medical News Today announced on January 2006 that there has been a recent research to develop a wireless device which must only be implanted around the nerve and is supplied from outside the body by radio waves (Radio Frequency-powered Neural Stimulator - RFNS). That gives another idea of implementing a kind of secondary winding around the nerve and use the external magnetic field to induce secondary side stimulating current in such transformer.

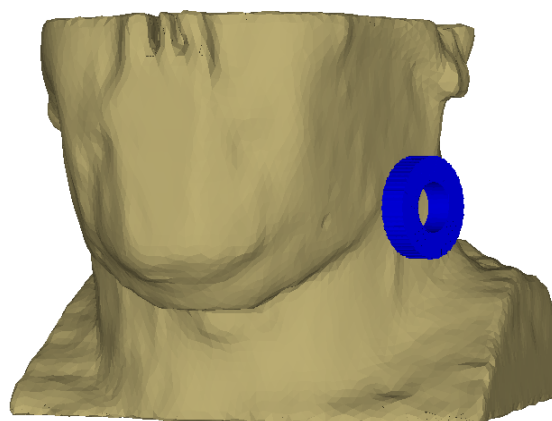


Figure 2. A 3D visualization of the concept of vagus nerve stimulation with an external magnetic field.

A 3D model has been already developed for vagus nerve and brain stimulation analysis by Sawicki and o. [1] allowing to estimate the phenomenon thoroughly but resulting in a large scale computational problem. Moreover, the model analyses the electromagnetic field inside the body model with omitting the stimulation source itself. That approach is justified as the induced currents are greatly smaller than exciting ones, thus they have no influence on the source. Using such model for optimization purposes is time consuming and enlarges the problem when more than one stimulating coil is used. In that case the model should be reworked to allow analysis of the coils interaction. That again enforces the need of modelling the body surroundings i.e. the coils and airspace what would result in a very complex computational problem.

Being aware of the constraints that draws from the 3D model, the authors decided to undertake the research towards finding the most relevant 2D model for VNS analysis. In general such model allows considering more aspects with less computation burden comparing to a three dimensional analysis.

The substantial dilemma in selecting the most adequate 2D model for nerve stimulation effect estimation is defining the factor that is responsible for the effect. Is it the magnitude of the induced field or it's intensity along the nerve is important for obtaining the best stimulation results? Answering to that question is subject to further research and thus it will imply the selection of the model. If the induced field magnitude is to be substantial, the axial symmetrical model with respect to the stimulation coil may be applied what significantly simplifies the calculations. If on the other hand the field distribution within the nerve that causes the potential difference is important, a 2D analysis in $x0y$ or $y0z$ plane is to be applied (see figure 3). Another question arises whether the potential difference has better effects when occurs along or across the nerve.

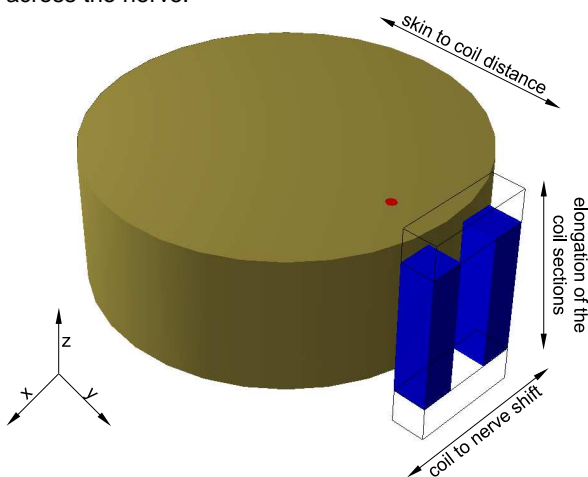


Figure 3. Geometrical primitives sketch in 3D for visualizing the concepts of VNS analysis in 2D domain together with potential degrees of freedom for optimization. The red cylinder states for the vagus nerve, which is located inside the larger primitive, representing the neck.

The researchers are generally inclining towards electromagnetic field analysis along the nerve, e.g. [2] and [3], thus such an approach was taken to begin with. However while taking such approach to the case, they are still aware that "despite accurate knowledge of the applied fields, many of the basic mechanisms underlying activation by these induced fields are still unclear" [3].

Another concern regarding the best stimulation effects is the stimulation source design. As it has been depicted in figure 3 the potential optimization factors are the coil to skin distance, elongation of the coil sections resulting in it's non-circular shape and the coil position in respect of the nerve fibre. The last factor arises from the further presented results which show that the amplitude of the induced eddy-currents is shifted geometrically aside of the coil windings.

The results reached in the process of optimization with use of the 2D model will be used as a start point for further analysis in more complex and computation demanding three dimensional domain.

Mathematical model

The simulations were made in two dimensional domain in order to speed up the analysis, while for the electromagnetic field description the complex vector magnetic potential \vec{A} was used. The two types of coordinates were used: the Cartesian $x0y$ and the polar $r0z$ for the axial symmetrical models. The mathematical description in Cartesian coordinates is given as follows:

$$(1) \quad \text{rot} \left(\frac{1}{\mu} \text{rot} \vec{A} \right) + j\omega\sigma\vec{A} = \begin{cases} 0 \\ |\vec{J}_s| \\ -\sigma|\text{grad}V|. \end{cases}$$

By such description one may introduce the excitation as the current density value or the gradient of the potential in normal direction for a particular subdomain. Although defining the current density value implies that the subdomain is considered as the set of infinitesimally thin conductors, i.e. the subdomain has no conductance in $x0y$ plane and $\sigma = 0$. Another possibility of introducing the excitation force to the model is by defining the total current value for a given subdomain. This requires an additional equation what leads to the following overall equations system:

$$(2) \quad \begin{cases} \text{rot} \left(\frac{1}{\mu} \text{rot} \vec{A} \right) + j\omega\sigma\vec{A} + \sigma\text{grad}V = 0 \\ \int_{\Omega} -\sigma \left(j\omega\vec{A} + \text{grad}V \right) d\Omega = \underline{I}, \end{cases}$$

where $\text{grad}V$ is not known.

Implementation and results

The algorithm has been implemented in C++ with use of the Diffpack library [7]. The application allows to introduce the excitation force value into the model by defining the current density, gradient of electric potential in normal direction or total current value in a given subdomain.

The 2D model for the first series of analysis was taken as the cross section along the $y0z$ plane of the model shown in figure 3. However it was assumed that the nerve is being stimulated with a toroidal coil of internal and external diameters of 2 and 5 cm respectively. The coil's windings had a square cross-section as presented in figure 4. The width of the subdomain modeling the nerve was 3 mm [4], which was located 20 mm under the skin surface [4, 5], the air gap between the coil and the body equals 5 mm. The conductivity of the nerve fibre was assumed as variable in the function of frequency as shown in figure 5, while the conductivity of the surrounding tissue was taken as constant and equal 0.33 S/m.

The time function of applied excitation as shown in figure 6 was modeled on the ones proposed in [5] and [6] for brain stimulation. The ratio of ascending to descending time

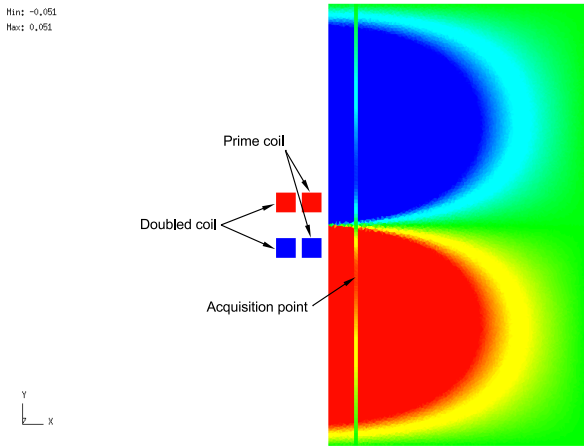


Figure 4. A 2D model of the nerve and excitation coils together with sample current density field.

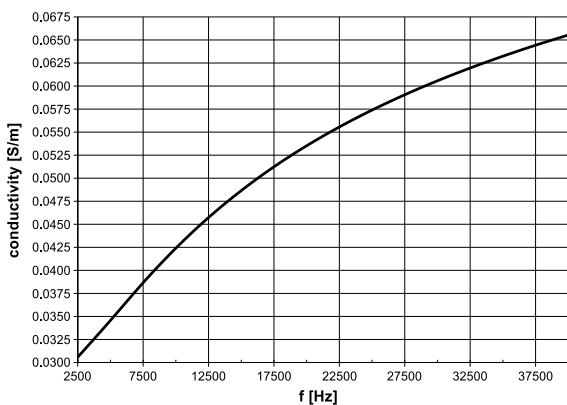


Figure 5. The nerve conductivity in function of frequency.

was about 1:6 with a total period of 0.4 ms. The function was transformed with FFT algorithm into 16 harmonics, which give the reconstructed excitation function of negligibly small MSE error of the order of $10^{-14}\%$.

In order to make a comparison between force introduction methods, the two example analysis with the same model were made. In the first simulation, the total current value in the coil subdomains was defined while in the other the current density value. The model was comprising of 93005 finite elements mesh nodes and 184857 elements. A total current value definition resulted in very long times of analysis as depicted in figure 7 with black points. That was caused by worse system conditioning arising from an additional equation as stated in formula 2. Several solvers and preconditioners were tested for solving the system and the best results were obtained with use of CGS solver coupled with SSOR preconditioner. Eventually the system could be solved for only 12 out of 16 harmonics i.e. up to $f = 30$ kHz. In the other analysis the current density value was chosen as the excitation force which allowed to obtain the system's convergence for every 16 harmonics. For such problem, the BiCGStab solver together with the RILU preconditioner gave the shortest solution time of 97 seconds average.

By defining the total current value flowing through the coil the assumption is made that the coil is monolithic. This implies that the eddy currents are being calculated within the winding. However the results obtained from the two simulations gave the same resultant field distribution within the

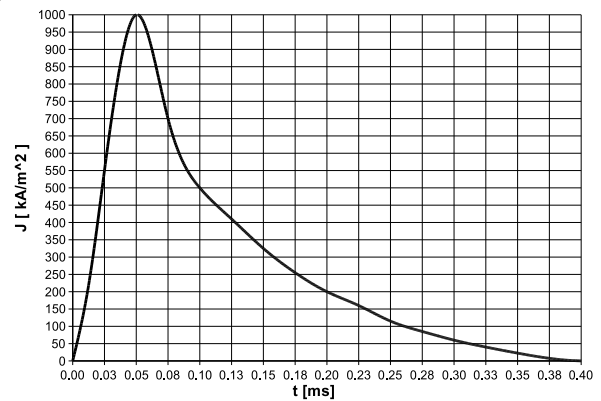


Figure 6. The waveform of the excitation function.

nerve. That allows to neglect the eddy currents phenomenon within the coil and make the calculations by defining the current density in order to obtain the results in shorter time.

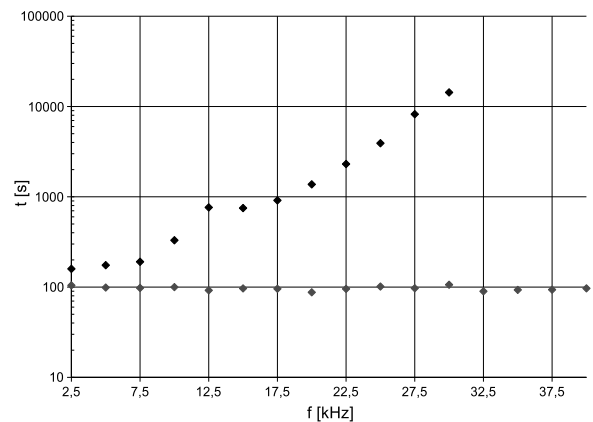


Figure 7. The system's convergence times for different ways of introducing the excitation forces: total current value defined in coil subdomains – black points and current density value – gray points.

The results were assembled from particular harmonics analysis to obtain the resultant electromagnetic field distribution within the model. The module of the complex current density distribution along the nerve's middle section for the basic harmonic of $f = 2.5$ kHz is shown in figure 8. It can be observed from the figures 4 and 8 that the amplitude of the induced current is shifted geometrically with respect to the excitation coil. That phenomenon prompts that either the air coil should be shifted aside of the nerve or the ferromagnetic core should be applied to the coil in order to obtain the best stimulation effect. The resultant time function of current density value measured in the selected acquisition point is depicted in figure 9 with the gray line.

The influence of the coil proximity on stimulation effect was estimated by moving the coil by 5 mm towards the skin surface. As the result, the amplitude of the induced current density has increased, while the response function nature remained the same (see figure 9).

Having the same coil to skin distance value of 5 mm another experiment was made with a twin coil. The other coil was placed next to the existing one (figure 4) with the distance of 5 mm between them. For the first attempt, the amplitude of the current density value defined in the coil sections was set to 0.5 A/mm^2 , i.e. half a value taken in the previous simulations with a single coil. Once again the nature of the response function had no change, however it's amplitude was

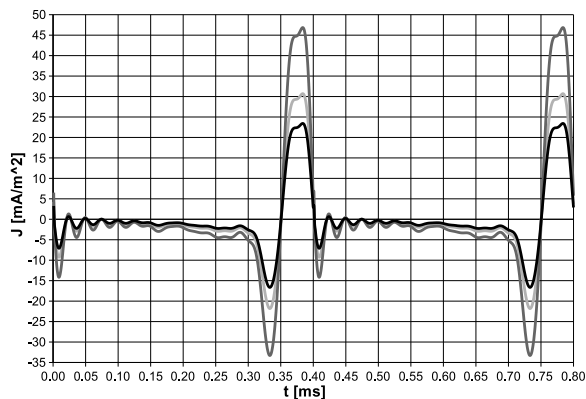


Figure 10. The comparison of induced current density functions for twin coil with excitation function amplitude of 0.5 A/mm^2 – black line, twin coil with doubled amplitude – gray and single coil with amplitude of 1 A/mm^2 – light gray.

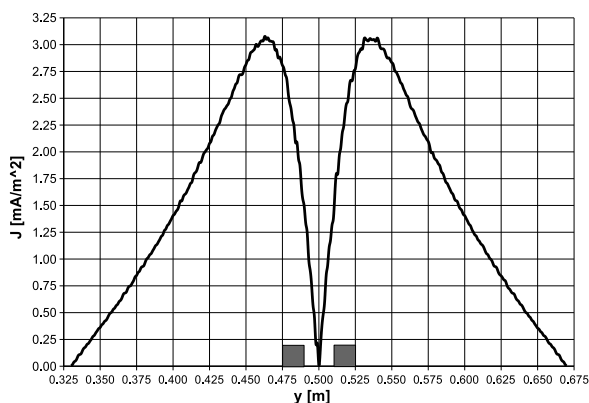


Figure 8. The module of the complex current density distribution along the nerve's middle section. The coil position is marked with gray squares for reference.

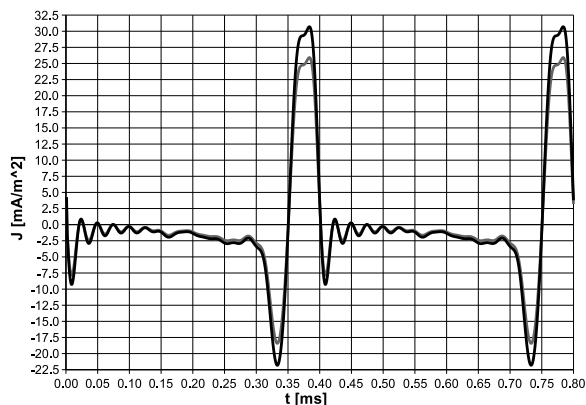


Figure 9. The resultant time functions of induced current density measured at selected acquisition point for two different distances from the coil to the skin surface: 5 mm – black line and 10 mm – gray line.

lower comparing to single coil, 1 A/mm^2 case roughly by only 8 mA/m^2 . In order to estimate the amplification effect in a twin coil configuration, the excitation current density value was set to 1 A/mm^2 . The simulation has shown that the amplitude of the response function was over twice as high as in the case where the excitation amplitude was set to 0.5 A/mm^2 . All the results discussed above are presented in figure 10 for comparison. The results suggest that the stimulation effect can be efficiently strengthened with use of doubled stimulating coil. That is of course the initial conclusion which needs to be further examined in the optimization process.

Conclusion

The obtained results allow to undertake further research towards the optimal design of the stimulator. It seems to be possible to use the 2D model at least to estimate the peak value of the stimulus.

The figure 1 is taken from the website of The Royal Children's Hospital in Melbourne [11].

This research was supported by the Polish Ministry of Science and Higher Education under Grant No. N510 030 31/1379.

REFERENCES

- [1] B. Sawicki, P. Płonecki, J. Starzyński, S. Wincenciak, *Scalar Potential Applied to Magnetic Stimulation Modelling*. Przegląd Elektrotechniczny, R. 83, Nr. 7-8/2007.
- [2] P.J. Maccabee, V.E. Amassian, L.P. Eberle, R.Q. Cracco, *Magnetic Coil Stimulation of Straight and Bent Amphibian and Mammalian Peripheral Nerve In Vitro: Locus of Excitation*. Journal of Physiology 460, pp. 201-219, 1993.
- [3] S.S. Nagarajan, D.M. Durand, *A Generalized Cable Equation for Magnetic Stimulation of Axons*. IEEE Transactions on Biomedical Engineering, Vol. 43, No. 3, March 1996.
- [4] R. Szmurło, P. Płonecki, B. Sawicki, J. Starzyński, S. Wincenciak, A. Rysz, *Elektryczna stymulacja nerwu błędnego – wstępna analiza numeryczna*. PTZE Workshop, Elektromagnetyczne Techniki w Ochronie Zdrowia, Łódź, 2006.
- [5] A. Barchanski, E. Gjonaj, H. De Gersem, T. Weiland, *Transient Calculation of the Induced Currents Inside the Brain During Magnetic Stimulation*. 12th International IGTE Symposium Proceedings, Graz, 2006.
- [6] Y. Hu, Y.M. Feng, M.S. Wang, W.W. Lu, *The Effect of Magnetic Stimulation on Potential Rhythm of Cerebral Cortex*. 20th Annual International Conference of the IEEE Engineering in Medicine and Biology Society Proceedings, Vol. 20, No 6, 1998.
- [7] H.P. Langtangen, *Computational Partial Differential Equations. Numerical Methods and Diffpack Programming*. Springer Verlag, Berlin-New York, 1999.
- [8] Website of The Royal Children's Hospital in Melbourne: <http://www.rch.org.au/>

Autorzy: mgr inż. Michał Chojnowski, dr inż. Jacek Korytkowski, Politechnika Warszawska, Wydział Elektryczny, Instytut Elektrotechniki Teoretycznej i Systemów, Informacyjno-Pomiarowych, ul. Koszykowa 75, 00-662 Warszawa, email: M.Chojnowski@iem.pw.edu.pl

PRZEGLĄD ELEKTROTECHNICZNY KONFERENCJE

Redaktor Naczelny: prof. dr hab. inż. Sławomir Tumański (e-mail: tusla@iem.pw.edu.pl)
Redakcja: e-mail: red.pe@iem.pw.edu.pl; red.pe@sigma-not.pl, Internet: www.red.pe.org.pl


RADA PROGRAMOWA

| | |
|---|---|
| Prof. dr hab. inż. Roman Barlik – PW | Prof. dr hab. inż. Jan Maksymiuk – PW |
| Prof. dr hab. inż. Jerzy Barzykowski – WAT | Prof. dr hab. inż. czł. PAN Jacek Marecki – PG |
| Prof. Janusz Białek – Univ. of Edinburgh, Wlk. Brytania | Prof. dr hab. inż. Teresa Orłowska-Kowalska – PWR |
| Prof. dr hab. inż. Leszek Czarnecki – Louisiana St. Univ. USA | Prof. dr hab. inż. Stanisław Osowski – PW |
| Prof. dr hab. inż. czł. PAN Mirosław Dąbrowski – PP | Prof. dr hab. inż. Maciej Pawlik – PŁ |
| Prof. dr hab. inż. Władysław Dybczyński – PBiał | Prof. dr inż. Andrzej Piłatowicz – Inst. Energetyki |
| Prof. dr hab. inż. Zdobysław Flisowski – PW | Prof. dr hab. inż. Stanisław Piróg – AGH |
| Prof. dr hab. inż. czł. PAN Tadeusz Kaczorek – PW | Prof. Paweł Ripka – Czech Technical University in Prague |
| Prof. dr hab. inż. Marian Kaźmierkowski (przewodniczący) - PW | Prof. dr inż. Ryszard Sikora – PSzcz |
| Prof. dr hab. inż. Krzysztof Kluszczyński – PŚI | Prof. Adam Skorek – Univ. du Québec a Trois-Rivieres, Kanada |
| Prof. dr hab. inż. Józef Korbicz – Uniwersytet Zielonogórski | Prof. Jan Sykulski – University of Southampton, Wlk. Brytania |
| Prof. dr hab. inż. Andrzej Krawczyk – CIOP | Prof. dr hab. inż. czł. PAN Tadeusz Śliwiński – Inst. Elektr. |
| Dr hab. Krzysztof Kurek – PŚI | Prof. dr hab. inż. czł. PAN i PAU Ryszard Tadeusiewicz – AGH |
| Prof. dr hab. inż. Jan Machowski – PW | Prof. dr hab. inż. Andrzej Wiszniewski – PWR |

INFORMACJE DLA AUTORÓW

Przeгляд Elektrotechniczny drukuje oryginalne prace naukowe, prace przeglądowe oraz recenzje książek, sprawozdania z konferencji z dziedziny szeroko rozumianej elektrotechniki. Wszystkie prace naukowe są recenzowane. Przyjmowane są prace w języku polskim lub angielskim. Prace powinny być dostarczone w postaci sformatowanej – wzór formatu zamieszczony jest na stronie internetowej (plik wzor.doc). Prace (artykuł oraz streszczenia polskie i angielskie, tytuł po angielsku, słowa kluczowe polskie i angielskie) powinny być nadsyłane na adres redakcji za pośrednictwem poczty elektronicznej (jedynie w przypadku dużych plików artykuł może być zgłaszany pocztą w formie CD).. Zgłoszenie powinno zawierać plik tekstu w formacie *.doc ze wstawionymi rysunkami. Redakcja nie przepisuje tekstów i nie wykonuje rysunków. Oprócz pliku *.doc zalecane jest, żeby autorzy dostarczali pliki źródłowe rysunków (najlepiej w formacie *.eps lub *.tif lub innym powszechnie używanym standardzie). Jeżeli nie jest to możliwe, w wyjątkowych przypadkach rysunek może być dostarczony w postaci wydrukowanej na arkuszu A4. Standardową szerokością rysunku jest szerokość kolumny 8 cm. Opisy na rysunku zmniejszonym do tej szerokości nie powinny być niższe niż 2 mm. Do artykułu powinien być dołączony adres do korespondencji i adres poczty elektronicznej autorów.

Autorzy proszeni są o uwzględnienie formuły, że Przeгляд adresowany jest do szerokiego środowiska inżynierów. Dlatego jeżeli artykuł dotyczy szczegółowego zagadnienia, powinien być poprzedzony wstępem omawiającym ideę metody i najnowsze osiągnięcia związane z tematem pracy. Bibliografia powinna uwzględniać aktualny stan wiedzy (z przedstawieniem najważniejszych pozycji literatury zagranicznej). Zalecane jest uwzględnienie w spisie literatury prac drukowanych w Przeглядzie Elektrotechnicznym. Zapraszamy do publikowania młodych autorów (np. autoreferaty prac dyplomowych lub doktorskich) oraz autorów z przemysłu (np. opisy wdrożeń lub wynalazków). Autorzy gwarantują, że zarówno treść pracy, jak i rysunki są ich oryginalną własnością. Autorzy zgłaszając artykuł przekazują Redakcji prawa do jego publikacji w formie drukowanej i w Internecie. Do zgłaszanej pracy powinien być dołączony formularz umowy zamieszczony na stronie internetowej (plik. umowa.doc).

| | |
|--|--|
| <p>WYDAWNICTWO CZASOPISM I KSIĄZEK TECHNICZNYCH</p>  <p>SIGMA-NOT Spółka z o.o.</p> <p>00-950 Warszawa skrytka pocztowa 1004 ul. Ratuszowa 11 www.sigma-not.pl</p> | <p>Internet: http://www.red.pe.org.pl lub http://www.sigma-not.pl E-mail: red.pe@sigma-not.pl</p> |
| | <p>Adres Redakcji: 00-950 Warszawa, Skrytka poczt. 1004, ul. Ratuszowa 11 Tel/fax: 22 818 9510, 0 693 428 056</p> |
| | <p>Prenumerata: e-mail: kolportaz@sigma-not.pl, tel./fax: 840-35-89 Wpłata na prenumeratę: Wydawnictwo SIGMA-NOT Sp. z o.o. Zakład Kolportażu, 00-950 Warszawa, skr. poczt. 1004 Konto: BPH PBK S.A. Oddział w Warszawie, pl. Gen. Hallera 6 Nr 53 1060 0076 0000 4282 1000 0012</p> |
| | <p>Możliwe jest też zamówienie prenumeraty za pośrednictwem naszego portalu www.sigma-not.pl</p> |
| | <p>Dział Reklamy i Marketingu, ul. Mazowiecka 12, 00-950 Warszawa skrytka pocztowa 1004, tel. 827-43-66, fax 826-80-16, E-mail: reklama@sigma-not.pl Redakcja nie odpowiada za treść ogłoszeń</p> |
| | <p>Egzemplarze archiwalne można nabyć w punkcie sprzedaży SIGMA-NOT 00-950 Warszawa, ul. Mazowiecka 12, tel. 826-80-16</p> |
| <p>Artykuły w formacie PDF poczynając od 2004 roku dostępne na naszym portalu www.sigma-not.pl</p> | |
| <p>Skład: Redakcja</p> | <p>Druk: Drukarnia SIGMA-NOT</p> |
| <p>nakład 150 egz. PL ISSN 1731-6103</p> | |

Professor Tadeusz Cholewicki (1907-1988)



Professor Tadeusz Cholewicki was born on October 23rd 1907 in Warsaw. After finishing the grammar school he got a humanistic education. In 1925 Tadeusz Cholewicki entered the Mathematical Department of Warsaw University and after graduating it in 1930 and his military service, he became a student of the Electrical Department at Warsaw Technical University. Tadeusz Cholewicki was qualified as an electrical engineer in 1935. In years 1935-1938 he worked at the Railway Electrification Company in Warsaw. In 1938-1944 Tadeusz Cholewicki as an engineer took part in a traction line construction of municipal power station. At the same time he started his work at the 2nd degree Technical School as a technical assistant. After the war he worked at the Operating team of Economical Committee of the Cabinet in Częstochowa then in Slask. In 1949 Tadeusz Cholewicki began to work at Warsaw Technical University, firstly, as a technical assistant, then as a tutor and later on as an assistant professor. The Professor worked at the Theoretical Electrotechnics Department of the Polish Academy of Sciences since 1952. In 1958 he went to France for three months. In 1954-1956 he was the dean of the Electrical Department and the Secretary of the Senate of Warsaw Technical University. In 1954 he became the head of the Theoretical Electrotechnics Department of this university, in 1962 an associate professor and a full professor in 1971. The General Meeting of members of the Polish Academy of Sciences elected him an associate member and then in 1980 a full member to the Polish Academy of Sciences. In 1966-1968 Professor was the member of the Society Council of Science Generalization of the Polish

Academy of Sciences and vice president of the Electrotechnical Committee; in 1969-1971 Tadeusz Cholewicki became the president of this Committee. Since 1967 the Professor was the editor-in-chief of the "Theoretical Electrotechnic Monographs" of the IV Department of the Polish Academy of Sciences and the member of Editorial Board of quarterly "Electrotechnic Papers". Professor was the charter member of the Polish Society of Theoretical and Applied Electrotechnics and vice-president of General Managerial Board of this society for a long time. Since 1959 Tadeusz Cholewicki became the member of Societe Francaise des Electriciens in Paris-Malqkoff. He was the member of many scientific councils, various institutes and research centers.

Professor's creative potential is very rich and extensive. It includes 85 entries, 67 papers published in the most important scientific periodicals in Poland and abroad, 11 monographs and school-books. Tadeusz Cholewicki was the first to apply the theory of matrices to electrotechnics. In 1952 his paper "The application of matrices in electrotechnics", showing the deep knowledge of this subject was published. Later on some of original papers dealing with this problem were published. In his monography "The matrix analysis of the linear networks", issued in 1958, Professor Tadeusz Cholewicki summarizes the applications of matrix algebra to the linear network analysis. This paper is cited by many Polish and foreign authors. In 1959 Professor Tadeusz Cholewicki's monography "The computation methods of electric circuit", presenting a modern and original approach to the subject was published. Later on the Professor was engaged in matrix analysis applications to electric circuit. In the monography "The analysis of electric circuit" published in 1962, Professor was the first who suggested the method of linear circuit analysis in the transient state based on Sylvester's formula. This monography was awarded the prize of the IV Department of the Polish Academy of Sciences, besides the first prize of the Minister of Higher Education for the best school-book and the second prize of the Polish Association of Electricians in 1969. Furthermore, Professor Tadeusz Cholewicki elaborated the theory of non-linear systems and in this field he was very creative. In 1960s Tadeusz Cholewicki published the papers dealing with oscillations and periodical Solutions of non-linear circuits and the ones described by Duffing's equation. All works of Professor Tadeusz Cholewicki, published in 1966-1967 are about the new elements of electric circuits (such as NIC, NIV, gyrators). In these papers the analysis of properties of complex transformers occurs. The subsequent papers deal with long-lines and heterogeneous ladder systems.

Tadeusz Cholewicki published his works mainly in the Bulletin of the Polish Academy of Sciences and in "Electrotechnics Archives". In 1974 he published the monography "Electrical long lines and heterogeneous ladder systems" which seems to be the summary of all his works in this field. In 1982 the "Analysis of electrical heterogeneous systems by the differential equations" was issued. The last years of his life Professor Tadeusz Cholewicki was engaged into analysis of chain four-terminal passive and active networks and heterogeneous ladder system. All Professor's papers and works are fundamental and comprehensive.

Professor Tadeusz Cholewicki was a brilliant teacher. His lectures of theoretical electrotechnics were highly appraised by students. Professor received a lot of awards. To appreciate his scientific and educational achievements he was awarded by the medal to Meritorious man of Warsaw Technical University (1978) and note to Honourable Book for Meritorious men of Warsaw Technical University (1980) and Gold Cross of Merit and Commandor's Cross, medal of the Committee of National Education and the title of Meritorious Teacher. Now we see that Professor Tadeusz Cholewicki a talented scientist and researcher worked hard all his life, possessed a deep sense of duty and responsibility for the further scientific development and progress of Theoretical Electrotechnics in Poland and abroad. His contribution to research is immense. Professor's friendly attitude to people attracted everybody. Professor had a lot of students, assistants who became his successors.